

IV

Applied Battery Research for Transportation

Introduction

Core and Enabling Support Facilities

Critical Barrier Focus —Voltage Fade in Li-ion Battery Cathode Materials

High Energy Cell R&D: “Improvements in Cell Chemistry, Composition, and Processing”

Process Development and Manufacturing R&D



IV. Applied Battery Research for Transportation

IV.A Introduction

The widespread adoption of electric vehicles is considered crucial to reaching both the environmental and energy security goals of the United States of America. Reaching the fleet electrification levels necessary could also enable a strong U.S.-based battery manufacturing sector. Absolutely critical to the invention → innovation → product process that has to take place, is the translation of materials discovery and device innovation in the R&D community into commercially viable products and processes. Such applied research activities are inherently high risk; coupling the frontier, cutting edge nature of materials discovery with the performance and cost needs of a market-changing new product.

A significant portfolio of VTO Energy Storage projects that meet these criteria are grouped together in the Applied Battery Research (ABR) for transportation program. The ABR program is and will continue to be comprised of high risk projects investigating issues and advances at the cell level. Success in ABR projects means electric drive vehicle energy storage products that can be realized (manufactured) and that lead to cost reduction; thus, fulfilling the energy storage component of EERE's EV Everywhere Initiative. Such improvements will be accomplished through novel materials, particularly the active components of the cell, but also through innovative cell design and electrode composition. As well, materials production, electrode processing, and cell manufacture are also important thrusts within ABR. Completing the suite of project modalities is the Critical Barrier Focus. Applied research programs always contain and can usually be defined by a major barrier, a set of structurally and functionally interrelated problems, that simultaneously appears intractable and that absolutely require mitigation or adaptation in order to achieve a particular technical target. Solutions, if possible, require understanding across the dimensions of the problem, and such understanding requires in-depth science practiced by a multi-disciplinary team—and a lot of data. This is the nature of a deep-dive investigation.

The R&D projects in the 2014 ABR portfolio are divided into four distinct but complementary groups:

- Core and Enabling Support Facilities.
- Critical Barrier Focus—Voltage Fade in Li-ion Battery Cathode Materials.
- High Energy Cell R&D: “Improvements in Cell Chemistry, Composition, and Processing”.
- Process Development and Manufacturing R&D.

Core and Enabling Support Facilities: Across several of the national laboratories, infrastructure has been created and resources grouped into facilities that support complex activities critical to applied battery research. This provides the U.S. energy storage research community a powerful tool to carry out scientific investigations using, for example, state-of-the-art fabricated Li-ion battery electrodes, commercially viable and high purity electrolyte additives, chemical and electrochemical analysis of cycled battery components, and component-level abuse response analysis. The services and products of these facilities are fully funded through the ABR program and are available hierarchically, with VTO funded projects first, followed by other DOE funded projects (BES, ARPA-E), then other government agencies down the line through to U.S. small businesses. The majority of these facilities came on line with Recovery Act funding in 2009 and have now a significant track record in supporting applied research. The anchor facility in ABR's Support Facilities is the Cell Analysis, Modeling, and Prototyping Facility (CAMP) located primarily at Argonne National Laboratory. The CAMP Facility is more than an arrangement of equipment, it is an integrated team effort designed to support the production of prototype electrodes and cells, and includes activities in materials validation (benchmarking), modeling, and diagnostics.

Critical Barrier Focus—Voltage Fade in Li-ion Battery Cathode Materials: Within the ABR program the first team-based, deep-dive project has been completed. As a coordinated research thrust, the voltage project has accomplished all it can: a significant body of high impact literature has been—and continues to be contributed to the body of scientific knowledge and technology innovation; methods, protocols, and data analysis tools have been developed and are available to the global technical community interested in this barrier; and rational, sophisticated hypotheses surrounding this phenomena have been proposed based on sound, reproducible experimental data. This initiating team-based deep-dive project was conceived as a possible route to ‘solving’ voltage fade, but no solution appears possible. That is because voltage fade is not a solitary characteristic of a material set—a problem to be ‘solved’—it is an intrinsic manifestation of the complex crystalline structure/electrochemical activity that defines these materials. The short answer is to realize the promise of these Li-, Mn-rich cathode materials, voltage fade cannot be designed out, only engineered around.

High Capacity Cell R&D: “Improvements in Cell Chemistry, Composition, and Processing”: Six financial assistance projects (grants) began this fiscal year and will each run until at least the beginning of FY2016. Each of the six teams proposed to address, at the cell level, advanced materials solutions that could reach the EV Everywhere Grand Challenge energy storage-specific goals: cutting battery costs to \$125/kWh by 2022. Relative to today's Li-ion battery cell chemistries, similar material themes are common:

- Active cathode materials are all either variations on the Li-, Mn-rich cathode materials discussed above or high nickel content NMCs.
- Active anode materials all contain a significant content of alloy-forming metals or semi-metals with silicon being the group ‘favorite’.
- Electrolyte formulations proposed all comprise co-solvents and additives under development to stabilize the anode SEI and to, potentially, enable higher voltage operation.

The proposed targets are extremely aggressive; these projects are not product development exercises. Significant challenges exist for energy content, cell lifetime, and materials specification across all six projects.

Process Development and Manufacturing R&D: The second phase of ABR, initiated in FY2012, contained the first process-R&D projects. The work in 2013 continued these initial projects, and the FY2014 effort builds on the experience and knowledge gained in the first two years. Critical to establishing a U.S.-based battery manufacturing industry is the development of process-oriented intellectual property. The reports in this section detail work that not only has led to IP creation on its own, the research teams have also leveraged the EERE-funded work to partner with American companies developing their own proprietary processing technologies. Over sixteen U.S. companies have collaborated within and among these five projects, ranging from multinational corporations to start-up small businesses. As new processing resources are developed, they are also being made available to the U.S. energy storage research community in line with the Support Facilities described above.

The remainder of this section provides technical highlights and progress on the Applied Battery Research program for FY 2014. Each report was prepared to capture the purpose, approach, and major gains and setbacks of the project (or project component) under review. For more technical detail, actual experimental methods, and data analytics please see the referenced scientific publications or contact the appropriate project lead.

IV.B Core and Enabling Support Facilities

IV.B.1 Cell Analysis, Modeling, and Prototyping (CAMP) Facility Production and Research Activities (ANL)

Andrew N. Jansen

Argonne National Laboratory

Collaborators:

Daniel P. Abraham, Argonne National Laboratory
Dennis W. Dees, Argonne National Laboratory
Wenquan Lu, Argonne National Laboratory
Bryant J. Polzin, Argonne National Laboratory
Stephen E. Trask, Argonne National Laboratory
Martin Bettge, Argonne National Laboratory
Yan Li, Argonne National Laboratory
Qingliu Wu, Argonne National Laboratory
Ye Zhu, Argonne National Laboratory
Organizations listed in this section

Start Date: October 1, 2012

End Date: September 30, 2014

Objectives

- The objective of this core-funded effort is to design, fabricate, and characterize high-quality prototype cells that are based on the latest discoveries involving high energy anode and cathode battery materials. Using this multi-disciplined facility, analytical diagnostic results can be correlated with the electrochemical performance of advanced lithium-ion battery technologies for plugin electric vehicle (PEV) applications.
 - Link experimental efforts through electrochemical modeling studies.
 - Identify performance limitations and aging mechanisms.

Technical Barriers

The primary technical barrier is the development of a high energy density battery for PEV applications that is safe, cost-effective, and has long cycle life.

- Interpret complex cell electrochemical phenomena.
- Identification of cell degradation mechanisms for a variety of novel high energy materials.

Technical Targets

- Fabricate prototype pouch cell build using battery grade silicon powder in the anode and a high-energy cathode.
- Recommend electrolyte additives and electrode compositions for high energy lithium-ion electrochemical couples.
- Validate performance of advanced battery materials and add to Electrode Library as needed.
- Determine n:p ratio effect on performance of LMR-NMC cells.
- Determine effect of rapid charging and discharging rates on LMR-NMC materials.
- Advance development of electrochemical models focusing on the impedance of LMR-NMC positive electrodes.

Accomplishments

- The CAMP Facility has successfully fabricated silicon-graphite electrodes with good flexibility, mechanical robustness, and capacity loading approaching 4 mAh/cm².
- Two pouch cell builds were conducted with silicon-graphite electrodes versus NCM523 cathodes and comparisons made to graphite-based pouch cell builds.
- Material selection and mixing processes were optimized extensively in FY14 to enable the production of a silicon-graphite electrode system that is used in pouch cell builds and available to outside organizations via the CAMP Facility Electrode Library.
- Over 18 pouch cell builds were performed to date with combinations of baseline NCM523, 5V spinel, and high energy composite structure cathode materials (LMR-NMC) from Toda Kogyo, ABR researchers, and the Materials Engineering Research Facility (MERF), and with graphite and graphite-silicon anodes.
- Electrolyte additive study on LMR-NMC cells suggests the combination of 2 wt% LiDFOB and 0.25 wt% PFO-PBE in the baseline electrolyte lowers cell impedance rise and improves capacity retention.

- An optimum n:p ratio exists for the best cell performance and was found to be n:p = 1.16 for LMR-NMC (HE5050) versus graphite in cells.
- The effect of fast discharging on cycle life can be more detrimental than fast charging for cells with LMR-NMC based positive and graphite-based negative electrodes.
- Differences in electrolyte volume to electrode area must be accounted for in formation protocols when using electrolyte additives.
- Examination of unique LMR-NMC positive electrode impedance behavior was completed using an intercalation active material electrochemical model. Confirmed the model's utility for describing LMR-NMC electrode electrochemical behavior under transportation application testing protocols.
- Distribution of electrodes from the CAMP Facility's Electrode Library increased to 871 sheets to 40 different organizations.
- A spreadsheet-based data processing tool developed by the CAMP Facility was copyrighted as the CAMP Analyzer and is available for use.
- Electrode swelling due to silicon lithiation must be accommodated in electrode designs.



Introduction

The “valley of death” is a phrase that is often used to describe the path that a new discovery must traverse to become a commercial product. This is especially true for novel battery materials that are invented in research laboratories around the world. Often researchers are resource limited and are only able to make gram quantities of their new material. A few grams is enough for several coin cells to prove the concept, but never enough for a battery manufacturer to test in a realistic format. Consider that a typical coin cell has a capacity near 4 mAh, while a cell in a PEV battery has a capacity near 40 Ah – four orders of magnitude larger. An unwarranted amount of resources could be gambled to make the tens of kilograms needed for a full-sized cell industrial demonstration. Many great materials may have been abandoned on the benchtop because the scale-up risks were deemed too excessive.

This is where the CAMP Facility is needed. The CAMP Facility is appropriately sized to enable the design, fabrication, and characterization of high-quality prototype cells using just a few hundred grams of the latest discoveries involving high energy battery materials. Prototype cells made in the CAMP Facility generally have near 400-mAh capacity, which straddles the gap between coin cells and full cells nicely – two orders of magnitude from each end point. Thus, a realistic and consistent evaluation of candidate

chemistries is enabled in a time-effective manner with practical quantities of novel materials in cell formats commonly used in industry.

The CAMP Facility is more than an arrangement of equipment, it is an integrated team effort designed to support the production of prototype electrodes and cells, and includes activities in materials validation (benchmarking), modeling, and diagnostics. It is not the aim of this facility to become a small battery manufacturer, but instead to be a laboratory research facility with cell production capabilities that adequately evaluate the merits and limitations of mid-to-long term lithium-ion chemistries in a close-to-realistic industrial format.

As new cell chemistries and systems progress, they reach the point where they are considered for further development in larger prototype cells. When this happens, a limited quantity of these materials, along with their preliminary data, are transferred from the inventor or originator to the CAMP Facility for materials validation to determine if they warrant further consideration. The source of these materials (anodes, cathodes, electrolytes, additives, separators, and binders) may originate from the ABR and BATT Programs, as well as from other domestic and foreign organizations such as universities, national labs, and industrial vendors. Electrochemical couples with high power and energy density are given extra priority. Lately efforts have focused on silicon-based anodes and lithium-manganese-rich nickel-manganese cobalt (LMR-NMC) cathodes.

The CAMP Facility has the capability to make two prototype cell formats in their 45 m² dry room: pouch cells (xx3450 format, with capacity around 0.4 Ah) and 18650 cells. Pouch cells are anticipated to be easier to assemble, but they may suffer from bulging if gases are evolved during cell aging and cycling. 18650s, which are rigid containers, may be used if the pouch cell format is deemed unreliable due to gassing, or if higher capacity cells are needed (greater than 1 Ah). Central to this effort is a pilot-scale coating machine that operates with slurry sizes that range from 20 grams to a few kilograms. This is a key feature of the CAMP Facility that enables a professional evaluation of small quantities of novel materials. If needed, the MERF is available for scaling up materials for these prototype cell builds.

In general, two types of modeling are employed within this effort. First, battery design modeling is a spreadsheet based simulation that is used to determine the impedance behavior, available capacity, and thermal effects for general and specific cell, battery module, and battery pack designs. The model is also capable of performing simulations on multiple battery designs for comparison and optimization. In addition, the battery design model includes a module that calculates battery costs by combining materials and components costs with manufacturing expenses based on a plant design. A

publicly available version of this work referred to as the battery performance and cost (BatPaC) model, represents the only public domain model that captures the interplay between design and cost of lithium-ion batteries for transportation applications.

Electrochemical modeling is aimed at associating electrochemical performance measurements with diagnostic studies conducted on lithium-ion cells. The methodology for the electrochemical model is described in detail in the literature [1-3]. Essentially, continuum based transport equations are combined with kinetic and thermodynamic expressions to allow the potential, concentration, and current distributions to be determined throughout the cell. Two versions of the cell electrochemical model with the same basis are utilized to fully examine the broad range of electrochemical studies. One version of the electrochemical cell model is used to simulate the cell response from Electrochemical Impedance Spectroscopy (EIS) studies, and the other model version is utilized for examining DC studies, such as controlled current or power cycling and diagnostic HPPC tests.

Approach

The general approach used in this effort is to start small and grow large in terms of cell size and amount of resources devoted to each novel battery material. At various points in the development process, decisions are made to either advance, modify, or terminate studies to maximize utilization of available resources.

Coin cells (2032 size) are used for materials validation purposes with initial studies performed at room temperature or 30°C. After formation cycles, the coin cells go through hybrid pulse power characterization (HPPC) testing, rate capability testing, and limited cycle life testing. Accelerated aging studies are also performed at 45°C to 55°C for promising materials to give a preliminary indication of life. Where appropriate, the thermal abuse response is studied using a differential scanning calorimeter.

Using the recommendations and results obtained by the materials validation of promising materials, single-sided electrodes are fabricated on the larger dry-room coater for diagnostic study. The new cell chemistries are studied in detail using advanced electrochemical and analytical techniques, including the employment of micro-reference electrode cells. Factors are identified that determine cell performance and performance degradation (capacity fade, impedance rise) on storage and on extensive deep-discharge cycling. The results of these tests are used to formulate data-driven recommendations to improve the electrochemical performance/life of materials and electrodes that will be incorporated in the prototype cells that are later fabricated in the dry room. This information also lays

the foundation for electrochemical modeling focused on correlating the electrochemical and analytical studies, in order to identify performance limitations and aging mechanisms.

The approach for electrochemical modeling activities is to build on earlier successful characterization and modeling studies in extending efforts to new PEV technologies. The earlier studies involved developing a model based on the analytical diagnostic studies, establishing the model parameters, and conducting parametric studies with the model. The parametric studies were conducted to gain confidence with the model, examine degradation mechanisms, and analyze cell limitations. Efforts are ongoing to expand and improve the model's capabilities with the focus on LMR-NMC active material cathodes, and eventually silicon-graphite composite electrodes.

In addition, the battery design spreadsheet model (BatPac) is used to determine the impact of advanced materials on the current technology. The performance of the materials within the battery directly affects the end energy density and cost of the integrated battery pack. Both modeling efforts complement each other and are specifically aimed at supporting the CAMP Facility goals.

If the results from diagnostics and modeling still look promising, full cell builds are conducted using double-sided electrodes. The electrodes are then either punched in the case of pouch cells, or slit in the case of 18650 cells and assembled into full cells in the dry room using the semi-automated cell assembly equipment. Formation procedures are conducted on the cells to encourage electrolyte wetting and solid-electrolyte-interface (SEI) formation. These cells undergo rigorous electrochemical evaluation and aging studies under the combined effort of the CAMP Facility team, and Argonne's Electrochemical Analysis and Diagnostic Laboratory (EADL) and Post-Test Facility. After testing, select cells are destructively examined by the Post-Test Facility to elucidate failure mechanisms. This information is then used to further improve the new chemistry, as well as future electrode and cell builds. The results of these tests are shared with other members of the ABR & BATT Programs and to the materials origin, and to battery developers (if appropriate).

Results

CAMP Facility Materials Validation (Benchmarking) results are reported in Section IV.B.2.

CAMP Facility Support of DOE Awards are not included in this section of the report, but do appear in other sections.

Silicon-based Anodes: Early Development: Several sources of silicon powder, including Alfa Aesar, American Element, and Nanostructured and Amorphous

Materials Incorporated (NanoAmor), have been investigated for cycling performance. In the early development, NanoAmor silicon powder and Timcal SFG-6L graphite powders had been chosen to develop a silicon-graphite blended anode because of their promising cycling performance, commercial availability, cost per gram, and various silicon particle sizes available (130 nm & 50-70 nm). As for the binder system, the lithiated poly(acrylic acid) (Li-PAA) binder outperformed other binders in terms of cyclability, coulombic efficiency, and fabrication of practical silicon-based electrodes with $>3 \text{ mAh/cm}^2$ capacity loading. However, PAA/Li-PAA binders typically have subpar physical electrode integrity, resulting in cracking and brittleness characteristics.

The Li-PAA binder solution is made with poly(acrylic acid) (PAA, see Figure IV - 1) from Sigma Aldrich. Several molecular weights are available, including 250,000, 450,000, and 1,250,000. The PAA (450,000 m.w.) arrives as a powder and is mixed with 18MΩ deionized water to make a 15 wt.% poly(acrylic acid) solution. The 15wt.% PAA solution has a pH of about 2.8. The pH can be adjusted by lithiating the PAA with lithium hydroxide (LiOH). A study of the pH effects on adhesion for PAA/LiPAA ranging from 3 to 11 resulted in the selection of a neutral pH range, which has the best adhesion properties to copper foil.

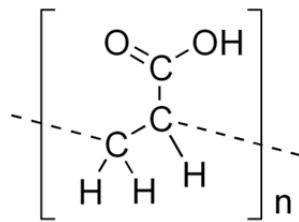


Figure IV - 1: Poly(acrylic acid)

The 450,000 molecular weight PAA was chosen for fabricating electrodes due to ease of slurry making with manageable viscosities, adequate mixing, and coating procedures. Slurry making involves mixing all the electrode components together, including the silicon, binder, graphite, carbon black, and water. The initial slurries made, using the PAA (450,000 m.w.) binder system, have been titrated with LiOH after the PAA was mixed with the other electrode components.

It became apparent early in development that silicon agglomerates form in high numbers that are difficult to break apart. Multiple mixing and dispersion methods were tried, including planetary centrifugal mixing which combines rotation and revolution centrifugal forces (Thinky), rotor-stator homogenizer mixing (Polytron), sonication horn pulsing, and high shear blade mixing (Ross), but all proved to be inadequate for breaking up the silicon agglomerates. The agglomerates have caused issues with both uniform coating and streaking of the electrodes and thus, these agglomerates need to be pulverized.

A new direction for mixing the silicon powder became clear. Aggressive mixing of the silicon, separate from the graphite, was needed to break up the silicon agglomerates. Water alone with silicon powder did not provide enough of a viscous medium to engage the silicon particles with the blade action in the mixers. Having a thickening agent, such as xanthan gum binder, allowed the silicon to engage the mixing blades. The Polytron mixer appeared to break up the silicon agglomerates most efficiently in this approach on small scale. This method provided some reduction of the agglomerates in the final slurry, but agglomerates were still present and caused some streaking during coating especially when coating at lower loadings, which is crucial since the mAh/g capacities for a silicon-graphite anode can be more than twice that of graphite only anodes. Proper mixing steps and mixing equipment have become paramount for the silicon-graphite anode.

The majority of the early evaluation of silicon/silicon-graphite materials and electrodes consisted of either Li metal (half-cell) or full coin cell studies. In order to make comparative evaluations between electrodes and their variables, a standard testing procedure was implemented. The major performance criteria used to characterize the silicon-graphite electrodes included the 1st cycle charge and discharge capacity (both should be larger than a graphite only system), 1st cycle efficiency, 2nd cycle through 10th cycle efficiency, and capacity fade. The testing procedure consists of 10 cycles at a C/10 rate, followed by a rate study (up to 2C rates), and then followed by C/5 cycling for 100 cycles. A 50 mV lower voltage cutoff is used in order to not over stress the silicon.

As for the electrolyte, the additive solvent fluoroethylene carbonate (FEC) has been shown to improve performance in silicon cells, thus it was utilized in all half-cell and full-cell testing where silicon was present in the anode. Based on previous work and literature, 10 wt.% FEC added to 1.2 M LiPF₆ in EC:EMC (3:7 wt.%) was used in all subsequent cell testing.

Numerous water based slurries and electrodes were constructed using ~15 wt.% NanoAmor silicon (130nm particle size) and ~73 wt.% Timcal SFG6-L graphite to target between 600 and 800 mAh/g of active material weight to balance the silicon benefits (high capacity) against negative side effects (volume expansion). Various wt.% of binder(s) and carbon black were investigated as well to improve electrode quality, adhesion, and performance.

The work that follows, highlights the Initial CAMP Facility xx3450 silicon-graphite pouch cell build using NanoAmor silicon (130 nm particle size) and Timcal SFG-6L graphite vs. Toda NCM 523 (Initial) and the reformulated CAMP Facility xx3450 silicon-graphite pouch cell build using NanoAmor silicon (50-70 nm particle size) and Hitachi MAGE graphite vs. Toda

NCM 523 (Reformulated-1 or Reform-1). The two pouch cell builds will be compared to a graphite only anode CAMP Facility xx3450 graphite pouch cell build using Phillips 66 CPreme A12 graphite vs. Toda NCM 523 (Baseline). The shorthand nomenclature will be used throughout the rest of the silicon-graphite anode work for quick reference.

The Baseline anode was fabricated using a composition of graphite with PVDF binder (92 wt.% Phillips 66 CPreme A12 graphite, 2 wt.% Timcal Super P Li carbon black, and 6 wt.% Kureha KF-9300 PVDF binder). The electrode had a single side coating thickness of 50 microns, 37.6% porosity, 1.34 g/cm³ coating density, 6.74 mg/cm² coating loading, and 2.05 to 2.14 mAh/cm² capacity (based on rate).

The Baseline cathode was fabricated using a composition of Toda NCM 523 with PVDF binder (90 wt.% Toda NCM 523, 5 wt.% Denka carbon, and 5 wt.% Solvay 5130 PVDF binder). The electrode had a single side coating thickness of 51 microns, 37.9% porosity, 2.51 g/cm³ coating density, 12.7 mg/cm² coating loading, and 1.64 to 1.82 mAh/cm² capacity (based on rate). The resulting n:p capacity ratio was 1.13 to 1.20.

Initial Silicon-Graphite Pouch Cell Build:

Results from early developments on the silicon-graphite anodes lead to incorporating the technology in the Initial xx3450 silicon-graphite pouch cell build. The Initial anode was fabricated using a composition of silicon-graphite blended with Li-PAA binder (15 wt.%

NanoAmor silicon (130nm particle size), 73 wt.% Timcal SFG6-L graphite, 5 wt.% Timcal C45 carbon, 6 wt.% LiPAA 450,000 m.w. binder, and 1 wt.% xanthan gum). The electrode had a single side coating thickness of 38 microns, 45.5% porosity, 1.14 g/cm³ coating density, 4.32 mg/cm² coating loading, and 1.71 to 2.28 mAh/cm² capacity (based on rate). The slurry was made in four steps. First the silicon, water, and xanthan gum was mixed with the PolyTron mixer. Second, in a separate container the graphite, PAA, water, and carbon black was mixed in the Thinky mixer. Third, the LiOH was then added to the mix of graphite, PAA, water, and carbon black to neutralize the PAA. Forth, both slurries were then combined in the Thinky mixer to complete the final mixing steps with media to aid in the dispersion.

The Initial cathode was fabricated using a composition of Toda NCM 523 with PVDF binder and was identical to the Baseline build. Using identical cathodes for the cell build allowed a direct comparison of apples to apples for improved evaluation of incorporating silicon into the anode. The resulting n:p capacity ratio for the Initial cell build was 1.27 to 1.46.

The xx3450 pouch cells consisted of 13 layers (5 double side cathodes, 2 single side cathodes, and 6 double side anodes) using 1.2 M LiPF₆ in EC:EMC (3:7 wt.%) with 10 wt.% FEC additive. A total of 8 pouch cells were put on test for formation, rate study, hybrid pulse power characterization (HPPC) testing, and cycle life testing.

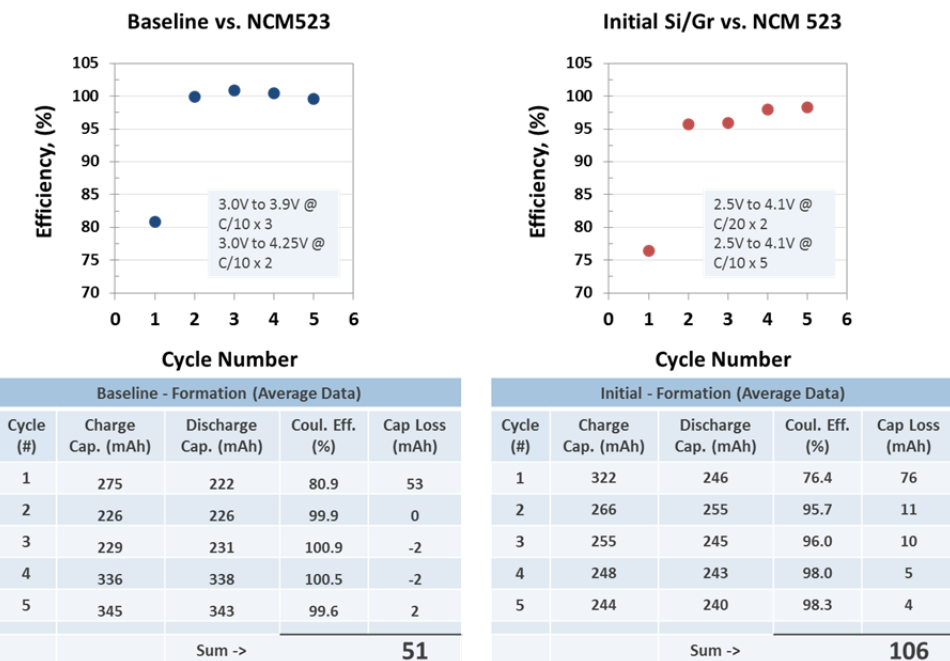


Figure IV - 2: Comparison of the formation cycling columbic efficiency of NCM 523 vs. Baseline & Initial xx3450 Silicon-Graphite Pouch Cell Builds. Plots are represented by using average data

The formation data comparing the graphite only anode to the silicon-graphite anode (Figure IV - 2) reveals higher capacity loss for the silicon-based cells, even after the first few cycles, as well as low coulombic efficiencies. These two items suggest that this silicon-based anode suffers from the lack of a robust SEI layer formation during breaking, thus causing a continuous consumption of electrolyte and lithium during cycling.

In the rate study, both the Initial and Baseline cells rate performance trend lines are similar, however the Initial xx3450 pouch cells had approximately 30 mAh/g less in capacity than the Baseline xx3450 pouch cells for each rate (C/24, C/5, C/2, 1C, and 2C). The mAh/g difference was also observed in the formation cycles and came as somewhat of a surprise because the Initial and Baseline cells were using identical cathode electrodes.

The Discharge ASI values for the silicon-graphite pouch cell are higher than the graphite only cells (Figure IV - 3), but for the values to be under 40 Ohm-cm² is promising for the system to handle higher rates. Also note the pulses for the silicon-graphite cells extend lower in voltage. Half-cell coin cell data reveal that most of the delithiation of graphite electrodes occurs around 100 mV to 200 mV plateau vs. Li metal, whereas the silicon-graphite electrodes occurs over a much larger and sloped window of 200 mV to 500 mV vs. Li metal. The differing delithiation windows influence the full cell discharge voltage profiles to extend to lower operating voltages when using silicon-graphite anodes.

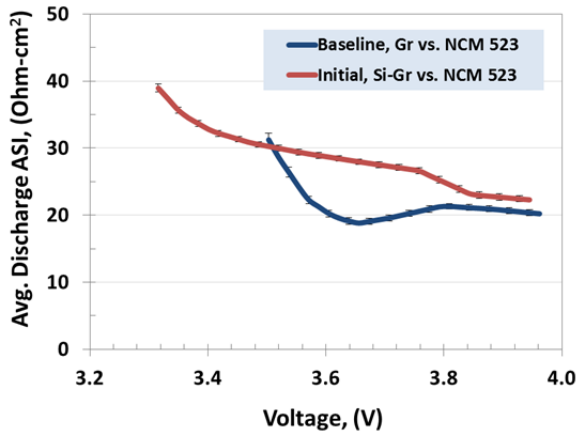


Figure IV - 3: HPPC Discharge ASI values for the NCM 523 vs. Baseline & Initial xx3450 Silicon-Graphite Pouch Cell Builds using a 5C discharge pulse for 10 seconds and 3.75C charge pulse for 10 seconds at each 10th% state of discharge. Data is averaged and interpolated with 1 σ SD error bars

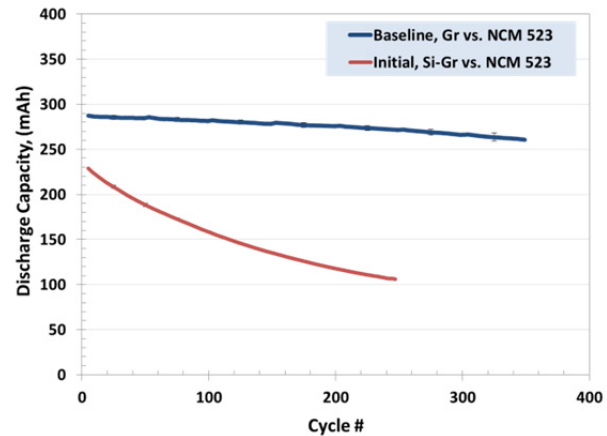


Figure IV - 4: Discharge capacity in mAh using the same cathode electrodes for NCM 523 vs. Baseline & Initial xx3450 Silicon-Graphite Pouch Cell Build

Cycling performance shows initial differences between the graphite only and silicon-graphite based anodes while using identical cathodes (Figure IV - 4). Future tests using reference electrode cells will show the individual anode and cathode voltage profiles while being cycled in a full cell format. The results of the reference electrode cells could then be compared to existing half-cell voltage profiles of the anodes and cathodes to determine failure mechanisms and understanding of stresses on the electrodes. The reference cells will also provide impedance behavior of each electrode.

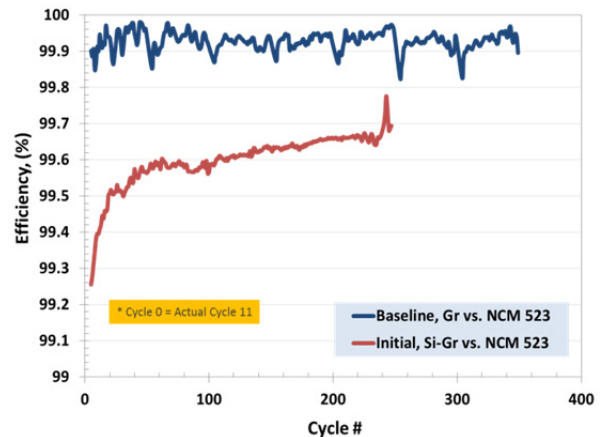


Figure IV - 5: Comparison of the cycle life columbic efficiency performance after formation cycles of NCM 523 vs. Baseline & Initial xx3450 Silicon-Graphite Pouch Cell Builds

Highlighting the coulombic efficiency performance for the cycle life testing shows the Baseline cells have around 99.9% efficiency, whereas the Initial silicon-graphite cells approach only 99.7% after 200 cycles (Figure IV - 5). While building the Initial silicon-graphite xx3450 pouch cells was an important first stepping stone, the overall cycling performance indicated that there is significant room for improvement in

the development of a high performance silicon-graphite anode.

Silicon-based Anodes: Recent Development:

New efforts have been taken to improve the practicality of the electrode in a commercial cell, with an emphasis on developing an electrode with $>3 \text{ mAh/cm}^2$. The approach involved testing silicon-graphite exploratory slurries on the CAMP Facility pilot-scale coating equipment (APro) to address any processing issues on the coater and verify the scalability of developments.

While the NanoAmor 50-70 nm silicon particle size costs more than the 130 nm particle size, earlier silicon studies in the CAMP Facility, and literature, suggest that smaller silicon particle sizes improve cycling performance. The inherent expansion of silicon when lithiated has less impact on smaller particles (decrepitation model) thus minimizing the degree of particle cracking, and better retaining electrical contact to the conductive network. On the one hand, the 50-70 nm silicon particle size is more difficult to work with because of low tap density and effects of static charge during handling, but on the other hand early slurries and coatings made using the 50-70 nm silicon particle size showed less agglomerates, improved flexibility and adhesion than the 130 nm particle size. With this in mind, the shift was made to using the 50-70 nm silicon particle size for further development.

A scan across various graphite materials to evaluate slurry making, coating ability, and resulting integrity of electrode was performed to identify whether graphite type affect these important characteristics. The reason for this investigation was made based on the observation that the Timcal SFG-6L graphite in PAA binder slurry showed signs of shear thickening, which drastically affected the coatability of the slurry with “waves” forming on the foil rendering the electrode unusable. However, when the SFG-6L graphite was in a Li-PAA binder slurry, the shear thickening characteristics were not present, resulting in a decent coating. Other graphite materials were tested in PAA binder to observe how the slurry and coating behaved. The other graphite materials included: Superior Graphite SLC1520P, Kureha hard carbon S(F), MCMB G15, and Hitachi MAGE. Surprisingly, only the SFG-6L graphite exhibited shear thickening with the PAA binder mix. It is thought that the flake like particles of SFG-6L caused the shear thickening action. In summary, the MAGE type graphite produced the better quality electrode and exhibited superior electrochemical performance (Figure IV - 6) when using LiPAA, as well as when mixed with silicon.

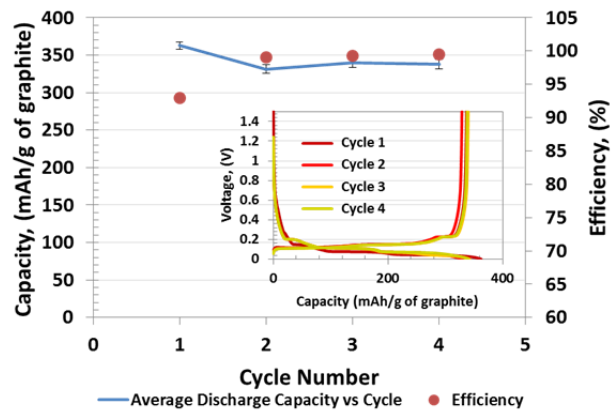


Figure IV - 6: Averaged discharge capacity and efficiency during formation vs. cycle number and corresponding voltage profile for MAGE graphite only vs. Li metal for comparison to silicon-graphite blends

A simple test (Soak Test) used by the CAMP Facility to determine adhesion and cohesion properties of a coating on a current collector involves soaking sample electrode punches in 2 mL of a standard 1.2 M LiPF₆ in EC:EMC (3:7 wt.%) electrolyte in a sealed vial under dry room atmosphere. The vial is placed in a 55°C oven and observed over a 2 week period to check for adhesion/delamination issues. A passing grade is determined if the electrode shows no signs of flaking apart or slipping off the current collector. A failing grade results if either flaking or slipping occurs. (One caveat to this soak test is the situation where a graphite material can raise the potential of the copper foil to the point of corrosion.) The Soak Test results for PAA and Li-PAA binder based electrodes typically resulted in acceptable cohesion and adhesion properties to the copper current collector. All the electrodes for Baseline, Initial, and Reformulated cells have passed the Soak Test.

Previously, the titration of the PAA (450,000 m.w.) for neutralization had been performed while in the slurry state for the Initial xx3450 pouch cell build. To streamline the slurry making process and not expose other components of the slurry to LiOH with potentially unwanted reactions, a stock solution of Li-PAA was created as a standalone solution. There were no noticeable differences in the slurry making procedure or coin cell testing results after switching to the Li-PAA stock solution.

Combining all the elements above lead to a usable slurry with a promising coating integrity, uniformity, and the ability to coat at higher loadings than before. Some coating parameters were needed to be adjusted such as fan speeds, coating speed, and temperature zones when using the water based binder system.

Silicon-Graphite Electrode for Electrode Library: Providing a usable and practical silicon-graphite electrode capacity matched to the Electrode

Library was a top priority for our team. While work to improve electrode integrity and cycling performance for silicon-graphite anodes is still needed, an electrode made using the CAMP Facility equipment would offer an opportunity for the battery research community to be provided with an electrode to perform other crucial research for silicon-graphite electrodes including electrolyte additive work. The anode constructed (A-A006) is a single-sided electrode combining our most recent breakthroughs of silicon particle size, graphite type, mixing protocol, and coating procedure.

The anode (A-A006) was fabricated using a composition of silicon-graphite blended with a pre-lithiated PAA binder (15 wt.% NanoAmor silicon (50-70nm particle size), 73 wt.% Hitachi MAGE graphite, 2 wt.% Timcal C45 carbon, and 10 wt.% LiPAA 450,000 m.w. binder). The electrode has a single side coating thickness of 25 microns, 42.4% porosity, 1.18 g/cm³ coating density, 2.94 mg/cm² coating loading, and 1.79-2.14 mAh/cm² capacity (based on rate). Coating the high capacity (mAh/g) silicon-graphite anode to match to the Electrode Library cathodes required a small wet coating gap, which relies on the improved pre-mixing method of silicon/carbon black, and LiPAA, and water in the Polytron mixer to prevent electrode streaking.

The photos in Figure IV - 7 demonstrate that winding the electrode around a mandrel for an 18650 cell would be possible without electrode disintegration (electrode passed the 3 mm diameter pin test). This improved flexibility is a significant development for silicon-graphite based anodes for practical use.

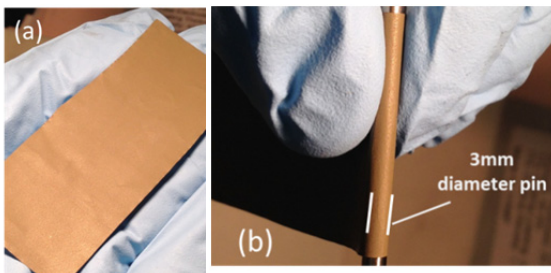


Figure IV - 7: (a) Photo showing the uniformity of the silicon-graphite based electrode in the Electrode Library (A-A006), and (b) Photo of the A-A006 electrode passing a 3 mm diameter pin test without visible cracking or adhesion issues

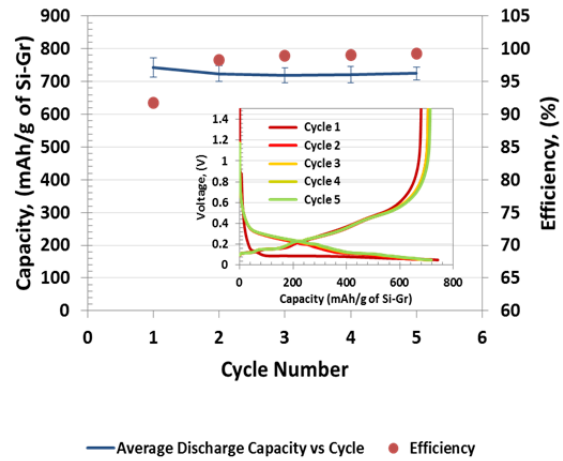


Figure IV - 8: Averaged discharge capacity during formation vs. cycle number with inset showing corresponding voltage profile for A-A006 vs. Li metal; 5 cycles @ C/10 from 1.5V to 0.050V

The formation data (Figure IV - 8) indicate that the A-A006 electrode has a relatively stable capacity near 700 mAh/g of active material (silicon + graphite). The 1st and 2nd cycle coulombic efficiencies at 91.7% and 98.3%, respectively, are markedly higher than previous silicon-graphite anodes. The voltage profile also reveals that the lithiation and delithiation of silicon occur at higher potentials than MAGE alone (see Figure IV - 6).

The rate study (Table IV - 1) and HPPC test (Figure IV - 9) for the A-A006 electrode show initial characterization of the electrode. These results demonstrate that this silicon-graphite electrode is appropriate for electrolyte additive work and general testing by the research community. Subsequent improved silicon-graphite electrodes will be added to the Electrode Library as new developments occur.

Mixing the silicon nanoparticles to reduce the agglomerates was not straight forward. Extensive mixing methods available were explored to break up the agglomerates. A major breakthrough came about with using a planetary ball mill (zirconia lined), with media, designed for grinding particles (Retsch). Agglomerates were significantly reduced using the planetary ball mill on a mix of silicon powder (50-70 nm), de-ionized water, Li-PAA, and carbon black, then mixing with graphite in the Thinky mixer. The breakthrough allowed for an electrode coating to be uniform and streak free. The Retsch mixer will be utilized in future silicon-graphite anode development.

Table IV - 1: Averaged delithiation (charge) capacity for various cycling rates for the A-A006 electrode vs. Li metal. Testing performed at various C-rates ranging from C/24 to 2C using a 1.5V to 0.050V voltage window for 3 cycles at each rate

A-A006 Average Delitiation Capacities		
C-rate	mAh/g	mAh/cm ²
2C	578	1.69
1C	615	1.79
C/2	651	1.90
C/5	699	2.04
C/10	735	2.14
C/24	780	2.28

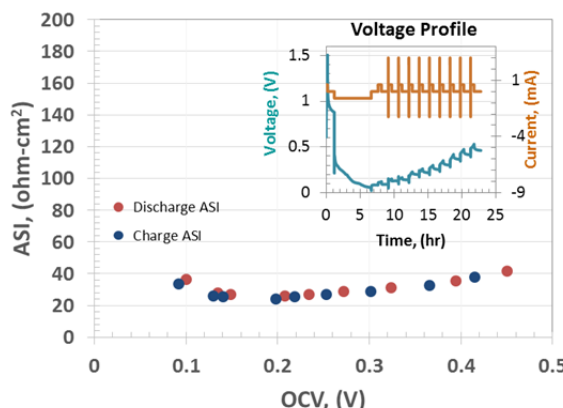


Figure IV - 9: HPPC Discharge and Charge ASI values for A-A006 electrode vs. Li metal. 1C charge (delithiation) pulse for 10 seconds and 0.75C discharge (lithiation) for 10 seconds at each 10th% state of charge

Reformulated Silicon-Graphite Pouch Cell

Build: A reformulated silicon-graphite anode pouch cell build was constructed to evaluate the performance in a full cell using the same electrode composition as the A-A006 electrode but at a higher coating loading to demonstrate the improved coating quality, which has both physical integrity, flexibility (passed 3 mm diameter pin test, see Figure IV - 10), and functionality for a realistic industrial cell targeting capacity loadings >3 mAh/cm².

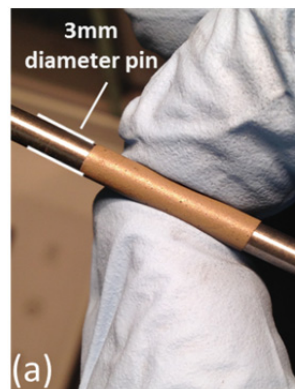


Figure IV - 10: Photo image of the Reformulated-1 silicon-graphite electrode (3.7 mAh/cm²) passing a 3mm diameter pin test without visible cracking or adhesion issues

The anode was fabricated using a composition of silicon-graphite blended with a lithiated PAA binder (15 wt. % NanoAmor silicon (50-70nm particle size), 73 wt. % Hitachi MAGE graphite, 2 wt. % Timcal C45 carbon, and 10 wt.% LiPAA 450,000 m.w. binder). The electrode had a single side coating thickness of 53 microns, 42.6% porosity, 1.17 g/cm³ coating density, 6.21 mg/cm² coating loading, and 3.7 mAh/cm² capacity. Mixing was performed using the Retsch planetary ball mixer to break up agglomerates.

The cathode was fabricated using a composition of NCM 523 with PVDF binder (90 wt.% Toda NCM 523, 5 wt.% Timcal C45 carbon, and 5 wt.% Solvay 5130 PVDF binder). The electrode had a single side coating thickness of 80 microns, 33.7% porosity, 2.69 g/cm³ coating density, 21.71 mg/cm² coating loading, and 2.82 to 3.13 mAh/cm² capacity (based on rate). The resulting n:p capacity ratio was 1.14 to 1.16.

The pouch cells consisted of 13 layers (5 double side cathodes, 2 single side cathodes, and 6 double side anodes) using 1.2 M LiPF₆ in EC:EMC (3:7 wt.%) with 10 wt.% FEC additive. A total of 8 pouch cells were put on test for formation, rate study, hybrid pulse power characterization (HPPC) testing, and cycle life testing (currently underway).

The 1st cycle efficiency from the Initial silicon-graphite pouch cell build to the Reformulated-1 silicon-graphite pouch cell build improved from 76.4% to 87.5% (Figure IV - 11). The 2nd cycle efficiency from the Initial to the Reformulated-1 pouch cell build improved from 95.7% to 99.6%. The mAh/g of oxide for Reformulated-1 is much improved compared to Initial.

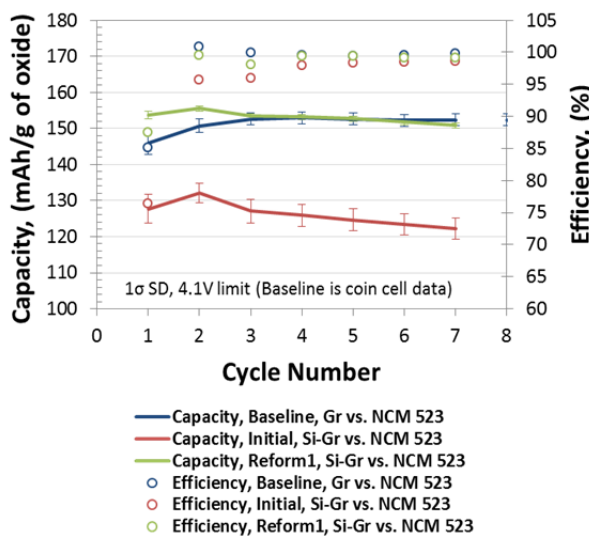


Figure IV - 11: Overlay of NCM 523 vs. Baseline, Initial, and Reformulated-1 silicon-graphite Formation testing in xx3450 pouch cells (NCM 523 vs. Baseline is coin cell data). Cells cycled to 4.1V UCIV

The rate capability of Reformulated-1 cell build (Figure IV - 12) improved noticeably from the Initial cell build, but there is still room to improve to the Baseline level of performance. Work to optimize the carbon black amount and mixing procedure with the planetary ball mill and silicon power are two paths that may help improve the rate performance.

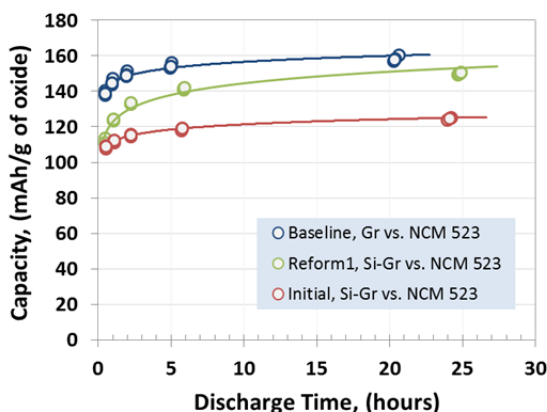


Figure IV - 12: Overlay of rate capability for NCM 523 vs. Baseline, Initial, and Reformulated-1 silicon-graphite testing in xx3450 pouch cells cycled to a 4.1V UCIV. Solid lines are trend lines based on rate performance. Open circles are actual data points for discharge capacities with corresponding discharge times for multiple cells

The HPPC data (Figure IV - 13) show that even with the Reformulated-1 pouch cell cathode coating loading almost double that of the Initial, cell impedance of the Reformulated-1 is even lower than the thinner Initial cathode loading suggesting that the thicker cathode is not adding to the cell impedance. Also, the HPPC data show the average voltage of the silicon-

graphite pouch cells is lower than that of the graphite only. The lower average voltage is attributed to the presence of silicon in the anodes, which has a higher delithiation voltage vs. Li metal than graphite vs. Li metal. Future studies will include reference cell studies to better understand the voltage profiles of both the cathode and anodes while cycling in a full cell format. The reference cells will also allow us to study the impedance of both electrodes as the cells age, which may suggest failure mechanisms of having silicon in the anode.

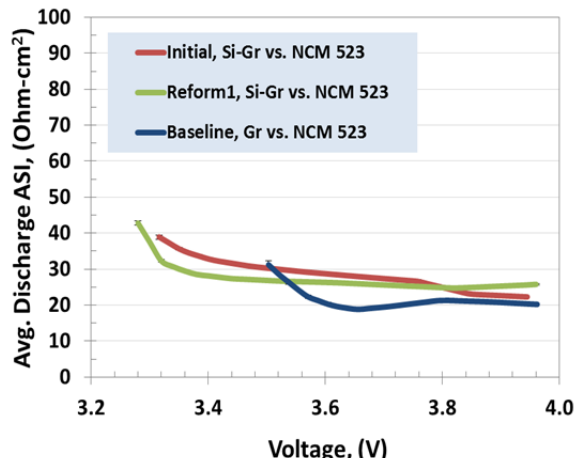


Figure IV - 13: Overlay of NCM 523 vs. Baseline, Initial, and Reformulated-1 silicon-graphite HPPC testing in xx3450 pouch cells using a 5C discharge pulse for 10 seconds and 3.75C charge pulse for 10 seconds at each 10th% state of discharge. Data is averaged with 1 σ SD error bars

A comparison of the Baseline, Initial, and Reformulated-1 electrodes and pouch cell builds is summarized in Table IV - 2. Of particular interest are the rows that show the thickness and capacity loading of the graphite and the silicon-graphite electrodes. Note that the Baseline and Reformulated-1 anodes have similar thickness (50 μm and 53 μm , respectively), while the capacity loading of the silicon-graphite anode is nearly 80% more than the graphite alone. This showcases the value of incorporating silicon into anode systems. However, the cathode loading was increased by 60 percent to match the improved silicon-graphite loading.

The Reformulated-1 silicon-graphite pouch cell build is currently in cycle life testing for continued evaluation of silicon-graphite capacity fade. An evaluation of capacity fade and coulombic efficiency will be made when the data become available.

The most significant breakthroughs came about because of the pre-mixing of silicon/carbon black/water/LiPAA binder in the Retsch planetary ball mill to break up the silicon agglomerates as the Thinky, rotor-stator, sonication, and planetary/shear mixers

could not break them up, which caused issues with coating/streaking.

Summary of key breakthroughs in the research and development of silicon-graphite anode:

- Implementing smaller particle size silicon (50 to 70 nm) to improve cyclability.
- Successfully breaking up agglomerates using planetary ball mill for grinding and pulverization (Retsch).
- Identifying the importance of graphite type for slurry preparation, coating, and cycling performance.
- Optimizing silicon compatible LiPAA binder solutions for acceptable cycling performance, slurry quality, and industrially practical coatings.

- Determination of coater settings to coat thicker electrodes using water-based slurries.

Swelling in Silicon-based Electrodes: Thickness studies of graphite vs. silicon-graphite electrodes before cycling, after formation, and at various states of charge have been performed by measuring the entire cell thickness change and the electrodes themselves after disassembly. Figure IV - 14 is a summary of the percent change in thickness for the anode only relative to the initial dry electrode. The silicon systems in general have a higher percent rise in thickness than graphite alone. In these cells, the cathode (and separator) changes were relatively insignificant. Accounting for the thickness changes in anode systems is an important feature to monitor when using silicon-based materials. This will be studied in more detail in the future.

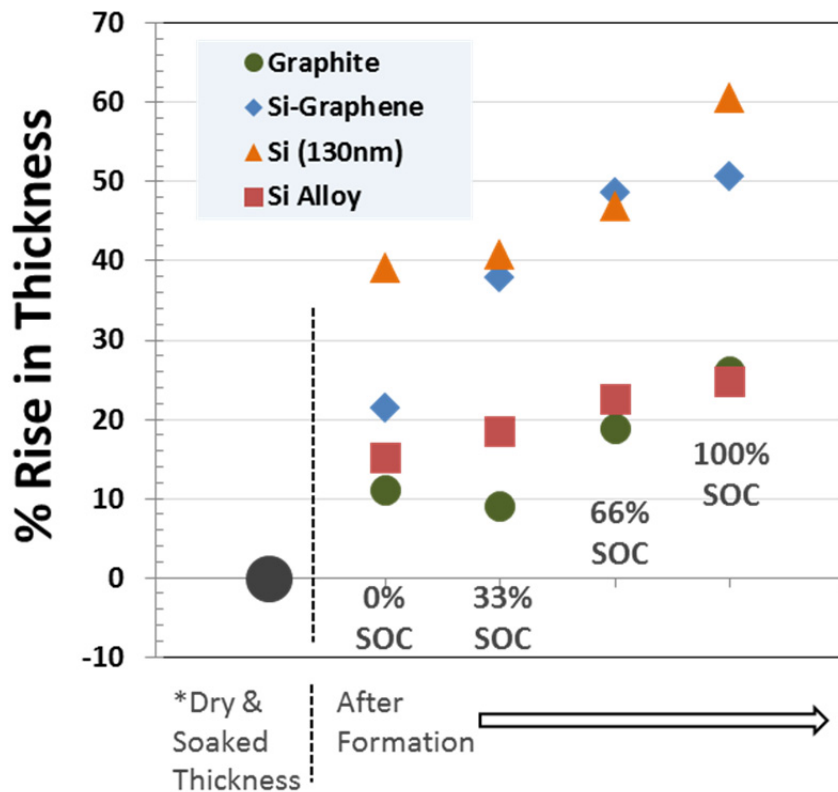


Figure IV - 14: Summary of electrode thickness changes as a function of state of charge for various electrodes with differing active materials

Table IV - 2: Summary of differences between Baseline, Initial, and Reformulated-1 silicon-graphite vs. NCM 523 in xx3450 Pouch Cell Builds. Capacity (mAh/cm²) range based on cycle rate data

	<u>Baseline</u> graphite vs. Toda NCM 523, xx3450 Pouch Cell Build	<u>Initial</u> silicon-graphite vs. Toda NCM 523, xx3450 Pouch Cell Build	<u>Reformulated-1</u> silicon-graphite vs. Toda NCM 523, xx3450 Pouch Cell Build
Silicon powder	-	NanoAmor, 130 nm particle size, spheres and nanotubes	NanoAmor, 50-70 nm particle size
Graphite powder	Phillips 66 CPreme A12	Timcal SFG-6L	Hitachi MAGE
Binder	Kureha KF-9300 PVDF	Sigma Aldrich PAA 450,000 m.w., titrated with LiOH in slurry, xanthan gum	Sigma Aldrich PAA 450,000 m.w., pre-titrated with LiOH•H ₂ O
Compositions (dry wt.%)	92/2/6 Gr/carbon black/PVDF	15/73/5/6/1 Si/Gr/carbon black/LiPAA/xanthan gum	15/73/2/10 Si/Gr/carbon black/LiPAA
Mixing method(s)	Ross planetary and dispersion mixer	Polytron, Thinky	Retsch, Thinky
Coating Thickness - Single Side (μm)	Anode: 50 Cathode: 51	Anode: 38 Cathode: 51	Anode: 53 Cathode: 80
Porosity (%)	Anode: 37.6 Cathode: 37.9	Anode: 45.5 Cathode: 37.9	Anode: 42.6 Cathode: 33.7
Coating Density (g/cm³)	Anode: 1.34 Cathode: 2.51	Anode: 1.14 Cathode: 2.51	Anode: 1.17 Cathode: 2.69
Coating Loading (mg/cm²)	Anode: 6.74 Cathode: 12.7	Anode: 4.32 Cathode: 12.7	Anode: 6.21 Cathode: 21.71
Capacity (mAh/cm²)	Anode: 2.05 to 2.14 Cathode: 1.64 to 1.82	Anode: 1.71 to 2.28 Cathode: 1.64 to 1.82	Anode: 3.7 Cathode: 2.82 to 3.13
Capacity (mAh/g of active material)	Anode: 330 to 345 Cathode: 145 to 160	Anode: 600 Cathode: 145 to 160	Anode: 700 Cathode: 145 to 160
Capacity (mAh)	300 @ 4.1V UCL	225 @ 4.1V UCL	500 @ 4.1V UCL
n:p ratio	1.13 to 1.20	1.27 to 1.46	1.14 to 1.16

Electrolyte Additives for LMR-NMC Cells:

Electrolyte additives are known to be an effective and economic approach to improving the stability of electrode surface films. In the past two decades, many organic and inorganic compounds have been identified as effective electrolyte additives: examples include vinylene carbonate (VC), ethylene sulfite (ES), vinyl ethylene carbonate (VEC), and fluoroethylene carbonate (FEC). In recent years, with the emergence of many high-voltage cathode materials, the anodic stability of common electrolytes is recognized as the main bottleneck limiting the calendar- and cycle- life of high-energy lithium-ion cells. Therefore, more attention has been devoted to improving stability of the cathode-electrolyte interface.

Ways are being examined to mitigate performance degradation of cells containing $\text{Li}_{1.2}\text{Ni}_{0.15}\text{Mn}_{0.55}\text{Co}_{0.1}\text{O}_2$ -based positive electrodes that are cycled at voltages

beyond 4.5 V versus Li. Studies indicate that common electrolyte additives such as VC, VEC, and FEC are not very effective at enhancing long-term cycling performance of these cells, *i.e.*, stable electrode passivation is not achieved with traditional SEI-forming additives. This observation underscores the need for new electrolyte additives that effectively form stable electrode passivation films in high-energy and high-voltage lithium-ion cells.

The synergistic effects of $\text{LiB}(\text{C}_2\text{O}_4)_2$ (LiBOB), $\text{LiF}_2\text{B}(\text{C}_2\text{O}_4)$ (LiDFOB), triphenylamine (Ph_3N), and 1,4-benzodioxane-6,7-diol (BDOD) as functional electrolyte additives were examined and reported in previous years. The influence of these additives, individually, and in different combinations, was evaluated using galvanostatic cycling of cells containing $\text{Li}_{1.2}\text{Ni}_{0.15}\text{Mn}_{0.55}\text{Co}_{0.1}\text{O}_2$ -based positive electrodes, graphite-based negative electrodes, and a LiPF_6 -based

electrolyte. It was noted that the addition of LiDFOB, Ph₃N, and BDOD to LiBOB-containing cells improves capacity retention and lowers impedance rise on extended cycling. However, even the best additive combination only slows down performance degradation and does not completely prevent it.

In the past year the CAMP Facility examined the effect of phenyl boronic acid ethylene glycol ester (PBE) as an additive to 1.2 M LiPF₆ in EC:EMC (3:7 by wt.) (referred to as Gen2) electrolyte in cells with the electrodes described above. The effects of a new modular additive, phenyl boronic acid perfluoroctyl ethylene glycol ester (PFO-PBE) were examined, which combines a PBE *head* group with a perfluoroctyl *tail* (see Figure IV - 15). This research builds on previous modular additive work in which a perfluoroalkyl chain (*tail*) was attached to ethylene carbonate (*head group*). The modular additives facilitate formation of a double layered film on electrode surfaces thereby reducing cell performance degradation. The influence of these additives was evaluated using galvanostatic cycling, electrochemical impedance spectroscopy (EIS), and linear sweep voltammetry (LSV).

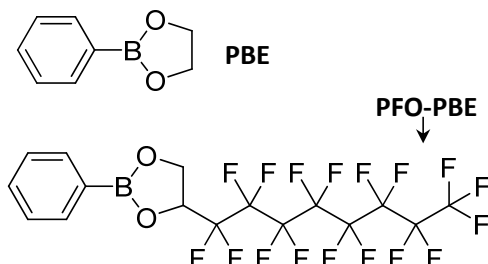


Figure IV - 15: Chemical structures of additives used in this work

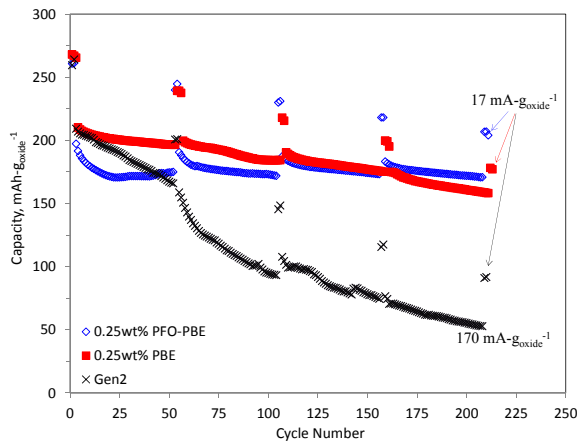


Figure IV - 16: Capacity vs. cycle number for full cells cycled at 30°C between 2.2–4.6 V with a 170 mA-g_{oxide}⁻¹ current and 17 mA-g_{oxide}⁻¹ current (after every 50 high current cycles). Data for cells with the Gen2 electrolyte (black), with 0.25 wt% PBE (red), and with 0.25 wt% PFO-PBE (blue) electrolyte additives are shown. The capacity and cycling current values are based on Li_{1.2}Ni_{0.15}Mn_{0.55}Co_{0.1}O₂ content in the positive electrode

The following conclusions can be reached from various tests conducted:

1. Small additions (0.25 wt.%) of PBE or PFO-PBE to the baseline electrolyte improve cell capacity retention (see Figure IV - 16) and reduce impedance rise (see Figure IV - 17).
2. Linear sweep voltammetry data indicate that both PBE (~4.5 V vs. Li/Li⁺) and PFO-PBE (~4.7 V vs. Li/Li⁺) are oxidized earlier than the baseline electrolyte, apparently providing protective films at the positive electrode that reduce impedance rise.
3. Studies in graphite//Li cells indicate that both PBE and PFO-PBE are reduced before the main EC reduction process at ~0.7 V vs. Li/Li⁺ apparently creating a more stable SEI.
4. Addition of 2 wt% LiDFOB to cells with 0.25 wt% PFO-PBE in the baseline electrolyte lowers cell impedance rise further, but does not improve capacity retention. Combining electrolyte additives that act synergistically are a practical, versatile, and economic means to extend cell life.

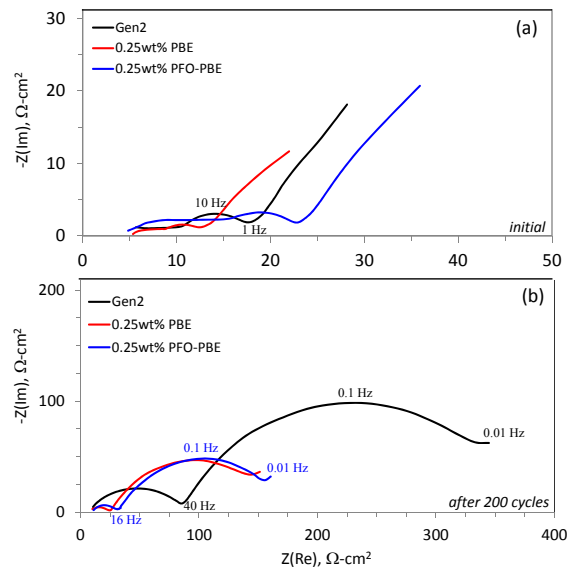


Figure IV - 17: AC impedance data from full cells containing the Gen2 electrolyte (black), 0.25 wt% PBE (red), and with 0.25 wt% PFO-PBE (blue) electrolyte additives after (a) initial cycling and (b) after more than 200 cycles between 2.2–4.6 V. The cells are charged to 3.75V and held for more than 4h before data are acquired at 30°C in the 100 kHz–10 mHz frequency range

Effect of n:p Ratios on Cell Performance: Full-cell performance depends critically on cell-level engineering. Apart from various material- and chemistry-dependent parameters, such as choice, size, and amount of active materials other parameters such as electrode porosities and negative-to-positive electrode capacity ratios (n:p ratio) affect cell performance. In this

report the effect of the negative-to-positive electrode capacity ratio (“n:p ratio”) on short and long term cycling performance is examined. Material details and electrode formulations are given in Table IV - 3. The active material loading of the negative electrode was varied by varying the coating thickness on the Cu current collector; however, the electrode constitution is exactly the same. All negative electrodes were coupled to a standard positive electrode from the CAMP Facility.

Table IV - 3: Positive and Negative Electrode Content

Active material	92 wt.% Toda HE5050 ($\text{Li}_{1.2}\text{Ni}_{0.15}\text{Mn}_{0.55}\text{Co}_{0.1}\text{O}_2$)	92 % wt. ConocoPhillips CGP A12 graphite
Binder	4 wt.% PVdF	6 wt.% KF-9300 Kureha
Additives	4 wt.% C45	2 wt.% C45
Current collector	Al, 15 μm	Cu, 20 μm
Electrolyte	1.2 M LiPF ₆ in EC:EMC (3:7 by wt.)	
Separator	25 μm thick, Celgard 2325	
Active loading	6 mg·cm ⁻²	
Electrode porosity	36%	(see text for details)
Laminate thickness	20 μm	

To evaluate cell performance, the protocol outlined in Table IV - 4 was chosen. All cycling was galvanostatic and carried out in coin cells with a 1.6 cm² electrode at 30°C. Cycling currents are given in terms of the active oxide weight, and are equal for all cells. Note that this implies that the graphite-specific currents for the negative electrode vary for each n:p ratio, while the oxide-specific currents remain the same. This is done deliberately, for two reasons – firstly, it ensures the same testing procedure for all cells. And secondly, it allows us to probe the cell performance only as a function of the n:p ratio for given currents.

Table IV - 4: Full cell cycling protocol

Formation	2 cyc	2.5V – 4.1V	0.09 mA (10 mA/g-oxide)
Activation	2 cyc	2.5V – 4.55V	0.09 mA (~C/25-C/30)
Rate study*	5 cyc	2.5V – 4.4V	0.45 mA (> C/4)
	5 cyc	2.5V – 4.4V	1.8 mA (> 1.2C)
	5 cyc	2.5V – 4.4V	4.5 mA (> 3.5C)
	2 cyc	2.5V – 4.4V	0.09 mA
Cycle life	2 cyc	2.5V – 4.4V	0.09 mA
ageing	100 cyc	2.5V – 4.4V	0.9 mA (100 mA/g-oxide)
	2 cycles	2.5V – 4.4V	0.09 mA

Figure IV - 18 highlights the effects of SEI formation and Li trapping on the gravimetric capacities (top panel) and coulombic efficiencies (bottom panel) during the first 2.5-4.1V cycle. At very low n:p ratios, the charge capacity is limited, because the upper cell voltage is impacted by the quickly dropping negative voltage (in the baseline cell this corresponds to ~95 mAh/g). As the n:p ratio is increased, the charge capacity increases nearly continuously because of the opposite effect: the higher negative voltage now pushes the positive voltage further up, resulting in higher capacities. Parasitic electrochemical side reactions, e.g. electrolyte reduction on the negative side, also contribute to this rising charge capacity, as the surface area on the negative side continuously increases with

increasing n:p ratio. Note that, despite the higher negative voltage, the activation plateau of the oxide is not accessed for the highest ratio (n:p = 4.5) at 4.1V, because this would otherwise result in significantly higher charge/discharge capacities and lower coulombic efficiencies.

The coulombic efficiencies are shown in the Figure IV - 18 bottom panel. As expected, coulombic efficiencies drop linearly at first, as the n:p ratio is increased. This linear relationship continues until n:p ~2.5 at which point the coulombic efficiency is ~50%. The linear decrease is related to increased SEI formation with the increased graphite content. Note that for n:p < 2.5, significant amounts of Li intercalate into the graphite voltage plateaus at <0.2V vs. Li/Li⁺ resulting in high coulombic efficiencies. For n:p > 2.5, lithium trapping in the SEI matches the lithium that intercalates into the graphite structure.

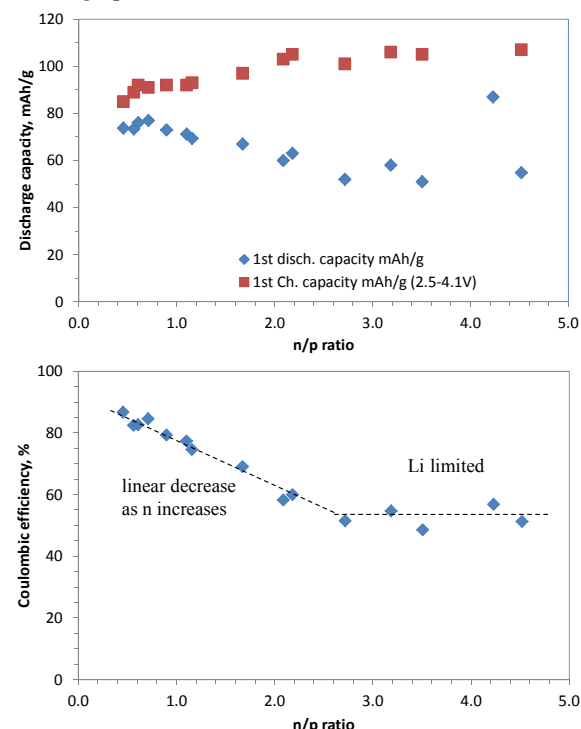


Figure IV - 18: Charge and discharge capacities during the first 2.5-4.1V cycle (top) and the corresponding coulombic efficiencies (bottom) as a function of n:p ratio

Figure IV - 19 confirms that higher n:p ratios lead to lower charge/discharge capacities, which are shown here for the first 2.5-4.55V activation cycle. The coulombic efficiencies, shown in the bottom panel, also decrease as the ratio increases. While decreasing capacities are expected, decreasing efficiencies are most probably related to some continuing SEI formation on the negative electrode, especially during this high voltage cycle pushing the negative voltage further down. Also included in these 5-12% “inefficiencies”, are the

so-called “irreversible losses” which are intrinsic to the oxide material. These losses in full-cells are related to structural changes occurring in the material during activation *and* simultaneous trapping of Li as previous studies have shown.

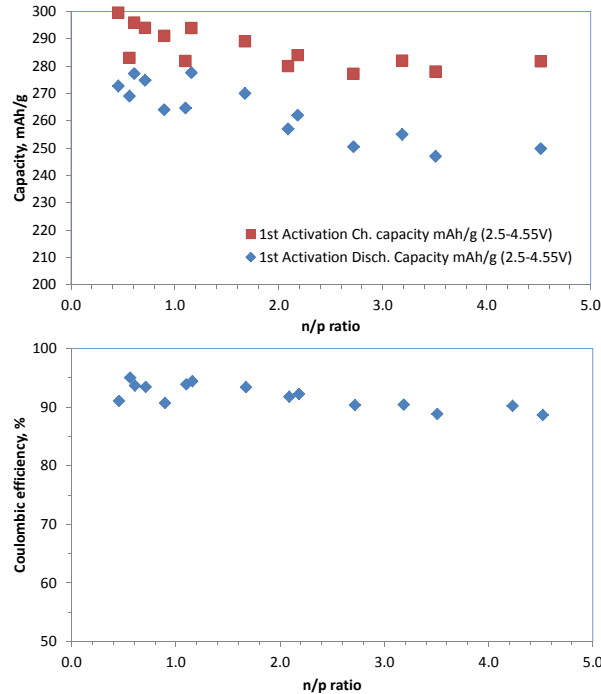


Figure IV - 19: Charge and discharge capacities during the first 2-4.55V cycle (top) and the corresponding coulombic efficiencies (bottom) as a function of the n:p ratio

Figure IV - 20 shows that the discharge capacities measured as a function of the n:p after the “rate study” follow a very different trend from the ones seen during the first activation cycle. In fact, a point of optimum performance emerges at around n:p=1.2, which is the ratio for the baseline cell. Also, the drop-off for higher n:p ratios is far less significant than the drop-off for lower ratios – implying that *high n:p cells are generally more rate, or abuse, tolerant than low n:p ratio cells*.

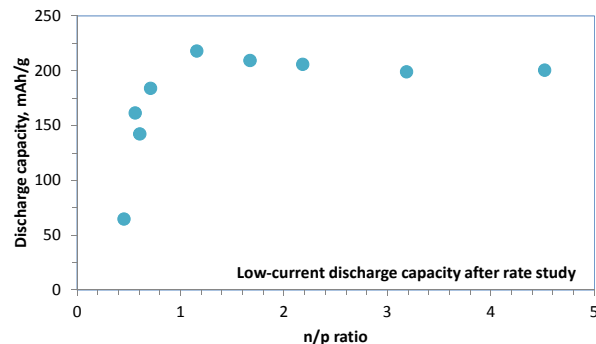


Figure IV - 20: Discharge capacities as a function of the n:p ratio after the rate study

Figure IV - 21 depicts the slow rate discharge capacities after 100 cycles with 100 mA-g⁻¹ current. All

cells continue to lose capacity. However, cells with n:p ratios below unity lose capacity most severely; and the n:p=1.2 cell remains the “best performing” cell, in terms of absolute capacity.

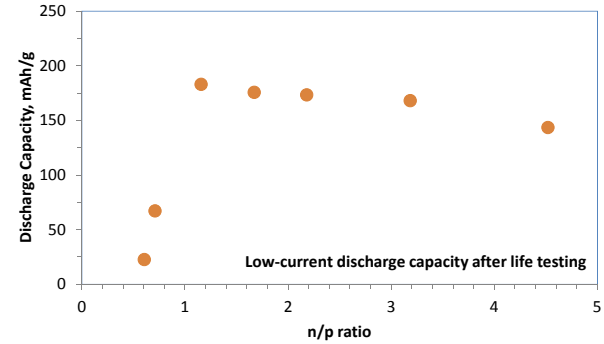


Figure IV - 21: Discharge capacities as a function of the n:p ratio after cycle life ageing, 100 cycles

The conclusions of these various data sets may be summarized as follows:

- An optimum n:p ratio exists for the best cell performance, in terms of cell capacity, after rate and cycle life testing. This ratio is found to be n:p = 1.16, which is similar to the value of our baseline cells.
- The rate performance for n:p < 1 is poor due to the larger current densities on the negative side, possibly triggering Li plating, graphite damage, and acceleration of SEI formation.
- For larger ratios of n:p > 4 , cycle life (i.e. capacity and capacity retention) worsens probably due to an unstable SEI triggered by high negative voltages.
- Cells with n:p > 1 are much more abuse tolerant than cells with n:p < 1.
- The negative electrode porosity has no apparent effect on cell performance. This is in contrast to earlier findings related to porosity of the positive electrode, for which porosity needs to be in the low 30’s for the electrode impedance to be low.
- No evidence was found that excess-Li, originating from the irreversible structural changes within the Li-rich oxide during activation, fully offsets the Li losses caused by negative SEI formation.

Investigation of Formation Protocols: In FY13 the CAMP Facility began to study the effects of LiDFOB and LiBOB on the performance of a cell containing Toda HE5050 LMR-NMC and Phillips 66 CPreme A12 graphite. In the initial diagnostics studies done, these bi-functional additives showed an improved performance in coin cells. Based upon these results, the additives were scaled up and placed in xx3405 pouch cells (~ 400 mAh capacity) made in the CAMP Facility. The initial results are shown in Figure IV - 22.

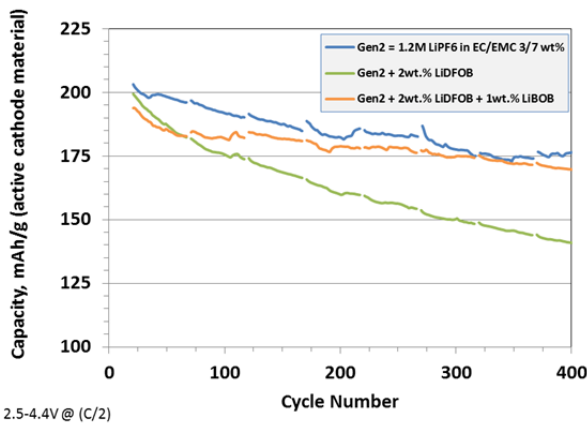


Figure IV - 22: Discharge capacities for electrolyte additives in baseline pouch cell build using HE5050 versus A12 graphite

The results show that from the initial cycling, the additive cells performed worse than the cells with the baseline electrolyte (Gen2 = 1.2M LiPF6 in EC/EMC 3/7 wt%). Based upon these results the CAMP Facility began to look at the initial differences between the baseline cells and the additive cells. The largest difference observed was in the tap charge profile between the cells. The tap charge profile of the cells and the dQ/dV plots are shown in Figure IV - 23 and Figure IV - 24.

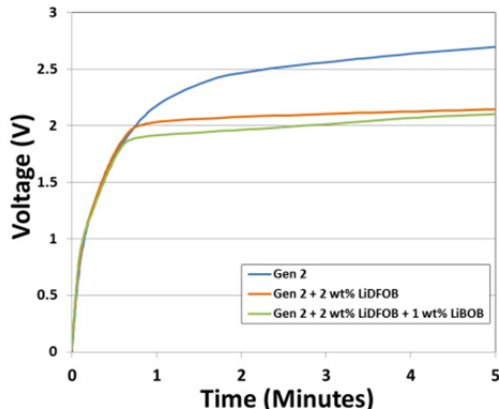


Figure IV - 23: Tap charge voltage profiles for electrolyte additives in baseline pouch cell build using HE5050 versus A12 graphite

In these cases we see that the additives are being activated during the tap charge, before the electrolyte has had a chance to wet the full cell. This could cause a non-uniform coating of the additives on the anode which is believed to affect the performance of the pouch cell.

In FY14 the CAMP Facility began to explore the differences between the initial coin cell data and the xx3450 pouch cells data to understand why the performance improvements were not seen in the pouch cells. In order to understand what the differences are

between the coin cell and pouch cell, the physical characteristics of the two different cells must be explored. Table IV - 5 summarizes the electrode area and electrolyte amounts in coin cells and pouch cells.

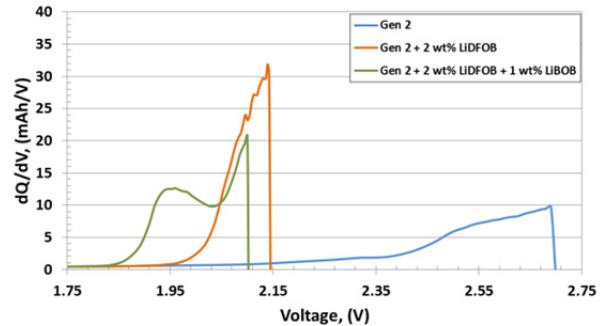


Figure IV - 24: Tap charge dQ/dV profiles for electrolyte additives in baseline pouch cell build using HE5050 versus A12 graphite

In the xx3450 pouch cells, the total anode area is 179 cm² and the cathode area is 169 cm² and uses 2.5 mL of electrolyte in the cell. The density of the Gen2 electrolyte is 1.2 g/cm³. For the coin cells, the total anode area is 1.6 cm² (9/16" diameter punch) and the cathode area is 1.6 cm² (9/16" diameter punch) and uses 10 drops of electrolyte. (1 drop = ~18 mg). By comparing the weight of the electrolyte/additive to the area of the anode and cathodes, in the table above, it is shown that for these two cell configurations, the coin cell has ~10 times the amount of electrolyte/additive than the xx3450 pouch cell. Since no additional electrolyte can be fit into the xx3450 pouch cell to make it equivalent to the 10 drop coin cell, the pouch cell conditions must be simulated in a coin cell.

When calculating the amount of electrolyte needed in a coin cell to simulate pouch cell conditions, one would need 3 drops of electrolyte for a matched 9/16" diameter anode and cathode. When doing initial studies with this amount of electrolyte, the cell assembly was difficult to ensure that all of the 3 drops of electrolyte made it between the anode, cathode and separator during assembly. Several studies were done to see the effects of the number of electrolyte drops in a coin cell on the cell assembly and cell performance. In order to balance the ease of assembly and electrolyte content, the decision was made to use 5 drops of electrolyte to simulate pouch cell conditions in coin cells. By using the 5 drops, the electrolyte/additive is only 3 times the amount that is in a pouch cell. It was agreed that this was a much better condition to run coin cells in than the 10 electrolyte drop amount. Table IV - 6 shows the basic pouch cell configuration compared to the 5 electrolyte-drop coin cell configuration.

Table IV - 5: Comparison of electrode areas and electrolyte volumes in different cell formats

Sample	Anode Area (cm ²)	Cathode Area (cm ²)	TTL Area (cm ²)	Electrolyte Composition	TTL Electrolyte Amount	TTL Electrolyte Amount (mg)	Base Electrolyte Amount (mg)	Additive Amount (mg)	Base Electrolyte Amount per Anode Area (mg/cm ²)	Base Electrolyte Amount per Cathode Area (mg/cm ²)	Base Electrolyte Amount per TTL Area (mg/cm ²)	Additive Amount per Anode Area (mg/cm ²)	Additive Amount per Cathode Area (mg/cm ²)	Additive Amount per TTL Area (mg/cm ²)
Pouch Cell	179	169	348	Gen2 (T)	2.5 ml	3000	3000.0	0.0	16.8	17.8	8.6	0.00	0.00	0.00
Pouch Cell	179	169	348	Gen2 (T) + 2 wt. % LiDFOB	2.5 ml	3000	2940.0	60.0	16.4	17.4	8.4	0.34	0.36	0.17
Pouch Cell	179	169	348	Gen2 (T) + 2 wt. % LiDFOB + 1 wt. % LiBOB	2.5 ml	3000	2910.0	90.0	16.3	17.2	8.4	0.50	0.53	0.26
Coin Cell	1.6	1.6	3.2	Gen2 (T)	10 drops	180	180.0	0.0	112.5	112.5	56.3	0.00	0.00	0.00
Coin Cell	1.6	1.6	3.2	Gen2 (T) + 2 wt. % LiDFOB	10 drops	180	176.4	3.6	110.3	110.3	55.1	2.25	2.25	1.13
Coin Cell	1.6	1.6	3.2	Gen2 (T) + 2 wt. % LiDFOB + 1 wt. % LiBOB	10 drops	180	174.6	5.4	109.1	109.1	54.6	3.38	3.38	1.69

Table IV - 6: Comparison of electrolyte additive amount to electrode area in different cell formats

Sample	Anode Area (cm ²)	Cathode Area (cm ²)	TTL Area (cm ²)	Electrolyte Composition	TTL Electrolyte Amount	TTL Electrolyte Amount (mg)	Base Electrolyte Amount (mg)	Additive Amount (mg)	Base Electrolyte Amount per Anode Area (mg/cm ²)	Base Electrolyte Amount per Cathode Area (mg/cm ²)	Base Electrolyte Amount per TTL Area (mg/cm ²)	Additive Amount per Anode Area (mg/cm ²)	Additive Amount per Cathode Area (mg/cm ²)	Additive Amount per TTL Area (mg/cm ²)
Pouch Cell	179	169	348	Gen2 (T)	2.5 ml	3000	3000.0	0.0	16.8	17.8	8.6	0.00	0.00	0.00
Coin Cell	1.6	1.6	3.2	Gen2 (T)	5 drops	86	86.0	0.0	53.8	53.8	26.9	0.00	0.00	0.00
Coin Cell	1.6	1.6	3.2	Gen2 (T) + 2 wt. % LiDFOB	5 drops	86	84.3	1.7	52.7	52.7	26.3	1.08	1.08	0.54
Coin Cell	1.6	1.6	3.2	Gen2 (T) + 2 wt. % LiDFOB + 1 wt. % LiBOB	5 drops	86	83.4	2.6	52.1	52.1	26.1	1.61	1.61	0.81

Now that a new coin cell configuration was established that was closer to the pouch cell conditions, variations on the tap charge and other formations cycles could be modified in a coin cell and transferred directly to a pouch cell process. By using coin cells to screening changes in the tap charge and formation cycles, results could be quickly and easily obtained.

The first change that was tested in coin cells was a variation on the tap charge. Since there was evidence of the LiDFOB and LiBOB being activated on the unlimited tap charge, a maximum voltage was set so that neither of the additives would be activated during the tap charge. Based upon the initial pouch cell data, a maximum voltage of 1.5 V was selected. An additional 15 minute hold step at the 1.5 V was also added to ensure that the potential on the anode was pulled up high enough during the 24 hour rest step to prevent copper corrosion. Figure IV - 25 shows the difference in voltage profiles as a function of time for the initial pouch cells and the coin cells with the modified tap charge process.

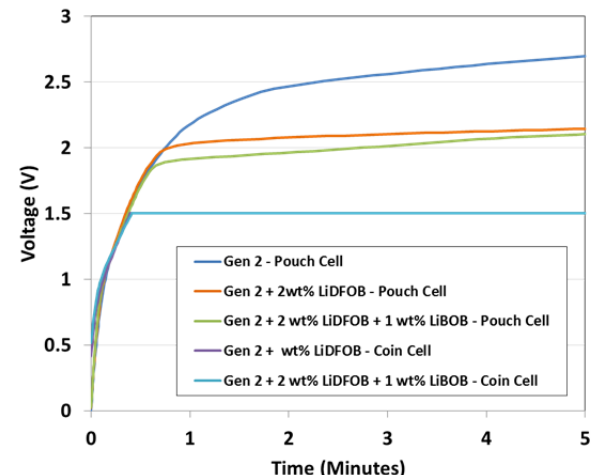


Figure IV - 25: Tap charge voltage profiles for electrolyte additives in baseline pouch cell build and coin cells with modified formation protocols using HE5050 versus A12 graphite

As seen in Figure IV - 25, the voltage of the coin cells never gets close to the previous levels of the pouch cells. Examination of the dQ/dV plots shows no activity on the coin cells with the new tap charge process. Once the formation process was completed on the coin cells, the cells were put on a life cycle test (~C/2 – 2.5-4.4V). The data for this test is shown in Figure IV - 26.

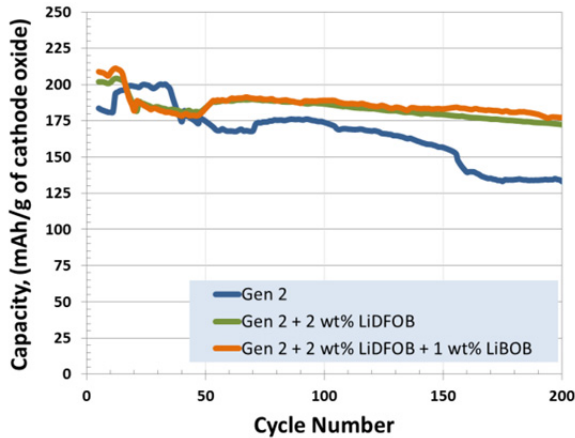


Figure IV - 26: Life cycle test for electrolyte additives in coin cells with modified formation protocols using HE5050 versus A12 graphite

From Figure IV - 26, it can be seen that the additive cells are out performing the baseline cells. The dips in the curves are due to some facility issues that were causing the room temperature to fluctuate. Since these conditions showed favorable results in the coin cell under simulated pouch cell conditions, the additives were scaled up and put into xx3450 pouch cells. The same formation process was used as in the coin cells, (Tap Charge Max 1.4V, 15 minute hold at 1.5V, 24hr hold) was used on the xx3450 pouch cells. Once the pouch cells finished the formation process, they were placed on a life cycle test (C/20 then 47 cycles at C/2, HPPC test, Voltage Window 2.5-4.4V). The results in Figure IV - 27 show the statistical analysis of the cells that were tested under these conditions.

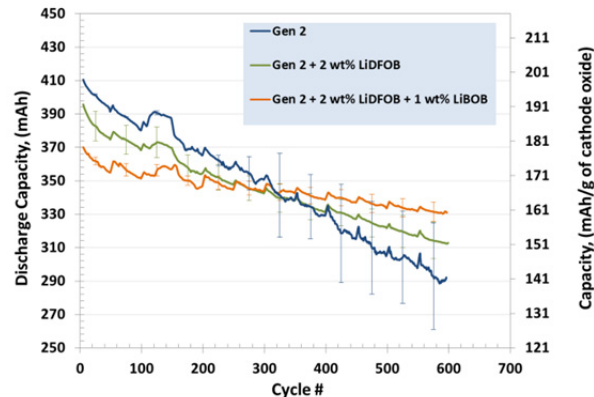


Figure IV - 27: Life cycle test for electrolyte additives in new pouch cell build with modified formation protocols using HE5050 versus A12 graphite

In the initial cycling of the cells, the baseline cells show the best performance early on, where the additive cells show a slightly lower initial capacity. At ~300 cycles we can start to see the benefit of the additives in the cells. At that point, the capacity fade of the additive cells is much less than the baseline cells. Looking at the impedance of the cells over the life of the cells shows a dramatic difference between the baseline and additive cells. Figure IV - 28 shows the discharge ASI at 3.75V as a function of cycle number.

In Figure IV - 28, the baseline cells show a doubling of the ASI when comparing the initial cycle to cycle 600. In the additive cells case, the 2% LiDFOB cells show a ~ 30% increase in the cells ASI and the 2% LiDFOB + 1% LiBOB cells show a ~15% increase in the cells ASI over the 600 cycles. This data would suggest that capacity fade in the baseline is a combination of impedance rise and voltage fade of the cathode material. In the additives case, the capacity fade of the cells are much more influenced by the voltage fade of the cathode material and there is minimal impedance rise.

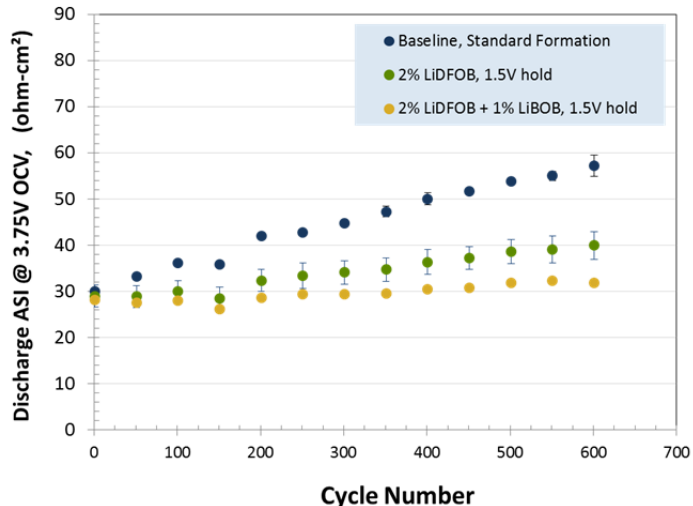


Figure IV - 28: Discharge ASI for electrolyte additives in new pouch cell build with modified formation protocols using HE5050 versus A12 graphite

Figure IV - 29 summarizes the comparison of the coin cell and pouch cell data. In the case of the coin cells, the additive cells at ~ cycle 40 perform better than the baseline cells. And after 200 cycles both additive coin cells showed a ~30% better capacity retention. In the case of the pouch cells, it takes ~320 cycles to show

an improved performance in the additive cells compared to the baseline cells. And when the 500th cycle of the additive and baseline cells are compared, the additive cells shows between a 5-10% better capacity retention than the baseline cells.

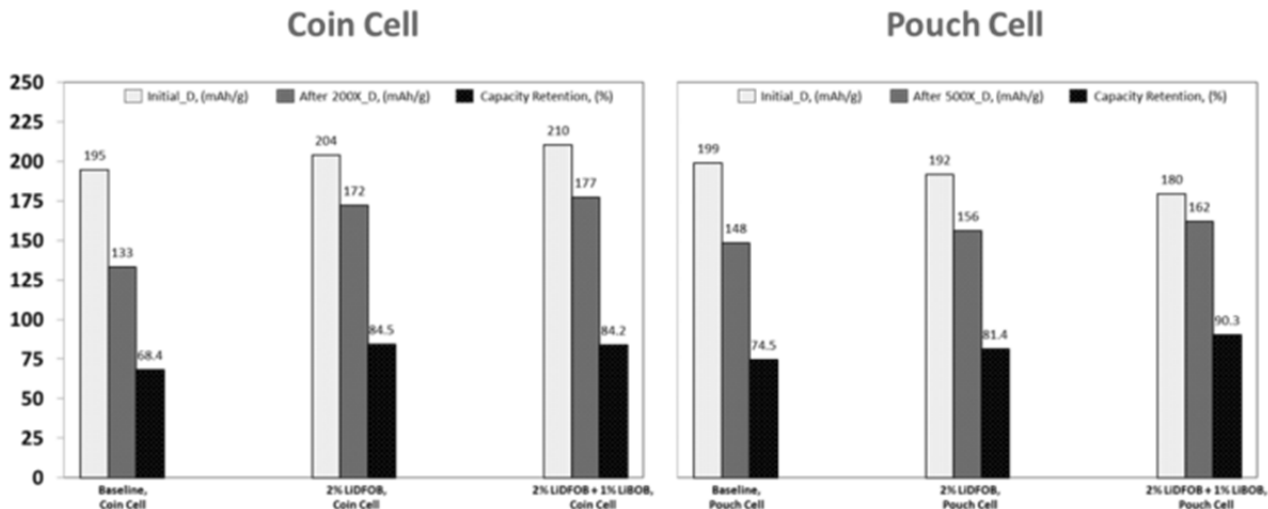


Figure IV - 29: Comparison of the coin cell and pouch cell data with modified formation protocols using HE5050 versus A12 graphite

Effect of Rapid Charging or Discharging on Cell Performance:

It is commonly accepted that fast charging shortens the cycle life of full cells much more than fast discharging when equal magnitudes of cell current are applied. The reason for this is believed to be the low operating voltage of the graphite anode once it is partially lithiated during charging. Polarization below the redox voltage of Li metal triggers Li plating on the anode surface, and the Li deposits react then with the

electrolyte irreversibly leading to capacity loss and impedance rise.

The goal of this study is to show how cycling conditions affect the cycle life of high-energy LMR-NMC oxide based full cells at high cut-off voltages. In particular, the effects of high charge and high discharge currents are compared and discussed.

Cell performance using different charge and discharge currents were studied with periodic measurements of cell impedance by AC impedance

spectroscopy (EIS). All tests were conducted in 2032-sized coin cells containing 1.6 cm^2 size electrodes at 30°C . The positive electrodes contained 92 wt% $\text{Li}_{1.2}\text{Mn}_{0.55}\text{Ni}_{0.15}\text{Co}_{0.1}\text{O}_2$, 4 wt% C45 carbons and 4 wt%

Table IV - 7 lists the general cycling procedure for every cell. The experimental conditions during initial formation, activation and impedance measurements (EIS) were identical for all cells. During the “asymmetric cycle life aging”, only the cycling currents were varied for the individual cells. This asymmetric cycling is the key experimental procedure: all cells were subjected asymmetrically to a low charge and a high discharge current - or vice versa. The low current is

PVDF; the negative electrodes contained 92 wt% graphite, 6 wt% PVDF and 2 wt.% C45. Some cells also contained LTO-based negative electrodes with 87 wt% $\text{Li}_4\text{Ti}_5\text{O}_{12}$, 8 wt% PVDF and 5 wt% C45.

always a “baseline” current of 0.15 mA, which corresponds to approximately a C/14 rate for a symmetrically cycled cell. Three different current levels were chosen in the corresponding fast charge or discharge of the graphite-containing cells, corresponding to a rate very close to C/3, 1C, and 3C. The LTO-containing cells were fast charged or fast discharged only at a 3C rate.

Table IV - 7: Full-cell cycling protocol for rate effect test

		Graphite (-) cells	LTO (-) cells	
Formation	2 cycles	2.5V – 4.1V	1.05V – 2.65V	0.09 mA
Activation	2 cycles	2.5V – 4.55V	1.05V – 3.1V	0.09 mA
EIS	100kHz-0.01Hz	3.75V	2.3V	$\pm 10\text{mV}$
1st asymm cycle	1 cycle	2.5V – 4.4V	1.05V – 2.95V	low current cycles: 0.15mA; $\pm 10\text{mV}$
EIS	100kHz-0.01Hz	3.75V	2.3V	
asymmetric cycle life ageing	102 cycles (with every 8 th cycle 2 lower current cycles)	2.5V – 4.4V	1.05V – 2.95V	low current cycles: 0.15mA; further details in Table C
EIS	100kHz-0.01Hz	3.75V	2.3V	$\pm 10\text{mV}$

Figure IV - 30 shows the cycle-life performance of six different tests, fast charging and fast discharging with three different current levels during the high current half-cycles. Note that after every rapid eight cycles, low current cycles are implemented to track the mobile Li inventory of the cells. Figure IV - 30A and Figure IV - 30B show the cycle life performance during fast charging and fast discharging, respectively.

Significant differences between the three current levels are seen for the fast discharge tests, while relatively small differences are seen for the fast charge tests. The high-current capacity decreases rapidly from cycle-to-cycle during fast discharging as the currents levels are increased, while the low-current capacity is remarkably similar for the three current settings. Regardless of fast charging or discharging, the low current capacity decreases continuously, almost linearly, as all cells continue to age – indicating a continuous loss of mobile Li in the cells, which is believed to result from Li trapping in the negative electrode SEI.

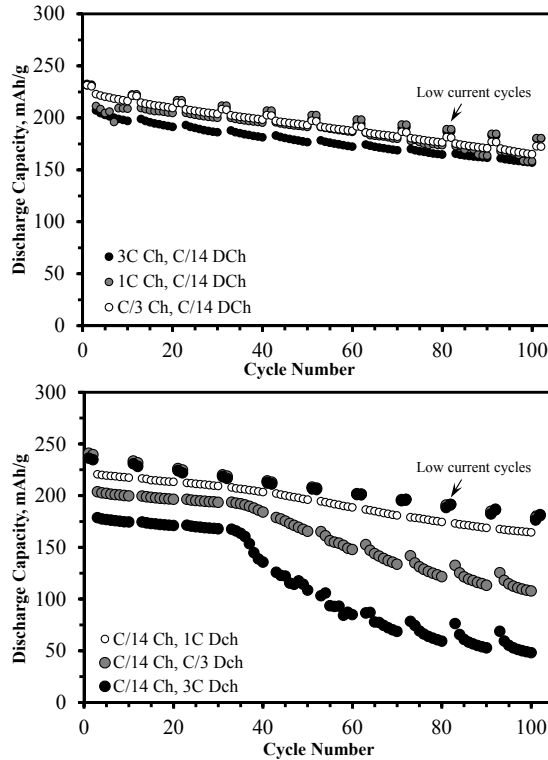


Figure IV - 30: Cycle life performance of full cells (A-Top panel) charged at various rates (3C, 1C, C/3) and discharged slowly and (B) charged slowly (C/14) and discharged at various rates

Of particular interest is also the abrupt drop in the high-current capacity that is encountered during fast discharging at the 1C and 3C rates after ~30 cycles. These capacity losses at high discharge currents are not due to excessive Li trapping, as the low current capacity is nearly identical for the two cases. It was surmised that the increasing difference between low and high current capacities arises from a significant increase in cell impedance during fast discharging. This impedance rise is shown in Figure IV - 31, wherein the two cases, fast charge and fast discharge, are compared. Significantly higher impedance is seen for the cell that was exposed to fast discharging.

As previous reports have confirmed, cells containing LMR-NMC oxide based electrodes suffer severely from a rise in cell impedance due to a degrading electrolyte, and a break-down of the electronic network within the positive electrode (possibly due to surface film formation and oxidation of the carbonaceous additives), as well as surface film formation on the cathode and also structural changes of the oxide. All these effects were previously linked to the high-voltage operation of the cathode. Loss of lithium because of trapping in the graphite SEI causes the positive electrode to cycle at increasingly higher average voltages, which ultimately causes the cell impedance to rise faster when the cell is exposed to series of rapid discharges.

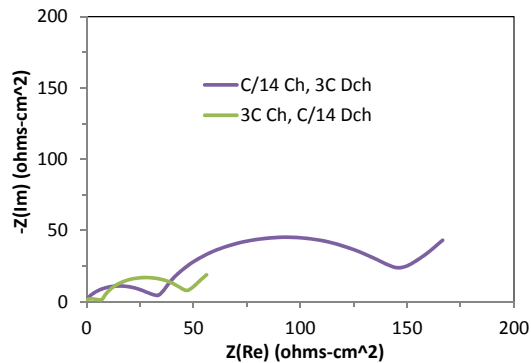


Figure IV - 31: AC impedance data (100 kHz-10 mHz, 30°C) from cells charged slowly but discharged rapidly and vice-versa. Impedance is significantly greater for the cell that underwent rapid discharge

Figure IV - 32 shows that impedance is similar for LTO-based cells that undergo either rapid charge or discharge. This result is a consequence of the superior capacity retention of these cells because the LTO-based negative electrode cycles at ~1.5 V vs. Li/Li⁺, has minimal SEI and does not trap lithium ions.

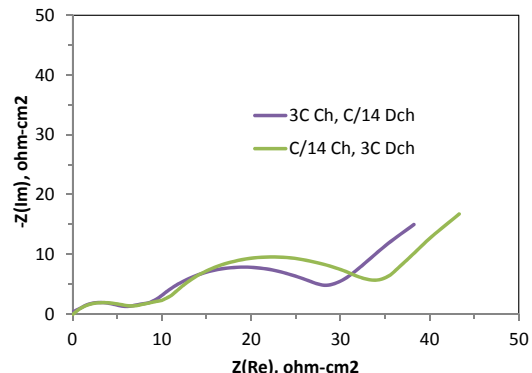


Figure IV - 32: AC impedance data (100 kHz-10 mHz, 30°C) for LTO-cells from cells charged slowly but discharged rapidly and vice-versa

In summary, this report shows that, contrary to common belief, the effect of fast discharging on the cycle life can be more detrimental than fast charging for cells with LMR-NMC based positive and graphite-based negative electrodes. This effect is primarily due to the rise in cell impedance which originates almost exclusively from the positive electrode. The cause for this impedance rise, as identified in earlier work, is ultimately linked to the breakdown of the electronic network of the positive electrode at higher voltages and also includes a break-down of the electrolyte due to its oxidation above ~4.3V vs. Li/Li⁺. It is important to note that the underlying reason for the positive electrode is pushed to higher voltages lies in the asymmetry of the material intrinsic impedance during charge and discharge, which is a consequence of the voltage hysteresis displayed by the LMR-NMC oxide.

Electrochemical Modeling: The EIS electrochemical cell model has been utilized to examine the impedance characteristics of LMR-NMC positive electrodes (i.e. this work focuses on the baseline HE5050 electrode). The data presented are electrode measurements taken on a micro-reference electrode cell. The model specifically addresses the surface layer impedance, but treats bulk material as a solid solution. Nevertheless, the standard intercalation model has proven quite useful for examining LMR-NMC electrodes, especially when using transportation application testing protocols.

The detailed theoretical description of the active material/electrolyte interface, commonly referred to as the solid electrolyte interphase or SEI, is based on post-test analytical diagnostic studies. The SEI region is assumed to be a film on the active material and layer at the surface of the active material. The film is taken to be an ill-defined mixture of organic and inorganic material through which Li-ions from the electrolyte must diffuse and/or migrate across to react electrochemically at the surface of the active material. The lithium is then assumed to diffuse through the surface layer and into the

bulk active material in the particle. Capacitive effects are incorporated into the model at the electrochemical interfaces and a localized electronic resistance between the current carrying carbon and the oxide interface is also included. The model can also accept multiple particle fractions with unique characteristics.

The EIS curve for these layered oxide positive electrodes consists of two circular arcs (i.e. a high-frequency arc and a mid-frequency arc) associated with the interface and a low frequency Warburg impedance associated with bulk diffusion of lithium ions in the oxide and salt in the electrolyte. For most standard electrolytes and well made electrodes, salt diffusive effects are usually small. In previous studies it has been well established that the impedance of the LMR-NMC electrode is much higher than observed for other layered oxide electrodes (e.g. NMC and NCA). The electrochemical model has been used to help eliminate differences in material physical characteristics, as well as electrode loading and formulation. A significant fraction of the higher impedance is caused by the relatively poor electronic conductivity of the LMR-NMC. This impedance occurs in the high frequency arc and is generally independent of the LMR-NMC state-of-charge (SOC). It can be significantly reduced through electrode formulation optimization.

The impedance of the layered oxide positive electrodes depends on their SOC. Typically, at low and high SOCs the impedance tends to increase. Further, the extremely long time constants in the LMR-NMC material, associated with the transport of lithium and accompanying structural changes during cycling, cause the impedance to be highly dependent on cell cycling history. As an example, two sets of EIS studies were conducted on the LMR-NMC electrode. One with a shorter wait time before the EIS measurements of a few hours, and one with a longer wait time of one hundred hours. Because of the voltage hysteresis, both sets of EIS studies were conducted during the charge and discharge. Typical of all these studies, most of the changes occur in the low frequency Warburg impedance and the mid-frequency arc. The main parameter variations associated with these changes are the active material lithium diffusion coefficients for the surface layer and bulk material (D_{Si} and D_{Sb}) and the kinetic exchange current density (i_0).

As previously reported, the shorter wait EIS data over the voltage range studied (between 3.3 and 4.0 volts vs. lithium) within the same half-cycle, either charge or discharge, the impedance increased as the SOC and electrode potential decreased. Further, the bulk lithium diffusion coefficient (D_{Sb}) dropped off faster than the interfacial (D_{Si}). Because of the hysteresis between charge and discharge, the two EIS sweeps taken at the same electrode potential, but differing SOCs, had significantly different impedance. Similarly, the two EIS sweeps taken at about the same SOC (i.e.

same lithium content) also had significantly different impedance. Generally, the charge and discharge behavior were similar. However, it was apparent from the limited data that the three model parameters did not correlate with either SOC or voltage.

The LMR-NMC kinetic and diffusion parameters for the longer wait data are shown in Figure IV - 33. With this more extensive set of measurements, it is quite evident that all the parameters fall off at low and high SOCs and again the bulk lithium diffusion coefficient (D_{Sb}) decreases faster than the surface layer lithium diffusion coefficient (D_{Si}) at low SOCs. Different from the shorter wait results, the longer wait charge and discharge electrochemical model parameters correlate well with electrode potential.

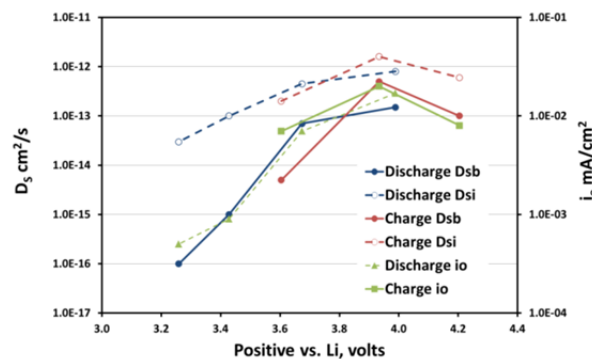


Figure IV - 33: Selected intercalation electrochemical model parameters from longer wait EIS studies on LMR-NMC electrode

Another difference can be seen in Figure IV - 34, using D_{Sb} as an example, all three model parameters are generally lower for the longer wait measurements, compared to the shorter wait parameters. Specifically, as you allow the LMR-NMC material to relax longer the interfacial and bulk impedance increases. As suggested above, the fundamental reasons for this behavior are related to the long LMR-NMC material time constants. To better understand this behavior requires an electrochemical model that specifically includes the LMR-NMC material domains, which is discussed in the Voltage Fade section.

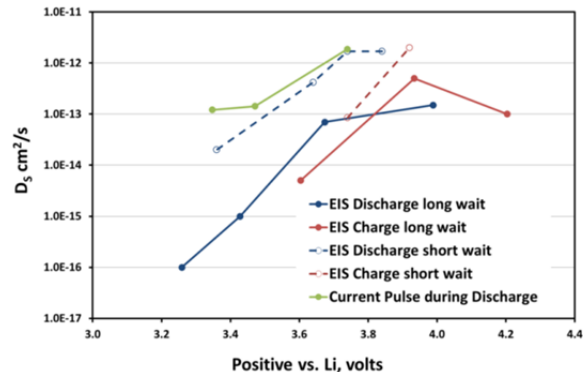


Figure IV - 34: Bulk lithium diffusion coefficient for LMR-NMC active material obtained from micro-reference cell

It is important to note that the increase in impedance at low and high SOCs is greater than observed for other layered oxides, which corresponds to the relatively steep slopes for the parameters in Figure IV - 33 and also observed for the shorter wait EIS study. This is important because the steep fall off causes a significant difference between charge and discharge ASIs in HPPC tests. Combining this observation with another that the LMR-NMC impedance is generally higher than other layered oxides suggests that the LMR-NMC electrode makes a much better high energy electrode than high power. Even for short current pulses, the steep parameter slope makes it very important to include the parameter variations within the electrochemical model to obtain an adequate fit of both charge and discharge data.

Most of this discussion has focused on the high impedance and unusual behavior of the LMR-NMC electrode. Indeed, the extremely low transport and kinetic parameters obtained from the long wait EIS measurements are particularly concerning for a battery developer. The intercalation electrochemical model can be used to address this point. Adequate fits have been obtained for a wide variety of electrochemical studies (e.g. EIS, controlled current discharge, and pulse power). As may be expected, tests more relevant to transportation applications yield parameters that are more in line with the lower impedance, shorter wait, EIS data. An example of this is given in Figure IV - 34 for the lithium diffusion coefficient obtained from discharge current pulse data. Finally, it is a major advantage to be able to model the electrode performance with a relatively simple intercalation model. It should be noted here to utilize this model, the LMR-NMC voltage hysteresis requires separate OCV curves for charge and discharge that would need to be modified for voltage fade as the cell ages.

Electrode Library: In the CAMP Facility's efforts to advance battery research not only at Argonne National Laboratory but also in industry, universities and other national laboratories, the Electrode Library was created several years ago. The Electrode Library

utilizes the industrial battery manufacturing coating and rolling equipment in the CAMP Facility to produce standard anode and cathode electrodes. The unique nature of the Electrode Library electrodes is that all the anodes and cathodes have a matched capacity. By doing this, any company, university or national laboratory that is working on one side of the cell will have multiple choices of materials to use on the other side of the cell in using the Electrode Library electrodes. By doing this, the quality and speed of research at these facilities are greatly improved.

In FY14, the CAMP Facility added a number of new materials/electrodes to the Electrode Library. These materials/electrodes include a new graphite electrode, (Superior Graphite SLC1520P), which will be used as the new baseline graphite electrode of all future full cell studies. (The previous baseline graphite was Phillips 66 CPreme CPG-A12 graphite) The second new anode that was added is a graphite-silicon composite electrode. This is the first openly available graphite-silicon electrode to companies, universities and national laboratories. The CAMP Facility will continue to characterize and improve upon this initial graphite-silicon electrode and add future versions into the Electrode Library.

As for the cathode side of the cell, four new cathode materials were added to the electrode library. These cathodes are Lithium Cobalt Oxide (LCO), Lithium Manganese Oxide (LMO), Lithium Nickel Cobalt Manganese Oxide (NCM 622), and Lithium Nickel Cobalt Manganese Oxide (NCM 424). Additionally, three new electrode formulations of existing materials were added, two compositions of Lithium Nickel Manganese Oxide (5V Spinel) and one composition of Lithium Nickel Cobalt Manganese Oxide (NCM 523). At the end of FY14 the Electrode Library contained ten anode electrodes and fifteen cathode electrodes. New material candidates are continuously being studied and may be added to the Electrode Library in FY15 if the need exists.

In FY14, a total of 40 different organizations utilized the CAMP Facility's Electrode Library. The breakdown of these organizations is as follows: 19 companies, 8 national laboratories (including ANL) and 13 universities. Figure IV - 35 is a summary of the many organizations that have used the CAMP Facility's services in the last several years. The total amount of electrodes used by all of the organizations was 871 sheets of electrodes (1 sheet = 220mm x 110mm), yielding a total electrode area of 21.1 square meters. This is over double of what was distributed in FY13. The 871 sheets breaks down to the following usage: 423 sheets to industry, 213 sheets to other national laboratories, 116 sheets to Argonne researchers, and 119 sheets to universities. The number of Electrode Library users is likely to increase further in FY15.



Figure IV - 35: Organizations that have used the CAMP Facility's services over the last several years.

CAMP Analyzer: In FY14 the CAMP Facility completed the electrochemical cell data processing tool, known as the CAMP Analyzer. This software package consists of seven Excel templates to be used for data processing, work instructions, example testing protocols, a revision log, and issue/improvement reporting form. This software package was copyrighted by Argonne National Laboratory on 5/23/14.

The CAMP Analyzer's data processing templates cover the following analysis areas; Formation, Rate Study, Hybrid Pulse Power Capability Test, Cycle Life, Extended HPPC Plotter, Average Cycle Life, and Average Extended HPPC Plotter. Each one of these templates allows the user to upload a testing data file, input basic cell information and have the software run analysis for a given test. The software then presents the data (for 1-8 cells) in a standard format with statistical analysis. This software is flexible in that it is not locked into a single cell chemistry and can equally handle half-cell data. The software was designed with this flexibility so that it could be used by a wide range of battery researchers. Some plots that depict the capabilities of the CAMP Analyzer are shown in Figure IV - 36 and Figure IV - 37.

Distribution of the CAMP Analyzer to organizations outside of Argonne was begun in FY14. Additionally, Argonne has begun to adopt this new software package for use in all new battery research and development projects. The CAMP Facility looks to further distribute the CAMP Analyzer to other companies, national laboratories and universities in FY15.

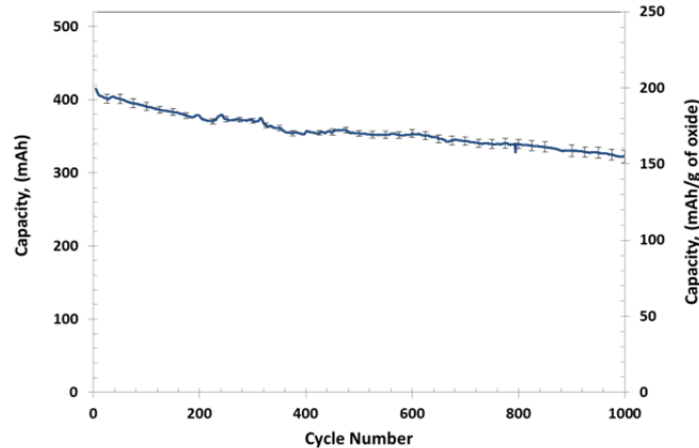


Figure IV - 36: Cycle Life Test analysis done with the CAMP Analyzer showing data with statistical error bars present. (8 Cells)

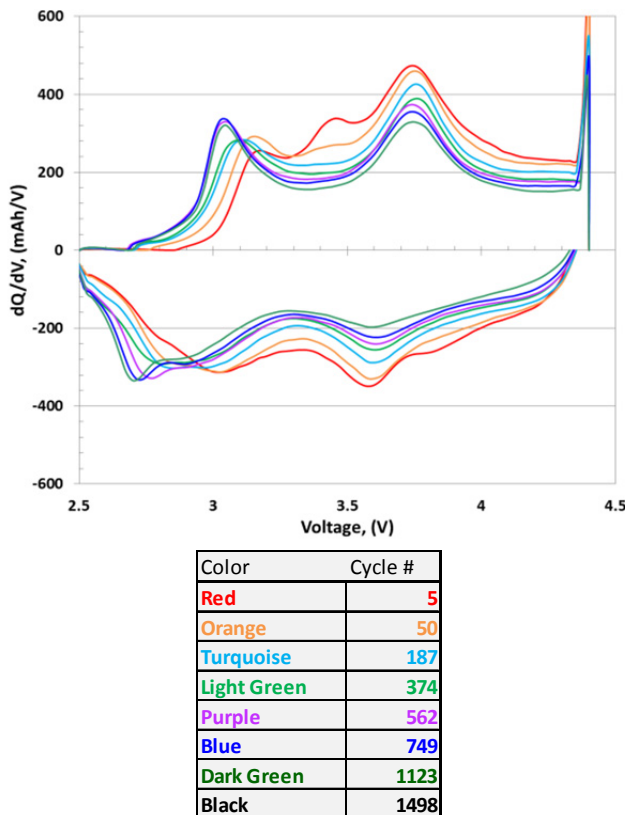


Figure IV - 37: Cycle Life Test analysis tracking the dQ/dV plot as a function of cycle number. The cycle numbers are selected by the user in the CAMP Analyzer

Conclusions and Future Directions

Significant effort was spent these past two years in developing a viable silicon-graphite anode that could be used in prototype pouch cell builds and in the Electrode Library. These efforts were very successful this year. The key to this success was a combination of: the selection of a commercially available silicon nanomaterial; optimization of the LiPAA binder system; selection of a graphite material with morphology conducive to mixing with silicon and LiPAA binder; and optimization of mixing processes with additional equipment. These results are discussed in detail in this report and will form the basis of future publications on silicon electrode development in the CAMP Facility.

Improvements were made to cell systems using LMR-NMC cathodes in terms of electrolyte additives and electrode designs. Much was learned via diagnostics, post-test analysis, and electrochemical modeling of this high energy cathode. Even though the emphasis on LMR-NMC cathodes has diminished due to the inherent problem of voltage fade in this class of materials, the knowledge and capability gained in this effort will be a great benefit to future endeavors in the CAMP Facility. One of the main messages from the

CAMP Facility is discoveries that work well in simple coin cell designs may not always work in full size cell systems. Validation in commercially recognized prototype cells is needed to save valuable resources later on.

In FY15, efforts will continue on improving the electrochemical and mechanical performance of the silicon-graphite anode. An emphasis will be placed on optimizing the LiPAA binder system for electrodes with capacity loadings $> 3 \text{ mAh/cm}^2$. The electrode swelling during lithiation will be monitored in this development work. Now that a viable silicon-graphite electrode is available for electrochemical studies, effort will be directed to developing electrolyte additives that can form a robust and harmonious SEI layer on the silicon and graphite surfaces. The main goal is to fabricate a pouch cell build using a silicon-based anode and a high energy (LMR-NMC) cathode.

The CAMP Facility will work closely with the new High Energy/High Voltage Program at Argonne with effort directed toward fabricating electrodes (and pouch cells) that use uncoated and coated NMC and/or LMR-NMC particles. A new class of lower-lithium LMR-NMC cathode materials are being scaled up within the MERF at Argonne that appear to be less affected by the problem of voltage fade. The CAMP Facility will

evaluate these materials in pouch cell builds as they become available.

Additional activities will be pursued to understand the mechanisms taking place in high energy cell systems. Chief among these is determining the effect of electrode thickness. Being able to use thicker (higher capacity loading) electrodes presents significant opportunities to lower the hardware cost of the cell/battery system (less foil and separator required).

Failure mechanisms of new energy storage chemistries will be determined, and remedies proposed, using diagnostic techniques within the CAMP Facility coupled with the support of the Post-Test Facility at Argonne.

A continuing effort to examine the unique LMR-NMC positive electrode impedance behavior using an intercalation active material electrochemical model was completed. The work confirmed the model's utility, as well as its limitations, for describing LMR-NMC electrode electrochemical behavior under transportation application testing protocols. The development of advanced electrochemical models focusing on high energy lithium ion electrochemical couples will continue. A small effort to model silicon-graphite electrodes will be expanded as high quality electrode data becomes available.

FY 2014 Publications/Presentations

1. "From coin cells to 400 mAh pouch cells: Enhancing performance of high-capacity lithium-ion cells via modifications in electrode constitution and fabrication", S.E. Trask, Y. Li, J.J. Kubal, M. Bettge, B.J. Polzin, Y. Zhu, A.N. Jansen, and D.P. Abraham, *J. Power Sources* **259** (2014) 233-244.
2. "Mitigating performance degradation of high-capacity lithium-ion cells with boronate-based electrolyte additives", Y. Zhu, Y. Li, and D.P. Abraham, *J. Electrochemical Society* **161** (2014) A1580-A1585.
3. "TOF SIMS characterization of SEI layer on battery electrodes", I.IV. Veryovkin, C.E. Tripa, A.IV. Zinovev, S.IV. Baryshev, Y. Li, and D.P. Abraham, *Nuclear Instruments and Methods in Physics Research Section B: Beam Interactions with Materials and Atoms* **332** (2014) 368-372.
4. "Effect of Interface Modifications on Voltage Fade in $0.5\text{Li}_2\text{MnO}_3 \bullet 0.5\text{LiNi}_{0.375}\text{Mn}_{0.375}\text{Co}_{0.25}\text{O}_{0.2}$ Cathode Materials", I. Bloom, L. Trahey, A. Abouimrane, I. Belharouak, X. Zhang, Q. Wu, W. Lu, D.P. Abraham, M. Bettge, J. Elam, X. Meng, A. Burrell, C. Ban, R. Tenant, J. Nanda, and N. Dudney, *J. Power Sources* **249** (2014) 509-514.
5. "Electrolyte Additive Performance in Lithium Ion Batteries: From Coin Cells to 400-mAh Pouch Cells", B. Polzin, S. Trask, Y. Zhu, Y. Li, M. Bettge, D. Abraham, and A. Jansen, presented at the *225th Meeting of the Electrochemical Society*, Orlando, FL, May 11-16, 2014.
6. "Mn(II) Deposition on Anodes and Its Effect on Capacity Fade in Spinel LiMn_2O_4 -Carbon System", Jun Lu, Chun Zhan, Jeremy Kropf, Tianpin Wu, Andrew N. Jansen, Yang-Kook Sun, Xinping Qiu, and Khalil Amine, presented at the *225th Meeting of the Electrochemical Society*, Orlando, FL, May, May 11-16, 2014.
7. "Bridging the Gap in Li-ion Technology": Examining Novel Materials and Designs in Cells Greater than 200 mAh", Stephen E. Trask, Yan Li, Joseph J. Kubal, Martin Bettge, Bryant J. Polzin, Ye Zhu, Andrew N. Jansen, and Daniel P. Abraham, poster presented at *31st Battery Seminar & Exhibit*, Fort Lauderdale, FL, March 10-13, 2014.
8. "Long Term Cycling Performance of High-Capacity Lithium-Ion Full Cells with $\text{Li}_{1.2}\text{Ni}_{0.15}\text{Mn}_{0.55}\text{Co}_{0.1}\text{O}_2/\text{Li}_4\text{Ti}_5\text{O}_{12}$ ", Y. Li, M. Bettge, Y. Zhu, J. C.M. Li, and D.P. Abraham, *225th Meeting of the Electrochemical Society*, Orlando, FL, May 11 – 15, 2014.
9. "Designing Electrolyte Additives for High-Capacity Lithium-Ion Cells", D.P. Abraham, Y. Zhu, Y. Li, and I. Shkrob, *International Battery Association (IBA-2014) Meeting*, Brisbane, Australia, March 3 – 7, 2014.
10. "Diagnostic examination of high-energy Li-ion cells containing alumina-coated $\text{Li}_{1.2}\text{Ni}_{0.15}\text{Mn}_{0.55}\text{Co}_{0.1}\text{O}_2$ -based positive electrodes", D.P. Abraham, M. Bettge, Y.Zhu, and Y. Li, *Materials Challenges in Alternative & Renewable Energy (MCARE 2014)*, Clearwater, FL, February 16 – 20, 2014.
11. "Designing Electrode Coatings to Enhance Life of Lithium-Ion Cells", D.P. Abraham, M. Bettge, Y.Zhu, and Y. Li, *Advanced Automotive Battery Conference (AABC-2014)*, Atlanta, GA, February 3 – 7, 2014.
12. "Pulsed Sonication for Alumina Coatings on High-Capacity Oxides: Performance in Lithium-ion Cells", IV.G. Pol, Y. Li, F. Dogan, E. Secor, M.M. Thackeray, D.P. Abraham, *J. Power Sources* **258** (2014) 46-53.
13. "High-Energy Cell Development in the Cell Analysis, Modeling, and Prototyping (CAMP) Facility at Argonne", Andrew N. Jansen, Bryant J. Polzin, Stephen E. Trask, Wenquan Lu, Daniel P. Abraham, and Dennis W. Dees, *Advanced Automotive Battery Conference, (AABC 2014)*, Atlanta, GA, February 3-7, 2014.

14. "Lithium-Ion Batteries: Endless Uses", A.N. Jansen, *Chemical Engineering Progress* (2013) 57–64.
15. "Mechanistic Insight into the Protective Action of Bis(oxalato)borate and Difluoro(oxalate)borate Anions in Li-Ion Batteries", I.A. Shkrob, Y. Zhu, T.W. Marin, and D.P. Abraham, *J. Phys. Chem. C* **117** (2013) 23750–23756.
16. "Perfluoroalkyl-substituted ethylene carbonates: novel electrolyte additives for high-voltage lithium-ion batteries", Y. Zhu, M.D. Casselman, Y. Li, A. Wei, D.P. Abraham, *J. Power Sources* **246** (2013) 184–191.
17. "Electrolyte Additive Combinations that Enhance Performance of $\text{Li}_{1.2}\text{Ni}_{0.15}\text{Mn}_{0.55}\text{Co}_{0.1}\text{O}_2$ -Graphite Lithium-ion Cells", Y. Zhu, Y. Li, M. Bettge, and D.P. Abraham, *Electrochimica Acta* **110** (2013) 191–199.
18. "Understanding Long-Term Cycling Performance of $\text{Li}_{1.2}\text{Ni}_{0.15}\text{Mn}_{0.55}\text{Co}_{0.1}\text{O}_2$ -Graphite Lithium-ion Cells", Y. Li, M. Bettge, B. Polzin, Y. Zhu, M. Balasubramanian, and D.P. Abraham, *J. Electrochemical Society* **160** (2013) A3006 – 3019.
19. "Improving High-Capacity $\text{Li}_{1.2}\text{Ni}_{0.15}\text{Mn}_{0.55}\text{Co}_{0.1}\text{O}_2$ -based Cells by modifying the positive electrode with alumina", M. Bettge, Y. Li, B. Sankaran, N.D. Rago, T. Spila, R.T. Haasch, I. Petrov, and D.P. Abraham, *J. Power Sources* **233** (2013) 346 – 357.
20. "Voltage Fade of Layered Oxides: Its Measurement and Impact on Energy Density", M. Bettge, Y. Li, K. Gallagher, Y. Zhu, Q. Wu, W. Lu, I. Bloom, and D.P. Abraham, *J. Electrochemical Society* **160** (2013) A1-A10.
21. "Correlating Cation Ordering and Voltage Fade in a Lithium-Manganese-Rich Lithium-Ion Battery Cathode Oxide: a Joint Magnetic Susceptibility and TEM Study", D. Mohanty, A.S. Sefat, J. Li, R.A. Meisner, A.J. Rondinone, E.A. Payzant, D.P. Abraham, D.L. Wood, III, and C. Daniel, *Physical Chemistry Chemical Physics* **15** (2013) 19496–19509.
22. "Neutron Diffraction and Magnetic Susceptibility Studies on a High-Voltage $\text{Li}_{1.2}\text{Ni}_{0.15}\text{Mn}_{0.55}\text{Co}_{0.1}\text{O}_2$ lithium-ion Battery Cathode; an Insight to the Crystal Structure", D. Mohanty, A. Huq, E.A. Payzant, A.S. Sefat, J. Li, D.P. Abraham, D.L. Wood, III, and C. Daniel, *Chem. Mater.* **25** (2013), pp 4064–4070.
23. 2014 U.S. DOE Vehicle Technologies Office Annual Merit Review and Peer Evaluation Meeting, Washington, D.C.
24. Additional publications and presentations are included in Section IV.B.2.

References

1. D. Dees, E. Gunen, D. Abraham, A. Jansen, and J. Prakash, *J. Electrochem. Soc.*, **152** (7) (2005) A1409.
2. D. Abraham, S. Kawauchi, and D. Dees, *Electrochim. Acta*, **53** (2008) 2121.
3. D. Dees, E. Gunen, D. Abraham, A. Jansen, and J. Prakash, *J. Electrochem. Soc.*, **155** (8) (2008) A603.

IV.B.2 CAMP Materials Benchmarking Activities (ANL)

Wenquan Lu (PI)

Argonne National Laboratory

9700 S. Cass Avenue

Argonne, IL 60439

Phone: (630) 252-3704; Fax: (630) 972-4414

E-mail: iuw@anl.gov

Collaborators:

Qingliu Wu (ANL)

Khadija Yassin-Lakhsassi (ANL)

Steve Trask (ANL)

Bryant Polzin (ANL)

Andrew Jansen (ANL)

Daniel Abraham (ANL)

Zhengcheng (John) Zhang (ANL)

Christopher Johnson (ANL)

Dennis Dees (ANL)

Khalil Amine (ANL)

Gary Henriksen (ANL)

Hui Zhao (LBNL)

Gao Liu (LBNL)

Cell Analysis Modeling and Prototyping Facility
(CAMPF-ANL)

Materials Engineering Research Facility (MERF-
ANL)

3M (U.S.)

Superior Graphite (U.S.)

PSI (U.S.)

FMC (U.S.)

Cabot (U.S.)

Toda Kogyo (Japan)

Daikin (Japan)

Subcontractor:

Illinois Institute of Technology, Chicago, IL

Start Date: October 1st, 2012

End Date: September 30th, 2014

Objectives

The primary objective is to identify and evaluate low-cost materials and cell chemistries that can simultaneously meet the life, performance, and abuse

tolerance goals for batteries used in PHEV and EV applications.

A secondary objective is to enhance the understanding of the impact of advanced cell components and their processing on the electrochemical performance and safety of lithium-ion batteries.

Technical Barriers

On one hand, an overwhelming number of materials are being marketed by vendors for lithium-ion batteries. It is a challenge to down select and screen these materials effectively within the allocated scope of this project.

On the other hand, there are no commercially available high energy materials that can produce a battery capable of meeting the 40-mile all-electric-range (AER) within the weight and volume constraints established for PHEVs by DOE and the USABC. Identification of new high-energy electrode materials is the primary goal for this project.

During the validation process, we often encounter a broad variation in chemical and physical properties when validating their electrochemical performance and safety related characteristics. This makes it very challenging to fabricate optimized electrodes with little knowledge of the impact of formulation and processing on electrode performance.

Technical Targets

- Higher energy density electrode materials identification and evaluation.
- Characterization of inert, but critical cell components which can enable the better cell performance.
- Technical support to the Cell Assembly Modeling and Prototyping (CAMP) facility and Materials Engineering Research Facility (MERF).

Accomplishments

- A high energy density silicon anode continues to be the focus for fiscal year. In addition to the previously tested silicon materials from XG sciences, Nanoamour, and Sigma-Aldrich, silicon materials from 3M and American Elements were also examined. Electrochemical characterization was completed using coin type cells, while pouch cells were fabricated and studied by the CAMP Facility.

- As a key component for silicon electrode, a conductive binder, developed at Lawrence Berkeley National Laboratory (LBNL) by Dr. Gao Liu, was successfully validated at ANL. It was found that pure silicon electrode with this binder alone (no conductive additives) can deliver over 2000mAh/g capacity with reasonable capacity retention. Furthermore, this conductive binder was scaled up at the Materials Engineering Research Facility (MERF) at ANL and its electrochemical performance was also validated.
- The high voltage and high energy capabilities of various lithium transition metal oxides (NCM424 and NCM523) were explored. Good capacity retention up to 4.5V with over 190mAh/g was observed.
- A PVDF separator was investigated. It was found that the PVDF separator with larger porosity can improve the electrochemical performance of lithium manganese rich composite cathode material (LMR-NMC).



Introduction

This benchmarking effort is conducted as part of the Cell Analysis Modeling and Prototyping (CAMP) facility (Refer to IV.B.1) to overcome the “valley of death”, which happens when a new discovery is traversed to commercial product. The CAMP Facility is appropriately sized to enable the design, fabrication, and characterization of high-quality prototype cells with around 400-mAh capacity, which straddles the gap between coin cells and full cells nicely – two orders of magnitude from each end point. Thus, a realistic and consistent evaluation of candidate chemistries is enabled in a time-effective manner with practical quantities of novel materials.

However, the CAMP facility is more than an arrangement of equipment, it is an integrated team effort designed to support the production of prototype electrodes and cells. In order to utilize the facility more efficiently and economically, cell chemistries are validated internally to determine if they warrant further consideration.

High energy density electrode materials are required in order to achieve the 40-mile AER within the weight and volume constraints established by DOE and the USABC. One would need a combination of anode and cathode materials that provide 420mAh/g and 220mAh/g, respectively, as predicted by Argonne’s battery design model, if one uses a 20% margin for energy fade over the life of the battery assuming an average cell voltage of 3.6 volts. Therefore, the search

for new high energy density materials is the focus of this project.

In addition to electrode materials, other cell components, such as separators, binders, current collectors, etc., are evaluated to establish their impact on electrochemical performance, thermal abuse, and cost.

Approach

Once the promising chemistries, from new commercially available materials, as well as new high energy density materials under development, are identified, coin cells (2032 size) will be used as test vehicle for the initial screening studies, which typically includes formation cycles, hybrid pulse power characterization (HPPC) tests, rate capability testing, and limited cycle life testing. Accelerated aging studies are also performed at 45°C to 55°C for promising materials to give a preliminary indication of life. Where appropriate, the thermal abuse response is studied using a differential scanning calorimeter.

After the validation, decision will be made to either advance, modify, or terminate studies to maximize utilization of available resources. If promising results are obtained with coin cells, the promising chemistries will be recommended for more extensive evaluation under the CAMP Facility, which includes advanced electrochemical analysis, electrochemical modeling, larger format cell design and long term testing.

Results

Silicon anodes have been recognized for several years as the most likely next generation high energy anode material. Despite of its inherent high energy density and many recognized breakthroughs, there still a long way for silicon to penetrate the transportation market for lithium ion batteries. In order to mitigate the gap, we have spent a significant effort to advance the energy density of lithium ion batteries by investigating the silicon material in the past few years. In this report, we will present two silicon composite materials from 3M and American Elements.

Silicon alloy from 3M is the closest to a drop-in replacement for the graphite anode of any material we have examined to-date. In this work, the electrode for validation is fabricated at 3M with composition listed in Table IV - 8. By introducing silicon alloy, the reversible specific capacity of the active material (including silicon alloy, KS6, and MAGE) can be boosted to over 460mAh/g (see Figure IV - 38) from about 350mAh/g of graphite. The electrolyte used for this study is 10%FEC in 1.2M LiPF₆ in EC/EMC. Also, the volume expansion of this electrode was greatly mitigated by only 15% silicon alloy.

Table IV - 8: The composition of silicon alloy electrode from 3M

Silicon Alloy	15wt.%
KS6	10wt.%
MAGE	65wt.%
LiPAA	10wt.%

In addition to its high energy density, this silicon electrode possessed excellent rate performance as shown in Figure IV - 39. It can be seen from this figure that there is almost no capacity loss up to 2C discharge. The half cell

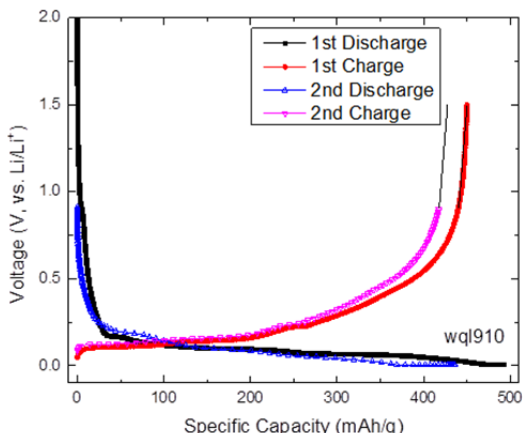


Figure IV - 38: Voltage profile of silicon alloy electrode received from 3M

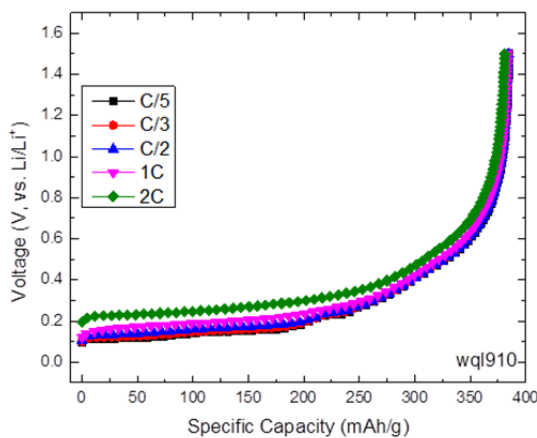


Figure IV - 39: Voltage profile of silicon alloy electrode received from 3M

Commercially available silicon from American Elements (AE) was tested as anode material for lithium ion batteries. The impact of particle size on the electrochemical performance was investigated using 50nm, 150nm, and 1μm particles. The electrode composition was Si:Graphene: PAA = 40%:40%:20%. The electrolyte used for this study was 10% FEC in 1.2M LiPF₆ in EC/EMC Total 5C rate test, C/5, C/3, C/2, 1C, and 2C, were applied to the electrodes consisting of various particle sizes following 3

formation cycles. There were three cycles for each rate. The specific capacity as a function of cycle number is shown in Figure IV - 40. It is very obvious that the electrode consisting of 1μm particles could not be cycled, exhibiting rapid capacity decay. With decreasing particle size, the capacity retention increased. The electrode with 50nm particle not only shows excellent rate performance, but also good capacity retention. This finding is consistent to the previous finding that the silicon with nano size can mitigate the volume expansion issue and provide promising electrochemical performance. Currently, the CAMP Facility is investigating the silicon electrode using 50nm silicon powder in a pouch cell format (Refer to the previous section IV.B.1)

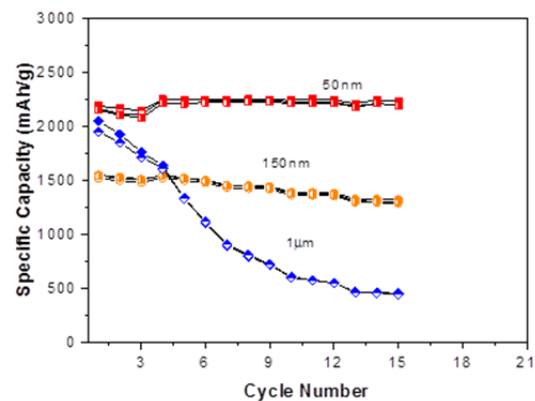


Figure IV - 40: Cycle performance of silicon electrodes consisting of various particle sizes

Conductive binder for silicon electrode was developed at LBNL by Dr. Gao Liu. This conductive binder can play a huge role in the success of the silicon electrode. We have tested and report the positive results last year by using the electrode fabricated at LBNL. This year, we validated the electrode making process by using the conductive binder Poly(9,9-dioctylfluorene-co-fluorenone-comethylbenzoic ester) (PFM) produced at LBNL. In this study, we fabricated electrode using various silicon materials (from NanoAmor and American Elements) with various particle sizes.

Figure IV - 41 shows the voltage profile of silicon electrodes using American Element silicon with high loading (more than 0.1mg/cm², top) and low loading (less than 0.1mg/cm², bottom). The particle size is 50nm. The electrode composition is 33% PFM and 67% silicon. The electrolyte used for this study is 10%FEC in 1.2M LiPF₆ in EC/EMC It can be seen clearly from this figure that all 5 electrodes with high loading can only be lithiated for less than one hour and no delithiation step at all during 1st cycle using C/10 rate. However, using the same composition, same silicon material, and same binder, all 4 electrodes with low loading can be charged and discharged normally except for one cell. The abnormal long lithiation of the peculiar electrode may

be due to a weighing error, since the loading was very low and the balance was close to its limit. Irrespective of the outlier, the results strongly suggested that the electrochemical performance of the silicon electrode using the conductive binder is very sensitive to the loading of the electrode, which needs to be addressed in its future development. During the investigation, we also fabricated the electrode using the large silicon particle (150nm) from same company (American Elements) and no electrochemical activity was observed, which indicated that the particle size also has impact on the binder performance.

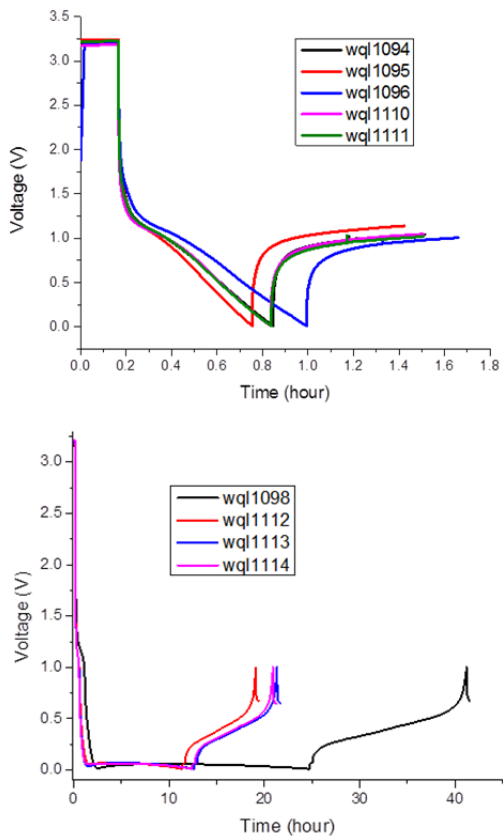


Figure IV - 41: Voltage profile of silicon electrodes with high loading (top) and low loading (bottom) using 50nm silicon particle from American Element. The PFM binder is provided by LBNL

The conductive PFM binder is being scaled up at MERF (ANL). The scaled-up binder materials were transferred to CAMP for electrochemical characterization. Using of the knowledge obtained previously, we fabricated an electrode using NanoAmor's 50nm silicon powder and the same electrode formulation. With the low material loading, all the half cells passed the electrochemical testing successfully. The electrochemical test result is shown in Figure IV - 42 below.

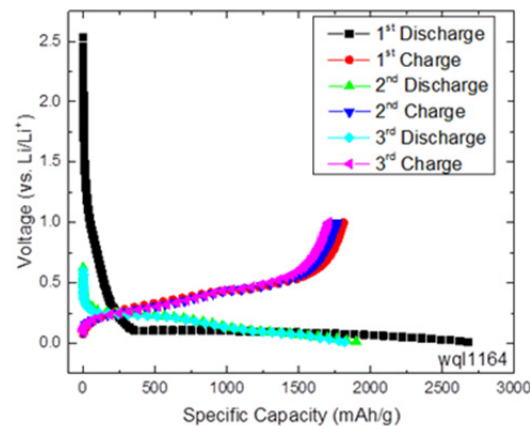


Figure IV - 42: Voltage profile of silicon electrodes with low loading using 50nm silicon particle from NanoAmor. The PFM binder is provided by MERF at ANL

High energy cathode materials are another major focus for benchmarking the cell chemistries. In the recent past, we have spent a lot of effort on lithium manganese rich (LMR) transition metal oxides, which were developed at ANL and can deliver over 900 Wh/kg. This year, we shifted the focus to nickel rich cathode materials, such as 40%, 50% or even 60% nickel in transition metals. These materials have been commercialized for years, but limited to lower cut-off voltage and low energy density compared to LMR. In this study, we have explored the possibility to charge the nickel rich cathode materials, including LiNi_{0.4}Co_{0.2}Mn_{0.4}O₂ (NCM424) and LiNi_{0.5}Co_{0.2}Mn_{0.3}O₂ (NCM523) from Toda, to higher voltages. The average voltage, discharge capacity, and specific energy density from first discharge at C/10 rate is listed in Table IV - 9. From the table, it can be seen that there is close to 68% specific energy density increase when the cut-off voltage is increased from 4.1V to 4.7V. The high specific energy density with highest cut-off voltage (886Wh/kg at 4.7V) is comparable to LMR, the state-of-art cathode material. The specific energy density increase is also significant, up to 44%, even when a lower cut-off voltage (4.5V) was used as cut-off voltage.

Table IV - 9: Average voltage, discharge capacity and energy density of NCM523 with various voltage windows at C/10 rate

Cut-off voltage	Average voltage	Capacity, mAh/g	Energy density, Wh/kg
4.1	3.77	141	531
4.3	3.84	171	657
4.5	3.90	196	764
4.7	4.08	217	886

Electrochemical cycleability of the NCM523 with various cut-off voltages was also tested and the preliminary results are shown in Figure IV - 43.

Apparently, up to 4.5V, the NCM523 electrode demonstrates very good capacity retention. Obvious capacity fading was observed when 4.7V was used as cut-off voltage. This result is obtained just using regular electrolyte, with no additives. The NCM523 material was used as received without further surface modification. Therefore, we believe that there is scope to further improve the electrochemical performance of this material when it is engineered and the better electrolyte is used.

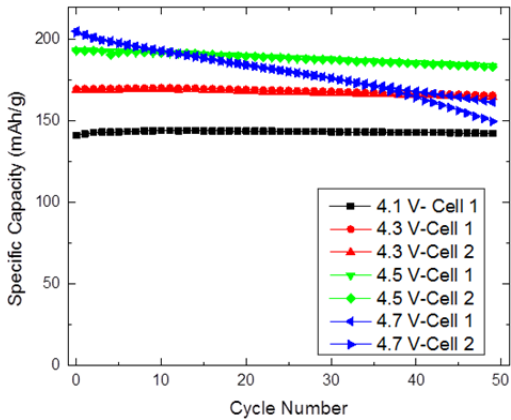


Figure IV - 43: Cycle performance of NCM523 half cell with various cut-off voltages

Other cell components, such as separator, binder, and additives, were evaluated to establish their impact on electrochemical performance, the test results were shared with material providers. A PVDF separator was investigated using full cells with Philips 66's graphite (A12) and LMR-NMC (Toda HE5050). The cycle life result is shown in Figure IV - 44. Compared to other commercially available polyolefin separator, the graphite/HE5050 full cells with PVDF separator show better capacity retention, only about 7% capacity loss after 50 cycle, which is considerably good for LMR-NMC material. The test results also indicate that less variation was obtained by using PVDF separator. The good capacity retention and reproducibility might be caused by the high porosity and good electrolyte absorption of PVDF separator, both of which can improve the conductivity and lower the resistance of the separator.

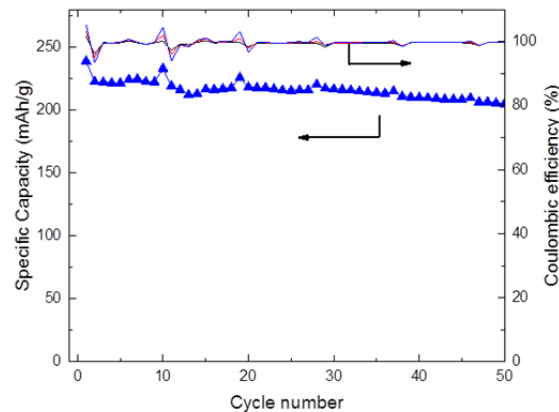


Figure IV - 44: Cycle performance of graphite/HE5050 full cell using PVDF separator

Conclusions and Future Directions

Under the material validation effort, several silicon anode materials were benchmarked using our internal electrochemical test procedure. The silicon alloy from 3M appears to be the drop-in replacement for conventional graphite anodes with higher specific capacity, good rate capability, and mitigated volume expansion. We also have better understanding of silicon particle size on its electrochemical performance. Good rate performance and capacity retention was obtained for silicon electrodes using commercially available nano size silicon powder from American Elements.

In another aspect of silicon electrode development, the conductive binders from both developer (LBNL) and scale up facility (MERF) at ANL were validated. Reasonable electrochemical performance was achieved by only using PFM conductive binder and silicon in the electrode formulation. However, further development is needed in order to address the loading issue.

Lithium transition metal oxide cathode materials were revisited by charging to higher voltages. The preliminary result of NCM523 indicated that this material can be at least charged to 4.5V, which can deliver close to 200mAh/g capacity, equivalent to 764Wh/kg. This finding opens a door for us to rethink the high energy density cathode materials for electric vehicle applications.

Other cell chemistries were investigated and electrochemical results of a PVDF separator were presented. In the future, we will continue to work on high energy cathode and anode, which can be used for automobile application. Other cell chemistries will be studies when they become available.

FY 2014 Publications/Presentations

1. Insight into the Structural Evolution of a High-Voltage Spinel for Lithium-Ion Batteries, Qingliu Wu, Yuzi Liu, Christopher S. Johnson, Yangxing Li, Dennis W. Dees, and Wenquan Lu, *Chem. Mater.*, 2014, 26 (16), pp 4750–4756.
2. Electrochemical and Thermal Studies of $\text{LiNi}_{0.8}\text{Co}_{0.15}\text{Al}_{0.05}\text{O}_2$ under Fluorinated Electrolytes, Aadil Benmayza, Wenquan Lu, Vijay Ramani, Jai Prakash, *Electrochimica Acta*, 01/2014; 123:7–13.
3. Rate-dependent, Li ion insertion/deinsertion behaviour of LiFePO_4 cathodes in commercial 18650 LiFePO_4 cells. Qi Liu, Hao He, Zhe-Fei Li, Yadong Liu, Yang Ren, Wenquan Lu, Jun Lu, Eric A Stach, Jian Xie, *ACS Applied Materials & Interfaces*, 2014, 6 (5), pp 3282–3289.
4. Silicon Based Nanomaterials for Lithium Ion Batteries - A Review Article, Xin Su, Qingliu Wu, Juchuan Li, Xingcheng Xiao, Amber Lott, Wenquan Lu, Brian Sheldon, and Ji Wu, *Advanced Energy Materials*, Vol. 4, 2014, 1300882.
5. Effect of Interface Modifications on Voltage Fade In Lithium-Manganese-Rich, Li-Ni-Mn-Co-O Cathode Materials, I. Bloom, L. Trahey, A. Abouimrane, I. Belharouak, H. Wu, Q. Wu, W. Lu, D. P. Abraham, M. Bettge, and A. Burrell, *J. Power Sources*, Vol. 249, 2014, p509-514.
6. Investigations on High Energy Lithium-Ion Batteries with Aqueous Binder, Qingliu Wu, Seonbaek Ha, Jai Prakash, Dennis W. Dees, and Wenquan Lu, *Electrochim. Acta.*, Vol. 114, 2013, p1-6.
7. Voltage fade of layered oxides: its measurement and impact on energy density, Martin Bettge, Yan Li, Kevin Gallagher, Ye Zhu, Qingliu Wu, Wenquan Lu, Ira Bloom, Daniel P. Abraham, *J. Electrochem. Soc.*, 160 (11), 2013, A2046-A2055.
8. Lithium Manganese Rich Transition Metal Oxide as Cathode for Lithium Ion Batteries, W. Lu, Q. Wu, D. Gosztola, IV. Maroni, Y. Liu, C. Johnson, and D. Dees, 2014 Electrochemical Conference on Energy & the Environment, Shanghai, PR China, March 13-16, 2014.
9. Aqueous Binders for Lithium Ion Batteries, W. Lu, *Battery Power 2014*, Denver, CO, U.S., Aug 6-7, 2014.
10. Electrochemical Characterization of Lithium and Manganese Rich Composite Material for Lithium Ion Batteries, Wenquan Lu, Qingliu Wu and Dennis W. Dees, 224 Electrochemical Society, San Francisco, CA Oct. 27-NoIV. 1, 2013.
11. Insight into the Structural Changes of High-Voltage Spinel during the Lithium Intercalation, Qingliu Wu, Yuzi Liu, Christopher Johnson, Dennis W. Dees, Wenquan Lu, 224 Electrochemical Society, San Francisco, CA Oct. 27-NoIV. 1, 2013.

IV.B.3 Impact of Materials on Abuse Response (SNL)

Christopher J. Orendorff, Ganesan Nagasubramanian, and Kyle R. Fenton
Sandia National Laboratories
P. O. Box 5800, Mail Stop 0614
Albuquerque, NM 87185-0614
Phone: (505) 844-5879; Fax: (505) 844-6972
E-mail: corendo@sandia.gov

Collaborators:
Prof. Steven George, CU-Boulder
Rob Privette, XG Sciences
Andrew Jansen, ANL

Start Date: October 2013
Projected End Date: September 2014

Objectives

- Elucidate degradation mechanisms in lithium-ion cells that lead to poor abuse tolerance (runaway thermodynamics, gas evolution, electrolyte combustion).
- Develop and evaluate advanced materials (or materials combinations) that will lead to more abuse tolerant lithium-ion cell and battery systems.
- Build 18650 cells in the SNL fabrication facility for cell level evaluation of new materials in support of all ABR thrust areas.

Technical Barriers

There are several technical barriers to achieving the goals stated above including:

- Develop advanced material components designed to improve the intrinsic abuse tolerance of lithium-ion cells and do not lead to high order catastrophic failures.
- Mitigate the gas evolution and decomposition of the electrolyte.
- Passivation of cathode runaway reactions and interfacial reactions with electrolyte.
- Limited quantities of advanced materials (and numbers of cells with new materials) to evaluate abuse response.

Technical Targets

- Quantify the thermal runaway response of materials at the cell level (18650).

- Determine the effect of high energy materials, electrolyte salts, solvents and additives on the abuse response of lithium-ion cells.
- Determine the effect of advanced material components on the abuse response of lithium-ion cells.
- Optimize electrochemical performance of new electrolyte components to meet DOE goals.

Accomplishments

- Continued evaluation of candidate electrolytes and salts that minimize the energetics of thermal runaway.
- Evaluation of additives, electrode coatings, and new materials to improve abuse response and safety of lithium-ion systems.
- Fabricated electrodes to aid in standardization of ABR materials across national laboratories (round robin).
- Demonstration of the baseline performance and abuse tolerance characteristics of NMC cells with LiF/ABA.



Introduction

As lithium-ion battery technologies mature, the size and energy of these systems continues to increase (> 50 kWh for EVs); making safety and reliability of these high energy systems increasingly important. While most materials advances for lithium-ion chemistries are directed toward improving cell performance (capacity, energy, cycle life, etc.), there are a variety of materials advancements that can be made to improve lithium-ion battery safety. Issues including energetic thermal runaway, electrolyte decomposition and flammability, anode SEI stability, and cell-level abuse tolerance continue to be critical safety concerns. This report highlights work with our collaborators to develop advanced materials to improve lithium-ion battery safety and abuse tolerance and to perform cell-level characterization of new materials.

Approach

The effect of materials (electrolytes, additives, anodes, and cathodes) on the thermal response of full cells is determined using several techniques. One of the most useful and quantitative techniques is accelerating

rate calorimetry (ARC). The ARCs at SNL are fitted with uniquely designed high pressure fixtures to not only measure quantitative heat flow but also gas generation under ideal adiabatic conditions during full cell runaway. Cells were fabricated using a variety of active materials, electrolytes, and additives in the SNL cell prototyping facility. The in-house prototyping capability gives us the versatility to target candidate materials, perform full cell evaluation, and correlate cell response to fundamental materials properties.

Abuse tolerance tests are performed which evaluate the response to expected abuse conditions and document and evaluate numerous outcomes including 1) failure point of energy storage device 2) conditions that cause failure 3) failure modes and abuse conditions using destructive physical analysis (DPA) 4) quantitate cell or module response to the abuse condition 5) provide feedback to develop new abuse test procedures that more accurately determines cell performance under the most likely abuse conditions.

Our approach to developing advance materials to improve abuse response focuses on redesigning lithium-ion cell electrolytes. This work starts with developing novel two-part electrolyte salts based on inherently stable lithium salts and anion binding agents (ABAs). The ABA components have two important design features: (1) improve the solubility of lithium salts in carbonate solvents by coordinating the salt negative ion at the electron withdrawing coordination site of the ABA and (2) passivate chemical decomposition

reactions at electrode interfaces or in the bulk electrolyte to minimize the consequences and severity of thermal runaway and electrolyte combustion.

Results

High Energy Materials: One objective for FY14 is to determine baseline safety performance and thermal stability of high energy lithium-ion materials, including silicon-composite anode materials. The largest barrier to the success of this effort to date has been the availability and access to these high energy materials. In FY14, we began collaboration with XG Sciences to evaluate their Si-C (graphene) composite anode material. Electrodes were prepared at SNL and cells evaluated to determine electrochemical performance to ensure consistency with what has been done at LBNL, ANL, and XG Sciences. In addition, initial thermal performance to determine abuse tolerance of Si-based electrode materials for lithium-ion was also evaluated. Figure IV - 45 shows the discharge capacity of NMC523 18650 cells with graphite (green trace) and the XG Si-C (blue trace) anode electrodes. It is important to note that the Si-C anode electrode is prepared at $\sim 3 \text{ mg/cm}^2$ loading, because of mechanical instabilities (cracking) at higher loadings. This low loading is consistent with observations made at other institutions on Si-composite anodes and work will continue in FY15 to improve the loading and specific energy of these materials.

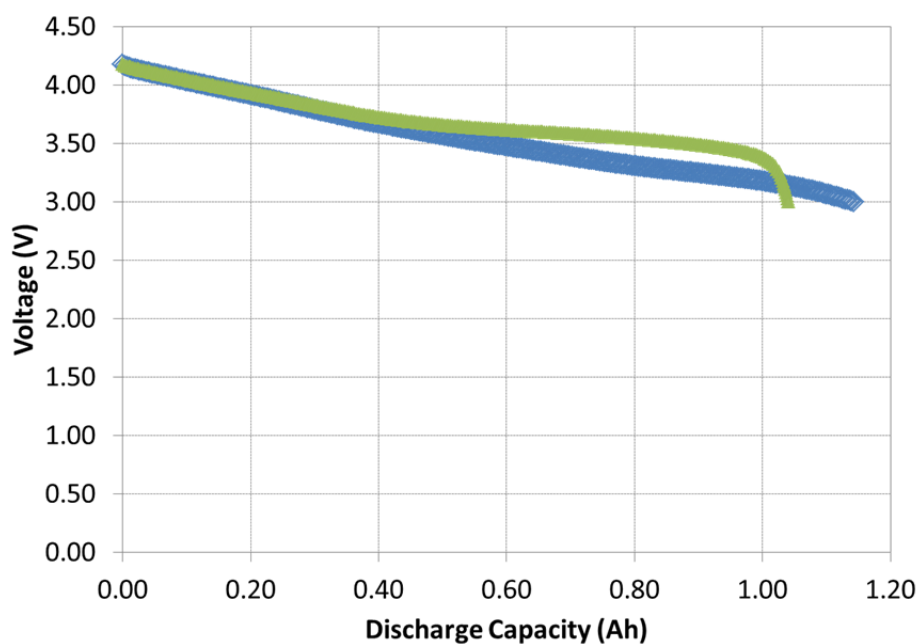


Figure IV - 45: Discharge capacity of NMC 523 18650 cells with graphite (green trace) and XG Si/C composite (blue trace) anodes

We also performed initial calorimetry work on 18650 cells to determine the baseline thermal performance of these materials. Figure IV - 46 shows the ARC profiles for representative NMC cells with Si-C and graphite anodes. The onset for the high rate runaway reaction is the same for both anodes. However, the NMC/Si-C cell shows a ~10% increase in the total

runaway enthalpy relative to the graphite cell with a greater total temperature rise during the runaway. This observation is consistent with the DSC measurements on the Si-C and graphite materials, shown in Figure IV - 47. The Si-C materials show ~10% greater specific heat output during decomposition and that heat generation is shifted to higher temperature relative to graphite.

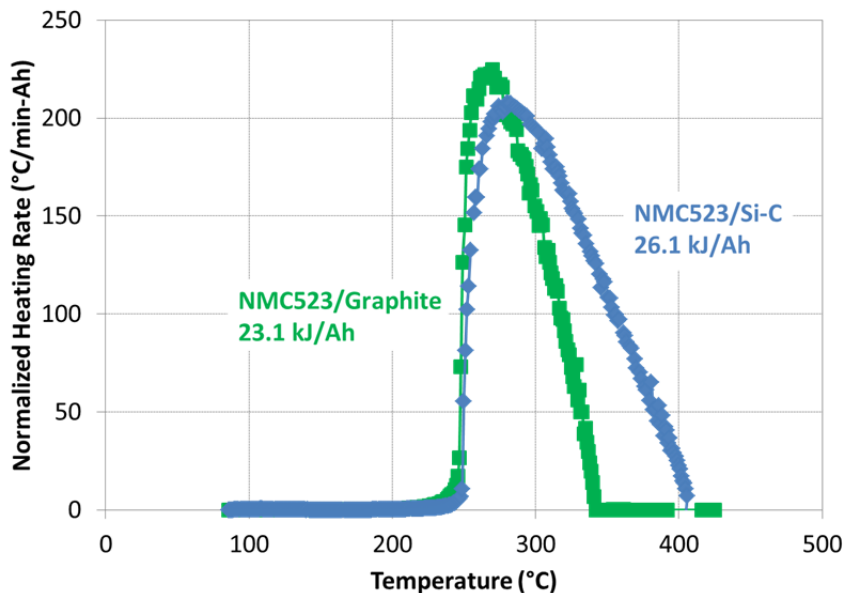


Figure IV - 46: ARC profiles during thermal runaway from NMC 523/graphite (green trace) and NMC523/Si-C (blue trace) 18650 cells

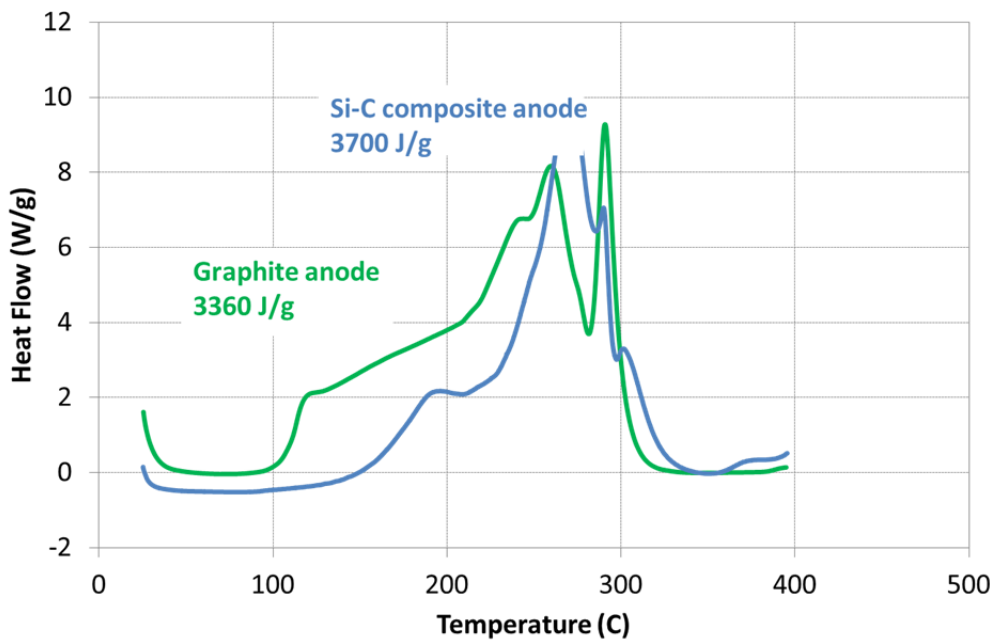


Figure IV - 47: DSC response for NMC graphite (green trace) and Si-C composite (blue trace) anode materials

Gas analysis (volume and chemical analysis) was also performed on cells with Si-C negative electrodes.

Figure IV - 48 shows the moles of gas produced in the calorimetry fixture during thermal runaway, plotted vs.

temperature. For a conventional NMC/graphite cell, the cell vent is observed at ~160 °C and there are ~0.02 moles of gas at the onset of the runaway reaction (~250 °C) (at ~750 psi). For one of the Si-C cells, the moles of gas generated are comparable to the NMC/graphite cell. However, for the cell tested, there is 5x the gas generated at the onset of thermal runaway (0.10 moles at ~250 °C). For this cell, the vent gas pressure actuates the pressure relief valve in the cell fixture at 2500 psi. There is some variability in these gas data that will need to be evaluated further to better understand the gas generation profiles for Si-C cells.

Gas species generated from graphite and Si-C cells were sampled and analyzed by GC-FID and GC-MS. Relative gas composition for each cell type is shown in

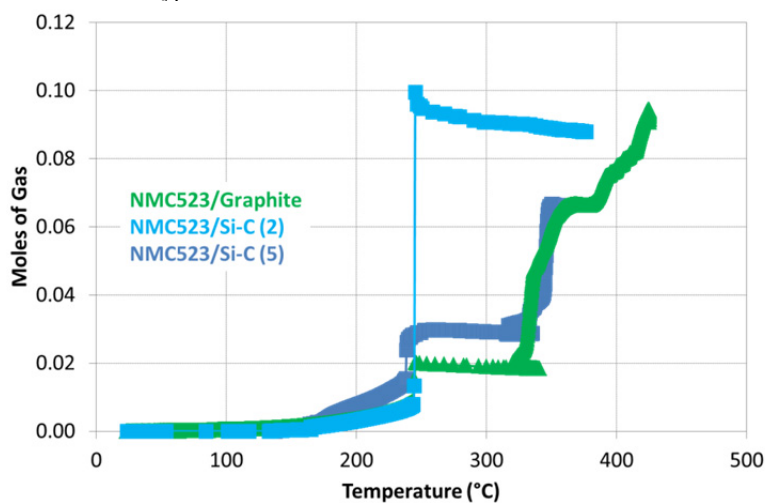


Figure IV - 48: Moles of gas as a function of temperature measured during a calorimetry experiment for NMC 523/graphite (green trace) and two NMC523/Si-C (light blue and dark blue traces) 18650 cells

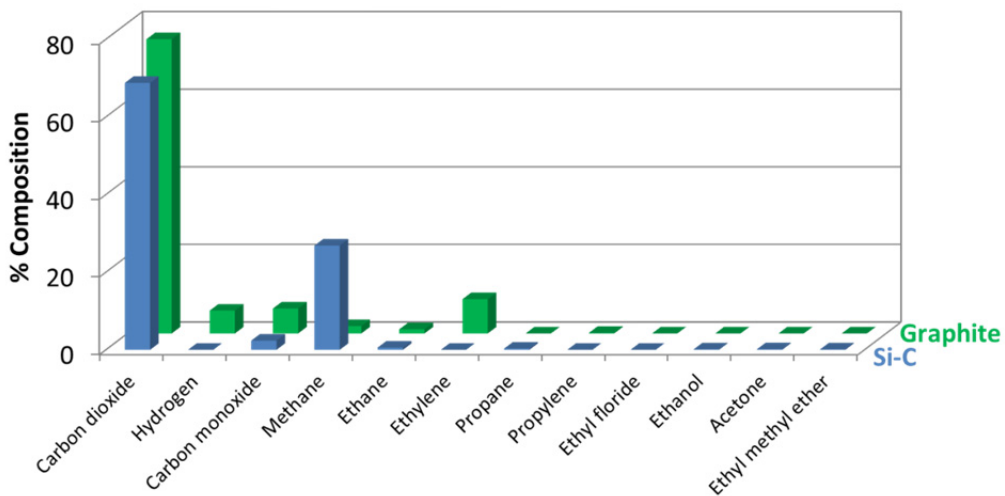


Figure IV - 49: Relative compositions of gas species generated from NMC/Si-C (blue) and NMC/graphite (green) cell during thermal runaway collected at 400°C

Coated Materials: For a number of years, the ABR program has focused on material coating strategies

Figure IV - 49 for gases sampled at 400 °C (end of thermal runaway). Results show a significant fraction of carbon dioxide generated from both cell types and a greater fraction of methane produced from the Si-C cells with very little other gas species produced. This suggests that electrolyte reactivity at the surface of the Si-C electrodes could be different than at graphite. Reactivity at Si-C interfaces could be either (1) more complete, breaking down the electrolyte more completely to methane and carbon dioxide, or (2) other decomposition products are adsorbed to the Si-C surface and not liberated as gas (or a combination of the two). Characterization work at the ANL Post-test facility will help elucidate that reaction mechanism.

to improve cell performance and reliability. In earlier work, we have shown AlF₃-coated NMC to have

improved safety performance, as well. In early FY14, we completed the thermal response and abuse tolerance of LiMPO₄-coated cathode materials developed by Physical Sciences Inc. (PSI) (where M = transition metal). NMC111 was coated with LiMPO₄ by PSI using their proprietary solution phase coating approach. In FY13, 2 kg of coated NMC111 was delivered to SNL. Figure IV - 50 shows DSC data for the coated and uncoated NMC111 harvested from 2032 coin cells at 100% state of charge (SOC). Both samples were prepared without excess electrolyte in order to elucidate differences with and without the cathode coatings without being convoluted with the large electrolyte

combustion specific heat. The coated sample has an onset temperature that is ~20 °C greater than the uncoated sample along with less activity between 200–280 °C. This suggests a stabilization of the coated cathode to thermal decomposition relative to the uncoated NMC111. Approximately 10 m of electrode was prepared and 18650 cells built. Figure IV - 51 shows the discharge capacity of a LiMPO₄-coated NMC cell and a control NMC cell at the end of formation (cycle 5). Through formation cycling, there is no observable difference between the coated and uncoated NMC.

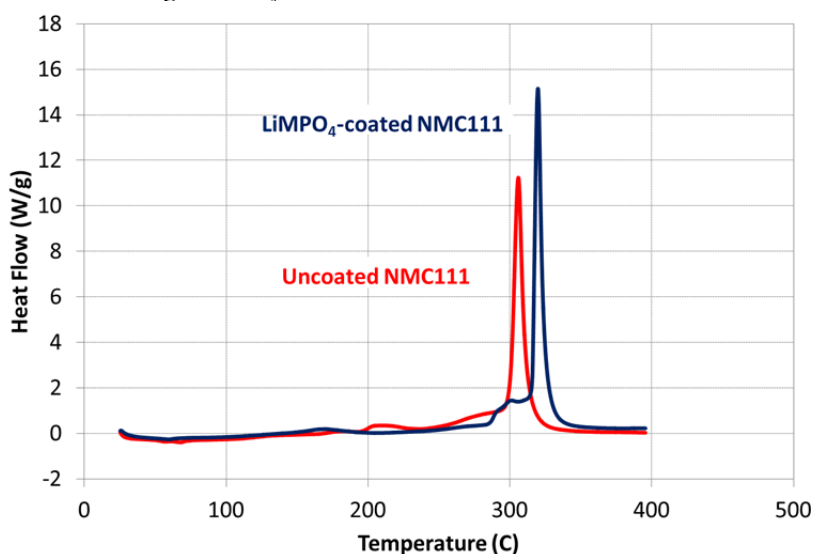


Figure IV - 50: DSC of LiMPO₄ coated NMC111 (navy blue trace) and uncoated NMC111 (red trace) from 2032 coin cells at 100% SOC (prepared without excess electrolyte)

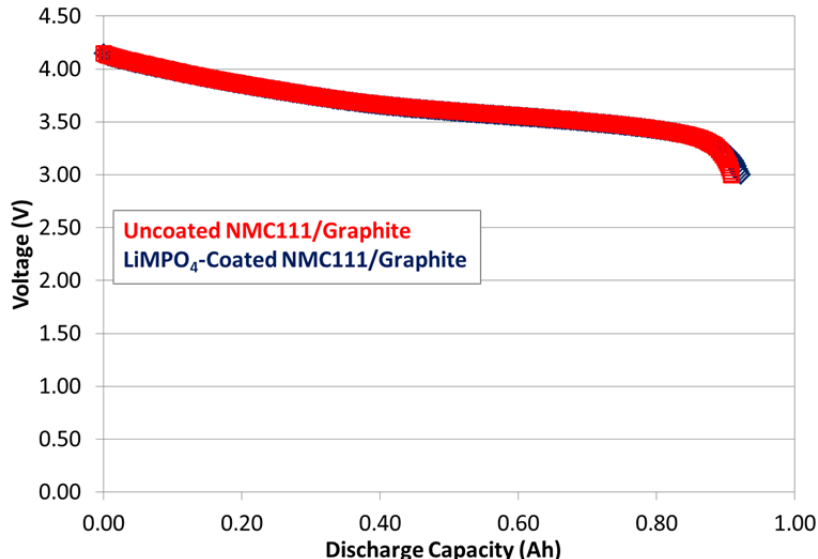


Figure IV - 51: Voltage vs. discharge capacity for LiMPO₄-coated and uncoated NMC/graphite 18650 cells

Accelerating rate calorimetry (ARC) measurements were performed on coated and uncoated cells. Figure IV

- 52 shows representative ARC normalized heating rate vs. temperature profiles from these experiments. The

control NMC cells show heating rates on the order of 200 °C/min and a total temperature rise from the runaway reaction of 350 °C (red trace). The LiMPO₄-coated NMC cells have a significantly diminished runaway response, with peak heating rates between 50–100 °C/min and a peak temperature rise of ~300 °C during thermal runaway. Results are consistent with DSC results on the coated materials, where the LiMPO₄ coatings act as a kinetic barrier to interfacial reactivity.

Abuse Resilient Component Development: The use of lithium fluoride (LiF) electrolyte salt has been considered as an alternative to LiPF₆ because of its chemical and thermal stability, but early generation anion binding agents (ABAs, used to improve LiF solubility) were large molecules that were inapplicable to lithium-ion cell systems (large molecular weights, low rate capability, low conductivity, voltage instability,

etc.). In collaboration with Binrad Industries we have developed LiF/ABA salts for lithium-ion cells to show improved thermal stability and to eliminate some of the shortcomings of using LiPF₆ salts.

The primary driver for the development of LiF/ABA-based electrolytes is their ability to stabilize a cell runaway reaction without impacting cell performance. Much of the effort in FY13 was focused on optimizing the performance of these electrolytes and improving the synthetic methods. FY14 has focused on evaluating LiF/ABA in full cells. Figure IV - 53 shows the discharge capacity of representative NMC523/graphite cells with conventional LiPF₆ and LiF/ABA-1 electrolytes. At C/5 (C/D rates used during formation cycling), there is no measureable difference in discharge capacity using LiPF₆ or LiF/ABA-1.

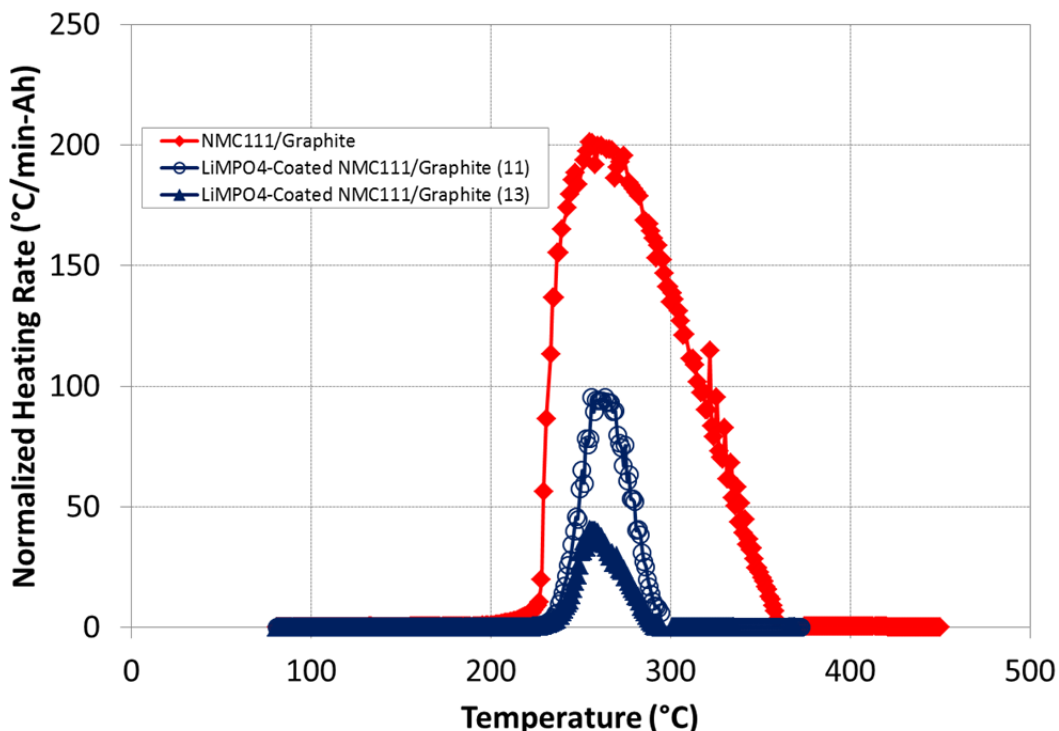


Figure IV - 52: ARC profiles of cell heating rate as a function of temperature for LiMPO₄-coated and uncoated NMC/graphite 18650 cells

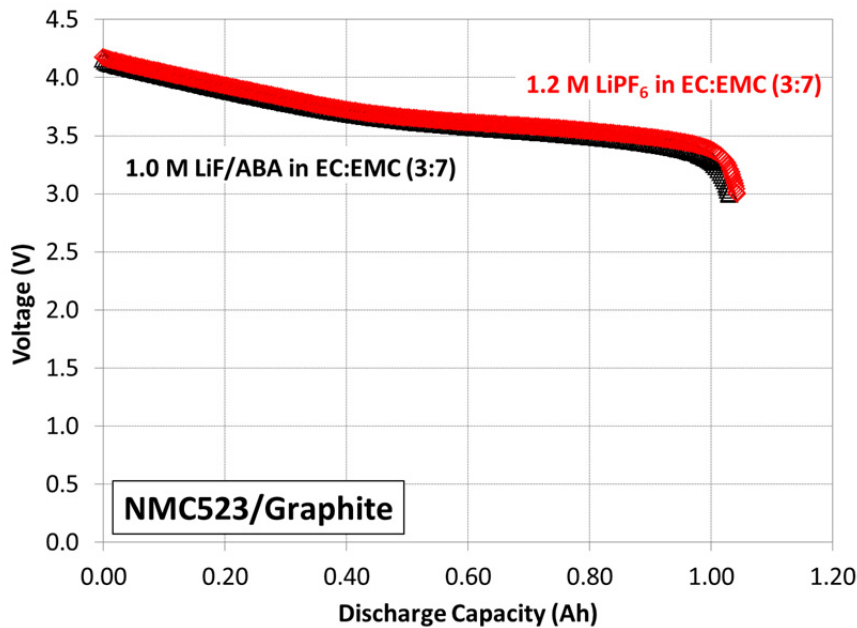


Figure IV - 53: 18650 cell discharge capacity of 523 NMC/Graphite cells with 1.0 M ABA-1 in EC:EMC (3:7) (black trace) and 1.2 M LiPF₆ in EC:EMC (3:7) (red trace) at C/5

In Q2 we reported on the ARC measurements of NMC523/graphite cells with LiF/ABA-1 relative to LiPF₆ electrolytes. Those data along with another LiF/ABA-1 cell and a LiF/ABA-2 cell are shown in Figure IV - 54. The response of ABA-1 is very reproducible from cell-to-cell showing only low rate heating (< 0.1 °C/min) during the entire exotherm and no high rate thermal runaway reactivity. ABA-2 (navy blue trace) shows similar behavior to ABA-1 below 200 °C, but does have a higher rate runaway than the

ABA-1 cells with a peak heating rate of 20 °C/min. However, it is important to note the thermal runaway response of the ABA-2 cell is significantly improved over the LiPF₆ control cell (red trace). The difference in the runaway response is likely attributed to differences in the structure of the ABA-1 and ABA-2 molecules and that there is a tradeoff between higher voltage stability (as observed for ABA-2) and improving thermal runaway response, as these molecules are designed.

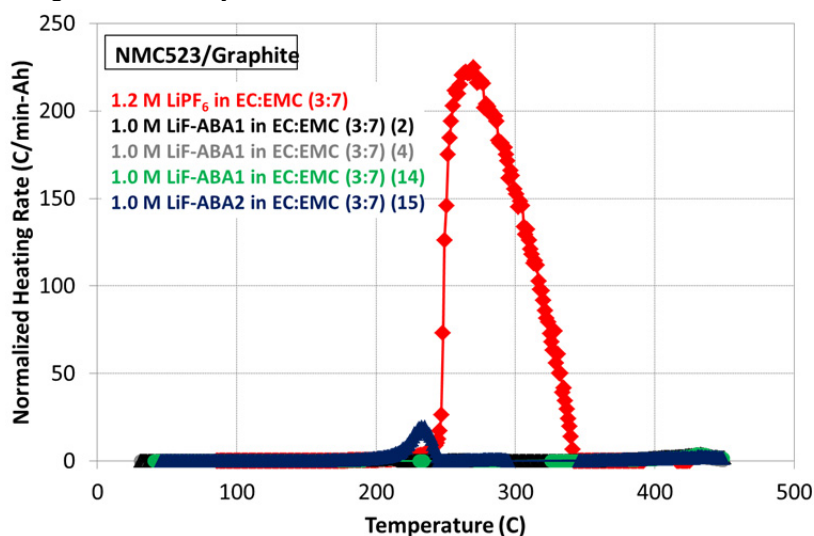


Figure IV - 54: Thermal runaway profiles of NMC/graphite cells in 1.0 M LiF/ABA-1 in EC:EMC (3:7) (black, gray, and green traces), 1.0 M LiF/ABA-2 in EC:EMC (3:7) (navy blue trace), and in 1.2 M LiPF₆ in EC:EMC (3:7) (red trace) measured by ARC

Cells were also evaluated for thermal and overcharge abuse tolerance to determine if LiF/ABA-1 is effective at mitigating thermal runaway under those conditions. Figure IV - 55 shows cell temperature and voltage during a thermal ramp abuse test for an NMC523 cell with LiPF₆ electrolyte (green), an NMC523 cell with LiF/ABA-1 electrolyte, and a COTS LFP cell. The runaway onset temperatures for each of the cells are comparable, between 210 and 230 °C. However, the peak cell temperature for the NMC-LiPF₆ cells is nearly 500°C, while the NMC523-LiF/ABA-1 cell peak temperature is more comparable to the COTS LFP cell at ~300 °C. In addition, the overcharge abuse tolerance of NMC523 cells with LiF/ABA-1 electrolyte

was also evaluated, shown in Figure IV - 56. Cells were overcharged at a 1C constant current with a compliance voltage of 20IV. At 155% SOC, the cell becomes resistive and the cell voltage increases and reaches the compliance voltage at 159% SOC without any cell venting or thermal runaway. The peak measured cell skin temperature is 115 °C. While this is a limited data set, results show that 18650 NMC523 cells with LiF/ABA-1 electrolyte have abuse tolerance characteristics that are more comparable to LFP cells than NMC523 cells with LiPF₆ electrolytes.

In Q4 FY14, the synthetic method for ABA-1 was delivered to ANL as a candidate material for scale-up at MERF.

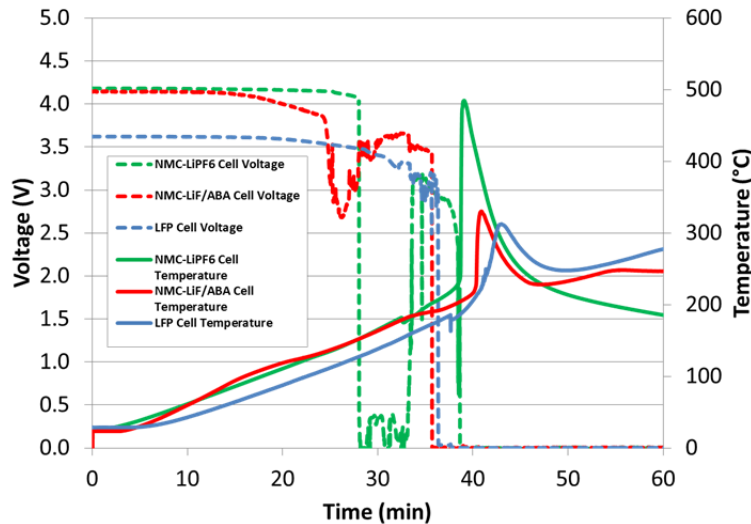


Figure IV - 55: Cell voltage and temperature during a thermal ramp abuse test for NMC cells with LiPF₆ (green trace) and LiF/ABA (red trace) electrolytes and a COTS LFP cell (blue)

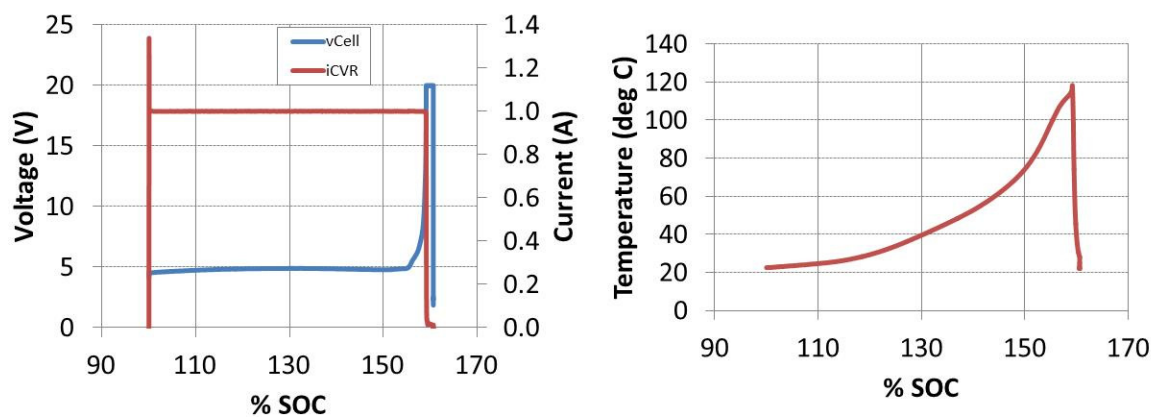


Figure IV - 56: Cell voltage and charging current (left panel) and cell temperature (right panel) as a function of cell state-of-charge (%SOC) during a 1C overcharge abuse test

Conclusions and Future Directions

This work demonstrates how specific advances in a variety of materials areas (anode, cathode, and electrolyte) can impact on cell-level safety and thermal characteristics. We have reported on the thermal runaway properties of cells containing Si-C anodes to better understand how these emerging, high energy class of high energy negative electrode materials will impact cell and battery-level abuse tolerance. Improved thermal runaway response was demonstrated with coated NMC materials based on LMPO₄. We have also shown LiF/ABA electrolytes to not only give appreciable electrochemical performance, but also significantly reduce the severity of thermal runaway reactions in NMC cells. Work will continue in this area to better understand the abuse response and thermal runaway

behavior of high energy materials for lithium-ion and other advanced energy storage technologies.

FY 2014 Publications/Presentations

1. C. J. Orendorff, “Inherent Safety Challenges with Battery Materials” NATTBAT meeting, January 2014.
2. 2014 DOE Annual Peer Review Meeting Presentation.
3. C. J. Orendorff “Battery Safety R&D at Sandia National Laboratories” 89th Lithium Battery Technical/Safety Group Meeting, September 2014.

IV.B.4 Post-Test Diagnostic Facility Activities (ANL)

Ira Bloom (Primary Contact)
Nancy Dietz Rago, Javier Bareño
Argonne National Laboratory
9700 South Cass Avenue
Argonne, IL 60439
Phone: (630) 252 4516; Fax: (630) 252 4176
E-mail: ira.bloom@anl.gov

Start Date: April 2010
Projected End Date: Open

Objectives

To accelerate the R&D cycle of DOE and industrial collaborators by developing and conducting standard procedures for post-test characterization of batteries in order to provide insight onto physicochemical causes of performance degradation.

Technical Barriers

This project addresses the following technical barriers as described in the USABC goals [1, 2, 3]:

- (A) Performance at ambient and sub-ambient temperatures.
- (B) Calendar and cycle life.

Technical Targets

- EV: 5-y calendar life; 1,000 80% DOD DST cycles.
- HEV: 15-year calendar life, 300,000 charge-sustaining cycles; EOL performance (min): 25 kW and 300 Wh.
- PHEV: 15-year calendar life, 300,000 charge-sustaining cycles, 5,000 charge-depleting cycles; EOL performance (min): 45 kW and 300 Wh.
- LEES: 15-year calendar life, 300,000 charge-sustaining cycles; EOL performance (min): 20 kW and 56 Wh.

Accomplishments

- Completed collaborations with industrial developers: JohnsonControls, Inc., Miltec, and Maxwell Technologies.
- Collaboration with Dalhousie University (Canada) is near complete.
- Started/continued collaborations with CAMP Facility, Jet Propulsion Laboratory, Army Research

Laboratory, University of Hawaii, CIC Energigune (Spain), Oak Ridge National Laboratory, University of Warwick (UK) and Illinois Institute of Technology.



Introduction

Batteries are evaluated using standard tests and protocols which are transparent to technology [1, 2, 3]. The evaluation provides a lot of information about how battery performance changes with time under a given set of conditions. Post-test characterization of aged batteries can provide additional information regarding the cause of performance degradation, which previously was inferred.

Approach

Post-test analysis consists of physical, spectroscopic, metallographic, and electrochemical characterization of battery components that have been harvested from aged cells. The aged cells have undergone standardized testing. The cells can come either from exploratory DOE programs, such as ABR and BATT, or from pre-competitive R&D programs managed by USABC and USDRIVE. The Post-Test Facility uses the experience and techniques developed in DOE's applied battery program in a standardized fashion.

Results

Cells, made by the CAMP Facility and containing HE5050 (cell A) and 5-V spinel (cell B) electrodes, were examined to determine possible causes of performance decline. Upon initial inspection, some staining on the electrodes and separator material in cell A was seen, as shown in Figure IV - 57. Staining was also seen on the separator and anode of cell B. In contrast to that seen in cell A, the staining in cell B had more of a zebra-stripe appearance, as shown in Figure IV - 58.

Anode material from cell A was characterized using FT-IR. These spectra are shown in Figure IV - 59 and show that there are differences in the colored bands. Here, the intensity of the bands may be indicative of film thickness. Difference in thickness, in turn, may be the cause of the different colors.

In places, white precipitates and shiny, metallic-looking crystals (dendrites?) were seen on the anode surface using the optical microscope. These materials were found intermixed on the anode (see Figure IV - 60). If the shiny material were lithium, its deposition on the anode could be a source of capacity fade.

In the SEM, EDS results show that there are chemical differences in the colored stripes on the anode in cell B. Indeed, the EDS results show that the lighter areas contain more fluorine and phosphorus than the dark areas, inferring that there may be higher concentrations of LiPF₆ plus electrolyte reaction products in these regions. EDS results from the separator shows that the light areas contain more fluorine. Together, these results indicate that the stripes may be from an uneven distribution of electrolyte or uneven current distribution.



Figure IV - 57: Photograph of the electrode and separator materials from cell A, showing staining patterns



Figure IV - 58: Photograph of the anode and separator material from cell B

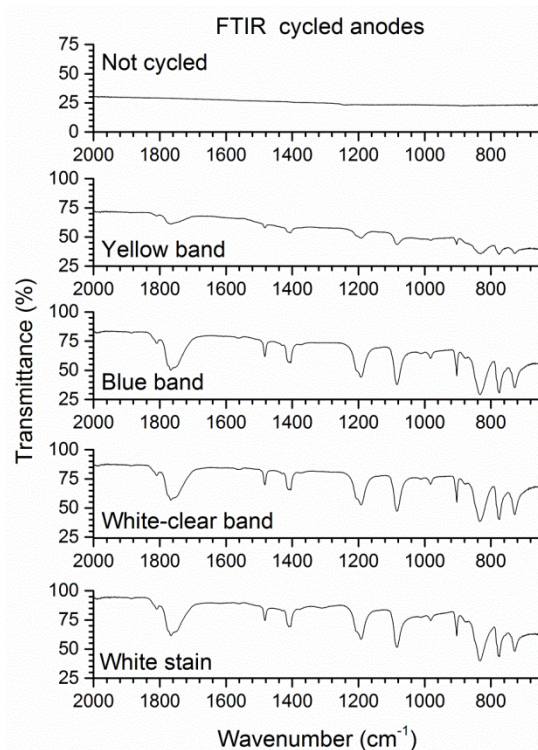


Figure IV - 59: FT-IR spectra of the colored bands on the anode material from cell A

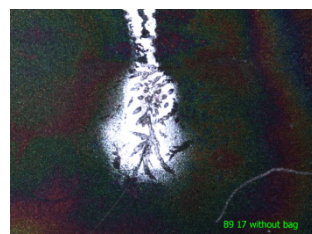


Figure IV - 60: Optical micrograph of cell A anode surface showing a white precipitate with metallic-looking crystals

Conclusions and Future Directions

In the examples above, performance decline can be from several factors, such as lithium deposition on the anode and electrolyte decomposition. Together, these may decrease cell capacity and increase cell resistance.

The next steps for the Post-Test Facility area as follows.

- Actively engage USABC and DOE battery contractors to help them understand the sources of performance decline.
- Collaborate with ABR, BATT and USABC programs.
- Participate/lead in the characterization of Si-binder interactions.

List of Abbreviations

- ABR: Advanced Battery Research
 ANL: Argonne National Laboratory
 BATT: Batteries for Advanced Transportation Technologies
 CAMP Facility: Cell Analysis, Modeling and Prototyping Facility at Argonne.
 DST: dynamic stress test, see reference 3.
 EDS: energy-dispersive x-ray spectroscopy
 EV: electric vehicle
 FT-IR: Fourier-transform infrared spectroscopy
 HEV: hybrid electric vehicle
 HE5050: $0.5\text{Li}_2\text{MnO}_3 \bullet 0.5\text{LiNi}_{0.375}\text{Mn}_{0.375}\text{Co}_{0.25}\text{O}_2$ (Toda Kogyo, Japan)
 LEESS: Low-Energy Energy Storage System
 PHEV: plug-in hybrid electric vehicle
 SEM: scanning-electron microscope
 SOC: state of charge
 USABC: United States Advanced Battery Consortium (DOE, GM, Chrysler and Ford)
 USDRIVE: US Driving Research and Innovation for Vehicle efficiency and Energy sustainability

FY 2014 Publications/Presentations

1. 2013 DOE Annual Peer Review Meeting Presentation.
2. **Post-Test Analysis of Lithium-Ion Battery Materials at ANL**, J. Bareño, N. Dietz-Rago, and I. Bloom, Advanced Automotive Battery Conference, Feb 3-7 2014, Atlanta GA, Session B2, Feb 4-5, 2014.
3. Post-Test Analysis of Lithium-Ion Battery Materials at Argonne National Laboratory, J. Bareño, N. Dietz Rago, and I. Bloom, American Physical Society, March 3-7, 2014, Denver CO.

4. Argonne National Laboratory's Post-Test Facility for Analysis of Lithium-Ion Battery Materials, N. Dietz Rago, J. Bareño, I. Bloom, and IV. Maroni, 247th American Chemical Society National Meeting, March 16-20, 2014, Dallas, TX.
5. Post-Test Analysis of Lithium-Ion Battery Materials at Argonne National Laboratory, J. Bareño, N. Dietz Rago, and I. Bloom, Materials Research Society Meeting, April 21-25 2014, San Francisco, CA.
6. Argonne National Laboratory's Post-Test Facility for Analysis of Lithium-Ion Battery Materials, N. Dietz Rago, J. Bareño, and I. Bloom, Materials Research Society Meeting, April 21-25, 2014, San Francisco, CA.
7. Post-test Analysis of Battery Materials: Another Part of the Question, I. Bloom, N. Dietz Rago, and J. Bareño, 225th Meeting of the Electrochemical Society, May 11-16, 2014, Orlando, FL.
8. Argonne National Laboratory's Post-Test Facility for Analysis of Lithium-Ion Battery Materials , N. Dietz Rago, J. Bareño, and I. Bloom, Microscopy and Microanalysis 2014, August 3-7, 2014, Hartford, CT.

References

1. FreedomCAR Battery Test Manual for Power-Assist Hybrid Electric Vehicles, DOE/ID-11069, October 2003.
2. FreedomCAR Battery Test Manual for Plug-In Hybrid Electric Vehicles, June 2010.
3. Electric Vehicle Battery Test Procedures Manual, Revision 2, January 1996.

IV.C Critical Barrier Focus —Voltage Fade in Li-ion Battery Cathode Materials

IV.C.1 Structure-Electrochemical Activity Relationships in LMR-NMC (ANL)

Voltage Fade Team

Argonne National Laboratory

9700 South Cass Avenue

Argonne, IL 60439

Phone: (630) 252-4516; Fax: (630) 252-4176

E-mail: Burrell@anl.gov

Start Date: October 2013

Projected End Date: September 2014

Objectives

Identify the fundamental causes of voltage fade and determine unknown electrochemical processes associated with the voltage fade phenomenon.

Technical Barriers

This project addresses the following technical barriers as described in the USABC goals:

- (A) Performance at ambient temperatures.
- (B) Cycle life.

Technical Targets

- PHEV specific energy targets (pack): 3.4 kWh (min) to 11.6 (max).
- EV specific energy targets (pack): 80 (min) to 200 (max) Wh/kg.

Accomplishments

- Established protocols for determination of voltage fade using electrochemical cycling. In addition presentation formats were determined and applied.
- Determined the electrochemical limits of the voltage fade process.
- Established the connection between hysteresis and voltage fade in lithium manganese rich materials.
- Discovered the connection between hysteresis and voltage fade.
- Development of a phenomenological model for the evolution of voltage fade.



Introduction

Layered materials in the Li-Mn-rich portion of the Li-Ni-Mn-Co-O phase diagram (LMR-NMC), which are structurally integrated composites of Li_2MnO_3 and $\text{Li}(\text{Ni},\text{Mn},\text{Co})\text{O}_2$ and are usually written as $a\text{Li}_2\text{MnO}_3 \bullet (1-a)\text{Li}(\text{Ni},\text{Mn},\text{Co})\text{O}_2$, are promising cathodes for use in lithium-ion batteries. However, with cycling, the shape of the voltage vs. capacity curve changes. A similar decline is also observed on charging, strongly suggesting that changes to the equilibrium electrochemical potential of the active material cause the voltage fade. In the literature, the continuous change in the shape of the discharge (and charge) curves has been attributed to the formation of a spinel-like phase. As a result of the loss in potential, there is a loss in energy, limiting the utility of these materials in energy-demanding applications, such as in electric vehicles.

Approach

Voltage fade is a process that occurs when the LMR-NMC is cycled between high and low voltages. This electrochemical process is at the heart of the physical changes that result in the cathode material, culminating in a shift in the voltage profile. Understanding this electrochemical process is key to determining the limits of the process, understanding possible solutions and the development of a functional understanding of voltage fade. We have carried out a comprehensive determination of the electrochemical processes for the LMR-NMC materials.

This began with the establishment of a clear set of testing procedures that enable comparison of materials and potential solutions. In addition we utilized a baseline material HE5050 in an attempt to enable all researchers to validate results.

To conclude we have utilized the extensive electrochemical data to develop a physical model of voltage fade that accounts for the growth of a low voltage Li phase at the expense of a high voltage Li phase due to the interaction energy of Li ions with transition metal ions that have migrated. The model was

re-cast in a general form and experimental LMR charge profiles were de-convoluted with the model to extract the evolutionary behavior of various components.

Results

Protocol to Track Voltage Fade – methodology, materials, experiments and results

Basic methodology

To track voltage fade, we calculate the average voltage for each charge and discharge. This is possible because the composition-dependent cell voltage $U(q)$, which continuously decreases throughout cycling, affects the measured average voltage \bar{U}_{meas} via $\bar{U}_{\text{meas}} = E/Q = (1/Q) \int U(q) dq$, with E and Q being the total energy and capacity of the cell. To correct for the many polarization losses that affect $U(q)$ and cause a difference between measured and true (i.e. near equilibrium) average voltages, we use an average cell resistance to obtain a resistance-corrected average voltage, $\bar{U}_{\text{corr}} = \bar{U}_{\text{meas}} - i\bar{R}$. (Note that a rise in cell resistance forces $U(q)$ to increase during charge and to decrease during discharge.) In this manner, we can compute an average open-circuit electrode potential for the compositional region of interest for each charge and discharge. This is henceforth referred to as “corrected average voltage”.

Materials

The material of prime interest in this voltage fade study is a structurally-integrated, Li- and Mn-rich layered metal oxide expressed as $\text{Li}_{1.2}\text{Ni}_{0.15}\text{Mn}_{0.55}\text{Co}_{0.1}\text{O}_2$, and as $0.5\text{Li}_2\text{MnO}_3 \bullet 0.5\text{LiMn}_{0.375}\text{Ni}_{0.375}\text{Co}_{0.25}\text{O}_2$ in the two-component notation. This material is denoted as “LMR-NMC” throughout the text. It is a promising material for battery applications where high energy densities and lower costs are imperative^[1]. The LMR-NMC exhibits high oxide-specific charge- and energy-densities exceeding $250 \text{ Ah}\cdot\text{kg}^{-1}$ and $900 \text{ Wh}\cdot\text{kg}^{-1}$ when charged beyond 4.5V vs. Li^+/Li . Details of cell chemistry, electrode formulation, and average cell resistances are given in Table IV - 10 for a set of standard baseline cells and “modified” cells. The modifications of the latter cells yield improved capacity retention and lower impedance rise in graphite-containing full-cells, as shown elsewhere^[2, 3].

Typical voltage fade of other oxide materials is also included in this report. These oxides include $\text{LiNi}_{0.8}\text{Co}_{0.15}\text{Al}_{0.05}\text{O}_2$ (also known as NCA), $\text{Li}_{1.05}(\text{Ni}_{1/3}\text{Mn}_{1/3}\text{Co}_{1/3})_{0.95}\text{O}_2$ (also known as NMC), $\text{Li}_{1.2}\text{Ni}_{0.4}\text{Mn}_{0.4}\text{O}_2$, $\text{Li}_{1.2}\text{Ni}_{0.2}\text{Mn}_{0.6}\text{O}_2$, $\text{Li}_{1.2}\text{Co}_{0.4}\text{Mn}_{0.4}\text{O}_2$, and $\text{Li}_{1.2}\text{Cr}_{0.4}\text{Mn}_{0.4}\text{O}_2$. The latter five compounds are also structurally-integrated composites and can be expressed in the two component notion as $x\text{Li}_2\text{MnO}_3 \bullet y\text{Li}(\text{M}_a\text{Mn}_b)\text{O}_2$ with M being Ni, Co, or Cr.

Electrodes from these materials were prepared by coating an Al foil with a mixture containing the oxide, SFG-6 graphite, acetylene black, and polyvinylidene fluoride (PVDF) binder (84:4:4:8 by weight). A complete compilation of all materials, their capacities, and experimental conditions is provided in Table IV - 11.

Table IV - 10: Electrode chemistry and formulation for baseline and modified cells

	Baseline cells	Modified cells
Active positive material	86 wt.% $\text{Li}_{1.2}\text{Ni}_{0.15}\text{Mn}_{0.55}\text{Co}_{0.1}\text{O}_2$ (Toda HE5050)	92 wt.% $\text{Li}_{1.2}\text{Ni}_{0.15}\text{Mn}_{0.55}\text{Co}_{0.1}\text{O}_2$ (Toda HE5050)
Binder	8 wt.% PVdF (Solvay 5130)	4 wt.% PVdF (Solvay 5130)
Electrode additives	4 wt.% SFG-6 graphite (Timcal) 2 wt.% SuperP (Timcal)	4 wt.% C45 (Timcal)
Current collector	Al, 15 μm	Al, 20 μm
Active loading density of oxide	6.64 mg·cm ⁻²	5.89 mg·cm ⁻²
Electrode porosity	37%	36%
Laminate thickness	35 μm	26 μm
Negative electrode	Li metal	
Separator	25 μm thick (Celgard 2325)	
Electrolyte	1.2 M LiPF_6 in ethylene carbonate (EC) : ethyl methyl carbonate (EMC), 3:7 by wt.	
Electrolyte additive	none	2 wt.% LiDFOB
Avg. cell resistance for all cells; 2 nd , 20 th discharge cycle	184 Ω , 309 Ω	174 Ω , 120 Ω

To measure and track voltage fade we used galvanostatic cycling experiments conducted in 2032-type coin cells (1.6 cm^2 area electrodes) with Li-metal counter electrodes. These cells contain a 1.2 M LiPF_6 in EC:EMC (3:7 by wt.) electrolyte (referred to as “Gen2 electrolyte”) and a Celgard 2325 (a polypropylene–polyethylene–polypropylene trilayer) separator. The cells are assembled in an Ar-atmosphere glove box and cycled at 30°C in an environmental chamber. The cycling protocol consists of a 10 mA·g_{oxide}⁻¹ (0.1 mA, ~C/25 rate) current for the first charge/discharge cycle between 2.0 and 4.7V vs. Li^+/Li and a 20 mA·g_{oxide}⁻¹ (0.2 mA, ~C/12 rate) for subsequent cycles in the same voltage range. The lower current during the first cycle promotes adequate wetting of the electrode and complete electrochemical activation of the active oxide.

Table IV - 11: Cycling conditions and specific capacities for selected layered oxides

Materials* (in one- and two- component notation)	Cycling windo w (V vs. Li)**	1 st charge (mAh·g ⁻¹) @ 10 mA·g ⁻¹	1 st discharge (mAh·g ⁻¹) @ 10 mA·g ⁻¹	20 th discharg e (mAh· g ⁻¹) @ 20 mA·g ⁻¹	Drop in corr. avg. charge voltage for 2 nd - 20 th cycle (mV)	Position of current interrupts (V vs. Li)	
		during charge	during discharge				
30°C LMR-NMC (baseline cell) $\text{Li}_{1.2}\text{Ni}_{0.15}\text{Mn}_{0.55}\text{Co}_{0.1}$, $0.5\text{Li}_2\text{MnO}_3 \bullet 0.5\text{LiMn}_{3/8}\text{Ni}_{3/8}\text{Co}_{1/4}\text{O}_2$	2-4.7	319	277	248	181	3.5, 3.9, 4.3	4.0, 3.6, 3.2
	2-4.6	325	281	245	141	3.5, 3.9, 4.3	4.0, 3.6, 3.2
	2-4.5	327	283	228	100	3.5, 3.9, 4.3	4.0, 3.6, 3.2
	2-4.4	333	289	209	65	3.5, 3.9, 4.3	4.0, 3.6, 3.2
	2-4.3	332	288	189	49	3.5, 3.9, 4.3	4.0, 3.6, 3.2
30°C LMR-NMC (modified cell) $\text{Li}_{1.2}\text{Ni}_{0.15}\text{Mn}_{0.55}\text{Co}_{0.1}$	2-4.7	333	288	269	200	3.5, 3.9, 4.3	4.0, 3.6, 3.2
	2-4.25	334	291	179	30 ⁺	3.05, 3.45, 3.85	4.1, 3.75, 3.4
55°C LMR-NMC (baseline cell) $\text{Li}_{1.2}\text{Ni}_{0.15}\text{Mn}_{0.55}\text{Co}_{0.1}$ NMC $\text{Li}_{1.05}(\text{Ni}_{1/3}\text{Mn}_{1/3}\text{Co}_{1/3})\text{O}_2$ $0.1\text{Li}_2\text{MnO}_3 \bullet 0.9\text{LiMn}_{0.25}\text{Ni}_{0.37}\text{Co}_{0.37}\text{O}_2$	2-4.7	328	296	264	202	3.5, 3.9, 4.3	4.0, 3.6, 3.2
	2-4.7	252	208	166	46	3.9, 4.3	4.0, 3.6
	2-4.25	251	206	146	-5 ⁺	3.05, 3.45, 3.85	4.1, 3.75, 3.4
NCA $\text{LiNi}_{0.8}\text{Co}_{0.15}\text{Al}_{0.05}\text{O}_2$	2-4.7	241	219	194	8	3.9, 4.3	4.0, 3.6
	2-4.25	241	221	180	-22 ⁺	3.05, 3.45, 3.85	4.1, 3.75, 3.4
0.5Li ₂ MnO ₃ •0.5LiNiO ₂ 0.5Li ₂ MnO ₃ •0.5LiMn _{0.5} Ni _{0.5} O ₂ 0.5Li ₂ MnO ₃ •0.5LiCoO ₂ 0.5Li ₂ MnO ₃ •0.5LiCrO ₂	2-4.7	279	169	172	76	3.9, 4.3, 4.7	4.0, 3.6
	2-4.7	291	197	197	144	3.5, 3.9, 4.3	4.0, 3.6, 3.2
	2-4.7	363	222	165	191	3.5, 3.9, 4.3	4.0, 3.6, 3.2
	2-4.7	313	177	150	84	3.5, 3.9, 4.3	4.0, 3.6, 3.2

Capacities are given with respect to the active oxide weight.

* Only the LMR-NMC is tested at 30°C and 55°C, all other materials at 30°C.

** For all materials the cycling window is 2-4.7V during the 1st cycle.

Experimentally measuring and tracking voltage fade

From the second cycle onwards, the protocol implements current interrupts to estimate resistances at various cell voltages during charge and discharge^[4]. The current is stopped for 10 minutes and the voltages are recorded before and after the stopping period to estimate the cell resistance (i.e. dU/dI). Cell resistances are recorded at a total of six different voltages, three during charge and three during the discharge cycle. Voltage locations of these current interrupts are based on their capacity-voltage profiles; the current interrupt locations for the various oxides are listed in Table IV - 11. The resistance-corrected average voltage is then calculated in three steps:

- 1) Average charge and discharge voltages are calculated by dividing the total cell's energy by the cell's capacity measured at 4.7V after charging and at 2.0V after discharging.
- 2) Average charge and discharge resistances are calculated from three interrupts for charge and discharge.
- 3) Resistance-corrected average voltages are then calculated by subtracting the averaged " $i\bar{R}$ " polarization losses from the measured average voltages.

Tracking voltage fade in such a manner is reasonably fast and can be carried out during normal cycling. The advantages of this protocol are as follows: i) it facilitates data comparison through quantification, ii) it is reasonably fast (in comparison to e.g., lengthy galvanostatic intermittent titration technique, GITT, measurements), iii) it records the corrected average voltages for each cycle under the testing conditions of interest, and iv) it tracks simultaneously average and state-of-charge dependent cell resistances. However, the protocol has obvious limitations, which include the following: (i) the mechanistic details are averaged out, and needs to be determined by other electrochemical techniques, (ii) similar cells with varying internal resistances can show small differences in voltage fade, as cycling would occur over different SOC ranges, and structural transformations and cell-level kinetics can be very temperature sensitive, (iii) the number, location, and duration of the current interrupts may shift the computed average voltages, depending on material and actual cycling conditions, and (iv) the data obtained are sensitive to experimental conditions, including test temperature, cycling rate and voltage window for cycling.

In general though the combination of moderate cycling currents, along with the resistance correction, allowed us to track voltage fade very reproducibly.

Voltage fade in $\text{Li}_{1.2}\text{Ni}_{0.15}\text{Mn}_{0.55}\text{Co}_{0.1}\text{O}_2$ ($0.5\text{Li}_2\text{MnO}_3 \bullet 0.5\text{LiMn}_{0.375}\text{Ni}_{0.375}\text{Co}_{0.25}\text{O}_2$) aka LMR-NMC

Figure IV - 61 shows a typical charge and discharge profiles for LMR-NMC. In Figure IV - 61A, a gradual cycle-to-cycle drop of the charge and discharge profiles, along with a relatively small capacity loss, is apparent. In Figure IV - 61B, the capacities are normalized for each half-cycle, showing this gradual drop in electrode potential more clearly. Both figures also show "electrochemical activation" of the material as a ~4.5 V plateau during 1st charge. After activation, charge and discharge profiles become gradually sloped, over nearly the entire compositional region, electrochemically revealing dramatic changes to the local Li environments. The drop in voltage from 1st to 2nd charge is especially striking.

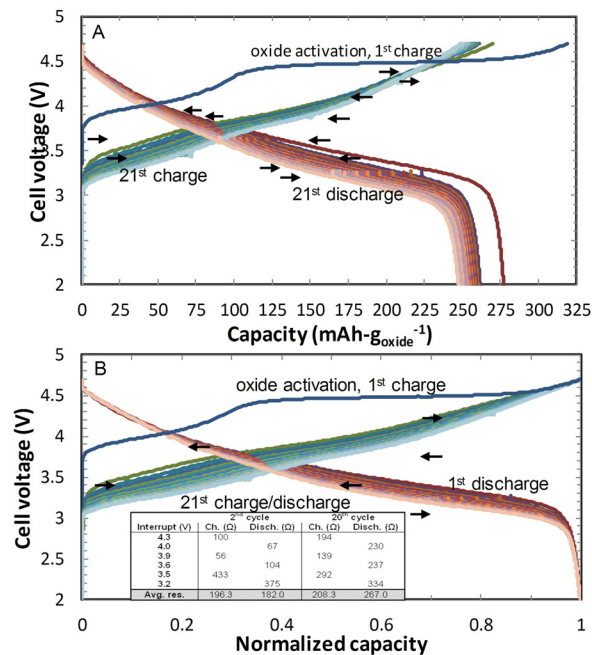


Figure IV - 61: The first 21 galvanostatic charge/discharge cycles for LMR-NMC vs. Li in the 2.0-4.7V range at 30°C, as-measured (A) and capacity normalized (B). A depression of the voltage profiles is apparent for charge and discharge curves after capacity normalization. A capacity of unity refers to 319 mAh-g_{oxide}-1 (after 1st charge), 277 mAh-g_{oxide}-1 (after 1st discharge), and 248 mAh-g_{oxide}-1 (after 20th discharge). Black arrows indicate the positions of the six current interrupts used to calculate the average resistances. The inset table in 1B table shows cell resistances as a function of the interrupt voltage for the 2nd and 20th cycle

Upon continued cycling, the profiles continue to drop to lower voltages. Note that the voltage decay during charge occurs *despite* a rise in average cell resistance that is caused by a degrading positive electrode^[1, 2]. Hence, irreversible structural changes of

the oxide are the origin of this potential change, and not cell-level charge transport kinetics. The measured cell resistances as a function of the interrupt positions and the corresponding average voltages are shown in the Figure IV - 61B table. Although the average resistances increase during cycling, some voltage-specific resistances can decrease (e.g. at 3.2 and 3.5V) because of state-of-charge (oxide-lithium-content) changes with cycling.

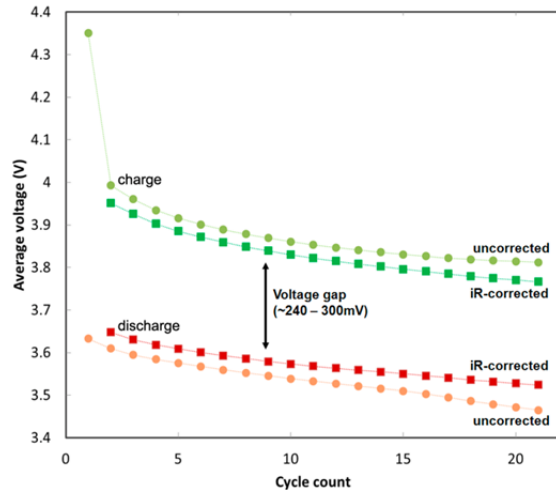


Figure IV - 62: Average voltages, corrected and uncorrected, as a function of cycle number for the LMR-NMC vs. Li. Average voltages during charge are plotted in light/dark green, and those during discharge are plotted in orange/red. Voltage fade and voltage gap are apparent. Corrected average voltages drop by a total of 185mV during charge and by 124mV during discharge. Thin dotted lines are intended only as a guide to the eye, and are also shown in all subsequent figures. HPPC results of CD sized cells delivered to INL for testing

Figure IV - 62 depicts voltage fade as a drop in uncorrected and resistance-corrected average voltages. The average cell voltages are calculated for charge and discharge as described above. The nonzero average “ $i\bar{R}$ ” polarization causes a difference of 30-70mV (at 0.2mA) between the uncorrected and corrected voltages; this polarization increases as cycling continues and cell resistance rises. A “voltage gap” between the corrected charge and discharge voltages of 240-300mV is the consequence of the material’s intrinsic hysteresis^[4, 5]. The corrected average voltages are not calculated during the 1st cycle because of uncertainties related to wetting of the electrode and structural changes of the oxide. Nevertheless, the abrupt drop in the uncorrected average voltage from 1st to 2nd charge, along with the difference between 1st charge and discharge, reflect the irreversible changes that occur within the material during its electrochemical activation. Upon continued cycling, a gradual decay in average voltage is clearly visible. For the first 20 cycles, the resistance-corrected average voltage drops by 185mV during charge and by 124mV during discharge which corresponds to a drop by ~3-5%,

or, alternatively, to ~6-10mV per cycle. The difference in charge- and discharge-decay rates gradually reduces the initial voltage gap. The rate of decay is more rapid in the early cycles and continues nearly in a linear manner for at least 50 cycles under standard cycling conditions (not shown here).

As described earlier, the measured voltage is affected by the experimental conditions; some of these factors are described below:

Cycling window: Upper and lower cut-off voltages affect the rate of fade. Figure IV - 63 shows the corrected average discharge voltages for different upper cut-offs. Clearly, as the cut-off is raised, the voltage fades faster; at voltages less than 4.4V, fade is negligible.

Temperature: Figure IV - 64 shows that the corrected average voltages are also affected by temperature. They are ~40-70 mV lower at 55°C than at 30°C. The lower average voltages for charge and discharge at the elevated temperature exclude again any cell-level kinetics as a possible reason for this behavior. The cycling data also show that the rate of fade during charge is higher, and that the average voltage gap (between charge and discharge) is larger, at elevated temperatures.

Cycle life and calendar life: Figure IV - 62 shows that the rate of fade is not constant throughout cycling; the highest rates occur during the initial cycles. Although the rate appears to slow down as cycling continues, various studies indicate that the voltage fade continues for several hundreds of cycles.

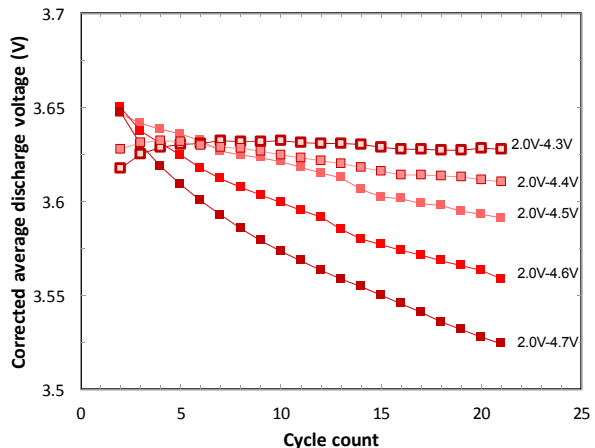


Figure IV - 63: Effect of cycling window on the corrected average voltage and its fade during discharge for the LMR-NMC baseline material. For the first activation cycle, the cycling window is kept constant for all samples, i.e. 2.0V – 4.7V. During cycling, only the lower cut-off is kept constant at 2V. The degree of voltage fade increases as the upper cut-off increases. Voltage relaxation at the beginning of discharge down to ~4.5V forces the average voltage after the 2nd discharge to be nearly the same for the data sets with the three highest cut-off voltages

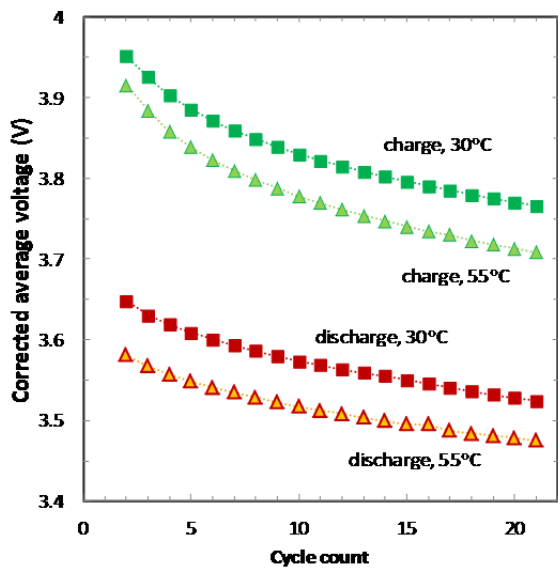


Figure IV - 64: Effect of temperature on the corrected average voltages of the LMR-NMC baseline material under otherwise identical cycling conditions.

Voltage Fade of Selected Layered Oxides

Another factor influencing voltage fade is the oxide composition. Figure IV - 65 and Figure IV - 66 show data for several Li-rich chemistries ($\text{Li}_{1.2}\text{M}_{0.8}\text{O}_2$, where “M” refers to any of the transition metals present), and for two oxides currently used in commercial cells – $\text{Li}_{1.05}(\text{Ni}_{1/3}\text{Mn}_{1/3}\text{Co}_{1/3})_{0.95}\text{O}_2$ (NMC) and $\text{LiNi}_{0.8}\text{Co}_{0.15}\text{Al}_{0.05}\text{O}_2$ (NCA). The cycling conditions for these materials follow the standard protocol given above, unless the material’s potential window required adjustments of the current interrupts.

The left hand side of Figure IV - 65 provides capacity-voltage profiles of the Li-rich chemistries over the 2.0-4.7V voltage range. The capacities are normalized to highlight the voltage decay; specific capacities and positions of the current interrupts are given in Table IV - 11. All materials show a 1st charge electrochemical activation near 4.5V, and display signs of voltage fade during subsequent cycles. Note that the activation plateau for $\text{Li}_{1.2}\text{Cr}_{0.4}\text{Mn}_{0.4}\text{O}_2$ is slightly lower in voltage and more gradually sloped than that for the other materials, which probably results from irreversible structural changes that have been described previously for this material [6]. Note also the presence of a 2V plateau for $\text{Li}_{1.2}\text{Ni}_{0.4}\text{Mn}_{0.4}\text{O}_2$ upon 1st discharge, which indicates formation of a Li_2MO_2 -like phase [7,8]. This plateau disappears after the first three cycles, probably due to rising cell resistance on cycling that depress the feature below the lower (2.0V) cutoff voltage.

The right hand side of Figure IV - 65 provides the corrected average voltages as a function of charge and discharge number. Again, all materials show voltage fade when cycled to 4.7IV. The total drop in charge voltage after 20 cycles lies between 76mV and 191mV for $\text{Ni}_{0.4}\text{Mn}_{0.4}$ and $\text{Co}_{0.4}\text{Mn}_{0.4}$, respectively, showing that the rate of fade depends on the materials chemistry. It also depends on the stoichiometry, as seen for e.g. $\text{Ni}_{0.4}\text{Mn}_{0.4}$ and $\text{Ni}_{0.2}\text{Mn}_{0.6}$ which show a drop of 76mV and 144mV, respectively. Similar to LMR-NMC, the rate of fade for these materials is on the order of a few millivolts per cycles, ranging from approximately 4mV to 11mV per *charge* cycle. The rate of fade during *discharge* is slightly lower, approximately 1mV to 10mV per *discharge* cycle. Note that the initial average voltage of $\text{Ni}_{0.4}\text{Mn}_{0.4}$ rises during discharge because of the disappearance of its 2V plateau.

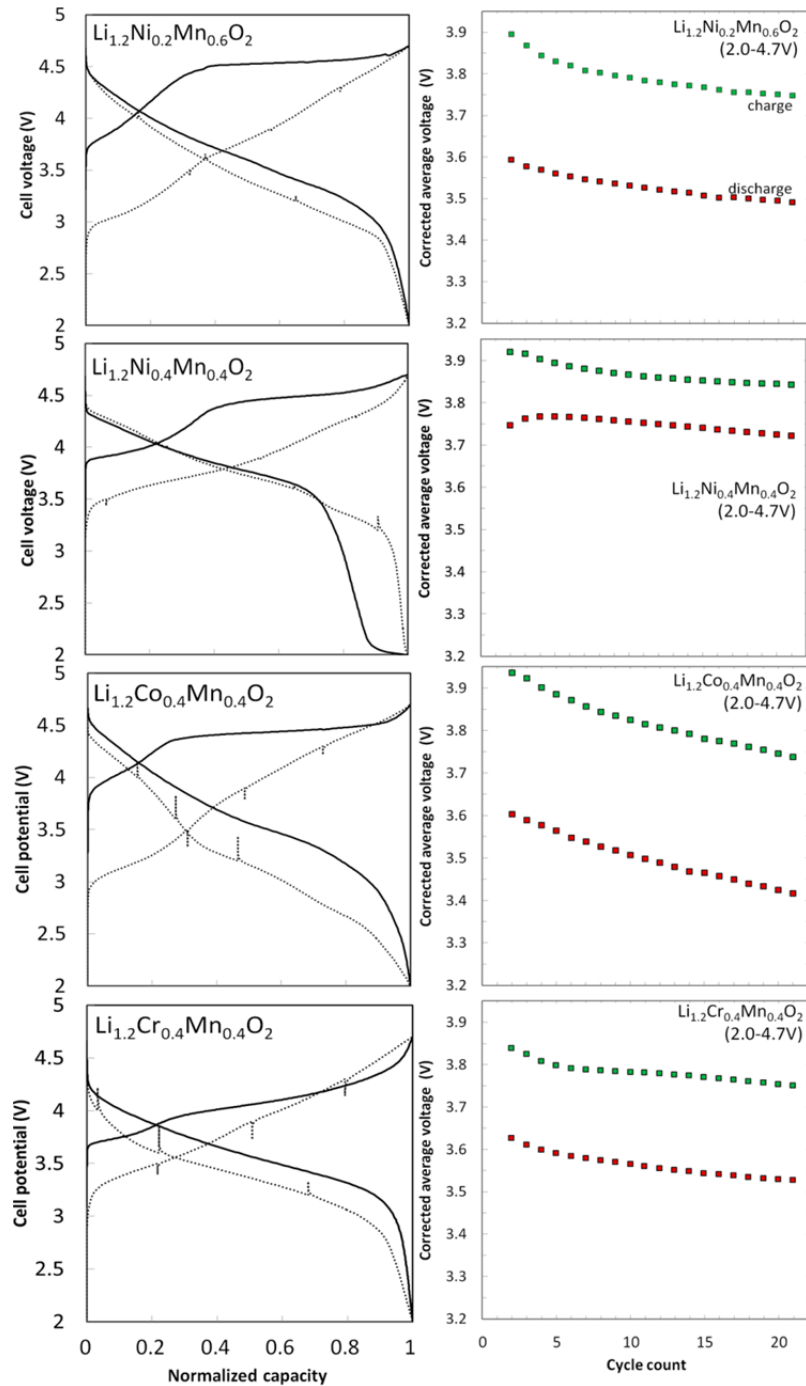


Figure IV - 65: Voltage profiles and corrected average voltages as a function of cycle number for selected layered oxides. The cycling window ranges from 2.0V to 4.7V. On the left hand side, all capacities are normalized. The solid line shows the 1st (“activation”) cycle; the dotted one the 20th cycle. On the right hand side, the top and bottom curves are the corrected average voltages during charge and discharge, respectively. All materials exhibit some degree of voltage fade if cycled to 4.7V vs. Li

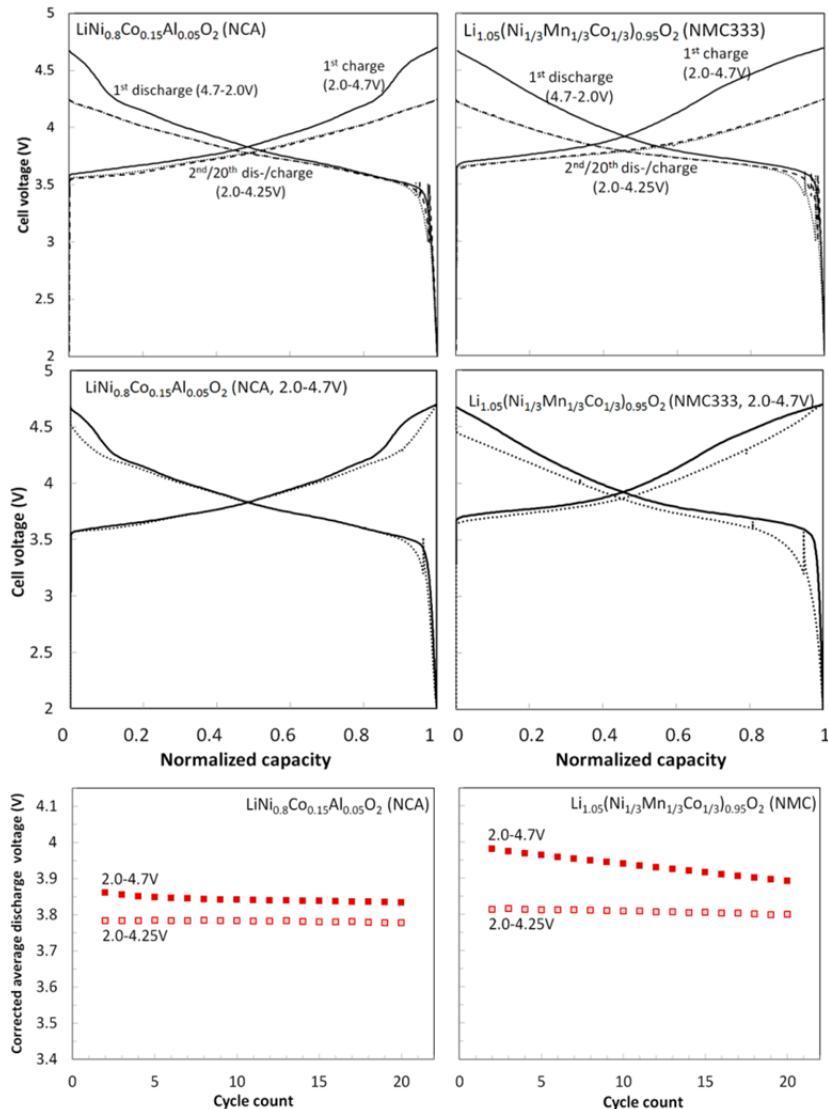


Figure IV - 66: Voltage profiles and corrected average voltages as a function of cycle number for NCA and NMC. Both materials are cycled over two different voltage windows, 2.0-4.25V (top panels) and 2.0-4.7V (middle panels), with the first cycle *always* ranging from 2.0V to 4.7V. All capacities are normalized. The solid line shows the 1st cycle; the dashed one the 2nd (only shown for the 2.0-4.25V window); the dotted one the 20th cycle. The lower panels show the corrected average discharge voltages for the two voltage ranges. Both materials exhibit some degree of voltage fade only when cycled up to 4.7V vs. Li.

Figure IV - 66 provides normalized capacity-voltage profiles for NCA and NMC over two different cycling windows, 2.0-4.25V and 2.0-4.7V vs. Li/Li⁺. The former range is depicted in the upper two panels of Figure IV - 66, the latter one is depicted in the middle panels. To ensure comparable testing conditions, the first cycle is always from 2.0V to 4.7V. Practically, no voltage decay exists, for both materials, during the lower voltage (4.25V) cycling, as the 2nd and 20th cycles are nearly identical. Some voltage fade is present at higher voltages (4.7V), although it is less than for the Li-rich chemistries described earlier. The corrected average *discharge* voltages, depicted in the bottom panels, confirm that practically no change in average

voltage occurs during the lower voltage (2-4.25V) cycling. When cycled to 4.7V, the *charge* voltage of NCA drops only by 8mV and that of NMC by 46mV; during *discharge* by 27mV and 88mV, respectively. Hence, the voltage gap widens for both materials.

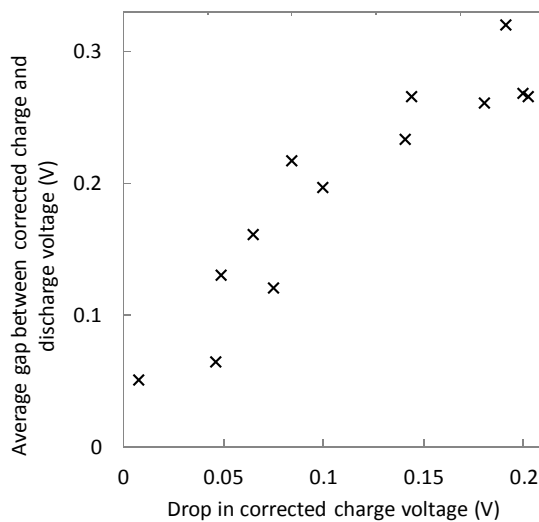


Figure IV - 67: Corrected average voltage gap plotted against the total drop of the corrected average voltage from 2nd to 20th charge ($\Delta \bar{U}_{corr}$). Individual data are collected from the same cells used for Figure IV - 66 through Figure IV - 69. Charge data are chosen because of their overall smaller cell-to-cell variability, as shown in Figure IV - 64. When a linear trend is assumed over this $\Delta \bar{U}_{corr}$ range, an R^2 -value of 0.85 is obtained

It is important to recognize that voltage fade and voltage gaps appear to be correlated. The scatter plot in Figure IV - 67 demonstrates this. Included here are data from the above compounds (same cells as in Figure IV - 68 and Figure IV - 69), from the LMR-NMC at 30°C and 55°C (same cells as in Figure IV - 66), and from the upper-cut-off voltage experiments (same cells as in Figure IV - 67). This apparent correlation agrees well with findings from recent variable window cycling studies supporting the hypothesis that both phenomena (i.e. hysteresis and voltage fade) share the same root cause.^[4]

Effect of Voltage Fade on Energy Density of Oxide Materials

Figure IV - 68 demonstrates the effect of voltage fade on energy density of LMR-NMC cells. The measured discharge energy densities are shown as a function of cycle number for baseline and modified baseline cells. In addition to voltage fade, capacity loss and resistance effects also cause the measured discharge energy to decrease; their physical origins have been identified and discussed elsewhere.^[1-3]

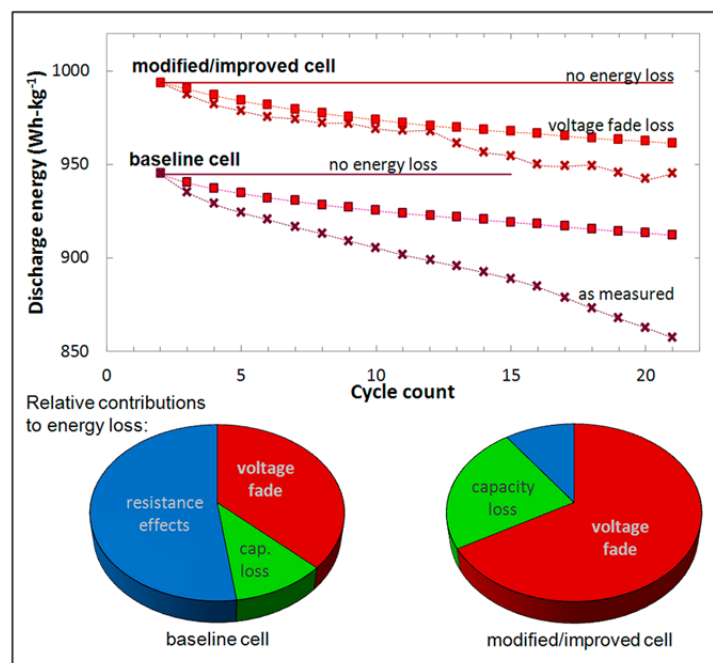


Figure IV - 68: Discharge energies as a function of cycle number for the LMR-NMC-based baseline and modified cells. The cycling window is 2.0–4.71V. The measured energy densities for both cells are given by the x-shaped data points. Energy loss comprises contributions from capacity loss, resistance effects, and voltage fade. Energy loss only due to voltage fade is given by the squared data points. The relative contributions of capacity loss (green), resistance effects (blue), and voltage fade (red) after 20 cycles after activation are measured separately and plotted for each cell in the pie charts. Voltage fade is a significant contributor to the overall energy loss

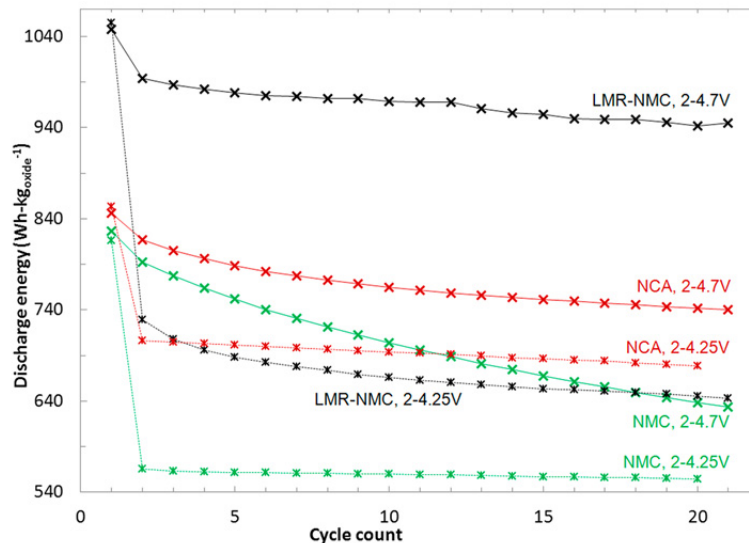


Figure IV - 69: Discharge energies for LMR-NMC (embedded in the modified baseline cell), NCA, and NMC for two voltage windows (2.0-4.25V and 2.0-4.7V) as a function of cycle number. Note that all materials are charged to 4.7V vs. Li/Li⁺ at 10 mA·g_{oxide}⁻¹ during the first cycle to ensure consistent testing among all materials and to ensure that the higher capacities of the LMR-NMC are accessed

The relative contributions of these three factors leading to the difference between 2nd and 21st discharge energies are shown as pie charts in Figure IV - 68. These charts are obtained by calculating the energy of the cell via $E(c) = \bar{U}(c)Q(c)$, with c being the cycle count and $E(c)$ the released energy upon discharge that decreases continuously throughout cycling. $\bar{U}(c)$ is the measured average cell voltage that decreases due to voltage fade and resistance effects; $Q(c)$ is the cell capacity that decreases due to resistance effects and *actual* loss in electrode capacity^[9]. Figure IV - 68 shows that voltage fade is significant to energy fade. In fact, once the increase in resistance is effectively mitigated through improved electrode and cell design, voltage fade becomes the largest contributor (>65%) to the overall energy fade.

Figure IV - 69 shows the oxide-specific energy density of three materials, LMR-NMC, NCA, and NMC, over 20 cycles and two voltage windows (2.0-4.25V and 2.0-4.7V). All cells were cycled initially to 4.7V to ensure complete activation and comparable testing conditions. At 4.7V, all three materials show energy fade. However, after 20 cycles, the oxide-specific energy density for LMR-NMC, NCA and NMC are 950 Wh·kg_{oxide}⁻¹, 740 Wh·kg_{oxide}⁻¹ and 630 Wh·kg_{oxide}⁻¹, respectively. That is, based on energy considerations, the LMR-NMC oxide is an excellent choice for cycling at high voltages (> 4.5 V vs. Li/Li⁺).

Voltage Fade – Observations from Differential Capacity Plots

Lithium- and manganese- rich transition metal oxides (LMR-NMC) are often described as

$x\text{Li}_2\text{MnO}_3 \bullet (1-x)\text{LiMO}_2$ (M = Ni, Co, Mn), i.e., as structurally integrated composites of Li_2MnO_3 and a Li-stoichiometric transition-metal bearing layered oxide^[10]. To achieve high energy densities (>900 Wh·kg⁻¹) the oxides are cycled at high voltages (>4.5 V vs Li/Li⁺). On extended cycling, however, cell energy decreases because of increasing cell resistance, loss of mobile lithium, and a continuous reduction in the average open circuit voltage of the oxide (termed “voltage fade”)^[11-13]. In addition to reducing usable energy voltage fade also complicates state-of-charge (SOC) determination, which is required for effective cell management.

Our studies show that voltage fade typically occurs when cells are cycled beyond the oxide “activation” plateau. An example of this oxide activation is shown in the inset of Figure IV - 70 which contains first 2-4.7 V cycle data at 30°C and 55°C for a $\text{Li}_{1.2}\text{Ni}_{0.15}\text{Mn}_{0.55}\text{Co}_{0.1}\text{O}_2$ vs. Li cell; this oxide has a theoretical capacity of 377 mAh·g⁻¹. Oxide delithiation commences at ~3.74 V at 30°C and at ~3.64 V at 55°C; the oxide activation commences at ~4.37 V at 30°C and at ~4.33 V at 55°C. The charge and discharge capacities at 30°C are 324 and 274 mAh·g⁻¹; the corresponding capacities at 55°C are 342 and 313 mAh·g⁻¹. Peaks corresponding to first oxide delithiation and oxide activation are seen in the differential capacity (dQ/dV) plots (Figure IV - 70). The peaks in these plots indicate the presence of lattice arrays that have distinguishably characteristic Gibbs energies^[14,15]; changes in the height and position of these peaks indicate crystal structure changes in the oxide.

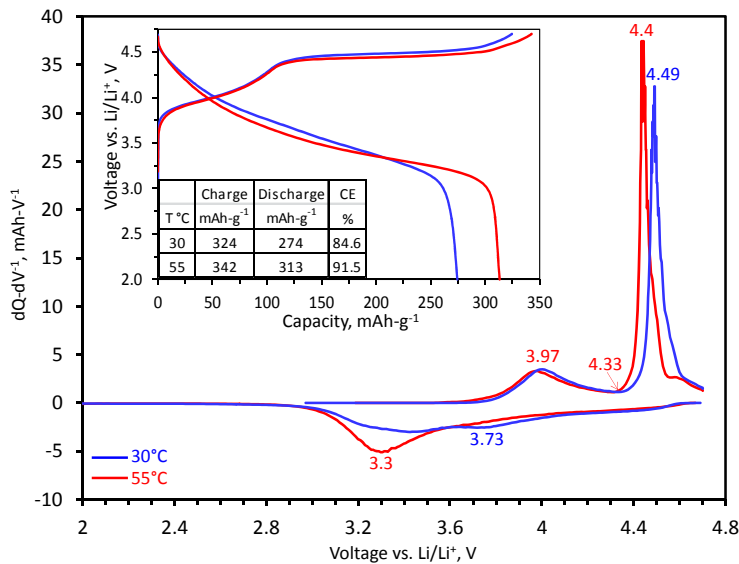


Figure IV - 70: First cycle differential capacity (dQ/dV) plots from $\text{Li}_{1.2}\text{Ni}_{0.15}\text{Mn}_{0.55}\text{Co}_{0.1}\text{O}_2$ vs. Li cells, cycled between 2-4.7 V with a 15 mA-g $^{-1}$ current at 30°C (blue) and 55°C (red). Inset shows the corresponding capacity-voltage plots. The columbic efficiency (CE) is the ratio of lithiation to delithiation capacity

Figure IV - 71 shows changes in the differential capacity plots from cycles 2 through 20 of a $\text{Li}_{1.2}\text{Ni}_{0.15}\text{Mn}_{0.55}\text{Co}_{0.1}\text{O}_2$ vs. Li cell cycled in the 2-4.7 V voltage range at 30°C. It is evident that the dQ/dV peaks between 3.0V and 3.5V shift down in charge voltage and grow at the expense of the higher voltage peak intensities (between ~3.8V and 4.7V) – a similar behavior is observed during discharge. As a result, the redox-active phase, initially located at ~3.5V (during

charge), appears to simultaneously transform and grow into one or more redox-active phase(s). The differential capacity plots reveal also another characteristic of the material: a large hysteresis caused by a major asymmetry between charge and discharge and by a relatively large voltage relaxation from 4.7V down to ~4.5V at the beginning of discharge. The voltage relaxation is partly caused by very sluggish kinetics even at very low cycling currents.

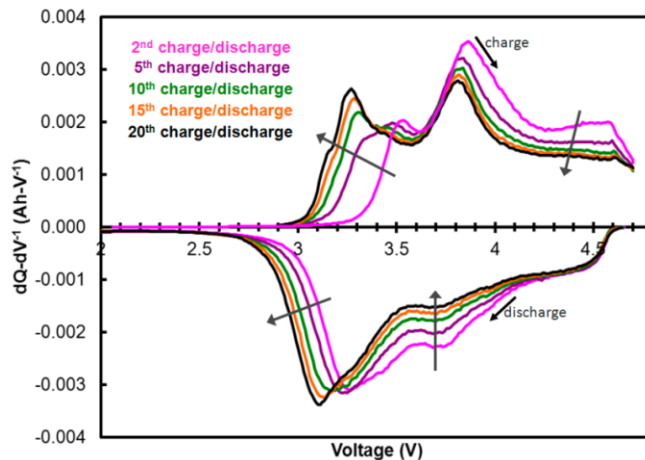


Figure IV - 71: Selected differential capacity plots from galvanostatic charge/discharge cycles 2 through 20, after initial activation of a $\text{Li}_{1.2}\text{Ni}_{0.15}\text{Mn}_{0.55}\text{Co}_{0.1}\text{O}_2$ vs. Li cell, in the 2.0-4.7V range at 30°C. The arrows indicate changes induced by the cycling. Increasing peak intensities and a shift to lower voltages around 3.1V reveal voltage fade

Because lithium metal impedance increases significantly after about 20 cycles, voltage fade data during extended cycling were obtained from $\text{Li}_{1.2}\text{Ni}_{0.15}\text{Mn}_{0.55}\text{Co}_{0.1}\text{O}_2$ vs. $\text{Li}_4\text{Ti}_5\text{O}_{12}$ cells. A typical dataset is shown in Figure IV - 72, wherein the cell was 1000 times between 0.75 – 3.15 V vs. LTO (2.3 – 4.7 V

vs. Li/Li $^{+}$) at 30°C. The crystal structure of $\text{Li}_4\text{Ti}_5\text{O}_{12}$ structure does not change during this extended cycling; therefore, all peak changes reflect crystal structure in $\text{Li}_{1.2}\text{Ni}_{0.15}\text{Mn}_{0.55}\text{Co}_{0.1}\text{O}_2$. Some features of Figure IV - 72 are as follows: (i) a continuous shift of the initial 3.5V charge peak to 3.15V; the corresponding peak on

discharge shifts to 2.95 V. These changes indicate cell capacity shifts to lower voltages on cycling, i.e., voltage fade; (ii) a continuous decrease of the initial 3.9 V charge (3.8 V discharge) peak, which reveals a continuous decreases in the originally present crystal structures; and (iii) a gradual increase of the 4.65 V charge peak, which suggests the growth of spinel ordering in the oxide. Note that the peak growth (also position change) rate, which corresponds to the voltage fade rate decreases, on cycling. The oxide voltage

profile appears to stabilize, i.e., the oxide appears to have attained a quasi-equilibrium structure, after about 400 cycles. On the other hand, the voltage hysteresis, which can be expressed as the difference between average voltages for the charge and discharge cycles, persists even after 1000 cycles. This observation indicates that the lithium atoms occupy different lattice sites during charge and discharge even though cell voltage and/or capacity is the same.

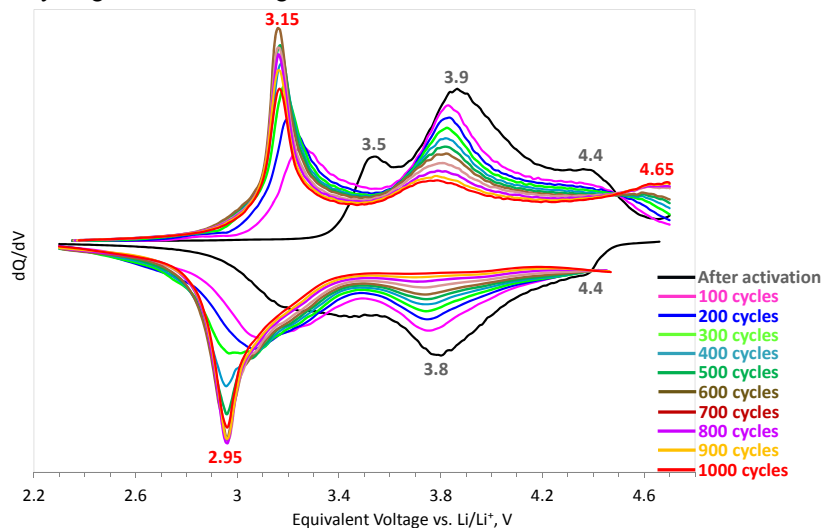


Figure IV - 72: Selected differential capacity plots from a $\text{Li}_{1.2}\text{Ni}_{0.15}\text{Mn}_{0.55}\text{Co}_{0.1}\text{O}_2/\text{Li}_4\text{Ti}_5\text{O}_{12}$ cell that was galvanostatically cycled in the 0.75 – 3.15 V (2.3 – 4.7 V vs. Li/Li^+) range at 30°C. Growth of the 3.15V charge peak (2.95V discharge peak) indicates voltage fade. Obvious changes are also observed for the other peaks as described in the text

Voltage Hysteresis and its Measurement by GITT experiments

Voltage hysteresis, which is the difference between average voltages for the charge and discharge cycles, is an apparent feature of LMR-NMC oxides cycled beyond the ~4.5 V activation plateau. This hysteresis arises from a variety of factors, which include thermodynamic (related to intrinsic, structural characteristics) and kinetic (related to transport/diffusional effects) features of the material. GITT (galvanostatic intermittent titration technique) experiments are one way to differentiate between the intrinsic material and extrinsic kinetic effects. In GITT experiments, the voltage response after a short current pulse is measured and is recorded as a voltage-time curve. By allowing the

samples to rest (zero current) sufficiently long after the current pulse the “equilibrium” voltages at various capacity values are obtained; this minimizes kinetic effects in the measured data.

Our GITT experiments were conducted on $\text{Li}_{1.2}\text{Ni}_{0.15}\text{Mn}_{0.55}\text{Co}_{0.1}\text{O}_2$ vs. Li cells and the resulting data are shown in Figure IV - 73 and Figure IV - 74. After an initial ‘activation’ cycle in the 2–4.7V voltage window, each cell followed a GITT cycling protocol, which consisted of 0.1 mA/cm² current pulse for 600s, followed by 6000s rest. The upper cutoff voltage (UCV) during the charge cycle was 4.7V and the lower cutoff voltage (LCV) during discharge was either 3.0V or 2.0V. Each charge-discharge cycle lasted a total of 22 days, which is equivalent to a C/250 cycling rate.

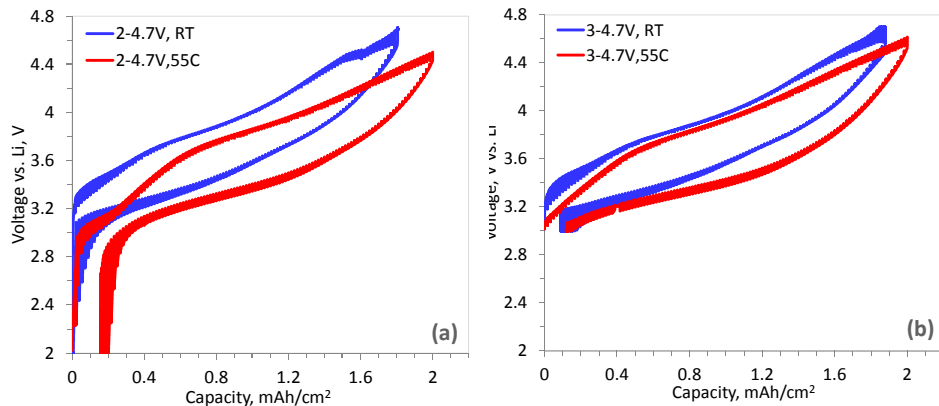


Figure IV - 73: (a) Capacity-voltage plots obtained by a GITT protocol from $\text{Li}_{1.2}\text{Ni}_{0.15}\text{Mn}_{0.55}\text{Co}_{0.1}\text{O}_2$ vs. Li cells in the (a) 2–4.7V, and (b) 3–4.7V voltage windows; the data were collected both at room-temperature (RT) and at 55°C

Figure IV - 73a shows the effect of cycling in the 2–4.7V voltage window at room temperature and at 55°C. Voltage hysteresis is evident at both test temperatures. Furthermore, the hysteresis is greater at 55°C than at room temperature, which indicates that the effect is an intrinsic feature of the oxide; kinetic factors, such as ion transport and diffusional effects are better, and would be expected to narrow the hysteresis loop at higher temperatures. A wider hysteresis loop at 55°C is also observed when the LCV is restricted to 3.0V as shown in Figure IV - 73b; this figure also indicates that the 3.0V LCV does not have a significant effect on the hysteresis. Other observations from Figure IV - 73a and Figure IV - 73b are the following: (i) a higher cell capacity is obtained at the higher temperature, (ii) a significant depression of the voltage profiles (voltage fade) is observed; this depression is non-uniform and varies depending on its location on the capacity-voltage profile. This non-uniform voltage fade is also observed in Figure IV - 74, which shows the effect of extended cycling (and associated calendar aging). Although the oxide energy density decreases on extended cycling, its energy efficiency improves as the voltage hysteresis decreases. However, the voltage gap never closes and the hysteresis persists even after long-term cycling as seen in other datasets.

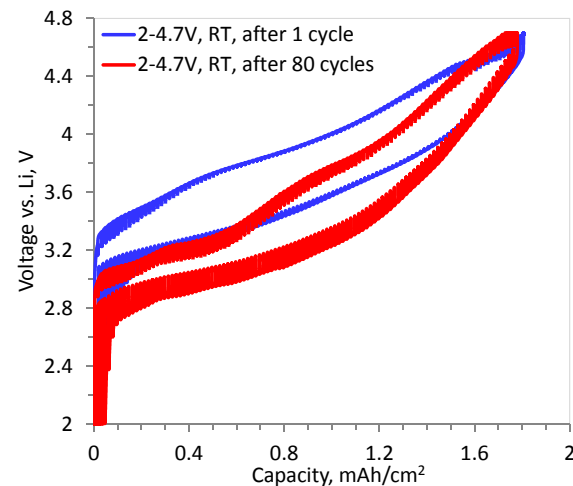


Figure IV - 74: Capacity-voltage plots, obtained with a room temperature GITT protocol, from a $\text{Li}_{1.2}\text{Ni}_{0.15}\text{Mn}_{0.55}\text{Co}_{0.1}\text{O}_2$ vs. Li cell showing the effect of cycle life aging in the 2–4.7V voltage window. The aged sample shows significant voltage fade; hysteresis persists even after aging.

Effect of Voltage Hysteresis on AC impedance data

Voltage hysteresis, which is the difference between average voltages for the charge and discharge cycles, is an apparent feature of LMR-NMC oxides cycled beyond the ~4.5 V activation plateau. In recent articles Croy and coworkers have shown that voltage fade is associated with voltage hysteresis^[16–18]. They propose that partially reversible migration of transition metal and/or lithium ions at high states of charge is responsible for these phenomena. The energy barrier that needs to be overcome for reversible migration of transition metal ions into the original octahedral sites is responsible for the voltage hysteresis. The transition metals that do not return to their original positions create new environments for lithium intercalation at lower voltages and, therefore, voltage fade.

Here we show that AC impedance data obtained on $\text{Li}_{1.2}\text{Ni}_{0.15}\text{Mn}_{0.55}\text{Co}_{0.1}\text{O}_2$ electrodes depends on whether the data were obtained on the charge or on the discharge portion of the cycling curve. Impedance data are important because they are a measure of the cell's ability to deliver and accept charge at relatively high-rates; for example, capacity data obtained at $\geq \text{C}/1$ rates could be strongly affected by cell impedance. Furthermore AC impedance data helps identify ohmic, charge-transfer, and diffusion-related contributions to

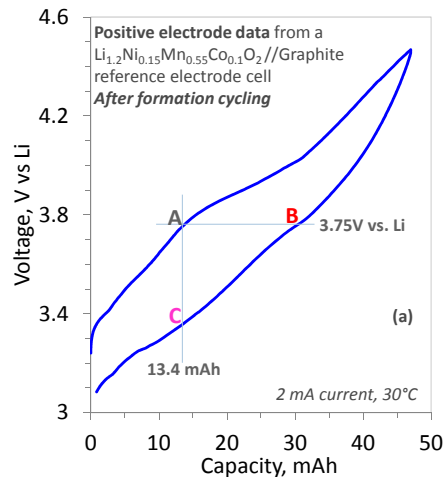
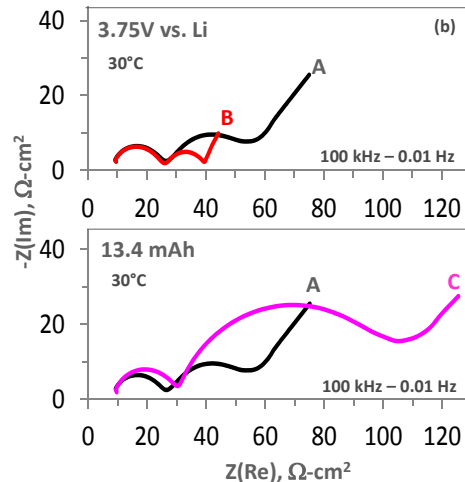


Figure IV - 75: (a) Positive electrode data from a $\text{Li}_{1.2}\text{Ni}_{0.15}\text{Mn}_{0.55}\text{Co}_{0.1}\text{O}_2$ // Graphite cell showing the voltage-capacity profile after formation cycling. The electrode voltage is shown vs. Li/Li^+ . AC impedance data (100 kHz–0.01 Hz, 30°C) were obtained at locations A, B and C shown on the plot. Locations A and B are at 3.75 V but on charge and discharge, respectively. Locations A and C are at 13.4 mAh but on charge and discharge, respectively. AC impedance data from locations A and B are compared in (b), and from A and C are compared in (c). It is evident that the impedance data are different during charge and discharge even though the cell voltage/cell capacity is similar

Figure IV - 75a shows voltage-capacity data from the positive electrode after the cells underwent formation cycling [21]. It is evident that the electrode voltage during charge is higher than the voltage during discharge. The difference between the charge and discharge voltage (i.e., the voltage hysteresis) depends on electrode capacity and appears to be greatest around 3.75 V vs. Li. AC impedance data were obtained at locations A (3.75 V, 13.4 mAh), B (3.75 V, 31 mAh) and C (3.3 V, 13.4 mAh); these data are shown in Figure IV - 75b and Figure IV - 75c. The data were obtained with a EG&G 273A potentiostat and a Solartron SI1260 frequency response analyzer controlled by ZPLOT measurement software. The cells were charged to the desired voltage and held for ~ 10 h before data were collected in the 100 kHz to 10 mHz frequency range, with a 10 mV perturbation around the hold voltage.

The positive electrode data shown in Figure IV - 75b and Figure IV - 75c exhibits several features including: (i) a high-frequency arc (with a maximum in the 10 kHz to ~ 1 kHz range), which can be attributed to the electronic network that links the oxide particles to the current collector; (ii) a mid-frequency arc (with a maximum in the 100 Hz to ~ 1 Hz range), which is

cell impedance. The data shown in Figure IV - 75 were obtained from a planar test cell containing 32 cm^2 area single-side coated positive and negative electrodes. The cells also contain a tin-coated $25 \mu\text{m}$ thick Cu wire, sandwiched between two Celgard 2325 separators; the tin coating is lithiated in-situ to form a Li-Sn alloy reference electrode that monitors potential at the positive and negative electrodes. Details of reference electrode preparation and cell assembly are discussed elsewhere [19,20].



associated with charge transport across the particle-particle and particle-electrolyte interfaces; and (iii) a Warburg impedance tail at frequencies < 1 Hz, which is associated with bulk diffusional effects in the cell, including diffusion of salt in the electrolyte and of lithium within the electrode active materials. More importantly, the data at locations A, B and C are significantly different.

For instance, in Figure IV - 75b, the impedances associated with mid-frequency arc and Warburg tail are smaller at location B than at A, even though the electrode voltage is 3.75 V vs. Li at both locations. The difference arises because of capacity differences; the lower oxide lithium content at B enhances ionic transport both at the interface and within the oxide bulk. In Figure IV - 75c, the impedance at location C is much greater than at A, even though the electrode capacity is the same, 13.4 mAh. This impedance difference indicates that, although lithium content of the oxide is the same, the sites occupied by the lithium atoms are very different.

Capacity-voltage profiles of the positive electrode change on extended cycling. Voltage fade, resulting

from structural changes in the oxide, causes a gradual decay in average electrode voltages. This decay is counteracted by the continuously increasing electrode resistance, which causes the average charge voltage to rise. Because the processes are non-uniform over the oxide capacity window the voltage hysteresis exhibits a non-uniform changes in the voltage-capacity profiles. These changes complicate cell state-of-charge (SOC) determination, which is required for effective battery management. Furthermore even though the hysteresis decreases it persists even after long-term cycling. That is, the cell impedance differences between charge and discharge portions of the cycle needs to be considered when designing the battery management modules.

Development of a Physical Theory of Voltage Fade

Lithium- and manganese-rich (LMR) cathode materials have been studied extensively, inside our project, with a wide range of experimental techniques aimed at characterizing voltage fade phenomena as shown. The primary experiments are electrochemical, and often times, extracting information on voltage fade phenomena relies on an interpretation of the voltage profile as a function of the number of charge/discharge cycles. Figure IV - 76 exemplifies voltage fade phenomena by showing the change in cell capacitance C_{cell} vs. cell voltage Φ_{cell} profiles for $\text{Li}_{1.2}\text{Ni}_{0.15}\text{Mn}_{0.55}\text{Co}_{0.10}\text{O}_2$ (TODA HE5050) in a lithium-titanate-oxide (LTO) coin cell from cycle 5 to cycle 45. Shaded regions I, II, III, and IV represent differences in low voltage charge capacity, high voltage charge capacity, high voltage discharge capacity and low voltage discharge capacity respectively. The capacity encompassed by the shaded regions are approximately: I = 0.93, II = 0.84, III = 0.81 and IV = 0.87 coulombs. The data suggest that decreases in high voltage capacity regions II and III are correlated with increases in low voltage capacity regions I and IV.

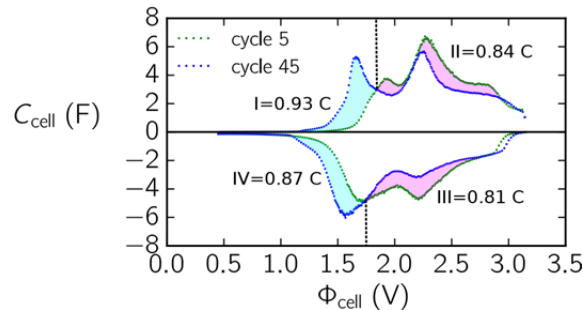


Figure IV - 76: Evolution of a capacitance vs. voltage profile for TODA HE5050 in a lithium-titanate-oxide (LTO) coin cell. The capacities of the shaded regions are indicated on the plot. Voltages are versus LTO

Theory and associated models that physically predict or de-convolute experimental voltage profiles can help resolve and quantify the causal relationships that are central to voltage fade phenomena. However,

there are two main requirements: (i) the models need to have physical relevance and (ii) the models must be simple enough such that they can be effectively compared with a wide range of voltage profiles under various conditions. Bearing the aforementioned stipulations in mind, a phenomenological model of voltage fade is proposed, recast into a generalized form and applied to de-convolute the cycle to cycle evolution of LMR charge profiles.

Though the phenomenological model and qualitative relation to proposed theories of voltage fade are coherent, quantitative descriptions are not as straightforward. The challenge for LMR is that the voltage profile has multiple components with differing physical origin, thus electrochemical fingerprints of voltage fade are often masked by overlapping processes.

Differential capacitance plots for charging of a typical LMR cathode material, TODA HE5050 in a Li coin cell as a function of cycling current are given in Figure IV - 77. We examine the qualitative effects of changes in rate because we want to establish a quasi-equilibrium voltage profile for which Eq. (1) may be valid, where Kelvin temperature is given by T . The standard voltage is given by Φ_n and an Li-Li interaction energy is given by ω_n .

$$\Phi_{cell} = \Phi_n + \frac{\omega_n}{f_n} \Theta_n^{\text{Li}} + \frac{k_b T}{e} \ln \left(\frac{\Theta_n^{\text{Li}}}{f_n - \Theta_n^{\text{Li}}} \right)$$

A differential capacitance plot is a convenient representation for rate comparison since LMR materials typically increase in capacity as the cycling rate decreases.

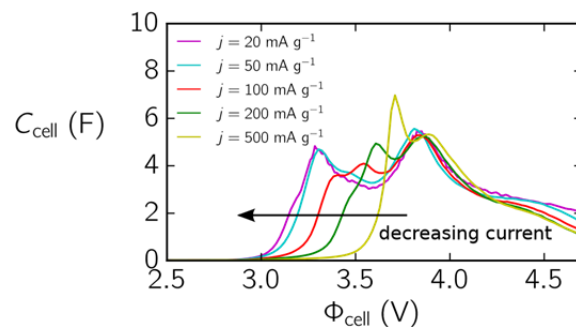


Figure IV - 77: Comparison of the effect of rate on differential capacity plots for post-activated (cycle 21) TODA HE5050 in a Li coin cell. Indicated currents are in mA g^{-1} . Voltages are vs. Li

Figure IV - 77 indicates that a quasi-equilibrium current is reached by 20 mA g^{-1} . We argue that qualitative changes in the differential capacitance plot via a decrease from 50 to 20 mA g^{-1} are much smaller than the changes from 100 to 50 mA g^{-1} . Even lower currents for quasi-equilibrium analysis are desired but

the marginal differences in the profiles upon decreases below 20 mA g^{-1} are outweighed by the prohibitive time of the experiment.

Voltage window studies can give insight into the number of components that we may need in our mean field approach. Figure IV - 78 shows charge profiles for TODA HE5050 as a function of cycle window. Over multiple cycles, the windows between 3.2-4.7 V as well as 3.1-4.7 V showed larger signatures of voltage fade phenomena in comparison to the other voltage windows. Furthermore, the windowing studies suggest three electrochemically distinct components as shown from a compositional perspective depicted in Figure IV - 78: These components are: A-voltage fade capacity, B-standard capacity LiMO_2 (where M = Mn,Ni,Co) related component, C - high capacity Li_2MnO_3 related component.

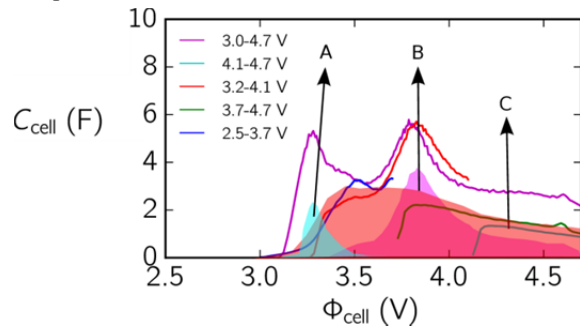


Figure IV - 78: Comparison of differential capacity plots in different voltage windows for post-activated (cycle 21) TODA HE5050 in a Li coin cell. Shaded regions represent hypothetical de-convolutions as described in the text. Voltages are vs. Li

In addition to rate and voltage window, the timescales of voltage fade are another experimental consideration that needs to be addressed. Voltage fade is a rather subtle phenomena that accumulates over a number of cycles. During the first cycle of activation the material undergoes a drastic change then over the next 10 to 50 cycles (short term) the initial stages of voltage fade emerge; from cycles 50 and onwards (long term) a more gradual and systematic trend emerges.

We apply the model to short term (6-20 cycles) and long term (100-500) cycling data of TODA HE5050 ($\text{Li}_{1.2}\text{Ni}_{0.15}\text{Mn}_{0.55}\text{Co}_{0.10}\text{O}_2$). In the short term test 20 post-

activation degradation (20 mA g^{-1}) cycles between 2.50 and 4.70 V vs. Li are performed. In the long term test 50 degradation (100 mA g^{-1}) cycles are performed followed by 3 diagnostic (20 mA g^{-1}) cycles between 1.15 and 3.10 V vs. LTO (2.70 and 4.65 V vs. Li). Only cycles with currents less than 20 mA g^{-1} were analyzed with the model. The range of cycles are analyzed iteratively with Eq. (1). More specifically, we start with an initial guess for the parameters of components A, B and C and compare with the profile of the first cycle in the sequence; then we perform a non-linear least squares parameter refinement for this cycle and use the refined parameters for the initial guess of the next cycle, then iterate through the desired range of cycles. Results are shown in Figure IV - 79 where a-e show the de-convoluted differential capacitance plot, f shows the evolution of the differential capacity profile for the components, g-i show how the standard voltages, fractions and interaction energies from Eq. (1) evolve with cycle number.

The standard voltages for B and C remain relatively constant while the standard voltage for A decreases slightly with cycle number. Interaction energies are also relatively constant; the high interaction energy for C gives the broad peak shape observed in the differential capacity plot. The fraction of component A increases at the same rate of decrease of component C while the fraction of component B remains unchanged.

For the long-term cycling data we analyze the second diagnostic cycle since rate effects obscure the first diagnostic charge cycle due to the switch from a fast to a slow cycle. Analyses are performed at 100,200,300,400 and 500 cycle increments. The fit of the model to the experimental data is given in Figure IV - 80. The standard voltages for A and B remain relatively constant and evenly spaced with a difference of approximately 0.7 V while the equilibrium voltage for component C increases slightly with cycle number. As with the short term cycles, interaction energies for A and B are much lower than that of C. Component fraction A increases with cycle number while component fraction B decreases with cycle number; the rates of change are similar.

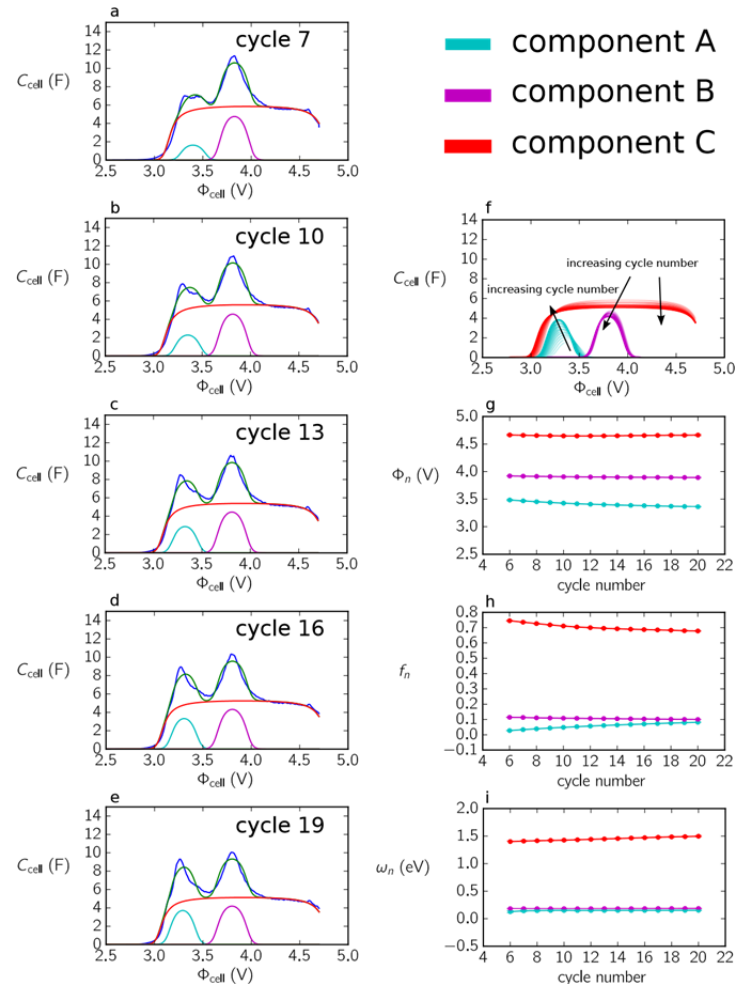


Figure IV - 79: Model-based diagnostic analysis of short-term cycling of TODA HE5050 in an Li coin cell. Voltages are vs. Li

In short term cycle analyses in the 6-20 cycle range it was found that the fraction of component A increased and the fraction of component C decreased at similar rates while component B was constant. While in long term cycle analyses in the 100-500 cycle range it was found that the fraction of component A increased and the fraction of component B decreased at similar rates while component C was constant. In a model-based compositional analysis we have shown that component C was proportional to the Li_2MnO_3 content, viz. it qualitatively represents the “extra” capacity that LMR

materials gain over their non Li rich layered counterparts. Indeed the broad general features of component C that we use in the model are unrealistic; masking hysteresis, diffusion phenomena as well as convoluting some overlapping characteristics of A, B and C as we have shown in Figure IV - 78. However, we argue that the de-convolution method captures the essential evolutionary features of component A and can be described within the framework of the phenomenological model.

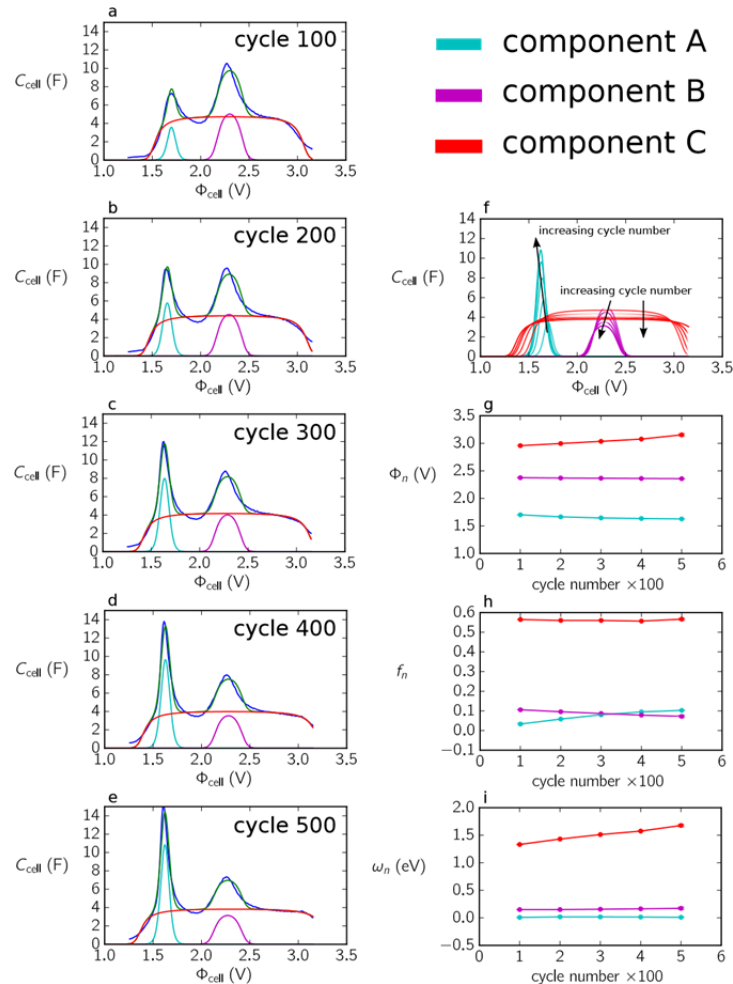
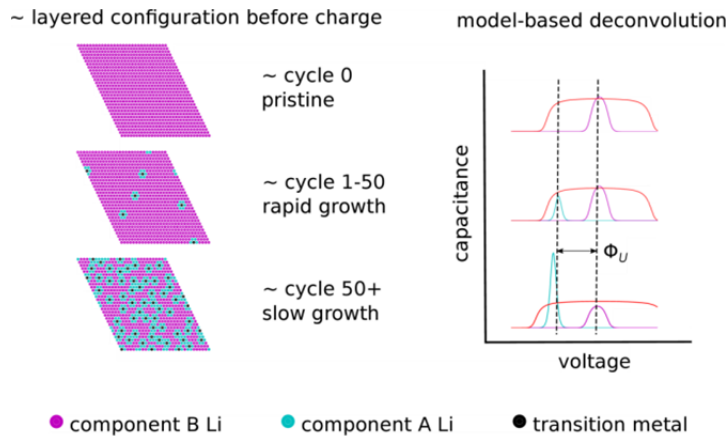


Figure IV - 80: Model-based diagnostic analysis of long-term cycling of TODA HE5050 in an LTO coin cell. Voltages are vs. LTO

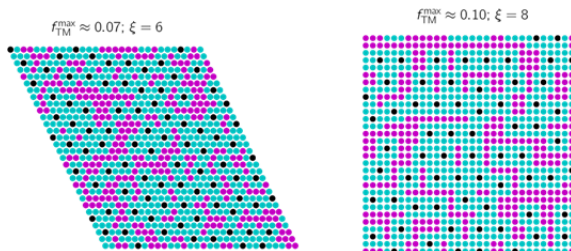
Figure IV - 81 gives a schematic view of a plausible relationship between the model and the deconvoluted differential capacity data for the long term test. A complex interplay between all components, the cycle window and the cycling rate determines the change in initial configuration from cycle to cycle. We demonstrate that local repulsive interactions between the migrated TM ions and nearest neighbor Li shell ions

result in a lower potential for the nearest-neighbor Li clusters. In Figure IV - 81 we speculatively allude to the idea that the difference in standard component voltages between components A and B, are due to these local TM-Li interactions; the relative fractions of A and B are related to the coordination factor ζ as well as the TM ion fraction f_{TM} .

**Figure IV - 81: Growth of voltage fade component**

From a mechanistic view: prior to activation, the Li layer, viz. Li similar to component B, has only a minor TM ion population. After activation and during each subsequent full cycle, a fraction of TM ions irreversibly migrate into the Li layer creating a cluster consisting of a TM ion and its associated nearest neighbor shell of Li, viz., component A Li. Within the theory, the growth rate would be limited by the free space available for clusters; as the number of clusters increases the growth rate will slow.

Accordingly, we assume that the growth of clusters and thus TM ions will be limited to a maximum amount, $f_{TM}^{\max} = \frac{1}{\xi} f_A^{\max}$. In Figure IV - 82, we show two approximate f_{TM}^{\max} values for a hexagonal and square lattice with different nearest neighbor coordination factors. These were generated using a random sequential adsorption algorithm and are shown for illustrative purposes only.

**Figure IV - 82: Hypothetical maximum TM ion occupations**

With the insights afforded by Figure IV - 81 and Figure IV - 82, a simple growth rate for the voltage fade component can be written as

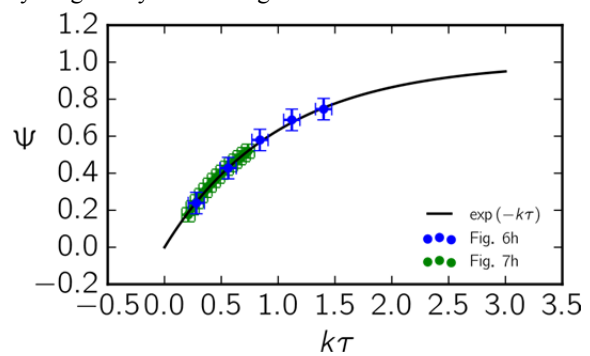
$$\frac{df_A}{d\tau} = (f_A^{\max} - f_A)k \quad (2)$$

where τ is cycle number and k is the fractional amount of TM ions that migrate into the Li-rich region per cycle. The parameter k depends on the details of the cycling protocol, viz. the cycling rate, window and

temperature. Assuming a negligible initial amount of f_A , Eq. (2) can be solved to give,

$$\Psi = \frac{f_A}{f_A^{\max}} = 1 - \exp(-k\tau). \quad (3)$$

In Figure IV - 83 we show re-scaled data generated from Figure IV - 79 and Figure IV - 80 with Eq. (3). The fit parameters for the short term cycling were $k = 0.035$ (2) cycles⁻¹ and $f_A^{\max} = 0.158$ (8) and for the long term cycling they were $k = 0.0028$ (2) cycles⁻¹ and $f_A^{\max} = 0.138$ (6) where the numbers in parenthesis are the error in the last digit. The re-scaling shows that both sets of data have similar values of f_A^{\max} but the rate constants differ by about an order of magnitude. This difference in growth rates is attributed to the fact that the 500 cycle experiment conducted cycling at 125 mA g⁻¹ between diagnostics cycles and the short term cycling conducted cycling solely at 20 mA g⁻¹.

**Figure IV - 83: Growth curve of voltage fade component for data extracted via model-based analysis**

In Figure IV - 84 we extend this growth rate analysis to a systematic study on the effect of cycling rate on voltage fade. The post-activation cycling protocol for these tests consisted of:

1) 3 window closing (2.0-4.7, 2.0-4.1, 2.0-3.7 V) diagnostic cycles at a current of 20 mA g^{-1} .

2) 8 degradation cycles at a specified current of 20, 50, 125, 250 or 500 mA g^{-1} .

3) Repeat 6 times.

We assume that the 2.0-3.7 V capacity from the diagnostic cycle can give a measurement based estimate of f_A . The adjustable parameters were the rate constants for each current and f_A^{\max} . We found that $f_A^{\max} = 56(4) \text{ mA h g}^{-1}$ and Figure IV - 84b shows the rate of TM ion migration as a function of cycling current.

Normalizing values of f_A^{\max} to the initial post-activated charge capacity (Figure IV - 84) or sum of component fractions (Figure IV - 83) we have $f_A^{\max} \approx 0.2$ for the data from Figure IV - 84 and for the analysis from Figure IV - 83. We can also compare the rates, $k \approx 0.04 \text{ cycles}^{-1}$, for the short-term cycling test and the 20 mA g^{-1} test since the cycling protocols were similar. The two de-convolution methodologies, model-based and measurement-based, agree.

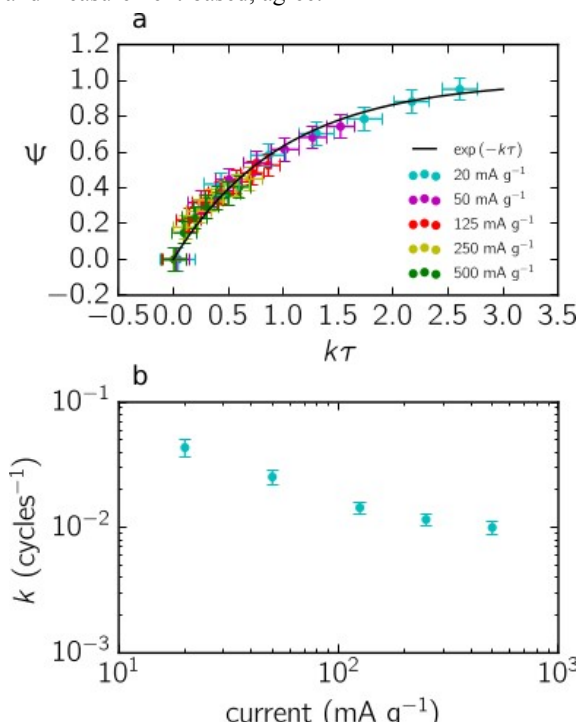


Figure IV - 84: Growth curve of voltage fade component for data extracted via measurement-based analysis

The rate parameter k declines sharply with increasing cycling current. This observation is in line with the hypothesis that voltage fade is a strong function of the state of lithiation/delithiation and the time spent within a particular state of lithiation/delithiation during the cycle. However, the rate appears to approach a constant value for currents greater than 100 mA g^{-1} . Based on this and previous work, the leveling off of the rate parameter is hypothesized to be the result of aging

induced by the diagnostic cycle. Future work will probe the effect of the frequency of diagnostic cycles to elucidate refined growth rate values under various conditions.

Here we outlined a phenomenological theory of voltage fade. The theory demonstrated the causal relationship between TM ion incorporation into Li-rich regions and the phenomena of voltage fade. Key parameters were the interaction energy voltage which determines the degree of separation between high and low voltage capacities and the TM ion coordination factor which determines the fractional amount of low voltage capacity. This theory is general and not bound to a specific crystallographic lattice or TM ion species.

The theory was put in the framework of a more generalized mean field model and we presented experiments that allowed us to rationally simplify the model to 3 essential components. The 3 component model was applied to de-convolute the evolutionary behavior of TODA HE5050 charge profiles. In general, components B and C decreased at the expense of component A. Additional analyses are required to isolate the contributions of components B and C separately.

Based on the phenomenological model proposed and the extracted component-wise evolutions, a differential growth law was proposed. The key parameters were the maximum TM ion fraction and the rate of TM ion migration per cycle. Data extracted from the analysis as well as experimentally generated voltage fade component evolution data all lie on a single growth curve. Thus model-based and measurement-based LMR voltage profile de-convolutions agree.

The relationship between TM ion migration rate per cycle and cycling current suggest that the dependencies of voltage fade on cycling conditions can be rationalized. We demonstrated that the per cycle rate of TM ion migration is lowest at high cycling rates but at high cycling rates the energy density is lower thus there is a balance between the rate of voltage fade and energy density. We speculate that parametric growth curves such as Figure IV - 84b can be generated for various stressors to give the rate of TM ion migration or voltage fade as a function of temperature, voltage window or Li_2MnO_3 content. Speculatively, there will be an optimal combination of stressors that will minimize the rate of transition metal migration and voltage fade while maximizing energy density.

Conclusions and Future Directions

Voltage fade reduces the energy density for a wide range of layered oxides as they are electrochemically cycled to higher voltages to improve energy and power densities. A protocol to measure and quantify voltage fade throughout cycling is proposed, and applied to

several materials demonstrating that this phenomenon is common for many layered oxides. The observations from our various electrochemical studies include the following:

- All lithium- and manganese-rich layered oxides display voltage fade and voltage hysteresis.
- Lithium-stoichiometric oxides, cycled to 4.7V vs. Li/Li⁺, also show voltage fade but at a much lower rate.
- In general, voltage fade rate is greater at higher temperatures, at higher upper cutoff voltages, and at longer aging periods.
- Oxide impedance data are strongly affected by the voltage hysteresis. For the same oxide potential and/or lithium-content, observed differences indicate that Li atoms occupy different sites during the charge and discharge cycles.
- Voltage Fade is not mitigated by surface coatings and electrolyte additives that form passivation films on the oxide particles.
- Voltage fade can be effectively circumvented by choosing lower cut-off voltages and possibly reduced by choosing lower temperatures. Such cycling, however, is undesirable when higher energy and power densities are required.
- Extended cycling data from Li₄Ti₅O₁₂ counter electrode cells indicate that the voltage profile stabilizes around 400 cycles. The voltage hysteresis decreases during this cycling but persists even after 1000 cycles.
- A mean field lattice gas model, which includes a parameter minimization and analysis package, has been developed to quantitatively deconvolute the various features observed in differential capacity charge profiles. The model provides a plausible causality relationship between transition metal migration and the nucleation and growth of a low voltage phase at the expense of a high voltage phase.

Future Directions

Voltage fade results from irreversible structural changes in the oxide that includes the relocation of transition metals from into the lithium layer, ultimately leading to the formation of spinel-structure frameworks. To minimize the fade, this irreversible transition metal migration needs to be inhibited and the layered structure needs to be stabilized to high voltages. Some questions that could be addressed in future work could include the following: (i) Which elements migrate during the high voltage cycling and what are their migration pathways? (ii) What makes cation migration irreversible and could it be reversed (or accelerated)? (iii) Does the first charge cycle electrochemical activation of the oxides affect

voltage fade and, if so, how? And, into what structure(s) do the layered oxides eventually transform into?

The Voltage Fade Team

Burrell, Anthony K.; Abouimrane, Ali; Abraham, Daniel; Amine, Khalil; Balasubramanian, Mahalingam; Barenco Garcia-Ontiveros, Javier; Belharouak, Ilias; Benedek, Roy; Bettge, Martin; Bloom, Ira D.; Long, Brandon R.; Chen, Zonghai; Croy, Jason R.; Dees, Dennis W.; Dogan, Fulya; Gallagher, Kevin G.; Henriksen, Gary L.; Iddir, Hakim; Ingram, Brian J.; Johnson, Christopher; Key, Baris; Li, Yan; Lu, Wenquan; Miller, Dean J.; Ren, Yang; Slater, Michael D.; Thackeray, Michael M.; Vaughey, John T.; Wu, Huiming; Wu, Qingliu; Zhu, Ye; Yang, Zhenzhen; Lee, Eungje; Aoun, Bachir; Vu, Anh D.; Lin, Chi-Kai; Rinaldo, Steven G.; Tenant, Robert; Ban, Chunmei; Nanda, Jagit; Bugga, Kumar; Yang, Xiao-Qing; Mohanty, Debasish; Li, Jianlin; Payzant, Andrew; Wood, David; Daniel, Claus; Jansen, Andrew; Polzin, Bryant; Trask, Steven; Krumdick, Greg.

FY 2014 Publications/Presentations

1. M. Bettge, Y. Li, K. Gallagher, Y. Zhu, Q. Wu, W. Lu, I. Bloom, D.P. Abraham, "Voltage Fade of Layered Oxides: Its Measurement and Impact on Energy Density", *J. Electrochemical Society* 160 (2013) A1-A10.
2. K.G. Gallagher, J.R. Croy, M. Balasubramanian, M. Bettge, D.P. Abraham, A.K. Burrell, M.M. Thackeray, "Correlating hysteresis and voltage fade in lithium- and manganese-rich layered transition-metal oxide electrodes", *Electrochemistry Communications* 33 (2013) 96–98.
3. Y. Li, M. Bettge, J. Barenco, D.P. Abraham, "Unexpected voltage fade in LMR-NMC oxides cycled below the "activation" plateau" *J. Electrochemical Society*, manuscript accepted for publication (2014).
4. S.G. Rinaldo, K.G. Gallagher, B.R. Long, J.R. Croy, D.P. Abraham, M. Bettge, J. Barenco, D.W. Dees, "Physical Theory of Voltage Fade", manuscript in preparation (2014).
5. D. Mohanty, A.S. Sefat, J. Li, R.A. Meisner, A.J. Rondinone, E.A. Payzant, D.P. Abraham, D.L. Wood, III, C. Daniel, "Correlating Cation Ordering and Voltage Fade in a Lithium- Manganese-Rich Lithium-Ion Battery Cathode Oxide: a Joint Magnetic Susceptibility and TEM Study", *Physical Chemistry Chemical Physics* 15 (2013) 19496–19509.
6. D. Mohanty, A. Huq, E.A. Payzant, A.S. Sefat, J. Li, D.P. Abraham, D.L. Wood, III, C. Daniel,

- “Neutron Diffraction and Magnetic Susceptibility Studies on a High-Voltage Li_{1.2}Ni_{0.15}Mn_{0.55}Co_{0.1}O₂ lithium-ion Battery Cathode; an Insight to the Crystal Structure”, Chem. Mater. 25 (2013), pp 4064–4070.
7. D. Mohanty, A.S. Safat, S. Kalnaus, J. Li, R.A. Meisner, E.A. Payzant, D.P. Abraham, D.L. Wood, C. Daniel, “Investigating Phase Transformations in Li_{1.2}Ni_{0.15}Mn_{0.55}Co_{0.1}O₂ lithium-ion battery cathodes during high-voltage hold (4.5V) via magnetic, X-ray diffraction and electron microscopy studies”, J. Mater. Chem. A 1 (2013) 6249.

References

1. Y. Li, M. Bettge, B. Polzin, Y. Zhu, M. Balasubramanian, D. P. Abraham, *J. Electrochem. Soc.* **160**, A3006 (2013).
2. M. Bettge, Y. Li, B. Sankaran, N. Dietz Rago, T. Spila, R. T. Haasch, I. Petrov, D. P. Abraham, *J. Power Sources* **233**, 346 (2013).
3. Y. Zhu, Y. Li, M. Bettge, D. P. Abraham, *J. Electrochem. Soc.* **159**, A2109 (2012).
4. K. G. Gallagher, J. R. Croy, M. Balasubramanian, M. Bettge, D. P. Abraham, A. K. Burrell, M. M. Thackeray, *Electrochem. Comm.* DOI: 10.1016/j.elecom.2013.04.022 (2013).
5. J. R. Croy, K. Gallagher, M. Balasubramanian, Z. Chen, Y. Ren, D. Kim, S.-H. Kang, D. W. Dees, M. M. Thackeray, *J. Phys. Chem. C* **117**, 6525 (2013).
6. M. Balasubramanian, J. McBreen, I.J. Davidson, P.S. Whitfield, I. Kargina, *J. Electrochem. Soc.* **149**, A176 (2002).
7. J. R. Mueller-Neuhaus, R. A. Dunlap, J. R. Dahn, *J. Electrochem. Soc.* **147**, 3598 (2000).
8. S.-H. Kang, W.-S. Yoon, K.-W. Nam, X.-Q. Yang, D. P. Abraham, *J. Mater. Sci.* **43**, 4701 (2008).
9. M. Bettge, Y. Li, K. Gallagher, Y. Zhu, Q. Wu, W. Lu, I. Bloom, D.P. Abraham, *J. Electrochemical Society* 160 (2013) A1-A10.
10. J. Bareño, M. Balasubramanian, S.H. Kang, J.G. Wen, C.H. Lei, S.IV. Pol, I. Petrov, D.P. Abraham, *Chemistry of Materials*, **23**, 2039 (2011).
11. Y. Zhu, Y. Li, D.P. Abraham, *Journal of The Electrochemical Society*, **161**, A1580 (2014).
12. S.E. Trask, Y. Li, J.J. Kubal, M. Bettge, B.J. Polzin, Y. Zhu, A.N. Jansen, D.P. Abraham, *Journal of Power Sources*, **259**, 233 (2014).
13. M. Bettge, Y. Li, B. Sankaran, N.D. Rago, T. Spila, R.T. Haasch, I. Petrov, D.P. Abraham, *Journal of Power Sources*, **233**, 346 (2013).
14. J. Thompson, *J. Electrochem. Soc.*, **126**, 608 (1979).
15. B. E. Conway, *Electrochim. Acta*, **38**, 1249 (1993).
16. K.G. Gallagher, J.R. Croy, M. Balasubramanian, M. Bettge, D.P. Abraham, A.K. Burrell, M.M. Thackeray, *Electrochemistry Communications*, **33**, 96 (2013).
17. J.R. Croy, K.G. Gallagher, M. Balasubramanian, Z. Chen, Y. Ren, D. Kim, S.-H. Kang, D.W. Dees, M.M. Thackeray, *The Journal of Physical Chemistry C*, **117**, 6525 (2013).
18. B.R. Long, J.R. Croy, F. Dogan, M.R. Suchomel, B. Key, J. Wen, D.J. Miller, M.M. Thackeray, M. Balasubramanian, *Chemistry of Materials*, **26**, 3565 (2014).
19. D.P. Abraham, S.D. Poppen, A.N. Jansen, J. Liu, D.W. Dees, *Electrochim. Acta*, **49**, 4763 (2004).
20. D.W. Dees, A.N. Jansen, D.P. Abraham, *J. Power Sources*, **174**, 1001 (2007).
21. Y. Li, M. Bettge, B. Polzin, Y. Zhu, M. Balasubramanian, D. P. Abraham, *J. Electrochem. Soc.* **160**, A3006 (2013).

IV.C.2 Spectroscopic and Imaging Characterization of the Voltage Fade Phenomena (ANL, ORNL)

Anthony Burrell (Primary Contact)

Voltage Fade Team
Argonne National Laboratory
9700 South Cass Avenue
Argonne, IL 60439
Phone: (630) 252-4516; Fax: (630) 252-4176
E-mail: Burrell@anl.gov

Start Date: October 2013

Projected End Date: September 2014

Objectives

Identify the fundamental causes of voltage fade and determine unknown electrochemical processes associated with the voltage fade phenomenon.

Technical Barriers

This project addresses the following technical barriers as described in the USABC goals:

- (A) Performance at ambient temperatures.
- (B) Cycle life.

Technical Targets

- PHEV specific energy targets (pack): 3.4 kWh (min) to 11.6 (max).
- EV specific energy targets (pack): 80 (min) to 200 (max) Wh/kg.

Accomplishments

Developed a fundamental understanding of the mechanism of voltage fade. Leading to the realization that this is an inherent property of the materials class when the cathode is cycled to extreme voltages.



Introduction

Lithium- and manganese-rich $x\text{Li}_2\text{MnO}_3 \bullet (1-x)\text{LiMO}_2$ (LMR-NMC, M=Mn, Ni, Co) electrode structures are currently the most promising class of cathodes for next-generation, lithium-ion batteries. These electrodes can provide capacities >230 mAh/g along with considerable energy densities. The stores of

excess lithium, relative to LiMO_2 structures, are contained within the transition metal (TM) layers of the Li- and Mn-rich, Li_2MnO_3 component. However, degradation of cathode performance accompanies the high-voltage cycling (>4.4 V vs. Li) necessary to access the excess Li. The first-cycle process of extracting the TM-layer Li, called “activation”, results in changes to the electrode structure on each subsequent cycle leading to a continuous decrease in energy output known as voltage fade. In addition, a significant hysteresis is developed between charge and discharge that decreases the round trip efficiency and may further complicate state of charge (SOC) management of cells. In order to advance this technology through rational design of more robust electrodes, the mechanisms of voltage fade must first be ascertained; specifically, what are the structure-electrochemical-property relationships of LMR-NMC electrodes?

Approach

We assembled a team of scientists who specified in the characterization of electroactive materials and used NMR, X-Rays, neutrons coupled with First principles calculations to elucidate the mechanism of voltage fade within the LMR-NMC class of materials.

Results

The first problem one encounters in deciphering the structure-property relationships of LMR-NMC cathodes is the inherent complexity of the pristine materials themselves. Since their introduction in ~2000 there has been no consensus in the community on the structural aspects of LMR-NMC's. Namely, the question has persisted, “Can LMR-NMC's be described as a solid solution, or, are they truly composite in nature, as suggested by the $x\text{Li}_2\text{MnO}_3 \bullet (1-x)\text{LiMO}_2$ notation?” The heart of the controversy is rooted in the identification of the long-range symmetry described by techniques such as X-ray diffraction (XRD). For example, LiMO_2 (trigonal, R-3m) and Li_2MnO_3 (monoclinic, C2/m) have structurally compatible oxygen lattices which allows an intimate integration of the two structures. In XRD data, all peaks in LMR-NMC patterns can be indexed to R-3m except the so-called superstructure peaks at $\sim 23^\circ 2\theta$ [copper K-alpha, $\sim 5.5^\circ 2\theta$ in Figure IV - 85(a)]. These peaks have been identified as a result of cation ordering in the TM layers, notably due to the formation of LiM_6 units (e.g., LiMn_6 , LiMn_5Ni_6) and are indexed with

respect to C2/m. Consequently, all peaks in the diffraction patterns of LMR-NMC can be indexed to the C2/m structure. As such, well-made materials (e.g., highly layered and crystalline) will give diffraction data consistent with the monoclinic structure and have been identified as solid solutions thereof.

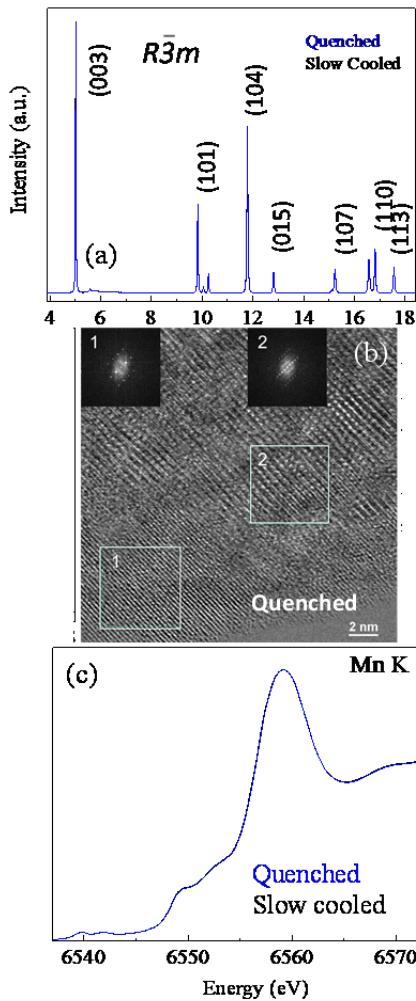


Figure IV - 85: (a) HR-XRD of 0.5Li₂MnO₃•0.5LiCoO₂ quenched and slow-cooled from 850°C. (b) HR-TEM image of a particle from the quenched 0.5Li₂MnO₃•0.5LiCoO₂ showing regions with LiCoO₂ (1) and Li₂MnO₃ (2) ordering. (c) Mn K-edge XANES of quenched and slow-cooled 0.5Li₂MnO₃•0.5LiCoO₂

This description of the material structure is, however, oversimplified and does not allow important aspects of some structure-property relationships to be ascertained. In order to accurately describe the properties of LMR-NMC's, a combination of complimentary, long- and short-range structural probes is necessary.

Figure IV - 85 shows a combination of high-resolution, synchrotron X-ray diffraction (HR-XRD), high-resolution, transmission electron microscopy (HR-TEM), and X-ray absorption spectroscopy (XAS) data

from 0.5Li₂MnO₃•0.5LiCoO₂ LMR-NMC electrode powders [ref]. The powders were synthesized at 850°C and either quenched (blue) or slow-cooled (black) to allow for the possibilities of disorder and phase separation, respectively, as reported in the literature [1]. As shown in Figure IV - 85 (a), both materials are highly crystalline and present well-defined and sharp HR-XRD peaks. The peaks are indexed to R-3m, except the aforementioned C2/m, superstructure peaks which appear at ~5.5° 2θ in the high-resolution data of Figure IV - 85 (a). As discussed, these types of data sets are often interpreted as a result of C2/m solid solution-type structures. However, Figure IV - 85 (b) shows HR-TEM images of the samples in 1(a) highlighting regions of two distinct orderings, one similar to LiCoO₂ (1) and one similar to Li₂MnO₃ (2). Furthermore, the near edge XAS data (XANES) in Figure IV - 85 (c) reveals that the average oxidation state of Mn in both samples is Mn⁴⁺, regardless of synthesis conditions, revealing additional clues about cation ordering.

Figure IV - 86(a) and (b) show the Mn and Co K-edge, extended X-ray absorption fine structure (EXAFS) data from 0.5Li₂MnO₃•0.5LiCoO₂ samples shown in Figure IV - 85. It is shown that the local environments have not been altered due to synthesis conditions between the quenched and slow-cooled samples. However, the differences between the Mn data (a) and the Co data (b) are significant. For example, the second-shell, Metal-Metal correlations (Mn-Co, Mn-Mn, Co-Co) are clearly different for the Mn and Co data in (a) and (b), respectively. The Co-M coordination at ~2.5 Å (not corrected for photoelectron wave shift) in (b) reveals a fully coordinated (i.e., 6 nearest neighbor metal atoms) second-shell as would be expected for a layered, R-3m-type oxide. In fact, the Co K-edge EXAFS in Figure IV - 85(b) bears a strong overall resemblance to that of pure LiCoO₂. Analysis of the Mn-M coordination shown in Figure IV - 85(a) gives a second-shell coordination of just ~3 and bears a strong resemblance to the local structure of pure Li₂MnO₃ where Li and Mn charge order to create LiMn₆ units in the TM layers.

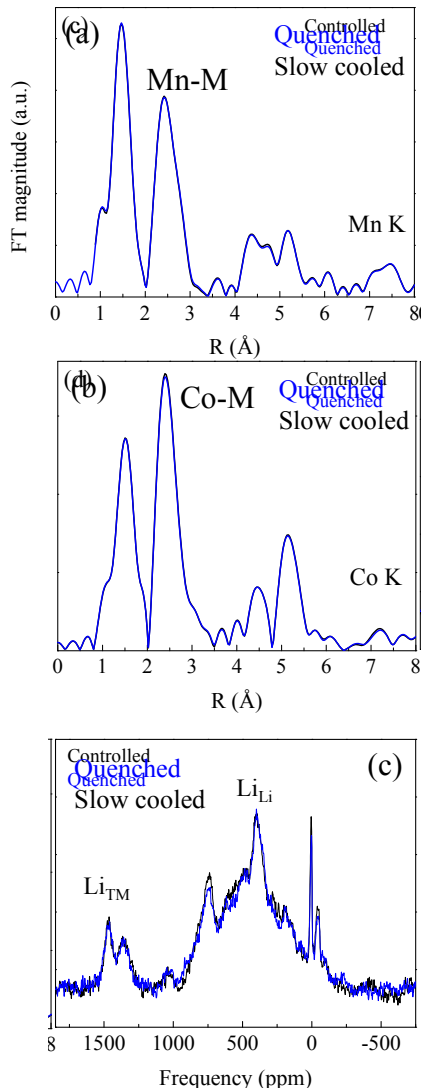


Figure IV - 86: (a) Mn and (b) Co K-edge EXAFS of $0.5\text{Li}_2\text{MnO}_3 \cdot 0.5\text{LiCoO}_2$ quenched and slow-cooled from 850°C . (c) ${}^6\text{Li}$ NMR of the samples in (a) and (b)

Because photoelectron scattering from Li is negligible in the EXAFS experiment, Li in the neighborhood of Mn in the $0.5\text{Li}_2\text{MnO}_3 \cdot 0.5\text{LiCoO}_2$ samples gives an apparent reduction in nearest-neighbor coordination. These data confirm that the excess lithium in these materials preferentially orders with Mn in the TM planes of the structure. Figure IV - 85 (c) shows ${}^6\text{Li}$ nuclear magnetic resonance spectroscopy (NMR) of the $0.5\text{Li}_2\text{MnO}_3 \cdot 0.5\text{LiCoO}_2$ samples. While the X-ray data of Figure IV - 86(a) and (b) gives a picture of the local environment with respect to the TMs, the NMR data is probing the local structure from the Li site point of view. The peaks labeled Li_{TM} between $\sim 1250 - 1500$ ppm are signatures of LiMn_6 units in the TM plane and also appear in pure Li_2MnO_3 . The EXAFS and NMR data unambiguously identify two distinct environments within the $0.5\text{Li}_2\text{MnO}_3 \cdot 0.5\text{LiCoO}_2$ samples; one rich in

Li and Mn with a local structure very similar to Li_2MnO_3 , and one rich in Co with a local structure very similar to LiCoO_2 . The fact that both data sets (quenched and slow-cooled) show similar cation ordering reveals that the driving force for the formation of the distinct domains is related to charge ordering; specifically, the very strong tendency for Li^+ and Mn^{4+} to order. This can be seen even in more complex compositions such as $0.5\text{Li}_2\text{MnO}_3 \cdot 0.5\text{LiMn}_{0.5}\text{Ni}_{0.5}\text{O}_2$. In this case, due to the ionic radius of Ni^{2+} (e.g., similar to that of Li), Ni can occupy Li sites in the TM layers as well as Li sites in the Li layers. As such, a more intimate mixing might be expected, especially when such compositions are quenched from high temperatures.

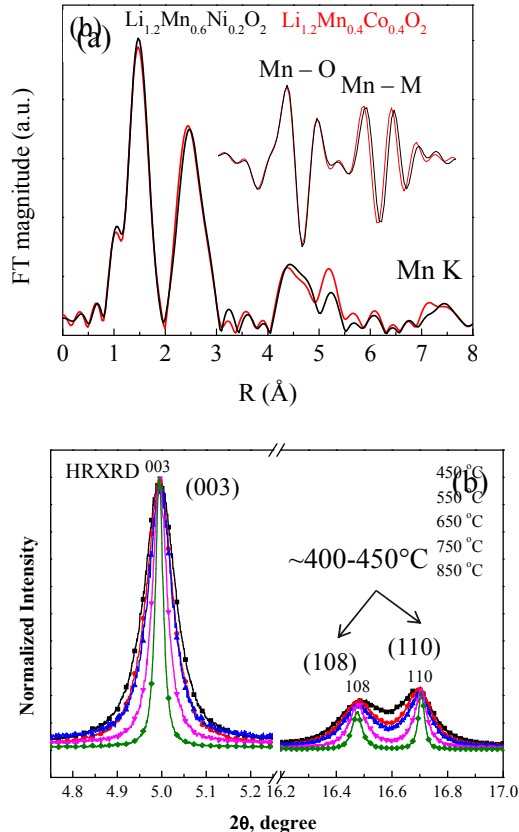


Figure IV - 87: (a) Mn K-edge EXAFS of $0.5\text{Li}_2\text{MnO}_3 \cdot 0.5\text{LiCoO}_2$ (red) and $0.5\text{Li}_2\text{MnO}_3 \cdot 0.5\text{LiMn}_{0.5}\text{Ni}_{0.5}\text{O}_2$ (black). Both samples were quenched from 850°C . (b) In-situ, HR-XRD during the synthesis of pure Li_2MnO_3

Figure IV - 87(a) shows a comparison of Mn K-edge EXAFS data from $0.5\text{Li}_2\text{MnO}_3 \cdot 0.5\text{LiMn}_{0.5}\text{Ni}_{0.5}\text{O}_2$ (black) and $0.5\text{Li}_2\text{MnO}_3 \cdot 0.5\text{LiCoO}_2$ (red) after both samples had been quenched from 850°C . As can be seen, the local environment around Mn in the Ni-containing sample is again quite similar to that of pure Li_2MnO_3 as well as the $0.5\text{Li}_2\text{MnO}_3 \cdot 0.5\text{LiCoO}_2$ sample. Differences at ~ 5.5 Å, as well as Mn-M bond distances (inset), can be attributed to Ni occupying Li sites in the TM layer as mentioned. Therefore, even in samples

where a more homogeneous ordering of TMs would be expected, Li and Mn ordering still persists to a large extent. This can be further illustrated in the behavior of pure Li_2MnO_3 . Figure IV - 87 (b) shows in-situ, HR-XRD data during the synthesis of pure Li_2MnO_3 from an initial mix of MnCO_3 and Li_2CO_3 . At temperatures as low as $\sim 400^\circ\text{C}$ the characteristic ordering peaks [(108), (110)] of the Li_2MnO_3 structure are seen to form. This indicates that in the synthesis of LMR-NMC materials, very early on in the process, Li and Mn ordering begins. Furthermore, it is strong enough to persist at high temperatures, as revealed by quenching experiments. Consequently, virtually all $x\text{Li}_2\text{MnO}_3 \bullet (1-x)\text{LiMO}_2$ materials, especially those with high x values, show two distinct environments. One of these environments, rich in Li and Mn, forms LiM_6 units (e.g., LiMn_6 , LiMn_5Ni) within the TM layers and is denoted as the Li_2MnO_3 component. The other, rich in TM's, consists of highly coordinated (i.e., ~ 6 TM neighbors) TM's with LiMO_2 ordering; where NiO -like rocksalt domains are also possible in certain compositions. The identification of distinctly different local environments in LMR-NMC's is critical and marks a substantial turning point in the effort to understand the mechanisms of certain phenomena such as voltage fade and hysteresis. By systematically looking at the local properties of LMR-NMC's we can begin to ascertain the effect of local structure on electrochemical performance.

Structure-Electrochemical Properties of LMR-NMC Electrodes

As shown above, the local structures of the Li- and Mn-rich domains are very similar to pure Li_2MnO_3 . However, because of the intimate integration of these domains, simply evoking " Li_2MnO_3 " as a pure component does not adequately reflect the material performance. For example, Figure IV - 88 shows a comparison of Mn K-edge XAS data from pure Li_2MnO_3 before (black) and after (red) the first electrochemical cycle compared with a $0.5\text{Li}_2\text{MnO}_3 \bullet 0.5\text{LiMn}_{0.375}\text{Ni}_{0.375}\text{Co}_{0.25}\text{O}_2$ LMR-NMC (Toda HE5050) after the first electrochemical cycle.

The HE5050 sample achieved ~ 310 mAh/g on charge and ~ 250 mAh/g on discharge (4.7-2.0 V, 10 mA/g, 30°C vs. Li). The charge capacity of the Li_2MnO_3 was ~ 440 mAh/g on charge ($\sim 96\%$ of theoretical) and 284 mAh/g on discharge (5.0-2.0 V, 10 mA/g, 30°C vs. Li). An important observation is the drastic shift to lower energy for the Li_2MnO_3 XANES after the first-cycle discharge compared to relatively minor changes to the cycled LMR-NMC, (a) and (b). This is definitive evidence for large-scale reduction of Mn^{4+} on the first-cycle discharge for Li_2MnO_3 while no such conclusions can be made for the LMR-NMC. The EXAFS data of Figure IV - 88 (c) reveals severe damping of all peaks for the Li_2MnO_3 after one cycle while only the first-shell, Mn-O correlations (~ 1.5 Å, uncorrected) are significantly effected for the LMR-NMC. Taken

together with the XANES data, (a) and (b), these observations suggest a significant fraction of Mn exists as Mn^{3+} in Jahn-Teller (JT) distorted environments in the cycled Li_2MnO_3 . A detailed EXAFS analysis, shown in Figure IV - 89, revealed several interesting features. The Li_2MnO_3 samples in Figure IV - 89 were synthesized at 850°C in order to create more crystalline structures that could be reliably fit in the EXAFS analyses. High temperature Li_2MnO_3 is generally believed to be inactive; however, specially prepared electrodes that facilitate intimate electrical contact between electrode particles can allow for high electrochemical capacities from crystalline Li_2MnO_3 .

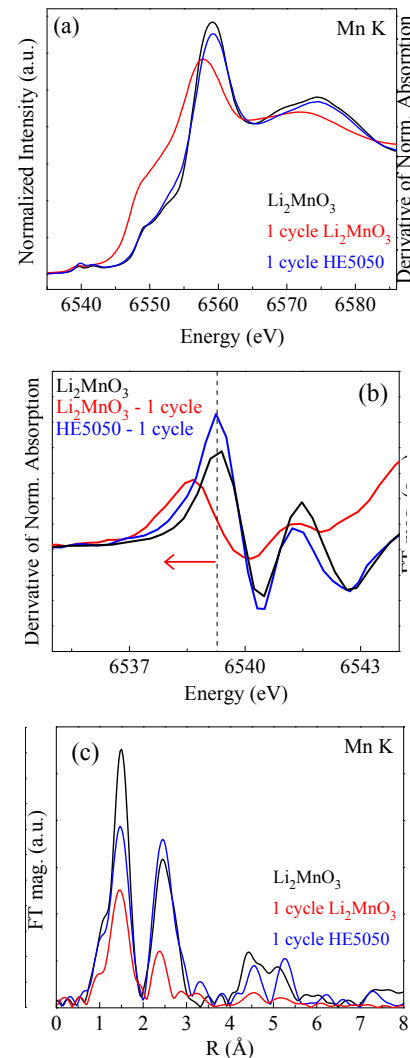


Figure IV - 88: (a) Mn K-edge XANES of pure Li_2MnO_3 before (black) and after (red) the first electrochemical cycle between 5.2-0 V (vs. Li) compared with a $0.5\text{Li}_2\text{MnO}_3 \bullet 0.5\text{LiMn}_{0.375}\text{Ni}_{0.375}\text{Co}_{0.25}\text{O}_2$ LMR-NMC (Toda HE5050). (b) Derivative of the pre-edge region shown in (a). (c) EXAFS data of the samples in (a) and (b)

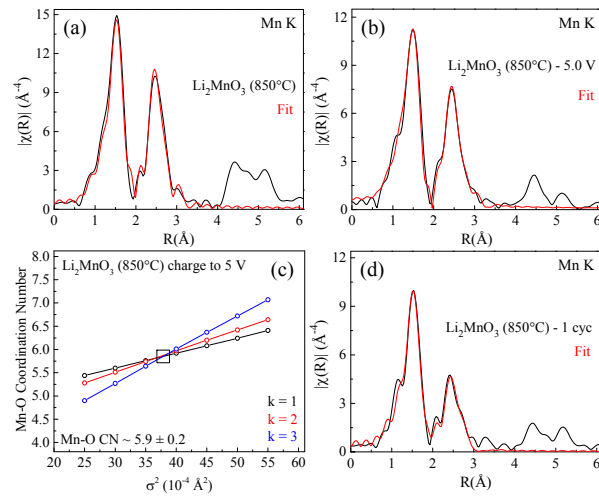


Figure IV - 89: EXAFS analysis of fresh Li_2MnO_3 (a), charged to 5.0 V (b), discharged to 2.0 V (d). (c) Detailed analysis of the first-shell Mn-O coordination in Li_2MnO_3 charged to 5.0 V (~94% delithiated)

The sample of Figure IV - 89 was charged to 5.0 V (10 mA/g, 30°C, vs. Li) and achieved ~430 mAh/g on charge (~94% of theoretical). Li NMR confirmed that this capacity was due to Li extraction and not unwanted side reaction. Details of the NMR and electrode preparation can be found in ref. [2]. The fitting shown in Figure IV - 89 (b) revealed that at the top of charge the highly delithiated Li_2MnO_3 maintained its overall average, local structure with a Mn-Mn, second-shell coordination number (CN) of 3, as in pure Li_2MnO_3 . Perhaps more interesting is the detailed analysis of the first-shell, Mn-O CN shown in Figure IV - 89 (c). The three intersecting lines represent 21 separate fits to the first-shell data under three different k-weights. This method of analysis allows the correlation between disorder (σ^2) and coordination (CN) to be largely broken resulting in an intersection [square in Figure IV - 89(c)] of the data that gives the true CN and σ^2 (within the error). As shown, the Mn-O CN in the highly delithiated Li_2MnO_3 remains very close to 6. Similar data analysis on an in-situ Li_2MnO_3 cell confirms these results. Figure IV - 89 (d) shows the fit to the discharged Li_2MnO_3 . This fits confirmed that a large fraction of Mn in the discharged Li_2MnO_3 was present as Mn^{3+} in JT-distorted local environments. Details of the EXAFS analyses and a table of fitted parameters can be found in ref. [2].

Contrary to the data presented for Li_2MnO_3 , a similar analysis of XAS data, collected in-situ, during the first charge of a $0.3\text{Li}_2\text{MnO}_3 \bullet 0.7\text{LiMn}_{0.5}\text{Ni}_{0.5}\text{O}_2/\text{Li}$ cell, shows that the first-shell, Mn-O CN decreases in a dramatic fashion during the first-cycle plateau (see Figure IV - 90).

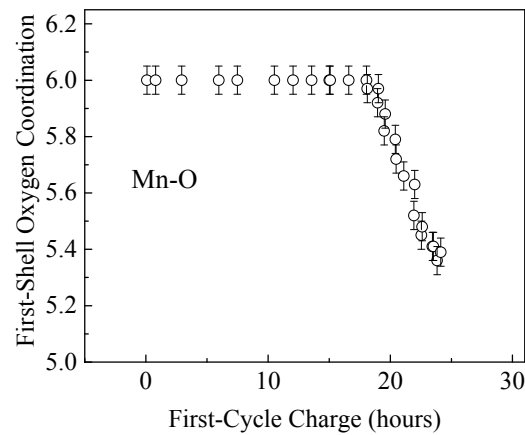


Figure IV - 90: Detailed analysis of the first-shell, Mn-O coordination of in-situ XAS data collected during the first charge of $0.3\text{Li}_2\text{MnO}_3 \bullet 0.7\text{LiMn}_{0.5}\text{Ni}_{0.5}\text{O}_2$

The data presented above reveal that although the Li- and Mn-rich, “ Li_2MnO_3 component” of LMR-NMC’s is structurally similar to pure Li_2MnO_3 , several major differences exists. 1) The role of oxygen in charge compensation and changes in local structures is different in Li_2MnO_3 and LMR-NMC; 2) Mn reduction from 4+ to 3+ clearly contributes in a significant way to the first cycle electrochemistry of Li_2MnO_3 but not to the first-cycle electrochemistry of LMR-NMC’s. Therefore, any understanding of the mechanisms at play in LMR-NMC’s must be had with a complete picture of the local structure (e.g., chemical inhomogeneity, cation ordering, and interfaces) properly accounted for. As a first indication of how the Li_2MnO_3 component behaves in working electrodes, XAS data was acquired on $0.5\text{Li}_2\text{MnO}_3 \bullet 0.5\text{LiMn}_{0.5}\text{Ni}_{0.5}\text{O}_2/\text{Li}$ cells. Figure IV - 91(a) and (b) show Mn and Ni K-edge EXAFS data from $0.5\text{Li}_2\text{MnO}_3 \bullet 0.5\text{LiMn}_{0.5}\text{Ni}_{0.5}\text{O}_2/\text{Li}$ cells as prepared (black), after three cycles (red), and after 50 cycles (blue). Cycling was done at room temperature between 4.6-2.0 V at a current rate of 15 mA/g.

The Mn EXAFS data in Figure IV - 91(a) shows that substantial changes to the local Mn environment occurred within the first several cycles. This is particularly evident with respect to the first-shell, Mn-O correlations (~1.5 Å). Changes in the shoulder at ~2.9 Å as well as the reduced amplitude of the ~4.5 Å region also involve some Mn-O correlations. From cycles three (red) to 50 (blue), limited changes are seen to occur, in agreement with cycling data which shows a slowing of, for example, the voltage fade phenomenon in the early stages of cycling. Contrary to the Mn data, the Ni EXAFS, Figure IV - 89(b), reveals that the overall average local Ni environment is fairly robust with cycling; showing only minimal changes over 50 high voltage cycles. These observations show that the Li_2MnO_3 component and, specifically, Li and Mn ordering, play a key role in the degradation of LMR-NMCs.

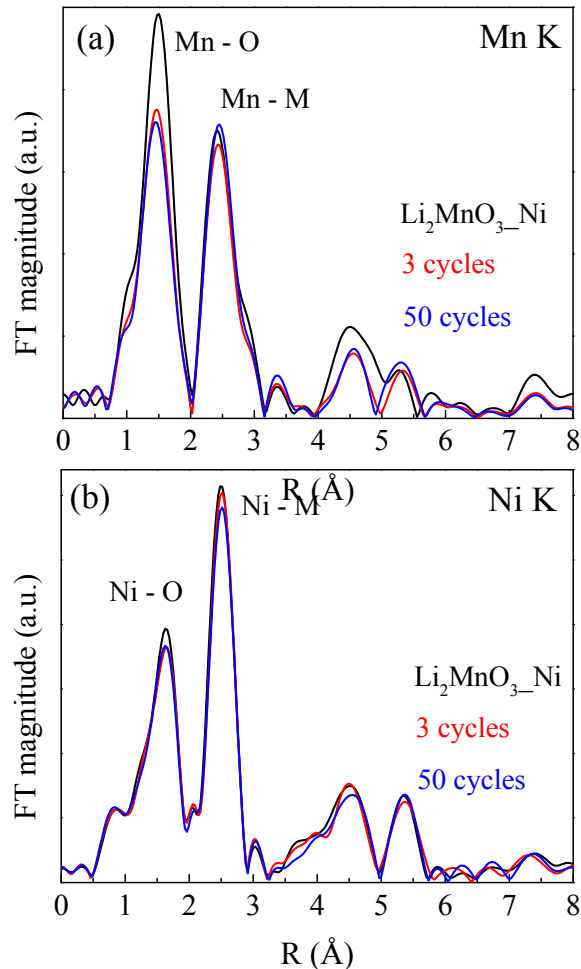


Figure IV - 91: Mn (a) and Ni (b) K-edge EXAFS of fresh and cycled $0.5\text{Li}_2\text{MnO}_3\bullet0.5\text{LiMn}_{0.5}\text{Ni}_{0.5}\text{O}_2/\text{Li}$ cells

To better understand the role of the Li-and Mn-rich Li_2MnO_3 component and, specifically, Li and Mn

ordering, systematic electrochemical and XAS studies were undertaken.

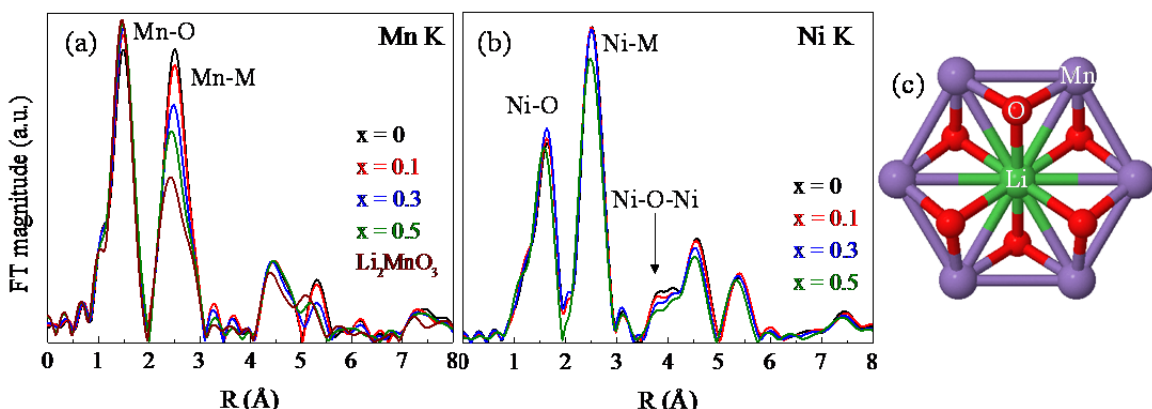


Figure IV - 92: Mn (a) and Ni (b) K-edge EXAFS of $x\text{Li}_2\text{MnO}_3\bullet(1-x)\text{LiMn}_{0.5}\text{Ni}_{0.5}\text{O}_2$ electrode powders. (c) Characteristic LiMn_6 unit of the Li and Mn layers in pure Li_2MnO_3

Figure IV - 92(a) shows Mn K-edge EXAFS data on a series of $x\text{Li}_2\text{MnO}_3\bullet(1-x)\text{LiMn}_{0.5}\text{Ni}_{0.5}\text{O}_2$ electrode powders with $x=0, 0.1, 0.3$, and 0.5 . Most evident in the

data is the clear trend of decreasing Mn-M correlations ($\sim 2.5 \text{ \AA}$) with increasing values of x , Figure IV - 92(a). As described previously, in pure Li_2MnO_3 Li and Mn

ordering forms LiMn_6 units as in Figure IV - 92(c). In these configurations, each Mn is coordinated to 3 Mn and 3 Li nearest-neighbor atoms. Because photoelectron scattering from Li is negligible, a K-edge EXAFS experiment gives a nearest-neighbor Mn-Mn CN of just 3 for Li_2MnO_3 . The decrease of the Mn-M correlations with increasing x seen in the $x\text{Li}_2\text{MnO}_3\bullet(1-x)\text{LiMn}_{0.5}\text{Ni}_{0.5}\text{O}_2$ series in Figure IV - 92 (a) is a consequence of increasing Li and Mn, LiM_6 -type ordering in the TM layers of these compositions (e.g., LiMn_6 , LiMn_5Ni). At x values of ~ 0.3 and above, the ordering is prevalent enough that the average local Mn environments tend towards pure Li_2MnO_3 configurations. The Ni K-edge EXAFS, Figure IV - 92 (b), of the $x\text{Li}_2\text{MnO}_3\bullet(1-x)\text{LiMn}_{0.5}\text{Ni}_{0.5}\text{O}_2$ series shows

that the overall average local structure is fairly constant with respect to x , contrary to the Mn data. Analysis reveals that the second-shell, Ni-M coordination is ~ 6 for all values of x , related to more LiMO_2 -type local ordering. Interestingly, the peak just below $\sim 4 \text{ \AA}$, which results from Ni-O-Ni correlations from Ni residing in the TM layers (e.g., Li/Ni exchange), decreases with increasing x . This implies that increasing x decreases the tendency for Li/Ni exchange creating a more layered structure. However, the fact that these correlations are not present in the Mn data indicates that most, if not all, Li/Ni exchange occurs in the Ni-rich, LiMO_2 regions. The decrease of the Ni-O-Ni correlations is only a consequence of the decreasing concentration of the Ni-rich domains with increasing x .

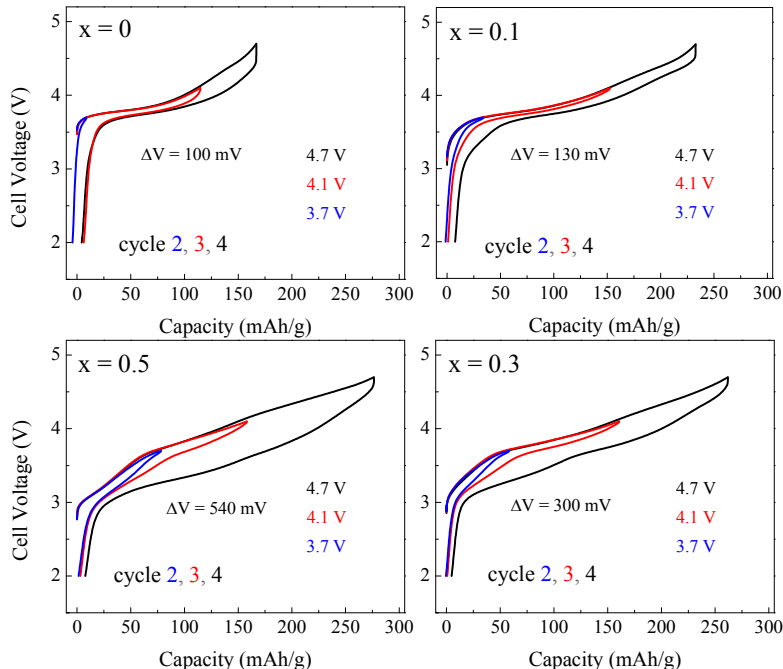


Figure IV - 93: Consecutive cycles to increasing upper cutoff voltages (lower cutoff of 2.0 V) for $x\text{Li}_2\text{MnO}_3\bullet(1-x)\text{LiMn}_{0.5}\text{Ni}_{0.5}\text{O}_2/\text{Li}$ cells. x values are given in the upper left, magnitude of the hysteresis at 50% SOC denoted as ΔV . All cells were activated between 4.7-2.0V, all cycles done at 5 mA/g at 30°C

Figure IV - 93 shows electrochemical profiles of the $x\text{Li}_2\text{MnO}_3\bullet(1-x)\text{LiMn}_{0.5}\text{Ni}_{0.5}\text{O}_2$ series of powders discussed in Figure IV - 92. The cells were activated between 4.7-2.0 V (5 mA/g, 30°C, vs. Li). Shown in Figure IV - 92 are consecutive cycles to increasing upper cutoff voltages (lower cutoff of 2.0 V) after the activation cycle. As shown, with increasing values of x there is an increase in the voltage gap (hysteresis) between charge and discharge, denoted ΔV . This hysteresis does not occur without the activation process; namely, traversing the first-cycle plateau and accessing the TM-layer lithium associated with the Li_2MnO_3 component. In addition, raising the upper cutoff voltage clearly increases the hysteresis between charge and discharge for $x>0$. Note that the overlap of the 4.1 V

(red) and the 4.7 V (black) cycles for the $x=0$ composition ($\text{LiMn}_{0.5}\text{Ni}_{0.5}\text{O}_2$) indicates that the voltage gap in this case is related to the slow kinetics of the material and not to the same phenomena occurring in the $x>0$ electrodes.

Figure IV - 94 shows the associated dQ/dV plots for the profiles in Figure IV - 93. The numbers along the charge and discharge portions of the dQ/dV plots represent the capacities (mAh/g) obtained in the regions marked by the dashed lines (e.g., in each voltage window used). The numbers, and curves, are color-coded and labeled (upper left) to match the upper cutoff voltage used. A careful accounting of the capacities in each window reveals that 1) capacities obtained above $\sim 4.0 \text{ V}$ on charge cannot be re-accommodated in the

structure until around ~3.0 V on discharge. This represents a ~1 V hysteresis for some fraction of the overall lithium content. 2) Capacities that evolve below ~3.6 V in the charge curves are reversible and also increase with increasing x . This capacity in the low-voltage charge region does not appear unless the first-cycle plateau is accessed and the Li- and Mn-rich portions of the material are activated. In addition, the capacities in this region grow with cycling and are directly responsible for lowering the average voltages in LMR-NMC's (i.e., voltage fade). These electrochemical studies, combined with the structural data presented so far, clearly illustrate an important structure-property relationship; Li and Mn ordering, and the utilization of the Li therein, results in both the electrochemical hysteresis and the voltage fade phenomena observed in LMR-NMC electrodes. To gain more insight into each of these phenomena several X-ray and electrochemical studies were conducted.

Figure IV - 95(a) shows charge and discharge curves on the 6th cycle, after activation, for $0.5\text{Li}_2\text{MnO}_3 \cdot 0.5\text{LiMn}_{0.375}\text{Ni}_{0.375}\text{Co}_{0.25}\text{O}_2/\text{Li}$, LMR-NMC (Toda HE5050) cells between 4.7-2.0 V (10 mA/g, 30°C). Red dots indicate example points along the curves at which XAS data was collected as shown in (b) and (c). The points chosen for data collection represent points of equal voltage and points of equal SOCs. These points, due to the existence of the hysteresis, are not symmetric with respect to charge and discharge. The Ni K-edge XAS in Figure IV - 95(b) and (c) serve to illustrate the important findings of the study.

Namely, even at points of equivalent lithium contents (equal SOCs) the average local structure and oxidation of Ni is different between charge and discharge. This can be followed in the shift of the Ni XANES (e.g., at ~75% SOC on charge and discharge) and in the JT distortions identifiable in the first-shell, Ni-O EXAFS data, Figure IV - 95(c). This data indicates that lithium does not have access to the same sites between charge and discharge, even when the same amount of lithium is present in the structure. This important finding reveals that the hysteresis that develops in LMR-NMC electrodes is structural in nature and results from dynamic changes, on a local scale, occurring in these materials during charge and discharge. The fact that this hysteresis cannot be attributed solely to kinetics has also been verified [3].

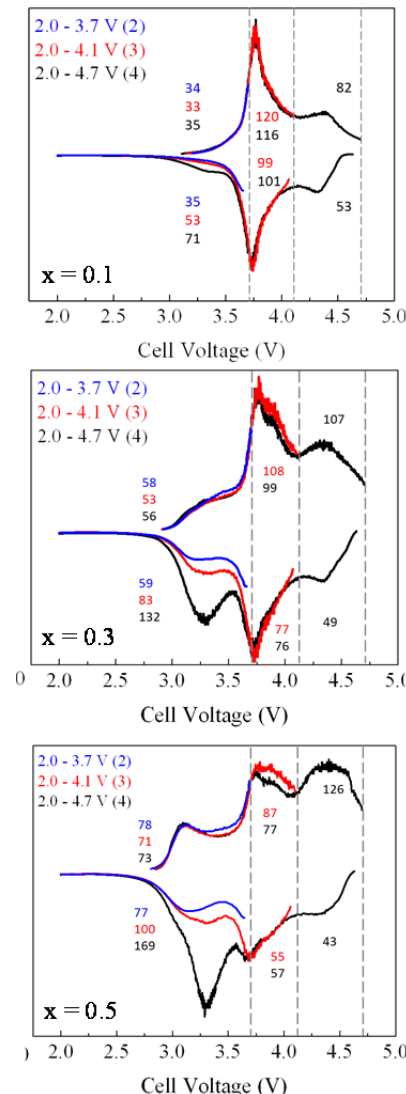


Figure IV - 94: dQ/dV plots of the window-opening cycles shown in the previous figure for the $x=0.1$, 0.3 , and 0.5 $\text{xLi}_2\text{MnO}_3 \cdot (1-\text{x})\text{LiMn}_{0.5}\text{Ni}_{0.5}\text{O}_2/\text{Li}$ cells. Numbers along the oxidation and reduction curves give the capacities obtained in each region (marked by the dashed lines) during charge and discharge, respectively, and are color-coded to match the cycling window used

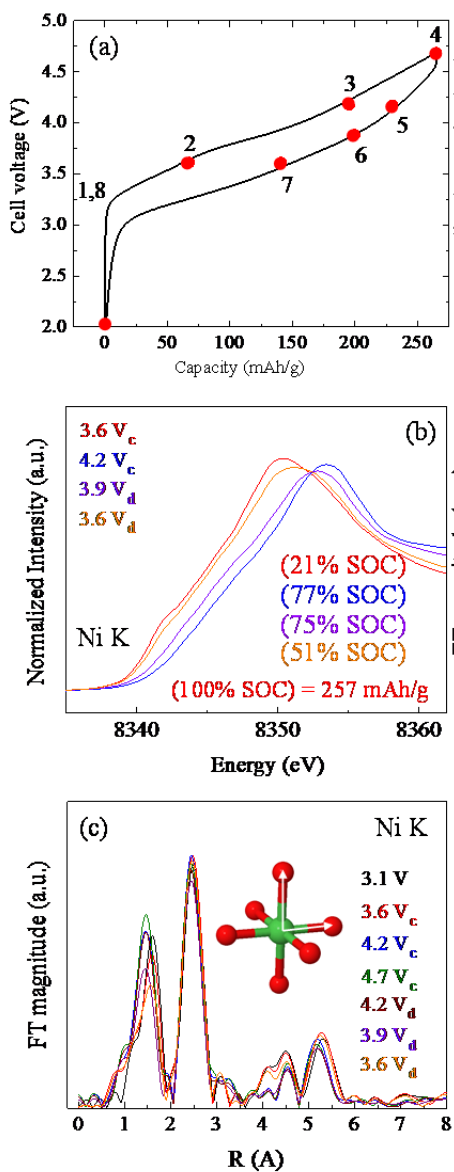


Figure IV - 95: (a) 6th-cycle charge/discharge for $0.5\text{Li}_2\text{MnO}_3 \cdot 0.5\text{LiMn}_{0.375}\text{Ni}_{0.375}\text{Co}_{0.25}\text{O}_2/\text{Li}$, LMR-NMC (Toda HE5050) cells between 4.7-2.0 V (10 mA/g, 30°C). Red dots indicate example points along the curves as which XAS data was collected as shown in the Ni K-edge data of (b) and (c). Inset shows the JT-distorted Ni-O environment of Ni³⁺ with two distinct Ni-O bond lengths

Because the onset and magnitude of both hysteresis and voltage fade can be directly correlated with the magnitude of Li and Mn ordering in the as-prepared electrodes, as shown above, the underlying mechanisms of these phenomena may also be related. Figure IV - 96 shows an electrochemical cycling study of $0.5\text{Li}_2\text{MnO}_3 \cdot 0.5\text{LiMn}_{0.375}\text{Ni}_{0.375}\text{Co}_{0.25}\text{O}_2/\text{Li}$ cells. The y-axis shows the magnitude of voltage fade (decrease in average discharge voltage) over the first ~20 cycles between 4.7-2.0 V, where the initial average discharge

voltage was determined from the second cycle (after activation). The x-axis shows the lower cutoff voltage used for cycling, where each group of cells shown (duplicates at each point) was charged to 4.7 V (i.e., fixed upper voltage for all cells shown). The red, dashed line is a guide to the eye and clearly reveals that decreasing the lower cutoff voltage increases the magnitude of voltage fade over the ~20 cycles shown. Furthermore, a maximum is seen to occur when cycling over a voltage window of ~4.7-3.2 V. This is the same lower cutoff voltage at which significant lithium is reinserted into the structure after charging above ~4.0 V as discussed in Figure IV - 94. The inset in Figure IV - 95 shows a calendar time plot of cells cycled in different voltage windows compared to cells that were charged to 4.7 V and held constant at that potential (red squares), after the first cycle between 4.7-2.0 V. The y-axis again shows the magnitude of voltage fade over the first ~20 cycles and the x-axis shows the time on test. Cells that were held constant at 4.7 V clearly show voltage fade in the early stages of the test, however, the effect quickly levels off and becomes less significant after a short time. The cells that were continuously cycled (purple circles, 4.7-2.0 V and green diamonds, 4.7-3.2 V) show a continuous fade over the time on test. Furthermore, cycling between 4.7-3.2 V accelerates voltage fade more than any other electrochemical exposure studied. These data show that while high voltage exposure has an effect on voltage fade, actually moving Li in and out of the structure (cycling), over the large voltage window where significant hysteresis occurs, plays an important part in the mechanisms that accelerate voltage fade; verifying that voltage fade and hysteresis are correlated.

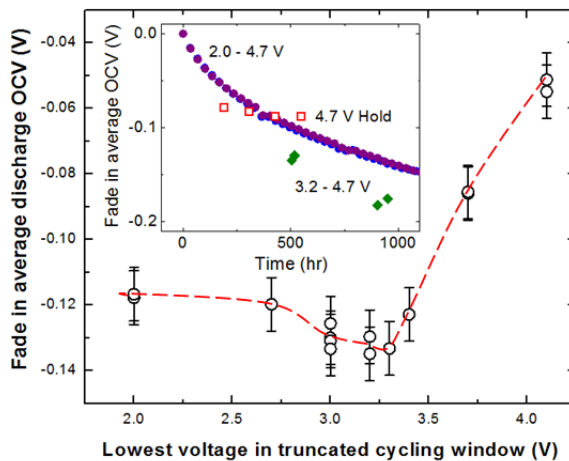


Figure IV - 96: Cycling window and calendar time plots (insets) for LMR-NMC cells, cycled as described in the text

Solid State NMR Characterization

Solid State NMR is a unique, complimentary characterization technique for Li-ion battery systems providing useful information on local structure, bonding, local dynamics of Li-ions, and the presence, or

absence, of lattice or non-lattice protons in the materials. It is a powerful, and quantitative, local-structure probe that can be used to determine which species are removed/inserted on charge/discharge and how the local structure changes on extended cycling. Furthermore, how these changes effect electrochemical processes such as voltage fade, hysteresis, and the overall performance of battery materials can be ascertained.

Initial studies were undertaken to understand the correlations between voltage fade, structural changes (from lithium local structure point of view), and the possible connections, if any, to proton insertion into cathode structures. Determination of local Li coordination numbers in pristine and activated LMR-NMC cathodes was carried out by ^6Li solid state NMR. ^2H solid state NMR measurements were used to identify possible proton environments within positive electrodes as a result of charge/discharge processes. The effect of domain size in LMR-NMC composite materials on electrochemical performance and voltage fade was probed through lithium local structure effects via ^6Li MAS NMR. Lastly, key lithium-6 NMR studies were completed on path-dependent lithium site occupation, correlated to structural reorganization of the metal oxide and the observed electrochemical hysteresis and voltage fade, during lithium insertion and extraction.

Investigation of Structural Proton Insertion and Effect on Voltage Fade

Electrochemical and chemical insertion of protons has been reported suggesting that protons generated in the electrolyte could be involved in electrochemical cycling which could play a similar role in the “ Li_2MnO_3 component” of lithium rich transition metal oxides. Therefore studies were done on the electrochemical insertion of structural protons, changes in lithium occupancy at various states of charge, and changes in local structure by ^2H solid state NMR. Deuterium is chosen to probe proton insertion into paramagnetic lattices because of the spectroscopic advantages of using low gyromagnetic nuclei to observe paramagnetic materials. Chemical protonation was attempted by stirring the Li_2MnO_3 powder in 5M DNO_3 or D_2SO_4 following a previous study by Paik *et al.*[4]. Our chemical protonation studies were mainly to form a model system for NMR characterization of electrochemical protonation of LMR-NMC materials. Both chemical and electrochemical protonation was initially studied on Li_2MnO_3 as electrochemical and chemical insertion of lattice protons have previously been proposed for Li_2MnO_3 . Similar electrochemical processes might then be expected to affect the “ Li_2MnO_3 component” of LMR-NMC composites. Electrochemical proton insertion studies were conducted with use of deuterated electrolyte during cycling and tracked with ^2H MAS NMR spectroscopy. ^2H MAS NMR data on acid leached samples (chemical proton insertion) show a broad resonance between 400-420

ppm indicating that deuterons have been inserted into the monoclinic Li_2MnO_3 lattice, Figure IV - 97(a). This is due to unpaired d-electron transfer from Mn^{+4} via empty p-orbitals of bridging oxygens (i.e. Fermi contact shift) and is consistent with previous reports showing resonances due to structural protons (deuterons) [4]. The data in Figure IV - 97 (a) reveal substantial proton insertion, at least when compared to non-lattice protonic accumulation (*i.e.* intensity of resonance at 1.2ppm), without significantly altering the host lattice, Figure IV - 97 (b).

We then tested the electrochemical activity and possible proton insertion on electrodes made from Li_2MnO_3 synthesized at low-temperature (LT, 450°C). LT- Li_2MnO_3 electrodes, made with 10% carbon and cycled up to 4.7 V, exhibited 280 mAh/g of charge capacity and 270 mAh/g of discharge capacity. These high capacities are somewhat surprising and have been attributed to electrolyte decomposition and protonic activity in previous reports. However, ^6Li MAS NMR data on cycled samples, Figure IV - 98(a), show that up to 95% of the Li has been removed from the lattice on the first-cycle charge. This agrees with the electrochemical observation of substantial Li removal observed in the electrochemistry; however it must be noted that this corresponds to about 60% of the 470 mAh/g theoretical capacity of Li_2MnO_3 . Upon the first-cycle discharge, up to 50% of the extracted Li can be reinserted back into the host lattice. It should also be noted that significant accumulation of diamagnetic Li salts, solid electrolyte interphase (SEI) build-up, and/or residual Li electrolyte species were observed (-3 ppm) upon charge and further discharge. The calculated Li insertion from the NMR data does not account for the full discharge capacity observed in the electrochemistry of the 1st discharge.

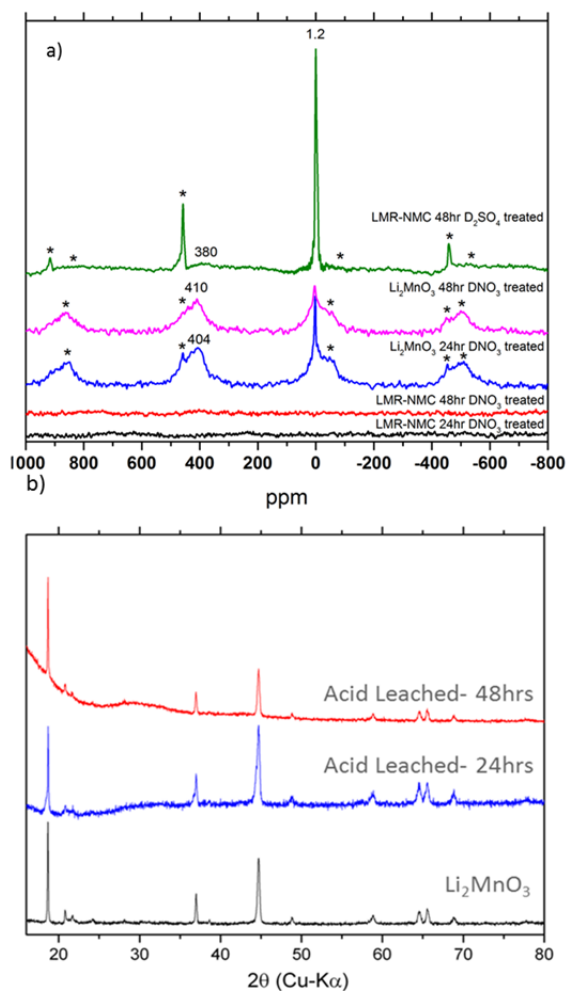


Figure IV - 97: a) ^2H MAS NMR of for acid leached HT- Li_2MnO_3 and $\text{Li}_{1.2}\text{Ni}_{0.2}\text{Co}_{0.2}\text{Mn}_{0.6}\text{O}_2$ powders (* indicates spinning sidebands, 35 kHz spinning speed at 11.7 T) b) XRD diffraction data for acid leached and pristine HT- Li_2MnO_3 ^2H MAS NMR data of the cycled, electrochemically active LT- Li_2MnO_3 material is shown in the next figure (b). All spectra contain a single, sharp diamagnetic resonance at 2 ppm indicating non-lattice proton (deuteron) bearing species, presumably due to surface decomposition species. No lattice proton (deuteron) species were observed

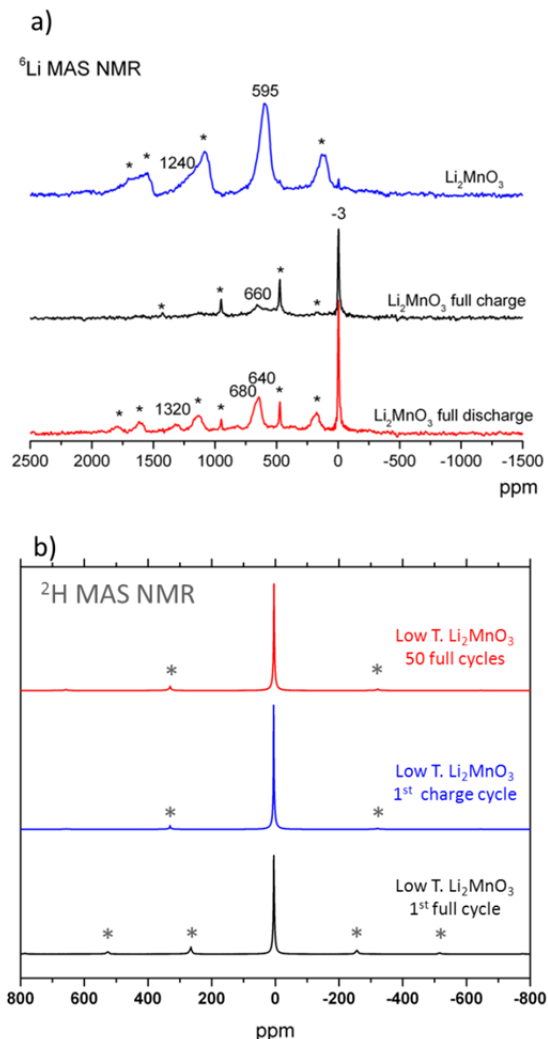


Figure IV - 98: a) ^6Li NMR data for pristine and cycled LT- Li_2MnO_3 (* indicates spinning sidebands, 35 kHz spinning speed at 11.7 T) b) ^2H MAS NMR data for cycled LT- Li_2MnO_3 (* indicates spinning sidebands, 25 kHz spinning speed for 1st and charge and 50 full cycles, 20 kHz for 1st full cycle data)

In an effort to investigate the correlation of electrochemically observed voltage fade and structural protons, $\text{Li}_{1.2}\text{Ni}_{0.2}\text{Co}_{0.2}\text{Mn}_{0.6}\text{O}_2$ samples were investigated with ^2H MAS NMR. Figure IV - 99(a) shows a stack plot of spectra for electrodes in a fully discharged state on the 1st, 10th, and 100th cycles. Similar to other electrochemically prepared Li_2MnO_3 electrodes, no paramagnetic ^2H , indicative of lattice protons, were observed. Again, a diamagnetic peak at 4.9 ppm was observed, suggesting residual electrolyte species on the particles. This residue appears to accumulate, and perhaps coordinate closely to the lattice, with increasing cycle number, indicated by the increased intensity, change in spinning sideband pattern and broadening of the 4.9 ppm resonance after 100 cycles (FWHM \sim 2ppm after 100 cycles as opposed to

0.2 ppm for cycles 1-10). An increase in the spinning sideband intensity is also observed, indicative of increased dipolar coupling which could be due to decreased symmetry of solid deuterium environments in the surface layer, or more likely, the interaction of this closely bound layer of deuterium bearing species near the core paramagnetic center bearing particles.

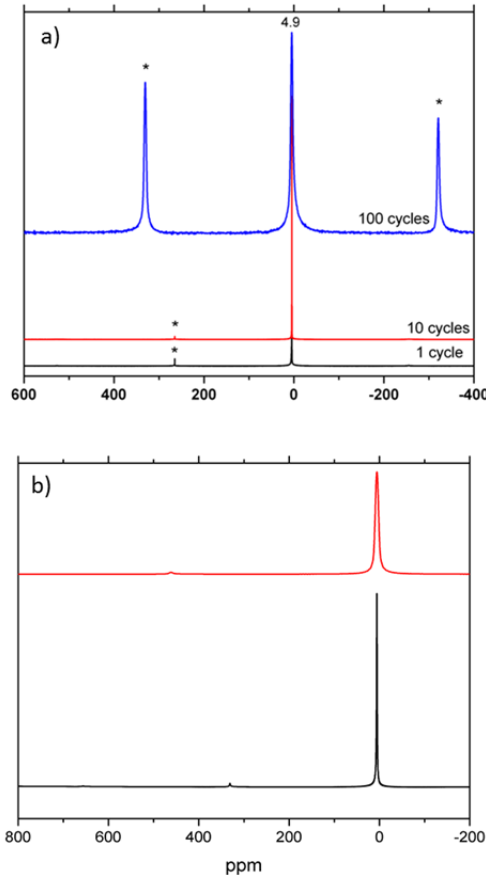


Figure IV - 99: ^2H MAS NMR of a) cycled LMR-NMC electrodes. (* indicates spinning sidebands, 20 kHz spinning speed for 1 and 10 cycle data, 25 kHz for 100 cycle data) b) pristine LMR-NMC electrode and charged stages (black 1st charge with 20 kHz spinning speed, red 3rd charge with 30 kHz spinning speed, * indicates spinning sidebands)

Possible protonation of the lattice was also investigated at the top of the charge cycles. The ^6Li NMR (shown in Figure IV - 100) shows that the majority of Li is deintercalated from the electrodes at the top of activation (1st charge) and at the top of the 3rd charge cycle. ^2H NMR of the same samples, reveal the absence of lattice protons, thereby, excluding their participation in voltage fade or the generation of measurable capacity. No evidence of electrochemically active structural protons were detected in this work for the electrochemically active electrode materials investigated; in opposition to the proton insertion

mechanisms previously proposed for Li-rich, transition metal oxides.

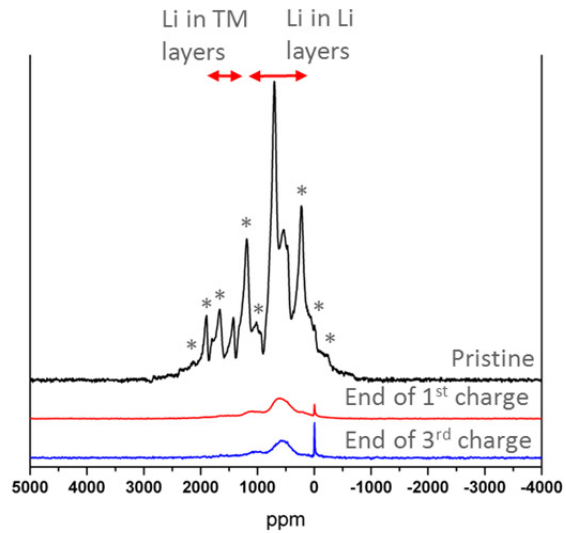


Figure IV - 100: ^6Li MAS NMR (11.7 Tesla, 30 kHz spinning speed) of pristine and charged LMR-NMC electrodes

Understanding the Voltage Fade Phenomena and its Correlation with Structural Changes

^6Li solid state NMR is a technique used for characterization of Li environments and local order present in LMR-NMC materials, both pristine and cycled. This powerful technique can be used to correlate changes in the local lithium environments to the observed electrochemical performance.

In Figure IV - 101, two groups of resonances are observed for Li species present in the lattice of a pristine LMR-NMC material; Li in Li layers around the 500-800 ppm region and Li in TM (transition metal) layers around the 1300-1500 ppm region.

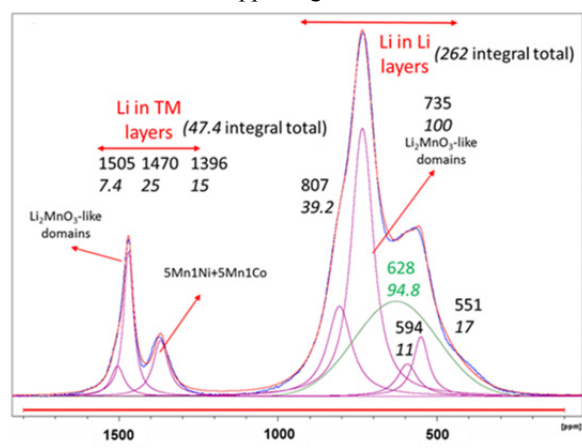


Figure IV - 101: ^6Li NMR data of pristine LMR-NMC material. Numbers on top of deconvoluted resonances indicate corresponding shift values and italic numbers indicate integral values

The deconvolution of the peaks observed for lithium in Li layers reveals at least five different lithium environments indicating different local ordering/domains from Fermi-contact shifts of neighbouring Li, Ni, Co and Mn. For lithium ions in TM layers, three resonances at 1396, 1470 and 1505 ppm were observed. Typically, the 735 and 1470 ppm pair is assigned to Li_2MnO_3 -like domains within the material, supporting the composite interpretation which agrees with previous literature [5-7]. Octahedral lithium sites are assigned to transition metal layers, two main resonances at 1396 (Li coordinated to 5Mn) and 1470 (Li coordinated to 6Mn) ppm. The 1505 ppm resonance exceeds typical, maximum shift values that could be obtained with 6TM-O-Li 90° interactions and, therefore, is tentatively assigned to a Li that has an additional TM neighbor in a tetrahedral site in the Li layer above or below. For the octahedral lithium sites in lithium layers, four, ordered Lorentzian resonances and a disordered Gaussian resonance were observed. Apart from the well-characterized 735 ppm Li_2MnO_3 -like domains, specific assignments of all these peaks are complicated. The peaks at 807 ppm, 594 ppm and 551 ppm are tentatively assigned to various lithium 2nd coordinations with a combination of transition metals and lithium cations. On the other hand, the significantly disordered Gaussian resonance(s) at 628 ppm (green peak in deconvolution, 95 integral units) is assigned, tentatively, to disordered Li due to the coexistence of two or more locally ordered domains. Such Gaussian features are also present in the presence of Mn, Ni, and Co in the Li layer and can, therefore, also indicate a combination of transition metals and lithium cations. The integrated intensities of individual resonances give additional information about the Li content in the lithium layers vs. transition metal layers. According to the composition, $\text{Li}_{1.2}\text{Ni}_{0.2}\text{Co}_{0.2}\text{Mn}_{0.6}\text{O}_2$, 1.0 Li is expected in the Li layers and 0.2 Li is expected in the TM layers, a 5:1 ratio. However integral values deduced from deconvolutions give a ratio of 5.53:1, indicating an 8.1% excess of Li in

Li layers. This excess Li is ascribed to an impurity spinel phase present in the electrode powder from the synthesis (spinel resonances overlap with Li in Li layer resonances), which manifests itself in the electrochemical profiles as a small plateau near 2.5V (approximately 7% capacity contribution) and also in XRD when carefully analysed.

To study the lithium local environment changes in LMR-NMC materials upon cycling, a tedious synthesis of $\text{Li}_{1.2}[\text{Ni}_{0.15}\text{Mn}_{0.55}\text{Co}_{0.10}]\text{O}_2$ composites, with fully ⁶Li-enriched cells (electrolyte, metal anode, and cathode), was carried out and a quantitative study with high resolution ⁶Li MAS NMR spectroscopy on the enriched, cycled materials was performed. Figure IV - 102(a) shows the NMR data for the pristine cathode material and after cycles 1 and 10. As clearly seen, a profound loss of order, or reordering, in the material is observed post activation. It is found that only 7.1% of the lithium ions go back to the “formal” octahedral sites in the transition metal layers. This is studied by deconvolution of the lithium resonances with shift values larger than 1300 ppm (by using integral values). The deconvolution of the majority of the spectrum can be made by keeping a minimum amount of lithium peaks only by introducing a Gaussian and two Lorentzian components. After a dynamic fit of the deconvolution of the peaks, the Lorentzian components observed match well with the fit for octahedral sites in the lithium layers of the pristine material.

However a new resonance(s) centered at 777 ppm is seen for the cycled samples. This resonance covers 34.5% of the lithium content of the cycled material whereas 58.4% of the lithium ions were found to be in the octahedral sites in the lithium layers. At this point a tentative assignment is made correlating this Li-occupancy to an extensive Li-Li dumbbell configuration composed of tetrahedral sites which are accessible after removal of octahedral Li from transition metal layers.

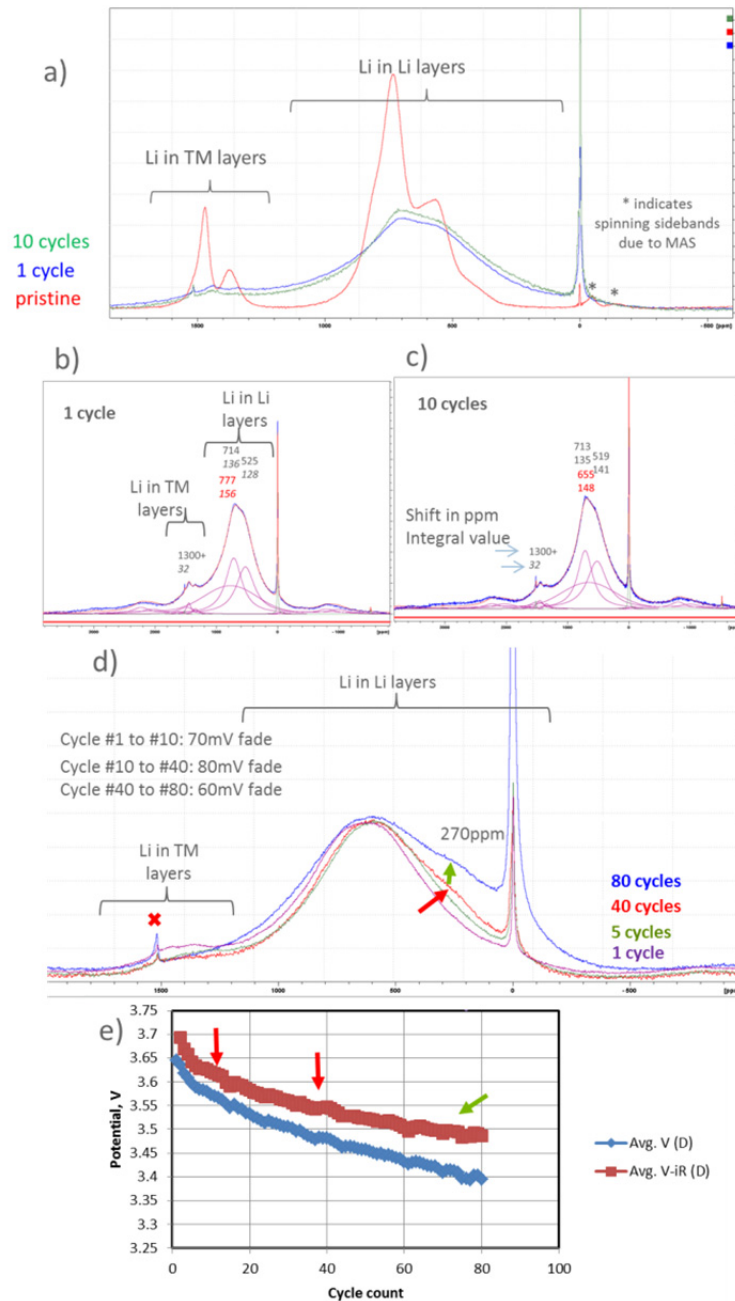


Figure IV - 102: ${}^6\text{Li}$ MAS NMR of a) pristine $\text{Li}_{1.2}[\text{Ni}_{0.15}\text{Mn}_{0.55}\text{Co}_{0.10}]\text{O}_2$ and after 1 and 10 cycles b) and c) the deconvoluted ${}^6\text{Li}$ MAS NMR $\text{Li}_{1.2}[\text{Ni}_{0.15}\text{Mn}_{0.55}\text{Co}_{0.10}]\text{O}_2$ after 1 and 10 cycles, respectively d) comparison of ${}^6\text{Li}$ MAS NMR data for cycled $\text{Li}_{1.2}[\text{Ni}_{0.15}\text{Mn}_{0.55}\text{Co}_{0.10}]\text{O}_2$ and d) the electrochemical performance

After 10 cycles, Figure IV - 102(c), the deconvolution reveals that the Lorentzian peak intensities and their shifts remain constant whereas there is a shift of 122 ppm peak to lower frequency for the Gaussian component. In order to correlate the effect of the shift with electrochemistry, additional experiments were performed after cycles 5, 40, and 80, Figure IV - 102(d). It is found that the shift gradually slows as the rate of voltage fade rate slows; between

cycle 1-10 being fastest (Figure IV - 102e). After 40 cycles the formation of a new lithium resonance at ~ 270 ppm is observed with solid state ${}^6\text{Li}$ NMR and there is a significant increase in its intensity after 80 cycles. The origin of this 122 ppm shift is currently unknown. However, such significant and progressive behavior could be explained by significant transition metal migration (presumably Mn since both NiMn and MnCo-

type Li rich materials exhibit voltage fade) and vacancy formation for transition metals and/or oxygen.

In order to compare the lithium ion local structure changes with further cycling, ${}^6\text{Li}$ MAS NMR experiments were performed on a non-enriched composite material after 500 cycles. Figure IV - 103 shows a comparison of NMR data after 80 and 500 cycles. It is clearly seen that there is no additional shift for the Gaussian component after 80 cycles (electrochemical characterization shows slowing down of the voltage fade) and the only major difference is the decrease in the peak width for the 770 ppm resonance, which, suggests an increase in the ordering for these specific lithium environments. The X-ray diffraction data collected for the sample after 500 cycles (not shown) still shows an ordered, layered structure similar to the activated (1 cycle) material with no spinel

formation. These observations support our tentative assignments on the formation of Li-Li dumbbell configurations composed of tetrahedral sites that are accessible after removal of octahedral Li from the transition metal layers.

Overall, the comparison of the electrochemical and structural characterization results show a direct correlation between the loss of lithium from the transition metal layers, post activation, and more importantly transformation/allocation of available lithium sites in lithium layers (tetrahedral crystallographic positions), and electrochemical voltage fade. These changes correlate quantitatively with the magnitude of voltage fade and require further, detailed analyses to narrow down the specific phenomena involved.

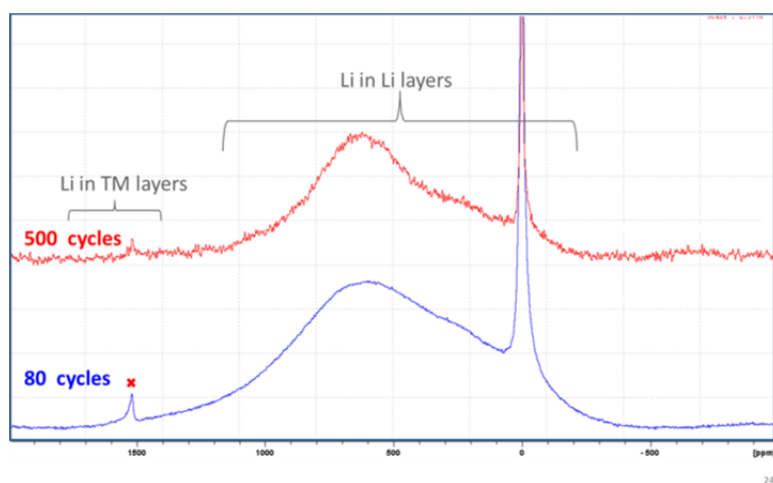


Figure IV - 103: Comparison of ${}^6\text{Li}$ MAS NMR data for cycled $\text{Li}_{1.2}[\text{Ni}_{0.15}\text{Mn}_{0.55}\text{Co}_{0.10}]_{\text{O}_2}$ (top) after 500 cycles, non-enriched sample, (bottom) after 80 cycles for enriched sample

Investigation of Domain Size Effect on Voltage Fade

In order to study cluster/ domain size effect on voltage fade and electrochemical performance; lithium-6 NMR experiments were initiated on $\text{Li}_{1.2}\text{Mn}_{0.4}\text{Co}_{0.4}\text{O}_2$ LMR-NMC composites. This composition is selected in order to utilize available calculation data from the Voltage Fade Theory Group and correlate with experimental observations of NMR shifts on this composition. Figure IV - 102 shows high resolution ${}^6\text{Li}$ MAS NMR data for the $\text{Li}_{1.2}\text{Mn}_{0.4}\text{Co}_{0.4}\text{O}_2$ composition. Two groups of resonances were observed for the Li species present in the lattice; Li in Li layers around 50-1100 ppm and Li in transition metal layers around 1300-1500 ppm. The deconvolution of the peaks observed for lithium in Li layers reveals many different lithium environments indicating different local ordering/ domains and domain boundaries from Fermi-contact shifts of neighboring Co and Mn. The preliminary assignment for domain-boundary lithium ions was

confirmed in this study by varying the synthesis conditions (duration) from 1 hr to 84 hrs and is represented by a broad Gaussian resonance centered at 350 ppm. This resonance is gradually lost (intensity transferred to ordered Lorentzian peaks corresponding to specific Li-O-TM coordinations) by increasing synthesis duration (constant 850°C) which presumably allows the small domains to coagulate and dendritic branches of the composite structure to grow during the high temperature annealing. To be specific, the ratio of Li in domain boundaries to the total amount of Li in the sample was 0.68 after a 1hr synthesis, 0.42 after a 12 hr synthesis, and near to 0 after an 84 hr synthesis. These deconvoluted Li intensities will be used by the theory group to estimate the average domain sizes/length-scales of the composite materials. The effect of this synthesis parameter on Li occupancy is also correlated to electrochemical performance and voltage fade as can be seen in Figure IV - 104(b). The voltage fade rate is found to be a minimum, but still significantly present,

for the composites with larger domains and less disorder (1 week annealing at 850°C). In addition, electrochemical discharge capacity and capacity retention values were a maximum for these samples. The

electrochemical performance drops and voltage fade rate increases as more domain boundary lithium ions are present in the structure, and as the domain sizes get relatively smaller (1 and 12 hour synthesis duration).

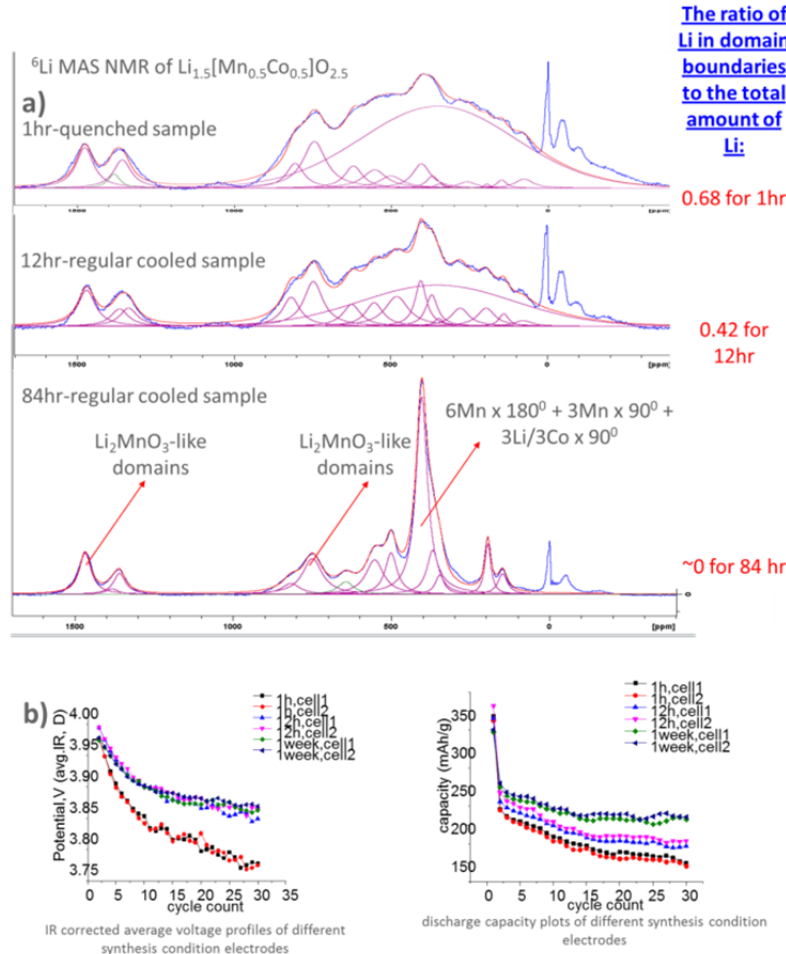


Figure IV - 104: a) ${}^6\text{Li}$ MAS NMR of pristine $\text{Li}_{1.5}[\text{Mn}_{0.5}\text{Co}_{0.5}]\text{O}_{2.5}$ compositions synthesized at 850°C for varying conditions b) electrochemical performance different synthesis condition electrodes. NMR resonances at 0 ppm and at negative shifts are due to diamagnetic Li in LiCoO_2 and spinning sidebands, respectively

A new set of samples was synthesized, with ${}^6\text{Li}$ enriched precursors, for a targeted $\text{Li}_{1.2}[\text{Ni}_{0.15}\text{Mn}_{0.55}\text{Co}_{0.10}]\text{O}_2$ composition to study similar domain size effect with samples prepared at 850°C varying the synthesis duration. Figure IV - 105(a) shows ${}^6\text{Li}$ MAS NMR of the as-prepared samples. Similar to the previous set of samples, two distinct lithium environments (lithium in lithium layers and lithium in transition metal layers) were observed with a similar, significantly disordered Gaussian resonance overlapping with the Lorentzian resonances. Again, a similar trend was observed with a decrease in the ratio of the intensity of the disordered resonance versus the overall intensity of the ordered resonances with increasing synthesis duration. In order to gain information on the evolution of mid- to long-range order of the composite material,

synchrotron XRD patterns were collected for the same samples, Figure IV - 105(a) inset. The expected evolution of increasing crystallinity with annealing time was observed where samples synthesized at 750°C and 850°C for 1 hr showed the lowest crystallinity. Interestingly, the highest crystallinity for a layered hexagonal composite lattice was reached at synthesis durations of 168 hours. Upon further annealing (672 hours), instead of an improvement in crystallinity, formation of a two phase mixture; a monoclinic lattice usually associated with Li_2MnO_3 and a hexagonal, layered lattice typical of NMC were observed. This result is consistent with the increase in local order and significant sharpening of the Li_2MnO_3 -like resonance observed in ${}^6\text{Li}$ MAS NMR for the same samples.

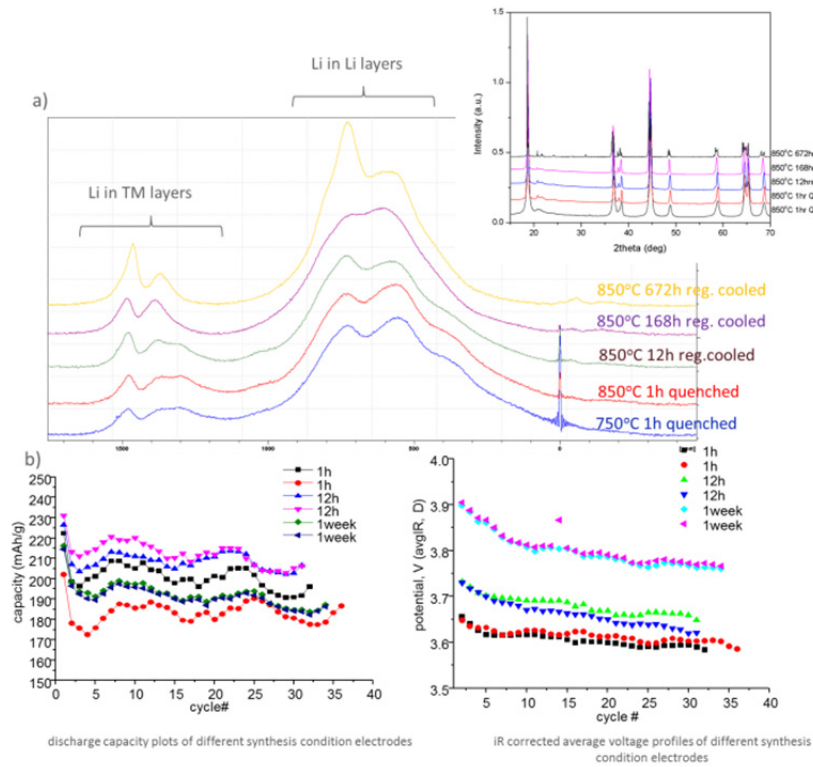


Figure IV - 105: a) Li MAS NMR of pristine $\text{Li}_{1.2}[\text{Ni}_{0.15}\text{Mn}_{0.55}\text{Co}_{0.10}]_{\text{O}_2}$ compositions synthesized at 850°C for varying conditions, the inset shows X-ray diffraction data for the same samples b) electrochemical performance different synthesis condition electrodes

The most likely interpretation of these experimental results can be summarized as follows: the well mixed, compatible lattices of the monoclinic Li_2MnO_3 structure and the hexagonal layered lattice of NMC materials, either in the well accepted dendritic domains or other nanodomain morphologies, begin to coagulate and form significant medium- to long-range order. It should also be noted that electrochemical performance of the sample annealed for 672 hours is very poor (below 150mAh/g discharge capacity, data not shown) which agrees well with the electrochemical inactivity of significant concentrations of crystalline Li_2MnO_3 traditionally prepared electrodes. As for samples which were annealed between 1-168hrs, preliminary electrochemical results [see Figure IV - 105(b)] still reveal significant voltage fade but suggest that optimized fade behavior, capacity, and capacity retention can be obtained by fine tuning annealing durations. *From the above data it can be concluded that optimum overall electrochemical behavior can be realized for a given composition (for Li rich NMC type materials) through optimization of synthesis parameters. However, regardless of the resulting domain sizes, shapes, and morphologies of the composite particles, the voltage fade phenomenon persists.*

Structural and Electrochemical Hysteresis and Voltage Fade: Lithium-Transition Metal Ordering

Voltage fade and hysteresis correlations, and their relationships to local structural changes, as discussed in the proposed mechanism in previous section, was further investigated by high resolution ^6Li solid state NMR spectroscopy. The study was a fully quantitative analysis utilizing ^6Li -enriched metal oxides, fully enriched cell components (electrolytes and ^6Li -anode), long data collection times, and was performed on activated $0.5\text{Li}_2\text{MnO}_3 \bullet 0.5^6\text{LiMn}_{0.5}\text{Ni}_{0.5}\text{O}_2$ electrode systems.

Tracking changes in local lithium environments is required to gain insights into the electrochemical potential of lithium as a function of path dependent site occupation. The changes in the local structures may then be related to the observed electrochemical hysteresis and voltage fade phenomena. Therefore, a detailed study of lithium extraction and insertion, after activation, through a quantitative ^6Li NMR approach was performed. The ^6Li peak intensities presented by NMR data represent the total lithium content in the materials. Data points were selected along the charge/discharge profiles in order to follow structural changes that occur at key potentials based on the previously-proposed model of hysteresis and voltage fade which is described in the conclusions [Figure IV - 106(a)].

At 2.0 V, point 1, Figure IV - 106(a), before the start of the 2nd cycle, a pronounced intensity loss for the TM layer lithium environments (Li_{TM}) is already observed relative to the pristine material, indicating that not all Li_{TM} are reinserted on the first discharge, accompanied by considerable ^6Li peak broadening due to a profound loss of order in the material, Figure IV - 106(c). During the early stages of the 2nd cycle charge [points 1 and 2, Figure IV - 106(a) and (b)] preferential removal of lithium-layer Li (Li_{Li}) from nickel-rich environments (~540 and lower and ~890 ppm, [6-8], concomitant with a slight shift in the Li_{Li} region at ~720 ppm, is observed due to rearrangement of TMs. At 4.38 V (point 3), simultaneous removal of Li_{Li} and Li_{TM} is observed with a considerable loss of intensity for Li_2MnO_3 -like (~720 ppm) and nickel-rich environments (~890 ppm). At the top of charge, 4.7 V, ~75% of the initial Li-ions are removed from the structure with the remaining ~25% residing in the lithium layers (Li_{Li}). These remaining lithium can be assigned to lithium ions that have migrated into lithium-layer tetrahedral sites adjacent to vacated octahedral sites of the TM layers, creating low energy, stable lithium-dumbbell configurations ($\text{Li}_{\text{Tet}}-\square-\text{TM}_{\text{Tet}}/\text{Li}_{\text{Tet}}$) [9, 10]. Interestingly, between points 1 and 2 (≤ 3.6 V), the electrochemical region that grows in capacity with cycling (i.e. voltage fade phenomenon), an unusual ^6Li peak evolution in the ~1600 ppm (TM-layer) region is captured for the first time, indicating a new ordering for Li_{TM} . It has to be noted that although there is lithium removal from the system at points 1 to 2, there is a clear increase in ^6Li -peak intensity associated with the TM layer region. The same ^6Li peak formation is once again

observed during the subsequent lithium insertion at 3.986 V (point 5) and between 3.2 and 2.0 V (points 7 and 8) where electrochemical hysteresis is observed, Figure IV - 94(a) and (c). Once again, lithium peaks are formed at point 7 (~1600 ppm) and the intensity is lost when 2.0 V is reached (point 8). ^6Li MAS-NMR spectra during lithium insertion from 4.7 V down to 2.0 V, including points at 3.986, 3.6 and 3.22 V [Figure IV - 106 (a)] on the second-cycle discharge are shown in Figure IV - 106(c). *A comparison of the NMR spectra given in Figure IV - 106(b) and Figure IV - 106(c) simply reveals that lithium extraction and insertion do not follow the same order.* From the end of the 2nd charge (4.7 V, point 4), relithiation starts with Li_2MnO_3 -like, ordered lithium sites (sharp peak at ~710 ppm) and distorted lithium layer sites (Li_{Li}) (broad, Gaussian peak ~630 ppm, Figure IV - 106). No significant lithium occupancy is seen for the nickel-rich environments (540 ppm and lower) until 3.6 V (point 6), although these sites were the first to be removed during the previous charge. This is consistent with previous reports on slow occupation of lithium sites next to Ni^{+2} , within lithium layers [8]. At lower voltages, between 3.22 and 2 V (points 7 and 8), the resonances due to nickel-rich environments at ~870 and ~540 ppm re-emerge along with an intensity increase for distorted Li_{Li} (~630 ppm Gaussian peak). *During discharge only ~7% of the initial Li_{TM} are reinserted back into TM layers where a drastic increase in occupation of these sites is observed between ~3.6 and ~3.2 V (points 6 and 7) as seen by peak formation between 1250-1500 ppm, Figure IV - 106 (c).*

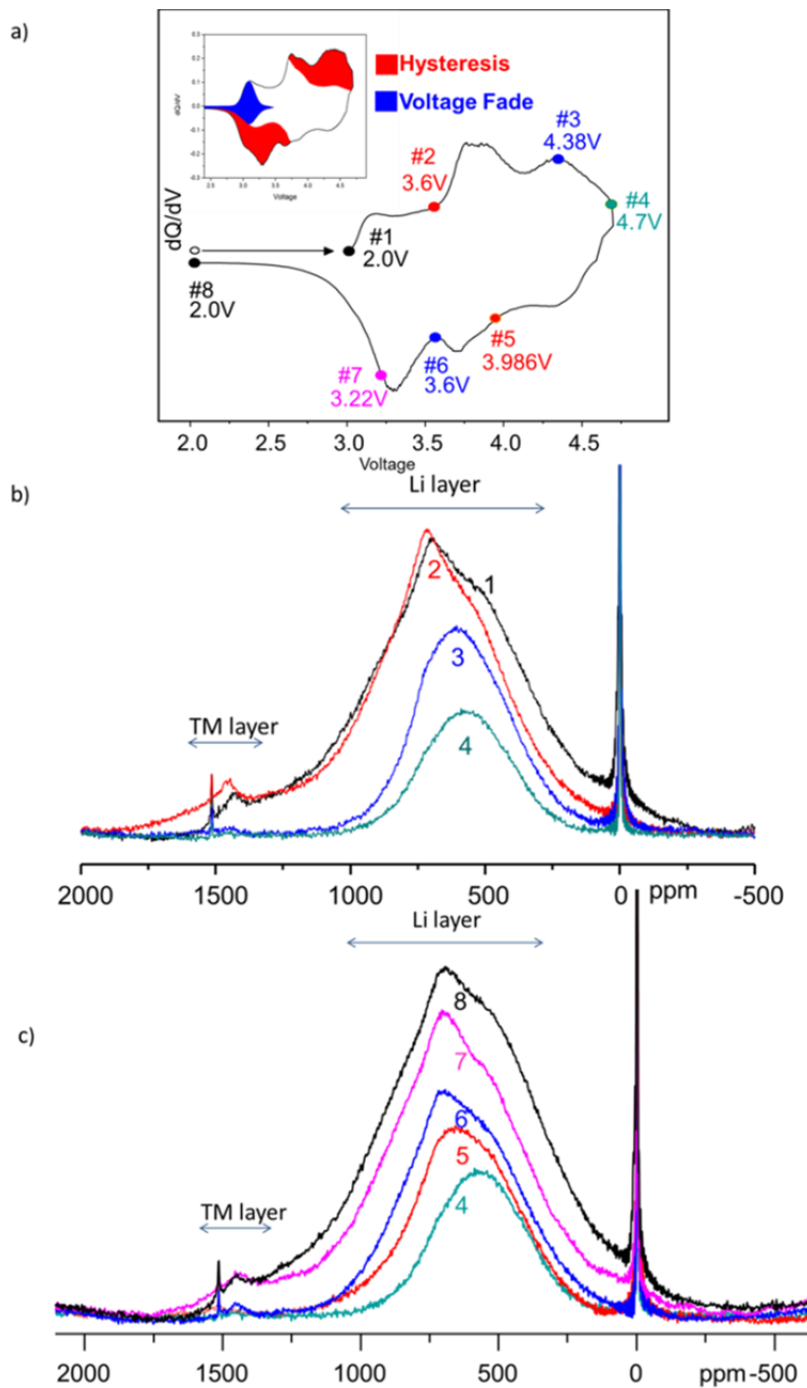


Figure IV - 106: a) Second- cycle dQ/dV plot with labels corresponding to voltages at which NMR spectra were acquired. Inset shows the schematic representation of electrochemical hysteresis and voltage fade with respect to dQ/dV during second-cycle charge/discharge. b) and c) show ^{6}Li MAS-NMR at various SOCs along the second-cycle charge and discharge, respectively

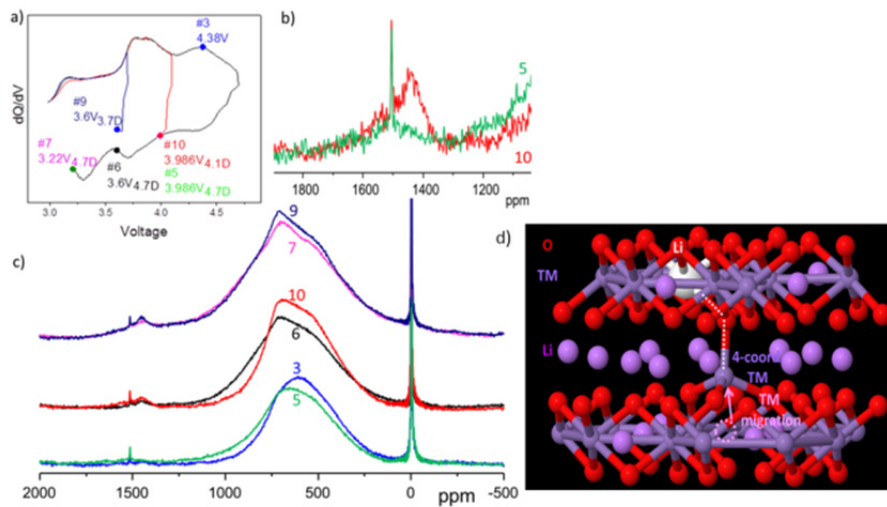


Figure IV - 107: a) dQ/dV plots for several samples charged/discharged to equivalent lithium contents and the corresponding voltages as labeled. Sample numbers correspond to the NMR spectra in b) and c). b) Magnified view of lithium environments in the TM region for points 5 and 10. c) ${}^6\text{Li}$ MAS-NMR of $0.5\text{Li}_2\text{MnO}_3 \cdot 0.5\text{LiMn}_{0.5}\text{Ni}_{0.5}\text{O}_2$ comparing samples charged/discharged to equivalent lithium contents

The structure-activity relationship can be revealed in further detail by comparing ${}^6\text{Li}$ NMR data on points selected at various voltages, but with equivalent lithium contents (states of charge, SOC), to observe the differences in lithium site occupancies (Figure IV - 107). For instance, at point 3 [Figure IV - 107 (a)] for a cell charged to 4.38 V, a mixture of lithium in dumbbells and lithium in octahedral sites in lithium layers is observed. However, a different local ordering is observed for a cell having the same Li content, but which was first charged all the way to 4.7 V and then discharged to 3.986 V (point 5). *The last lithium ions that are removed from Li_{Li} on charge are not the first sites to be lithiated on discharge, i.e. hysteresis.* This effect of cycling above 4.1 V and accessing the hysteresis component is further highlighted in Figure IV - 107 (b) (points 5 and 10). *The spectra reveal that Li_{TM} are not removed until charging above 4.1 V and are not reinserted into the structure until at least after 3.986V on discharge.* In another instance, a significant change in lithium ordering is observed in sample 6, which has undergone a charge to 4.7 V followed by discharge to 3.6 V, relative to sample 10 having the same Li content as 6, which was only charged to 4.1 IV. These correlate well with the electrochemical hysteresis component in the high voltage region above 4.1 V, Figure IV - 106(a) inset. On the other hand, the hysteresis voltage difference these materials exhibit can be shown structurally by comparing points 9 and 7. A cell that is cycled to high voltage which accesses the hysteresis component (point 7) must be discharged to a significantly lower voltage ($\sim 1\text{V}$) before the Li ordering is similar to a cell without the high voltage charging (point 9). This data related to local lithium structure and

site occupancy correlates well with the electrochemical hysteresis discussed in the previous sections.

As discussed previously, at points 2 and 7 in Figure IV - 94(b) and (c), a broad high frequency ${}^6\text{Li}$ peak is observed at 1600 ppm. This peak is first observed at low voltages, post-activation, on charge, and appears once again on discharge. In order to have a total hyperfine shift for a Li_{TM} resonance at ~ 1600 ppm, additional TMs must be coordinated to LiMn_6 units via the presence of a tetrahedral or octahedral TM in the layers immediately above or below. This can be concluded based on previous ${}^6\text{Li}$ NMR chemical shift values reported on similar cathode materials and our heuristic shift calculations [6, 8, 12, 13] and is shown schematically for tetrahedral manganese in Figure IV - 107(d) for a partially delithiated oxygen vacancy bearing lattice. *This assignment represents the first direct ${}^6\text{Li}$ NMR observations of Li-TM coordination changes and TM migration via the shift effect on Li_{TM} resonances at specific states of charge in LMR-NMC electrodes.* This new ${}^6\text{Li}$ resonance is now denoted as $\text{LiTM}_6\text{-TM}_{\text{tet/oct}}$. The relative intensity loss of the lithium sites associated with $\text{LiTM}_6\text{-TM}_{\text{tet/oct}}$ defects (~ 1600 ppm) from charge to discharge (Figure IV - 106, comparing points 2 and point 7, respectively) indicates limited reversibility of the spectroscopically-detected TM migration. This correlates directly with the proposed model of hysteresis and voltage fade where partially reversible TM migration is indicated as a key mechanism.

In order to study the evolution of resonances arising from $\text{LiTM}_6\text{-TM}_{\text{tet/oct}}$ defects, detailed deconvolutions of the NMR data at specific SOCs have been analyzed. Figure IV - 108 shows the deconvoluted spectra for cells charged to 3.6 V on cycles 2, 11, and 20, respectively.

The 1600 ppm region involves two distinct, small peaks at ~1550 and 1688 ppm. The former (1550 ppm) likely indicates the presence of tetrahedral Mn but could also been attributed to the presence of octahedral Ni⁺³ in the lithium layers. However, lithium-ions are assumed to be removed from the vicinity (1st and 2nd coordination shell) of oxidized Ni (+3 and +4), corresponding to electrochemical activity [6].

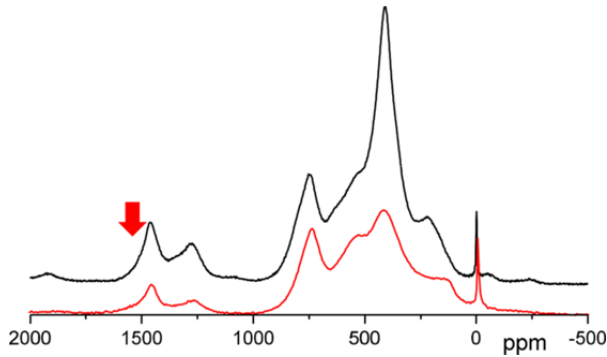


Figure IV - 108: ⁶Li MAS-NMR of; 0.5Li₂MnO₃•0.5LiMn_{0.5}Co_{0.5}O₂, (top) charged to 4.3V, 1st cycle spinning at 67kHz, and (bottom) charged to 4.35V, 1st cycle spinning at 64kHz. Red arrow highlights ~1550ppm resonance due to LiMn₆-Mn_{ter}

Furthermore, the distinct loss of ordering observed for the Li₂MnO₃-like coordinations (724 and 765 ppm) post activation indicate Mn activity/migration. In addition to this, spectra collected along the 1st cycle at similar data points presented herein, for a system where nickel is substituted with cobalt (Figure IV - 108), have produced very similar shifts suggesting that the TM activity observed arises predominantly from Mn_{ter}. Therefore, the 1550 ppm resonance has been assigned to LiMn₆-Mn_{ter}. Interestingly, the detected migration does not occur within an electrochemical window where Mn⁺³ forms, a requirement shown for Mn migration in layered oxides [17]. The 1688 ppm resonance indicates the presence of a Mn_{oct} in the layer above or below the TM layer or an unreacted Ni⁺² in an octahedral site in the lithium layers (an unlikely scenario due to the

magnitude of shift and possibility of 2+ oxidation states of Ni at this state of charge). Lastly, presence of a Mn_{oct} in the layer above or below of a LiMn₂Ni unit could also be a minor contributor to the intensity of the 1550 ppm resonance. Besides the significance of the migrated TM assignments described above, one important point to note is the dramatically low concentrations of lithium coordinations associated with these migrated TMs (see green and blue areas in Figure IV - 109). Quantification of the integrated areas for 1550 ppm and 1688 ppm regions indicates that only 1.91% and 1.24% of the overall lithium content are associated with LiTM₆-TM_{ter/oct} coordinations, respectively. These results are surprising in that the effect of transition metal migration/coordination change and defect formation on lithium local environments is small with respect to the electrochemical hysteresis observed. It is only through the use of very high signal-to-noise, ⁶Li NMR data and full quantification that detection of these defects is made possible.

The effect of increasing cycle number on the intensity of LiTM₆-TM_{ter/oct} resonances (1550 and 1688 ppm) has also been studied. Figure IV - 109 shows cells that have been charged to 3.6 V on cycles 2, 11, and 20. As shown with % integration values the intensities and relative frequencies of these lithium environments decrease significantly with increasing cycle number (from a combined 3.15% on cycle 2 to 2.73% by cycle 11 and 1.86% by cycle 20). A minor contribution to the loss of intensity also comes from capacity loss (about 11.6% of the intensity loss after 11 cycles). This correlates well with stabilization of TM ordering, i.e., a decrease in TM migration and a slowing down of the electrochemical voltage fade phenomenon. It is also significant to note that with a few percent TM migration and defect site formation, a 1 V hysteresis is created involving 10% lithium removed above 4 V and inserted back in the structure below 3.5IV. This is a clear and important example of defect sites governing structural activity and electrochemical activity.

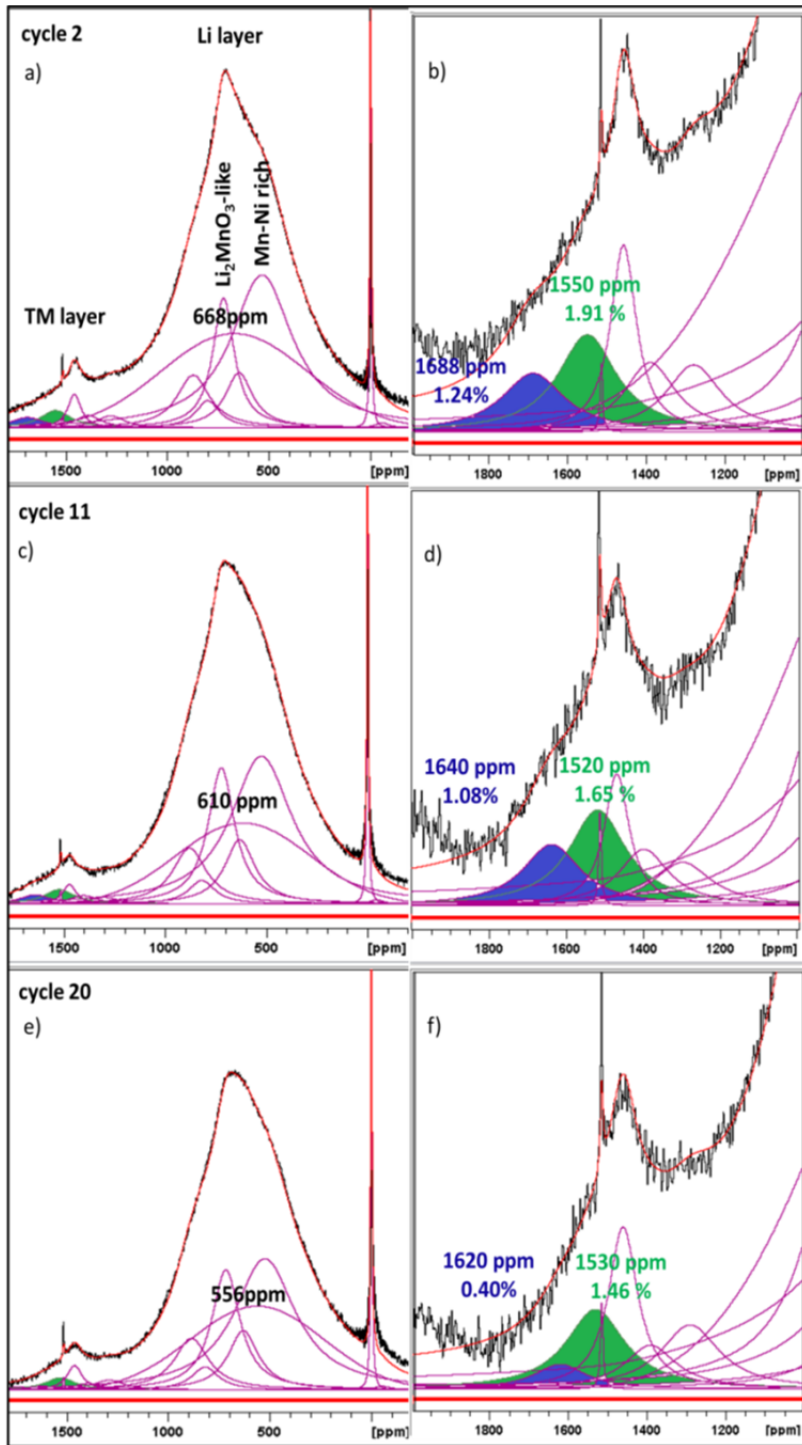


Figure IV - 109: ${}^6\text{Li}$ MAS-NMR deconvolutions for samples charged to 3.6V at cycles 2, 11 and 20. (Right) Li_{TM} region for the same data. Blue and green peaks show the lithium peaks coordinated to octahedral nickel and tetrahedral manganese, respectively. Lithium contents for the specific sites were calculated with the integrated area of the corresponding lithium peak within the mass normalized spectra

In summary, this part of the study has helped identify structural causes of reversible hysteresis and voltage fade phenomena observed for Li-rich composite

materials. There are two main structural processes identified from the experimental results obtained:

- 1) *Lithium removal and reinsertion from and into the activated composite structure is found to be path dependent in terms of Li-sites, i.e., structural hysteresis. The structural hysteresis is found to be reversible and correlates directly with electrochemical hysteresis. Furthermore, it is dependent on a surprisingly low concentration of defect sites formed post-activation within the electrode structure.*
- 2) *⁶Li resonances are observed due a hyperfine shift of tetrahedral TMs coordinated to LiMn₆ units above or below the lithium layer as well as TMs in octahedral lithium sites. This process indicates electrochemically induced TM migration and is found to be only partially reversible. The resulting partial TM reordering in the local structure correlates directly with the phenomena of voltage fade due to, presumably, lowered Li-site energies without corresponding to any new distinct long range order (e.g., spinel).*

These two processes have been found to progress simultaneously, post-activation, upon cycling and bolster the spectroscopic evidence in support of the structural hysteresis and voltage fade model previously proposed for Li- and Mn-rich composite electrodes.

Understanding the layered to spinel (LS) structural transformation mechanism in LMR-NMC by neutron diffraction

Our approach was to employ neutron diffraction (ND) technique on pristine and cycled HE5050 oxides to extract detailed crystallographic information in pristine and cycled oxides in order to visualize the atom migration paths. Unlike X-ray scattering, neutron interaction with materials is not atomic number (z) dependent. Therefore, the approach takes advantage of the uniqueness of the ND technique for locating lighter atoms in the presence of heavier atoms, and, therefore, makes it possible to get more accurate structural information about lithium and oxygen in a transition metal ion (M) environment. Locating the exact site occupancies of cations and anions will enable to propose the cation migration path(s) that are responsible for LS structural rearrangements in HE5050 oxide. Our inquisition is focused on answering these important questions:

- 1) What is the structure of HE5050 pristine oxide?
- 2) Is there any cation site interchange present in the unit cells?
- 3) Which transition metal ions migrate or relocate in the structure to form the spinel framework after cycling?
- 4) What sites do the relocated transition metal and lithium ions occupy?
- 5) What type of spinel phase is formed, and how is it formed?
- 6) What is the migration path for LS structural rearrangements?

Experimental: The HE5050 powder was obtained from Argonne National Laboratory. The composition of

the HE5050 was verified as Li_{1.2}Mn_{0.55}Ni_{0.15}Co_{0.1}O₂ and the *ex situ* XRD, particle morphology, selected area electron diffraction (SAED), high-resolution transmission electron microscopy image, and electrochemical performance data can be found in previous publications[Physical Chemistry Chemical Physics 2013, 15, 19496, Journal of Power Sources 2013, 229, 239-248]

Neutron diffraction for pristine HE5050 powder: In this case, HE5050 powder (~1gram) was filled in a 6mm vanadium can in a glove box containing Helium. Room temperature ND experiments were carried out on the POWGEN beam line at the Spallation Neutron Source (SNS) at Oak Ridge National Laboratory. The 24 sample changer was used to collect the room-temperature ND pattern using a frame of neutrons with center wavelength of 1.066 Å. The experimental pattern was refined by Rietveld method using GSAS and EXPGUI interface.

Neutron diffraction for cycled HE5050 oxides:

Materials, slurry preparation and electrode coating

The electrodes for this study were fabricated at the U.S. Department of Energy (DOE) Battery Manufacturing R&D facility (BMF) at Oak Ridge National Laboratory (ORNL). Polyvinylidene fluoride (PVDF) (Solvay 5130), and Super P Li (Timcal) in 86/8/6 wt% were dispersed in N-Methyl-2-pyrrolidone (NMP) with a planetary mixer (Ross PDM-1/2). The HE5050 cathode was coated on one side of a 15-μm thick Al foil by a slot-die coater (Frontier Industrial Technology, Inc.). The wet coating thickness was 118.5 μm, and the areal weight was 9.8 cm². For the anode, A12 natural graphite (ConocoPhillips) was used.³

Pouch cell fabrication and electrochemical cycling

Uncalendared HE5050 cathodes and graphite anodes were punched into layers. The areas of a single layer of cathode and anode were 47 and 50 cm², respectively. Three layers of HE5050 cathodes and graphite anodes were assembled into pouch cells at the ORNL BMF. The reason for making a 3 × 3 layer pouch cell was to obtain enough material for ND experiments at the POWGEN beam line at the ORNL Spallation Neutron Source (SNS), which generally requires a sample size of ~1 g for this family of materials to obtain refinable patterns. Celgard 2325 was used as the separator; the electrolyte was 1.2 M LiPF₆ in ethylene carbonate: diethyl carbonate (3/7 wt % ratio, Novolyte). All cells underwent formation cycling following a procedure similar to that reported by Abraham's group[Journal of the Electrochemical Society 2013, 160 (5), A3006] carried out in two steps. Next, the cells were cycled between 2.5 and 4.7 V for 26 cycles at a rate of 20 mA/g. Oxide electrode samples for neutron diffraction studies were collected at different cell voltages during the second and 26th charge-

discharge cycles after the formation cycling. All pouch cells were disassembled in an argon-atmosphere glove box, washed with dimethyl carbonate (DMC), and dried for several hours in the glove box. Cycled HE5050 oxide powder materials (along with the PVDF and carbon black) were removed from the Al current collectors after being dried. In order to track the structural rearrangement in the HE5050 material, cycled samples were collected at the voltages shown in Figure IV - 110a and Figure IV - 110b for the second and 26th cycles, respectively. Cell voltages of 3.2, 3.5, 4.1, and 4.5 V were selected as points of interest for structural characterization (Figure IV - 110). The cells underwent a holding/resting period to attain structural equilibrium, and sufficient caution was taken to attain the desired voltages before the cells were disassembled. That is, the reported voltages represent completely relaxed and stabilized HE5050 oxide samples.

Neutron diffraction

Cycled HE5050 powder materials were filled in air-tight 6 mm vanadium sample cans in an argon-filled glove box. The cans were transported to the ORNL SNS, where room-temperature ND experiments were carried out on the POWGEN beam line. The 24-sample changer was used to collect the room-temperature ND patterns using a frame of neutrons with center wavelength of 1.066 Å. The experimental patterns were refined by the Rietveld method using GSAS and the EXPGUI interface [A. C. Larsen; R. B. Von Dreele, General Structure Analysis System (GSAS). Los Alamos National Laboratory Report LAUR 86-748, 2004, B. H. Toby, Journal of Applied Crystallography 2001, 34, 210].

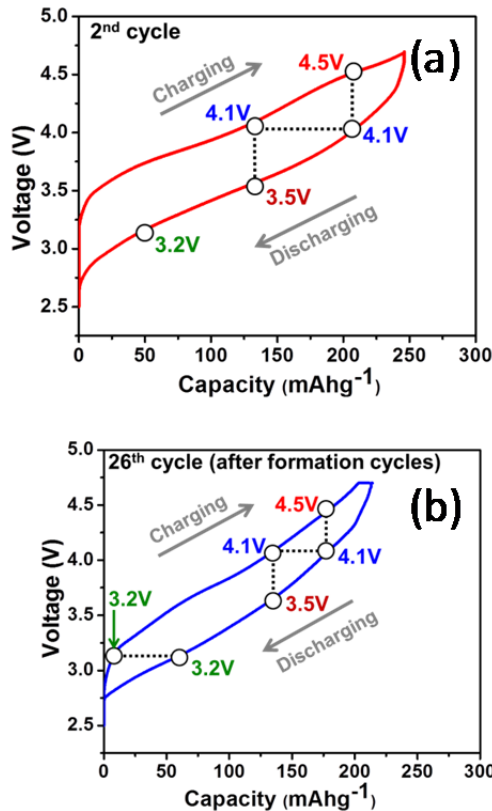


Figure IV - 110: The voltage-capacity curve during the second (a) and 26th cycle (b). The HE5050 oxides were collected at the designated cell voltages for characterization. The connected lines represent the samples collected at same voltage or same capacity

Results and Discussion:

Neutron diffraction of pristine HE5050 oxide:

Rietveld refinement of experimental ND patterns from the HE5050 powder was performed by using two models *viz.* Model 1: Monoclinic ($C2/m$ space group), and Model 2: Monoclinic ($C2/m$) + Trigonal ($R\bar{3}m$). The model with only the trigonal phase was not considered here since the experimental ND pattern contains ordering peaks (see blue arrow mark in Figure IV - 111) that could not be indexed by considering a trigonal phase alone. Our results considering model 2 (two phase model) shows slightly better agreement parameter. The crystallographic information derived from Rietveld analysis of pristine HE5050 oxide is provided in Table IV - 12 and corresponding refined neutron diffraction pattern is given in Figure IV - 111.

Table IV - 12: Refined crystallographic parameters for HE5050 with combined monoclinic Li_2MnO_3 and trigonal LiMO_2 ($\text{M}=\text{Co, Ni, Mn}$) unit cells

Overall Composition: $\text{Li}_{1.21}\text{Co}_{0.086}\text{Mn}_{0.563}\text{Ni}_{0.141}\text{O}_2$						
Agreement parameters: $R_{WP}=5.05\%$ $R_p=8.09$ $\chi^2=1.50$						
Phase 1: Crystal System: Trigonal, SG: $\text{R}\bar{3}m$						
Composition: $\text{LiCo}_{0.25}\text{Mn}_{0.375}\text{Ni}_{0.375}\text{O}_2$						
Lattice constants: $a=b=2.85525(12)$ $14.2483(10)$, $V=100.596(7)$, $Z=3$						
Phase percentage : 50% ($\delta=0.01$)						
Site	Atom	X	Y	z	SOF	Uiso
3b	Li	0	0	0.5	1	0.0285(3)
3a	Co	0	0	0	0.25(4)	0.0345(3)
	Mn				0.375(4)	
	Ni				0.375(4)	
6c	O	0	0	0.2594 (20)	1	0.0093(6)
Phase 2: Crystal System: Monoclinic SG: $\text{C}2/\text{m}$						
Composition: Li_2MnO_3						
Lattice constants: $a=4.9464(27)$, $b=8.5624 (5)$, $c=5.0332(21)$, $\beta=109.3221 (32)$, $V=201.186 (9)$, $Z=4$, Phase percentage: 50% ($\delta=0.01$)						
Site	Atom	X	y	z	SOF	Uiso
2c	Li	0	0	0.5	1	0.0132(2)
4h	Li	0	0.6606	0.5	1	0.0132(2)
2b	Li	0	0.5	0	1	0.0132(4)
4g	Mn	0	0.1670	0	1	0.0101(4)
4i	O	0.2189(1 0)	0	0.2283(9)	1	0.0027(4)
8j	O	0.2548(7)	0.3202 (20)	0.2243(6)	1	0.0048(8)

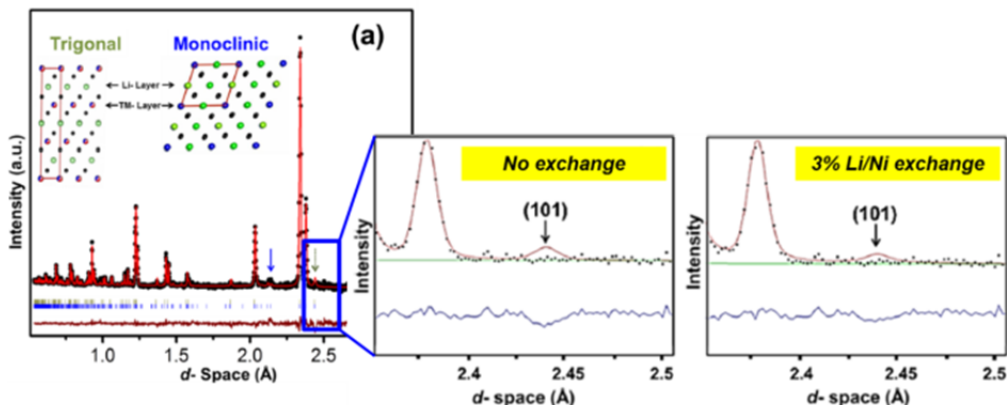


Figure IV - 111: Refined powder neutron diffraction (a) and x-ray diffraction (b) for HE5050 by considering a composite monoclinic Li_2MnO_3 and trigonal LiMO_2 ($\text{M}=\text{Co, Ni, Mn}$) unit cell. The different color of the atoms in the TM layer represents different TM ions (Co, Mn, Ni) present in same site. In figure a, the solid blue arrow shows the cation-ordering peaks exclusively from monoclinic Li_2MnO_3 unit-cell and the dotted arrow represents the (101) reflection in the trigonal phase and (130)/(201̄) reflections in the monoclinic phase. (b-c) show the trigonal (101) plane intensity before Li/Ni exchange (b) and after 3% Li/Ni exchange (c)

Interestingly, in model 2, one extra reflection corresponding to d - spacing of 2.44 Å (see highlighted box in Figure IV - 111) was observed in the calculated pattern; however, it was not observed in the experimental pattern. This peak was assigned to a (101) reflection in the trigonal phase and (130)/(201̄) reflections in the monoclinic phase. To address this

intriguing observation, model 2a was proposed, which is similar to the model 2. In model 2a, however, the Li/Mn atoms in the monoclinic phase and Li/Ni atoms in the trigonal phase were allowed to exchange sites between lithium and transition metal layers. Allowing Li/Mn to exchange in the monoclinic phase did not alter the peak intensity of this extra reflection, but when Li and Ni atoms were exchanged between Li/Ni sites in the

trigonal phase, the intensity of this reflection was minimized in the calculated pattern (see Figure IV - 111b and Figure IV - 111c for comparison). At this stage, only the occupancy of Li and Ni was varied while keeping Mn and Co occupancies constant as model 2, and refinement showed 3% of the Li site could be occupied by Ni. Further increasing this value did not result in significant improvement in the fit.

Therefore, the composition of LMR-NMC HE5050 was found to be 0.50 $\{Li_{1-x}Ni_x\}$ $\{Li_{0.20+x}Co_{0.25}Mn_{0.375}Ni_{0.375-x}\}O_2 \cdot 0.50 Li_2MnO_3$ where $x=0.0354$ in a composite structure.

Neutron diffraction of cycled HE5050 oxide:

After 26 cycles, significant voltage drop was observed (Figure IV - 112) with 15% drop in discharge capacity. The neutron diffraction patterns were collected at different SOCs during second cycle and 26th cycle (see Figure IV - 110) and Rietveld refinements were performed carefully until reasonable agreement parameters were achieved.

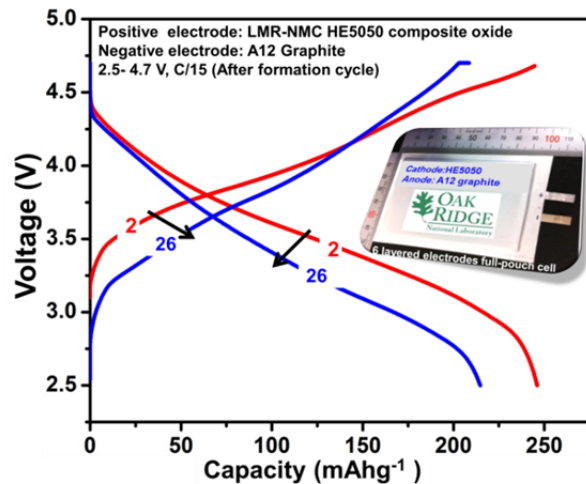


Figure IV - 112: Voltage profile of a full-pouch cell containing three HE5050 cathodes and three graphite anodes. The arrow shows the voltage fade phenomena

Evidence of growth of spinel phase after 26th cycles

Our initial investigations on neutron diffraction patterns collected from cycled HE5050 oxides during second and 26th cycles at different SOCs are:

- i) Structural modification might occur during the initial cycles, but that it might be minimal and reversible. This is evidenced by ND peak analysis, where the peaks from LMR oxides after the second cycle (3.2-V discharged state) attain the initial positions very close to the starting material (see Figure IV - 113a)
- ii) ND showed an increase in lattice spacing of (110), and (108) reflections (Figure IV - 113b) and a new spinel-like (4 4 0) peak at $d=1.13 \text{ \AA}$ (Figure IV - 113c) at 3.2V discharged state after extended (26) cycling suggests LS structural rearrangement occurs after extended cycling.

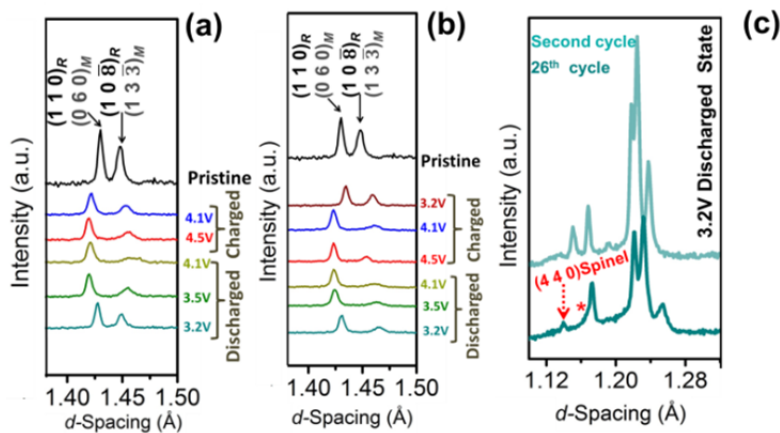


Figure IV - 113: (108), and (110) peak positions in second (a) and 26th (b) cycle. The peaks retains the original positions after completion of second cycle, however, changes the positions after 26th cycle. the New peaks at $d=1.13 \text{ \AA}$ appear at the 3.2 V discharged state after the 26th cycle but not observed after the second cycle(c)

iii) Rietveld refinements of the cycled HE5050 oxides in the 26th cycle showed improved agreement by the addition of a spinel component (LiMn₂O₄ model) spinel. In contrast, no improvements in the fitting were observed for oxides from the second cycle. The refinement indicated ~15% by weight of a spinel component in the oxide structure after the 26th charge-

discharge cycle. Figure IV - 114 shows fitting patterns and agreement parameters from the Rietveld refinements of oxides discharged to 3.2 V for the 26th cycle, in which a LiMn₂O₄ spinel phase was not included (Figure IV - 114a) and included (Figure IV - 114b)

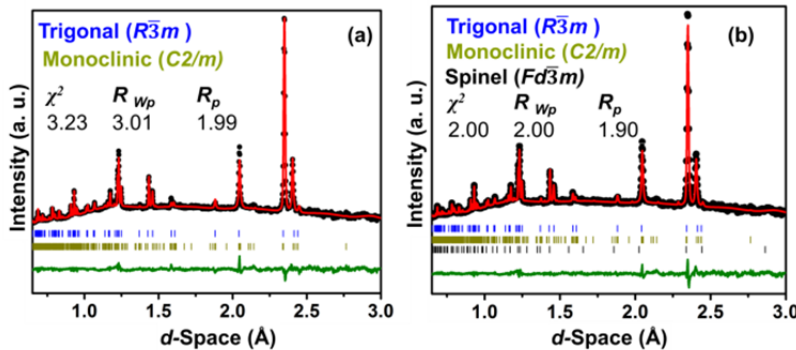


Figure IV - 114: The refined ND patterns for HE5050 oxide collected after 26th cycle at 3.2 V discharged state without spinel phase (a), and with the spinel phase (b) in the model. The model includes spinel phase shows better agreement parameter as compared to the model without the spinel phase

The results above confirm that HE5050 oxide undergoes a LS structural transformation after extended cycling (26 cycles in this study), which is in agreement with the high-resolution TEM and SAED data reported previously [Physical Chemistry Chemical Physics, 15, 19496, (2013)]. The formation of a spinel phase in the host layered HE5050 oxide after subsequent charge-discharge cycles likely alters the lithium (de)intercalation process. It is important to note that the relocation of lithium ions in different crystallographic site(s) of the cycled HE5050 oxides might alter the site energy (possible Li-Li interaction), which will adversely affect the lithium (de)intercalation chemistry and might ease lithium-ion movement during the lithium (de)intercalation process. As a consequence, the average operating voltage of the cell could decrease causing a depression of the voltage profile.

Cation(s) site occupancies in HE5050 oxide during second and 26th cycles

Trigonal layered ($R\bar{3}m$ space group) and spinel ($Fd\bar{3}m$ space group) unit cells are structurally correlated by group-subgroup schemes in the Bärnighausen formalism [H. B. Yahia; M. Shikano; H. Kobayashi, Chemistry of Materials 2013, dx.doi.org/10.1021/cm401942t]. Similar to the trigonal unit cell, a spinel unit cell is also O₃ stacked and the LS structural transformation can occur via layer gliding and/or a direct movement of cations within the fixed oxygen anion (vacancy) arrays. The difference between the layered trigonal and the spinel (for example, if one considers LiMn₂O₄ spinel as model compound) structure is that in the LiMn₂O₄ spinel, a lithium atom is present in the tetrahedral site and the TM(Mn) atom is in the octahedral site of the lithium layer²⁷ whereas in the

trigonal phase, all the M and Li ions are in the octahedral sites of their respective layers. The tetrahedral occupancy in the spinel structure increases the symmetry from $R\bar{3}m$ to $Fd\bar{3}m$ spacegroup. Therefore, to track the LS transformation pathways in the cycled HE5050 oxide, the key is to investigate the cation occupancies at different cell voltages Figure IV - 110 and compare the crystallographic information of the second and 26th cycles. In order to obtain the cation migration paths for LS rearrangement, Rietveld refinements were performed, the details of Rietveld refinement process and the crystallographic parameters obtained from refinement process are described elsewhere [Chem. Mater., 2014, DOI: 10.1021/cm5031415]. The percentage of site occupancy factors of cations at different crystallographic sites for pristine and cycled HE5050 oxides at different SOCs during second and 26th cycle are plotted in Figure IV - 115. The structural refinement was initiated for the HE5050 oxide collected at the 4.1-V charge state during the second cycle by a two phase refinement of a trigonal unit cell where all the M (Co, Mn, Ni) ions were in octahedral sites of the metal layer (3a), and the lithium ions were in the octahedral sites of the lithium layer (3b) (model 1). The agreement parameters with model 1 were found to be $R_{wp}=2.30\%$, $R_p=3.44$, and $\chi^2=3.67$. The presence of 6% lithium in the octahedral sites (3a) of the transition metal layer (Li_{TM}) and 9% Ni in the octahedral sites (3a) of lithium layer (Ni_{Li}) resulted in $R_{wp}=2.08\%$, $R_p=3.18$ and $\chi^2=3.01$. During refinement, a Mn deficiency in the 3a site was observed, and the χ^2 value was further reduced by about 10% by placing 3% Mn in the octahedral sites (3b) of lithium layer (Mn_{Li}). Therefore, with Li/Ni disorder and Mn_{Li} in the trigonal phase (model 2), a

better fit was obtained, as compared to model 1 where Li/Ni disorder and Mn_{Li} were absent. The refined ND pattern with model 2 is shown in Figure IV - 116a. Closer observation of the refined and experimental patterns revealed that, in some cases, the experimental peak intensity, for example the (006) peak intensity, does not match the calculated intensity (see inset of Figure IV - 116a). Substantial improvement in the peak fitting (for example, see the fitting of (006)) and further improvements in the agreement parameter value (χ^2 was reduced to 1.5) were obtained by model 3 (Figure IV - 116b), in which 11% lithium atoms and 12% Mn atoms were placed in the tetrahedral 6c site of lithium layer (0, 0, x; x = 0.125). Further, ND refinements showed 13% oxygen deficiency in overall composition that improved the agreement parameters ($R_{WP} = 1.78\%$, $R_p = 3.08$, $\chi^2 = 1.35$) (model 4); note that oxygen vacancies are expected in this oxide after the activation/formation cycle. The oxygen deficiency after initial cycle(s) is consistent with the report by Liu et. al. [H. Liu; C. R. Fell; K. An; L. Cai; Y. S. Meng, Journal of Power Sources 2014, 240, 772], where authors report the formation of oxygen vacancies and conclude that the activation barriers for transition metal migration is significantly reduced by the presence of these vacancies. Although the current study is unable to confirm whether the oxygen loss occurs only from the oxide surface or both from the surface and bulk, it clearly shows oxygen deficiency in the cycled HE5050 oxides, which could assist in the cation migration for LS transformation.

From this point on, model 4 was considered as an initial model for refinement for the cycled HE5050 oxides.

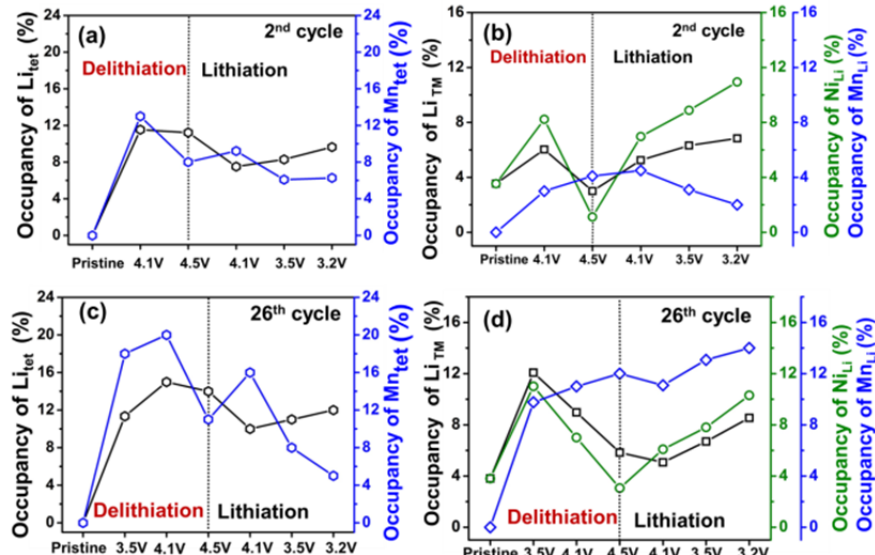


Figure IV - 115: Percentage of Li_{tet} , Mn_{tet} , Li_{TM} , Ni_{Li} , and Mn_{Li} at different SOCs during second electrochemical cycle(a-b) and 26th cycle(c-d)

In the following section, we present how the SOFs of Li and M ions vary during the charge and discharge processes as a function of cell voltage for the HE5050 oxides collected during the second cycle (Figure IV - 115). The Li_{tet} concentration is higher at 4.1V than the pristine oxide. At 4.5 V, the percentage of Li_{tet} remained constant. In contrast, the occupancy of Mn_{tet} decreased in comparison to 4.1V charged state. The Mn_{Li} concentration increased, and the Ni_{Li} concentration decreased significantly. The agreement parameters with model 3 were $R_{WP} = 1.78\%$, $R_p = 3.08$, and $\chi^2 = 1.76$.

Interestingly, when the lithium ions and oxygen SOF in the monoclinic unit cell were less than one, the agreement parameter was slightly improved. At the 4.1-V discharge state, the percentage of Li_{tet} decreased and Mn_{tet} slightly increased. The Ni_{Li} occupancy increased; however, the Mn_{Li} occupancy nearly remained constant. With further discharging, the Mn_{tet} slightly decreased at

3.5 V and remained constant at 3.2 V at 3.2 IV. In contrast, the occupancy of Li_{tet} increased on further discharging to 3.5 V and 3.2 IV. The Li_{TM} and Ni_{Li} occupancies increased during the discharge process regardless of the discharge voltage. These results yield a higher percentage of Ni_{Li} in the structure than the percentages of Mn_{Li} and Li_{TM} (see Figure IV - 115b). In summary, at 3.2 V after completion of the second cycle, the HE5050 oxide structure was more likely to contain a composite of trigonal and monoclinic phases with significant amount of Mn and Li in the tetrahedral sites of Lithium layer of trigonal phase. Therefore, the atomic distribution was not exactly like that of the pristine HE5050 oxide. The compound after the second cycle, the layered trigonal phase, can be written as $\{[(1-x-y-m)Li_x yNi_{Li} \square]_{3b} (xLi_{tet} zMn_{tet})_{6c}\} \{mLi_{TM} (0.375-y)Ni (0.375-z)Mn 0.25Co\}_{3a} \{O_{2-8}\}_{6c}$ where \square denotes the vacancies in the lithium layer. The presence of Li_{tet} , Mn_{tet} in the lithium layer of layered trigonal phase after

completion of second cycle might indicate a ‘defective/intermediate spinel’ with formula $[A_{1-x}B_x]^{tet}[A_{x/2}B_{1-x/2}]_2^{Oct}O_4$; where A= Li and B=Mn. However, no ‘spinel peaks’ were observed at 3.2V discharged state after completion of second cycle.

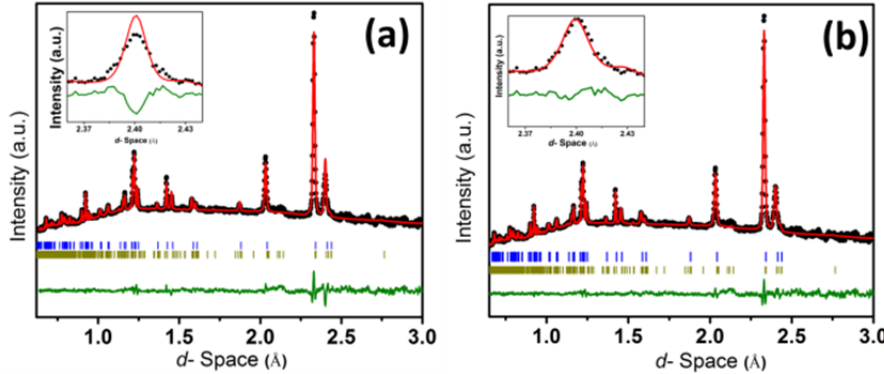


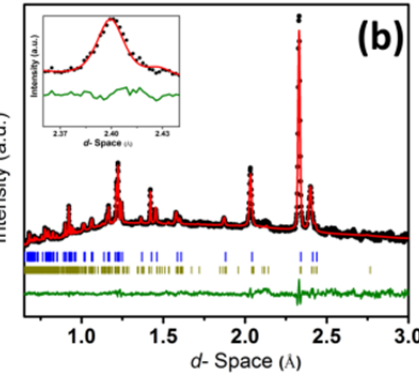
Figure IV - 116: The refined ND patterns for HE5050 oxide collected at 4.1 V charged state without Li in the tetrahedral site of lithium-layer in the trigonal phase, model 2 (a) and with Li in the tetrahedral site of lithium-layer in the trigonal phase, model 3 (b). Presence of Li in tetrahedral sites increases the profile matching

The change in cation occupancies in the cycled HE5050 oxides after 26 cycles to different SOCs were similar to the second cycle; however, there are a few noteworthy distinctions to be made: i) a higher percentage of Litet in the structure; ii) the Mn_{tet} concentration increased during charging and decreased at 3.2 V; iii) the concentration of MnLi increased during charging and did not decrease during discharging, suggesting an “irreversible” MnTM → MnLi migration; and v) after discharging to 3.2 V, the phase percentage of LiMn₂O₄ spinel compound was calculated as 15%.

Therefore, the structure of HE5050 oxide after the 26th cycle is not structurally similar to the HE5050 oxide obtained after the second cycle or the pristine HE5050 oxide. The structure of HE5050 oxide after 26th cycle is a combination of trigonal, monoclinic, and spinel phases. From the current study, it is difficult to be certain whether there are many defects in a single phase (‘splayered’ phase as proposed by Grey group) or three separate phases are present in the cycled (25 cycled) HE5050 oxide. However, the ND analysis clearly provides evidence of irreversible Mn migration from the octahedral M layer to the octahedral lithium layer and of the presence of excessive lithium in the tetrahedral site after 26 cycles, which could be the route for forming a spinel phase via the LS rearrangement mechanism (see below).

The finding that the percentage of LiMn₂O₄ is 15% after 26 cycles also indicates that major LS “restructuring” occurred during this period. Other spinel phases (for example: defective spinel where Mn is in tetrahedral site) should not be ruled out, however our ND refinement shows with LiMn₂O₄ model (where lithium in tetrahedral site and Mn in octahedral site), better agreement parameters could be achieved.

Therefore, we speculate that the presence of Li_{tet} and Mn_{tet} in the lithium layer of trigonal phase after second cycle might be the route to form a spinel-like framework over subsequent (26) cycles.



Atomistic Simulations of Layered-Layered Composites

First principles calculations were performed to elucidate the physical and electrochemical properties of LMR-NMC materials. The calculations employed the VASP code, primarily at the GGA+U level of density functional theory. The work has followed three general directions: Property simulations (such as atomic structure), Spectroscopy prediction (NMR and x-ray absorption) to assist the interpretation of experimental measurements, and exploration of a strategy to develop high-capacity fade-free composites. This report on atomistic simulations of layered-layered composite materials is divided into three sections:

- I. Structure of the pristine material.
- II. Instabilities in activated layered-layered composites.
- III. Design of high capacity composites.

I. Atomic Structure of Pristine Material

Composite phase diagram: simulations of solubility of Li₂MnO₃ in LiCoO₂

We addressed first the issue of whether the LMR-NMC materials are composite materials or solid solutions. The simulations indicated that at typical synthesis temperatures, the solubility of Li₂MnO₃ is only of order 1% in LiCoO₂, so that phase separation is expected at thermodynamic equilibrium. The relatively small domain sizes observed in TEM, we believe, results from kinetic barriers to further growth.

a. Initial first charge voltage of a MnCo composite.

A prediction of our simulations is that the onset voltage during the first charge is lower by ~200 meV in a MnCo composite (~3.7 V) than in pure LiCoO₂ (~3.9

V), owing to the attraction of a Li vacancy to the domain-matrix interface. The amount of lowering depends on the structure of the interface. This effect has not yet been investigated experimentally.

b. *Co-vacancy migration energy.*

The kinetics of domain formation depend on diffusion in the metal layer. Our analysis indicated that self-diffusion activation energies in LiCoO_2 are small enough that domain formation can occur at typical LMR-NMC synthesis temperatures (Figure IV - 117).

c. *Bond-pathway simulations of NMR Spectra of a MnCo composite.*

The NMR spectra of pristine MnCo composites have been analyzed, using the bond pathway model, to gain insight into domain structure. In general, the measured spectra give strong evidence that a typical domain has a thin ribbon-like structure. No single domain shape or morphology, however, can account for all of the observed features. By superposing the spectra of striped domains (with a thickness of 4 atomic rows) with two different orientations (relative to layer crystal axes) and with non-unique stacking along the c-axis, however, the bond-pathway simulation predicts most features observed in the experimental spectrum.

d. *Structure of L333: simulation of NMR spectra.*

We investigated the transition metal ordering of $\text{Li}(\text{NiMnCo})_{1/3}\text{O}_2$. DFT calculations were performed for several dozen local atomic arrangements of NMC in the metal layer, using a 48 ion/layer supercell. The lowest energy configuration was an ordered ($\sqrt{3}\times\sqrt{3}$) NMC superstructure. The experimental measurement (by the Grey group), however, shows a broad spectrum, which indicates the presence of some disorder. We found that the experimental measurement could be well reproduced by considering a superposition of the lowest energy configurations.

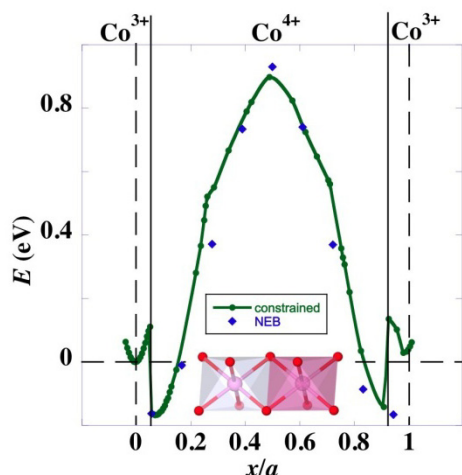


Figure IV - 117: Energy along path of Co ion migration from a site near $x/a=0$ toward a Co vacancy at $x/a=1.0$. Insert shows the octahedral coordination of two nearest neighbor Co

II. Atomic Structure Instabilities during first charge activation

Li_2MnO_3

We performed simulations to gain insight into the first charge of Li_2MnO_3 . Owing to the complexity of simulating the charge process incrementally (e.g., as a function of x , for $\text{Li}_{2-x}\text{MnO}_3$), most of the simulations were performed on the composition $\text{Li}_{0.5}\text{MnO}_3$, with half or all of the Li-layer Li removed. After removing of all of the Li-layer Li, a strong compressive stress exists along the c-axis. Different metastable structures may be obtained, depending on the details of the simulation protocol. In general the lithium deficient stoichiometries $\text{Li}_{2-x}\text{MnO}_3$ create a thermodynamic driving force to transform the initial ($\text{C}2/\text{m}$ or $\text{R}-3\text{m}$) structure, in which the bonding is purely heteropolar (i.e., Mn-O and Li-O) and homopolar (O-O) bonding are present. For example, the energy of $\text{Li}_{0.5}\text{MnO}_3$ can be lowered by removing two oxygen ions from the oxygen layers, and inserting them, essentially as an O_2 molecule, into the delithiated Li layer. The kinetic barriers to this process, however, may be high, and we have not attempted to determine them from simulation. We note that EXAFS experiments, performed by Croy et al. within the ANL VF project, showed relatively few vacancies in charged Li_2MnO_3 , i.e., much fewer than would be the case if an oxygen vacancy were created for every two Li ions extracted ($\text{Li}_2\text{MnO}_3 > \text{Li}_{2-x}\text{MnO}_{3-x/2} + x\text{Li}_2\text{O}$). Therefore, kinetic barriers may exist to the creation of oxygen vacancies, which prevent thermodynamic equilibrium from being established in the experiments. In the composite materials, however, oxygen vacancy creation may occur at domain boundaries, and more vacancies in the oxygen sublattice may be created, as discussed below.

Simulations in support of EELS measurements on e-irradiated Li_2MnO_3 :

Electron irradiation experiments performed in-situ in an aberration corrected electron microscope simulate lithium and oxygen extraction processes observed during electrochemical cycling, while allowing for atomic-resolution, real-time observations of specific particles. This technique also allows for irradiation dose quantification ($\#e^-/\text{area}$). The results demonstrate that typical imaging conditions are not severe enough to induce damage to the pristine oxide, and that the irradiation process triggers Li removal followed by the creation of O vacancies. Simulations were performed to investigate the effect of Li/O vacancies on the EELS O-K edge spectra. Density functional theory calculations were used to calculate the projected density of states (PDOS) of unoccupied O_{2p} states in the presence of Li vacancies (Figure IV - 118).

To avoid any inconsistencies in the determination of reference energy when comparing different PDOS from different vacancy configurations/supercells, we

performed calculations where both Li and O vacancies were present in the same supercell. A line of oxygen vacancies along the (100) direction (4 O) and two lines of Li vacancies (8 Li) along the same direction (similar to the TEM direction of observation), a composition that provides charge compensation was used. This approach allowed us to also avoid the creation of shallow defect levels that result from uncompensated charge defects within the cell.

The DFT results show that near Li vacancies, the O-K pre-peak intensity is increased, and shifts to lower energies, consistent with the experimental observations. The increase in the intensity of the O-K pre-peak, which is attributed to transitions from the O1s core states to the unoccupied O2p states hybridized with Mn3d states, is a reflection of increased hybridization between O2p and Mn3d as Li is removed. Li vacancies will decrease the number of Mn d-electrons, and hence increase the number of empty d-states available for the excited electrons to occupy. This decrease in Mn d-electrons will also decrease the anti-bonding contribution to the Mn-O bond, leading to an increase in the Mn-O covalent binding character. The intensity increase (peak C) of the main peak, in the calculated PDOS as well as the observed experimental EELS spectra which appears as a shoulder around 540 eV, is also a signature of increased O2p-Mn4s hybridization. Contrary to the case of Li vacancies, though as expected, the intensity of the O-K pre-peak near O vacancies is decreased. In this case, when O vacancies are produced, the number of Mn d-electrons is increased, and hence decreasing the number of available empty states. With extended beam exposures, the feature at 540 eV is now vanishing, another indication of increased oxygen vacancy concentration in the sample.

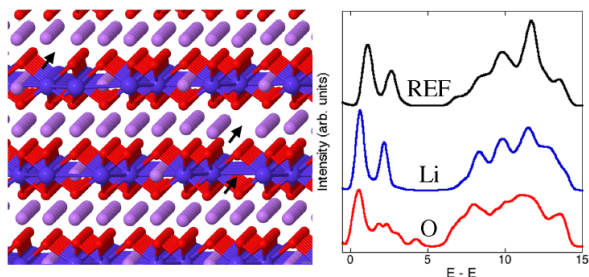


Figure IV - 118: The Li_2MnO_3 supercell used for the DFT calculations (Mn - blue, O - red, Li - purple) with rows of either O (left) or Li (right) vacancies arrowed, and the resulting O K-edge spectra for O atoms either far from the vacancies (black - reference), near the Li vacancies (blue), or near the O vacancies (red). Note that the intensity to the left and to the right of the text labeling each spectrum represents the pre- and the main peak, respectively

Composites:

i. Instability of oxygen sublattice of MnCo, MnNi composites:

Simulations were performed of the atomic structure at the end of the first charge of MnCo and MnNi composites. In the case of MnNi, we treated the composition $\text{Li}_{7/6-x}\text{Ni}_{1/4}\text{Mn}_{7/12}\text{O}_2$, with $x=1$ Li ion extracted in the charged state. (As in the simulations for Li_2MnO_3 described above, we did not investigate partially delithiated states). For this system, MD simulations were performed (at 1000K to accelerate the dynamics), to enable oxygen vacancies to be created by dynamical processes, without the introduction of unnecessary biases. Following the MD simulation, a steepest descents relaxation is performed to allow local atomic structures to equilibrate. The concentration of oxygen vacancies created in by this simulation protocol was found to be close to the limit of one vacancy per two Li ions extracted. This value was also in close agreement to that obtained from analysis of EXAFS experiments for a MnNi composite within the ANL VF program; the behavior is also consistent with x-ray (Dahn group) and neutron-scattering (Meng group) structure refinements.

ii. Migration of Mn in presence of O vacancies: low and high concentrations

Based on previous work by the Ceder group, the migration of Mn ions from the metal layer to the Li layer of composites is expected to have high barriers in the presence of a fully occupied oxygen sublattice. Both simulation and experiment, however, indicate that oxygen vacancies are created during the first charge. Simulation of Mn migration in the presence of oxygen vacancies was therefore performed to investigate their effect. Migration of a Mn ion coordinated to a single oxygen vacancy, in an otherwise perfect Li_2MnO_3 crystal is energetically unfavorable, but in the presence of two oxygen vacancies, migration of Mn to a tetrahedral site (in the Li layer) is either energy neutral, or slightly favorable, particularly in the vicinity of a domain boundary. The assumption of isolated oxygen vacancies in a relatively perfect crystal environment, however, probably is not realistic for a highly charged composite. In the simulations for a MnNi composite described above (MD/steepest descents for $\text{Li}_{1/6}\text{Ni}_{1/4}\text{Mn}_{7/12}\text{O}_2$), we find that one quarter of the Mn ions in the Li_2MnO_3 domains migrate to the delithiated Li layer. In the highly distorted environment that results from the large oxygen vacancy concentration, the migrated Mn ions don't possess either octahedral or tetrahedral symmetry.

iii. Migration of Li

The delithiation of the Li layer in both MnCo ($\text{Li}_{7/6-x}\text{Co}_{1/2}\text{Mn}_{1/3}\text{O}_2$) and MnNi ($\text{Li}_{7/6-x}\text{Ni}_{1/4}\text{Mn}_{7/12}\text{O}_2$) composites was found to create a driving force for Li

migration from the metal layer to the Li layer. This was seen both in static and molecular dynamics simulations (Figure IV - 119). For $x=1$, dynamical calculations for the MnNi composite indicate that all the metal-layer Li migrate to the Li-layer.

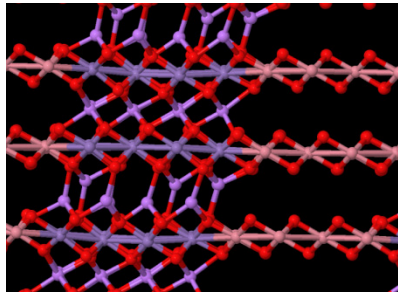


Figure IV - 119: Structure of $\text{Li}_{7/6-x}\text{Co}_{1/2}\text{Mn}_{1/3}\text{O}_2$ composite after delithiation of the Li-layer ($x=1$), AIMD at 1000K, for 0.567ps, followed by the steepest descent relaxation. Migrated Li from the metal-layer is now occupying tetrahedral and octahedral sites in the Li-layer

iv. Discharge simulations of MnNi composites

Starting from the relaxed structures of the MnNi composites after charge ($x=1$) as indicated above, and the creation of few oxygen vacancies (by taking O-O molecules formed out of the simulation cell) we performed a combination of DFT-AIMD-DFT sequence to simulate the discharge by re-introducing groups of 6 Li atoms into the structure at a time. The AIMD were performed at 800K for about 0.4 to 0.5 ps to enable the structure to find a more stable configuration. During discharge some of the Mn ($\text{CN}=4$), as well as Li from Li-Layer moved back into the metal-layer (Figure IV - 120), hence contributing to the reversible process component of the first cycle. The discharge simulations are still underway (70%). The preliminary results show that Mn ions in the octahedral sites in the Li-layer are more stable than the low coordinated Mn.

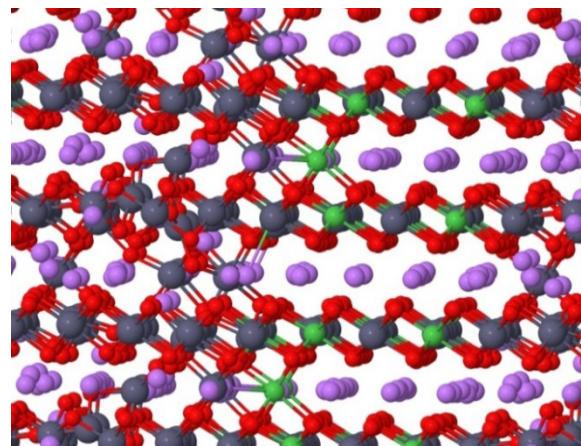


Figure IV - 120: Structure of $\text{Li}_{7/6-x}\text{Ni}_{1/4}\text{Mn}_{7/12}\text{O}_{2-y}$ composite at 70% discharge state ($\text{Li}_{76}\text{Ni}_{24}\text{Mn}_{56}\text{O}_{176}$) ($y=1/6$, $x=3/8$). Some Mn, Ni and O remain in the metal-layer. Mn is shown in dark gray, Ni in green, O in red, and Li in light purple

v. Oxygen molecules and their migration

A key issue for understanding composite behavior during the first charge is the subsequent bonding and migration of the interstitial oxygen ions displaced to form oxygen vacancies. Our simulations for $\text{Li}_{1/6}\text{Ni}_{1/4}\text{Mn}_{7/12}\text{O}_2$ show that the displaced oxygen ions form O-O pairs with bond lengths in the range 1.3 -1.6 Å. It is natural to identify the pairs with the small bond length of 1.3 Å as superoxide anions, and such pairs are relatively isolated from the rest of the system, with no other bond lengths of less than 2 Å. These superoxide molecules are mobile within the channel formed in the (delithiated) lithium layer of the domain, sandwiched between two distorted oxygen layers. As the oxygen-ion pairs move through the channel, they may encounter, at relatively close range, oxygen ions from the sandwich, which trap the pair, or present a barrier to their further migration.

The O-O pairs with pair bond lengths > 1.3 Å are not isolated, but may belong to larger clusters (Figure IV - 121). At least one member of the pair has a short bond length with a lattice oxygen ion, so that such pairs are relatively immobile. Although the O-O pairs (“molecules”) are more mobile than lattice oxygen ions (which are strongly bonded to Mn), they are likely not sufficiently mobile to diffuse to a surface from the bulk within a laboratory time scale.

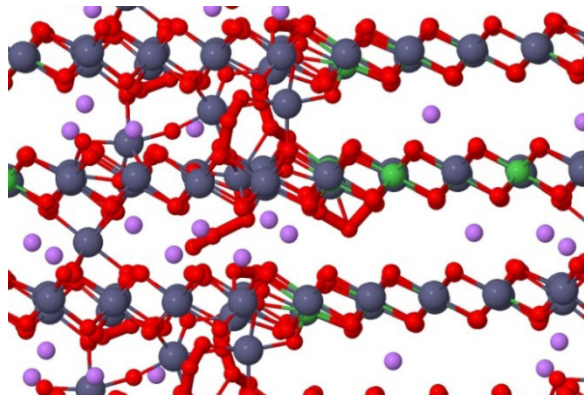


Figure IV - 121: Simulated atomic structure of $\text{Li}^{7/6-x}\text{Ni}_{1/4}\text{Mn}_{7/12}\text{O}_2$ after first charge ($x=1$). The domain “ribbon” is shown on the left side of the figure, and the LiMO_2 ($M=\text{Ni}_{0.5}\text{Mn}_{0.5}$) region is on the right side. Relatively, well-ordered rows of O ions (and NiMn) are seen in the LiMO_2 part of the cell. Oxygen is considerably disordered in the domain, with about 20% of the oxygen in this region (O-O bonds <1.6 Å shown) showing homopolar (O-O) bonding as well as heteropolar (O-M) bonding. Some Mn migrated to the Li layer, in the domain region

X-ray spectroscopy

XAS, particularly EXAFS and pre-edge spectra, are sensitive to local environment, and were applied by the ANL VF team to MnNi (in situ) and MnCo (ex situ) composites during the first charge. Most attention was given to the Mn spectra, which reflect the loss in coordination associated with oxygen vacancies in the nearest-neighbor shell. Simulations were performed to help interpret the results.

i. EXAFS

Analysis of EXAFS measurements has provided values of the coordination number deficit $\Delta CN(\text{Mn}) = 6 - CN(\text{Mn})$ as a function of state of charge during first cycle activation. Analysis for the composition $0.3\text{Li}_2\text{MnO}_3 \bullet 0.7\text{LiMn}_{0.5}\text{Ni}_{0.5}\text{O}_2$ yield $\Delta CN(\text{Mn}) = 0.6$ at the top of the first charge. A simple model relates the oxygen vacancy concentration in domains: $\Delta CN(\text{Mn}) = 6 c(V_O)$, where $c(V_O)$ is the oxygen vacancy concentration in domains. For the above composition, under the assumption that one oxygen vacancy is created per two Li ions extracted, we predict $\Delta CN(\text{Mn}) = 0.69$. The close agreement is gratifying, however, we note that two approximations were not corrected for: (i) the Mn ions located at domain boundaries may have different $\Delta CN(\text{Mn})$ from the interior of the domain, and (ii) the displaced oxygen ions that create the 6c lattice vacancies may remain in close proximity, and therefore coordinated to Mn ions, which would lower $\Delta CN(\text{Mn})$. Nevertheless, the EXAFS results appear to confirm the presence of a large concentration of oxygen vacancies at the top of the first charge.

ii. Pre-edge spectra

The pre Mn K-edge spectrum in principle provides an independent measure of local Mn coordination. The pre-edge intensity is found experimentally to increase during the first charge activation, which is attributed to enhanced hybridization with O2p orbitals. DFT simulations of electronic densities of states, not presented in detail here, corroborate this behavior. At present, however, we lack a procedure to derive specific structural information by quantitative comparison of simulated and experimental pre-edge spectra.

iii. Design of high (pre-activation) capacity composite material

Composite cathode materials such as HE5050 with composition $x\text{Li}_2\text{MnO}_3 \bullet (1-x)\text{LiMO}_2$ yield high initial capacity when charged to voltages above 4.5 IV. The voltage degradation with cycling, however, has delayed their commercial utilization, and provided the impetus for the ANL Voltage Fade program. One strategy to improve upon the standard materials is to replace (partially or fully) the Mn in the Li_2MnO_3 component of the composite with a late transition element that possesses a 4+/5+ (and perhaps 5+/6+) redox, to increase the pre-activation capacity below the onset of oxygen oxidation at about 4.5 IV. Ideally, the replacement element would (a) form a composite $x\text{Li}_2(M'_y\text{Mn}_{1-y})\text{O}_3 \bullet (1-x)\text{LiMO}_2$ in which the majority of M' would reside in the $\text{Li}_2M'_y\text{Mn}_{1-y}\text{O}_3$ component (“domains”) in the pristine material ($M = \text{Mn}_{0.5}\text{Ni}_{0.5}$ is a convenient composition for development purposes); (b) be stable with respect to M' migration (from its initial octahedral site) to Li-layer tetrahedral (or octahedral) sites in both 4+ and higher oxidation states during cycling; and (c) have 4+/5+ redox energies in a suitable range (say, 3.5-4.0 V).

The obvious candidates for M' are the late transition elements. The first transition series elements (e.g., V, Cr and Fe), however, don’t have favorable chemistries in this context (at least for full replacement), and attention has therefore focused on $M' = \text{Ru}$ or Mo , both of which adopt structures similar to Li_2MnO_3 at the composition $\text{Li}_2M'\text{O}_3$. Efforts by the ANL VF Team to synthesize the composite with $M' = \text{Ru}$ and $M = \text{Mn}_{0.5}\text{Ni}_{0.5}$ (E. Lee and C. Johnson) are presently in progress.

If synthesis (of the substituted composites) proves feasible, simulations are expected to be helpful to characterize properties of the $x\text{Li}_2(M'_y\text{Mn}_{1-y})\text{O}_3 \bullet (1-x)\text{LiMO}_2$ composite, and assist in material optimization. As a preliminary step in this direction, calculations were performed of the relative energy of replacing Mn with in Li_2MnO_3 and $\text{Li}(\text{Mn}_{0.5}\text{Ni}_{0.5})\text{O}_2$. For $M' = \text{V}, \text{Ti}, \text{Cr}, \text{Fe}, \text{Ru}$ and Sn , simulation indicates that substitution in the former is lower in energy than in the latter by 0.02-0.04 eV per substitution. The preference of M' for the Li_2MnO_3 phase is therefore small at synthesis

temperatures. This result suggests that if synthesis of a (hypothetical) composite $x\text{Li}_2\text{MnO}_3 \bullet (1-x)\text{Li Mn}_{0.5}\text{Ni}_{0.5}\text{O}_2$ with a fraction of the Mn replaced were feasible, M' would be present in both phases, and the resultant composition would be $x\text{Li}_2 M'_y \text{Mn}_{1-y} \text{O}_3 \bullet (1-x)\text{Li} M'_{0.5(1-z)} \text{Mn}_{0.5(1-z)} \text{Ni}_{0.5}\text{O}_2$. Further efforts on the simulation of substituted composites (e.g., properties (b) and (c) mentioned above) have been postponed until a determination is made regarding the feasibility of synthesis.

Conclusions and Future Directions

A model has been introduced to explain, in part, voltage fade and hysteresis based on the data presented above. Namely:

- 1) The inherent, composite nature of LMR-NMC's is dominated by charge ordering. Specifically, the strong tendency for Li^+ and Mn^{4+} to order (e.g., LiMn_6) results in two distinct, average, local environments, one rich in Li and Mn (e.g., Li_2MnO_3) and the other in TM's (LiMO_2).
- 2) These distinct environments have direct and observable effects on the electrochemical performance of LMR-NMC's that can be tracked during

electrochemical cycling. The TM-rich, LiMO_2 behaves largely as a “standard”, layered electrode; for example, structurally and electrochemically reversible in nature. The Li- and Mn-rich, Li_2MnO_3 plays a key role in voltage fade and hysteresis, whereby, accessing the TM layer Li from this component (activation) triggers the onset of both phenomena. In addition, the magnitude of both voltage fade and hysteresis are directly correlated with the magnitude of Li and Mn ordering in as-prepared electrodes.

3) The energetics between charge and discharge are different, even at equivalent Li contents (SOC's), due to structural differences within the bulk of electrode particles. Therefore, the hysteresis observed in LMR-NMC's is a stable, structural hysteresis. This means that Li does not have access to the same sites between charge and discharge at equivalent SOC's.

4) Voltage fade and hysteresis are correlated. Accessing Li above ~4.0 V causes local structural changes which prohibit the re-accommodation of this Li until ~3.0 V on discharge (hysteresis). Moving Li in and out of the structure (cycling) over this voltage window (e.g., 4.7–3.2 V) accelerates voltage fade more than any other electrochemical exposure studied.

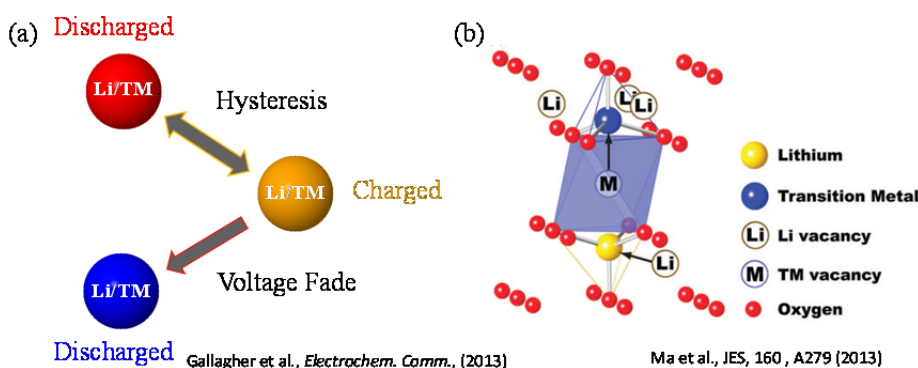


Figure IV - 122: (a) Simplified schematic of hysteresis/voltage fade mechanism as described in the text. (b) octahedral and tetrahedral sites associated with dumbbell configurations in layered Li-TM-oxides

Figure IV - 122(a) shows a simple model describing the hysteresis and mechanism and how it contributes to voltage fade. Starting with an activated electrode in the discharged state, Li and/or TM's (red) can be induced to migrate once a sufficient SOC is reached on charge. Specifically, once charged beyond ~4.0 V the Li vacancy concentration is high enough to promote Li/TM migration from octahedral sites of the TM layers to tetrahedral sites of the Li-layers. Calculations show that when this happens, additional Li ions will migrate to fill the adjacent tetrahedral sites opposite the TM-layer vacancy. For example, $\text{Li}_{\text{tet}}-\square-\text{Li}_{\text{tet}}/\text{TM}_{\text{tet}}$ “dumbbells” are formed where Li_{tet} and TM_{tet} are Li and TM's that occupy tetrahedral sites on either side of a TM-layer, octahedral vacancy (\square). The

dumbbell configuration is shown schematically in Figure IV - 122(b). Because the tetrahedral sites of the Li layer share faces with three surrounding octahedral Li sites (now vacant due to charging), it is energetically unfavorable to refill these octahedral sites on discharge once the tetrahedral sites are occupied. However, once sufficient Li insertion has occurred on discharge a critical content (Li_c) is reached at which point three possibilities exist. 1) The tetrahedral cations are forced to migrate back to their original sites. This process represents a reversible migration at the expense of an energy penalty, paid in the form of a hysteresis when cycling over large voltage windows (e.g., 4.7–3.2 V). 2) The cations are forced further along their migration path and come to occupy new sites (e.g., octahedral sites of

the Li layer). This changes the local structure and lowers the associated Li site energies with respect to further extraction and insertion, contributing to the observed voltage fade. 3) Cations can become trapped in the

tetrahedral sites of the Li layers. This process would be expected to contribute to both capacity loss and impedance rise with extended cycling. The effect on the overall lattice structure is shown in Figure IV - 123.

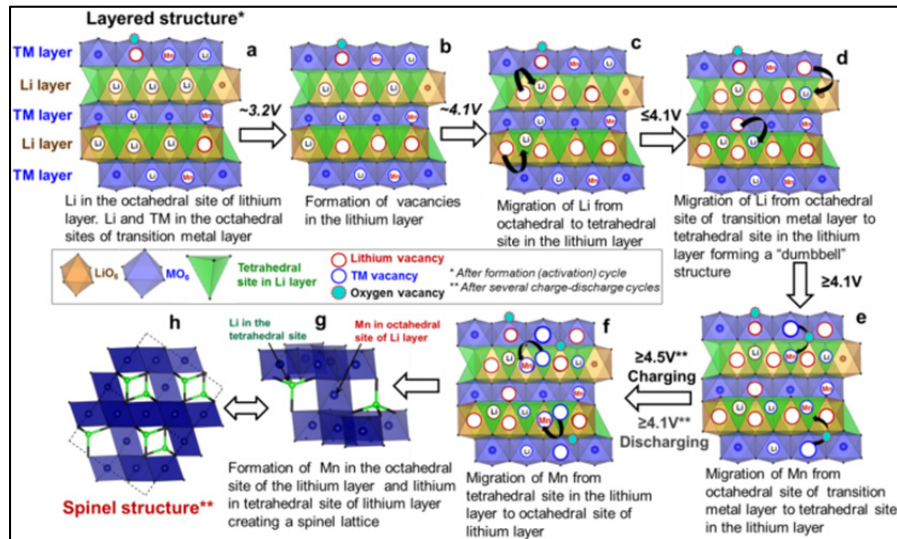


Figure IV - 123: Proposed LS transformation mechanism in HE5050 LMR composite oxide via formation of tetrahedral lithium in the lithium layer and migration of Mn from octahedral TM layer to octahedral site of lithium layer

The above processes occur on each charge and discharge cycle where the hysteresis mechanism is reversible for only part of the migrated cations. Cations that migrate to occupy new sites contribute to voltage fade. The model, then, predicts a slow decay of the hysteresis at the expense of a growing “voltage fade configuration”; that is, the growth of new, local orderings due to the migration of cations from cycle to cycle. Figure IV - 124 shows long-term cycling between 4.7-2.0 V for $x\text{Li}_2\text{MnO}_3 \bullet (1-x)\text{LiMn}_{0.5}\text{Ni}_{0.5}\text{O}_2/\text{Li}$ cells with $x=0.1, 0.3$, and 0.5 . As described in Figure IV - 124, the voltage fade capacity is a direct consequence of the integration and utilization of the Li_2MnO_3 component (Li and Mn ordering) and can be tracked in the low-voltage (≤ 3.6 V) region during charge, whereas the hysteretic capacity can be tracked in the charge region above ~ 4.0 V. These regions are clearly defined in the high quality $x\text{Li}_2\text{MnO}_3 \bullet (1-x)\text{LiMn}_{0.5}\text{Ni}_{0.5}\text{O}_2$ samples shown in Figure IV - 124 when cycled at low rates (5 mA/g). A careful accounting of capacities over the 30 cycles on test confirmed that the decrease in capacity in the high-voltage, hysteresis component was accompanied by corresponding increases in capacity in the low-voltage, voltage fade region. Thus, the electrochemical tests of Figure IV - 124 confirm one prediction of the proposed model.

It should be emphasized that voltage fade and hysteresis are driven by defects in the structure (e.g., dumbbells), the concentrations of which are dependent on vacancy concentrations (e.g., Li, O). As such, the more Li that is accessed on charge the more prevalent the effects become. Therefore, in studying the effects

and mitigation of voltage fade and hysteresis, comparisons should be made among materials that 1) have similar compositions, as it has been shown that Li and Mn ordering, dictated by composition, plays a key role in both phenomena. And 2) similar capacities (Li vacancies) must be obtained by all samples compared so as not to mask the underlying mechanisms. A final point to note is that the concentration of defects responsible for the hysteresis mechanism is very small.

For example, it can be estimated that roughly ~5% or less of the TM's may be involved from cycle to cycle in defect formation and migration. And although the XAS data presented above clearly reveal, from the TM point of view, the structural differences between charge and discharge as a consequence of these defects, a critical step in verifying the proposed mechanisms and building a more complete picture is to probe the local structure from the Li site point of view.

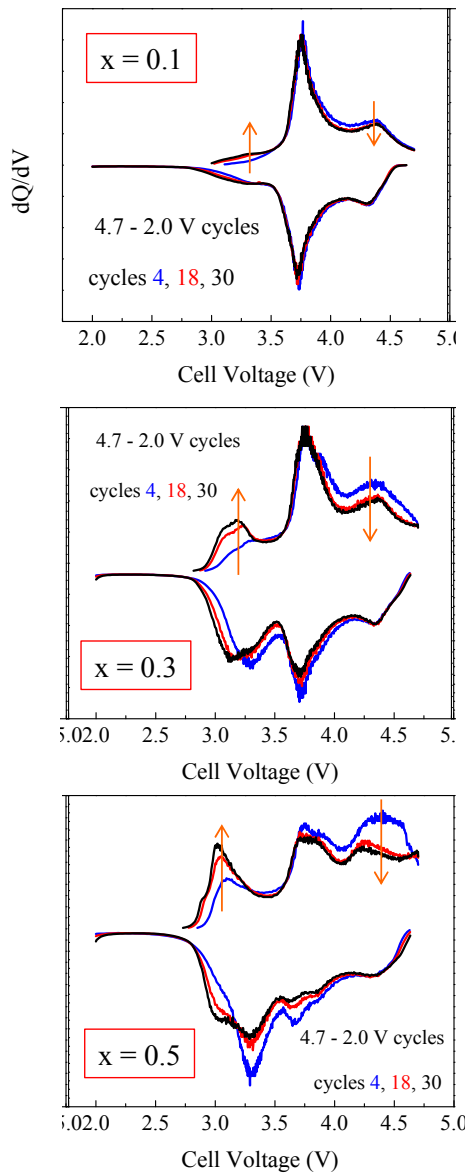


Figure IV - 124: Cycling between 4.7-2.0 V for $x\text{Li}_2\text{MnO}_3 \bullet (1-x)\text{LiMn}_{0.5}\text{Ni}_{0.5}\text{O}_2/\text{Li}$ cells with $x=0.1, 0.3$, and 0.5 . Arrows indicate decreasing capacities associated with hysteresis and increasing capacities associated with voltage fade

FY 2014 Publications/Presentations

1. Croy, J. R.; Gallagher, K. G.; Balasubramanian, M.; Long, B. R.; Thackeray, M. M. Quantifying Hysteresis and Voltage Fade in $\text{Li}_2\text{MnO}_3 \bullet (1-x)\text{LiMn}_{0.5}\text{Ni}_{0.5}\text{O}_2$ Electrodes as a Function of Li_2MnO_3 Content. *J. Electrochem. Soc.* 161, A318 (2014).
2. Long, B. R.; Croy, J. R.; Dogan, F.; Suchomel, M. R.; Key, B.; Wen, J. G.; Miller, D. J.; Thackeray, M. M.; Balasubramanian, M. Effect of Cooling Rates on Phase Separation in 0. $\text{Li}_2\text{MnO}_3 \bullet 0.5\text{LiCoO}_2$ Electrode Materials for Li-Ion Batteries. *Chem. Mat.* 26, 3565 (2014).
3. Croy, J. R.; Gallagher, K. G.; Balasubramanian, M.; Chen, Z. H.; Ren, Y.; Kim, D.; Kang, S. H.; Dees, D. W.; Thackeray, M. M. Examining Hysteresis in Composite $\text{Li}_2\text{MnO}_3 \bullet (1-x)\text{LiMO}_2$ Cathode Structures. *J. Phys. Chem. C* 117, 6525 (2013).
4. Gallagher, K. G.; Croy, J. R.; Balasubramanian, M.; Bettge, M.; Abraham, D. P.; Burrell, A. K.; Thackeray, M. M. Correlating hysteresis and voltage fade in lithium- and manganese-rich layered transition-metal oxide electrodes. *Electrochim. Commun.* 33, 96 (2013).
5. Dogan, Fulya; Croy, Jason; Balasubramanian, Mahalingam; Slater, Michael; Iddir, Hakim; Johnson, Christopher; Vaughey, John; Key, Baris, Solid State NMR Study of Li_2MnO_3 and Li-rich NMC Cathodes: Proton Insertion, Local Structure, and Voltage Fade. *J. Electrochem. Soc.*, accepted (2014).
6. H. Iddir and R. Benedek, First-principles analysis of phase stability in layered-layered composite cathodes for lithium-ion batteries. *Chem. Mater.*, 26(7), (2014)
7. Croy, J.R.; Park, J.S.; Dogan, F.; Johnson, C.S.; Key, B.; Balasubramanian, M. First-Cycle Evolution of Local Structure in Electrochemically Activated Li_2MnO_3 . *M. Chem. Mat.*, submitted (2014).
8. P.J. Phillips, H. Iddir, D.P. Abraham, R.F. Klie, Direct observation of the structural and electronic changes of Li_2MnO_3 During electron irradiation, Accepted to *Appl. Phys. Lett.*
9. Fulya Dogan, Brandon R. Long, Jason R. Croy, Kevin G. Gallagher, Hakim Iddir, John T. Russell, Mahalingam Balasubramanian, and Baris Key, Defect Driven Structural and Electrochemical Hysteresis in Lithium Rich Composite Cathodes, submitted (2014).

10. Hakim Iddir, John Russell, Baris Key, Fulya Dogan, Brandon Long, Javier Bareño and Roy Benedek, Bond pathway analysis of NMR spectra for $\text{Li}_{1.2}\text{Mn}_{0.4}\text{Co}_{0.4}\text{O}_2$: pristine material and first charge, in preparation.
11. Jason R. Croy, Hakim Iddir, Kevin Gallagher, Roy Benedek, and Mahalingam Balasubramanian, Instabilities of layered-layered lithium-ion-battery materials: oxygen vacancy formation and Mn migration, in preparation.
12. D. Mohanty, J. Li, A. Huq, D. P. Abraham, A. Sefat, E. A Payzant, D. L. Wood, C. Daniel, "Unraveling the Voltage Fade Mechanism in High-Energy-Density Lithium-ion Batteries: Origin of the Tetrahedral Cations for Spinel Conversion" *Chemistry of Materials*, ASAP DOI: 10.1021/cm5031415 (2014).
13. D. Mohanty, A. Huq, E. Andrew Payzant, A. Safa-Sefat, J. Li, D. P Abraham, D.L. Wood, and C. Daniel, "Neutron Diffraction and Magnetic susceptibility studies on a High-voltage $\text{Li}_{1.2}\text{Mn}_{0.55}\text{Ni}_{0.15}\text{Co}_{0.10}\text{O}_2$ Lithium-ion Battery Cathode; In-sight into the Crystal Structure" *Chemistry of Materials*, 25, 4064 (2013)
14. D. Mohanty, A. Sefat, J. Li, R.A. Meisner, R. A. Justine, E. A. Payzant, D.P. Abraham, D.L. Wood, and C. Daniel, "Correlating Cation Ordering and Voltage Fade in a Lithium- and Manganese-Rich Layered-Layered Lithium-ion Battery Cathode Oxide; a Joint Magnetic Susceptibility and TEM study," *Physical Chemistry Chemical Physics*, 15, 19496, (2013).
15. D. Mohanty, S. Kalnaus, R.A. Meisner, K.J. Rhodes, E.A. Payzant, D.L. Wood, and C. Daniel, "Structural Transformation of a Lithium-Rich $\text{Li}_{1.2}\text{Co}_{0.1}\text{Mn}_{0.55}\text{Ni}_{0.15}\text{O}_2$ Cathode During High Voltage Cycling Resolved by In-Situ X-Ray Diffraction," *Journal of Power Sources*, 229, 239–248 (2013).
16. D. Mohanty, S. Kalnaus, R.A. Meisner, A. Safa-Sefat, J. Li, K.J. Rhodes, E.A. Payzant, D.L. Wood, and C. Daniel "Structural Transformation in a $\text{Li}_{1.2}\text{Co}_{0.1}\text{Mn}_{0.55}\text{Ni}_{0.15}\text{O}_2$ Lithium-Ion Battery Cathode During High-Voltage Hold," *RSC Advances*, 3, 7479–7485 (2013).
17. D. Mohanty, A. Safa-Sefat, S. Kalnaus, J. Li, R.A. Meisner, E.A. Payzant, D.P. Abraham, D.L. Wood, and C. Daniel, "Investigating Phase Transformation in $\text{Li}_{1.2}\text{Co}_{0.1}\text{Mn}_{0.55}\text{Ni}_{0.15}\text{O}_2$ Lithium-Ion Battery Cathode During High-Voltage Hold (4.5 V) via Magnetic, X-ray Diffraction and Electron Microscopy Studies," *Journal of Materials Chemistry A*, 1, 6249–6261 (2013).

References

1. McCalla E., Lowartz, C. M., Brown, C. R., Dahn, J. R. *Chem. Mat.* 25, 912 (2013).
2. Croy J.R., Park J.S., Dogan F., Johnson C.S., Key B., Balasubramanian M. *Chem. Mat.* submitted (2014).
3. Croy J. R., Gallagher, K. G., Balasubramanian, M., Chen, Z. H., Ren, Y., Kim, D., Kang, S. H., Dees, D. W., Thackeray, M. M. *J. Phys. Chem. C* 117, 6525 (2013).
4. Younkee, P.; Grey, C. P.; Johnson, C. S.; Jeom-Soo, K.; Thackeray, M. M. *Chem. Mat.* 14, 5109 (2002).
5. M. Jiang, B. Key, Y. S. Meng and C. P. Grey, *Chem. Mat.* 21, 2733 (2009).
6. C. P. Grey and N. Dupre, *Chem. ReIV*. (Washington, DC, U. S.), 104, 4493 (2004).
7. W. S. Yoon, S. Iannopollo, C. P. Grey, D. Carlier, J. Gorman, J. Reed and G. Ceder, *Electrochem. Solid State Lett.* 7, A167 (2004).
8. Zeng, D., Cabana, J., Breger, J., Yoon, W.-S. & Grey, C. P. *Chem. Mat.* 19, 6277 (2007).
9. Breger J., Meng, Y. S., Hinuma, Y., Kumar, S., Kang, K., Shao-Horn, Y., Ceder, G. Grey, C. P. *Chem. Mat.* 18, 4768 (2006).
10. Grey, C. P., Yoon, W. S., Reed, J. & Ceder, G. *Electrochem. Solid State Lett.* 7, A290 (2004).
11. Van der Ven A., and Ceder, G. *Electrochem. Comm.* 6, 1045 (2004).
12. Breger J., Jiang, M., Dupre, N., Meng, Y. S., Shao-Horn, Y., Ceder, G. Grey, C. P. *J. Solid State Chem.* 178, 2575 (2005).
13. Yoon, W.-S., Kim, N., Yang, X.-Q., McBreen, J. & Grey, C. P. *J. Power Sources* 119–121, 649 (2003).
14. Chen, H. & Grey, C. P. *AdIV. Mater.* (Weinheim, Ger.) 20, 2206 (2008).

IV.C.3 Mitigation Approaches: Synthetic and Coating Strategies (ANL)

Voltage Fade Team

Argonne National Laboratory
9700 South Cass Avenue
Argonne, IL 60439
Phone: (630) 252-4516; Fax: (630) 252-4176
E-mail: Burrell@anl.gov

Start Date: October 2013

Projected End Date: September 2014

Objectives

Identify the fundamental causes of voltage fade and determine unknown electrochemical processes associated with the voltage fade phenomenon.

Technical Barriers

This project addresses the following technical barriers as described in the USABC goals:

- (A) Performance at ambient temperatures.
- (B) Cycle life.

Technical Targets

- PHEV specific energy targets (pack): 3.4 kWh (min) to 11.6 (max).
- EV specific energy targets (pack): 80 (min) to 200 (max) Wh/kg.

Accomplishments

- Determined the coating do not mitigate voltage fade.
- Determined that synthesis method does not mitigate voltage fade.
- Determined that morphology does not mitigate.
- Determined that composition does have a limited effect on voltage fade.
- Determined simple doping of the lattice does not mitigate voltage fade.
- Determined that simple structural modification does not mitigate voltage fade.
- Determined that lower lithium levels result in less voltage fade as the amount of high voltage lithium cycling is reduced. Achieved by either reducing the lithium excess and/or by limiting the cyclizing window to lower voltages.



Introduction

New cathode materials are required for high-energy density Li-ion batteries in order to enable greater mileage range for electric vehicles in transportation applications within the U.S. and worldwide. The Li- and Mn-rich chemistries or LMR-NMC class of cathodes ('layered-layered' composites) appear to be the best option to date as reversible specific capacities are well above 250 mAhg⁻¹. With this value and an operating voltage above 3 V results in energies that approach 950 Whkg⁻¹. The capacity is stable over 1000s of cycles in full cells. Unfortunately materials based on LMR-NMC compositions suffer from voltage suppression during cycling leading to energy density loss over time. This behavior limits their widespread use in next generation Li-ion cells. Further, low rate capability and low tap density limit practical performance and these issues are being addressed in the battery community as well.

Approach

New cathode materials are required for high-energy density Li-ion batteries in order to enable greater mileage range for electric vehicles in transportation applications within the U.S. and worldwide. The Li- and Mn-rich chemistries or LMR-NMC class of cathodes ('layered-layered' composites) appear to be the best option to date as reversible specific capacities are well above 250 mAhg⁻¹. With this value and an operating voltage above 3 V results in energies that approach 950 Whkg⁻¹. The capacity is stable over 1000s of cycles in full cells. Unfortunately materials based on LMR-NMC compositions suffer from voltage suppression during cycling leading to energy density loss over time. This behavior limits their widespread use in next generation Li-ion cells. Further, low rate capability and low tap density limit practical performance and these issues are being addressed in the battery community as well.

The voltage suppression, also termed voltage fade (hereafter in this report), appears to be correlated to the activation of the material on the first charge whereby a voltage plateau occurs, generally, for LMR-NMC type cathodes (Figure IV - 125, label B feature). Therefore we surmise that the structural transformation of the material during the first charge cycle leads to an altered state with scrambling of the transition metals and oxygen movement within the lattice.

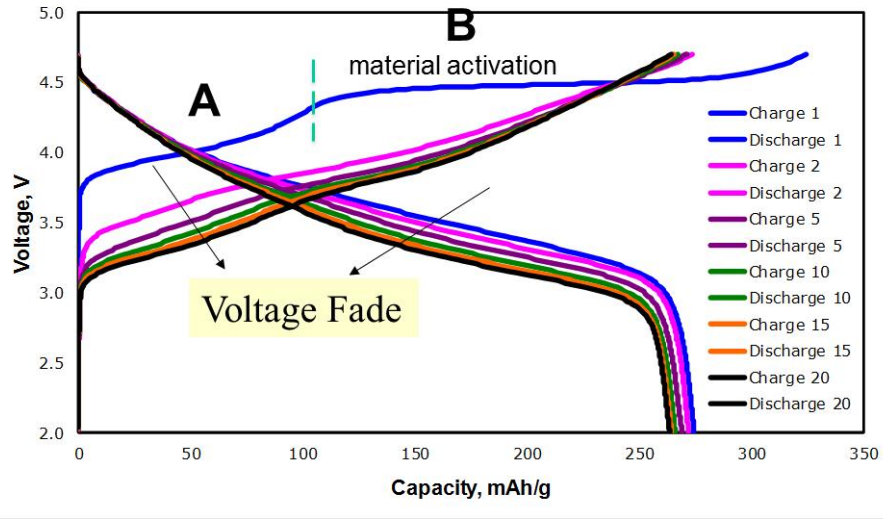


Figure IV - 125: Voltage profiles of $\text{Li}/0.5\text{Li}_2\text{MnO}_3 \cdot 0.5\text{Li}[\text{Ni}_{0.375}\text{Mn}_{0.375}\text{Co}_{0.25}]\text{O}_2$ during the first 20 cycles (as labeled). Feature B is the activation plateau

This transformation of the lattice may be related to a movement of transition metals from the transition metal layer of the layered structure to the Li layer during the excessive removal of nearly all Li (many vacancies) from the material. As such, atom movement in this manner would yield a spinel-like atomic arrangement with O₃ stacking. Since the as-prepared layered LMR-NMC oxide is also O₃ stacked, it is logical that the activation barrier for movement of transition metals into

the Li layer is low. Note that for O₃ designation, there is an ABC repeat unit in the O sub-lattice and the sites are all octahedrally coordinated. Figure IV - 126 depicts the layer stacking of various layered oxide and spinel oxide polymorphs with O₃ stacking, and the green arrow depicts movement of Mn (Ni, Co; as well as Mn in Li_2MnO_3) into the Li layer without perturbation of the lattice.

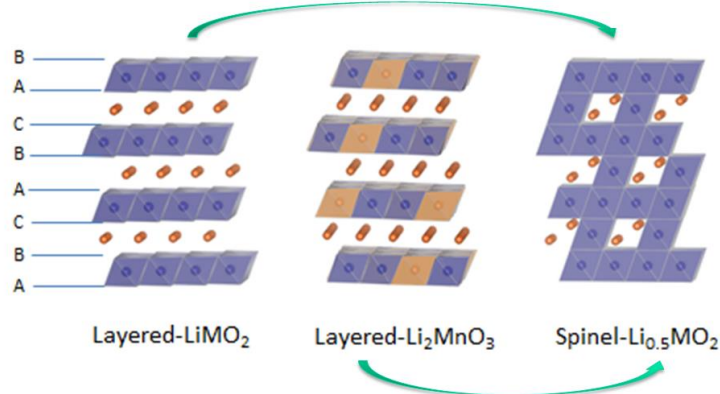


Figure IV - 126: O₃ stacking arrangements for oxygen closest-packed oxide structures

In this work a number of synthesis strategies were employed in order to attempt to mitigate the voltage fade phenomenon. Towards this objective the following approaches were implemented.

- Coatings.
- Composition.
- Sol-gel and co-precipitation routes.
- Cation distribution (honeycomb strategy).
- Cation substitution.

- Structural alterations.
- pO₂ atmosphere (firing conditions).

Results

a. Coatings and Surface Modifications

Three national laboratories, Argonne National Laboratory, the National Renewable Energy Laboratory and Oak Ridge National Laboratory, investigated the effects of using cathode coatings and electrolyte

additives on the voltage fade phenomenon. In the literature, coatings, surface modifications, and additives of many descriptions have been used to stabilize the capacity of cathode materials and enhance cycling ability, enhance the rate capacity of cathode materials, lessen their thermal reactivity, lessen their reactivity towards the organic electrolytes, and promote secondary electrolyte interface layer formation on the cathode. The effects of the coatings Al_2O_3 , LiAlO_x , ZrO_2 , TiO_2 , AlPO_4 , and lithium phosphorus oxynitride (LiPON) and of the electrolyte additives 3-hexylthiophene and lithium difluoro-oxalatoborate (LiFOB) on voltage fade were investigated. It should be noted that both electrolyte additives are very effective in forming a protective layer on the surface of the positive electrode at high potentials.

Effect of coating conditions on capacity retention (blank; no coating applied). Although it has been conclusively confirmed that coatings on cathode particles or laminates do not lessen the extent of voltage

fade, coating have been shown to improve capacity retention. The question remains – is it the chemistry of the coating, or the treatment conditions of applying the coating, that positively impact capacity retention? To address this we've compared the electrochemical cycling of “mock coated” laminates in coin cells to appropriately coated laminates. To perform a mock coating, atomic layer deposition conditions that yielded the TiO_2 , ZrO_2 , and LiAlO_x coatings reported previously, namely increased temperature under nitrogen for a specific length of time, were applied to laminates which were then cycled using the voltage fade protocol. No chemical or physical deposition of any material was introduced, just the temperature and gas requirements of the coatings. Basic comparison between the uncoated laminates, mock-coated laminates, and ALD-coated laminates (Figure IV - 127) suggests that the chemistry of the coating is indeed responsible for the observed increased capacity in coated laminates.

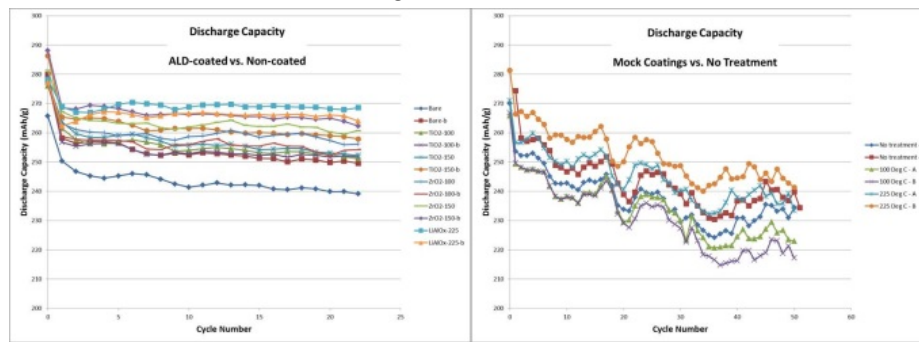


Figure IV - 127: (left) Capacity retention vs. cycle count for coated and uncoated laminates. (right) Capacity retention vs. cycle number for uncoated laminates and mock-coated laminates

The graph at left in Figure IV - 127 shows the capacity retention vs. cycle number for uncoated laminates and ALD-coated laminates. The coatings, which did not impact voltage fade, are shown to enhance capacity retention over 20 cycles. All of the samples shown were tested within a short timeframe (days).

At the right in Figure IV - 127 is a plot of capacity retention vs. cycle number for uncoated laminates and mock-coated laminates. The 6 coin cells represented in the graph at right were initiated at the same time. The close tracking of the capacity curves with respect to each other are due to temperature variations in the laboratory and highlight the superiorly uniform nature of the laminates, which were received from the ANL CAMP Facility. Just like in the coated case, the laminates treated at 225°C, which is the temperature used for LiAlO_x ALD-coatings, shows slightly higher capacity retention than the other cells, however the non-treated laminates exhibit the median performance on the graph. Within the error of measurement, the mock coatings do not appear to improve capacity retention. Indeed it is the chemistry of the coating that has the

capacity retention benefit. If more data shows that the 225°C N_2 treatment is truly beneficial for capacity retention, we expect the effect to be related to the binder in the laminate.

Effect of coatings and additives: A list of cathode compositions, using HE5050 as the common cathode material, is given in Table IV - 13. Each was assembled into coin cells with lithium metal as the counter electrode. The cells were cycled at ambient temperature ($\sim 23^\circ\text{C}$) using the voltage fade protocol.

As expected, the cell discharge capacity faded with cycling for cells containing the electrolyte additives and the coated or uncoated cathode materials, as shown in Figure IV - 128. The baseline showed the greatest amount of capacity fade, which was due to impedance rise and loss of active sites in the positive electrode when cycled to 4.7 IV. Figure IV - 128 shows that the capacity fade rate of the coated materials is sensitive to the nature of the coating; some coated materials display greater capacity loss rates than others. It was interesting to note that the loss of capacity in cells containing an electrolyte additive were different, with the cell

containing LiDFOB displaying about 25% of the capacity loss of the cell containing 3-hexylthiophene. Of more importance, the data in Figure IV - 128 clearly show that the capacity of cells containing coated cathode materials or electrolyte additives fades slower than that of the cell containing either no additive or uncoated materials. This trend is consistent with reports in the literature.

In these experiments, the cells containing either coated cathodes or an additive behaved similarly as those that were uncoated or contained no additive. Examples of the aging behavior of cells containing an uncoated cathode and coated cathode are shown in Figure IV - 129, and Figure IV - 130 respectively. The first charge cycle is believed to activate the Li_2MnO_3 portion of the composite cathode material, a process needed to achieve high capacity density. With continued cycling, the cathode material loses voltage, as indicated by the changes in the voltage vs. normalized capacity curves (Figure IV - 128, Figure IV - 129, and Figure IV - 130); this loss of voltage behavior is consistent with that seen by others. The iR-corrected, average voltage value for a given cycle was calculated using the data shown in Figure IV - 128. It should be noted that the shape of the average voltage curve was not sensitive to the presence of a coating or its nature, or to the presence of an electrolyte additive.

Table IV - 13: Cathode compositions used in this work

Designation	Cathode
Baseline	86 wt% HE5050 4 wt% SFG-6 graphite 2 wt% SuperP carbon black 8 wt% PVDF
TiO_2 (100°C) TiO_2 (150°C)	92 wt% active material
ZrO_2 (100°C) ZrO_2 (150°C)	4 wt% C45 conductive additive
LiAlO_x	4 wt% Solyve 5130 binder
AlPO_4	86 wt% active material 4 wt% SFG-6 graphite 2 wt% SuperP carbon black 8 wt% PVDF
5 ALD cycles Al_2O_3 (120°C) 100 ALD cycles Al_2O_3 (120°C)	86 wt% active material 4 wt% SFG-6 graphite 2 wt% SuperP carbon black 8 wt% PVDF
LiPON (1 h) LiPON (2 h) LiPON (3 h)	85 wt% active material 7.5 wt% SuperP carbon black 7.5 wt% PVDF
LiDFOB (2.0 wt%)	92 wt% active material 4 wt% C45 conductive additive 4 wt% Solyve 5130 binder
3-hexylthiophene (0.1 wt%)	92 wt% active material 4 wt% C45 conductive additive 4 wt% Solyve 5130 binder

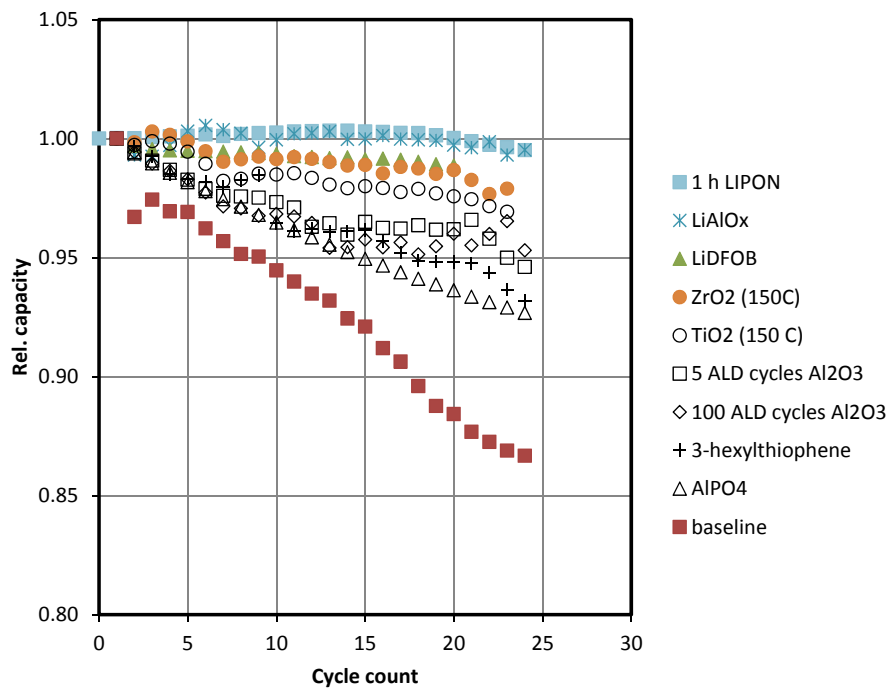


Figure IV - 128: Rel. cell capacity vs. cycle count, showing capacity decline with cycle count. The capacity of coated materials tended to decline slower than that of uncoated materials. The relative cell capacity vs. cycle count for the 2- and 3-h LiPON coatings behaved similarly to that seen for the 1-h coating. These data were omitted for the sake of clarity

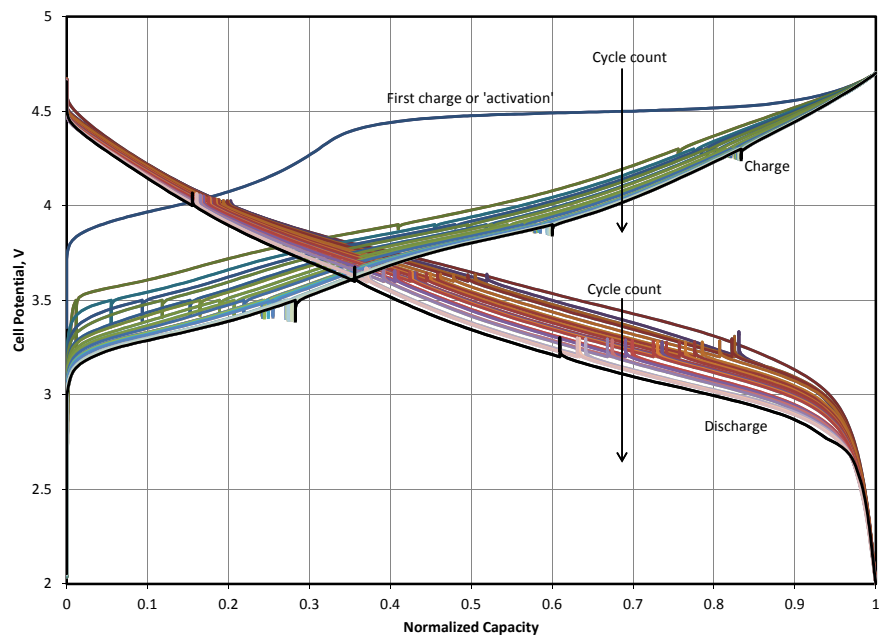


Figure IV - 129: Cell potential vs. normalized capacity, representing the typical charge and discharge voltage response of a cell containing an uncoated cathode in these experiments. Selected curves were removed for the sake of clarity. During the first charge, the LMR NMC material was activated. With continued cycling, the voltage response for both the charge and discharge subcycles changed. The downward tick marks on the charge curves and upward tick marks on the discharge curves represent current interrupts

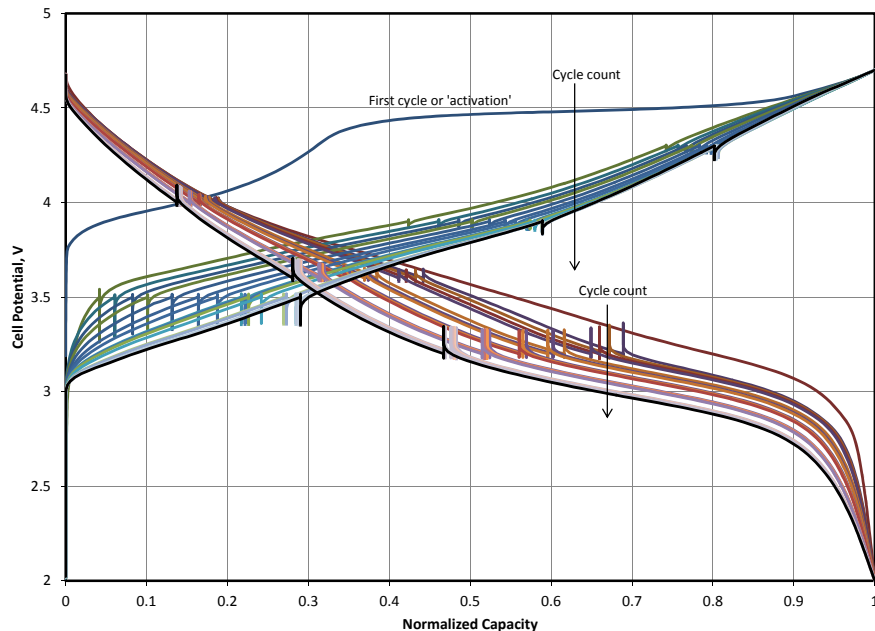


Figure IV - 130: Cell potential vs. normalized capacity, representing the typical charge and discharge voltage response of a cell containing a coated cathode in these experiments. This particular cell contained a zirconia-coated cathode (150°C). Selected curves were removed for the sake of clarity. During the first charge, the LMR NMC material was activated. With continued cycling, the voltage response for both the charge and discharge subcycles changed. The downward tick marks on the discharge curves and upward tick marks on the charge curves represent current interrupts

The relative change in average voltage, calculated from Eqn. 1, for the cells is given in Table IV - 14. In some cases, there was more than one cell for a given coating. This is indicated by the presence of a value for standard error (s.e.). Examining the values for the discharge subcycle shows that, after 20 cycles, most were within about 17% of the value given for the baseline material, and the value for LiPON (3 h) was almost twice that given for the baseline. The values given for the relative change in average voltage during the charge subcycle show a similar pattern after 20 cycles. Most values were within about 30% of the value

given for the baseline, and that for LiPON(3 h) was twice that given for the baseline.

It is interesting to note that neither the thickness of the Al_2O_3 layer nor the deposition temperature of the TiO_2 and ZrO_2 layers had a significant effect on the relative change in the average voltage. The voltage loss from cathodes containing LiAlO_x was approximately the same as those containing TiO_2 or ZrO_2 layers.

Table IV - 14: Relative change in average voltage in baseline cells and in cells containing an electrolyte additive or a coated cathode

Coating/Additive	100 × Rel. Change in Average Voltage after 20 Cycles (100 × s.e.)	100 × Rel. Change in Average Voltage after 50 Cycles (100 × s.e.)
Discharge		
Baseline	3.14 (0.10)	4.81
3-hexylthiophene	2.88	4.52
LiDFOB	3.38	
Al ₂ O ₃ (5 ALD cycles)	3.40	5.30
Al ₂ O ₃ (100 ALD cycles)	3.22	5.47
AlPO ₄	3.68	5.48
LiAlO _x	3.32 (0.07)	
TiO ₂ (100°C)	3.14 (0.04)	
TiO ₂ (150°C)	3.20 (0.07)	
ZrO ₂ (100°C)	3.17 (0.01)	
ZrO ₂ (150°C)	3.26 (0.03)	
LiPON (1 h)	2.69	
LiPON (2 h)	2.60	
LiPON (3 h)	5.20	
Charge		
Baseline	3.97 (0.49)	4.52
3-hexylthiophene	3.16	4.20
LiDFOB	4.89	
Al ₂ O ₃ (5 ALD cycles)	3.52	5.15
Al ₂ O ₃ (100 ALD cycles)	3.14	4.70
AlPO ₄	3.66	5.03
LiAlO _x	5.21 (0.05)	
TiO ₂ (100°C)	4.39 (0.01)	
TiO ₂ (150°C)	4.60 (0.01)	
ZrO ₂ (100°C)	4.62 (0.02)	
ZrO ₂ (150°C)	4.85 (0.03)	
LiPON (1h)	3.67	
LiPON (2 h)	3.75	
LiPON (3 h)	7.97	

$$\text{Rel. change in avg. voltage} = \frac{\text{Avg. voltage}_{\text{first cycle}} - \text{Avg. voltage}_{\text{last cycle}}}{\text{Avg. voltage}_{\text{first cycle}}} \quad \text{Eqn. 1}$$

The data in Table IV - 14 show that the values given for the 1-h and 2-h LiPON layers were outside the statistical range for the discharge subcycles and within the statistical range for the charge subcycles. The additional hour of sputtering time did not markedly change the voltage fade response characteristic.

However, at 3 h, voltage fade increased by about a factor of 2 for both the charge and discharge subcycles, which was due to the increase in electronic resistance of the LiPON film surrounding the cathode particles.

After 20 cycles, the values given for the AlPO₄ layer and the electrolyte additives are also outside the

statistical range. The values for the electrolyte additives indicate that the average voltage decreased slightly less than the baseline. The value for AlPO₄ indicates that the average voltage decreased slightly more than the baseline. After 50 cycles, the values indicate a greater loss.

The central question underlying this work concerned the origin of voltage fade. That is, is the voltage fade phenomenon controlled by a reaction at the cathode-electrolyte interface? Theoretically, if voltage fade were caused by the loss of oxygen (e.g., during electrochemical activation) or the loss of a soluble constituent, such as Mn²⁺, changing the nature of the exposed cathode surface should change the rate at which the reaction proceeds by a significant amount.

In the literature and in this work, coatings and electrolyte additives were shown to be very effective in controlling capacity loss. The rates of these reactions displayed significant changes in the presence of an interface-modifying organic or inorganic material. However, the results in the present work indicate that using interface-modifying materials or additives had little-to-no effect on voltage fade. Under the cycling conditions used in these experiments, voltage fade appears to derive from an intrinsic property of the LMR-NMC materials, such as thermodynamic instability, and proceeds at a rate of a few millivolts per cycle.

Adjusting the cycling window was found to be one practical approach to reduce voltage fade.

b. Effect of Composition

Combinatorial synthesis. Our approach is to use combinatorial synthetic methods to identify factors that contribute to voltage fade as part of a team effort. This part of the effort will investigate the effects of Li, Mn, Ni, Co and oxygen stoichiometries on the voltage fade phenomenon.

One-hundred, forty-seven compositions (see Table IV - 15), spanning the low-cobalt portion of the Li₂MnO₃-LiCoO₂-LiNiO₂-LiMnO₂ phase diagram, were identified for investigation. Selected compositions were made by sol-gel methods for characterization in terms of XRD, elemental analysis and electrochemical performance. Based on the XRD results, the phase distribution of the materials prepared is given in Table IV - 16. High lithium content was important to obtain the desired phase.

Only those materials crystallizing with the layered-layered structure were characterized in terms of elemental analysis and electrochemical performance. These compositions were assembled into coin cells. Lithium metal was the anode.

Table IV - 15: Group numbers and compositions for this study

Group	Li	Ni	Co	Mn	Group	Li	Ni	Co	Mn
1	1~1.6	0.15	0	0.85	12	1~1.6	0.25	0.2	0.55
2	1~1.6	0.15	0.05	0.85	13	1~1.6	0.3	0	0.7
3	1~1.6	0.15	0.1	0.75	14	1~1.6	0.3	0.05	0.65
4	1~1.6	0.2	0	0.8	15	1~1.6	0.3	0.1	0.6
5	1~1.6	0.2	0.05	0.75	16	1~1.6	0.3	0.15	0.55
6	1~1.6	0.2	0.1	0.7	17	1~1.6	0.35	0	0.65
7	1~1.6	0.2	0.15	0.65	18	1~1.6	0.35	0.05	0.6
8	1~1.6	0.25	0	0.75	19	1~1.6	0.35	0.1	0.55
9	1~1.6	0.25	0.05	0.7	20	1~1.6	0.4	0	0.6
10	1~1.6	0.25	0.1	0.65	21	1~1.6	0.4	0.05	0.55
11	1~1.6	0.25	0.15	0.6					

Table IV - 16: Found compositions and phase distribution of materials made for this study

Group	Li	Ni	Mn	Co	Phase Distribution
1-A	0.956	0.159	0.841	0.000	layered-layered+Li ₂ MnO ₃
1-B	1.059	0.152	0.848	0.000	layered-layered+Li ₂ MnO ₃
1-C	1.179	0.155	0.845	0.000	layered-layered+Li ₂ MnO ₃
1-D	1.241	0.144	0.856	0.000	layered-layered+Li ₂ MnO ₃
1-E	1.383	0.152	0.848	0.000	layered-layered+Li ₂ MnO ₃
1-F	1.452	0.149	0.851	0.000	layered-layered
1-G	1.573	0.152	0.847	0.000	layered-layered
2-A	0.929	0.178	0.767	0.055	layered-layered+Li ₂ MnO ₃
2-B	1.037	0.155	0.792	0.052	layered-layered+Li ₂ MnO ₃
2-C	1.157	0.158	0.788	0.054	layered-layered+Li ₂ MnO ₃
2-D	1.236	0.149	0.803	0.049	layered-layered+Li ₂ MnO ₃
2-E	1.351	0.148	0.799	0.053	layered-layered+Li ₂ MnO ₃
2-F	1.427	0.151	0.796	0.052	layered-layered
2-G	1.493	0.156	0.790	0.054	layered-layered
3-D	1.330	0.150	0.750	0.100	layered-layered
3-E	1.419	0.148	0.755	0.097	layered-layered
3-F	1.565	0.150	0.752	0.098	layered-layered
3-G	1.618	0.150	0.751	0.991	layered-layered
4-A	0.843	0.244	0.756	0.000	spinel + Li ₂ MnO ₃
4-B	0.947	0.223	0.777	0.000	spinel + Li ₂ MnO ₃
4-C	1.101	0.205	0.795	0.000	spinel + Li ₂ MnO ₃
4-D	1.156	0.195	0.805	0.000	spinel + Li ₂ MnO ₃
4-E	1.267	0.220	0.780	0.000	spinel + Li ₂ MnO ₃
4-F	1.352	0.220	0.780	0.000	spinel+Li ₂ MnO ₃ +layered-layered
4-G	1.437	0.226	0.774	0.000	spinel+Li ₂ MnO ₃ +layered-layered
5-A	0.879	0.219	0.730	0.051	spinel + Li ₂ MnO ₃
5-B	0.968	0.217	0.738	0.046	spinel + Li ₂ MnO ₃
5-C	1.094	0.214	0.736	0.050	spinel + Li ₂ MnO ₃
5-D	1.212	0.211	0.743	0.046	spinel + Li ₂ MnO ₃
5-E	1.335	0.220	0.732	0.048	spinel+Li ₂ MnO ₃ +layered-layered
5-F	1.467	0.205	0.749	0.046	layered-layered
5-G	1.544	0.205	0.745	0.050	layered-layered
6-A	0.924	0.209	0.690	0.101	spinel + Li ₂ MnO ₃
6-B	1.002	0.210	0.690	0.100	spinel + Li ₂ MnO ₃
6-C	1.081	0.210	0.685	0.106	spinel+Li ₂ MnO ₃ +layered-layered
6-D	1.213	0.203	0.699	0.098	spinel+Li ₂ MnO ₃ +layered-layered
6-E	1.304	0.208	0.692	0.100	layered-layered+Li ₂ MnO ₃
6-F	1.409	0.203	0.696	0.101	layered-layered
6-G	1.510	0.205	0.693	0.103	layered-layered
7-A	0.936	0.211	0.631	0.158	spinel+Li ₂ MnO ₃ +layered-layered
7-B	1.054	0.203	0.648	0.149	spinel+Li ₂ MnO ₃ +layered-layered
7-C	1.172	0.199	0.652	0.150	spinel+Li ₂ MnO ₃ +layered-layered
7-D	1.382	0.195	0.663	0.142	spinel+layered-layered
7-E	1.330	0.205	0.644	0.151	layered-layered
7-F	1.418	0.200	0.649	0.152	layered-layered
7-G	1.478	0.208	0.643	0.149	layered-layered
8-A	0.981	0.252	0.748	0.000	spinel + Li ₂ MnO ₃
8-B	1.086	0.254	0.746	0.000	spinel + Li ₂ MnO ₃
8-C	1.191	0.261	0.739	0.000	spinel + Li ₂ MnO ₃
8-D	1.285	0.240	0.760	0.000	spinel + Li ₂ MnO ₃
8-E	1.374	0.251	0.749	0.000	spinel+Li ₂ MnO ₃ +layered-layered

Group	Li	Ni	Mn	Co	Phase Distribution
8-F	1.473	0.250	0.750	0.000	spinel+Li ₂ MnO ₃ +layered-layered
8-G	1.740	0.252	0.748	0.000	layered-layered
12-A	0.952	0.257	0.546	0.198	layered-layered
12-B	1.041	0.256	0.543	0.201	layered-layered
12-C	1.028	0.314	0.498	0.188	layered-layered
12-F	1.383	0.256	0.541	0.203	layered-layered
12-G	1.407	0.256	0.540	0.204	layered-layered
13-A	0.937	0.316	0.683	0.000	spinel + Li ₂ MnO ₃
13-B	1.030	0.298	0.702	0.000	spinel + Li ₂ MnO ₃
13-C	1.157	0.299	0.701	0.000	spinel + Li ₂ MnO ₃
13-D	1.289	0.292	0.708	0.000	spinel+Li ₂ MnO ₃ +layered-layered
13-E	1.362	0.298	0.702	0.000	spinel+Li ₂ MnO ₃ +layered-layered
13-F	1.425	0.305	0.695	0.000	spinel+Li ₂ MnO ₃ +layered-layered
13-G	1.503	0.316	0.684	0.000	layered-layered+Li ₂ MnO ₃
16-A	0.941	0.298	0.554	0.148	spinel+Li ₂ MnO ₃ +layered-layered
16-C	1.011	0.296	0.553	0.151	spinel+Li ₂ MnO ₃ +layered-layered
16-C	1.091	0.299	0.550	0.150	spinel+Li ₂ MnO ₃ +layered-layered
16-D	1.191	0.301	0.546	0.153	layered-layered+Li ₂ MnO ₃
16-E	1.282	0.305	0.542	0.153	layered-layered
16-F	1.338	0.300	0.552	0.149	layered-layered
16-G	1.380	0.299	0.549	0.152	layered-layered
17-A	0.912	0.348	0.652	0.000	spinel + Li ₂ MnO ₃
17-B	1.020	0.346	0.654	0.000	spinel + Li ₂ MnO ₃
17-C	1.114	0.361	0.639	0.000	spinel+Li ₂ MnO ₃ +layered-layered
17-D	1.178	0.346	0.654	0.000	layered-layered+Li ₂ MnO ₃
17-E	1.313	0.348	0.652	0.000	layered-layered+Li ₂ MnO ₃
17-F	1.364	0.328	0.671	0.001	layered-layered+Li ₂ MnO ₃
17-G	1.438	0.345	0.655	0.000	layered-layered+Li ₂ MnO ₃
20-A	0.902	0.434	0.565	0.000	spinel+Li ₂ MnO ₃ +layered-layered
20-B	1.077	0.416	0.584	0.000	spinel+Li ₂ MnO ₃ +layered-layered
20-C	1.144	0.412	0.588	0.000	layered-layered+Li ₂ MnO ₃
20-D	1.246	0.417	0.582	0.000	layered-layered+Li ₂ MnO ₃
20-E	1.306	0.411	0.588	0.000	layered-layered
20-F	1.454	0.411	0.589	0.000	layered-layered
20-G	1.566	0.382	0.618	0.000	layered-layered
21-A	0.884	0.415	0.532	0.052	spinel+Li ₂ MnO ₃ +layered-layered
21-B	1.021	0.408	0.544	0.048	spinel+Li ₂ MnO ₃ +layered-layered
21-C	1.086	0.414	0.533	0.052	layered-layered+Li ₂ MnO ₃
21-D	1.185	0.407	0.545	0.048	layered-layered+Li ₂ MnO ₃
21-E	1.241	0.412	0.536	0.052	layered-layered+Li ₂ MnO ₃
21-F	1.322	0.409	0.543	0.049	layered-layered
21-G	1.347	0.408	0.541	0.051	layered-layered
NMC-1	1.205	0.419	0.581	0.000	layered-layered
NMC-2	1.260	0.371	0.629	0.000	layered-layered
NMC-3	1.331	0.311	0.689	0.000	layered-layered
NMC-4	1.485	0.255	0.745	0.000	layered-layered
NMC-5	1.553	0.265	0.733	0.002	layered-layered

All cells were cycled between 2 V and 4.7 V at 10 mA/g for the first cycle, and then between 2 V and 4.7 V (vs. Li⁺/Li) at 20 mA/g for the following cycles. The cells were cycled between 2 and 4.7 V for a minimum of

20 and a maximum of 50 times. While cycling, current interrupt measurements were carried out at 3.5, 3.9, 4.3, and 4.7 V during charge and at 4.0, 3.6, 3.2, and 2.0 V during discharge. Estimates of cell resistance were

calculated from the values of cell voltage and current at times t_0 and t_1 using Eq. 2.

$$R = \left| \frac{v_{t_1} - v_{t_0}}{i_{t_1} - i_{t_0}} \right|, R = \left| \frac{v_{t_1} - v_{t_0}}{i_{t_1} - i_{t_0}} \right|, \quad \text{Eq. 2}$$

where v_{t_1} and v_{t_0} are the cell voltages at t_1 and t_0 , respectively; i_{t_1} and i_{t_0} are the respective currents.

The activation charge subcycle and the discharge immediately following it were omitted from further analysis in this work. After that subcycle, the energy (Wh) and capacity (Ah) values were either extracted directly from the cycling data or were calculated from the raw data using Microsoft Excel®. The average voltage for a given charge or discharge subcycle was calculated as Wh/Ah. The resistance values at the first three voltages were averaged and used to correct the average voltage value for the average resistance of the cell during a given cycle, examples are shown in Figure IV - 131.

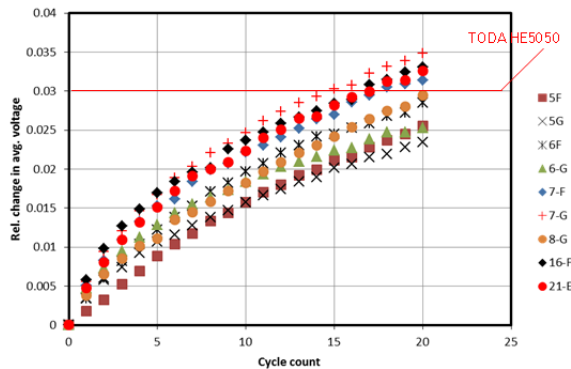


Figure IV - 131: Relative change in average voltage vs. cycle count. The abbreviations in the legend reflect different Li, Mn, Ni, and Co stoichiometries (see associated table)

These relative average voltage values (hereafter called ΔAvgV ; see Eq. 2) then were used for plotting and subsequent analyses. The values of ΔAvgV was found to be sensitive to composition. The behavior of ΔAvgV with cycle count is shown in Figure IV - 132 for selected compositions.

$$\Delta\text{AvgV} = \frac{\text{Avg.voltage}_0 - \text{Avg.voltage}_i}{\text{Avg.voltage}_0} \quad \text{Eq. 2.}$$

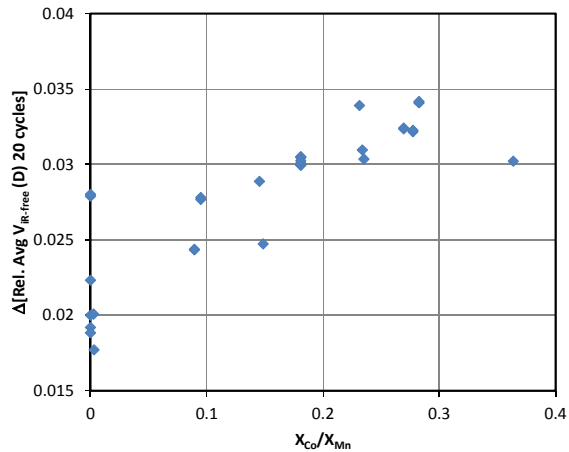


Figure IV - 132: Change in the relative change in average voltage vs. $X_{\text{Co}}/X_{\text{Mn}}$

From the experimental data, ΔAvgV for HE5050 was ~3% over the course of 20 cycles. The lowest observed ΔAvgV was 1.28% from composition 12-G, $\text{Li}_{1.48}\text{Ni}_{0.25}\text{Mn}_{0.52}\text{Co}_{0.23}\text{O}_2$. This is about 1/3 of the value observed for HE5050.

Simplex Modeling of ΔAvgV . A model was constructed as an aid to guide the search for compositions with values of ΔAvgV lower than that of HE5050. Modeling was limited to those compositions that crystallize in the R-3m space group (layered-layered materials). The ΔAvgV data were treated by multiple linear regression analysis using the cubic simplex equation for four-component mixtures, based on the work of Scheffé. The complete cubic equation is given below.

$$Y = a_1x_1 + a_2x_2 + a_3x_3 + a_4x_4 + a_{12}x_1x_2 + a_{13}x_1x_3 + a_{14}x_1x_4 + a_{23}x_2x_3 + a_{24}x_2x_4 + a_{34}x_3x_4 + a_{123}x_1x_2x_3 + a_{124}x_1x_2x_4 + a_{134}x_1x_3x_4 + a_{234}x_2x_3x_4 + b_{12}(x_1 - x_2) + b_{13}(x_1 - x_3) + b_{14}(x_1 - x_4) + b_{23}(x_2 - x_3) + b_{24}(x_2 - x_4) + b_{34}(x_3 - x_4), \text{ where } x_j \text{ is the mole fraction of the } j\text{th component and } a_j \text{ and } b_k \text{ are fitting constants.}$$

The relative change in the iR-corrected average voltage was calculated by comparing the value from the first discharge or charge subcycle to the respective value at the 20th discharge or charge subcycle, as shown in Eq. 3.

$$\begin{aligned} \text{Rel. change in avg. voltage} &= \\ \frac{\text{Avg.voltage}_0 - \text{Avg.voltage}_{20}}{\text{Avg.voltage}_0} &\text{ Rel. change in avg. voltage} = \\ \frac{\text{Avg.voltage}_{\text{firstcycle}} - \text{Avg.voltage}_{\text{lastcycle}}}{\text{Avg.voltage}_{\text{firstcycle}}} &\quad \text{Eq. 3.} \end{aligned}$$

Of 26,333 possible solutions, candidate fits of the equation to the data must include the first four terms; use the fewest number of terms; have a high value of r^2 , typically greater than 0.98; and have low RMS error. With the current data, a candidate fit was found using

eleven terms, shown below. Here, the value of r^2 was greater than 0.99 and the RMS error was 0.046.

$$Y = a_1x_1 + a_2x_2 + a_3x_3 + a_4x_4 + a_{12}x_1x_2 + a_{13}x_1x_3 + a_{23}x_2x_3 + b_{12}(x_1 - x_2) + b_{13}(x_1 - x_3) + b_{24}(x_2 - x_4) + b_{34}(x_3 - x_4)$$

The compositions beginning with “NMC” in Table IV - 16 were selected based on the model. The calculated values of relative change in average voltage was much less than 1%; however, the actual values were much greater, but the compositions were single phase and crystallized with the R-3m structure.

Examining the data shows that there are trends in the data. For example, Figure IV - 132 shows that there is a trend between the change in the relative, average voltage and the ratio of X_{Co}/X_{Mn} . When X_{Co}/X_{Mn} is greater than 1, this trend does not appear to hold.

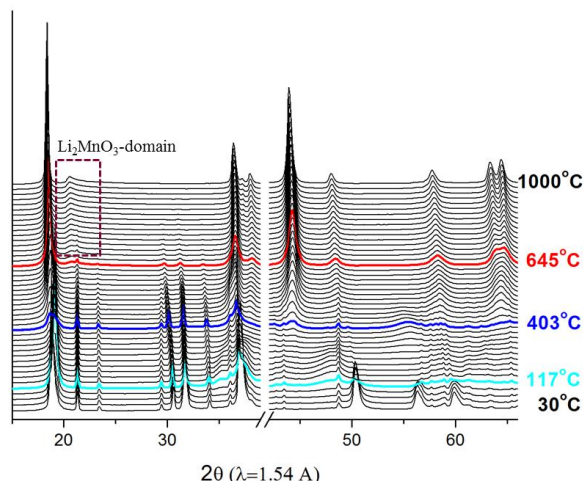


Figure IV - 133: Operando study of the formation of LMR-NMC from hydroxide precursor and lithium carbonate

Preferential formation of Li_2MnO_3 : *operando* XRD of LMR-NMC. The tendency for the formation of domains of Li_2MnO_3 embedded within a matrix of $LiMO_2$ is strong and may be considered important effect in the synthesis of these LMR-NMC materials. In Figure IV - 133, presents an *operando* XRD study of the formation of LMR-NMC (with $Li/Ni+Mn+Co=1.5$) as the sample hydroxide precursor with hereby Li_2CO_3 are heated together under air. At about 120°C, the $Ni_xMn_yCo_z(OH)_2$ decomposes. At 400°C a layered oxide phase is produced, followed by crystallization of Li_2MnO_3 domain at 645°C (highlighted in red). Therefore, synthetically, we must take into account the prevalence to form $LiMn_6$ clusters in the TM plane.

c. Cation Distribution

Disordered network materials: formation of honeycomb ‘layered-layered’ composites. Taking into account the pressure to form $LiMn_6$ clusters in LMR-NMC, it was reasoned that if the oxide was to be formed in a non-domain configuration, it will be necessary to

form the material below 650 °C as documented in the *operando* XRD work (above). Towards this objective we attempted a synthesis route to create a precursor coordinated bonded network consisting of a honeycomb of transition metals.

Microscale segregation of transition metals in Li-ion battery cathode materials affects critical performance attributes, including the structural evolution during cycling that gives rise to voltage fade. Better control of transition metal distribution at all steps in materials synthesis will be required for mitigating this phenomenon.

Cathode material precursors prepared by traditional precipitation reactions tend to produce secondary particles with compositional gradients induced by poorly controlled differences in reactivity between the transition metals. In our approach, an ordered precursor is produced using a modular synthesis in which the different transition metals are incorporated in different building blocks (see schematic in Figure IV - 134). One block is a trioxalato complex of a +3 oxidation state metal, while the other is a +2 oxidation state metal with labile ligands. As the two components assemble into the final structure, the oxalato ligands take on the $m^2-h^2:h^2$ bonding mode, bridging the two metals and forming the ordered 2D network (*J. Mater. Chem.*, 16, 2685 (2006)).

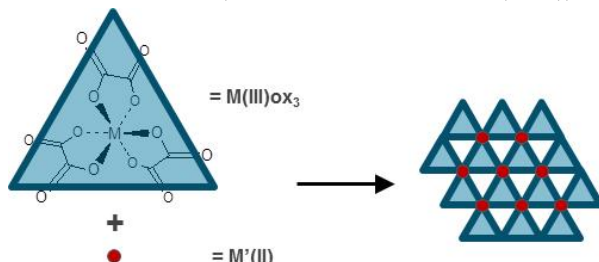
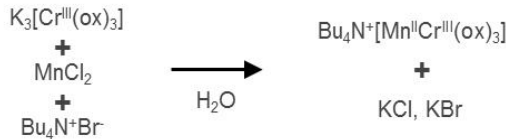


Figure IV - 134: Schematic of honeycomb network for synthesis of modified homogeneously distributed divalent metal precursors

The initial attempts at ordered oxalate precursors made use of the somewhat unstable $K_3[Mn^{III}(ox)_3] \cdot 3H_2O$ as the trivalent metal component. The only products that could be isolated according to the published procedure turned out to be associated with decomposition of the Mn(III) compound to produce $(Ni^{II}_{0.5}Mn^{II}_{0.5})_2C_2O_4$, analogous to a coprecipitated Ni-Mn oxalate.

In order to rely on more firmly established chemistry, Cr was used the trivalent metal component, in the form of $K_3[Cr^{III}(ox)_3] \cdot 3H_2O$, which is stable and easily produced by reduction of dichromate with oxalic acid. Now Mn can be incorporated as the divalent metal component, an oxidation state in which it is much more stable. Combining these two in the presence of the templating tetrabutylammonium cation produced the expected product $Bu_4N^+[Mn^{II}Cr^{III}(ox)_3]$:



The conditions for converting the mixed Mn(II)-Cr(III) precursor to a lithiated oxide are being explored including low-temperature ion-exchange and direct solid state methods. This material will be evaluated electrochemical and compared to similar compositions prepared by standard methods. As the voltage fade program ends, this project has been abandoned.

d. Cation Substitution

Al and Ga substitution in HE5050. In this synthesis segment, we performed a systematic evaluation to determine the effect of cation substitution on the voltage fade for LMR-NMC cathode materials. We chose a prototypical Co-containing $0.5\text{Li}_2\text{MnO}_3 \bullet 0.5\text{Li}(\text{Ni}_{0.375}\text{Mn}_{0.375}\text{Co}_{0.25})\text{O}_2$ layered-layered composite as the representative example for our study. We prepared a series of Al- or Ga-substituted $\text{Li}_{1.2}\text{Ni}_{0.15}\text{Mn}_{0.55}\text{Co}_{0.1}\text{O}_2$ (i.e. the layered notation for $0.5\text{Li}_2\text{MnO}_3 \bullet 0.5\text{Li}(\text{Ni}_{0.375}\text{Mn}_{0.375}\text{Co}_{0.25})\text{O}_2$ as designated hereafter in the report) cathode samples by the sol-gel synthesis method and measured their electrochemical properties.

The electrochemical properties related to voltage-fade are the interests and focus of this paper. Using a voltage fade testing protocol, we quantitatively compared the degree of voltage fade in pristine and cation-substituted samples and determined the effectiveness of non-redox active Al or Ga substitution on suppressing the voltage fade.

Sol-gel synthesis— It is important, in the study of cation substituted LMR-NMC, to make sure that the substituting cations (here, Al or Ga) are homogeneously mixed with Ni, Mn, and Co. We prepared samples using sol-gel synthesis method that ensures good atomic mixing between multiple cations. In order to confirm the equivalence of the sol-gel synthesized samples, the electrochemical performance of the baseline $\text{Li}_{1.2}\text{Ni}_{0.15}\text{Mn}_{0.55}\text{Co}_{0.1}\text{O}_2$ sol-gel material is compared with that of a commercial grade sample having the same composition (HE5050, Toda). Figure IV - 135 shows the initial voltage profiles of the two samples. The overlapping voltage profiles indicate that the initial electrochemical characteristics (including activation of Li_2MnO_3 component) of the two samples are equivalent to each other.

In Figure IV - 135b, the voltage fades in the two samples are compared by plotting the relative fade in the iR-corrected average voltages (V_{avg} , iR-corr) as a function of cycle number. The two samples show the same degree of voltage fade confirming the efficacy of employing our sol-gel method in the synthesis of

cathode materials during the study of cation substituted LMR-NMC.

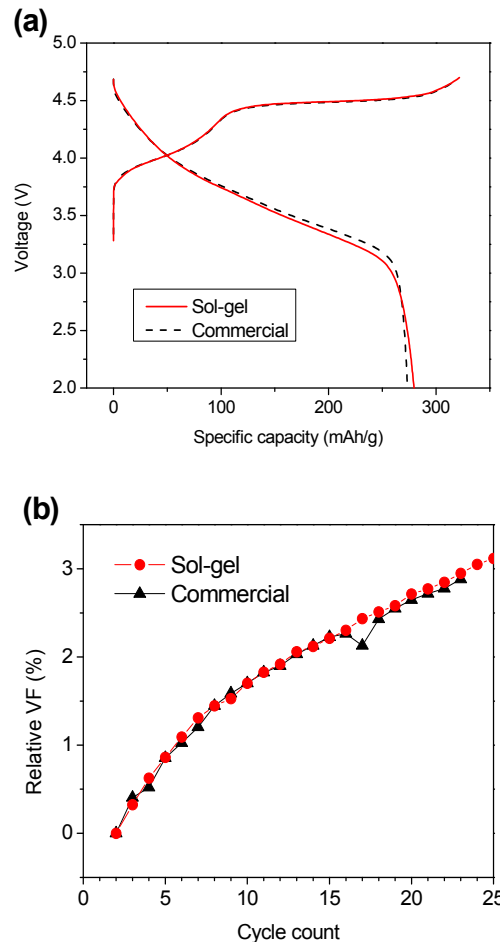


Figure IV - 135: (a) Voltage profiles and (b) changes in iR-corrected average discharge voltage in sol-gel prepared and commercial (HE5050, Toda) $\text{Li}_{1.2}\text{Ni}_{0.15}\text{Mn}_{0.55}\text{Co}_{0.1}\text{O}_2$ baseline samples

Cation substitution— Two series of Al- and Ga-substituted $\text{Li}_{1.2}\text{Ni}_{0.15}\text{Mn}_{0.55}\text{Co}_{0.1}\text{O}_2$ samples were prepared for this study. For each series, 2.5%, 5%, and 10% levels of substitutions were tried at the expense of the transition metals, $\text{Ni}_{0.15}\text{Mn}_{0.55}\text{Co}_{0.1}$, in stoichiometric ratio.

The target and actual compositions of the synthesized samples are summarized in Table IV - 17. The actual ratio of cations in each sample is similar to the nominal ratio. Although slightly lower than expected values, the actual percent substitutions of cations in samples are close to the target values. Figure IV - 136 shows SEM images of the pristine and cation-substituted sample. The overall morphologies of all powder samples are similar, generally consisting of agglomerates of spherical primary particles. The size of primary particles is $\sim 100 - 300 \mu\text{m}$. The SEM analysis

confirms that the cation substitution itself does not affect the particle morphologies.

Table IV - 17: Elemental analysis of cation-substituted $\text{Li}_{1.2}\text{Ni}_{0.15}\text{Mn}_{0.55}\text{Co}_{0.1}\text{O}_2$

Sample	Cation ratio (Ni : Mn : Co : M)		Actual percent substitution (%)
	Nominal	Actual (ICP-MS)	
Al-0%	0.15 : 0.55 : 0.1 : 0	0.150 0.539 0.111 0.000	:
	0.14625 : 0.53625 : 0.0975 : 0.02	0.145 0.527 0.108 0.019	0
	0.1425 : 0.5225 : 0.095 : 0.04	0.141 0.518 0.103 0.038	2.4
Al-5%	0.135 : 0.495 : 0.09 : 0.08	0.132 0.490 0.098 0.079	:
	0.15 : 0.55 : 0.1 : 0	0.150 0.540 0.110 0.000	4.7
	0.14625 : 0.53625 : 0.0975 : 0.02	0.147 0.524 0.111 0.018	9.9
Ga-0%	0.1425 : 0.5225 : 0.095 : 0.04	0.142 0.514 0.109 0.035	:
	0.135 : 0.495 : 0.09 : 0.08	0.135 0.490 0.102 0.073	0
	0.15 : 0.55 : 0.1 : 0	0.150 0.540 0.110 0.000	2.2
Ga-5%	0.14625 : 0.53625 : 0.0975 : 0.02	0.147 0.524 0.111 0.018	4.4
	0.135 : 0.495 : 0.09 : 0.08	0.135 0.490 0.102 0.073	9.1

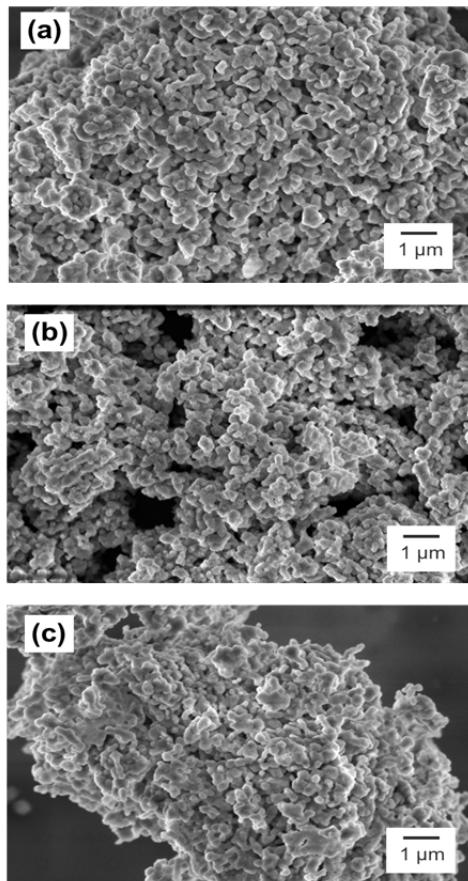


Figure IV - 136: Particle morphology of (a) pristine $\text{Li}_{1.2}\text{Ni}_{0.15}\text{Mn}_{0.55}\text{Co}_{0.1}\text{O}_2$, (b) 5% Al-substituted, and (c) 5% Ga-substituted powder samples

Figure IV - 137 shows typical XRD patterns for the Li-Mn-rich layered-layered composite materials. They are indexed with the R-3m space group despite the appearance of the Li-Mn ordering super-lattice peaks at 20-22°.

In Figure IV - 137a, the Al-substituted samples have no impurity phases up to 10% substitution. The Li-Mn ordering peaks become broader as the Al content increases, suggesting that the Li-Mn ordering is perturbed by the presence of Al in the transition metal plane. The Ga-substituted samples also present similar XRD patterns in Figure IV - 137b. However, small impurity peaks, which are assigned to LiGaO_2 (JCPDS Card# 72-1640), are also observed with excessive 10% Ga substitution.

Figure IV - 138 plots the lattice parameter values as a function of percent cation substitution. The average lattice parameters of three pristine samples are presented as black square symbols with error bars. The 10% Ga sample, which contains an impurity phase, is marked as open triangles and excluded from further interpretation. The plots show that, as the Al contents increase, the lattice parameters decrease in both the a- and c-axis

lattice parameters. In contrast Ga substitution increases the lattice constants. The observed trends correspond well with the ionic radii of the substituted cations ($r_{\text{Al}}^{3+} = 53.5 \text{ pm}$ and $r_{\text{Ga}}^{3+} = 62 \text{ pm}$). The average ionic radius for the transition metals in the stoichiometric ratio, r_{NMC} ($\text{NMC} = \text{Ni}_{0.15}\text{Mn}_{0.55}\text{Co}_{0.1}$), is 56.2 pm; hence, the ionic radius of the cations increases in the order $r_{\text{Al}}^{3+} < r_{\text{NMC}} < r_{\text{Ga}}^{3+}$, indicating lattice contraction with Al substitution and lattice expansion with Ga substitution. This difference confirms the effective incorporation of the substituents into the parent lattice structure without formation of a significant amount of secondary phase.

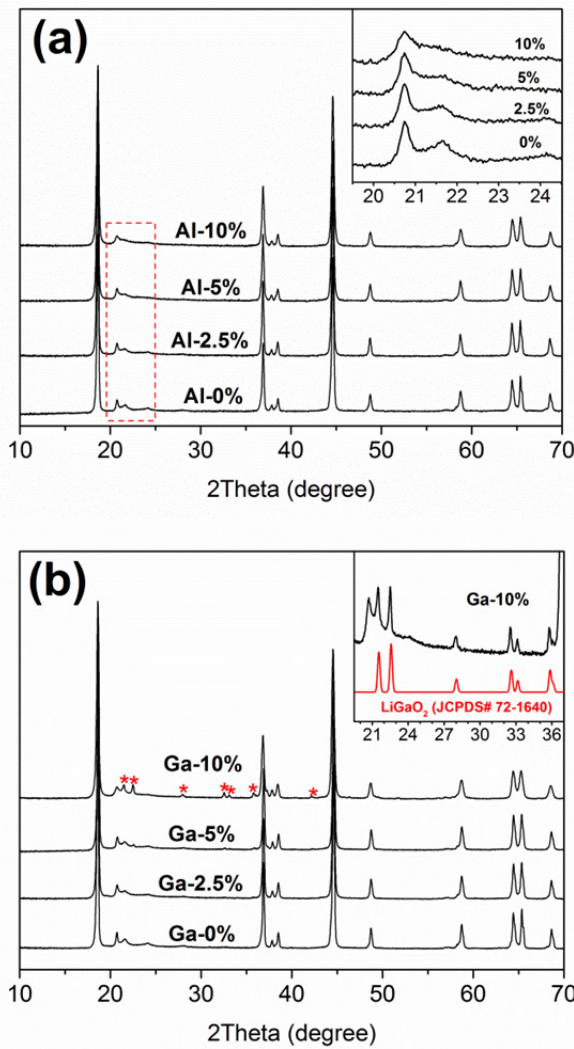


Figure IV - 137: XRD patterns of (a) Al- and (b) Ga-substituted $\text{Li}_{1.2}\text{Ni}_{0.15}\text{Mn}_{0.55}\text{Co}_{0.1}\text{O}_2$

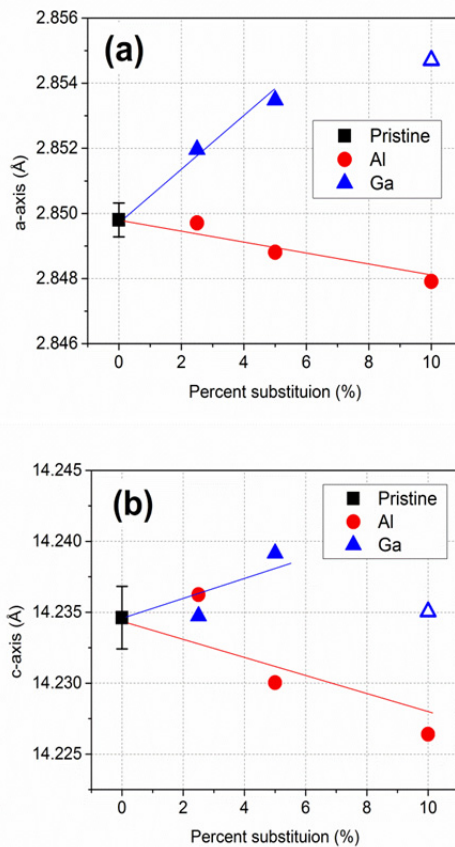


Figure IV - 138: Plots of lattice parameters in (a) a-axis and (b) c-axis as a function of percent substitution of Al and Ga. For baseline data, three batches of pristine samples are used to obtain average lattice parameter values. The samples containing impurity phases (10% Ga) are marked with hollow symbols. Solid lines are for visual guidance

Electrochemical performance—Figure IV - 139 shows the voltage profiles during the initial activation cycle for the cells with Al- or Ga-substituted cathode material. The voltage profiles are characterized by a long 4.5 V plateau on the 1st charge. While the detailed mechanism of the electrochemical activation process is not clearly understood yet, it is generally believed that oxygen loss and irreversible structural change occur in the plateau region. In Figure IV - 139a, and Figure IV - 139b, the voltage profiles for the two pristine samples (no Al or Ga substitution) are identical. The initial charge and discharge capacities for the pristine samples are, respectively, 320 and 275 mAh/g. These values are comparable to the initial capacity of a commercial sample with the same nominal composition. Also consistent with cation substitution, the initial specific capacity is decreased due to the presence non-redox Al and Ga ions.

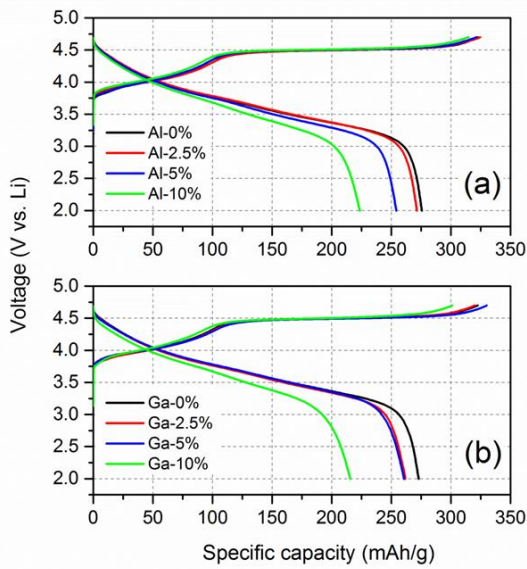


Figure IV - 139: Initial voltage profiles of (a) Al- and (b) Ga-substituted $\text{Li}_{1.2}\text{Ni}_{0.15}\text{Mn}_{0.55}\text{Co}_{0.1}\text{O}_2$. (Voltage window: 2 – 4.7 V vs. Li; current: 10 mA/g)

Figure IV - 140 compares the discharge capacity as a function of cycle number. After the initial activation cycle (10 mA/g) the coin cells were repeatedly charged and discharged at 20 mA/g in the subsequent cycles. The abrupt drop in capacity between the 1st and 2nd cycle is due to the increased current density. In general, only a small change in cycle performance occurs with cation substitution. The specific capacity values for each sample at the 2nd and 20th cycles are compared in Table IV - 18. The pristine samples have ~89% capacity retention after 20 cycles.

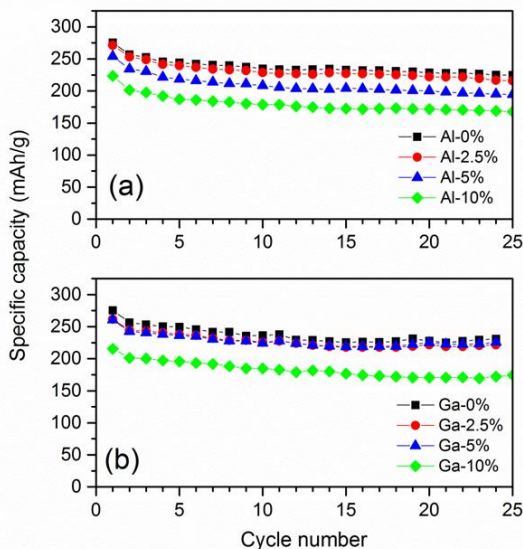


Figure IV - 140: Capacity retention of (a) Al- and (b) Ga-substituted $\text{Li}_{1.2}\text{Ni}_{0.15}\text{Mn}_{0.55}\text{Co}_{0.1}\text{O}_2$. (Voltage window: 2 – 4.7 V vs. Li; current: 10 mA/g for the 1st cycle and 20 mA/g for the following cycles)

Table IV - 18: Specific capacity at the 2nd and 20th cycle number and percent retention

Sample	Specific capacity (mAh/g)		Capacity retention (%)
	At 2 nd cycle	At 20 th cycle	
Al-0%	256.7	228.5	89.0
Al-2.5%	253.3	222.1	87.7
Al-5%	234.5	200.1	85.3
Al-10%	201.4	171.7	85.3
Ga-0%	256.5	227.7	88.8
Ga-2.5%	244.5	221.7	90.7
Ga-5%	242.6	225.1	92.8
Ga-10%	201.2	170.6	84.8

The cation substitution shows only a marginal influence on the cycle performance within the cycle counts used here. The capacity retention slightly decreases with Al substitution to 87.7% for the 2.5% Al samples and 85.3% for the 5% Al samples. Several groups have reported a beneficial effect from Al_2O_3 -coatings and Al-infused surface phase on the cycle performance of $\text{Li}_{1.2}\text{Ni}_{0.15}\text{Mn}_{0.55}\text{Co}_{0.1}\text{O}_2$, in contrast to bulk Al-substituted samples found elsewhere and this work. Note, instead a slight increase in cycle performance is observed with Ga substitution (90.7% for 2.5% Ga and 92.8% for 5% Ga), which may be attributed to possible Ga atom surface segregation thus forming some sort of surface-protecting secondary phase. *Voltage fade*—Voltage fade in these LMR-NMC cathodes effectively lowers the energy density (ED) over the lifetime of the battery. The question arises; what is the diagnostic feature for this ED change? Figure IV - 141 depicts the normalized voltage profiles and differential capacity plots for the pristine and cation-substituted samples. In these voltage profiles, the capacities are normalized for each half-cycle to present changes in electrode potential more clearly. After the activation cycle (1st cycle, not shown here), all of the materials' voltage profiles exhibit a cycle-to-cycle depression in both charge and discharge. Note that the depression in charge curves is a better indicator for the voltage fade than that observed in discharge curves. Since the two major causes of energy density loss arise from cell impedance increase and voltage fade, the charge curve actually better represents the voltage fade phenomena. The two effects simultaneously depress the discharge curve, but are competing against each other in the charge curves: the impedance rise effect increases the over-potential pushing the charge curves to higher voltage, but the voltage fade lowers the equilibrium voltage for the charge process. Therefore, the observed depression in the charge voltage curves during cycling suggests that the voltage fade process is the main cause for the ED losses in the tested materials.

The voltage fade is also noticed by the peak shifts in the differential capacity plots ($dQ/dV \times 1/Q$ plots). During the first 25 cycles with the pristine material, the

charge peaks at 3.0 – 3.5 V grow stronger and shift to lower potential, whereas the peak intensity decreases at 3.8 – 4.7 IV. A similar behavior is observed for the corresponding discharge peaks. These irreversible changes in the differential capacity plots are interpreted in the literature as the transformation of an initial phase(s) that is redox active at high potential (> 3.5 V)

into one or more redox-active phases located below 3.5 IV. The phase change from layered-type to spinel-type structure has been proposed for LMR-NMC with experimental evidences by neutron diffraction methods. A redox process for lithium manganese oxide spinel-type material ($\text{Li}_{1+x+y}\text{Mn}_{2-x}\text{O}_4$; $0 < x < 0.1$; $y > 1$) would typically appear at ~3.0 IV.

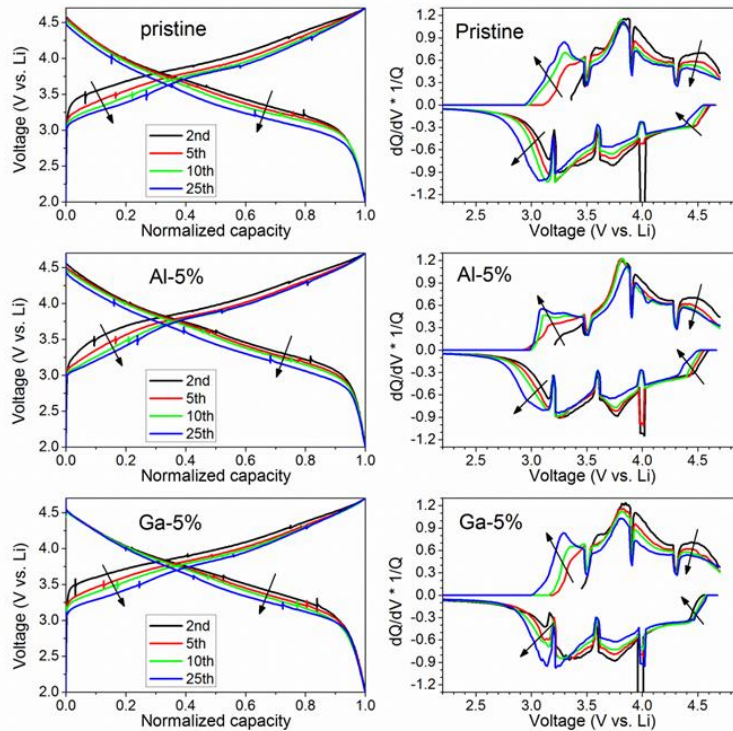


Figure IV - 141: Normalized voltage profiles (left side) and $(\text{d}Q/\text{d}V)^*1/\text{Q}$ plots (right side) for pristine and cation-substituted samples. Arrows indicate the movements of the curves on progressive cycling

Notably, the differential capacity plots for both Al and Ga substituted samples show similar shape changes as cycling progresses. However, a detailed comparison indicates cation substitutions may have some influence on the way the high-potential phases decay and the low-potential phases increase and evolve. In the 3.0–3.5 V region of the $\text{d}Q/\text{d}V^*1/\text{Q}$ curve during charge, each cation-substituted sample exhibits different doublet peak shapes after 25 cycles. While the pristine sample has a strong peak at ~3.3 V with a shoulder peak at ~3.1 V, the 5% Al sample clearly exhibits faster growth for the ~3.1 V peak, leading to a different $\text{d}Q/\text{d}V^*1/\text{Q}$ curve shape in the 3.0–3.5 V region after 25 cycles. In contrast, the growth of the ~3.1 V peak seems suppressed for the 5% Ga sample.

The effect of Al and Ga substitution on voltage fade of $\text{Li}_{1.2}\text{Ni}_{0.15}\text{Mn}_{0.55}\text{Co}_{0.1}\text{O}_2$ was quantitatively evaluated by comparing the changes in resistance-corrected average voltage ($V_{\text{avg}, \text{iR-corr}}$). We excluded the 10% Al and 10% Ga samples from this evaluation to

avoid any biased conclusion that might arise from the much lower specific capacities of those samples. The different specific capacity values (hence, the different cumulative amounts of cycled lithium ions) imply different levels of structural stress imposed on the different cathode materials. Furthermore, only the $V_{\text{avg}, \text{iR-corr}}$ values within the initial 25 cycles are considered because (1) major structural relaxation followed by the initial activation process is manifested within early cycles, (2) impedance effect becomes more dominant at longer cycle numbers, and (3) even a small difference in specific capacity values or cycle capability could cause a significant difference in the cumulative amounts of cycled lithium ions after a greater number of cycles.

Figure IV - 142a shows plots of $V_{\text{avg}, \text{iR-corr}}$ vs. cycle number for the Al-substituted samples. The $V_{\text{avg}, \text{iR-corr}}$ continuously decreases as cycle number increases. For the pristine sample (no Al) after 20 cycles, the value drops by 151 mV during charge and by 101 mV during discharge. The plot of relative voltage fade in Figure IV

- 142b does not reveal any beneficial effect from Al substitution in $\text{Li}_{1.2}\text{Ni}_{0.15}\text{Mn}_{0.55}\text{Co}_{0.1}\text{O}_2$, showing similar percent voltage fade of $\sim 3.8\%$ during charge and $\sim 2.8\%$ during discharge. In contrast, the Ga substitution plots in Figure IV - 143a appear to show some influence on the charge voltage decays; the average charge voltages for the Ga-substituted samples are slightly higher than the pristine (0% Ga) sample data. This effect is better represented in the relative voltage fade plot in Figure IV - 143b. During the initial 20 cycles, the relative voltage fade for 2.5% and 5% Ga samples is, respectively, 3.3% and 3.1% on charge, which is lower than that of 0% Ga sample (3.8%). This suppression of voltage drop echoes the suppressed $dQ/dV^*1/Q$ peak at 3.1 V, as shown in Figure IV - 141.

The layered-type to spinel-type phase transition requires major rearrangements of transition metals from the transition metal layers to lithium layers. The migration of transition metals occurs through the tetrahedral sites, as represented in Figure IV - 144. The different shape change in the $dQ/dV^*1/Q$ curves for the cation-substituted samples may be related to the cations deflecting the migration path of the transition metals. Indeed, Balasubramanian and coworkers have observed that Ga^{3+} ions have a stronger tendency to migrate from octahedral sites to tetrahedral sites during charging of $\text{LiNi}_{0.908}\text{Co}_{0.085}\text{Ga}_{0.003}\text{O}_2$.

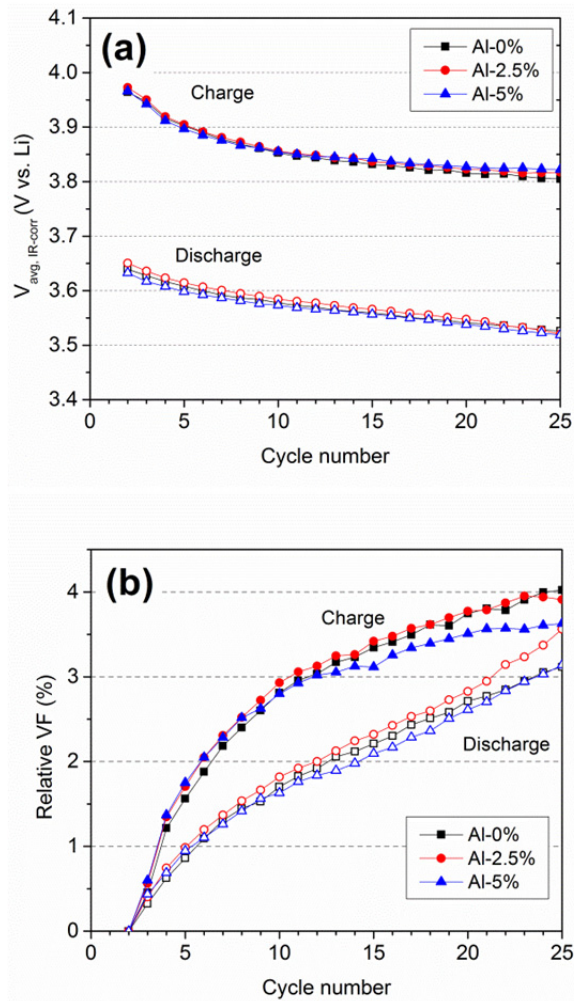


Figure IV - 142: Plots of (a) iR-corrected average voltage ($V_{\text{avg}, \text{iR-corr}}$) and (b) relative voltage fade (VF) as a function of cycle number in Al-substituted $\text{Li}_{1.2}\text{Ni}_{0.15}\text{Mn}_{0.55}\text{Co}_{0.1}\text{O}_2$. The relative voltage fade is defined as the percent decay in $V_{\text{avg}, \text{iR-corr}}$ relative to $V_{\text{avg}, \text{iR-corr}}$ at 2nd cycle

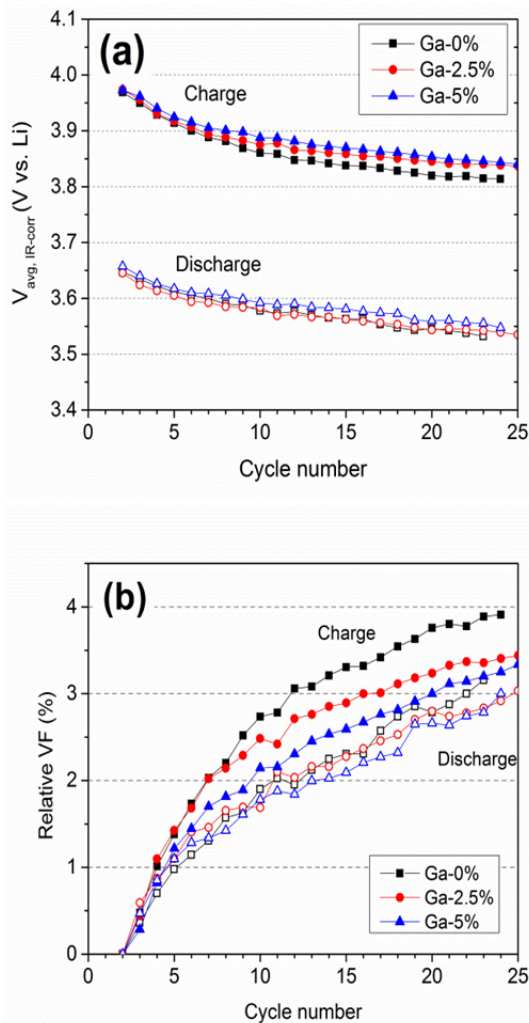


Figure IV - 143: Plots of (a) iR-corrected average voltage (V_{avg} , iR-corr) and (b) relative voltage fade (VF) as a function of cycle number in Ga-substituted $\text{Li}_{1.2}\text{Ni}_{0.15}\text{Mn}_{0.55}\text{Co}_{0.1}\text{O}_2$. The relative voltage fade is defined as the percent decay in $V_{\text{avg}, \text{iR-corr}}$ relative to $V_{\text{avg}, \text{iR-corr}}$ at 2nd cycle

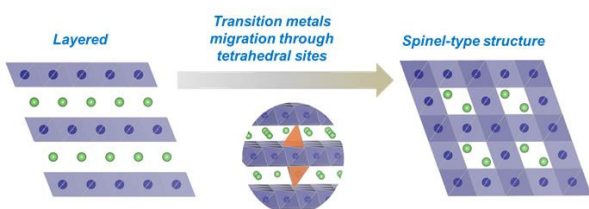


Figure IV - 144: Schematic illustration of layered to spinel-type phase transition

Therefore, the presence of Ga^{3+} ions in the transition metal layer and its preferential migration to tetrahedral sites may affect (block) the irreversible migration of other transition metals and, subsequently,

voltage fade during charge cycles. Nevertheless, the voltage fade during discharge, which is more directly related to the performance of the material, does not show a meaningful improvement due to the Ga substitution (see voltage fade during discharge in Figure IV - 143a and b). Note that the suppression of voltage fade only in the charge profile leads to an increase in hysteresis between the charge and discharge profiles and, hence, a lower energy efficiency. This result indicates that the path of structural change leading to voltage fade is unaltered by Al or Ga substitution. It has been reported that Al or Ga substitution for Mn in layered LiMnO_2 materials marginally slows the layered to spinel transformation, but does not completely stop it. Certainly, for LMR-NMC, the large stoichiometric content of Mn could undergo the same fate. The formation of Jahn-Teller distorted trivalent Mn octahedra in the local environment during the discharge reduction cycle could be related to the transformation. However, reports in the literature have not precisely determined large Mn redox change, and accordingly a Jahn-Teller driven mechanism leading to spinel then voltage fade has not been invoked to this point. In contrast, the same degree of voltage fade observed in Al or Ga substituted LMR-NMC implies the material's strong tendency to undergo cation rearrangements as a result of the creation of oxygen vacancies during the initial activation cycle and not due to Jahn-Teller effects. More efforts are required to understand and control the initial activation process for LMR-NMC materials if the voltage fade problem and energy loss are to be solved.

The effects of Al and Ga substitution on suppressing voltage fade in $\text{Li}_{1.2}\text{Ni}_{0.15}\text{Mn}_{0.55}\text{Co}_{0.1}\text{O}_2$ cathode materials were systematically evaluated by using a voltage fade test protocol. The data show little-to-no effect from the cation substitution. Despite some hints of structural modification during charge via electrochemical measurements, the $\leq 10\%$ degree of cation substitution may not be enough to impose significant structural stability to the layered-layered composite cathode, which is subject to significant rearrangement of transition metals as a result of oxygen loss and lithium extraction from the transition metal layer during the initial charge activation. Subsequent cycles presumably involve continued transition metal migration from octahedral sites in the transition metal layer through tetrahedral sites and into the lithium layer. The cation rearrangement adds impedance but also contributes to voltage fade and energy loss. While we expect that Al and Ga can reside in tetrahedral sites in the structure and potentially block transition metal movement, the approach did not appear to be effective. The results indicate that the voltage fade is a global process, which is difficult to be completely stopped by small modification through non-redox atom substitution.

Cr substitution. The incorporation of Cr into a Li-Ni-Mn-O based LMR-NMC was completed. The

XRD patterns of the synthesized phases are shown in Figure IV - 145.

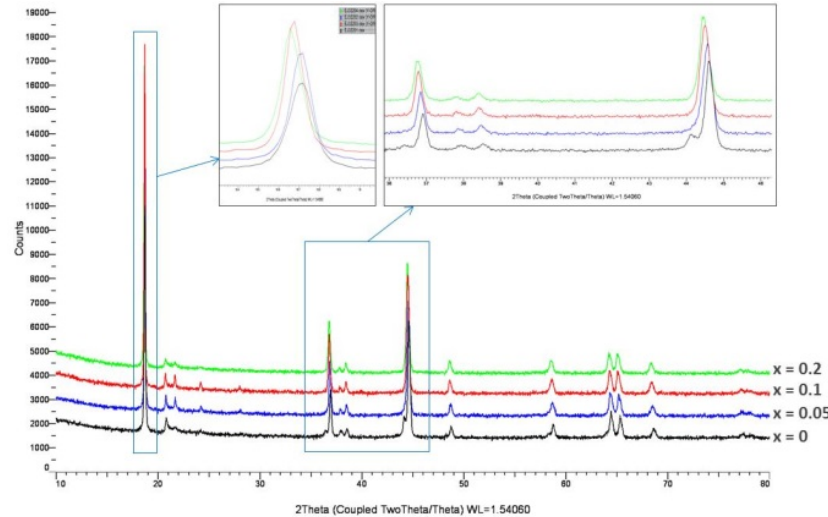


Figure IV - 145: Powder XRD patterns of Cr-substituted $\text{Li}_{1.2}\text{Ni}_{0.2-x/2}\text{Mn}_{0.6-x/2}\text{Cr}_x\text{O}_2$

The pristine sample shows a spinel marker, but with Cr-substitution the spinel phase begins to disappear at the expense of Mn decreasing amount. The layering low-angle peak reflection is shifted to lower angles as the result of Cr-substitution which is indicative of lattice expansion as a result of larger Cr^{3+} cations: ($R[\text{Ni}^{+2}_{1/4}\text{Mn}^{+4}_{3/4}] = 0.57\text{\AA}$, $R[\text{Cr}^{3+}] = 0.615\text{\AA}$). The LiMn_6 cluster ordering peaks become stronger with low degree of Cr-subst. at $x=0.05$ and $x=0.1$.

Figure IV - 146 shows the electrochemical voltage profile of the Cr series of materials. The greater the content of Cr, then the shorter the activation plateau which is indicative of the decrease in Mn in the composition. The activation plateau could be associated with the content of LiMn_6 units in the composite.

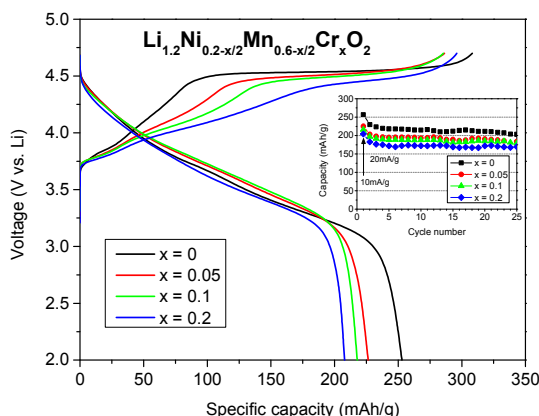


Figure IV - 146: Electrochemical voltage profile of the first cycle for Cr-subst. LMR-NMC series of compounds with $\text{Li}_{1.2}\text{Ni}_{0.2-x/2}\text{Mn}_{0.6-x/2}\text{Cr}_x\text{O}_2$

The extent of voltage fade is not countered from the alteration of the phase in Cr samples as is evident in the plot in Figure IV - 147. In fact the rate of voltage fade appears larger in such samples.

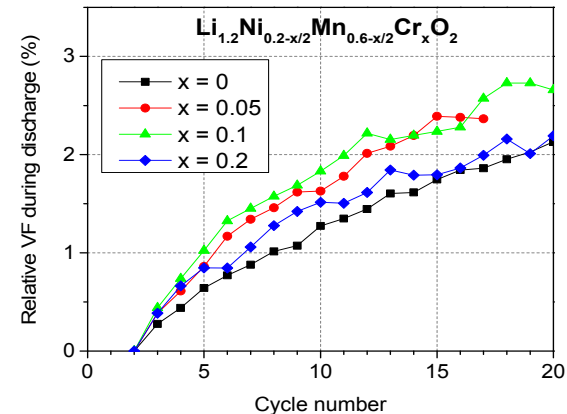


Figure IV - 147: Voltage fade percent change as a function of cycle number for $\text{Li}_{1.2}\text{Ni}_{0.2-x/2}\text{Mn}_{0.6-x/2}\text{Cr}_x\text{O}_2$

e. Structural Alterations

Layered-layered-spinel compositions. The particle size of the starting materials and the homogeneity of the transition metals likely puts a lower bound on domain size. The ultimate domain size is controlled by the diffusion lengths of the metals during synthesis. This is a function of the time, temperature, particle morphology, precursor structure, etc.

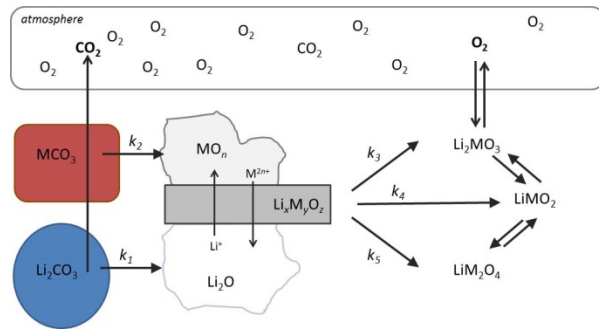


Figure IV - 148: Schematic of reaction mechanism which represents formation of LMR-NMC materials

The schematic in Figure IV - 148 represents a mechanism of formation of the LMR-NMC. Five rate constants are supposed for the mechanism wherein the decomposition of the carbonates is first taken into account. As the resultant lithium oxide and metal oxide products begin to calcine the formation of $\text{Li}_x\text{M}_y\text{O}_z$ takes place. Rearrangement of the lattice to accommodate either LiMO_2 , Li_2MnO_3 , or spinel LiMn_2O_4 will be controlled and are defined by the other three rate constants. The k_3 rate constant is likely large and dominates in formation of LMR-NMC materials.

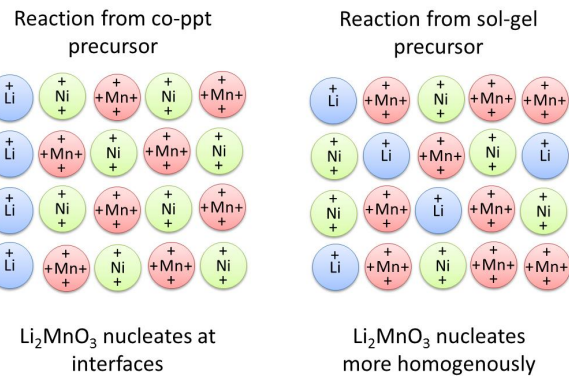


Figure IV - 149: Schematic of microscopic view of the synthesis of LMR-NMC

In Figure IV - 149, this schematic visually represents the scenario where the diffusion of Li will either form nucleates of Li_2MnO_3 at interfaces in LMR-NMC for a reaction involving transition metal precursors like oxalates, hydroxides or carbonates, or the situation where, Li is originally in the sol-gel matrix that would favor the nucleation of Li_2MnO_3 in LMR-NMC more homogeneously.

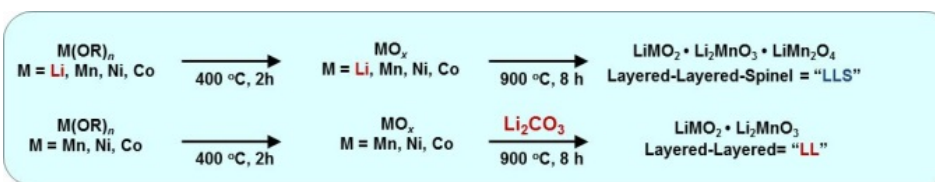


Figure IV - 150: Synthetic protocol for synthesizing either 'layered-layered' (LL) or 'layered-layered-spinel' (LLS) composites for studying voltage fade behavior in LMR-NMC cathodes

The control of the redistribution of Li as outlined in Figure IV - 150 in the reaction protocol for synthesis of nominal Toda HE5050 $\text{Li}_{1.2}\text{Mn}_{0.55}\text{Co}_{0.1}\text{Ni}_{0.15}\text{O}_{2+\delta}$ is possible based on the order of addition of Li. Figure IV - 151 compares the voltage profile of the nominal material on the first cycle. The LLS seems to result in a

splitting of LiMO_2 into Li_2MnO_3 and LiMn_2O_4 components effectively making a longer first charge cycle voltage plateau, and a small plateau at about 2.8 V indicative of a spinel signature in the material. The XRD pattern of the samples supports this interpretation of the electrochemical data.

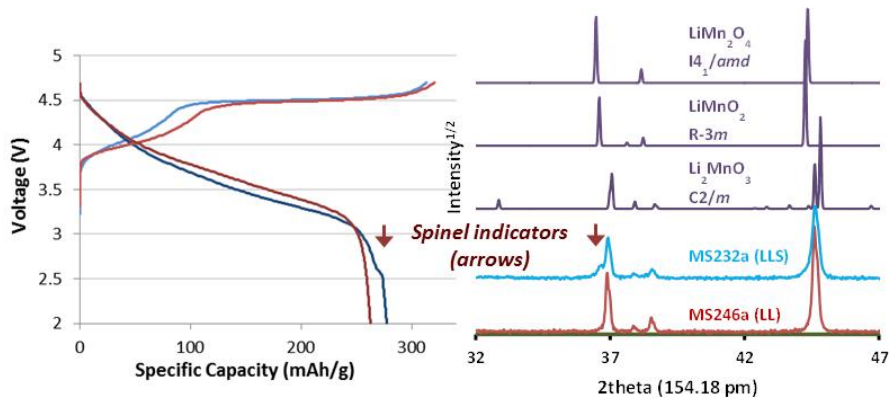


Figure IV - 151: Left side: voltage profile (first cycle) of LL and LLS with nominal composition: $\text{Li}_{1.2}\text{Mn}_{0.54}\text{Co}_{0.1}\text{Ni}_{0.15}\text{O}_{2+\delta}$. Right side: powder XRD patterns of products from LL and LLS synthesis. The LLS or LL can be tuned based on the order of addition of Li salt in the reaction. The arrows in both figures shows the markers for spinel as either a short plateau in the voltage profile at about 2.8 V, and a diffraction peak that corresponds to spinel at about 36 degrees 2-theta

For Figure IV - 152, we see the electrochemical summary showing the capacity observed for LL and LLS over 20 cycles. A direct voltage fade comparison of the two classes of materials are possible since the amount of Li cycled is approximately equivalent.

Unfortunately there is not a mitigation of voltage fade in either case. While exhibiting similar specific capacity LLS composite has lower average V-iR. The LL composite essentially evolves into a LLS composite after a few cycles.

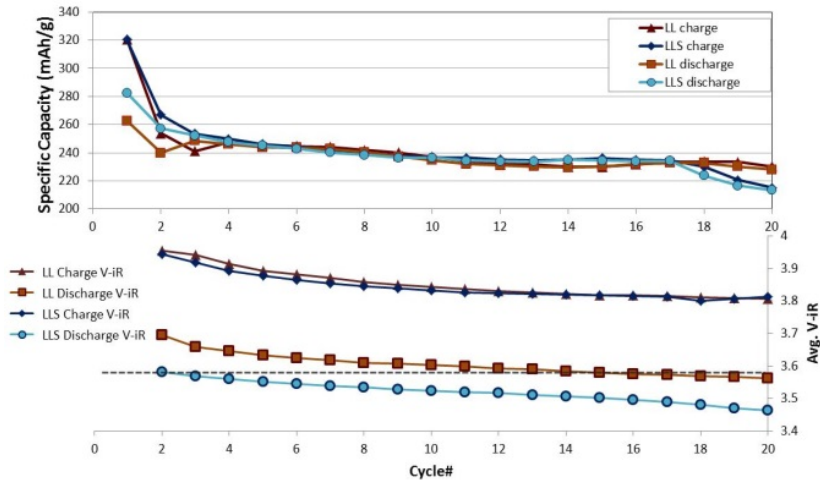


Figure IV - 152: Specific capacity of LL and LLS cathode materials (top), and the voltage fade response (lower figure)

f. Effect of Oxygen Partial Pressure During Synthesis

How oxygen chemistry and oxygen partial pressures affect the performance of LMR-NMC materials is relatively unexplored. It is not known, for example, how different oxygen partial pressures used in the calcination step affected the electrochemical behavior of LMR-NMC materials.

It is possible that oxygen chemistry or vacancies play a role in the voltage fade phenomenon. Oxygen vacancies or O_2^{n-} species may facilitate the migration of metal ions, which, in turn, have been suggested as the cause of the voltage fade phenomenon, transforming the layered-layered ($R\bar{3}m$) structure to one that is spinel-like ($Fm\bar{3}m$) structure during the charge-discharge

process. Oxygen vacancies may be formed during the activation of Li_2MnO_3 when lithium and oxygen are simultaneously removed from its structure. According to Qian et.al., the presence of one oxygen vacancy next to a manganese ion will lower the activation energy for the migration of that ion to as low as 0.7 eIV.

The redox chemistry of oxygen as proposed by Delmas, et al. as part of the mechanism of voltage fade in $\text{Li}_{1.20}\text{Mn}_{0.54}\text{Co}_{0.13}\text{Ni}_{0.13}\text{O}_2$. The presence and possible involvement of oxygen species other than O^{2-} in the voltage fade process has recently been reported by Tarascon. They observed electron paramagnetic resonance signals characteristic of O_2^- during cycling experiments using the model compound, $\text{Li}_2\text{Ru}_{1-x}\text{Sn}_x\text{O}_3$.

In this work, we report the effect of material preparing conditions, such as the oxygen partial pressure and the cooling rate, on their chemical composition, structure and electrochemical performance. The materials, $\text{Li}_{1.45}\text{Ni}_{0.15}\text{Co}_{0.167}\text{Mn}_{0.683}\text{O}_2$ and $\text{Li}_{1.25}\text{Ni}_{0.15}\text{Co}_{0.167}\text{Mn}_{0.683}\text{O}_2$, were chosen for study because the ratios of the transition metals were similar to those in the well-studied TODA HE5050 cathode material.

Hydroxide precursors with the transition metal ratio of 0.15:0.167:0.683 for Ni, Co and Mn, respectively, were obtained from the Materials Engineering Research Facility at Argonne National Laboratory. Two nominal compositions, $\text{Li}_{1.45}\text{Ni}_{0.15}\text{Co}_{0.167}\text{Mn}_{0.683}\text{O}_x$ and $\text{Li}_{1.25}\text{Ni}_{0.15}\text{Co}_{0.167}\text{Mn}_{0.683}\text{O}_y$ were obtained by homogeneously mixing the precursor with the appropriate amount of $\text{LiOH} \cdot \text{H}_2\text{O}$. These materials are denoted as high-lithium (HL-NMC) and low-lithium (LL-NMC), respectively. The HL-NMC and LL-NMC materials were annealed at 850°C for 12 h under oxygen

partial pressures of 1.0, 2.0×10^{-1} , 2.0×10^{-2} , and 2.0×10^{-3} atm. The balance of the gas mixtures was argon.

After being sintered for 12 h at 850°C, the materials were cooled to room temperature by either quenching or slow cooling. In the quenching experiment, the material was cooled by placing the powder between two thick metal plates, which were pre-cooled with liquid nitrogen. It took ~2–3 seconds to cool the materials to 25°C using this method. In the slow cooling experiment, the material was cooled to room temperature at a rate of 1°C/min.

These materials were then assembled into coin cells. Lithium metal was the anode and the cells were cycled using the voltage fade protocol. The elemental composition, determined by ICP-Mass spectrometry, of these materials is given in Table IV - 19.

Table IV - 19: Metals-only composition of materials prepared in this study

Sample name	pO_2 , atm	Composition				Lithium retained, %
		Li	Mn	Co	Ni	
Slow-cooled HL-NMC	2.0×10^{-3}	1.418	0.679	0.165	0.156	90.87
	2.0×10^{-2}	1.431	0.680	0.165	0.155	90.05
	2.0×10^{-1}	1.437	0.680	0.164	0.156	91.25
	1.0	1.448	0.679	0.163	0.157	91.95
Quenched HL-NMC	2.0×10^{-3}	1.427	0.678	0.165	0.157	90.58
	2.0×10^{-2}	1.429	0.679	0.165	0.155	90.71
	2.0×10^{-1}	1.432	0.680	0.165	0.155	90.91
	1.0	1.436	0.680	0.164	0.156	91.18
Slow-cooled LL-NMC	2.0×10^{-3}	1.241	0.681	0.161	0.158	90.92
	2.0×10^{-2}	1.275	0.681	0.162	0.158	93.40
	2.0×10^{-1}	1.278	0.681	0.162	0.157	93.63
	1.0	1.436	0.680	0.164	0.156	91.18
Quenched LL-NMC	2.0×10^{-3}	1.198	0.683	0.160	0.156	87.76
	2.0×10^{-2}	1.245	0.681	0.162	0.157	91.21
	2.0×10^{-1}	1.257	0.682	0.161	0.157	92.07
	1.0	1.269	0.681	0.162	0.158	93.00

Table IV - 19 shows that there is a correlation between the content of retained lithium and the oxygen partial pressure. This trend is shown in Figure IV - 153 for the LL-NMC materials. Clearly, the lithium content in the oxide was directly related to the oxygen

partial pressure. Using pure oxygen, the amount of lithium retained was higher than that using 2.0×10^{-3} atm oxygen. The relationship between pO_2 and lithium content in the HL-NMC materials was more

complex, but the general trend was the same as seen in Figure IV - 153.

LL-NMC cathodes: All the major peaks in the XRD patterns of the slow-cooled and quenched HL-NMC cathodes calcined under 2.0×10^{-2} atm or higher

oxygen partial pressure could be indexed in the $R\bar{3}m$ space group except for a few weak peaks in the 20° region between 20° and 27°. These peaks were indexed to the C2/m space group.

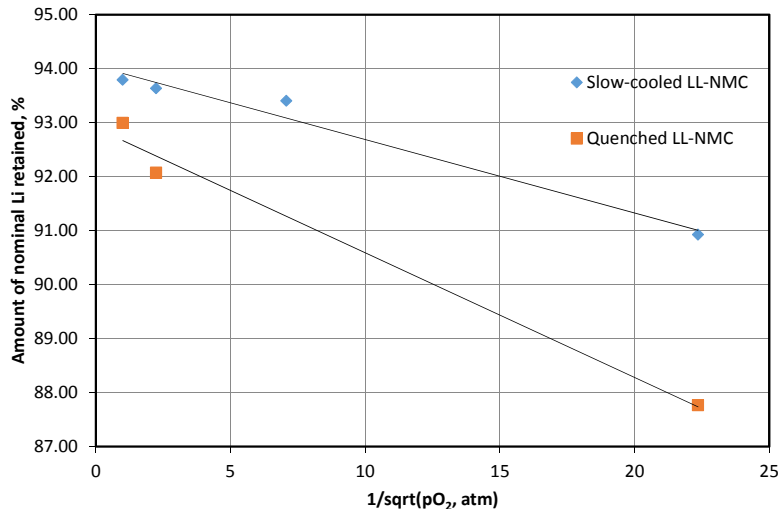


Figure IV - 153: Amount of nominal lithium retained vs. $1/\sqrt{p_{O_2}}$. The markers represent the data points and the lines, the least-squares fit of those data. The value of the regression coefficient, r^2 , in both cases was 0.98 or greater. High oxygen partial pressures are on the left-hand side of the x-axis

An important feature is the presence of a shoulder near 36.5° in the XRD patterns of slow-cooled HL-NMC cathodes calcined under low oxygen partial pressure (Figure IV - 154). Quenching seemed to

suppress the formation of this phase as the peak is more symmetrical in these samples. In general, all HL-NMC materials did not show this behavior clearly.

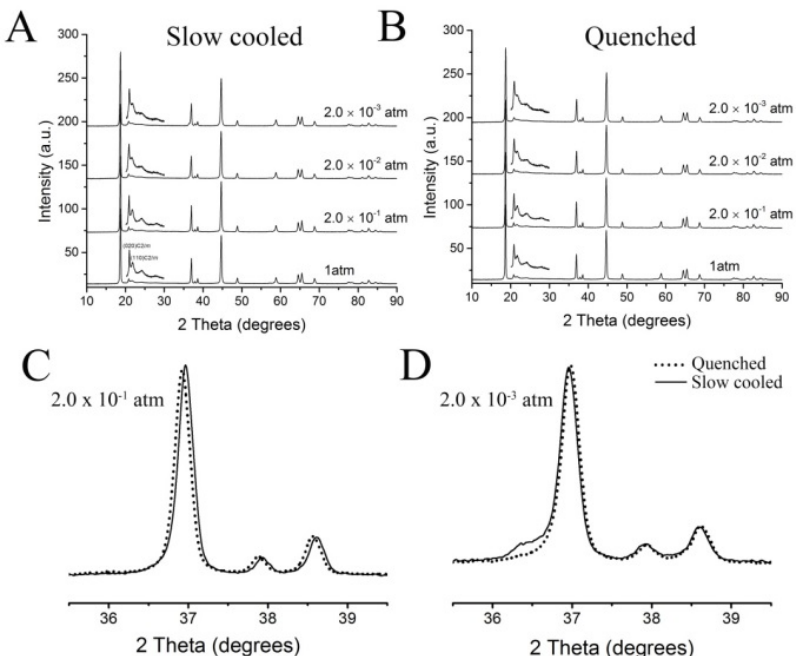


Figure IV - 154: A and B) XRD patterns of slow-cooled and quenched HL-NMC cathode materials calcined under different oxygen partial pressures with the patterns are indexed to $R\bar{3}m$ space group. **C and D)** comparison between slow-cooled and quenched HL-NMC samples showed the effect of quenching rate on the shape of the peak at ~36.5°. ($\lambda = 1.5406 \text{ \AA}$)

All the major peaks in the XRD patterns of LL-NMC materials were also indexed in the $R\bar{3}m$ space group. The biggest differences between XRD patterns of the LL-NMC and the HL-NMC materials were the clearly-visible peak near 36.5° and the shoulder near 44° in LL-NMC samples. Figure IV - 155 clearly shows the development of these features in the LL-NMC materials with the decrease of the oxygen partial pressure. The small shoulder near 36.5° , observed in the sample calcined under 1 atm oxygen, grew into a sharp peak at 2.0×10^{-2} atm oxygen partial pressure.

Figure IV - 154 and Figure IV - 155 present XRD spectra of, respectively, the HL-NMC and LL-NMC series of samples as a function of oxygen partial pressure and cooling rate during synthesis. All XRD patterns consist of a series of fundamental reflections (main peaks) that can be indexed to a layered ($R\bar{3}m$) structure, as well as a series of weak peaks in the 2θ region between 20° and 27° . These weak peaks are monoclinic ($C2/m$) superreflections stemming from regions with local Li_2MnO_3 order in the transition metal planes of the structure and are a common occurrence in LMR-NMC materials.

In addition to the expected peaks for standard LMR-NMC materials, the LL-NMC series shows additional superreflections that cannot be attributed to a layered structure. For example, figures 31.C and 31.D show a detail of the $35.5^\circ < 2\theta < 39.5^\circ$ region, containing the (101), (006) and (102) peaks at 37° , 38° and 38.75° , approximately. There is an additional peak closer to 36° , which in the slow cooled 2×10^{-1} atm O₂ sample is closer to the (101) reflection, showing as a shoulder at $\sim 36.5^\circ$. This peak, which cannot be attributed to a layered-layered structure, is indicative of spinel-like ordering of the lithium and transition metal atoms in some regions of the material, akin to the monoclinic Li_2MnO_3 regions responsible for the superreflections in the $20^\circ - 27^\circ$ range. In opposition to the rest of the HL-NMC series, the slow cooled 2.0×10^{-3} atm. O₂ HL-NMC sample also shows a very weak peak at $20 \sim 36.5^\circ$. This peak is absent in the corresponding quenched HL-NMC sample (see Figure IV - 154D), indicating that the cooling rate also plays a role in the development of spinel character in the structure.

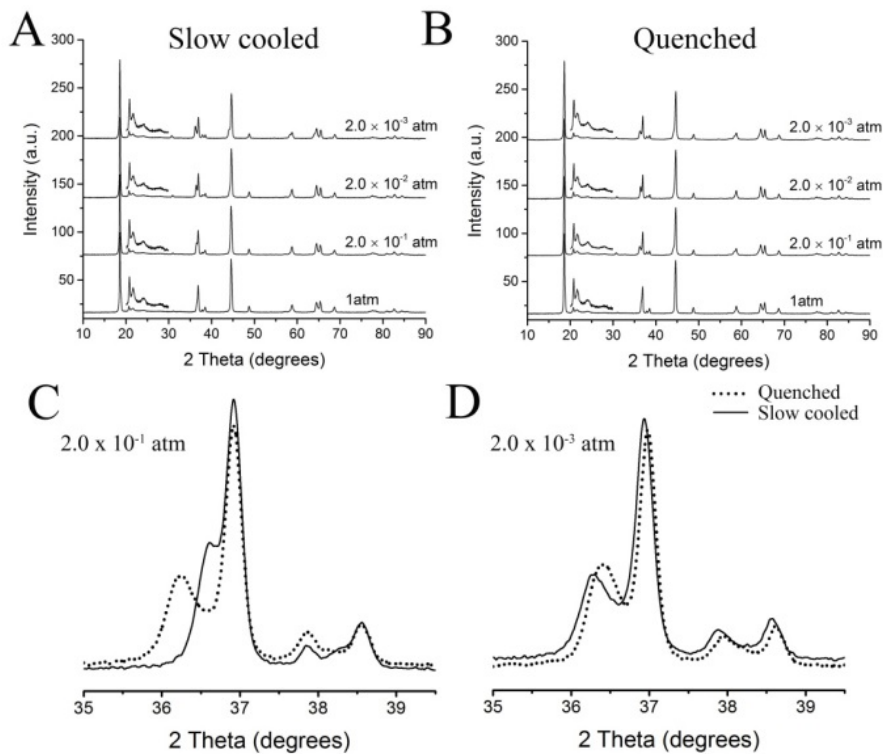


Figure IV - 155: A and B) XRD patterns of slow-cooled and quenched LL-NMC cathode materials calcined under different oxygen partial pressures. C and D) comparison between slow-cooled and quenched LL-NMC samples showing the effect of quenching rate on the shape of these peaks. ($\lambda = 1.5406 \text{ \AA}$)

The cooling rate also had an effect on the development of these features (see Figure IV - 154C and D). The XRD patterns of the quenched LL-NMC samples calcined using high oxygen atmospheres, $2.0 \times$

10^{-1} and 1.0 atm, actually showed sharper peaks near 36.5° than those seen in the XRD patterns from the slow-cooled samples. However, the cooling rate, apparently, did not affect the XRD patterns of the

samples calcined under 2.0×10^{-2} atm oxygen. Under this partial pressure, the peaks in the range of 20–27°, corresponding to the Li₂MnO₃ component, were also observed for all LL-NMC samples calcined under 0.002 atm oxygen and higher.

The initial charge and discharge capacity for Charge0 and Discharge0, respectively, as well as the capacity of the 20th discharge cycle of materials studied are given in Table IV - 20.

In general, those materials prepared at high oxygen partial pressures tended to display higher initial charge and discharge capacities. The measured capacities show strong correlation with the lithium retention after calcination as shown in Table IV - 19, as expected. For LL-NMC materials, the cooling method also impacted the initial charge and discharge capacities. For a given

pO₂, the slow-cooled materials tended to display higher capacities than the quenched ones.

Additionally, there was less irreversible capacity loss for HL-NMC prepared at 2.0×10^{-1} and 1 atm oxygen partial pressures, ~17%, than those prepared at 2.0×10^{-3} and 2.0×10^{-2} atm, 22–59%. For LL-NMC materials, those prepared using 1 atm oxygen displayed less capacity loss (~21%) than those prepared using lower oxygen partial pressures (~26%).

All samples displayed voltage fade during the cycling experiment. To facilitate the comparison on the rate of voltage fade, a plot of the change in relative average voltage is shown in Figure IV - 155. Here, all materials displayed a similar degree of voltage fade, ~2.5–3.5%, over the course of 20 cycles.

Table IV - 20: Dependence of charge and discharge capacity on pO₂, lithium content and cooling method

Material	pO₂, atm	Capacity, mAh g⁻¹		
		Charge0	Discharge0	Discharge20
Slow-cooled HL-NMC	2.0×10^{-3}	316.82	243.68	190.85
	2.0×10^{-2}	328.13	257.34	200.47
	2.0×10^{-1}	322.15	268.16	223.80
	1.0	321.68	268.46	225.47
Quenched HL-NMC	2.0×10^{-3}	326.38	256.44	204.98
	2.0×10^{-2}	326.78	254.57	202.16
	2.0×10^{-1}	327.97	265.22	203.39
	1.0	328.28	273.24	224.35
Slow-cooled LL-NMC	2.0×10^{-3}	245.1	182.51	169.33
	2.0×10^{-2}	246.37	181.32	170.77
	2.0×10^{-1}	278.61	209.27	179.52
	1.0	291.58	231.21	190.74
Quenched LL-NMC	2.0×10^{-3}	264.09	193.46	160.28
	2.0×10^{-2}	222.35	157.07	152.87
	2.0×10^{-1}	266.19	194.94	156.16
	1.0	277.36	210.38	182.62

Particle size shape and texture and the impact on voltage fade-Imaging of LMR-NMC: Particles and Electrode Laminates

The imaging work herein aims to establish the correlation between microstructural characteristics and electrochemistry for a better understanding of battery materials degradation at the single particle level. One possible approach to controlling voltage fade was particle morphology and while the different synthesis methods described above gave significantly different

particle size and morphology a detailed analysis of them interaction of morphology and electrochemistry was undertaken. Nanoscale X-ray fluorescence imaging is used to measure the changes in transition metal elemental composition in single particles of LMR-NMC before and after electrochemical cycling, as well as after lamination. The volume to surface area ratios of the particles is determined with nanotomography. The combination of fluorescence measurements with 3-D nanotomography reconstruction procedures can provide detailed qualitative and quantitative elemental

information. Such procedures allow mapping of the inside volume of the single particles with nanometer size resolution (30-50 nm) to obtain local differences in elemental concentrations.

Experimental

A laminate containing Toda HE5050 LMR-NMC cathode was cycled vs. graphite in Gen 2 electrolyte at C/2 in a pouch cell. The laminate was made and cycled by the ANL CAMP Facility. After 1000 cycles, the test was terminated; the laminate was removed from the cell in an Ar filled glovebox and washed with DMC. Particles from the cycled laminate and particles from the same *uncycled* laminate were scraped off from the Al foil and physically broken up. Next, the particles were soaked in NMP and sonicated for 15 min, three times. The solution was filtered using 2 μm filter paper. Then the solids were scraped off from the paper and dissolved in NMP again. The sonication and filter steps were repeated in order to separate the oxide particles from other laminate residues. The solids caught from the second filtering were dispersed in a large amount of NMP so as to produce a clear the solution. Drops of this solution were placed on substrates and the NMP was allowed to dry overnight before mounting in the SEM. Pristine particles (never laminated) were also prepared as described but without filtering. The single particles were ultimately mounted on a tungsten tips using Pt and C solders from the FIB at the EMC by PI Miller.

The tips mounted with LNR-NMC single particle were measured at beamline 26 ID-C. Images were obtained by the use of a CCD X-ray camera, with an incident X-ray energy of 10 keV. A full tomography data set was collected from -90°-90° with 1° steps, 5 exposures, and exposure time of 1 s for each step. Total collection time was approximately 30 min for each tomography set. Images were corrected using background images which were taken after every 5 scans. Full Florescence data sets were taken at 0, -45, -90, +45, and +90 degrees with about 50 nm resolution.

The pouch cell was subjected to electrochemical cycling from 2.5 to 4.4 V with a constant current density of 200 mA/cm² (C/2 rate). Figure IV - 156 shows the cycle performance for the cell. As illustrated in Figure IV - 156a, the electrode material can deliver a capacity of ca. 400 mAh during the first few cycles. But it shows gradual capacity decay with cycling. After 650 cycles the cell shows a capacity of 320 mAh, with 25% capacity fading. The detailed voltage profiles are presented in Figure IV - 156b. Expectedly, the shape of the curves changes with cycling. In particular, voltage fade is significant during the early cycles (first 6 cycles), and slows with cycle number. Since this was a full cell with many layers of anodes and cathodes, the cell underwent 3 formation cycles before the activation cycle in cycle 4.

X-ray tomography of three different types of samples including a fresh, pristine particle (FP), an

uncycled laminate particle (LP), and a cycled laminate particle (CLP) were first collected in transmission mode, which gives 3D maps of the density with a resolution of about 14.8 nm per pixel. The cross-sectional images (generated by rotating and translating the sample) produce accurate representations of thin slices of the test particle. Figure IV - 157 shows the 2D slices of each type of particle based on the classical Filtered Back-projection (FBP) reconstruction method. Since we measure the absorption contrast, the gray levels in a slice image correspond to X-ray attenuation. Thus, the density and composition of the material are being imaged, allowing a direct comparison of the observed features in the reconstruction for different samples. The resulting 2D slices were stacked to form the 3D volume.

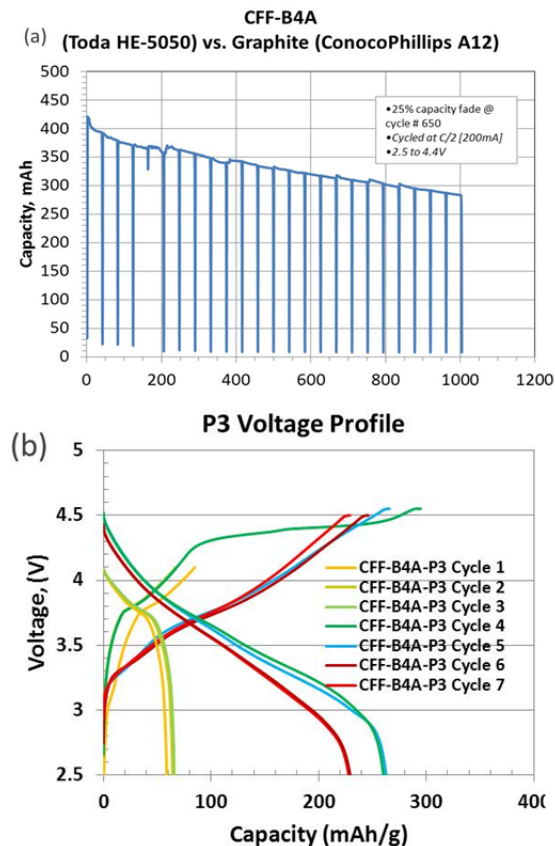


Figure IV - 156: (a) Cycle life performance; (b) Voltage profiles for the first 7 cycles

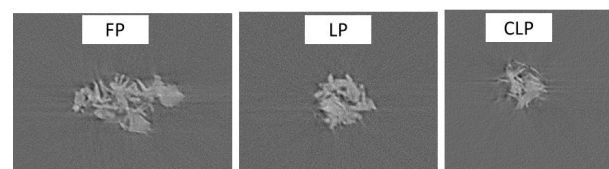


Figure IV - 157: A typical cross-section reconstructed by FBP, approximately through the center of the particle by tomographic reconstruction of the raw data

Figure IV - 158 shows the 3D cropped volume rendering of the single particle of FP and CLP acquired with the technique. This 3D volume is used to study the internal three-dimensional structure, and is particularly important for observing the morphology of complex nanostructures. The platelet-like texture of the particle is clear visible in the fresh particle, but it is not evident in the cycled particle.

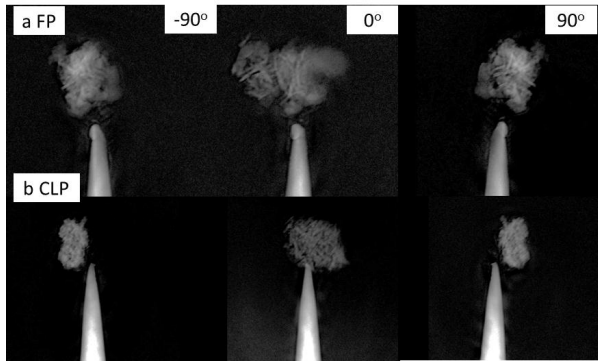


Figure IV - 158: Cropped volume rendered view of the reconstructed data from earlier figure. The data for complete 3D reconstruction were composed of 180 such images as they were collected through a total of 180° rotation

Data analysis to date has revealed a drop in the volume to surface area ratio of the particles as a function of both laminating and cycling. High resolution images of 3 of the 9 particles (one of each type) are shown in Figure IV - 159.

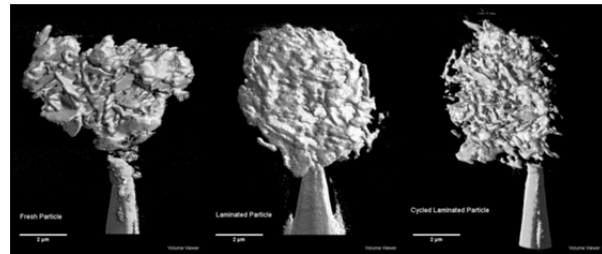


Figure IV - 159: 3-D renderings of FP (left), LP (middle), and CLP (right)

The corresponding volume to surface area ratios for all 9 particles are plotted in Figure IV - 160 (top). With the exception of one outlier among the cycled particles, we can deduce that the surface area of the particles increases because the volume is assumed fixed, albeit no single particle was analyzed both before and after cycling. Increases in particle surface area can arise from cracking during lamination/rolling, or cracking from activation and cycling which is more prevalent. Pictures in Figure IV - 157, when viewed with rotation, indicate that the cycled particles have much higher internal surface areas, perhaps due to the erosion of surfaces in contact with electrolyte. It is believed that the particle – electrolyte contact area can increase due to the strain on the particle during activation (i.e., if oxygen is being expelled in any quantity). Crack formation during cycling has been seen with *in situ* TEM by PI Miller.

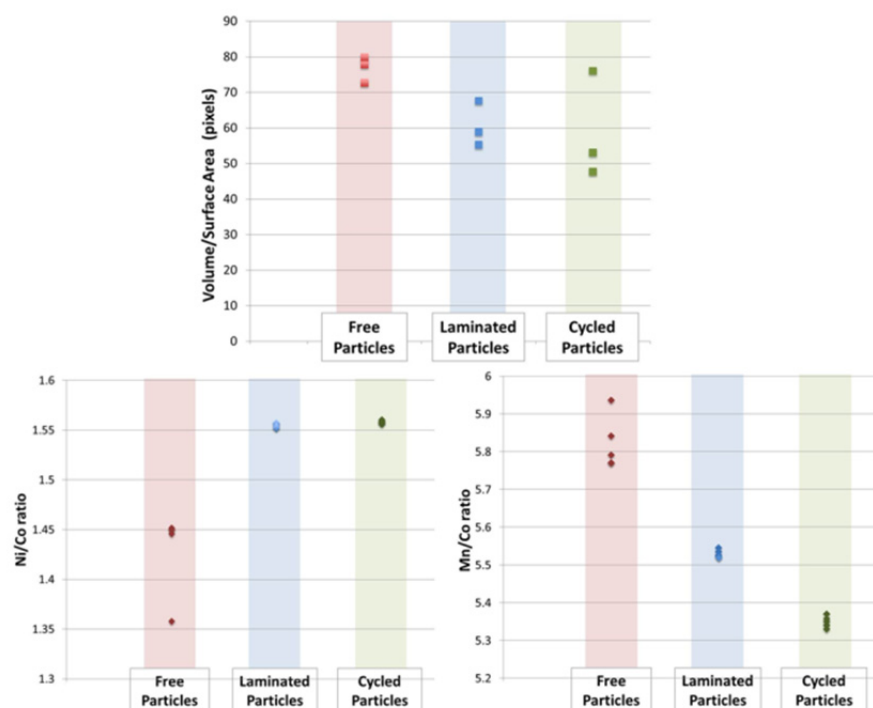


Figure IV - 160: (top) Volume to surface area ratios (in pixels) for all nine particles analyzed with nanotomography. (bottom) Three readings of transition metal ratios in each of one particle per type as determined by fluorescence

Fluorescence data averaging the total transition metal ratios in each particle are shown in Figure IV - 160 (bottom). One early conclusion from this data is that the particles, on average, have more homogenous transition metal distributions, particularly in reference to Mn, after prolonged cycling. The free particles show the largest spread in Mn/Co ratio throughout the sample. This ratio lessens, likely due to Mn-loss, and the spread in the measurement decreases with cycling.

Data analysis and manuscript preparation for the Advanced Photon Source nanofluorescence and nanotomography studies of single particle Toda HE5050 is ongoing. The final data sets will show the distribution of the three transition metals (Co, Ni, Mn) on the surface of the particles and core of the particles before and after cycling. Figure IV - 161 shows steps in the process of modeling this data. First a cross section is binarized to show matter from non-matter. Then, erosion and dilation modeling is performed to accurately determine the size of the cross section. From here, maps of the transition metals are overlaid onto the cross-sections, information is gathered on the fit, and the process is iterated. The lead scientist for this effort is Benjamin Stripe. This information will be compared to previous reports of Ni-segregation at grain boundaries [1], densification of the material [2], and changes in transition metal homogeneity [3]. Whether or not there are significant changes, the resulting information will play a part in the cumulative understanding of voltage fade.

Layered-Layered-Spinel Electrodes

There is general consensus based on the structural work within the voltage fade project that the voltage fade phenomenon results from the migration of transition metals into the lithium-rich layer, which leads to highly complex atomic configurations in

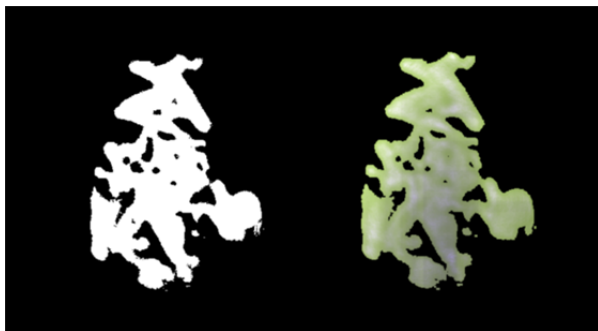


Figure IV - 161: (left) Binarized cross-sections of single particle. (right) A step in the process of overlaying Mn (green) onto the cross section

electrochemically activated and cycled cathode structures; it has been proposed that a partially reversible migration of the transition metals between sites in alternate layers of the close-packed electrode

structure during charge and discharge is responsible for the hysteresis effects in the charge/discharge profiles of the cells. The concept of synthetically embedding a structurally-compatible and stabilizing spinel component into ‘layered-layered’ composites to form ‘layered-layered-spinel’ composite structures has been explored. The rationale behind this approach is that in $\text{Li}[\text{M}_2]\text{O}_4$ (and in electrochemically lithiated spinel $\text{Li}_2[\text{M}_2]\text{O}_4$ (rocksalt) products) 25% of the M cations are located in the lithium-rich lithium layers, thereby providing significant binding energy to maintain the stability of the close-packed oxygen array during lithium extraction. Two different synthetic methods have been utilized to synthesize ‘layered-layered-spinel’ composites by lowering the lithium content in various $x\text{Li}_2\text{MnO}_3 \bullet (1-x)\text{LiMO}_2$ ($\text{M}=\text{NMC}$) electrode compositions and by tailoring the voltage window to stabilize the electrode against electrochemically-induced degradation. The first method involved the acid-treatment of a Li_2MnO_3 precursor in the presence of the desired amounts of transition metal ions for a particular electrode composition following a previously reported procedure [Croy, BATT project]. This method is referred to as the ‘ Li_2MnO_3 method’. The second synthesis method was an oxalate co-precipitation route using transition metal oxalate precursors, MC_2O_4 ($\text{M}=\text{Mn, Ni, Co}$). This synthesis method is referred to as the ‘oxalate method’. Research of ‘layered-layered-spinel’ materials, particularly the development of alternative synthesis methods, compositional and electrochemical optimization, and surface protection, is currently being undertaken in a performance-driven BATT project (Thackeray et al.). In order to study the metrics associated with voltage fade and the stabilization of ‘layered-layered’ electrodes, various ‘layered-layered-spinel’ compositions were selected and evaluated as part of the voltage fade program. The baseline ‘layered-layered’ compounds were, in composite notation, $x\text{Li}_2\text{MnO}_3 \bullet (1-x)\text{LiMn}_y\text{Ni}_{0.125}\text{Co}_{0.250}\text{O}_2$ with $x = 0.25$ and 0.33 and $y = 0.125, 0.25$, and 0.375 . ‘Layered-layered-spinel’ compounds with targeted spinel contents of 6%, 15% and 25% were prepared by reducing the Li content following a previously reported procedure [Park]. Note that these are targeted compositions because it is difficult to control the precise oxygen content in these materials; indeed, in our studies conducted thus far, the electrochemical profiles suggest that the amount of the spinel component is less than the targeted amount and that there is a corresponding increase in layered character. Transmission electron microscopy confirmed the presence of spinel domains in a ‘layered-layered-spinel’ product synthesized by the Li_2MnO_3 method that targeted a slightly lithium-deficient $0.25\text{Li}_2\text{MnO}_3 \bullet 0.75\text{LiMn}_{0.375}\text{Ni}_{0.375}\text{Co}_{0.250}\text{O}_2$ composition with 15% spinel, as shown in Figure IV - 162.

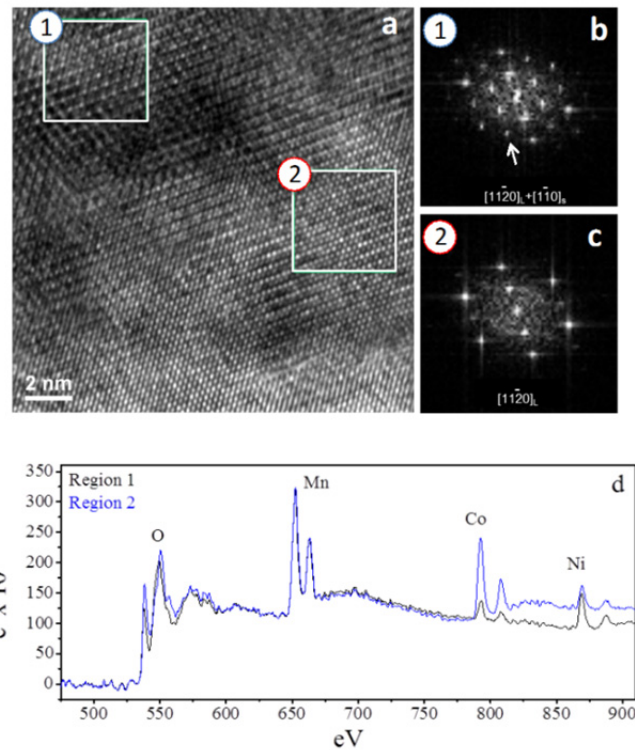


Figure IV - 162: (a) HRTEM image and (b-c) local structural information from Fast-Fourier Transforms of regions 1 and 2. Extra rows of spots indicated by the white arrow in (b) indicate that region 1 contains a spinel structure. (d) EELS data from regions 1 and 2 in (a) and normalized to the Mn edge, indicating that the spinel region contains more Ni than Co

Figure IV - 162a shows a HRTEM image revealing a domain structure within the product grain. Local structure information extracted from the HRTEM image using a Fast Fourier Transform (FFT) for the regions marked in Figure IV - 162a is shown in Figure IV - 162b and Figure IV - 162c. The row of spots, indicated by the white arrow in Figure IV - 162b, corresponds to a spinel configuration, which is not present in the ‘layered-layered’ region of Figure IV - 162c.

Compositional information obtained by electron energy loss spectroscopy (EELS) for the two domains marked in Figure IV - 162a is provided in Figure IV - 162d. Normalized to the Mn edge, these spectra show that the spinel domains (spectra 1, black line) have less Co and relatively more Mn and Ni compared to the ‘layered-layered’ domain (spectra 2, blue line). The characterization results showed that the spinel component is well integrated into the ‘layered-layered’ composite material.

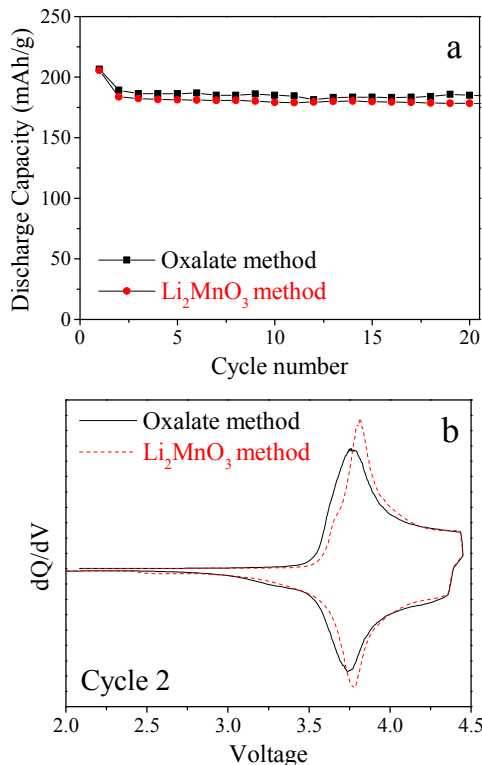


Figure IV - 163: Electrochemical comparison of ‘layered-layered-spinel’ electrodes fabricated by the ‘oxalate’ and ‘ Li_2MnO_3 ’ methods showing (a) discharge capacities as a function of cycle number, and (b) second cycle $d\text{Q}/d\text{V}$ profiles

An electrochemical comparison of two ‘layered-layered-spinel’ electrodes with a targeted 15% spinel content prepared by the ‘oxalate’ and ‘ Li_2MnO_3 ’ methods (i.e., the same lithium-deficient $0.25\text{Li}_2\text{MnO}_3 \bullet 0.75\text{LiMn}_{0.375}\text{Ni}_{0.375}\text{Co}_{0.250}\text{O}_2$ composition used for the TEM studies) is shown in Figure IV - 162. Cells were initially charged to 4.6 V to activate the Li_2MnO_3 component, and thereafter cycled between 2.0 V and 4.45 V at 15 mA/g. These cycling conditions were chosen to extract as much capacity as possible while maintaining stability, both structural and related to electrolyte decomposition, both of which are compromised with cycling to higher voltages. On the second and subsequent cycles, both electrodes delivered ~ 190 mAh/g (Figure IV - 163a). The $d\text{Q}/d\text{V}$ plots of the charge/discharge profiles (Figure IV - 163b) confirmed the similarity in electrochemical behavior of the electrodes when made by different methods, the ‘ Li_2MnO_3 method’ producing an electrode that provided a slightly higher cell voltage and slightly sharper redox features. The results showed that different synthetic routes can be utilized to yield ‘layered-layered-spinel’ composites with similar performance.

A series of ‘layered-layered-spinel’ electrode compositions with varying spinel content, synthesized by the ‘oxalate method’, was investigated

electrochemically. A plot of first-cycle capacity and first-cycle efficiency vs. lithium (spinel) content of a lithium cell containing the ‘ $\text{Li}_{x}\text{Mn}_{0.53125}\text{Ni}_{0.28125}\text{Co}_{0.18750}\text{O}_{\delta}$ ’ electrode ($0.25\text{Li}_2\text{MnO}_3 \bullet 0.75\text{LiMn}_{0.375}\text{Ni}_{0.375}\text{Co}_{0.250}\text{O}_2$) is shown in Figure IV - 165a.

The top x-axis shows the increasing target spinel content as a function of decreasing lithium content. The electrodes were first charged to 4.6 V and discharged to 2.0 V in lithium coin cells. The plot of solid squares indicates that the electrode capacity reaches a maximum by lowering the lithium content corresponding to spinel content of approximately 6%, after which the electrode capacity decrease. Lowering the lithium content, and thereby increasing the spinel content, increases the first-cycle efficiency significantly (open squares). Figure IV - 164b shows the discharge capacity for the series of samples with increasing spinel (Figure IV - 164a) with increasing rate. Increasing the spinel content significantly improves the rate performance when cycled between 2.0 – 4.6 V at the specified current density. The 25% target spinel content in particular shows dramatic improvement in discharge capacity at a current density of 150 mA/g. Figure IV - 164c shows the cycle 20 $d\text{Q}/d\text{V}$ plots for the series of increasing spinel content samples when continuously cycled between 2.0 – 4.45 V at 15 mA/g. The results showed that increasing the spinel content results in electrochemical activity at higher voltages on both the charge and discharge, which is indicative of the stabilizing role of the spinel component.

A comparison of the electrochemical behavior of ‘layered-layered-spinel’ electrodes derived from lithium deficient $x\text{Li}_2\text{MnO}_3 \bullet (1-x)\text{LiMn}_y\text{Ni}_y\text{Co}_{1-2y}\text{O}_2$ electrodes with a 15% targeted spinel content, for $x=0.25$ and 0.33 (i.e., different Li_2MnO_3 content) and $y=0.125$, $y=0.250$ and $y=0.375$, when cells are first activated at 4.6 V and subsequently cycled between 4.45 and 2.0 V, is provided in Figure IV - 165(a-c). The data indicate that, although electrodes with a higher Li_2MnO_3 content ($x=0.33$) provide the highest cycling capacities (open symbols in Figure IV - 165a), their electrochemical behavior is compromised by considerably more redox activity at lower potentials and a more pronounced voltage fade relative to those with a lower Li_2MnO_3 content ($x=0.25$).

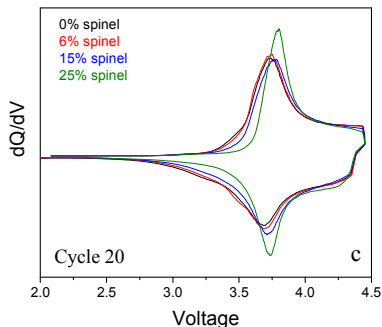
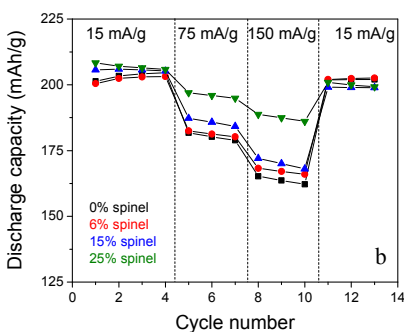
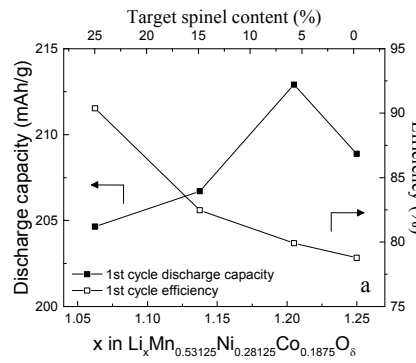


Figure IV - 164: (a) First cycle discharge capacity (■) and first cycle efficiency (□) as a function of x in $\text{Li}_x\text{Mn}_{0.53125}\text{Ni}_{0.28125}\text{Co}_{0.1875}\text{O}_\delta$, i.e., the target spinel content in the ‘layered-layered-spinel’ samples. (b) Discharge capacity for increasing spinel content as a function of increasing current density. (c) Cycle 20 dQ/dV for the series of increasing spinel content when cycled between 2.0 – 4.45 V at 15 mA/g

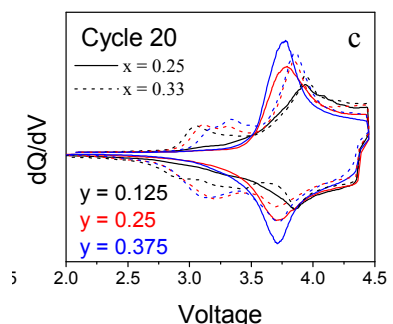
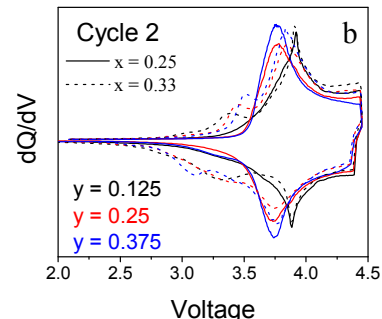
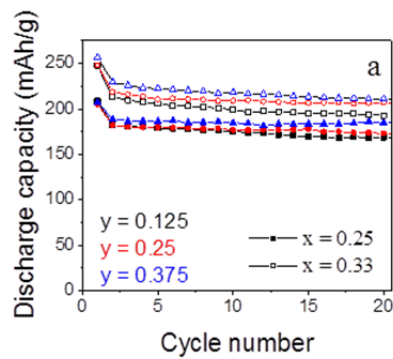


Figure IV - 165: (a) Cycle performance for lithium cells with ‘layered-layered-spinel’ electrodes derived from $x\text{Li}_2\text{MnO}_3 \cdot (1-x)\text{LiMn}_y\text{Ni}_{1-y}\text{O}_2$ compositions with $x=0.25$ (closed symbols) and $x=0.33$ (open symbols) for various values of y , and a targeted 15% spinel content. dQ/dV plots for (b) cycle 2 and (c) cycle 20 of the electrochemical data in (a)

The data also shows that reducing the Co content in the samples from $y = 0.125$ to $y = 0.375$ results in increased capacity as well as a sharper and more well-defined dQ/dV profile. The electrochemical data highlight the importance of optimizing Mn:Ni:Co ratio and the ratio of ‘layered-layered’ and spinel components in ‘layered-layered-spinel’ electrode structures. A rechargeable capacity of ~190 mAh/g and enhanced cycling stability with minimal voltage fade have been demonstrated when a voltage window of 4.45 - 2.0 V is used. This composition has therefore been selected for scale up and further electrochemical evaluation using the voltage fade test protocol at Argonne’s Materials Engineering Research Facility (MERF).

Conclusions and Future Directions

As the text above indicates the voltage fade team tackled all of the obvious approaches to modifying the LMR materials and in no case did they discover a material that eliminated the phenomena. There are several promising indications. First the lower lithium materials gave lower rates of voltage fade, but this was accompanied by lower energy density in the cathode material. Clearly composition has an effect on the rate of voltage fade but as yet no composition shows zero rate at high energy densities. However our detailed structure/synthetic analysis indicates that morphology has no impact on the rate of voltage fade. Alternative composite materials like the layer-layer spinel also show voltage fade when cycled to higher voltages. At this moment the only path for no voltage fade is to not to cycle the lithium that results in the unstable transition state leading to voltage fade.

The path forward for synthesis will involve discovering the most stable high energy composition where voltage fade is limited to slow or no rate. This is likely to require sacrifices on both capacity and energy density.

The Voltage Fade Team

Burrell, Anthony K.; Abouimrane, Ali; Abraham, Daniel; Amine, Khalil; Balasubramanian, Mahalingam;

Bareno Garcia-Ontiveros, Javier; Belharouak, Ilias; Benedek, Roy; Bettge, Martin; Bloom, Ira D.; Long, Brandon R.; Chen, Zonghai; Croy, Jason R.; Dees, Dennis W.; Dogan, Fulya; Gallagher, Kevin G.; Henriksen, Gary L.; Iddir, Hakim; Ingram, Brian J.; Johnson, Christopher; Key, Baris; Li, Yan; Lu, Wenquan; Miller, Dean J.; Ren, Yang; Slater, Michael D.; Thackeray, Michael M.; Vaughey, John T.; Wu, Huiming; Wu, Qingliu; Zhu, Ye; Yang, Zhenzhen; Lee, Eungje; Aoun, Bachir; Vu, Anh D.; Lin, Chi-Kai; Rinaldo, Steven G.; Tenant, Robert; Ban, Chunmei; Nanda, Jagit; Bugga, Kumar; Yang, Xiao-Qing; Mohanty, Debasish; Li, Jianlin; Payzant, Andrew; Wood, David; Daniel, Claus; Jansen, Andrew; Polzin, Bryant; Trask, Steven; Krundick, Greg.

References

1. M. Gu, I. Belharouak, A. Genc, Z. Wang, D. Wang, K. Amine, F. Gao, G. Zhou, S. Thevuthasan, D. R. Baer, J-G. Zhang, N. D. Browning, J. Liu, C. Wang, *Nanoletters*, 12, 5186 (2012).
2. A. Boulineau, L. Simonin, J-F. Colin, C. Bourbon, S. Patoux, *Nanoletters*, 13, 3857 (2013).
3. F. Yang, Y. Liu, S. K. Martha, Z. Wu, J. C. Andrews, G. E. Ice, P. Pianetta, J. Nanda, *Nanoletters*, 14, 4334 (2014).

IV.C.4 Adaptation Approaches: Synthetic and Operational Regime Approaches (ANL)

Voltage Fade Team

Argonne National Laboratory

9700 South Cass Avenue

Argonne, IL 60439

Phone: (630) 252-4516; Fax: (630) 252-4176

E-mail: Burrell@anl.gov

Start Date: October 2013

Projected End Date: September 2014

Objectives

Identify the fundamental causes of voltage fade and determine unknown electrochemical processes associated with the voltage fade phenomenon.

Technical Barriers

This project addresses the following technical barriers as described in the USABC goals:

- (A) Performance at ambient temperatures
- (B) Cycle life

Technical Targets

- PHEV specific energy targets (pack): 3.4 kWh (min) to 11.6 (max).
- EV specific energy targets (pack): 80 (min) to 200 (max) Wh/kg.

Accomplishments

- Voltage fade cannot be taken to “completion” by simple accelerated cycling
- Voltage fade cannot be accelerated by cycling at 65 C.



Introduction

Layered materials in the Li-Mn-rich portion of the Li-Ni-Mn-Co-O phase diagram (LMR-NMC), which are structurally integrated composites of Li_2MnO_3 and $\text{Li}(\text{Ni},\text{Mn},\text{Co})\text{O}_2$ and are usually written as $a\text{Li}_2\text{MnO}_3 \bullet (1-a)\text{Li}(\text{Ni},\text{Mn},\text{Co})\text{O}_2$, are promising cathodes for use in lithium-ion batteries. However, with cycling, the shape of the voltage vs. capacity curve

changes. A similar decline is also observed on charging, strongly suggesting that changes to the equilibrium electrochemical potential of the active material cause the voltage fade. In the literature, the continuous change in the shape of the discharge (and charge) curves has been attributed to the formation of a spinel-like phase. As a result of the loss in potential, there is a loss in energy, limiting the utility of these materials in energy-demanding applications, such as in electric vehicles.

Approach

One alternative to finding a solution to the inherent property of voltage fade is developing a method to accelerate the voltage fade so the process is over within very few cycles. Several approaches were considered, temperature and cycling methodology.

To assess the possible limitations of “break-in” cycling and its impact we have created a comprehensive electrochemical model that describes the processes occurring in the LMR-NMC system.

Results

Can we accelerate voltage fade through calendar life aging?

In a series of recent articles, we examined the effects of lower and upper cut-off voltages (LCV and UCV) during cycle life aging, and the effect of extended holding at high voltages (for example, 4.7V vs. Li/Li^+) on the rate of voltage fade (VF)^[1,2]. We found that VF is greatest during cycle life aging, especially when high UCVs are chosen. The VF rate is fastest when $\text{Li}_{1.2}\text{Ni}_{0.15}\text{Mn}_{0.55}\text{Co}_{0.1}\text{O}_2$ (LMR-NMC oxide) is cycled between ~3.2V and 4.7V vs. Li/Li^+ ; this rate even exceeded the value measured after extended holding at 4.7IV. This observation indicates that simple transition metal migration at the top of charge (in the delithiated state) does not suffice to explain the structural transformation(s) that cause VF.

However, if an LCV of around 3.0-3.4V, and simultaneously an UCV of 4.7V, are needed to obtain the highest VF rate, it is reasonable to assume that a single charge state exists in-between at which the fade rate is highest. Identifying such a single charge state was the primary goal of this effort. This work is of practical relevance because if such a single charge state exists below 4.7V at which voltage fade is pronounced, then VF can be accelerated and materials with little-to-no

further fade can be obtained by electrochemical means. i.e., we can design an initial cycling protocol to enable the oxide to achieve a “stable” crystal structure that shows no further fade.

Experimental

All tests were conducted in half cells containing the baseline TodaHE5050 oxide electrode^[1]. The cells first underwent one complete activation cycle (2-4.7V vs. Li/Li⁺). Then they were charged (or discharged) to various states of lithiation and rested for extended periods of time. After the resting period, the cells were first discharged to 2.0V, then examined by our standard VF testing protocol.

A few points to note: (i) Given the inherent hysteresis, we always need to differentiate between charge and discharge lithiation states. This means that a rest period at 3.55V during *charge* implies that the cells were charged from 2.0V to 3.55V. A rest period of 4.45V during *discharge* required a complete charge from 2.0V to 4.7V with a subsequent discharge to 4.45V. (ii) For practical reasons, we decided to probe the material’s VF after resting (zero current), and not after holding at the indicated voltages. No cycler channels are needed to monitor the material during rest, and therefore this approach is more convenient. Extended rest periods, however, are associated with a small, but continuous self-discharge, i.e., the cell voltage changes during the rest period. Rest periods

after the initial material activation were implemented after charge at 3.55V and after discharge to 4.45V. Testing was conducted for 1, 12, and 23 days at 30°C, 55°C, and 65°C.

Observations

Tests were conducted on multiple cells and large quantities of test data were collected. Only the most relevant data are presented here to highlight the trends displayed by the oxide; these trends are compared to the published VF data obtained on the baseline electrodes^[1].

Figure IV - 166 shows the effect of the state of charge on VF. Here, the corrected average voltages for charge and discharge, obtained from the VF protocol, are plotted for each cycle. When compared to the baseline, both cells rested at 3.55V and 4.45V show obvious differences. The cells rested at 4.45V upon discharge, show lower average voltages than the baseline electrode during charge and discharge. Although the corrected average voltages are lower than that of the baseline – one cannot explicitly claim that VF is “accelerated”. The testing time for these particular cells is 23 days plus about 1 day for each subsequent cycle during which the average voltage is measured. That is, the lower voltage is simply an effect of calendar-aging. Furthermore, the VF protocol shows that the oxide voltage continues to decrease. i.e., structural transformations continue in the material.

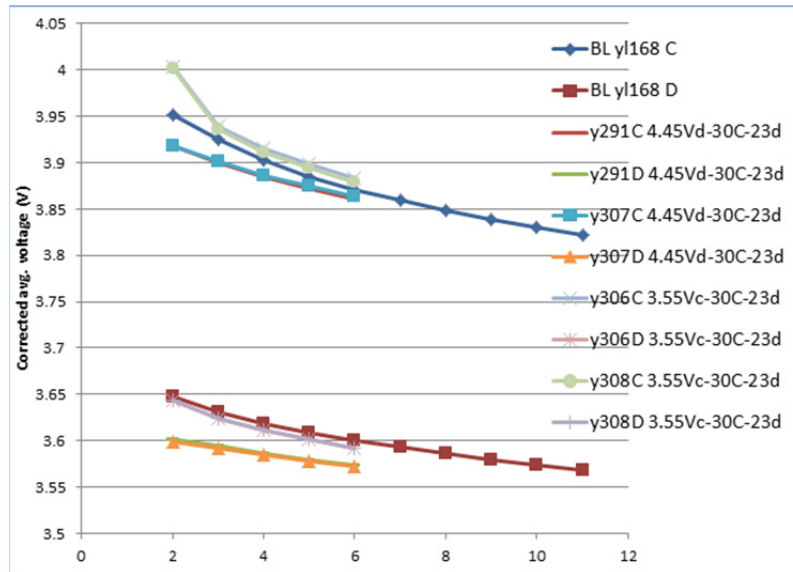


Figure IV - 166: State-of-charge effects during resting on VF at 30°C after 23 days. Corrected average charge and discharge voltages are plotted against the cycle number

Somewhat unexpected is the higher initial average voltage for the cells rested at 3.55V upon charge. This higher average voltage (“voltage rise”) occurs only during the initial charge; and the subsequent discharge reveals almost no difference to the baseline material, with average voltage and rate of fade being nearly the

same when compared to the baseline cell. Note that small differences can occur during cycling due to some inherent limitations of the measurement methodology^[1], and may not necessarily reflect structural differences. In any case, the initial rise of the average voltage is real, as

all measurements are conducted by cycling between 2.0V and 4.7IV.

Figure IV - 166 and Figure IV - 167 show how temperature and rest time affect voltage for the cells rested at 4.45V during discharge. Figure IV - 166 shows that higher the temperature, greater the fade. Figure IV - 168 shows that longer the rest period, greater the fade. The VF protocol on the cell held for 23 days at 65°C shows negligible fade for the discharge voltage; however, the charge voltage continues to

decrease suggesting that structural transformation continue within the oxide. Cells resting at 3.55V during charge behave in a similar manner as discussed in Figure IV - 166: the initial rise in average charge voltage increases as temperature and rest time are increased. However, this effect is limited to the first charge after resting. The corrected average voltages for these cells fall right back onto the profile of the baseline with the first discharge.

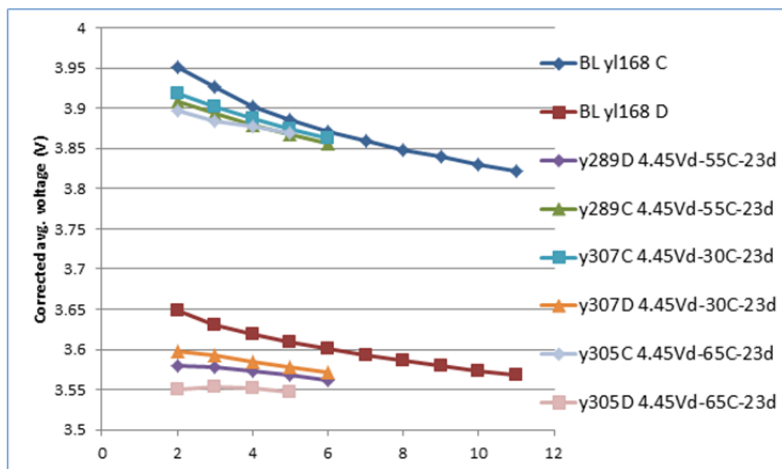


Figure IV - 167: Temperature effects on VF for cells rested at 4.45V during discharge after 23 days. Corrected average charge and discharge voltages are plotted against the cycle number

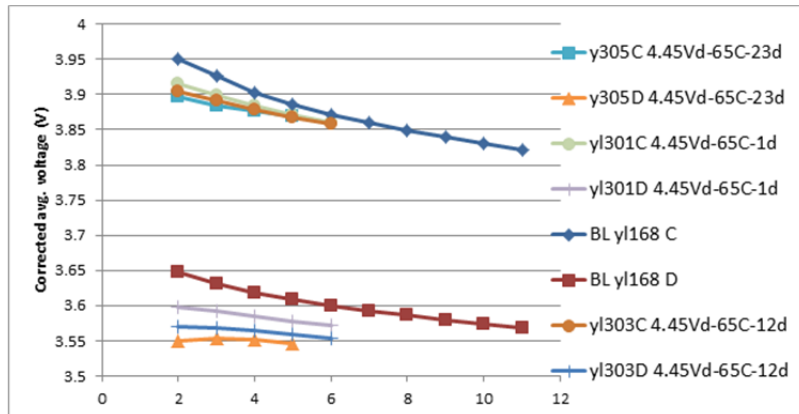


Figure IV - 168: The effect of rest time on VF for cells rested at 4.45V during discharge at 65°C. Corrected average charge and discharge voltages are plotted against the cycle number

Figure IV - 169 shows the voltage vs. time curves during resting for a few selected, monitored cells for two different temperatures. During the first few minutes of resting, the cell voltage first rises to approximately

4.48V due to cell equilibration phenomena after discharging, before it continuously decays over hundreds of hours due to self-discharge and VF.

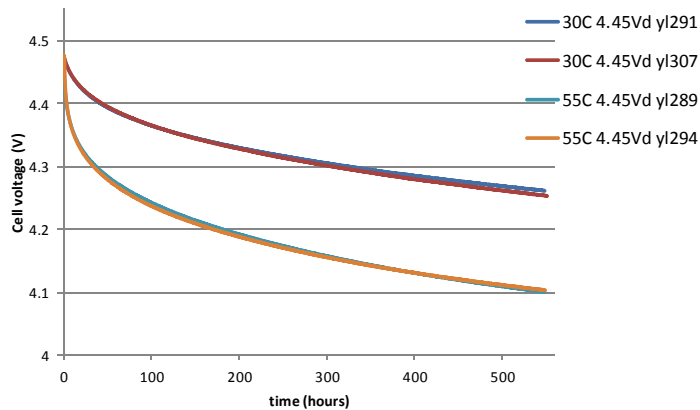


Figure IV - 169: Voltage decay for cells rested at 4.45V during discharge for about 22 days at 30°C and 55°C

Additional testing was also carried out at 3.55V, 3.8V, and 4.05V during *discharge* for 21 days at 65°C, in a similar manner to the experiments described above. The motivation for these additional experiments was to probe charge states between the above experiments (i.e. between 3.55V during charge and 4.45V during discharge), while avoiding any areas that lead to “voltage rise”. An elevated temperature of 65°C was chosen to increase the rate of fade. We find that the fade rate at these three states is always lower than that observed at 4.45V during discharge at 65°C, suggesting that the voltage fade measured during resting increases with increasing states of delithiation. This conclusion is in agreement with the 30°C holding data at 4.7V at very high states of delithiation, as reported by Gallagher^[2].

Additional testing was carried out at 3.55V during charge to check whether “voltage rise” impacts VF. Figure IV - 170 shows for one cell two consecutive VF protocols, each carried out after extended resting at 3.55V during charge. As described above, the first period includes a rest of 23 days, the second one a rest of 6 days. For comparison, data for one cell resting at 4.45V over the same amount of time are also included. Figure IV - 170 shows unambiguously that voltage rise occurs repeatedly, when the cell is rested at 3.55V upon charge. This voltage rise during charge is *entirely independent* from the VF typically observed, as each subsequent discharge follows again the profile of the baseline cell with practically no difference. This shows that oxide retains its voltage fade memory despite the apparent voltage rise.

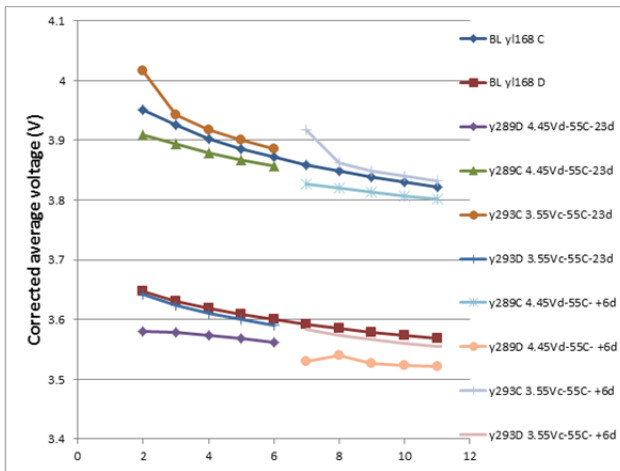


Figure IV - 170: Effect of multiple rests on VF for two cells rested at 3.55V during charge and at 4.45V during discharge. All testing is done at 55°C

The data are different for the cell resting twice at 4.45V upon discharge. Here, each time the cell rests, the average voltage continues to drop below the voltage measured for the baseline cell. Hence, the voltage rise at the lower state of charge (3.55V) is only a temporary effect, and is presumably active only until the higher

states of delithiation are reached. It does, however, contribute to the observed hysteresis along with the hysteresis contribution seen at higher states of delithiation.

This observation suggests that there are at least two different processes in the material contributing to the

observed voltage-capacity profiles. The fact that VF is most pronounced during cycling over a wide voltage range (in comparison to VF during resting/holding) strongly suggests that VF requires, in fact, multiple steps to occur sequentially – perhaps with an initiation step at higher states of delithiation, and at least one further step at lower voltages leading to higher degrees of structural relaxation. Such interpretation is in agreement with our previous model [2].

Electrochemical Modeling

As detailed in the other sections, the activated LMR-NMC cathode material is a rather complex structure. As with most lithium ion oxide positive electrode active materials, the active material secondary particles (typically 10-20 μm in diameter) are composed of micron to sub-micron size primary particles. A simplified continuum-based drawing of a piece of a primary particle near the solid electrolyte interphase (SEI) showing its structural makeup is given in Figure IV - 171. The activated LMR-NMC cathode material is made of nanometer scale LiMO_2 and Li_2MnO_3 domains that are highly integrated, but have unique electrochemical properties. The LiMO_2 domains (domain 1) are considered to be relatively stable to changes in lithium concentration. However, the Li_2MnO_3 domains go through a slow reversible structural transition during cycling (domains 2 and 3), as well as an irreversible structural change (VF domain) that is the source of the voltage fade. The transition between domains 2 and 3 generates the observed voltage hysteresis by the open circuit voltage (OCV) curves for these domains being offset by a significant voltage. Further, the high voltage domain (3) is stable fully discharged, while the low voltage domain (2) is stable fully charged. Finally, the LMR-NMC is also known to have an oxide surface layer that is different compositionally, structurally, and electrochemically from the bulk.

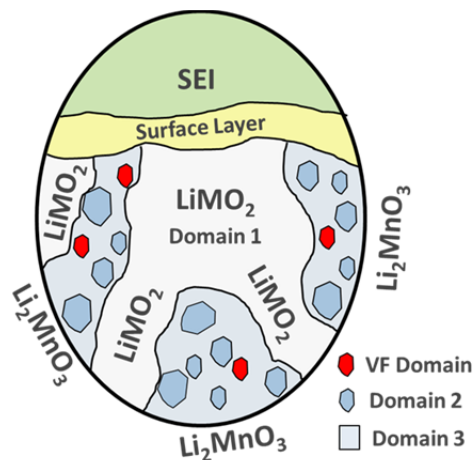


Figure IV - 171: View of activated LMR-NMC material

There is a wide range of electrochemical experimental data available to utilize for these modeling studies. They include cycling studies, electrochemical impedance spectroscopy (EIS) measurements, and galvanostatic intermittent titration technique (GITT) studies (i.e. applied current, followed by relaxation, and repeated). These studies are mostly done on half-cells (i.e. LMR-NMC electrode vs. lithium) and some full cells (i.e. LMR-NMC electrode vs. graphite or LTO electrode). Ideally, one would use a reference electrode cell to enable better examination of the LMR-NMC electrode or at least a cell where the impact of the counter electrode can be accurately accounted. With typical lithium ion cell thicknesses being less than 100 μm , it is difficult to make a good reference electrode cell [3]. More commonly, half-cells are employed to conduct electrochemical studies. Fortunately, there is enough reference electrode cell data to establish the impedance of the standard LMR-NMC electrode (i.e., made with HE5050 active material). As shown in Figure IV - 172, the impedance of the lithium electrode can be estimated by comparing half-cell area specific impedance (ASI) taken after approximately one second of applied current to LMR-NMC reference electrode cell interfacial EIS measurements. The ASI data from one half-cell, Figure IV - 172(a), is similar to the EIS reference electrode data, meaning the lithium electrode impedance is relatively small. Conversely, there is a significant offset attributed to a much higher impedance lithium electrode in the second cell, Figure IV - 172(b).

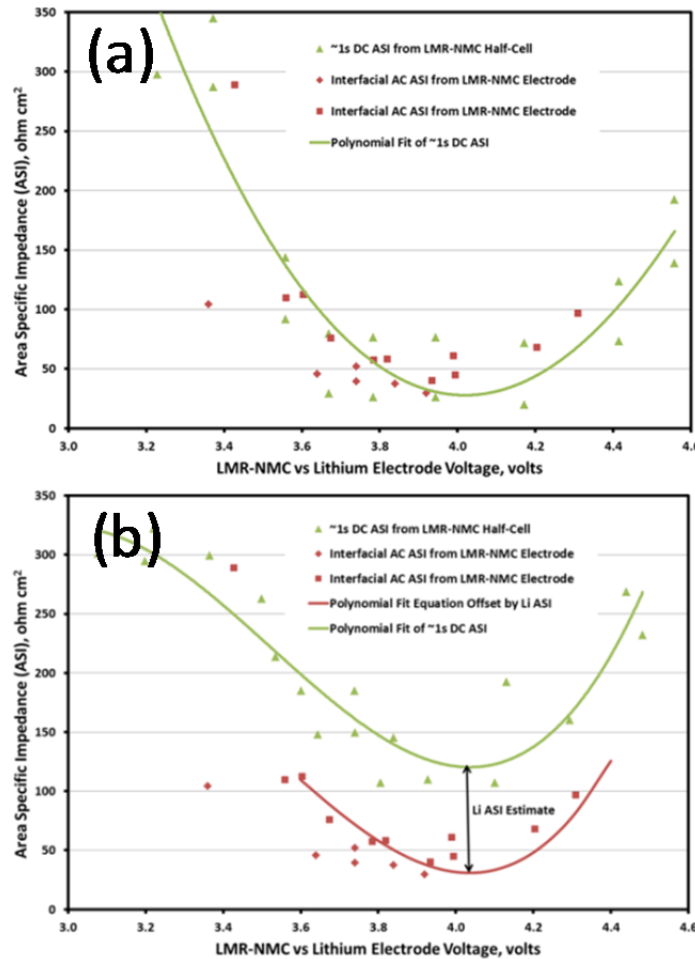


Figure IV - 172: Li electrode ASI estimated by comparing half-cell to LMR-NMC electrode reference electrode cell interfacial impedance. Data from two different half-cells are shown

Accounting for lithium electrode cell-to-cell differences within the model is relatively straight forward. The more important issue is the stability of the lithium during the experiment. The lithium electrode is notoriously unstable, yet Argonne and essentially everybody else uses it regularly as a counter electrode [4]. Lithium electrode stability is particularly important in these voltage fade studies because the LMR-NMC active materials tend to have extremely long time constants (i.e. 100's if not 1000's of seconds) associated with the transport of lithium and accompanying structural changes during cycling. In the absence of a reference electrode, reproducibility between multiple cell tests becomes the primary indicator of the quality of the data. As an example, the two cells studied in Figure IV - 172 both exhibited similar behavior, despite the significantly different lithium electrode impedance. It should also be noted that researchers at Argonne and elsewhere use LTO as a counter electrode in some studies. This electrode has lower impedance and is much more stable than lithium, but does not have the effectively infinite source of lithium ions.

In general, two types of electrochemical models were used to examine the LMR-NMC material and electrode with two levels of complexity. An electrochemical model for intercalation active material electrodes and complex active material/electrolyte interfacial structure was applied to LMR-NMC electrodes. This model specifically addresses the surface layer impedance, but treats bulk material as a solid solution. Nevertheless, the standard intercalation model has proven quite useful for examining LMR-NMC electrodes, especially when using transportation application testing protocols. This was mostly a parameter fitting exercise using an existing model applied to LMR-NMC electrode results obtained from a micro-reference electrode cell. The other electrochemical model of bulk LMR-NMC materials and electrodes was developed that specifically address the domains and structural changes in the active material. This model incorporates and extends earlier work on volume-averaged, multi-phase, and phase-change active material electrodes. It captures much of

the observed LMR-NMC electrode electrochemical behavior, including the voltage hysteresis.

Electrochemical Model Describing the Bulk Lithium Transport and Structural Transitions in LMR-NMC

The focus of this effort is on the unique behavior LMR-NMC electrode materials that separate them from other layered oxide materials. Probably the most obvious example is the hysteresis that LMR-NMC electrode materials are known to exhibit between their charge and discharge voltage curves, even at very slow cycling rates (e.g. C/300). Experimental studies on LMR-NMC materials also suggest a link between the hysteresis and the voltage fade phenomenon, thus emphasizing the importance of a valid electrochemical model for this class of materials. A number of different models have been examined with varying degrees of success. The electrochemical model development described below combines and extends some earlier work [5-10]. As discussed below, this model exhibits characteristics that account qualitatively for many of the observed phenomena. Also, the model is flexible enough to quantitatively match much of the observed experimental results.

Volume-averaged continuum-based diffusion equations are used to describe the transport of lithium through the material. A separate transport equation is used to account for the movement of lithium through each of the domains. Specifically, there are three separate equations for the three domains, the stable LiMO₂ domain (domain 1) and the unstable Li₂MnO₃ domains (domains 2 and 3) that go through a slow reversible structural transition during cycling. The flux of lithium between two adjacent domains denoted *i* and *j* (N_{ij}) is described by an electrochemical potential (μ_{Li}) driven mass transport expression, Equation 1, where k_{ij} is the mass transfer coefficient. The electrochemical potential can be easily associated with the OCV of the specific domain.

$$N_{ij} = k_{ij} [\mu_{Li}(i) - \mu_{Li}(j)] \quad [1]$$

The structural transitions from domain 2 to 3 and from domain 3 to 2 are assumed to follow the Avrami phase change expression (see Equation 2), where k is a lithium concentration driven rate constant and ε_{Si} is the volume fraction of domain *i*.

$$\varepsilon_{Si} = 1 - \exp(-kt^n) \quad [2]$$

The full system of equations used to describe the transport and structural transitions in the LMR-NMC active material is given in Figure IV - 173. A particle model was developed based on the system of material equations with Butler Volmer kinetics and a resistive component to account for other cell effects. The particle model was used to examine extremely slow cycling (i.e. slower current rate than C/20) of the LMR-NMC

material in half-cells. At these very slow rates there is little or no difference between the single particle and the full cell simulations. A half-cell electrochemical model for intercalation electrodes was modified for LMR-NMC electrodes that included the bulk phenomena for the active material. The half-cell electrochemical model was used in examining the GITT studies.

Bulk Transport and Structural Transitions

$$\begin{aligned} \frac{\partial \varepsilon_{S1} c_{S1}}{\partial t} &= \nabla \cdot \left(\frac{\varepsilon_{S1} D_{S1}}{\tau_{S1}} \nabla c_{S1} \right) + a_{S21} N_{21} + a_{S31} N_{31} \\ \frac{\partial \varepsilon_{S2} c_{S2}}{\partial t} &= \nabla \cdot \left(\frac{\varepsilon_{S2} D_{S2}}{\tau_{S2}} \nabla c_{S2} \right) - a_{S21} N_{21} + a_{S32} N_{32} - c_{S2} R_{23} + c_{S3} R_{32} \\ \frac{\partial \varepsilon_{S3} c_{S3}}{\partial t} &= \nabla \cdot \left(\frac{\varepsilon_{S3} D_{S3}}{\tau_{S3}} \nabla c_{S3} \right) - a_{S31} N_{31} + a_{S23} N_{23} - c_{S3} R_{32} + c_{S2} R_{23} \\ \frac{\partial \varepsilon_{S2}}{\partial t} &= R_{32} - R_{23} & R_{ij} = k_{Sj} \Delta c_i^* \varepsilon_{Si} H(\Delta c_i^*) \\ N_{ij} &= k_{ij} [\mu_{Li}(i) - \mu_{Li}(j)] = k_{ij} F[U_j - U_i] & k_{ij} = \frac{k_{Dj} D_{Si} k_{Di} D_{Sj}}{(k_{Dj} D_{Si} + k_{Di} D_{Sj})} \end{aligned}$$

Figure IV - 173: Electrochemical model equations for the lithium transport in the LMR-NMC electrode active material

As one may expect, determining the individual parameters and characteristics for each of the domains is a huge challenge. As a starting point we can look at the characteristics of NMC and Li₂MnO₃ electrodes [11]. This can be quite useful as a guide. For example, the lithium transport in the NMC material is much faster than the Li₂MnO₃ material. However, there is significant structural diagnostic evidence that the cycling of the Li₂MnO₃ material is quite different from the cycling of the Li₂MnO₃ domain in the LMR-NMC material, which makes directly using parameters and characteristics from the individual materials problematic [12].

The challenge of creating a parameter set for the electrochemical model begins with establishing the individual OCV curves for the domains. First, to create the voltage hysteresis within the electrochemical model it is important that the individual OCV curves for the unstable domains (domains 2 and 3) are offset by a significant voltage (i.e. roughly at or greater than one volt). Further, the high voltage domain should be stable fully discharged, while the low voltage domain should be stable fully charged. A simple thermodynamic-like expression with two adjustable parameters (i.e. α_i and β_i), given in Equation 3, is assumed for OCV curve of each of the domains, where x_{Si} is the ratio of the lithium concentration in the specific domain divided by its maximum concentration. For further simplicity, a single parameter expression is used for the Li₂MnO₃ domains (i.e. $\alpha_i = \beta_i$).

$$U_i = U_i^0 + \frac{RT}{F} [\alpha_i \ln(1 - x_{Si}) - \beta_i \ln(x_{Si})] \quad [3]$$

Figure IV - 174 has the assumed OCV curve for each of the domains, as determined from slow cycling of

LMR-NMC half-cells described below. The actual OCV curves are inevitably more complicated.

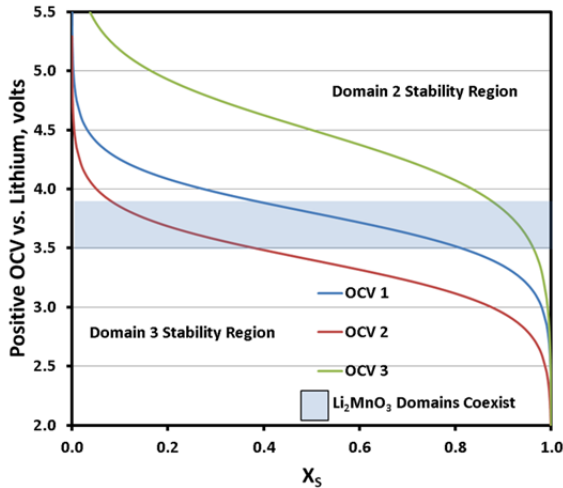


Figure IV - 174: Assumed open circuit voltage curve as a function of relative lithium concentration in domain. Also the stability ranges of domains 2 and 3 are shown

By offsetting the individual domain OCV curves and making the structural transitions and lithium transport between domains extremely slow (i.e. very small rate constant and mass transfer coefficient); the electrochemical model exhibits a hysteresis between charge and discharge, even at a C/300 rate, that agrees well with experiment (see Figure IV - 175).

Experimental observations also indicate that a piece of the LMR-NMC voltage hysteresis is rate independent. That is, the electrode will exhibit a hysteresis no matter how slow it is cycled. Building a rate independent hysteresis component into the model can be accomplished by requiring the two Li_2MnO_3 domains to have a voltage range where both domains coexist, as indicated in Figure IV - 174.

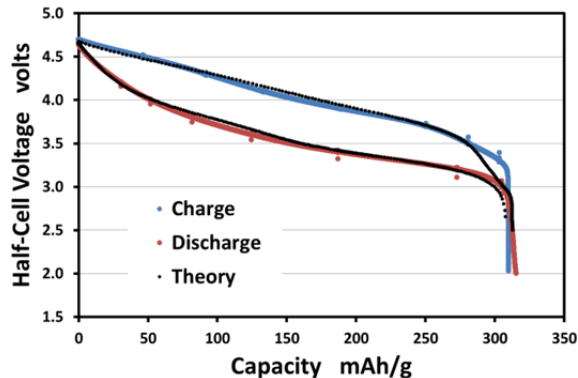


Figure IV - 175: Electrochemical particle model simulation of LMR-NMC standard electrode half-cell charge and discharge curves at a C/300 rate

As indicated above, the half-cell slow constant current cycling data was utilized with the particle model to develop a working set of parameters. This data is not

as sensitive to the lithium transport as the GITT studies. Primarily, the cycling data was used to fit the OCV curves of the three domains and establish average rate constants for the domain transitions, as well as their range of stability. Unfortunately, but not surprisingly, there is an array of parameter sets that result in an adequate fit. The best fit found to-date of the C/300 data is shown in Figure IV - 175. While an adequate fit was obtained, it was also clear from this effort that a very good fit of data is not possible without allowing the transition rate and transport parameters to be concentration dependent. The parameter set for the particle electrochemical model established with the C/300 half-cell cycling data was compared to C/40 cycling data performed on another cell. It was clear that the same parameter set would not fit the data from both cells. Further, a common set of parameters could not be found that would yield an adequate fit of both sets of data. However, an adequate fit could be obtained by adjusting the domain structural rate change constant, possibly suggesting the Avrami phase change expression or at least the concentration driving force may not be sufficient.

The changes in the Li_2MnO_3 domains with cycling are apparent by examining the relative amounts of domains 2 and 3 as the material is cycled (see Figure IV - 176). As indicated above, domain 2 is stable when fully charged and domain 3 is stable when fully discharged. Modeling of the slow cycling data indicates that domain 3 is the dominate phase below 3.5 volts vs. lithium and domain 2 is the dominate phase above 3.8 volts. The sluggishness of the transition rates cause the material to never be at equilibrium at any reasonable cycling rate. Further, the slow transition rates and relative stability ranges result in the changes to appear to be out-of-phase with the cycling. Finally, increasing the cycling rate reduces the transition between domains 2 and 3 in the Li_2MnO_3 regions. At C/1 there is little or no change in the volume fractions during cycling. This is one of the reasons why the intercalation model is valid to describe cycling rates relevant to transportation applications.

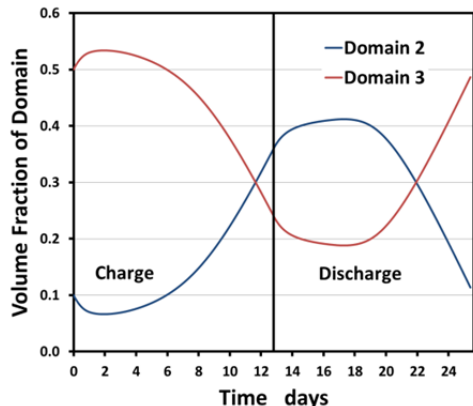


Figure IV - 176: Volume fraction of domains 2 and 3 in LMR-NMC active material from electrochemical model simulation of charge and discharge at a C/300 rate

Because of their similarities to cyclic voltammetry studies, with constant current cycling data it is common to create a dQ/dV plot (also called a capacity plot) from the cycling data. Taking the derivative of the C/300 cycling data presented in Figure IV - 174 is somewhat problematic because the small changes in voltage makes the plot rather noisy, as shown in Figure IV - 176(a), which can be smoothed using a moving average. Also shown in Figure IV - 176 (a) is the electrochemical model simulation for comparison. Having the model simulation allows one to see the contributions of the individual domains, as shown in Figure IV - 176 (b). At the slow cycling rate the individual contribution from each domain is mostly governed by thermodynamics and the relative amounts of domains 2 and 3.

A series of GITT studies were examined with the electrochemical model to more rigorously study the transport through the individual domains. Like the cycling studies, the GITT measurements were obtained on standard LMR-NMC half-cells. In the majority of the GITT studies a C/18 current is applied for 10 minutes followed by a 100 minute rest, which is then repeated through a complete cycle. Figure IV - 177 contains the results from selected current pulses overlaid across a full charge. As can be easily seen, the material electrochemical characteristics changes dramatically with SOC.

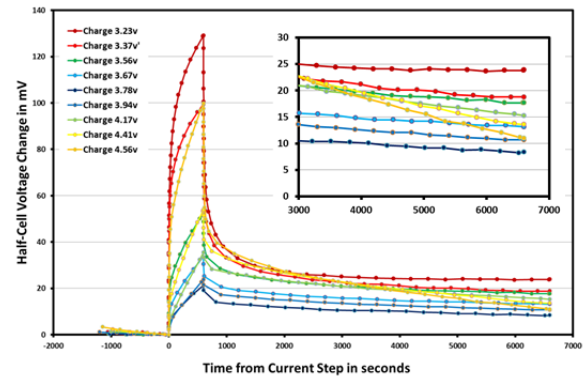


Figure IV - 177: Overlaid selected GITT measurements at indicated voltage on standard LMR-NMC electrode half-cell (600 second C/18 charge pulse and 6000 second relaxation) across full charge. Inset shows expanded view of last hour of relaxation

The inset in Figure IV - 177 also shows that the material is not fully relaxed from the 10 minute current pulse, even after one hundred minutes. The modeling indicates that the lithium concentration gradients relax relatively quickly, but that the slow decay is associated with the structural transition between domains 2 and 3 within the Li₂MnO₃ regions and the transport of lithium between domains.

The particle model was integrated into the half-cell electrochemical model to use in fitting the GITT half-cell data. The approximately 30 model parameters associated with the LMR-NMC material allows for more than enough degrees of freedom to adequately fit all the data. Creating a consistent parameter set across the full range of data is the real challenge. The focus here with the GITT experiments is to first examine the lithium transport within and between individual domains. As discussed above, it is expected that the LiMO₂ domain in general allows for much faster transport of lithium than the Li₂MnO₃ domains. This is most likely to be the case at SOCs where the lithium content of the Li₂MnO₃ domains is either nearly full or empty, and the LiMO₂ domain is moderately populated. Using the thermodynamic information gleaned from the constant current cycling data, this would occur at voltages between 3.6 and 4.0 volts. Further, examining the slow relaxation portion of the GITT charge results with the electrochemical model suggests that the lithium diffusion coefficient in the Li₂MnO₃ domains needs to be at least an order of magnitude slower than the LiMO₂ domain. A factor of 20 was used. A typical fit of the electrochemical model to the GITT results is shown in Figure IV - 178. Over the voltage range studied, the lithium diffusion coefficient for the LiMO₂ domain obtained from the electrochemical model simulations varied from approximately 2×10^{-13} to $2 \times 10^{-12} \text{ cm}^2/\text{s}$. This is in good agreement with the intercalation electrochemical model EIS study results given in Figure IV - 177.

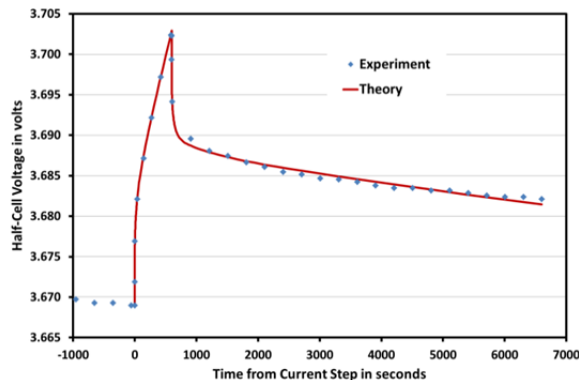


Figure IV - 178: Electrochemical model simulation of standard LMR-NMC electrode half-cell GITT experiment (600 second C/18 charge pulse and 6000 second relaxation at about 3.67 volts)

Examining the lithium transport in the LMR-NMC at low and high SOCs becomes more problematic; where the transport in one domain may not be dominate over the others. To avoid this situation, a special set of GITT-like studies (i.e. current pulse followed by a rest) were conducted on a LMR-NMC reference electrode cell. The formed electrode was operated below 3.5 volts vs. lithium and then brought to approximately 3.3 volts and allowed to rest till the Li_2MnO_3 regions had ample time to convert to domain 3. Under these conditions the thermodynamics indicate that domains 1 and 3 are almost fully loaded with their lithium content at approximately the same fraction. Since both domains are at similar low SOCs, it is reasonable to assume that the lithium transport in domain 1 is again much better than the transport in domain 3. It is important to note that allowing the Li_2MnO_3 regions to fully relax generally creates a domain that is either almost fully loaded or fully empty of lithium, and thus has relatively poor lithium transport properties. It is the slow structural transition of the Li_2MnO_3 regions that allows for the existence of either domain 2 at low SOCs or domain 3 at high SOCs, which creates the pathways for faster lithium transport. A consequence of this characteristic is that allowing the LMR-NMC material to rest generally increases its impedance.

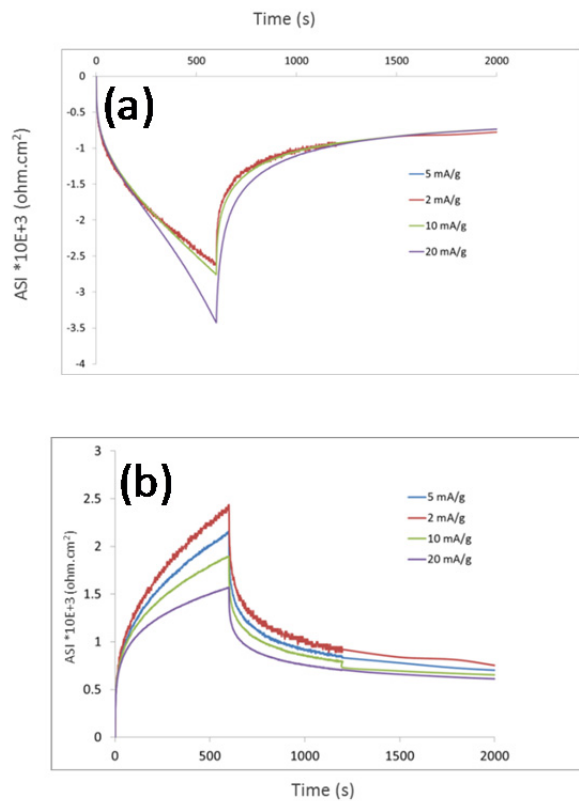


Figure IV - 179: Current pulse experiment on LMR-NMC reference electrode cell (10 minute current pulse and 7 hour relaxation at about 3.3 volts). (a) discharge (b) charge

Starting at 3.3 volts, a sequence of charge for 10 minutes, rest for 7 hours, discharge for 10 minutes, and rest for 7 hours was applied to the LMR-NMC reference electrode cell for four different current rates: 2, 5, 10, and 20 mA/g. Even with no slow structural transition of the Li_2MnO_3 regions, the longer wait times were needed to allow the transport between domains to fully relax. The range of current rates was used to examine its impact at these low SOCs. The results of these tests are plotted as ASI ($\Delta V/I$) in Figure IV - 179 so that the differences between charge and discharge are more apparent. One immediately notices that the ASIs are generally very large and the discharge ASIs are significantly greater than the charge ASIs for all rates except the 2 mA/g. Also, the ASI curves do not overlay. A strong non-linear transport system (i.e. where D_{Si} is lithium concentration dependent) will generate ASI curves that do not overlay. At these low SOCs, on charge the ASI should decrease with current rate and increase on discharge. Finally, the charge results appear to indicate a stronger lithium concentration dependence of the diffusion coefficient than the discharge data.

For these simulations, the volume of domain 2 was set to zero in the electrochemical half-cell model. While the model was already non-linear, a linear concentration dependence of the diffusion coefficient

was specifically added. With no Li_2MnO_3 structural transition and the longer rest, the system thermodynamics was less complex. Two thermodynamic expressions were considered, one linear and the other logarithmic, based on the change from the initial voltage and concentration of lithium. The data was examined with the model variations. The linear concentration dependence of the diffusion coefficient combined with logarithmic thermodynamics produced an adequate fit of all the data with a unified set of kinetic and transport parameters. A typical fit of the data is shown in Figure IV - 180. The lithium diffusion coefficient for the LiMO_2 domain obtained from the electrochemical model simulations at 3.3 volts vs. lithium was $6 \times 10^{-14} \text{ cm}^2/\text{s}$, which is considerably higher than the intercalation electrochemical model EIS study results given in Figure IV - 170. Some of this difference can be attributed to the tortuosity of the LiMO_2 domain. Also, the DC model does not specifically account for a surface diffusion layer on the oxide which is significant at the low SOC. Finally, a possibility not considered in the modeling effort to improve the model is that the D_{Si} concentration functionality is non-linear (i.e. possibly D_{Si} levels off to a constant value as x_{Si} approaches one).

The methodology described above allows for a full parameter set for the model to be determined. Multiple iterations of working with the data would be needed to optimize the parameter set, as well as the model. Further, the utility of the electrochemical model has been demonstrated to accomplish more than just determining parameters. The model describes a wide variety of observed phenomenon for the LMR-NMC material. As indicated above, a portion of the voltage hysteresis is rate independent, which is built into the model by creating a voltage range where both unstable domains coexist (2 & 3). As an example, model simulations exhibit a significant voltage hysteresis even at a C/5000 rate. Also observed experimentally and using the model, the hysteresis is lessened if the LMR-NMC material is cycled in narrower voltage ranges from the top and bottom of charge. Further, the model shows that the time constant for previous cycling history impacting performance is extremely long. Finally, early in the charge half-cycle if the cell is allowed to relax for long times the voltage will first drop and then rise as the domain transition (i.e. domain 2 to domain 3) starts to control the process.

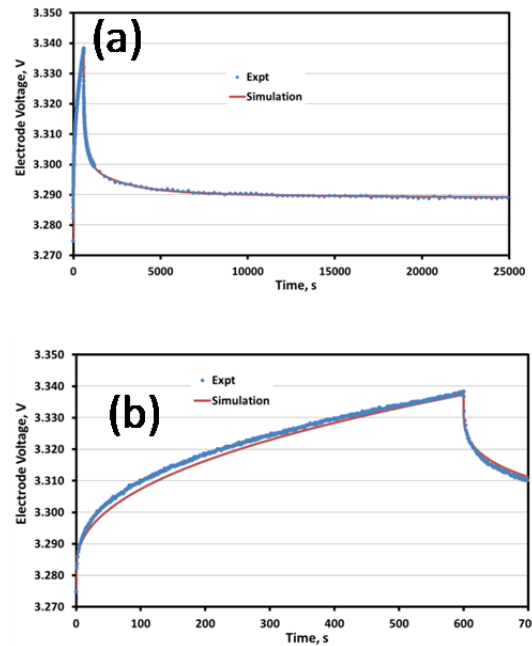


Figure IV - 180: Simulation of current pulse experiment on LMR-NMC reference electrode cell (10 minute 5 mA/g charge pulse and 7 hour relaxation at about 3.3 volts). (a) full experiment (b) approximately first 12 minutes

Conclusions and Future Directions

While the process of voltage fade is a thermodynamic relaxation of the lattice within the LMR-NMC it appears the process cannot be accelerated by simple thermal treatments. Moreover the complexity of the voltage fade process as demonstrated by the electrochemical model indicates that relaxations within the lattice are extremely slow and accelerating voltage fade at reasonably achievable temperatures or voltages is not practical.

The Voltage Fade Team

Burrell, Anthony K.; Abouimrane, Ali; Abraham, Daniel; Amine, Khalil; Balasubramanian, Mahalingam; Barenco Garcia-Ontiveros, Javier; Belharouak, Ilias; Benedek, Roy; Bettge, Martin; Bloom, Ira D.; Long, Brandon R.; Chen, Zonghai; Croy, Jason R.; Dees, Dennis W.; Dogan, Fulya; Gallagher, Kevin G.; Henriksen, Gary L.; Iddir, Hakim; Ingram, Brian J.; Johnson, Christopher; Key, Baris; Li, Yan; Lu, Wenquan; Miller, Dean J.; Ren, Yang; Slater, Michael D.; Thackeray, Michael M.; Vaughey, John T.; Wu, Huiming; Wu, Qingliu; Zhu, Ye; Yang, Zhenzhen; Lee, Eungje; Aoun, Bachir; Vu, Anh D.; Lin, Chi-Kai; Rinaldo, Steven G.; Tenant, Robert; Ban, Chunmei; Nanda, Jagit; Bugga, Kumar; Yang, Xiao-Qing; Mohanty, Debasish; Li, Jianlin; Payzant, Andrew,

Wood, David, Daniel, Claus, Jansen, Andrew, Polzin, Bryant; Trask, Steven, Krundick, Greg.

References

1. M. Bettge, Y. Li, K. Gallagher, Y. Zhu, Q. Wu, W. Lu, I. Bloom, D. P. Abraham, "Voltage Fade of Layered Oxides: Its Measurement and Impact on Energy Density", *J. Electrochem. Soc.*, 160 (11) A2046-A2055 (2013).
2. K. G. Gallagher, J. R. Croy, M. Balasubramanian, M. Bettge, D. P. Abraham, A. K. Burrell, M. M. Thackeray, "Correlating hysteresis and voltage fade in lithium- and manganese-rich layered transition-metal oxide electrodes", *Electrochim. Comm.* 33 (2013) 96–98.
3. D. P. Abraham, S. D. Poppen, A. N. Jansen, J. Liu, and D. W. Dees, *Electrochim. Acta* 49(26), 4763-4775 (2004).
4. C. M. Lopez, J. T. Vaughey, and D. W. Dees, *J. Electrochem. Soc.* 156(9), A726-A729 (2009).
5. D. Dees, E. Gunen, D. Abraham, A. Jansen, and J. Prakash, *J. Electrochem. Soc.* 152(7), A1409-A1417 (2005).
6. D. P. Abraham, S. Kawauchi, and D. W. Dees, *Electrochimica Acta* 53, 2121-2129 (2008).
7. D. Dees, E. Gunen, D. Abraham, A. Jansen, and J. Prakash, *J. Electrochem. Soc.* 155(8), A603-A613 (2008).
8. S. E. Trask, Y. Li, J. J. Kubal, M. Bettge, B. J. Polzin , Y. Zhu, A. N. Jansen, and D. P. Abraham, *J. Power Sources* 259, 2330-244 (2014).
9. D. W. Dees, S. Kawauchi, D. P. Abraham, and J. Prakash, *J. Power Sources* 189(1), 263-268 (2009).
10. K. G. Gallagher, D. W. Dees, A. N. Jansen, D. P. Abraham, and S.-H Kang, *J. Electrochem. Soc.* 159(12) A2029-A2037 (2012).
11. W. Lu, Q. Wu, and D. W. Dees, *J. Electrochem. Soc.* 160(6) A950-A954 (2013).
12. J. R. Croy, K. G. Gallagher, M. Balasubramanian, B. R. Long, and M. M. Thackeray, *J. Electrochem. Soc.* 161(3) A318-A325 (2014).

IV.C.5 The Voltage Fade Deep-Dive: Outcomes and Future Directions (ANL)

Voltage Fade Team

Argonne National Laboratory
9700 South Cass Avenue
Argonne, IL 60439
Phone: (630) 252-4516; Fax: (630) 252-4176
E-mail: Burrell@anl.gov

Start Date: October 2013

Projected End Date: September 2014

Objectives

- Improve materials level performance of Li- and Mn-rich layered transition metal oxide cathodes (LMR-NMC) necessary to significantly improve upon existing Li-ion cathodes (pack level cost and energy density).
- Specific focus on understanding the voltage fade phenomena present in the current generation of LMR-NMC materials.

Technical Barriers

This project addresses the following technical barriers as described in the USABC goals:

- (A) Performance at ambient temperatures
- (B) Cycle life

Technical Targets

- PHEV specific energy targets (pack): 3.4 kWh (min) to 11.6 (max).
- EV specific energy targets (pack): 80 (min) to 200 (max) Wh/kg.

Accomplishments

- Determined the mechanism of voltage fade.
- Established atomic, materials and cell level models for voltage fade.
- Determined that voltage fade is a fundamental property of the material.
- Determined coatings do not mitigate voltage fade.
- Determined additives do not mitigate voltage fade.
- Determined synthesis method does not mitigate voltage fade.
- Determined morphology does not mitigate voltage fade.

- Determined composition does have a limited effect on voltage fade.
- Determined simple doping of the lattice does not mitigate voltage fade.
- Determined simple structural modification does not mitigate voltage fade.
- Determined lower lithium levels result in less voltage fade as the amount of high voltage lithium cycling is reduced. Achieved by either reducing the lithium excess and/or by limiting the cyclizing window to lower voltages.
- Completed the research project one year early.



Introduction

Energy density is an important characteristic for Li-ion batteries. For a given volume or mass, it determines, among other factors, the duration and range of the battery's operational autonomy and the cost of the battery pack. Unfortunately, the deliverable energy of practical Li-ion cells fades when repeatedly charged and discharged. This energy loss can typically be traced back to three major causes: chemical trapping and loss of mobile lithium within the cell, loss of available lithium-hosting sites, and rising cell resistances. Under certain conditions, there exists yet another mechanism which causes the cell's energy output to decrease: a continuous cycle-to-cycle decrease of the cell voltage, during charge and discharge. This decrease is typically associated with the drop in equilibrium voltage of the positive electrode, as observed for many Li-intercalating oxides. This phenomenon, occasionally referred to as "voltage fade" reduces the usable energy because the voltage of the cell integrated over the capacity equals the cell's energy. It also complicates state-of-charge (SOC) determination which is crucial for effective battery management.

Although varying degrees of voltage fade have been observed in a range of materials over the past years, several issues remained unaddressed. First, the actual physical mechanisms leading to voltage decay are largely unknown, although theories exist but had not been experimentally verified. Second, no comprehensive studies exist which establish structural and experimental conditions for voltage fade to occur. In fact, it is not even clear whether the impact of voltage fade is technologically significant. And last, no formal description of voltage fade and its measurement exists. Especially, the latter one is critically important to

successfully address the other issues and to evaluate effectiveness of proposed strategies to mitigate this voltage decay.

The objective of the voltage fade project was to take a comprehensive approach to determining the cause of voltage fade and to come up with a “fix”. This was to be a large team deep dive where the advantages of a multidisciplinary approach could lead to a conclusion on an accelerated timeline.

Approach

The following team was assembled to work on the voltage fade project: Burrell, Anthony K.; Abouimrane, Ali; Abraham, Daniel; Amine, Khalil; Balasubramanian, Mahalingam; Bareno Garcia-Ontiveros, Javier; Belharouak, Ilias; Benedek, Roy; Bettge, Martin; Bloom, Ira D.; Long, Brandon R.; Chen, Zonghai; Croy, Jason R.; Dees, Dennis W.; Dogan, Fulya; Gallagher, Kevin G.; Henriksen, Gary L.; Iddir, Hakim; Ingram, Brian J.; Johnson, Christopher; Key, Baris; Li, Yan; Lu, Wenquan; Miller, Dean J.; Ren, Yang; Slater, Michael D.; Thackeray, Michael M.; Vaughey, John T.; Wu, Huiming; Wu, Qingliu; Zhu, Ye; Yang, Zhenzhen; Lee, Eungje; Aoun, Bachir; Vu, Anh D.; Lin, Chi-Kai; Rinaldo, Steven G.; Tenant, Robert; Ban, Chunmei; Nanda, Jagit; Bugga, Kumar; Yang, Xiao-Qing; Mohanty, Debasish; Li, Jianlin; Payzant, Andrew; Wood, David; Daniel, Claus; Jansen, Andrew; Polzin, Bryant; Trask, Steven; Krundick, Greg.

While the majority of the participants were based at ANL members include scientists from ORNL, BNL, NREL and JPL. In addition the voltage fade protocols and processing metrics were distributed to any of the research community who asked.

To approach this issue we proposed to assess the following issues:

- Definition of the problem and limitations of the composite cathode materials.
- Data collection and review of compositional variety available using combinatorial methods.
- Modeling and Theory.
- Fundamental characterization of the composite cathode materials.
- Understand the connections between electrochemistry and structure.
- Synthesis.
- Post treatment/system level fixes.

The testing and data analysis protocols were critical to the success of the project. The selection of a method for comparing materials, additives and other cell modifications was critical for the decision process in

moving forward toward a clear outcome. The most interesting aspect of this was the final realization that the protocols need not be perfect but simply had to be followed by all researchers. The same issue arises when considering a standard material. The choice of a “base line” sample was essential to the determination of post synthesis methods for correcting voltage fade. In the end we selected Toda HE5050 for several reasons. This material is available in the CAMP facility in Kg quantities, as fully characterized laminates and extensive electrochemical data related to HE5050.

Underpinning data collection and methodology

Baseline Materials Selection

While there cannot be a “perfect” baseline material in the LMR-NMC class due to the breath of potential materials compositions and almost infinite processing variations we selected a commercial batch of HE5050 ($0.5\text{Li}_2\text{MnO}_3 \bullet 0.5\text{LiMn}_{0.375}\text{Ni}_{0.375}\text{Co}_{0.25}\text{O}_2$) as our initial reference point. We have 10kg of well characterized material which has been validated in our Materials Validation Facility and electrodes prepared in the Cell Fabrication Facility (CFF). The Toda HE5050 electrodes have also been sent to ARL, JPL, LBNL, BNL, ORNL, NREL and INL and as such present the most well characterized sample of an LMR-NMC material known. This baseline material will be used to validate any post formation modifications (coating for example).

Materials and Experimental Details

The LMR-NMC, $0.5\text{Li}_2\text{MnO}_3 \bullet 0.5\text{LiMn}_{0.375}\text{Ni}_{0.375}\text{Co}_{0.25}\text{O}_2$, is supplied by Toda according to specifications provided by Argonne. It is commonly referred to as “TodaHE5050”.

LMR-NMC baseline performance

Figure IV - 181 shows charge and discharge voltage profiles of the first 20 cycles. Some capacity loss is apparent. Most of this occurs during and after the activation cycle (0th cycle). This is well known, and is likely due to loss of oxygen from the active oxide, but also due to additional electrolyte reduction/oxidation processes. A gradual capacity loss from then on is related to a variety of degradation processes, including surface structural changes of the oxide particles, transition-metal ion dissolution from them, particle isolation, as well as cell resistance increase (apparent at the end of charging). Electrochemical cycling and impedance spectroscopy of three-electrode cells show that cell resistance predominantly originates from the positive side, and is related to surface film formation between the active oxide and electrolyte which impedes Li-ion motion, as well as a degrading electronic network.

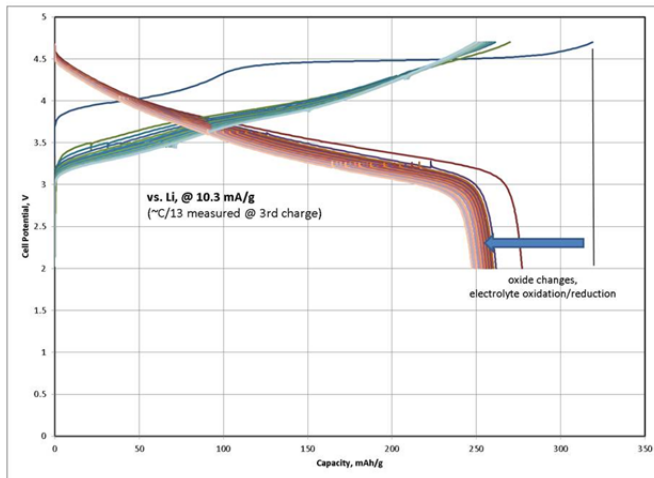


Figure IV - 181: Charge discharge profile of the LMR-NMC $0.5\text{Li}_2\text{MnO}_3 \cdot 0.5\text{LiMn}_{0.375}\text{Ni}_{0.375}\text{Co}_{0.25}\text{O}_2$, cycled against Li for 20 cycles

LMR-NMC is a remarkable cathode material with the very high practical capacity for a layered material. The overall stability of the cathode material toward extensive lithium exchange is shown in Figure IV - 182 where a LMR-NMC cathode has been cycled 1500 times in a balanced graphite cell, followed by harvesting

of the LMR-NMC cathode and reassembly into a lithium half-cell. The overall capacity loss is minimal and can be accounted for by physical damage to the electrode resulting in active material becoming electrically isolated.

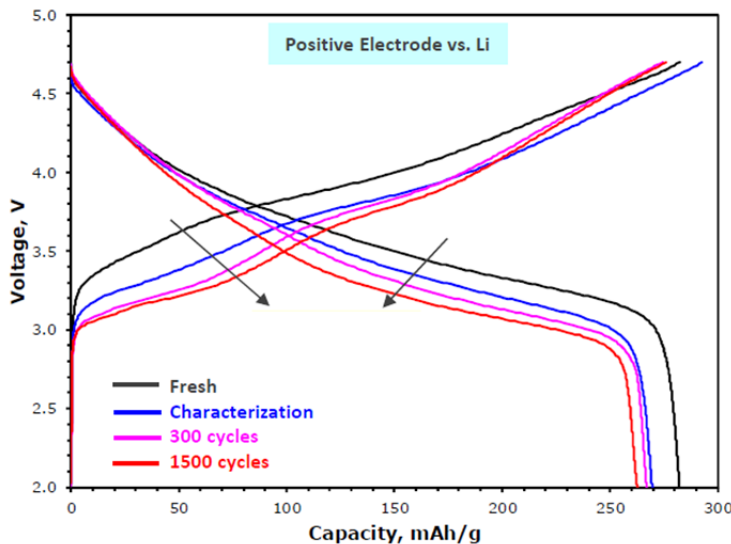


Figure IV - 182: LMR-NMC cathodes cycled for 1, 300 and 1500 cycles in full cells, cathodes harvested and reassemble in to half cell. Capacity for a fresh electrode 282 mAh/g and a cathode cycled 1500 times is 262 mAh/g

While there is effectively no capacity fade from the cathode there is a significant change in the overall voltage profile. This has a major impact on both the energy density and the ability for OEM's to implement traditional state-of-charge measurement.

A preliminary assessment of the factors that affect the energy density in LMR-NMC cells indicated that the impedance growth of the full cell was the dominant effect, Figure IV - 183. However, when we consider that there are traditional approaches to controlling

impedance rise voltage fade becomes one of the largest energy loss mechanisms. Most significantly voltage fade was the lost mechanism where there was no known mitigation Strategy.

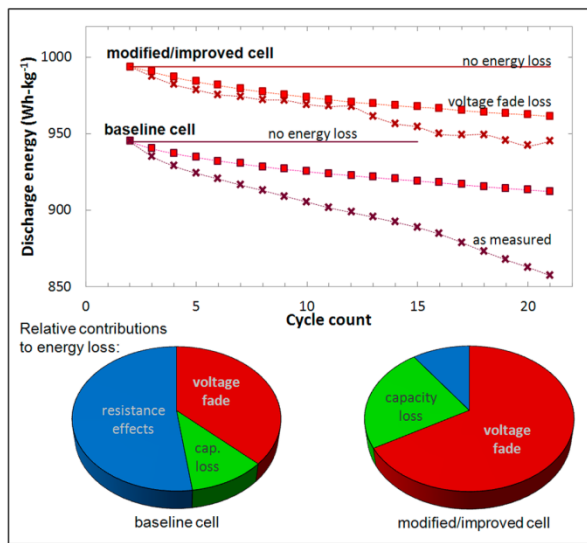


Figure IV - 183: Analysis of cell energy loss indicated voltage fade was a significant factor with no known mitigation strategy

To identify voltage fade, capacity loss and increasing cell resistance need to be factored out first. One way of doing this is to show capacity-normalized

voltage profiles. This is done in Figure IV - 184. If the normalized charge profiles drop in voltage, despite an increase in cell resistance, the oxide material experiences severe voltage fade. Figure IV - 184 also shows normalized profiles during discharging. Here, however a drop in voltage can also be partly related to increasing cell resistance. Nevertheless, it is clear that cell potentials drop over a wide range of charge states and discharge depths throughout cycling.

Another way of demonstrating voltage fade is to calculate average charge and discharge voltages and plot them versus cycle number. This is done in Figure IV - 185 in which resistance-corrected average voltages are shown. Voltage fade is clearly evident: The average charge voltage decreases from 3.95 V to 3.77 V (~0.24% or 10 mV per cycle, excluding 0th and 1st cycles); and the average discharge voltage decreases from 3.65 V to 3.53 V (~0.17% per cycle) after 20 cycles. Note that the biggest drop in average voltage within one cycle occurs after the initial activation charge, clearly evident in Figure IV - 181, Figure IV - 182, and Figure IV - 183.

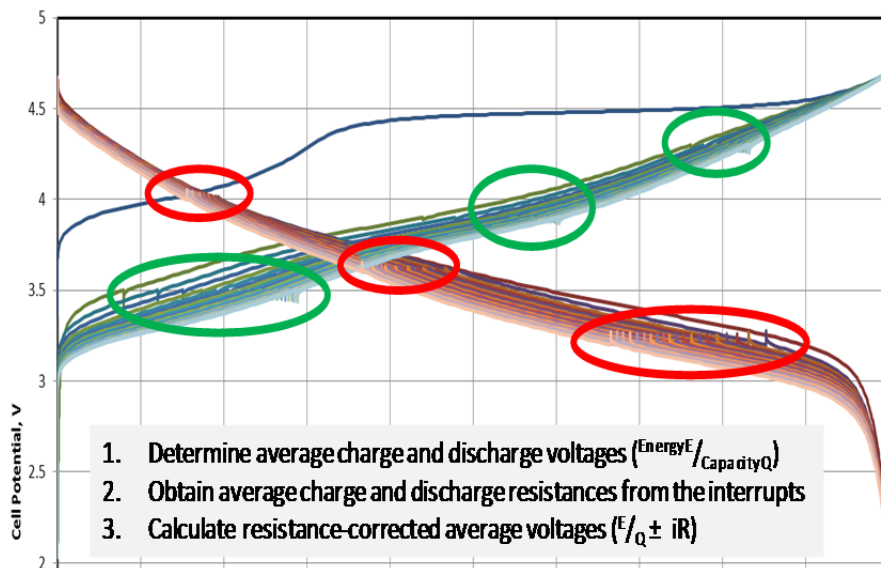


Figure IV - 184: Critical to the team's success was the initial establishment of a unified testing and data analysis protocol which all partners utilized

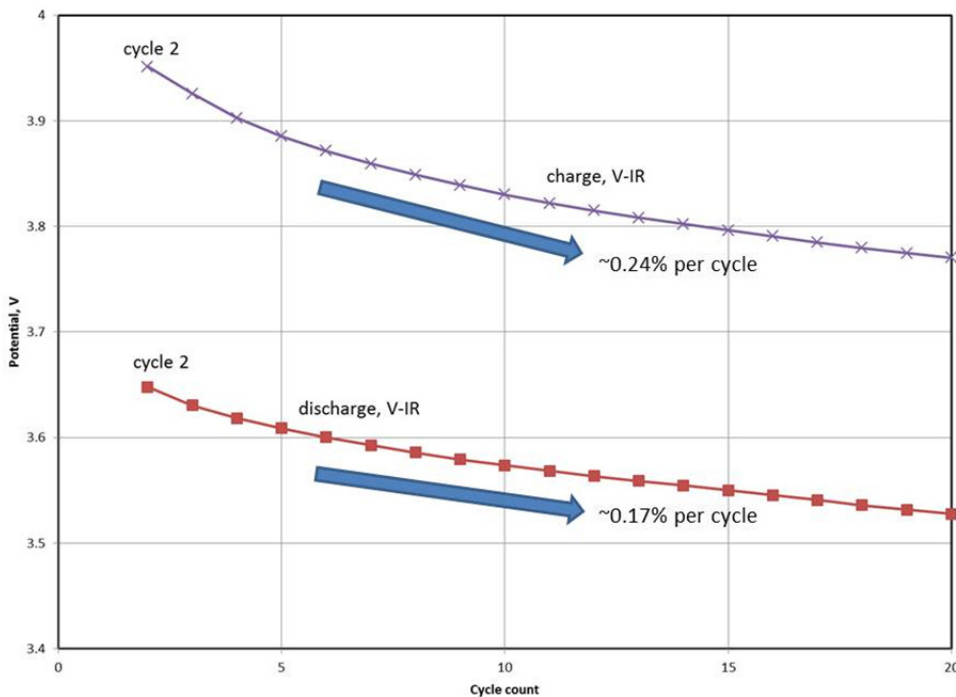


Figure IV - 185: Resistance-corrected average cell potentials versus cycle number. A continuous drop in average potential exceeding 0.1V is apparent during charging and discharging. The drop in average charge potential is larger than the drop in average discharge potential. The average potential is calculated by dividing the measured total energy (current x time x voltage) by the measured cell capacity

Testing Protocols

Based upon our understanding of the baseline material and the use of the economic model we selected a standardized test protocol has been established to reliably measure the average OCV for all investigators in the ABR program. The protocol was written to correct for ohmic losses and maximize the fraction of Li-ions accessed within the LMR-NMC material. Initial testing is completed at room temperature to expand the range of accessible test stations. If voltage fade is minimal, accelerated testing is then completed at 55 °C. We created an Excel Macro that automatically processes the cycling data for average voltage, ohmic loss correction, and plots various figures of interest. Results for the Toda HE5050 material are shown in Figure IV - 186.

The initial test protocols are:

- Electrode fabrication (lamine preparation).
- The cathode material should be prepared with a specific capacity near 1.5-1.75 mAh/cm². This translates to a specific active mass loading of 6 to 7 mg/cm² for a cathode material with 250 mAh/g of reversible capacity. This loading was chosen as it will likely balance to premade graphite negative electrodes (e.g. Saft made A12 graphite electrode).

Further assessment of first cycle capacity and other measurements is necessary to assure a well-balanced cell.

- The electrode is also recommended to be made with the standard electrode composition of 84 wt% active material, 8 wt% PVDF binder, 8 wt% Super P Li carbon black. Alternate compositions may be used as the tester sees fit, but the change should of course be reported.

Cycling Protocol

- 1st Electrochemical Evaluation.
- Cell configuration: Lithium metal as negative.
- Temperature: room temperature.
- First cycle: as the tester desires; 2-4.7V 10 mA/g recommended. Cycling procedure: 20 mA/g and 2 V to 4.7 V; Current interrupts will be implemented at (charge) 3.5V, 3.9V, 4.3V and (discharge) 4.7V, 4.0V, 3.6V, 3.2V, and 2.0V each with a 10 minute rest to measure a quasi-OCIV. Further testing protocols at 55C are implemented for any material that passes this initial testing.
- Number of cycles: >20.
- Total test time: >20 days.

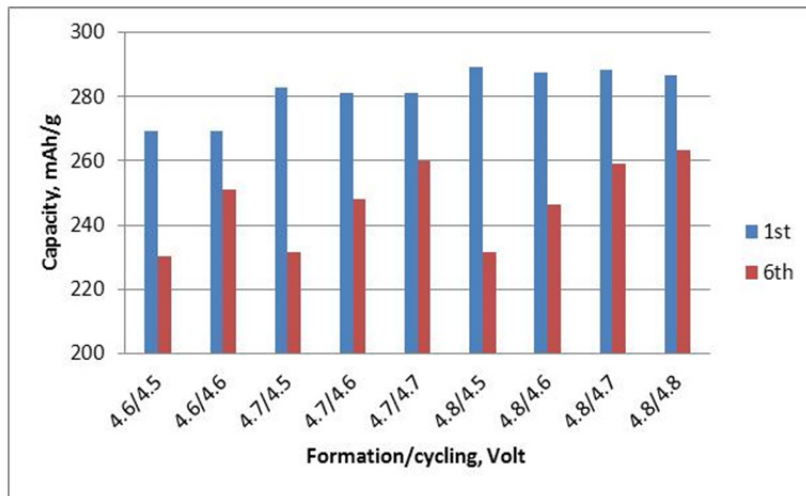


Figure IV - 186: Discharge capacity after 1st and 6th cycles under various testing conditions

Confirmation on the effectiveness of the test protocols an evaluation of the effect that both initial charge voltage and cycling voltages have on voltage fade in HE5050 ($0.49\text{Li}_2\text{MnO}_3$ • $0.51\text{LiNi}_{0.37}\text{Co}_{0.24}\text{Mn}_{0.39}\text{O}_2$, Toda) was carried out. Figure IV - 186 shows the 1st and 6th discharge capacity for a range of cells charged to different voltages and then cycled to different maximum voltages. It is apparent that the discharge capacity increases with increasing the high cut-off voltage. In addition, the discharge capacity on the 6th cycle is largely independent of the charging voltage. It appears that the only factor that limits capacity in this study is the high voltage cut-off. Finally, the capacity seems increasing linearly with cut-off voltage until 4.7V cut-off voltage, there is not significant advantage in cycling to greater than 4.7V regardless of charging voltage.

Results

With the establishment of methodology that enables direct comparison of data the team set testing the geranial approaches that had been suggested by the VF project and others that were proposed in the literature. These fell within the following classes.

- Type of Synthesis.
- Composition.
- Surface Treatments.
- Cycling protocols.
- Electrolytes.
- Morphology.

In these areas data was collected and the following overall process (Figure IV - 187) was used to determine if the modification was effective in correcting voltage fade.

Overall the following conclusions were obtained from this data driven consensus process:

- Coating do not mitigate voltage fade.
- Additives do not mitigate voltage fade
- Synthesis method does not mitigate voltage fade
- Morphology does not mitigate voltage fade
- Composition does have a limited effect on voltage fade.
- Simple doping of the lattice does not mitigate voltage fade
- Simple structural modification does not mitigate voltage fade
- Lower lithium levels result in less voltage fade as the amount of high voltage lithium cycling is reduced. Achieved by either reducing the lithium excess and/or by limiting the cyclizing window to lower voltages.

Understanding Voltage Fade

The determination of this study is that voltage fade is a fundamental property of LMR-NMC materials and cannot be eliminated where the materials is cycled to low lithium content. We have developed three levels of models to explain both the mechanism of voltage fade and the limitations it imposes upon the material.

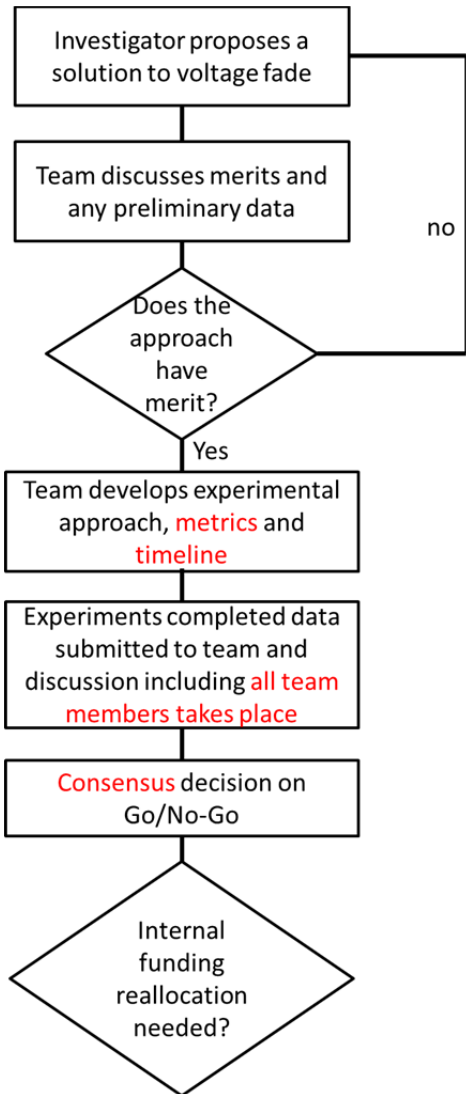


Figure IV - 187: Flow chart for consensus decision making within the project

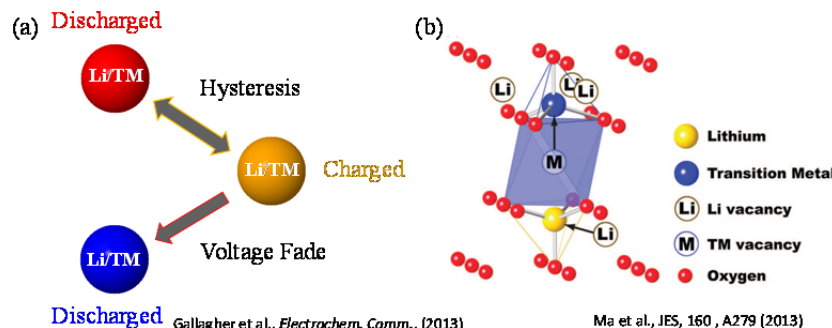


Figure IV - 188: (a) Simplified schematic of hysteresis/voltage fade mechanism as described in the text. (b) octahedral and tetrahedral sites associated with dumbbell configurations in layered Li-TM-oxides

Figure IV - 188(a) shows a simple model describing the hysteresis and mechanism and how it

Molecular Level Model

A model has been introduced to explain, in part, voltage fade and hysteresis based on the data presented above. Namely:

1) The inherent, composite nature of LMR-NMC's is dominated by charge ordering. Specifically, the strong tendency for Li^+ and Mn^{4+} to order (e.g., LiMn_6) results in two distinct, average, local environments, one rich in Li and Mn (e.g., Li_2MnO_3) and the other in TM's (LiMO_2).

2) These distinct environments have direct and observable effects on the electrochemical performance of LMR-NMC's that can be tracked during electrochemical cycling. The TM-rich, LiMO_2 behaves largely as a "standard", layered electrode; for example, structurally and electrochemically reversible in nature. The Li- and Mn-rich, Li_2MnO_3 plays a key role in voltage fade and hysteresis, whereby, accessing the TM layer Li from this component (activation) triggers the onset of both phenomena. In addition, the magnitude of both voltage fade and hysteresis are directly correlated with the magnitude of Li and Mn ordering in as-prepared electrodes.

3) The energetics between charge and discharge are different, even at equivalent Li contents (SOC's), due to structural differences within the bulk of electrode particles. Therefore, the hysteresis observed in LMR-NMC's is a stable, structural hysteresis. This means that Li does not have access to the same sites between charge and discharge at equivalent SOC's.

4) Voltage fade and hysteresis are correlated. Accessing Li above ~4.0 V causes local structural changes which prohibit the re-accommodation of this Li until ~3.0 V on discharge (hysteresis). Moving Li in and out of the structure (cycling) over this voltage window (e.g., 4.7–3.2 V) accelerates voltage fade more than any other electrochemical exposure studied.

contributes to voltage fade. Starting with an activated electrode in the discharged state, Li and/or TM's (red) can be induced to migrate once a sufficient SOC is

reached on charge. Specifically, once charged beyond ~4.0 V the Li vacancy concentration is high enough to promote Li/TM migration from octahedral sites of the TM layers to tetrahedral sites of the Li-layers. Calculations show that when this happens, additional Li ions will migrate to fill the adjacent tetrahedral sites opposite the TM-layer vacancy. For example, $\text{Li}_{\text{tet}} \square - \text{Li}_{\text{tet}}/\text{TM}_{\text{tet}}$ “dumbbells” are formed where Li_{tet} and TM_{tet} are Li and TM’s that occupy tetrahedral sites on either side of a TM-layer, octahedral vacancy (\square). The dumbbell configuration is shown schematically in Figure IV - 188(b). Because the tetrahedral sites of the Li layer share faces with three surrounding octahedral Li sites (now vacant due to charging), it is energetically unfavorable to refill these octahedral sites on discharge once the tetrahedral sites are occupied. However, once sufficient Li insertion has occurred on discharged a

critical content (Li_c) is reached at which point three possibilities exist. 1) The tetrahedral cations are forced to migrate back to their original sites. This process represents a reversible migration at the expense of an energy penalty, paid in the form of a hysteresis when cycling over large voltage windows (e.g., 4.7-3.2 V). 2) The cations are forced further along their migration path and come to occupy new sites (e.g., octahedral sites of the Li layer). This changes the local structure and lowers the associated Li site energies with respect to further extraction and insertion, contributing to the observed voltage fade. 3) Cations can become trapped in the tetrahedral sites of the Li layers. This process would be expected to contribute to both capacity loss and impedance rise with extended cycling. The effect on the overall lattice structure is shown in Figure IV - 189.

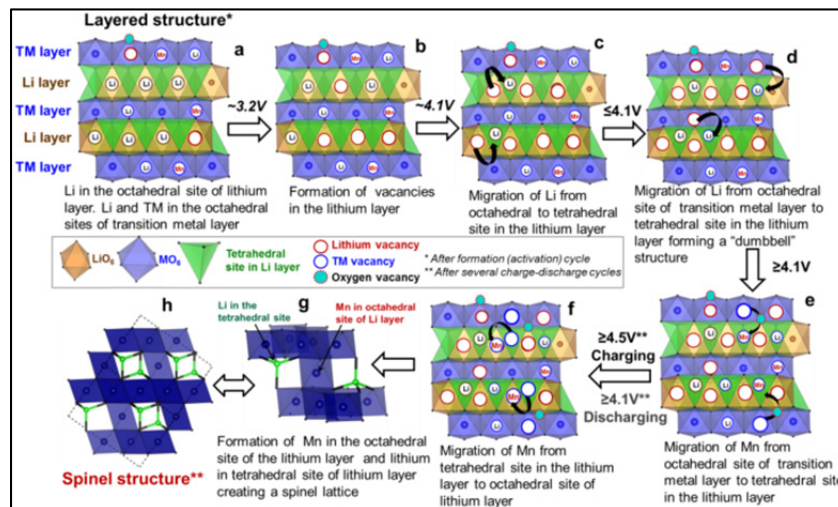


Figure IV - 189: Proposed LS transformation mechanism in HE5050 LMR composite oxide via formation of tetrahedral lithium in the lithium layer and migration of Mn from octahedral TM layer to octahedral site of lithium layer

Phenomenological Theory of Voltage Fade

This theory demonstrates the causal relationship between transition metal ion incorporation into Li-rich regions and the phenomena of voltage fade. Key parameters were the interaction energy voltage which determines the degree of separation between high and low voltage capacities and the TM ion coordination factor which determines the fractional amount of low voltage capacity. This theory is general and not bound to a specific crystallographic lattice or TM ion species.

The theory was put in the framework of a more generalized mean field model and we presented experiments that allowed us to rationally simplify the model to 3 essential components. These components are: A-voltage fade capacity, B-standard capacity LiMO_2 (where M = Mn, Ni, Co) related component, C - high capacity Li_2MnO_3 related component. The 3 component model was applied to de-convolute the evolutionary behavior of TODA HE5050 charge profiles. In general, components B and C decreased at

the expense of component A. Additional analyses are required to isolate the contributions of components B and C separately.

Based on the phenomenological model proposed and the extracted component-wise evolutions, a differential growth law was proposed. The key parameters were the maximum TM ion fraction and the rate of TM ion migration per cycle. Data extracted from the analysis as well as experimentally generated voltage fade component evolution data all lie on a single growth curve. Thus model-based and measurement-based LMR voltage profile de-convolutions agree.

The relationship between TM ion migration rate per cycle and cycling current suggest that the dependencies of voltage fade on cycling conditions can be rationalized. We demonstrated that the per cycle rate of TM ion migration is lowest at high cycling rates but at high cycling rates the energy density is lower thus there is a balance between the rate of voltage fade and energy density. Speculatively, there will be an optimal

combination of stressors that will minimize the rate of transition metal migration and voltage fade while maximizing energy density.

Electrode Level Model

This model describes a wide variety of observed phenomenon for the LMR-NMC material. As indicated above, a portion of the voltage hysteresis is rate independent, which is built into the model by creating a voltage range where both unstable domains coexist. As an example, model simulations exhibit a significant voltage hysteresis even at a C/5000 rate. Also observed experimentally and using the model, the hysteresis is lessened if the LMR-NMC material is cycled in narrower voltage ranges from the top and bottom of charge. Further, the model shows that the time constant for previous cycling history impacting performance is extremely long. Finally, early in the charge half-cycle if the cell is allowed to relax for long times the voltage

will first drop and then rise as the domain transition starts to control the process.

Conclusions and Future Directions

Status of LMR-NMC

Based upon this project it is clear that voltage fade cannot be solved but it can be lived with. There are several options moving forwards. First we should remember that the LMR-NMC materials is still the highest energy cathode material current under development, as seen in Figure IV - 190, and has many extremely desirable properties. Even if LMR-NMC is limited to an upper voltage cutoff of 4.3V where no voltage fade is apparent the energy density is comparable to NCA at a significantly lower materials cost as shown by Figure IV - 191.

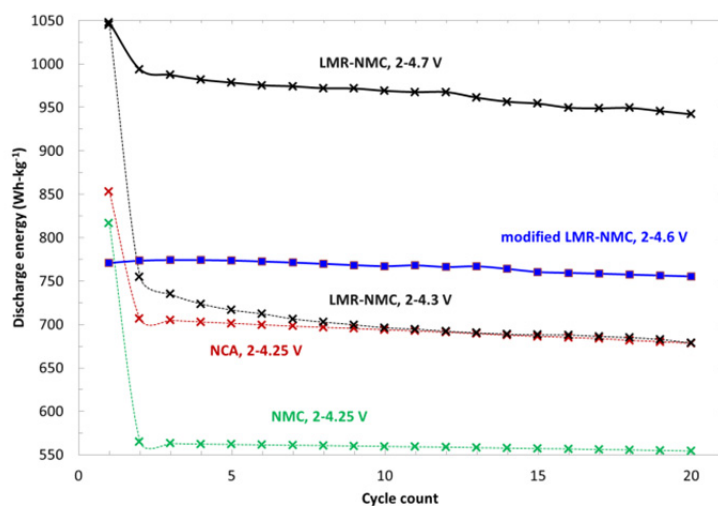


Figure IV - 190: Relative energy densities for cathode materials

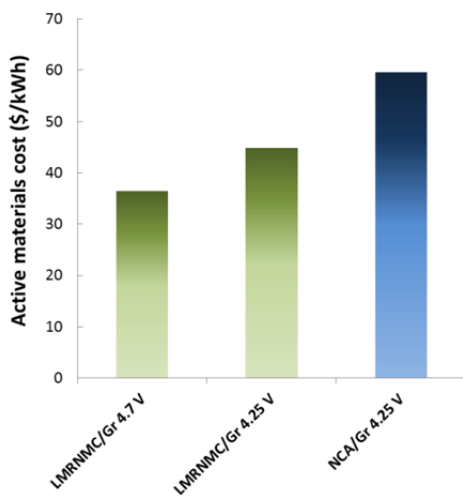


Figure IV - 191: Relative materials costs for cathode materials is dependent upon energy density and composition.

www.cse.anl.gov/batpac

One thing than should be remembered in this story is that to achieve the very highest energy densities from LMR-NMC upper charging voltages of greater than 4.5V (preferably 4.7V) are required. In full cells cycling to such high voltages has dramatic negative effects beyond the effect of voltage fade.

There are compositions of the LMR-NMC cathode material yet to be identified with an optimal combination of energy density and voltage fade but this research will not require a large team effort and is perhaps better suited to single PI projects. The scientific understanding, cycling protocols and data analysis tools this team created provide the foundation for future research into minimizing voltage fade in LMR-NMC materials. In addition before the full capability of LMR-NMC can be realized it must be possible to cycle, high

energy cells employing either a graphic or silicon based anode at 4.7V for thousands of cycles.

Perhaps the single greatest achievement of the voltage fade project was the team itself. The researchers worked together to tackle a serious issue which at the beginning of this project was only poorly understood. The work encompassed multiple PI's, research groups and institutions all with a clear outcome in mind. They readily stopped working on approaches that proved to be unsuccessful and down-selected to approaches with the most promise. This project was slated to take three years and the team work, focus on the task and adherence to the research plan enabled its completion one year early.

The Voltage Fade Team

Burrell, Anthony K.; Abouimrane, Ali; Abraham, Daniel; Amine, Khalil; Balasubramanian, Mahalingam; Barenco Garcia-Ontiveros, Javier; Belharouak, Ilias; Benedek, Roy; Bettge, Martin; Bloom, Ira D.; Long, Brandon R.; Chen, Zonghai; Croy, Jason R.; Dees, Dennis W.; Dogan, Fulya; Gallagher, Kevin G.; Henriksen, Gary L.; Iddir, Hakim; Ingram, Brian J.; Johnson, Christopher; Key, Baris; Li, Yan; Lu, Wenquan; Miller, Dean J.; Ren, Yang; Slater, Michael D.; Thackeray, Michael M.; Vaughey, John T.; Wu, Huiming; Wu, Qingliu; Zhu, Ye; Yang, Zhenzhen; Lee, Eungje; Aoun, Bachir; Vu, Anh D.; Lin, Chi-Kai; Rinaldo, Steven G.; Tenant, Robert; Ban, Chunmei; Nanda, Jagit; Bugga, Kumar; Yang, Xiao-Qing; Mohanty, Debasish; Li, Jianlin; Payzant, Andrew; Wood, David; Daniel, Claus; Jansen, Andrew; Polzin, Bryant; Trask, Steven; Krundick, Greg.

IV.D High Energy Cell R&D: “Improvements in Cell Chemistry, Composition, and Processing”

IV.D.1 New High Energy Electrochemical Couple for Automotive Applications (ANL, BNL, LBNL)

Peter Faguy (Program Manager)
Subcontractor: Argonne National Laboratory

Khalil Amine, Ph.D
Argonne National Laboratory
9700 South Cass Avenue
Argonne, IL 60439-4837
Phone: (630) 252-3838; Fax: (630) 972-4451
E-mail: amine@anl.gov

Collaborators:
Huiming Wu, Argonne National Laboratory
Zonghai Chen, Argonne National Laboratory
Ali Abouimrane, Argonne National Laboratory
Jun Lu, Argonne National Laboratory
Yangie Cui, Argonne National Laboratory
Xiao Qing Yang, Brookhaven National Laboratory
Liu Gao, Lawrence Berkeley National Laboratory

Start Date: October, 2014 (New Project)
Projected End Date: September, 2016 (last report)

Objectives

The main objective of the proposal is to develop a new redox couple that meets and exceeds the DOE targeted energy density of 200 Wh/kg and exhibits outstanding cycle and calendar life, low cost, and excellent abuse tolerance.

Technical Barriers

The primary technical barrier is the development of a safe and cost-effective battery with 40 mile range for a plug-in hybrid electric vehicle that meets or exceeds all DOE performance goals.

Technical Targets

The technical target of this project is to develop a redox couple that provides specific energy in excess of 200 Wh/kg with cycle life of at least 500 cycles. This

couple is to be based on (1) a high-voltage (~4.4 V) and high-capacity cathode composed of lithium manganese, cobalt, and nickel metal oxide (~230 mAh/g) with full gradient concentration across each particle (FCG) to stabilize the material at high voltage, and (2) a high-capacity and high-density composite anode composed of $\text{SiO-Sn}_x\text{Co}_y\text{Fe}_{1-y}\text{C}_z$ with conductive binder to enhance cycle life. These active materials will be assembled in a high-energy prismatic cell (0.4 Ah) for independent testing and validation.

Accomplishments

- Scaled up 50 wt% SiO-50 wt% $\text{Sn}_{30}\text{Co}_{30}\text{C}_{40}$ anode to 500 g level for use in baseline cell.
- Acquired 25 kg of $\text{LiNi}_{0.6}\text{Mn}_{0.2}\text{Co}_{0.2}\text{O}_4$ cathode from industry for use in baseline cell.
- Engineered cathode and anode electrodes using conventional polyvinylidene fluoride (PVDF) binder, built a full baseline cell, and carried out cycling tests.
- Set up a continuously stirred co-precipitation reactor for carrying out development of a FCG cathode.
- Prepared dense FCG cathode using hydroxide process (2.7 g/cc).
- Confirmed thermal stability of FCG cathode using synchrotron soft X-ray at different temperatures.



Introduction

Lithium-ion batteries exhibit the highest power and energy density of any existing commercial battery system and offer many advantages for applications in the transportation sector. Among existing cathode chemistries used in lithium batteries, LiMn_2O_4 spinel (LMO) and LiFePO_4 olivine (LFP) show considerable promise for high-power applications such as hybrid electric vehicles (HEVs), where power is more important than energy. However, these cathodes offer very limited capacity and, thus, are not suitable for plug-in hybrid vehicles (PHEVs) and all-electric vehicles

(EVs). The layered oxide materials such as $\text{LiNi}_{0.8}\text{Co}_{0.1}\text{Mn}_{0.1}\text{O}_2$ or $\text{LiNi}_{0.8}\text{Co}_{0.15}\text{Al}_{0.05}\text{O}_2$ (NCA) and $\text{Li}_{1.1}[\text{Ni}_{1/3}\text{Mn}_{1/3}\text{Co}_{1/3}]_{0.9}\text{O}_2$ (NMC) offer higher capacity than LMO and LFP but not high enough to meet the PHEV (with 40 mile electric range) and full EV demands within a required volume and weight that does not compromise the trunk volume and vehicle performance. Therefore, cathodes possessing very high capacity (over 200 mAh/g), good cycle and calendar life, and outstanding safety are urgently needed for use in EVs and PHEVs-40, which require thousands of charge-depleting cycles and 15 years of calendar life.

Among the cathode technologies that have the potential of providing either very high capacity or high voltage are the layered lithium mixed metal oxides such as Argonne's layered composite oxide $x\text{Li}_2\text{MnO}_3 \bullet (1-x)\text{LiMO}_2$ ($M=\text{Ni, Co}$) and $\text{LiNi}_{1-x}\text{Mn}_x\text{Co}_z\text{O}_2$ for high energy, and $\text{LiNi}_{0.5}\text{Mn}_{1.5}\text{O}_4$ (4.8 V), $\text{LiCo}_{0.5}\text{Mn}_{1.5}\text{O}_4$ (5.1 V), LiMnPO_4 (4.1 V), and LiCoPO_4 (5.1 V) for high voltage.

The practical capacity of layered lithium mixed metal oxides, such as $\text{LiNi}_{0.8}\text{Co}_{0.1}\text{Mn}_{0.1}\text{O}_2$, NCA, and NMC, is only 50% of theoretical (275 mAh/g) under the operating potential window of 4.2 V~3 IV. Operating at voltages higher than 4.3 V can lead to a significant increase in the specific capacity up to 220 mAh/g. However, at high potential, the cycle life of this material is very poor. This fast capacity decay is caused by the high interfacial reactivity of the fully charged electrode with the electrolyte, which leads to film growth at the surface of the cathode and an increase in the cell interfacial impedance with cycling. The high reactivity with the electrolyte is caused by the high concentration of unstable tetravalent Ni during high voltage charge, which reduces to stable divalent Ni and leads to O_2 release from the particle surface, oxidation of the electrolyte, and formation of a polymeric film at the surface of the cathode. Similar characteristics, mainly capacity increase at high voltage, accompanied by capacity fade during cycling, were also observed for NCA and NMC.

Approach

Argonne (ANL) is working closely with Brookhaven (BNL) and Lawrence Berkeley National Laboratory (LBNL) to develop an advanced electrochemical couple. The cathode is a high-voltage, high-capacity, and dense FCG with full gradient concentration across each particle to stabilize the material, and the anode is a high-capacity and high-density $\text{SiO-Sn}_x\text{Co}_y\text{Fe}_{1-y}\text{C}_z$ composite that offers capacities higher than 600 mAh/g. This system will be investigated in cell tests using two electrolytes: a conventional electrolyte with additives that stabilize the interface of both cathode and anode and a fluorinated electrolyte that will be supplied by industrial partners.

At the initial stage, a cathode of $\text{LiNi}_{0.6}\text{Mn}_{0.2}\text{Co}_{0.2}\text{O}_2$ with constant composition coupled with an anode of $\text{SiO-Sn}_x\text{Co}_y\text{Fe}_{1-y}\text{C}_z$ composite will be used as the baseline chemistry. The performance of the baseline chemistry will be compared to that of an FCG cathode with the same average composition, $\text{LiNi}_{0.6}\text{Mn}_{0.2}\text{Co}_{0.2}\text{O}_2$. The optimum chemistry based on an FCG cathode and carbon/ $\text{SiO-Sn}_x\text{Co}_y\text{Fe}_{1-y}\text{C}_z$ anode will be built and delivered to an independent laboratory for testing and validation.

Results

Baseline Chemistry

Initial effort in this project was focused on building the baseline chemistry. The baseline $\text{LiNi}_{0.6}\text{Mn}_{0.2}\text{Co}_{0.2}\text{O}_2$ cathode material (25 kg) was acquired from ECOPRO and is used by a number of battery companies in Asia. The $\text{SiO-Sn}_x\text{Co}_y\text{Fe}_{1-y}\text{C}_z$ material was scaled up by Argonne to the 0.5-kg level. The design of the baseline chemistry cell is summarized below:

- Anode:
- ✓ 90 wt% SiO-SnCo-C ; 5 wt% Timcal C-45; 5 wt% UBE U-Varnish A
 - Total Electrode Thickness: 13 microns.
 - Cu Foil Thickness: 10 microns.
 - Total Electrode Loading: 2.41 mg/cm^3 .
 - Porosity: ~45%.
- Cathode:
- ✓ 90 wt% ECOPRO NCM 622; 5 wt% Timcal C-45; 5 wt% Solvay 5130 PVDF
 - Total Electrode Thickness: 77 microns.
 - Al Foil Thickness: 20 microns.
 - Total Electrode Loading: 14.83 mg/cm^3 .
 - Porosity: ~36%.
- Separator:
- ✓ Celgard 2325 PP/PE/PP Tri-Layer.
- Electrolyte:
- ✓ Tomiyama Pure Chemicals -1.2M LiPF_6 in EC:EMC (3:7 wt%) with 10 wt% Solvay FEC.

Figure IV - 192 shows the performance of the baseline chemistry at the full cell level. The cell shows good cycle life (Figure IV - 192a) and low area specific impedance (ASI) of 40 ohm cm^{-1} (Figure IV - 192b) after applying a high-pulse characterization test at 3C discharge and 2.25C charge. This result is very encouraging since the anode used 90 wt% un-optimized SiO-SnCo-C , which has very large initial irreversible capacity loss.

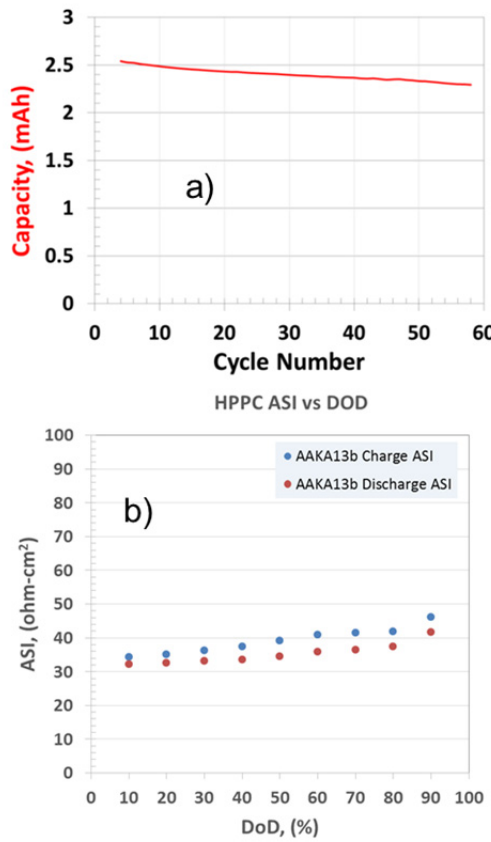


Figure IV - 192: Electrochemical performance of baseline cell: (a) capacity for more than 50 cycles and (b) area specific impedance (ASI) vs. depth of discharge (DoD)

Table IV - 21 shows the expected usable energy density in Wh/kg and Wh/l as well as the power density at minimum state of charge (SOC) in W/kg during a 10-s pulse. These data were calculated from the BatPAC model based on two cell sizes: 20 Ah and 40 Ah. The predicted usable gravimetric energy densities of the baseline cell are 216 Wh/kg and 271 Wh/kg for the 20 Ah and 40 Ah cell, respectively. The volumetric energy densities are 511 Wh/l and 650 Wh/l for the 20 Ah and 40 Ah cells, respectively. Finally, the calculated power densities for the 20 Ah and 40 Ah cells are 1880 W/kg and 1177 W/kg, respectively. These BatPAC model results indicate that the baseline alone with the new high energy anode meets and exceeds the DOE energy performance requirements.

Table IV - 21: Battery performance based on baseline chemistry determined by BatPAC model

Deliverable	Device	Battery Performance (Cell Level)			
		Usable Specific Energy (Wh/kg)	Energy Usable Density (Wh/l)	Power at SOCmin (W/kg, 10 sec)	Technology Info
baseline	20Ah Cell 40Ah Cell BatPac Design	(-216) (-271)	(~511) (~650)	(-1880) (-1177)	Si-Sn Composite And NMC (6:2:2)

Cathode Material

As stated before, our objective is to achieve capacities as high as 220 mAh/g for layered lithium metal mixed oxide by increasing the operating voltage to 4.4 V and stabilizing the surfaces using an FCG across the whole cathode particles. Argonne has developed an FCG layered manganese nickel cobalt system

(Figure IV - 193) where each particle has a central bulk that is rich in nickel and a manganese-rich outer layer with decreasing Ni concentration and increasing Mn concentration as the surface of the particle is approached. The former provides very high capacity at high voltage, as in the case of NCA, while the latter improves the electrode stability with respect to the electrolyte and provides excellent cycle life and safety characteristics. In this case, the particle surface has a high concentration of Mn.

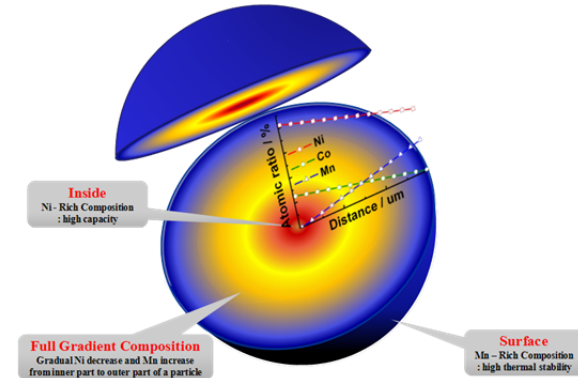


Figure IV - 193: Schematic of full continuous concentration gradient cathode material (FCG)

Figure IV - 194a shows energy dispersive X-ray analysis (EDAX) of FCG cathode material prepared using a carbonate-based precursor. In this case, the material has a composition of $\text{LiNi}_{0.6}\text{Mn}_{0.25}\text{Co}_{0.15}\text{O}_2$. Also, the Ni concentration is high at the bulk and progressively reduced toward the outer layer of the particle. The Mn concentration remains constant across the particle, and the Co concentration increases slowly toward the particle surface. Figure IV - 194b presents the results from electron probe micro-analysis (EPMA) of a cross section of a particle. This cathode material has

a low tab density of 2.2 g/cc due to a significant CO₂ release during the calcination process.

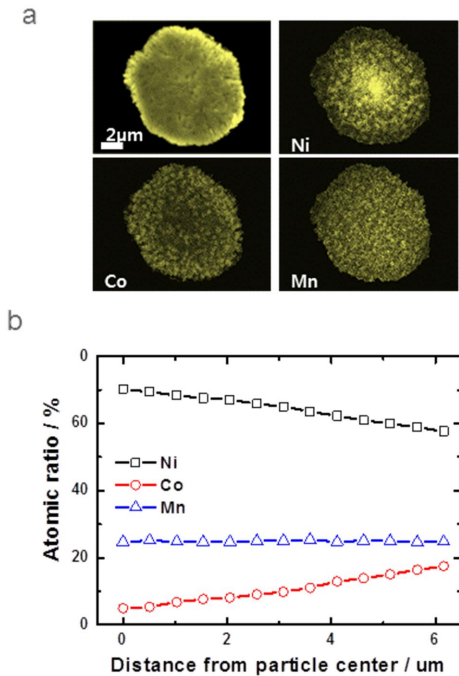


Figure IV - 194: (a) EDAX of FCG cathode and (b) EPMA result showing the composition gradient at the particle level

Figure IV - 195a shows the initial electrochemical performance of the FCG cathode in half cells both at room temperature and 55°C. The cathode shows capacities of 220 mAh/g at the C/10 rate. Figure IV - 195b compares the cycling performance of a half-cell based on the FCG cathode and a cathode that has the same average formula LiNi_{0.6}Mn_{0.25}Co_{0.15}O₂ with constant composition (core). The capacity retention of the cell based on FCG cathode is much better than that of the core cathode during the first 100 cycles. In this case, the cells were cycled between 4.3 V and 2.7 V at a rate of C/5.

Since the carbonate process has led to a packing density of 2.2 g/cc, which is very low for a Ni-rich cathode material, we have focused our synthesis optimization on the hydroxide process to increase the tab density and thus the loading of active material in the electrode.

Figure IV - 196 shows a scanning electron microscopy (SEM) image of FCG precursor Ni_{0.6}Mn_{0.2}Co_{0.2}(OH)₂ made by the co-precipitation process and the final FCG (LiNi_{0.6}Mn_{0.2}Co_{0.2}O₂) cathode. In both cases, the particles are spherical and very dense, with the final FCG cathode having a packing density of 2.7 g/cc.

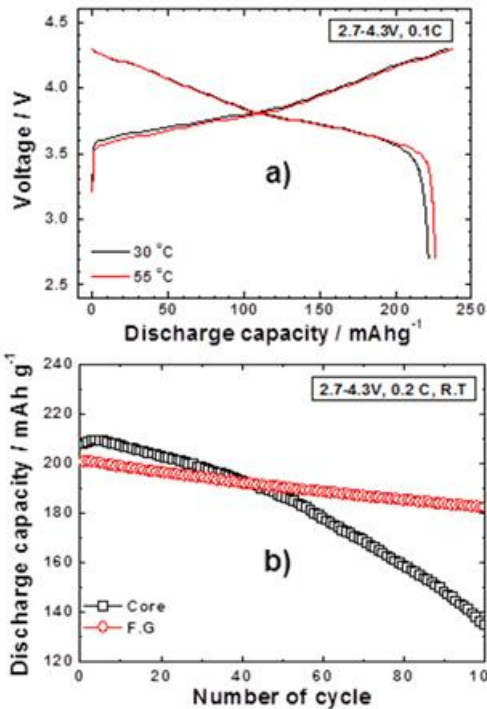


Figure IV - 195: (a) Initial charge and discharge at 30°C and 55°C of half-cell based on FCG cathode and (b) comparison of cycling performance of cell based on FCG cathode and cathode that has the same average formula LiNi_{0.6}Mn_{0.25}Co_{0.15}O₂ with constant composition (core)

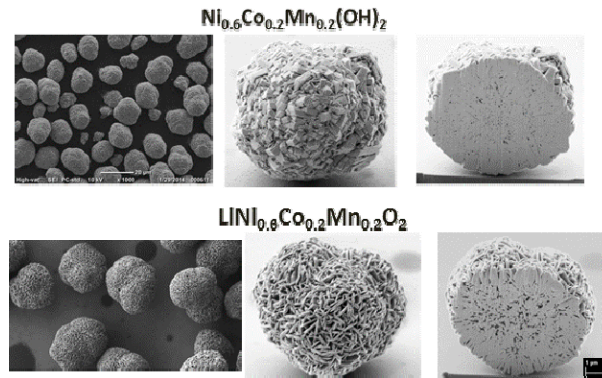


Figure IV - 196: SEM images of FCG precursor Ni_{0.6}Mn_{0.2}Co_{0.2}(OH)₂ and LiNi_{0.6}Mn_{0.2}Co_{0.2}O₂

Figure IV - 197 shows the initial charge and discharge capacity of a half-cell based on the FCG cathode made by the hydroxide process. This cell was cycled between 4.3 V and 2.75 V at a C/3 rate. The cell attained a capacity of 182 mAh/g with a first-cycle efficiency of 94%. It showed no capacity fade after 100 cycles. Further development is underway to improve the discharge capacity to over 200 mAh/g by optimizing the hydroxide process and the calcination patterns.

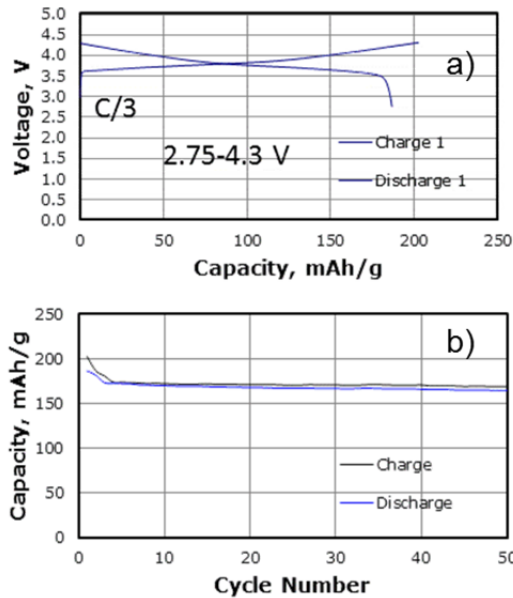


Figure IV - 197: (a) Initial charge and discharge of half-cell based on FCG cathode prepared by hydroxide process and (b) cycling performance of FCG cathode

Time-resolved x-ray diffraction (TR-XRD) data for the FCG sample together with reference NCA samples were collected at beam-line X7B ($\lambda=0.3196\text{\AA}$) of the National Synchrotron Light Source using an image plate detector in the transmission mode. Approximately 3.5~4.0 mg of the charged cathode sample was loaded into a quartz capillary with an inner diameter of 0.7 mm and two open ends. One end of the capillary was connected to He carrier gas, and the other end was connected to a residual gas analyzer mass spectrometer (RGA200, Stanford Research Systems) with a flow meter to detect gas species released from the sample during heating. Quartz wool was placed on each side of the sample to prevent its movement due to the He carrier gas flow. The TR-XRD patterns (about ~4 minutes for each XRD scan) and mass spectrum were simultaneously collected in a continuous manner as the sample was heated from room temperature to 600°C for 4 h (at a heating rate of $\sim 2.4\text{ }^{\circ}\text{C min}^{-1}$). The XRD patterns of selected samples were refined by Le Bail methods using the GSAS package with the EXPGUI interface.

The TR-XRD patterns for the FCG sample in comparison with NCA samples, as well as the oxygen release data collected through the mass spectrum, are plotted in Figure IV - 198. For the FCG sample, the phase transition from layer structure to the spinel phase (Figure IV - 198a) occurred at higher temperatures and covered a wider temperature range than the NCA sample. Figure IV - 198(b) shows less oxygen release of the FCG than bulk NCA samples. In addition, the oxygen release of the FCG sample covered a much broader temperature range than that of the NCA sample.

The small and broadened oxygen release temperature range might be able to suppress the drastic exothermic reaction between O₂ and flammable electrolyte and improve the thermal stability of the FCG materials in comparison with the NCA material.

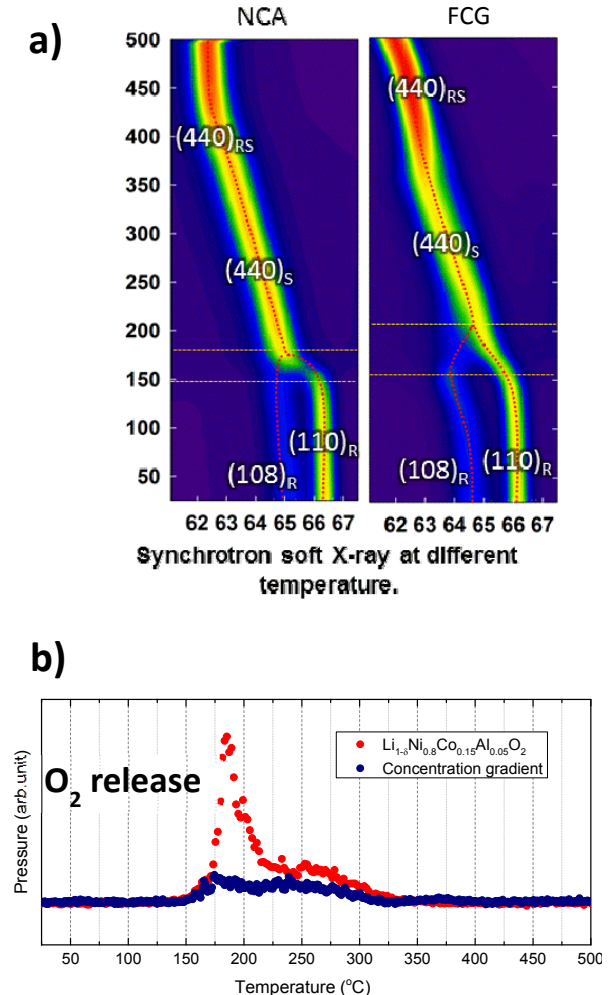


Figure IV - 198: (a) Contour plots of the TR-XRD patterns at the selected 2θ range for the charged FCG and NCA sample and (b) mass spectroscopy profiles for the oxygen release (O₂, m/z=32) collected simultaneously during measurement of TR-XRD and the corresponding temperature region of the phase transitions for the FCG and NCA samples

Anode Material

Silicon monoxide can produce high capacity but suffers from poor cycle life. Also, Sn-Co-C has good cyclability and high tap density, but its reversible capacity is not significantly better than that of the commercial carbon anode. Our work reports on a new anode material, based on 50 wt.% SiO-50 wt.% Sn₃₀Co₃₀C₄₀ composite (molecular composition: SiSn_{0.23}Co_{0.23}C_{0.3}O), which was synthesized by a custom-made ultra-high energy ball milling (UHEM) method. The SiO-Sn_xCo_yC_z composite has the potential

to combine the advantageous properties of both SnCoC (long cycle life) and SiO (high capacity) and, thereby, improve the overall electrochemical performance.

Mechanical ball milling, which is known to produce nano-sized particles, is often used for improving electrochemical properties. The ball milling method is employed not only to reduce the particle size, but also to synthesize non-equilibrium alloys starting from blended elemental or pre-alloyed powders. Traditional ball mills adopt stirred mills or vibration mills. However, these mills exhibit a limitation regarding product fineness: a size limit of 1 μm is often observed after several hours of grinding. This limitation is due to the particles being weakly confined in the breakage zone of these mills. Our custom-made milling machine works by a planetary mill method that creates a very high centrifugal field, confining the particles in the milling area and reducing the “dead zone” effect (see Figure IV - 199).

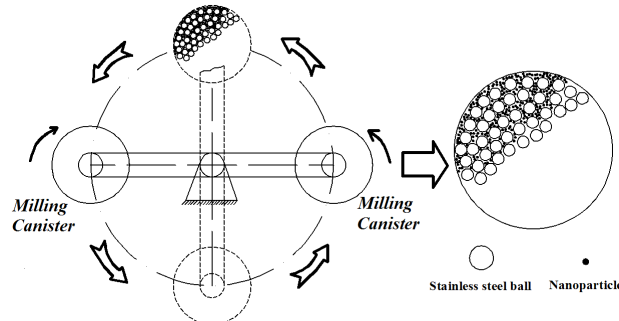


Figure IV - 199: Scheme for ultra-high energy ball milling machine

Figure IV - 200 shows the SEM of $\text{SiO-Sn}_x\text{Co}_y\text{C}_z$ (Figure IV - 200a) and the energy dispersive x-ray (EDX) mapping images for Si, O, Sn, Co, and C in a UHEM sample. The results indicate that Si (Figure IV - 200e) and Sn (Figure IV - 200f) exhibit very similar distribution, especially in the yellow-circled areas. This result indicates that Si and Sn may be alloying during the ball milling process.

Figure IV - 201 shows the XRD patterns of the UHEM sample. The Bragg peaks from tin and graphite are not observed. Graphite readily loses its crystalline structure under external stress. This may account for graphite being invisible in the XRD pattern. Metal oxide peaks not being detectable in Figure IV - 201 implies that milling occurred without oxidation. The inset image shows the conventional XRD pattern. Due to the amorphization of the as-milled samples, the conventional XRD apparatus is limited by low energy and low resolution to index peaks. Therefore, we performed high-energy XRD. As shown in Figure IV - 201, diffraction peaks for CoSn_2 and Co are clearly present in the high-energy XRD pattern for the UHEM sample. Commercial SiO is known to be an amorphous phase, and the structure of SiO consists of

nanoparticles of Si distributed in a matrix of amorphous SiO_2 .

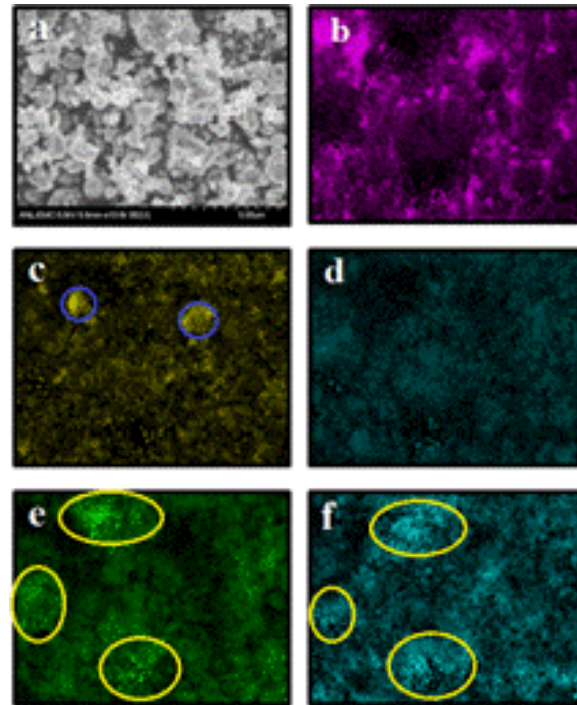


Figure IV - 200: SEM image (a) and EDX elemental mapping of (b) C, (c) Co, (d) O, (e) Si, and (f) Sn for the UHEM $\text{SiO-Sn}_{30}\text{Co}_{30}\text{C}_{40}$ composite

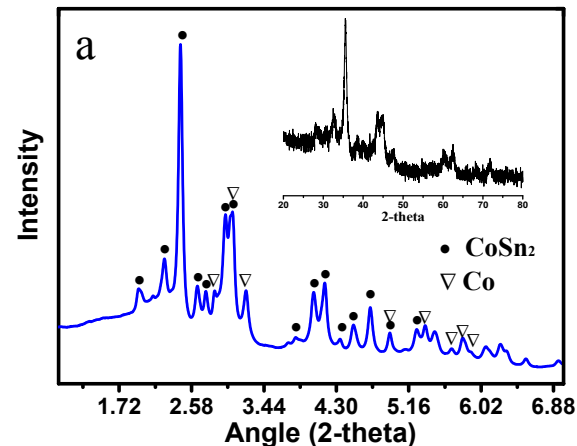


Figure IV - 201: XRD patterns of UHEM sample

Galvanostatic charge-discharge experiments with the composite anode material were carried out at current rates of 100 mA g^{-1} , 300 mA g^{-1} , and 900 mA g^{-1} within a voltage window of $0.005\text{-}1.5 \text{ V}$ (Figure IV - 202). In the first cycle, the UHEM anode exhibits charge and discharge capacities of 1030 mA h g^{-1} and 1480 mA h g^{-1} at 300 mA g^{-1} ($\sim\text{C}/3$). All the discharge capacity is delivered below 0.4 V . A small variation is observed in the voltage profile with continued cycling at 300 mA g^{-1} (Figure IV - 202a) and 900 mA g^{-1} (Figure IV - 202b),

indicating excellent capacity retention after 100 cycles. The major issue in this cell is the large irreversible loss in the first cycle. Our focus will be to increase the first-cycle efficiency to 90% by exploring a composite of this anode with active graphite (both natural and artificial) coupled with suitable electrolyte additive and a conductive binder under development by LBNL.

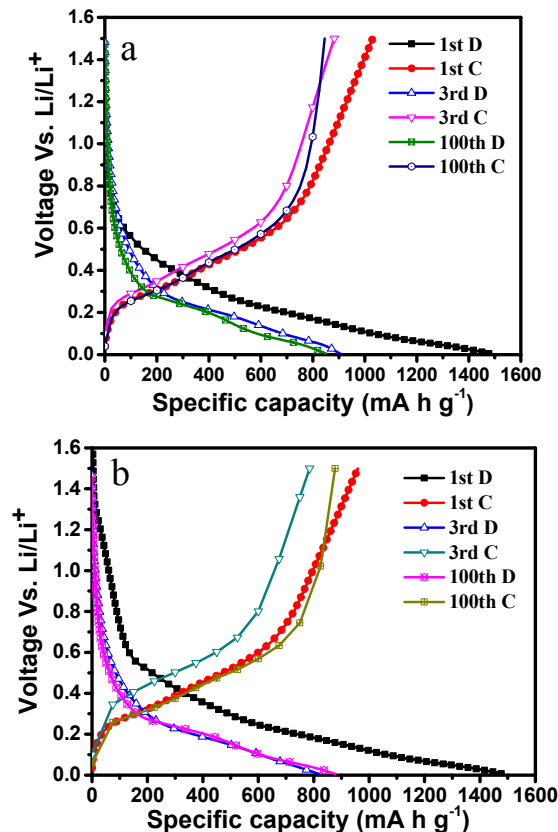


Figure IV - 202: Charge-discharge curves of cells with UHEM anode cycled at rates of (a) 300 mA g⁻¹ (~C/3) and (b) 900 mA g⁻¹ (~1C)

While carrying out the above study, ANL is developing the high-energy composite $\text{SiO-Sn}_x\text{Co}_y\text{Fe}_{1-y}\text{C}_z$ as anode for the proposed electrochemical couple. The focus will be on reducing the irreversible loss by exploring a graphite- $\text{SiO-Sn}_x\text{Co}_y\text{Fe}_{1-y}\text{C}_z$ composite with conductive binders from LBNL. Also, the effect of electrolyte additives to provide a stable passivation film will be investigated. These materials will be scaled up, and cells based on this redox couple will be made and their performance will be validated.

FY 2014 Publications/Presentations

1. Liu, B.; Abouimrane, A.; Balasubramanian, M.; Ren, Y.; Amine, K., *Journal of Physical Chemistry C* **2014**, 118, 3960.
2. Cui, Y.; Abouimrane, A.; Sun, C.-J.; Ren, Y.; Amine, K., *Chemical Communications* **2014**, 50, 5576.
3. Noh, H.-J.; Chen, Z.; Yoon, C. S.; Lu, J.; Amine, K., *Chemistry of Materials* **2013**, 25, (10), 2109-2115.
4. Liu, B.; Abouimrane, A.; Brown, D. E.; Zhang, X.; Ren, Y.; Fang, Z. Z.; Amine, K., *Journal of Materials Chemistry A* **2013**, 1, (13), 4376-4382.
5. Sun, Y.-K.; Chen, Z.; Noh, H.-J.; Lee, D.-J.; Jung, H.-G.; Ren, Y.; Wang, S.; Yoon, C. S.; Myung, S.-T.; Amine, K., *Nature Materials* **2012**, 11, (11), 942-947.

Presentations

6. Amine, K. In 2014 Electrochemical Society and SMEQ (Sociedad Mexicana de Electroquímica) Joint International Meeting, Cancun, Mexico, October 5-10, 2014.
7. Amine, K. In 224th Electrochemical Society Meeting, San Francisco, CA, October 27–November 1, 2013).

Conclusions and Future Directions

Argonne will continue to work closely with BNL and LBNL to develop an advanced electrochemical couple based on a high-voltage, high-capacity, and dense cathode of FCG with full gradient concentration across each particle to stabilize the material, and a high-capacity and high-density anode composed of a $\text{SiO-Sn}_x\text{Co}_y\text{Fe}_{1-y}\text{C}_z$ composite. Now that ANL has successfully developed a hydroxide process that provides a FCG cathode with very high tab density, the next step will focus on optimizing the composition of the full continuous gradient materials and fabrication processes that can lead to high Mn concentration at the surface of the particle for effective stabilization against reactivity with the electrolyte.

IV.D.2 High Energy Novel Cathode / Alloy Automotive Cell (3M, GM, Unicore, Leyden, LBNL, ARL)

John Tabacchi (DOE Program Manager)

Subcontractor: 3M Company

Jagat D. Singh (Program Manager)

3M Center, Building 209-2C-26

St Paul, MN 55144

Phone: (651) 575-1230; Fax: (651) 736-7478

E-mail: jdsingh@mmm.com

Start Date: October 2011

Projected End Date: January 2015

Objectives

The objectives of the project are

- Develop a >2 Ampere Hour (Ah) Cylindrical wound or stacked pouch cell with high energy density at low cost for automotive application.
- Integrate advanced chemistries including an advanced high-voltage cathode, high capacity alloy anode and advanced electrolyte materials as well as enabling technologies related to electrode preparation and cell build such as binder, conductive agent, and processing aids.

Technical Barriers

This project addresses the following technical barriers associated with the combination of high energy cathode and advanced alloy anode material:

- Low Cycle Life.
- Low Rate Capability.
- High irreversible capacity leading to low overall cell energy density.
- Large volume expansion of alloy anode.

Technical Targets

- Establish a baseline cell with similar energy density to USABC EV targets with commercial $\text{LiMn}_{1/3}\text{Ni}_{1/3}\text{Co}_{1/3}\text{O}_2$ (NMC 111) cathode and graphite anode.
- Provide an advanced cell with at least 40% (1.4 x base/L) increase in energy density compared to the baseline cell.

- Demonstrate as good or superior thermal stability, long-term cycling, and rate capability, of the advanced cell compared to baseline test cell.
- Demonstrate by calculation at least 25% lower cost per unit energy at the cell level for comparative integrated advanced materials cell to a baseline materials cell.

Accomplishments

- Down selected high energy core shell cathode and Si alloy anode materials for 18650 performance optimization.
- Demonstrated material scale up to 100+ kg levels.
- Further optimized pilot process parameters to improve process robustness. Identified parameters to control process variability.
- Demonstrated >40% energy increase, with intermediate design (C/S||Si) in 18650 cells over baseline (NMC || Graphite).
- Sampled 18650 format cells to ANL for testing; 18 cells with baseline materials and 6 cells with intermediate materials.
- Post mortem cycled 18650 to identify root cause for rapid capacity fade.
- Improved cycle life in 60% energy window.
- Identified voltage windows (60% energy) for better performance.
- Reduced 18650 formation time to a commercially viable time.



Introduction

In order to design a lithium ion cell with a step function increase in energy, it is necessary to start from scratch with new well designed and matched active materials. First, the cathode needs to have a Cathode Energy Factor (CEF) beyond the traditional LCO and NMC materials. This invariably requires charging to higher cell voltage. Second, the cathode irreversible capacity has to "match" the irreversible capacity of the composite alloy anode. In fact, for cell balance and control of the lower cut off cell voltage, it is convenient if the irreversible capacity of the composite cathode is slightly larger than that of the anode. For the Active alloy it is critical to have the proper morphology (amorphous active phase), the proper particle size

(microns), and the proper activity leading to a volume expansion of 110 to 120% upon lithiation. Next, the composite electrode has to be formulated with graphite for highest density and best inter particle contact, while still providing the required volumetric energy when fully lithiated. Finally, the electrolyte and separator must be stable against the two active composite electrodes, across the complete cell voltage range, to eliminate any parasitic reactions.

Approach

3M team has been leveraging its expertise in R&D of Lithium Ion Batteries to develop a high energy cell using synergistically matched anode and cathode electrodes. To achieve the goal, a three phase approach has been taken. The phases are:

- Phase I - Verify baseline materials performance, and select advanced cell material candidates for further evaluation and optimization.
- Phase II - Integration of individual optimized materials into full cells and optimization of EV test cell.
- Phase III - Final Optimization of integrated advanced materials in EV test cells, complete cell evaluation, fabrication of final cells and submission of final cells to National Labs.

Results

Cathode Material Development: The team has successfully developed a core shell (C/S) based high energy cathode material. Table IV - 22 compares the two developed cathode material with baseline NMC material. 126T shows >35% CEF increase over the baseline.

Table IV - 22 : Cathode Energy Factor comparison of different cathodes when matched to graphite or a Si composite

	Oxide	Capacity	X	Density	X	Voltage	X	Irrev Factor	=	Cathode Energy Factor
Electronics	LCO	0.179		3.75		3.99		0.95		2.54 (graphite)
	LCO	0.179		3.75		3.99		0.88		2.36 (alloy)
	NCA	0.196		3.5		3.78		0.97		2.51 (graphite)
Automotive	NMC	0.160		3.3		3.90		0.98		2.01 (graphite)
	NMC	0.160		3.3		3.90		0.95		1.96 (alloy)
Core-Shell	126M	0.230		3.4		3.84		0.95		2.85 (alloy)
	126T	0.220		3.4		3.88		1.00		2.90 (alloy)

The materials were successfully scaled up from few grams to 100+ kg. Figure IV - 203 compares the dQ/dV of the three scales.

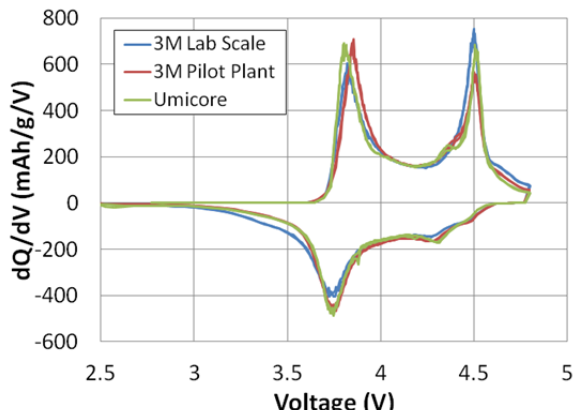


Figure IV - 203: Material Validation in coin cells vs. Li

Anode Material Development: The team successfully developed a new Si anode composition, studied parameters for process optimization and scaled up material production. L20772 was down selected is

being tested for performance optimization. Table IV - 23 summarizes the different Si alloy based anode materials developed with the help of DOE funding

Table IV - 23: Si alloy anodes developed with DOE support

Material Type	Specific Capacity (mAh/g)	1 st Cycle Efficiency (%)	Scalability	DOE Support
L-20772	860	89.6%	No	
C-L-20772	850	88.2%	No	EE-
V4	1250	76.4%	Yes	000650
V5	1004	83.5%	NA	
V6	1060	85.0%	Yes	EE-
CV6	837	84.1%	Yes	005449

The team also performed analysis to fit dV/dQ and help determine the relative positions of anode and cathode during testing (Figure IV - 204).

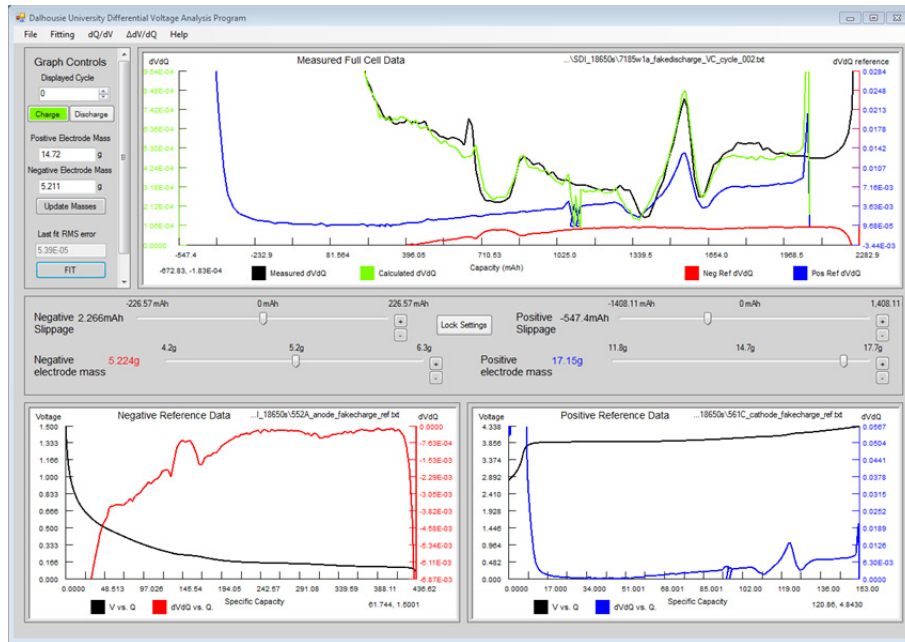


Figure IV - 204: Snap shot of the dV/DQ software

Electrolyte Development: Electrolytes which can enable performance at high voltages were tested for performance evaluation. Figure IV - 205 compares the

effect of FEC and L20446 during OCV storage against standard electrolyte systems.

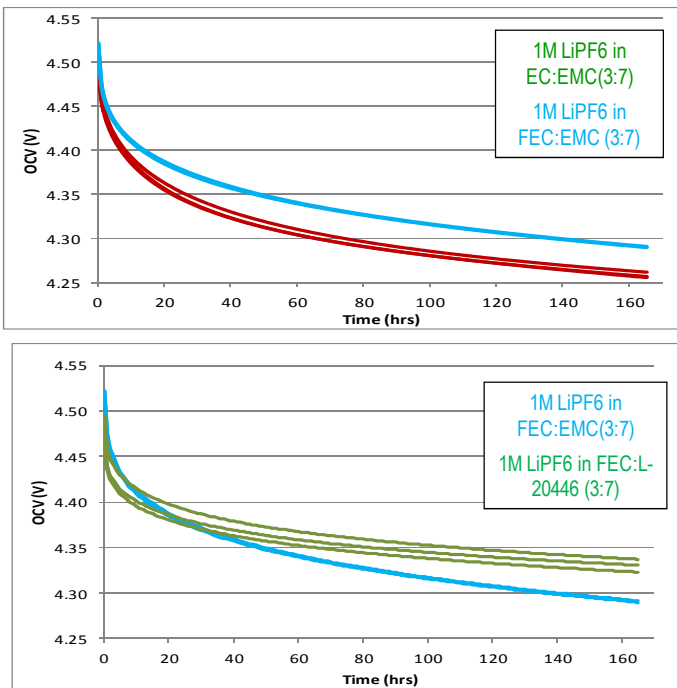


Figure IV - 205: High Voltage stability of FEC and L-20446

Cell Development: The advantage of the core shell cathode and Si anode is shown in Figure IV - 206. The matched irreversible capacity helps to prevent the anode from going to a high potential during the bottom of full cell discharge.

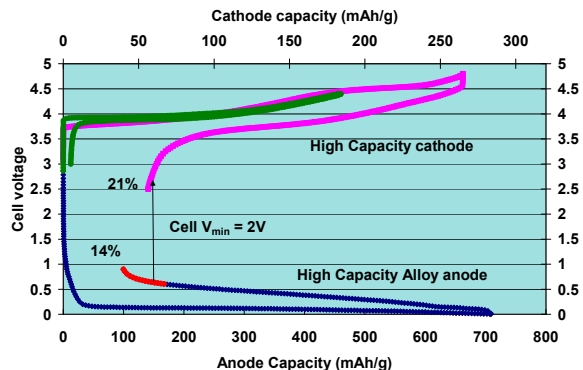


Figure IV - 206: Matching 1st cycle efficiencies maximizes benefit of both materials

18650 cells with Core shell cathode matched to Si anode show higher energy at the beginning of Life but after 100 cycles start to fade rapidly as shown in Figure IV - 207.

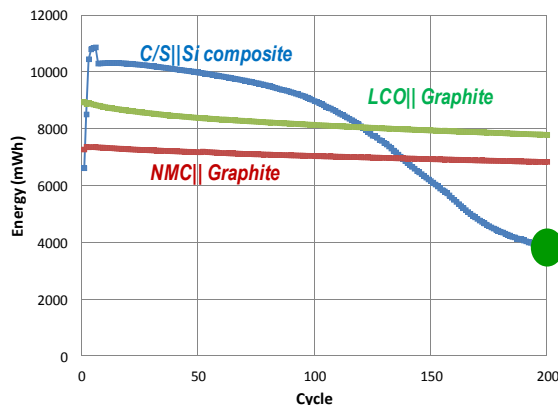


Figure IV - 207: Cycle life of Core shell || Si anode composite

The cell was post mortemed after 200 cycle (shown by the big green dot in Figure IV - 207). Figure IV - 208 shows the picture of the dry jelly roll. Half coin cells (both anode and cathode) were assembled from the unrolled jelly roll. Fresh electrolyte was used in these half cells, Figure IV - 209 shows the initial capacity of these cycled electrode.



Figure IV - 208: Picture of post mortemed 18650 jelly roll

The majority of the capacity is regained suggesting that the active materials are not dead.

During the period a new formation process was also developed by the team to reduce the formation time from 1 week to 1 day. Figure IV - 210 shows similar performance with both formation protocols.

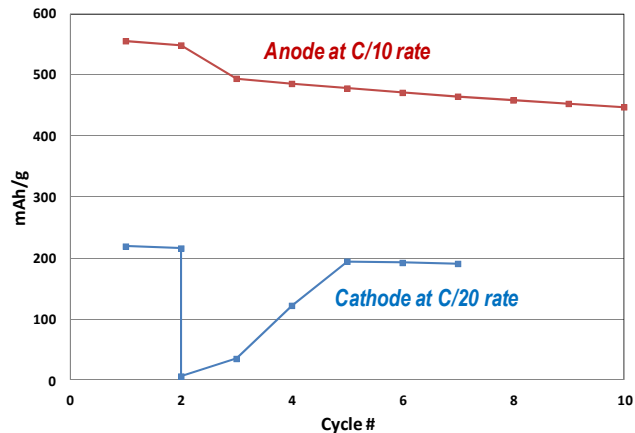


Figure IV - 209: Half cell performance of electrodes from the post mortem 18650 cell

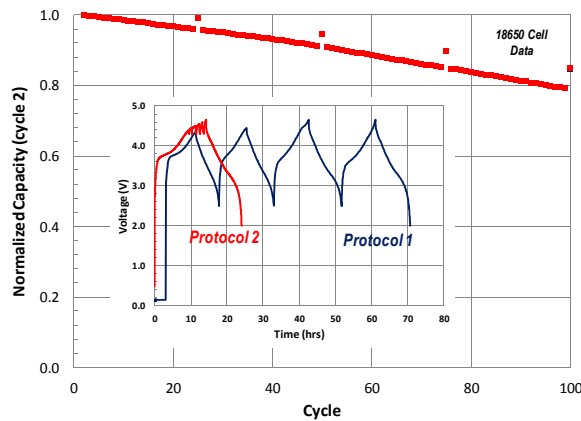


Figure IV - 210: Protocol 2 reduces formation time with similar life performance

Apart from looking at novel high voltage electrolytes, we also started looking at shallow cycling for cycle life improvement. A 60% energy window was chosen and three different voltage windows were identified for study (Figure IV - 211).

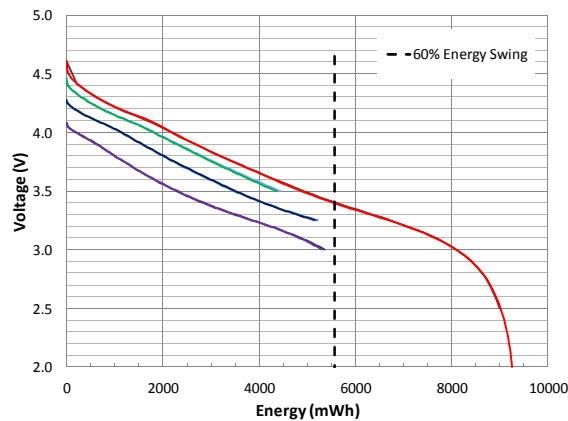


Figure IV - 211: Voltage windows yields 60% cell energy

Figure IV - 212 summarizes the cycle life in shallow voltage windows. 4.2V to 2.9V and 4.35V to 3.15V show significant improvement in capacity retention.

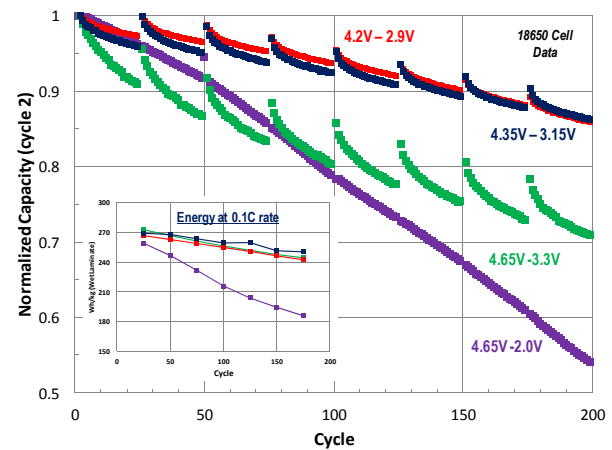


Figure IV - 212: Cycle life in 60% energy windows

Conclusions and Future Directions

The anode and cathode materials were down selected for future cycle life optimization. The team successfully demonstrated capability to scale up advanced materials in 100+ kg levels. 18650 format cells were assembled and showed >40% improvement in energy over the baseline design. The baseline data package was completed and 18650 cells with baseline and intermediate materials were shipped to ANL for energy validation.

The development of high voltage electrolyte is a key challenge to this project. As shown the active material still have majority of their initial capacities after the cell dies. Formation time was significantly reduced to a commercially viable time of 1 day during this period. Shallow cycling with a 60% energy swing has helped improve the cell life performance. It is interesting to see that shallow cycled cells have better energy at slow rates (every 25th cycle).

Going forward, the team plans to test cells for EV testing and prepare for the shipment of final deliverable cells.

FY 2014 Publications/Presentations

1. 2014 DOE Annual Peer Review Meeting Presentation.

IV.D.3 High Energy Density Li-ion Cells for EVs Based on Novel, High Voltage Cathode Material Systems (Farasis E, ANL, LBNL, Nanosys, Dupont)

Keith Kepler (Principle Investigator)

Farasis Energy, Inc.
21363 Cabot Boulevard
Hayward, CA 94545
Phone: (510) 732-6600 x203
E-mail: kkepler@farasis.com

Subcontractors:

Argonne National Laboratory, Argonne, IL
Lawrence Berkeley National Laboratory, Berkeley, CA
Nanosys, Inc.

Partners:

DuPont

Start Date: October 2013

Projected End Date: September 2015

Objectives

- Develop advanced electrode materials and cell components to enable stable high-voltage operation.
- Design and demonstrate a Li-ion cell using these materials that meets the PHEV40 design targets.

Technical Barriers

The major challenge to creating stable high specific energy cells with long cycle life is system integration. Although materials that can give high energy cells are known, stabilizing them towards long-term cycling in the presence of other novel cell components is a major challenge. This is being addressed using design of experiment and iterative development approaches.

Technical Targets

- Develop a Ti-doped, high-voltage stabilized layered NCM cathode material with reversible capacities >230 mAh/g.
- Develop a layered-layered-spinel (LLS) composite cathode material capable of reversible capacities of >250 mAh/g at 1C rate.

- Develop an optimized composite positive electrode based on blending different positive electrode active materials.
- Develop a Si/C composite negative electrode with >1600 mAh/g reversible capacity.
- Develop electrolytes for these electrode systems that enable stable high-voltage cycling.
- Integrate materials into PHEV40 cell designed to achieve 250 Wh/kg.

Accomplishments

- Successful scale-up synthesis of nanocomposite LLS materials prepared using ion-exchange chemistry.
- Identification of a lower-cost route to Ti-doped NCM cathode materials.
- Completion of processing parameter optimization and composite electrode formulation for nano-Si/C composite anode materials.
- Development of novel electrolyte formulations that increase capacity retention in full cells.
- Delivery of state-of-the-art Li-ion cells to Idaho National Laboratory for baseline testing.



Introduction

Farasis proposed to develop high-energy density, high power Li-ion cells based on novel high-voltage/high-capacity materials. In collaboration with our partners, multiple material classes are being developed simultaneously. On the positive electrode side, layered NCM materials are being developed and stabilized for high voltage operation using various coating technologies. Simultaneously, high capacity layered-layered-spinel composites are being explored using novel synthetic approaches based on ion-exchange reactions. High capacity negative electrode development is focused on silicon-carbon composites. Tying the cell together are electrolyte/separator systems optimized for high-voltage performance.

Approach

The approach taken by Farasis to succeed in this project is to develop multiple materials in parallel, with

periodic integration of materials in design of experiment studies to evaluate higher-order interactions between components. This approach relies on close collaboration with our partners, leveraging the strengths of each organization to accelerate development.

Results

Cathode materials

Two types of high-energy positive electrodes are being investigated in this project. The first class of materials, being developed in conjunction with Lawrence Berkeley National Laboratory, is based on NCM-type layered oxides of the general formula $\text{LiNi}_{1-x-y}\text{Co}_x\text{Mn}_y\text{O}_2$. These compounds have been shown to be stabilized by aliovalent substitution with Ti and have improved cycle life relative to undoped versions when cycled to high upper cutoff voltages. In spite of the promising results, the synthetic route used to prepare the Ti-doped materials involved complicated modifications of conventional synthetic approaches and raised some

questions about scalability. Recently, cost-effective approaches to incorporating Ti using commercially available precursor materials have been explored. The promising initial results are shown in Figure IV - 213 in which the Ti-doped material prepared by this new process shows clear advantages over the baseline after only 10 cycles.

The second class of positive electrode materials is manganese-rich nanocomposites of the layered-layered-spinel type, discovered by, and being developed in conjunction with Argonne National Laboratory. Research has focused on optimization of composition and synthesis procedures. The particular synthetic approach being used involves an ion-exchange step which leads to a certain amount of disorder in the material. The structural defects associated with this method presumably create lower-energy pathways for Li migration, reflected in lower impedance relative to materials made by conventional means, while still maintaining high specific capacity. This effect is illustrated in Figure IV - 214.

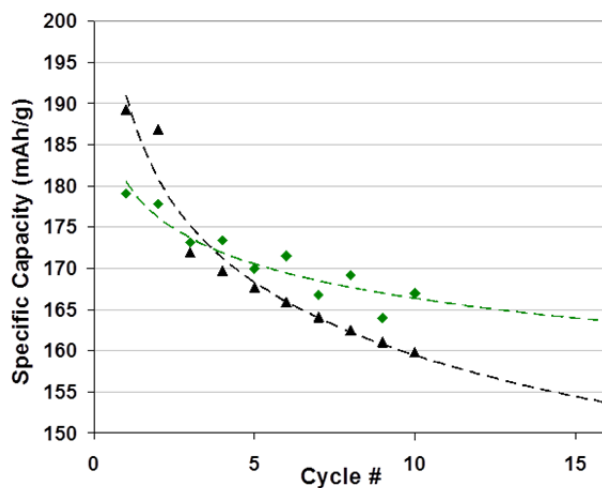


Figure IV - 213: Improved cycling stability of a Ti-doped NCM compared to a baseline material

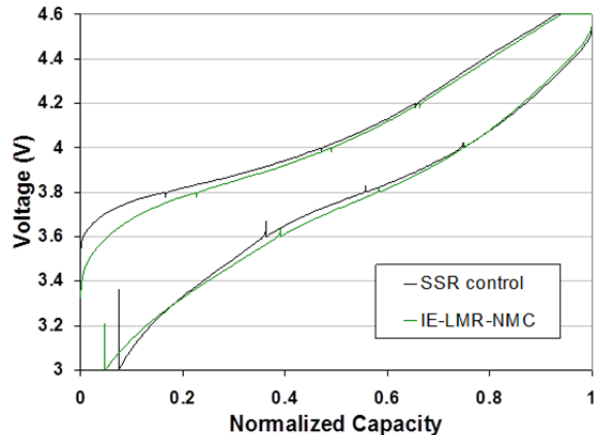


Figure IV - 214: Materials prepared via ion-exchange exhibit lower impedance, indicated by less voltage relaxation during current interrupts

Anode Materials

Negative electrode material development has focused on silicon-carbon composites. Blends of nanostructured silicon with conventional carbon-based materials have enabled development of negative electrodes that exhibit sufficiently stable cycling at capacities of 400 and 600 mAh/g. Current research is focused on improving cycle life for higher capacity electrode formulations, which are required to meet EV cell design goals. This research is intimately related to electrolyte development as Si is well known to require certain additives for stable performance.

Electrolyte Development

Electrolyte development is, perhaps, the most critical challenge in enabling stable high-voltage cycling. Farasis has evaluated a number of advanced

electrolytes incorporating novel solvents and additives using the project baseline electrodes. Extensive testing has identified several formulations that offer greatly improved cycling stability at higher cutoff voltages. Typical data is shown in Figure IV - 215, in which it is clear that the optimized electrolyte dramatically improves capacity retention relative to the baseline.

Cell Development: An initial set of baseline cells, representing the state of the art, were built and delivered to Idaho National Laboratory and are currently undergoing testing. At the end of the first year of this project, the developmental materials are being integrated into several different full cell designs to get an early indication of the specific cell level challenges we can expect to encounter as we continue to optimize material and system properties.

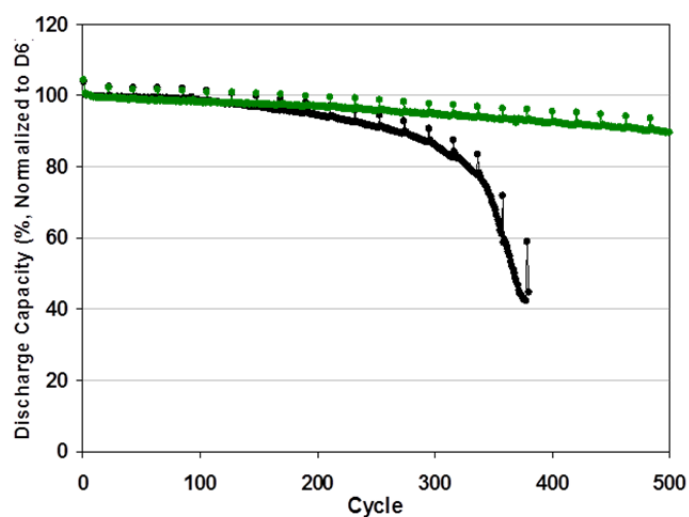


Figure IV - 215: Improved electrolyte formulations lead to extended cycling stability

Conclusions and Future Directions

Farasis and its partners have succeeded in optimization and scale-up of cathode, anode, and electrolyte components for high-energy density Li-ion cells. These materials are currently being combined into several different full cell designs targeting PHEV40 performance goals. Information from this round of testing will feed back into the materials development efforts and subsequent cell builds.

FY 2014 Publications/Presentations

1. 2014 DOE Annual Peer Review Meeting Presentation.

IV.D.4 Develop high energy cells for PHEV applications (Envia, LBNL, ORNL, GM)

Bruce Mixer (ABR Program Manager)

Subramanian Venkatachalam

(Principal Investigator)

7979 Gateway Boulevard, Suite 101

Newark, CA 94560

Phone: (510) 962-3688; Fax: (510) 790-7012

E-mail: mani@enviasystems.com

Subcontractor:

General Motors, Warren, MI

Lawrence Berkeley National Laboratory, Berkeley, CA

Oak Ridge National Laboratory, Oak Ridge, TN

Start Date: October 2013

Projected End Date: September 2015

Objectives

- 1) Understand the root cause of the DC-R issues of HCMR™ (lithium rich cathode material) systems via analytical techniques such as spectroscopic, microscopic and electrochemical techniques.
- 2) Mitigate the DC-R issues via different surface coating strategies – (a) ionic coating (LiPON) (b) Carbon coating (PE-CVD) (c) Atomic Layer Deposition (ALD) and solution based nanocoating (AlF_3 , Al_2O_3 , TiN, etc.) and (d) conducting polymer based surface coatings.
- 3) Perform atomistic modeling of DC-R, phase change, and voltage sag issues.
- 4) Apply theoretical solutions from atomistic modeling to mitigate phase change/voltage sag and DC-R challenges – doping of other metal ions.
- 5) Perform cell level modeling – understand the response at cell level that contributes to the DC-R of HCMR™ cathodes.
- 6) Develop suitable conducting polymeric binders for Si-anodes to enhance cycle life and meet the PHEV targets.

Technical Barriers

Unfortunately the higher specific capacity layer-layer cathode materials suffer from a fundamental problem of high resistance and transition metal-ion dissolution, which leads to reduced power, low usable

energy, poor cycle life and poor calendar life, making it highly compromising when considering it for automotive applications, particularly plug-in hybrid electric vehicles (PHEVs). Silicon-based anodes have been integrated with HCMR™ cathodes and shown to be critical components enabling cell requirements and cost targets. In order to utilize Si-based anodes, novel binders will be developed and screened to mitigate cycle life concerns associated with the large volume expansion of silicon.

Technical Targets

- Develop a cell to meet the PHEV goals.
- Develop a lithium rich cathode material with low DC-R, voltage fade and good cycling stability.
- Develop an anode formulation that is suitable for a PHEV application, particularly capable of >5000 cycles.
- Utilize computational modeling to understand the structural changes to the cathode material and apply understanding to developing cathode materials with improved stability.

Accomplishments

- LiPON coating showed much improved energy retention.
- DC-R from the two different deposition times for ALD coating from 4 different chemistries (AlF_3 , Al_2O_3 , AlN and TiN) showed no negative impact.
- Chemically incorporating PEDOT-PSS conducting polymer show improved electrochemical properties.
- In-situ cell designed to look at the Raman spectroscopy response of the cathode material shows appreciable signal from the sample in an assembled state.



Introduction

Envia proposed to develop a new battery system based on a novel cathode material and anode formulation that could meet the PHEV requirements while maintaining long life, excellent safety, and low cost. At the conclusion of this program, we will demonstrate a lithium ion battery (LIB) with energy density greater than 200Wh/kg (80% of which is usable

energy) while maintaining other performance requisites of PHEVs, including usable energy, power, and cycle life of 5000 cycles (the target metrics stated by the Advanced Battery Research for Transportation Program). This will be achieved through a collaborative effort across several organizations, which include two national laboratories (Lawrence Berkeley National Laboratory - LBNL and Oak Ridge National Laboratory - ORNL), a major US automotive OEM (General Motors - GM) and Envia Systems. Each will provide expertise on a specific component of the material and/or cell. Computational modeling will be used to understand the mechanisms and identify proper cathode compositions (and dopants) to improve cycle life and calendar life, while already identified coating and binder technologies will be incorporated to improve DC resistance, power, usable energy and cycle life.

Approach

Envia is working with GM, LBNL, and ORNL to develop lithium rich cathode materials with low DC resistance and silicon based anodes that have good stability. GM and LBNL have experience developing coatings for cathode materials as well as atomistic modeling. LBNL also has experience with binders for silicon based anodes. ORNL has experience with

LiPON materials and will develop coatings for the cathode material. Envia has experience in developing and synthesizing novel cathode and anode materials. Envia is capable of producing sufficient cathode material for large format cell builds. Envia will synthesize base cathode materials and LBNL, GM, and ORNL will apply novel coatings. Envia will build cells with the coated cathode materials. Envia will also utilize novel binders developed by LBNL. Envia will demonstrate the capability of the HCMR/Silicon cell in a large format pouch cell.

Results

LiPON coating: LiPON, an ionic conducting solid electrolyte, has been coated onto HCMR™ class of materials in order to understand the effect that an ionic conducting layer has on DC-R and growth in DC-R. As shown in the Q4 report, the presence of LiPON has improved usable energy by 3-4%, possibly due to the improvement of Li-ion diffusion at low SOC's. However, when the LiPON coated material is cycled, there is no appreciable arrest of DC-R growth. In other words, there is a continuous loss in the usable energy with respect to cycling both with and without LiPON coating. (See Figure IV - 216.)

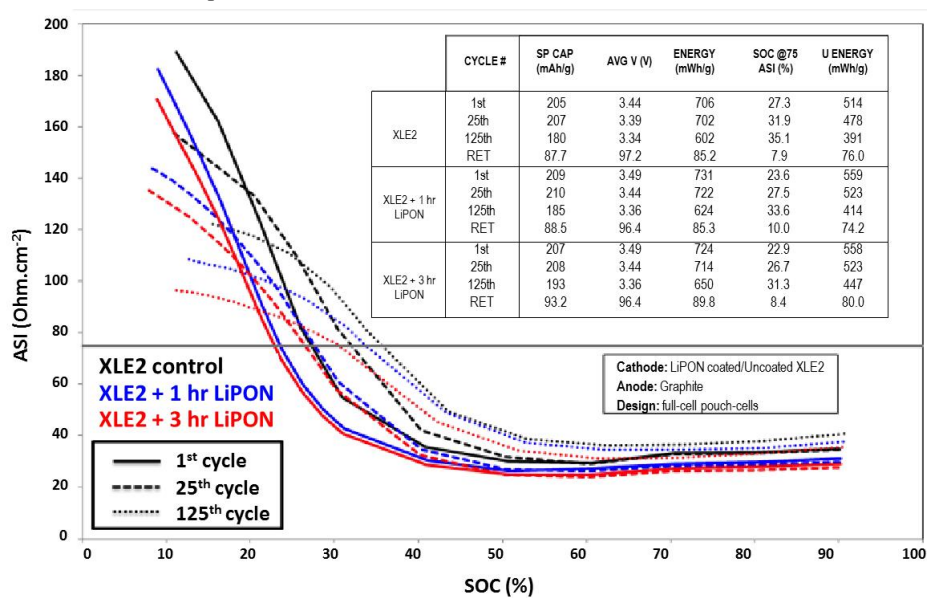


Figure IV - 216: Change in useable energy with respect to cycling for HCMR™ XLE2 and LiPON coated HCMR™ XLE2 cathode materials in a single layer pouch cell configuration

Polymer Coating: LBNL is developing new conductive polymeric coatings so as to address the effect of an electronic conducting coating on the DC-R of the HCMR™ cathode. Various conducting polymers such as PANI, PAN etc. were coated on to the cathode surface either via in-situ polymerization or mixing with

the polymers mainly to improve the electronic conductivity.

ALD Coating: At General Motors, various iterations were carried out for the ALD coating on both powders and electrodes with different chemistries and thicknesses. Details are presented in Q1 to Q4 reports.

Based on an initial screening of ALD coatings on powder, optimized chemistry and thickness ALD coatings were performed on electrodes. These nanocoatings include AlF₃, Al₂O₃, AlN and TiN. DC-R studies on the ALD-coated electrodes show no

significant impact of ALD on initial DC-R of the cathode material, which is a positive result because it is expected that the ALD coating will reduce DC-R growth over time. (See Figure IV - 217.)

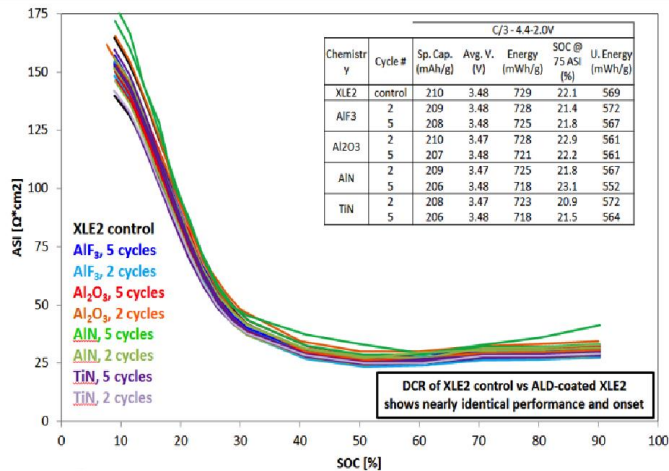


Figure IV - 217: DC-R of four select ALD chemistries (AlF₃, Al₂O₃, TiN and AlN) deposited on electrodes at two different thicknesses

Conducting Carbon for Cathode Material:

Envia has shown that incorporating a highly conducting carbon into the cathode material via solid-state processes will increase the usable energy of the cathode system. However, this solid-state process involves large quantities of the HCMR™ material, resulting in a challenge when needing to combine carbon-coating with coatings such as ALD or LiPON. An alternative to the solid-state carbon-coating is the PE-CVD driven carbon coating, one of the most effective and efficient processes to uniformly coat high conducting carbon at low temperatures.

Computational Techniques for Analyzing

Material Structure: After an extensive screening of various analytical techniques during the first year of this project, Electrochemical Impedance Spectroscopy (EIS) in combination with Hybrid Pulse Power Characterization (HPPC) have been identified as promising techniques to study DC-Resistance as a function of the state-of-charge (SOC). Analyzing the cathode material via EIS and HPPC at different SOC's provides a pathway for distinguishing between electronic and ionic conductivity deficiencies that cause DC-R growth. LBNL's atomistic modeling helps understand the causes of DC-R at the single-crystal level. These atomistic models allow prescribing new dopants that could mitigate phase changes that cause loss of power with cycling.

Conclusions and Future Directions

Envia is developing a of new class of pristine HCMR™ material (XE) that will be engineered based on the results we have achieved from the exercise during the first year of the ABR program. With the learning on the best ALD chemistry and thickness, LiPON thickness and the polymer coating, the new XE materials will be applied with these coatings to further improve the electrochemical performance. From the present data, we believe that the single nanocoating might not be a solution. Rather, it will be a combination of two or more surface coatings in order to achieve the best electrochemical performance for the HCMR™ cathode materials.

Currently, Envia is optimizing the scale-up process of XE class of materials, and the scale-up material will be shipped this quarter with the exact prescription of focused tasks to all the partners. During the next two quarters the final material composition (involving the dopants as suggested by theory) and nanocoating(s) will be frozen and the cell build towards meeting the final ABR project objective of 200 Wh/kg and cycle life > 5000 cycles will begin.

FY 2014 Publications/Presentations

1. 2014 DOE Annual Merit Review Presentation.

IV.D.5 High Energy, Long Cycle Life Lithium-Ion Batteries for PHEV Application (Penn State U, UT Austin, LBNL, ANL, EC Power)

Christopher Johnson (Program Manager)
Subcontractor: Pennsylvania State University

Donghai Wang (Project Manager)
328 Reber Building
University Park, PA 16802
Phone: (814) 863-1287; Fax: (814) 863-4848
E-mail: dwang@psu.edu

Subcontractors:
University of Texas at Austin
EC Power

Collaborators:
Lawrence Berkley National Laboratory
Argonne National Laboratory

Start Date: September 30, 2013
Projected End Date: September 30, 2015

Objectives

- Demonstrate a 2.5 Ah prismatic Li-ion battery cell capable of:
 - an energy density of 330 Wh/kg (770 Wh/L) at C/3 rate.
 - a power density of 1600 W/L while maintaining an energy density above the DOE PHEV goal of 200 Wh/kg.
 - a long cycle life with 95% capacity retention in 500 cycles at C/3 and 1C rate at 80% depth of discharge (DOD).

Technical Barriers

The development of the proposed Li-ion battery presents technical barriers for each of the system's components: anode, cathode, binder, and electrolyte. Although silicon-alloy anode materials have shown remarkable capacities above 2000 Ah/g, the silicon will undergo large volume change (~400%) upon lithiation/delithiation. In effect, other issues arise including unstable SEI, pulverization and aggregation of the Si particle, and low coulombic efficiency (less than 99.8%) compared with graphite (higher than 99.9%). Furthermore, layered oxide cathode materials will need to overcome a relatively low practical capacity (~170

mAh/g), along with other issues such as chemical and structural instability, transition metal dissolution, and transition metal redox potential changes. The technical barriers for the anode and cathode may partially be addressed with an appropriate binder/electrolyte; however the chemical composition of these components must be optimized to ensure compatibility.

Technical Targets

Anode:

- Si alloy-carbon anode with 1500 mAh/g capacity, 95% capacity retention after 100 cycles at 1C, coulombic efficiency >99%.

Cathode:

- LiFePO₄-coated, Ni-rich layered oxide cathode with 190 mAh/g capacity, 95% capacity retention after 100 cycles at 1C.

Polymer Binder:

- Develop two polymer binders specifically optimized for use with the PSU micro-sized porous Si-C composite anode material.

Electrolyte:

- Formulate a suitable electrolyte for silicon alloy anodes through investigating a variety of fluorinated solvents.

Accomplishments

- **Anode:** **Q1:** The team has achieved a silicon-based anode with high mass loading (ca. 4mg/cm²). **Q2:** A novel micro-sized graphene/Si-C composite (G/Si-C) material was synthesized and exhibited low electrical resistance and high areal capacity after 100 cycles at high mass loadings. **Q3:** Developed a synthesis process for a silicon-based carbon (Si-C) composite, which is designed to achieve areal capacities above 4 mAh/cm². **Q4:** A novel intermediate Si-based anode material, B-Si/SiO₂/C, and deformable gel polymer binder, PAA-PVA, have been developed, enabling excellent silicon anode performance.
- **Cathode:** **Q1:** Electrochemical testing has shown that the optimum range of nickel content for the cathode. **Q2:** Three new Ni-rich cathode materials have been prepared based on single- and two-step synthesis process and evaluated through electrochemical characterization. **Q3:** By coating

the concentration gradient (Ni-rich in core, Mn-rich surface) electrode with 10nm Al₂O₃ layer, the capacity fading over 100 cycles has decreased without sacrificing capacity. **Q4:** Developed high tap density Ni-rich cathode materials. The LiNi_{0.8}Co_{0.1}Mn_{0.1}O₂ material prepared at a pH = 11.5 exhibits an excellent cycling performance and low voltage fade.

- **Electrolyte:** **Q1:** Argonne carried out the new additive synthesis, characterization and purification. **Q2:** The effects of Gen2 electrolyte and fluorinated electrolyte on the performance of the high capacity cathode/Li metal half cells were investigated. **Q3:** The high-temperature performance of cathode/Li half-cells has been improved and the electrochemical performance of Si/Li half cells has been improved through the addition of 10% FEC to the conventional Gen 2 electrolyte. **Q4:** Evaluated the performance of the fluorinated electrolyte FEC 2 (1.0 M LiPF₆ in FEC/F-EMC/F-EPE=3/5/2 by volume) with the new cathode material from UT-Austin and compared with Gen 2 electrolyte. Also conducted research on the PSU Si anode (SiO₂-C material) and have screened a couple of additives to improve the performance of the baseline electrolyte (Gen 2+10wt.% FEC).
- **Baseline cell:** Delivered 2.0 Ah prismatic Li-ion battery cells with an energy density of 200 Wh/kg (500 Wh/L) at C/3 rate and a long cycle life with 90% capacity retention in 100 cycles at C/3 and 1C rate at 80% depth of discharge (DOD)



Introduction

With a relatively high energy density and long lifespan, Li-ion batteries have naturally become the state-of-the-art technology for plug-in hybrid electric vehicle (PHEV) and electric vehicle (EV) applications. However, mainstream adoption of the current generation of PHEVs and EVs has been hindered by high-cost batteries, limited travelling distance, and restrained vehicle size. In effect, research in the field of battery chemistry and material science has focused on the

development of complementary battery components that will significantly improve the practical performance of the Li-ion battery and optimize it for transportation applications. Within the last decade, these primary components - cathode, anode, binder, and polymer - have been enhanced through careful modification in chemical composition, although often independent of each other. In this effect, it is clear that realizing a Li-ion battery suitable for the rising demands in transportation applications can only be achieved when research on individual battery components are performed in conjunction.

Approach

The development of a high energy/power Li-ion battery suitable for PHEV and EV applications can be accomplished through the expertise and experience of a multiple organizational team with facilities and collaboration spanning Penn State University (PSU), University of Texas at Austin (UT-Austin), Lawrence Berkley National Laboratory (LBNL), Argonne National Laboratory (ANL), and industrial partner EC Power (ECP). PSU and UT-Austin will use extensive knowledge in the state-of-the-art anode and cathode materials, respectively, to develop optimized and compatible electrodes in the Li-ion battery. Innovative polymer binders and electrolytes solutions will be developed by LBNL and ANL, respectively, based on their well-established expertise in this area. Finally, the culmination of these state-of-the-art battery components will be realized through the intelligent cell design and fabrication techniques of ECP.

Results

Anode: During the first quarter of the ABR project, the team at Penn State achieved a silicon-based anode material with a high mass loading (ca. 4mg/cm²). The Umicore Si nanoparticles were chosen as the active material for the thick-coating electrodes, combined with graphite flakes, Super P, and polymer binder in a mass ratio of 60:20:5:15 (i.e. silicon : graphite flakes : Super P : binder). The expected electrode component morphology is shown in Figure IV - 218.

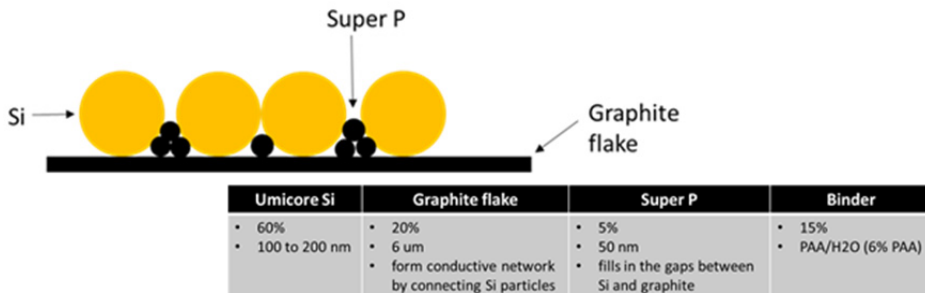


Figure IV - 218: The expected microstructure of the thick-coating electrode and material information of the constituent materials

The polyacrylic acid (PAA) binder was employed from a mixture of PAA-H₂O (6% PAA). The gap thickness of 375 microns was used to draw the electrode slurry over the raw copper current collector and a desiccator was used to decrease the drying rate of the slurry and relax the stresses associated with the drying process. With the fabrication method for a thick-coating electrode confirmed, the next phase of research will

involve the electrochemical testing of the material via lithium half cells.

In the second quarter of the ABR project, the Penn State team improved on its previous electrode composition by incorporating graphene, forming a novel micro-sized graphene/Si-C composite. TEM and SEM images of the micro-sized active material is shown in Figure IV - 219.

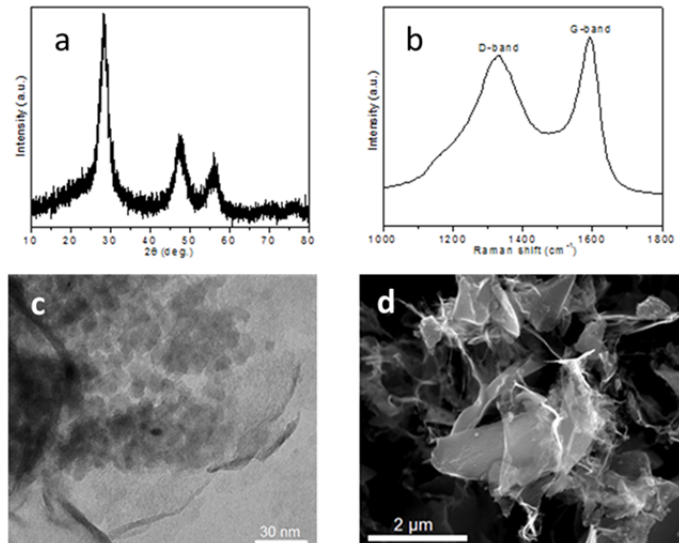


Figure IV - 219: (a) XRD pattern and (b) Raman spectrum of G/Si-C. (c) Low-magnification TEM and (d) SEM image of G/Si-C

The graphene-wrapped micro-sized Si-C composite was successfully prepared via a facile approach. The graphene provides additional electron pathways for the whole electrode by forming a conductive network that connects different Si-C particles, giving the G/Si-C conductive networks both within and between particles. As a result, low electrical resistance can be maintained at high mass loading, as shown in Figure IV - 220, which enables a high degree of material utilization. For the electrochemical testing of the new anode material, electrodes with three different active material mass loadings (around 1.2, 2.0 and 3.2 mg/cm^2) were

fabricated for each composite, and were designated G/Si-C@low, G/Si-C@medium, G/Si-C@high, Si-C@low, Si-C@medium and Si-C@high, where low, medium, and high referred to mass loading.

Correspondingly, the graphene-wrapped Si-C composite exhibits a high areal capacity of 3.2 mAh/cm^2 after 100 cycles with high coulombic efficiency, as shown in Figure IV - 221. These findings demonstrate the importance of building a conductive network at the electrode level for high material utilization at high mass loading and have shed light on future designs of Si-based anodes with high areal capacity.

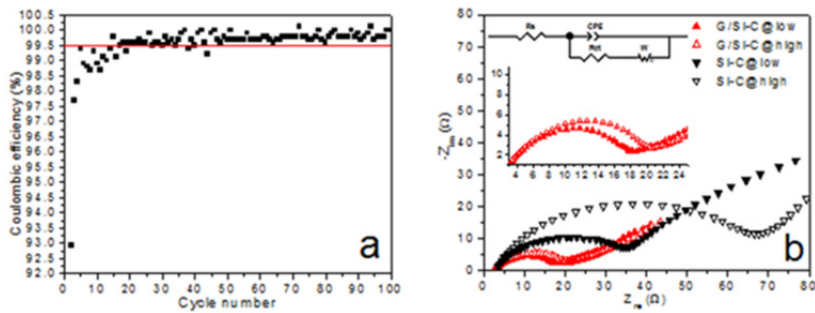


Figure IV - 220: (a) Coulombic efficiency (2nd to 100th cycle) of G/Si-C@high. (b) Impedance spectra of G/Si-C and Si-C at low and high mass loadings. Insets in (b) are the Randles equivalent circuit and enlarged spectra showing difference between G/Si-C@low and G/Si-C@high, respectively

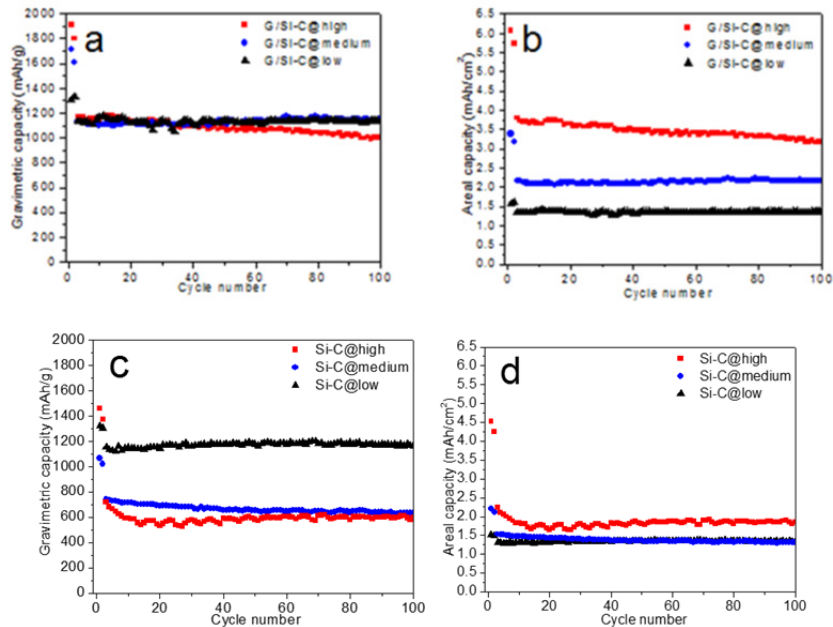


Figure IV - 221: Cycling performance of G/Si-C (a & b) and Si-C (c & d)

In an endeavor to develop a stable silicon-based anode material for incorporation into a large-scale pouch cell, the most compatible features of our previous electrode compositions and designs were incorporated into a new version of Si-C material during the 3rd quarter of the project. The general composition of the silicon-based electrode is Si-C : Carbon : PAA in an

approximate ratio of 4 : 5 : 1 (weight %), as shown in Figure IV - 222a. More specifically, Figure IV - 222b details the various types of carbon incorporated into the composition, each offering unique benefits to minimizing coating fracture, improve electrical conductivity, and reduce the damaging effects during silicon volume expansion.

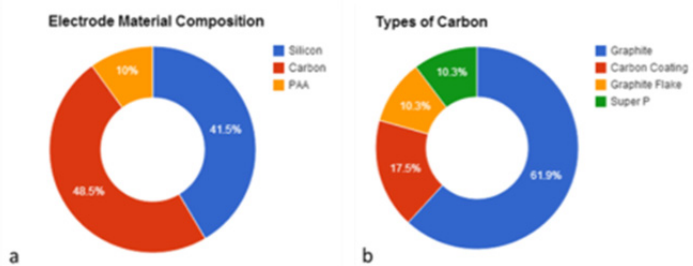


Figure IV - 222: Percentage composition of a) the overall electrode and b) the carbon components

The Si-C anode material described above was characterized through galvanostatic testing at a constant current of 50 mA/g over a voltage range of 1.5 – 0.01 V at room temperature, which are similar conditions to the previously tested baseline material, Umicore silicon. Our newest Si-C anode performed remarkably better than the Umicore silicon control electrode, as shown in

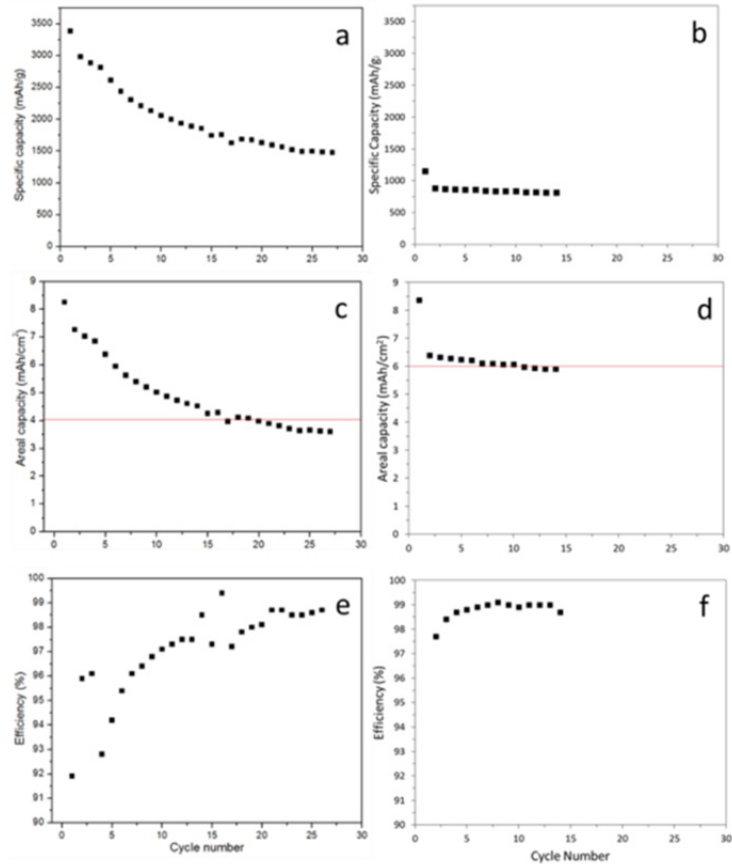


Figure IV - 223: Electrochemical performance comparison between Umicore Si (a,c,e) and Si-C (b,d,f)

Following the success of previous Si-based anode iteration, an intermediate Si-based anode material (B-Si/SiO₂/C) has been developed. The cycling stability and rate performance of the anode material were improved by size reduction, carbon coating, and boron doping of commercial silicon monoxide (SiO) without any HF etching. As shown in the SEM image (Figure IV - 224a), B-Si/SiO₂/C is composed of micro-sized particles with an average size of about 3 μm and sub-micron particles. Figure IV - 224b shows the TEM image of B-Si/SiO₂/C, in which the thickness of the carbon layer (marked by white arrows) was found to be around 20-30 nm.

The electrochemical performance was evaluated by galvanostatic cycling in Li-ion half-cells. For comparison, boron-doped Si/SiO₂/C (B-Si/SiO₂/C-325) using SiO, which was not ball-milled, and undoped Si/SiO₂/C using ball-milled SiO were prepared.

Figure IV - 223. Although the specific capacity of the Si-C electrode is significantly lower than the Umicore silicon, the Si-C electrode offers a much higher lithium capacity per unit area, maintained at about 6 mAh/cm² over the course of 15 cycles, and greatly reduced capacity fading.

Figure IV - 225a shows the cycling performance of B-Si/SiO₂/C and B-Si/SiO₂/C-325 at a current density of 600 mA/g with the first two cycles activated at 300 mA/g. It is clear that B-Si/SiO₂/C exhibits better cycling stability than B-Si/SiO₂/C-325. A capacity of 1279 mAh/g was obtained by B-Si/SiO₂/C after 100 cycles, equating to 92.7% capacity retention (based on the lithiation capacity of the 3rd cycle), while B-Si/SiO₂/C-325 only delivered 990 mAh/g after 100 cycles, only 75% of its initial capacity. The doping effects on reduced-size Si/SiO₂/C were examined by charge/discharge at different current densities. As shown in Figure IV - 225b, the difference in the specific capacities of doped and undoped ball-milled Si/SiO₂/C becomes more and more pronounced with increasing current density. At a high current density of 6.4 A/g, B-Si/SiO₂/C delivers a capacity of 685 mAh/g, 2.4 times that of Si/SiO₂/C (286 mAh/g). After the current density was restored to 400 mA/g, B-Si/SiO₂/C showed

excellent reversibility, with a capacity similar to its initial capacity, while Si/SiO₂/C showed lower capacity

and poor stability. It is worth noting that the CE of B-Si/SiO₂/C remains a round 99.7% even at high rates.

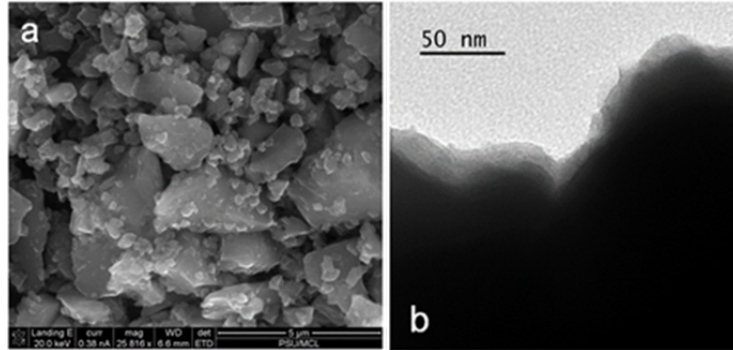


Figure IV - 224: (a) SEM and (b) TEM images of B-Si/SiO₂/C

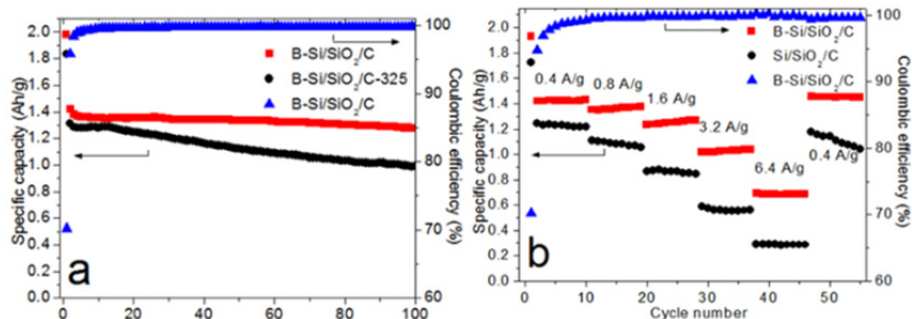


Figure IV - 225: (a) Cycling and (b) rate performance of B-Si/SiO₂/C

A novel deformable gel polymer binder through an in-situ thermal crosslinking of water soluble poly(acrylic acid) (PAA) and poly(vinyl alcohol) (PVA) has been developed to stabilize Si anode materials. Commercial silicon nanoparticles in elliptical or spherical shapes with diameters in the range of 30 to 100 nm were used to demonstrate the performance of PAA-PVA. Noticeably, the Si anode with the PAA-PVA binder exhibited an excellent battery performance, when compared to alternative binder as shown in Figure IV - 226. A specific capacity of 3616 mAh/g was achieved in the initial cycle by using novel interpenetrated gel polymer binder, which is about 86% of the theoretical capacity (4200 mAh/g). Furthermore, this cell also gave an excellent cycling stability, with a capacity of 2283 mAh/g remaining after 100 cycles. Moreover, this novel binder also showed a relatively high initial Coulombic efficiency of 83.9%, which increased to ~97.7% at the third cycle, and finally stabilized at ~99.3% in subsequent cycles (Figure IV - 226b).

Combining the intermediate B-Si/SiO₂/C anode materials and the PAA-PVA crosslink binder, thick electrodes with high mass loading were prepared and evaluated. As shown in Figure IV - 227, a high gravimetric capacity of around 1000 mAh/g (based on the whole electrode excluding the mass of current

collector) was obtained. The areal capacity has been maintained around 4 mAh/cm² during cycling, which meets the requirement of cell design to achieve high energy density of full cells.

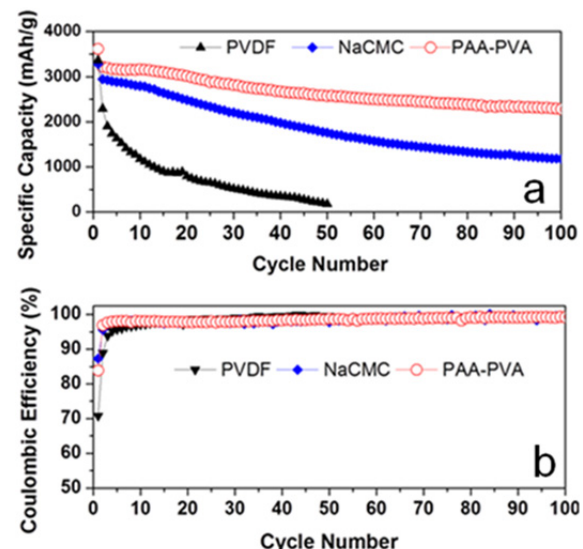


Figure IV - 226: (a) cycling performance and (b) coulombic efficiency of Si electrodes with PAA-PVA, NaCMC, and PVDF binders

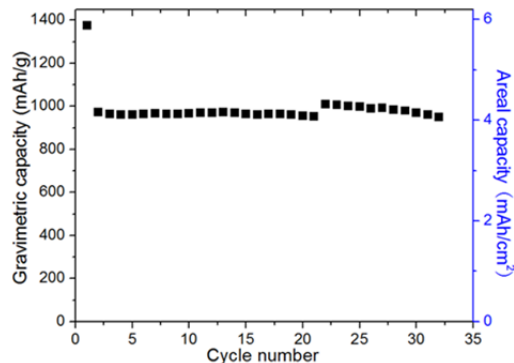


Figure IV - 227: Cycling performance of intermediate B-Si/SiO₂/C electrodes with PAA-PVA binder

Cathode: In the first quarter of the ABR project, the UT-Austin team worked to find the optimum range of nickel content for their cathode material. Synthesis of several samples with various Mn:Co:Ni ratios indicated that a nickel content of above 0.5 but below 0.7 in Li[Mn,Co,Ni]O₂ is an optimum range to realize high capacity. The material does not seem to transform from layered structure to spinel structure during cycling as the sloping discharge profile is maintained even at the 100th cycle, unlike the lithium-rich layered oxide cathodes. Additionally, as shown in Figure IV - 228, the nickel-rich composition LiNi_{0.62}Mn_{0.24}Co_{0.14}O₂ displays an impressive capacity of 220 mAhg⁻¹ in the first cycle at C/5 rate. However, the sample exhibits some irreversible capacity loss in the first cycle and capacity fade during cycling as seen in both Figure IV - 228 and Figure IV - 229. The capacity fade is due to the chemical instability of the cathode surface with the electrolyte at voltages above 4.3IV.

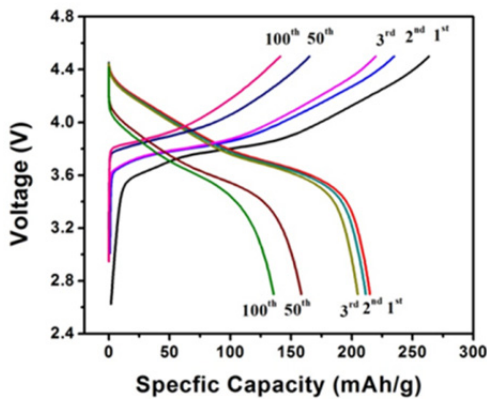


Figure IV - 228: Charge-discharge profiles of the LiNi_{0.62}Mn_{0.24}Co_{0.14}O₂ cathode at 2.7 – 4.5 V at C/5 rate

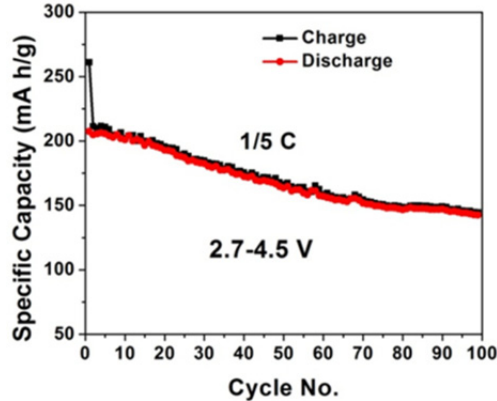


Figure IV - 229: Cyclability of the LiNi_{0.62}Mn_{0.24}Co_{0.14}O₂ cathode at 2.7 – 4.5 V at C/5 rate for 100 cycles

Based on the results from the 1st quarter and to overcome the capacity fade problem, structure modification experiments (with a Ni-rich “core” and Mn-rich “shell” to obtain a concentration gradient structure) were carried out. For a comparison, three Ni-rich materials were prepared: (i) LiNi_{0.8}Co_{0.2}O₂ by a single-step synthesis, (ii) LiNi_{0.62}Mn_{0.24}Co_{0.14}O₂ by a single-step synthesis, and (iii) a Ni-rich “core” and Mn-rich “shell” Li[Ni_{0.8}Co_{0.2}]_{0.7}[Ni_{0.2}Mn_{0.8}]_{0.3}O₂ concentration gradient Ni-rich material by a two-step synthesis. The three Ni-rich samples exhibit different electrochemical performances despite the similar morphologies and tap densities. Figure IV - 230a-c shows the charge/discharge curves for three cycles recorded with coin cells fabricated with the three samples at 2.7 – 4.5 IV.

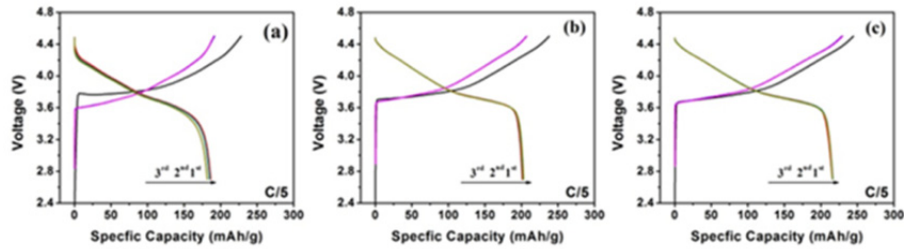


Figure IV - 230: First three charge-discharge curves of the three Ni-rich samples at 2.7 – 4.5 V: (a) $\text{LiNi}_{0.8}\text{Co}_{0.2}\text{O}_2$, (b) $\text{LiNi}_{0.62}\text{Mn}_{0.24}\text{Co}_{0.14}\text{O}_2$, and (c) concentration-gradient $\text{Li}[\text{Ni}_{0.8}\text{Co}_{0.2}]_{0.7}[\text{Ni}_{0.2}\text{Mn}_{0.8}]_{0.3}\text{O}_2$

All three samples deliver first charge capacities of 210 – 230 mA h g⁻¹, however concentration gradient $\text{Li}[\text{Ni}_{0.8}\text{Co}_{0.2}]_{0.7}[\text{Ni}_{0.2}\text{Mn}_{0.8}]_{0.3}\text{O}_2$ had a higher Mn content on the surface, which lead to a better capacity retention. Even after operating the $\text{Li}[\text{Ni}_{0.8}\text{Co}_{0.2}]_{0.7}[\text{Ni}_{0.2}\text{Mn}_{0.8}]_{0.3}\text{O}_2$ electrode at 1C rate for 100 cycles, a discharge capacity of ~160 mA h g⁻¹ is maintained, with a high coulombic efficiency of 97.7%.

In addition, coating of three other Ni-rich compositions with different Ni, Mn, and Co contents

($\text{LiNi}_{0.8}\text{Mn}_{0.1}\text{Co}_{0.1}\text{O}_2$, $\text{LiNi}_{0.7}\text{Mn}_{0.15}\text{Co}_{0.15}\text{O}_2$, and $\text{LiNi}_{0.6}\text{Mn}_{0.2}\text{Co}_{0.2}\text{O}_2$) with Al_2O_3 was also investigated to improve the cyclability. As seen in Figure IV - 231, the Al_2O_3 -coated samples show consistent improvement in cycling stability in the potential window of 3.0 – 4.5 V at C/5 for all of the three samples. The Al_2O_3 coating also results in a suppression of voltage decay during cycling, as seen in Figure IV - 232.

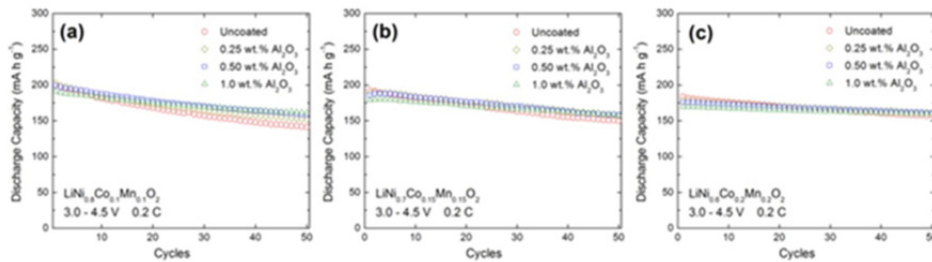


Figure IV - 231: Cyclability of the (a) $\text{LiNi}_{0.8}\text{Mn}_{0.1}\text{Co}_{0.1}\text{O}_2$, (b) $\text{LiNi}_{0.7}\text{Mn}_{0.15}\text{Co}_{0.15}\text{O}_2$, and (c) $\text{LiNi}_{0.6}\text{Mn}_{0.2}\text{Co}_{0.2}\text{O}_2$ samples with and without coating with various amounts of Al_2O_3 at C/5 rate at 3.0 – 4.5V

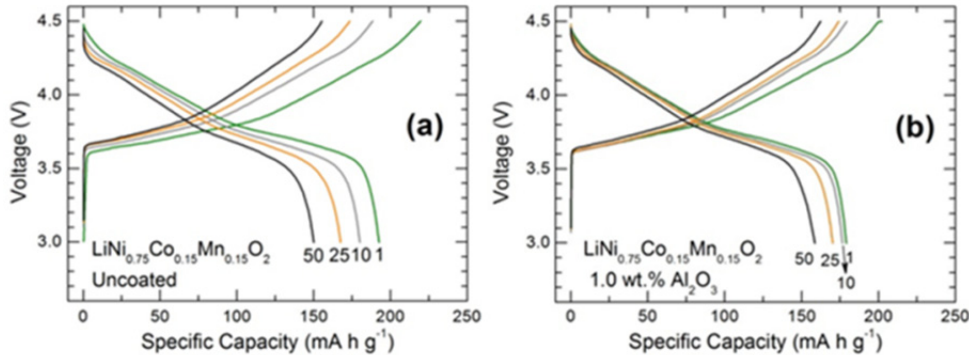


Figure IV - 232: Galvanostatic charge-discharge profiles of the $\text{LiNi}_{0.7}\text{Mn}_{0.15}\text{Co}_{0.15}\text{O}_2$ sample (a) without and (b) with 1.0 wt. % Al_2O_3 coating

To overcome the capacity fade problem mentioned above, surface modification experiments, involving Al_2O_3 coatings, were carried out during the 3rd quarter.

The presence of the Al_2O_3 layer was confirmed through TEM, SEM, and EDS analysis, as shown in Figure IV - 233 and Figure IV - 234.

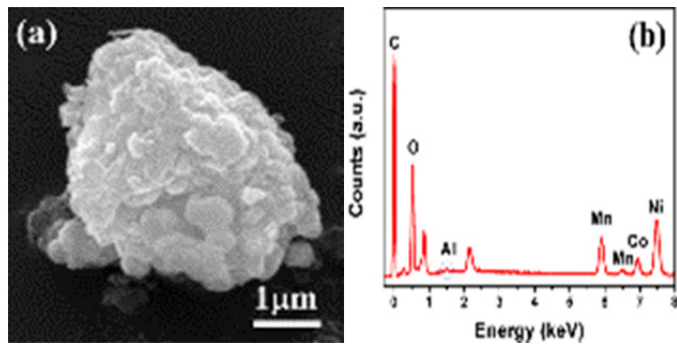


Figure IV - 233: SEM image (a) and EDS pattern (b) of the Al_2O_3 -coated concentration gradient Ni-rich electrode

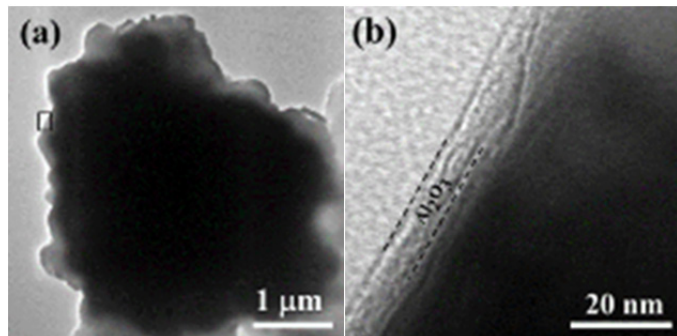


Figure IV - 234: TEM image (a) and HRTEM image (b) of the Al_2O_3 -coated concentration gradient Ni-rich material

Figure IV - 235 shows the discharge capacity retention at C/5 of concentration-gradient (CG) and Al_2O_3 -coated concentration gradient (Al_2O_3 -CG) electrodes. After being activated by Li ions during the first several insertion/extraction cycles, the discharge capacity of the Al_2O_3 -coated CG had remained much more stable than the uncoated electrode.

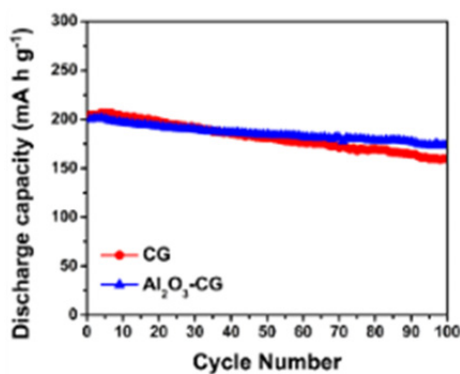


Figure IV - 235: Cycling performances at 4.5 – 2.7 V of the concentration-gradient (GC) and Al_2O_3 -coated concentration-gradient (Al_2O_3 -CG) at C/5 rate

In addition, coating of three other Ni-rich compositions with different Ni, Mn, and Co contents ($\text{LiNi}_{0.8}\text{Mn}_{0.1}\text{Co}_{0.1}\text{O}_2$, $\text{LiNi}_{0.7}\text{Mn}_{0.15}\text{Co}_{0.15}\text{O}_2$, and $\text{LiNi}_{0.6}\text{Mn}_{0.2}\text{Co}_{0.2}\text{O}_2$) with Al_2O_3 was also investigated to improve the cyclability. Electrochemical testing of these compositions, shown in Figure IV - 236, showed that the Al_2O_3 -coated samples had consistent improvement in cycling stability in the potential window of 3.0 – 4.5 V at C/5 and that the Al_2O_3 coating results in a suppression of voltage decay during cycling, as seen in Figure IV - 237.

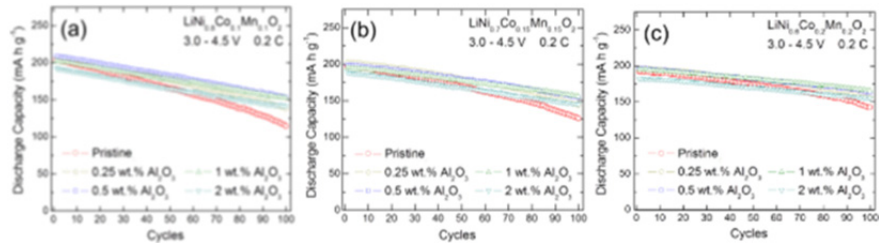


Figure IV - 236: Cyclability at C/5 rate at 3.0 – 4.5 V of the (a) $\text{LiNi}_{0.8}\text{Mn}_{0.1}\text{Co}_{0.1}\text{O}_2$, (b) $\text{LiNi}_{0.7}\text{Mn}_{0.15}\text{Co}_{0.15}\text{O}_2$, and (c) $\text{LiNi}_{0.6}\text{Mn}_{0.2}\text{Co}_{0.2}\text{O}_2$ samples with and without coating with various amounts of Al_2O_3

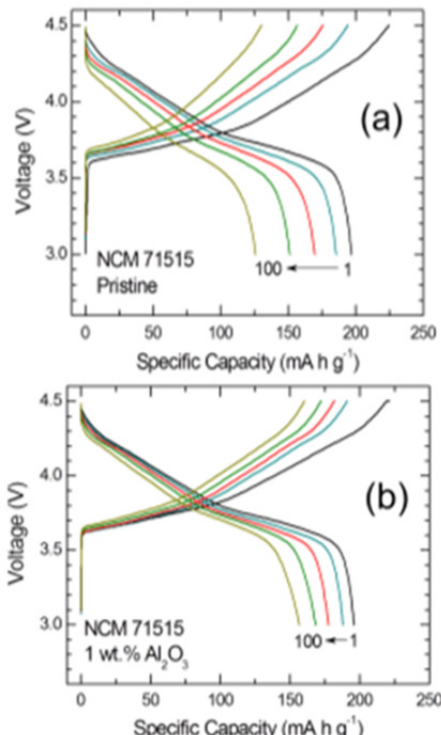


Figure IV - 237: Galvanostatic charge-discharge profiles of the NCM 71515 ($\text{LiNi}_{0.7}\text{Mn}_{0.15}\text{Co}_{0.15}\text{O}_2$) samples (a) without and (b) with 1 wt % Al_2O_3 coating

Furthermore, various approaches have been tried to synthesize samples with a larger secondary particle size to further increase the reversible capacity with superior cyclability. To achieve this goal, Ni-rich materials using Na₂Co₃ as the reaction agent were prepared and performance compared against Umicore NCM. For the synthesized Ni-rich electrode, a discharge capacity of ~185 mA h g⁻¹ is maintained after 30 cycles, which is higher than that of the commercial Umicore NCM, as shown in Figure IV - 238.

The 4th quarter work has been dedicated to achieving high tap density with Ni-rich cathode materials, where a hydroxide/carbonate co-precipitation method to prepare spherical particles has been implemented. The materials generally exhibit higher tap

density than those composed of irregular particles. We then systematically investigated the effects of pH value on the performance of the Ni-rich cathode materials LiNi_{0.8}Co_{0.1}Mn_{0.1}O₂ and LiNi_{0.62}Co_{0.08}Mn_{0.23}O₂.

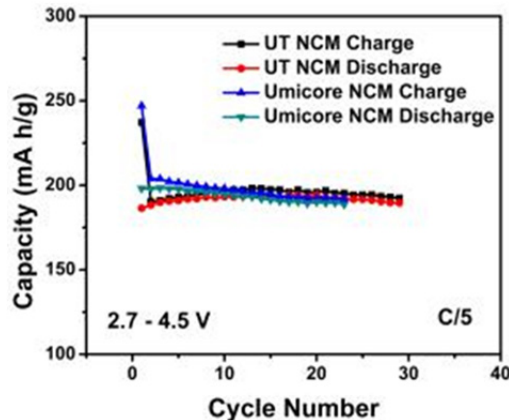


Figure IV - 238: (a) Comparison of the cyclability of our Ni-rich cathode ($\text{LiNi}_{0.69}\text{Mn}_{0.23}\text{Co}_{0.08}\text{O}_2$) with that of the commercial Umicore NCM ($\text{LiNi}_{0.5}\text{Mn}_{0.2}\text{Co}_{0.3}\text{O}_2$) at C/5 rate at 2.7 – 4.5V. (b) Cyclability of our Ni-rich cathode with a higher cutoff voltage (2.8 – 4.6 V) at C/5

Figure IV - 239 compares the charge/discharge performance at C/5 of the LiNi_{0.8}Co_{0.1}Mn_{0.1}O₂ cathodes prepared at different pH values. The material that was prepared at the pH value of 11.5 shows the highest initial discharge capacity of 210 mA h g⁻¹, as presented in Figure IV - 239a. Additionally, this same material shows the highest capacity retention (82.3%) and least voltage fade (0.15V) during cycling compared to the material prepared at other pH values.

To gain insight on the structural stability of material prepared at pH = 11.5, an EDS line scan was carried out on the material prepared at pH 10.7 and pH 11.5 and the result of Mn/Ni intensity ratio is shown in Figure IV - 240. Interestingly, it is found that the Mn/Ni intensity ratio across the particle, especially at the edge of the particle, of the material prepared at pH = 11.5 is higher than the one prepared at pH = 10.7. A relatively higher concentration of Mn content at the particle surface could significantly enhance the surface structural stability of Ni-rich cathode materials.

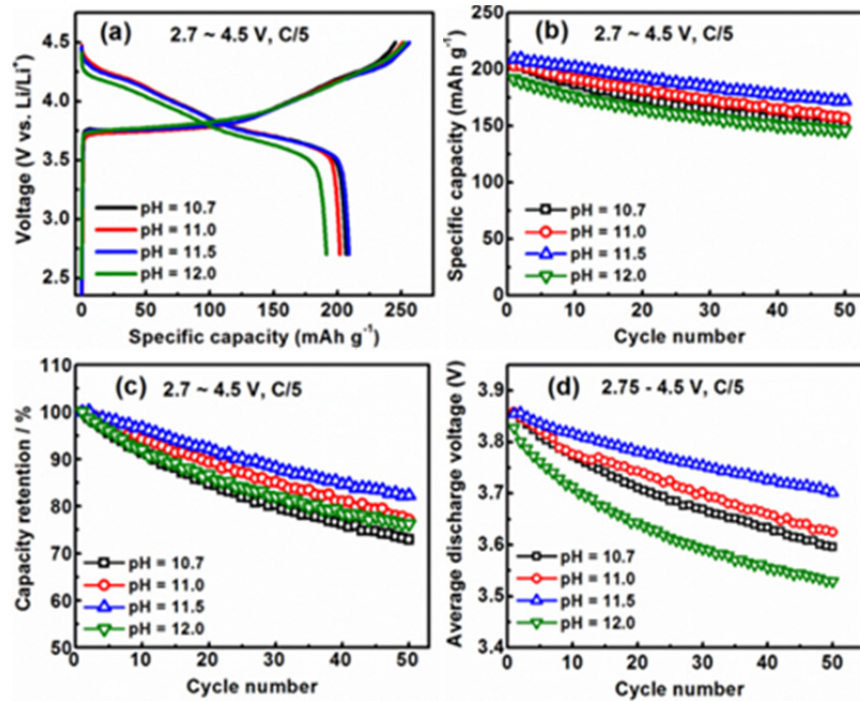


Figure IV - 239: (a) Charge/discharge profiles, (b) cycling performance, (c) capacity retention, and (d) average discharge voltage of $\text{LiNi}_{0.8}\text{Co}_{0.1}\text{Mn}_{0.1}\text{O}_2$ materials prepared at different pH values at C/5 rate over the voltage range of 2.7 - 4.5 V

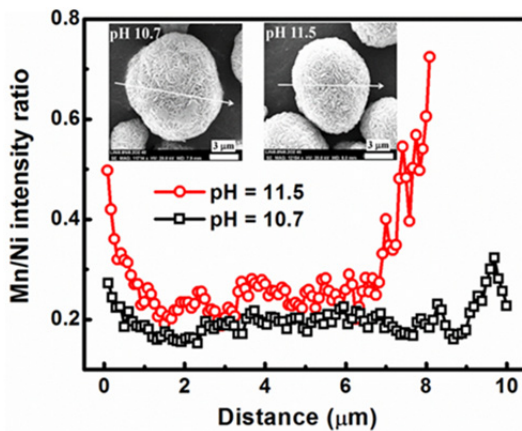


Figure IV - 240: Comparison of Mn/Ni intensity ratios across the precursor particles of materials prepared at pH = 10.7 and pH = 11.5

To further increase the tap density by increasing the secondary particle size, modified co-precipitation conditions were applied for NCM 71515 ($\text{LiNi}_{0.7}\text{Co}_{0.15}\text{Mn}_{0.15}\text{O}_2$, tap density: 2.3 g cm^{-3}) syntheses. Since the goal of the 4th quarter research is to determine the most desirable average particle size, large and uniform spherical particles of the NCM 71515 material with homogeneous size distributions around 10, 15, and 20 μm were synthesized, as shown in Figure IV - 241.

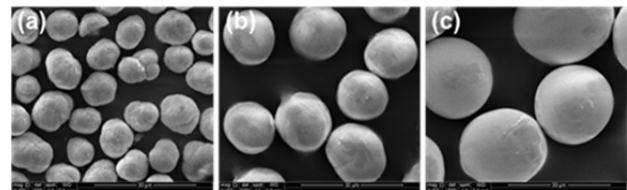


Figure IV - 241: SEM images of three recent batches of the NCM 71515 hydroxide precursor ($\text{LiNi}_{0.7}\text{Mn}_{0.15}\text{Co}_{0.15}\text{O}_2$) with different average particle size: (a) $\sim 10 \mu\text{m}$, (b) $\sim 15 \mu\text{m}$, and (c) $\sim 20 \mu\text{m}$

To further improve the cycle life and safety compared to the constant-concentration nickel-rich oxides, concentration-gradient cathode materials have

been prepared. The SEM image and the electrochemical performance are shown in Figure IV - 242. Compared to the constant-concentration material, the concentration-gradient materials (Figure IV - 242a) have similar morphology with a particle size of around 12 μm . However, in Figure IV - 242b, the concentration gradient materials show superior cyclability to the constant-concentration material.

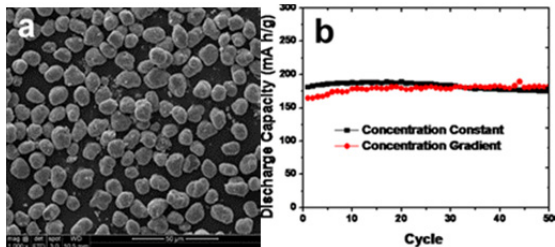


Figure IV - 242: (a) SEM image of the concentration-gradient $\text{LiNi}_{0.62}\text{Co}_{0.08}\text{Mn}_{0.23}\text{O}_2$ prepared at $\text{pH} = 8.3$ and (b) cycling performance of the concentration-gradient $\text{LiNi}_{0.62}\text{Co}_{0.08}\text{Mn}_{0.23}\text{O}_2$ and the constant-concentration material

As indicated in Figure IV - 242b, the concentration-gradient Ni-rich cathode prepared with Na_2CO_3 base agent has excellent stability, but a lower capacity of < 200 mA h g^{-1} , which is slightly lower than our goal. Therefore, instead of using Na_2CO_3 , NaOH was applied as the base agent to prepare new concentration-gradient samples. Figure IV - 243 compares the SEM images of samples prepared by different co-precipitation steps using NaOH. As shown in Figure IV - 243, all three

samples have uniform size, but the particle size gradually increases from ~3 μm to 5 μm to 7 μm after the third step. Since the Ni content decreases and Mn content increases in the metal solution from step 1 to step 3, the Ni content should decrease and the Mn content should increase gradually from the center towards the surface, which was confirmed by the EDS line scan shown in Figure IV - 244. In Figure IV - 244a, Ni and Co concentrations decrease from center to surface and the Mn concentration increases from center to surface.

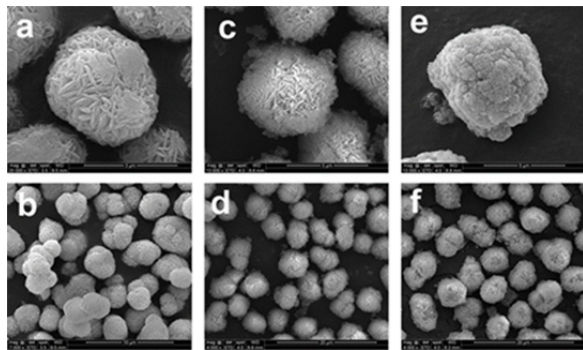


Figure IV - 243: SEM images of (a, b) $[\text{Ni}_{0.9}\text{Co}_{0.1}](\text{OH})_2$, (c, d) $[\text{Ni}_{0.9}\text{Co}_{0.1}]_{0.44}[\text{Ni}_{0.7}\text{Co}_{0.08}\text{Mn}_{0.22}]_{0.56}(\text{OH})_2$, and (e, f) $[\text{Ni}_{0.9}\text{Co}_{0.1}]_{0.4}[\text{Ni}_{0.7}\text{Co}_{0.08}\text{Mn}_{0.22}]_{0.5}[\text{Ni}_{0.5}\text{Co}_{0.05}\text{Mn}_{0.45}]_{0.1}(\text{OH})_2$

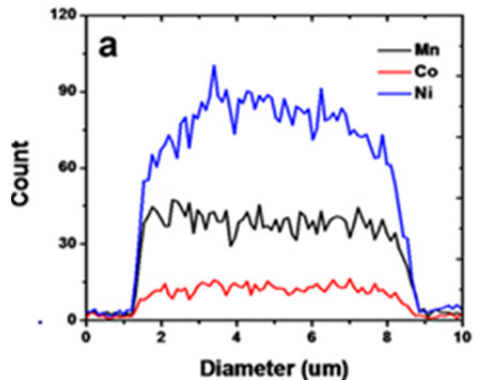


Figure IV - 244: EDS line scan across the $[\text{Ni}_{0.9}\text{Co}_{0.1}]_{0.4}[\text{Ni}_{0.7}\text{Co}_{0.08}\text{Mn}_{0.22}]_{0.5}[\text{Ni}_{0.5}\text{Co}_{0.05}\text{Mn}_{0.45}]_{0.1}(\text{OH})_2$ sample

Electrolyte: In the first quarter, Argonne has carried out the new additive synthesis, characterization and purification. Based on the DFT calculation, the LUMO energy level of a molecule will be reduced when an electron-withdrawing group is introduced onto the structure, making it easily reduced on the anode surface forming a robust electrode/electrolyte interphase.

We first designed and synthesized the fluorinated additive 4-(2,2,3,3-tetrafluoropropoxy)methyl-1,3-dioxolan-2-one (ANL-FA-1) as shown in Scheme 1. The reaction can be run at sub-gram and multi-gram scales at room temperature and atmospheric pressure with good conversion. For a 10-gram scale reaction, the reaction

proceeded cleanly to the desired product with 80% conversion after 24 hours (GC-MS) and >97% conversion after four days. Crude product was obtained after solvent removal. Pure product was obtained in 45% overall yield by vacuum distillation (90 °C/0.3 mmHg) for two times. The purified product was characterized by GC-MS, ^1H NMR, ^{13}C NMR, and FT-IR. The purity is determined to be 99.8% by GC-MS as shown in Figure IV - 245. Water content is 80 ppm as determined by Karl-Fischer titration. The fluorinated cyclic carbonate derivative may be used as a potential electrolyte/additive for high-energy NMC/Si cell. New electrolyte composed of 1.2 M LiPF_6 in TFPPCE/EMC

(3/7 v/v) was examined in $\text{LiNi}_{0.5}\text{Mn}_{1.5}\text{O}_4$ (LNMO) half-cell. The preliminary test results indicate the new additive is not compatible with the high voltage cathode LNMO as indicated by the fast capacity fading of the LNMO/Li cell (Figure IV - 246), but could be a good

cathode passivating additive. In the next quarter, we will conduct the electrochemical performance of this additive for both high voltage cathode and graphite and Si anode.

Scheme 1: Synthesis of fluorinated cyclic carbonates from epoxides and CO_2

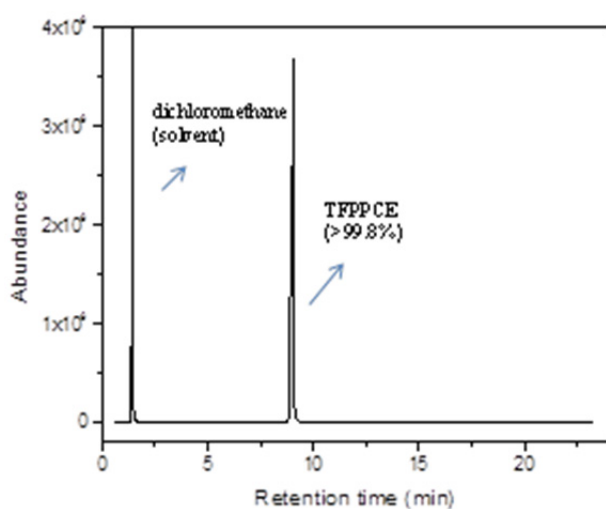
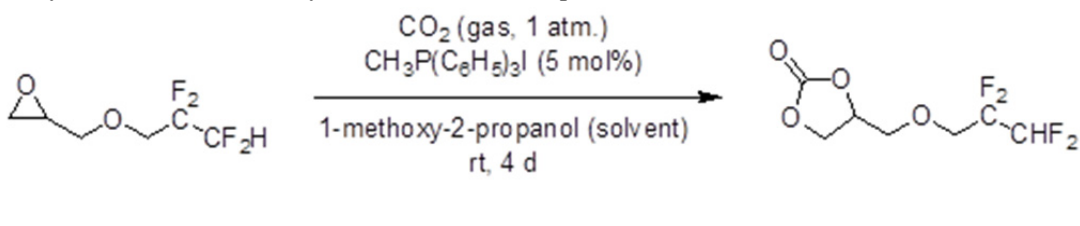


Figure IV - 245: GC-MS of the synthesized new additive

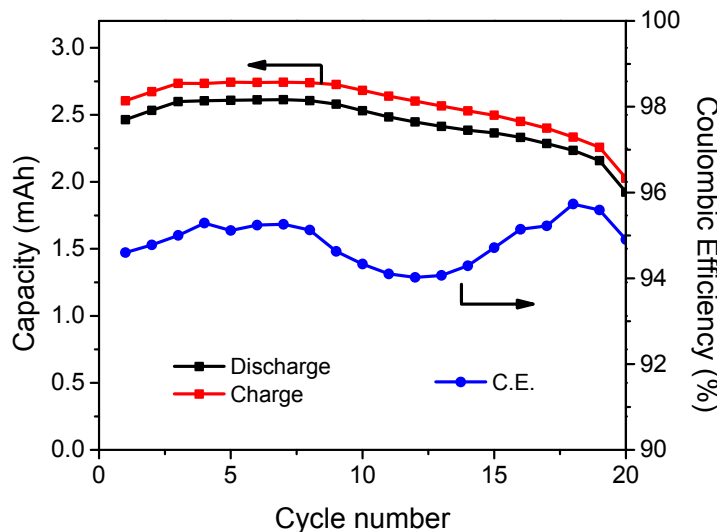


Figure IV - 246: LNMO/Li cell capacity retention profile using 1.2 M LiPF_6 in TFPPCE/EMC (3/7, v/v). Voltage window: 4.95–3.5 V, Current: 0.8 mA (C/3)

In the second quarter, we have investigated the effect of different electrolytes on the performance of the

high capacity cathode Li metal half cells. The cathode material is from UT Austin, named UTC#0. To begin

with, we used the Gen 2 electrolyte (LiPF_6 in EC/EMC = 3/7 by weight) as the base line and cycled the cell between 4.5–2.7 V at C/5 cycling rate. The capacity retention and voltage profile of the cell is shown in Figure IV - 247a and Figure IV - 247b. At the same time, we tested a fluorinated electrolyte formulation using the same testing condition, and the result is shown

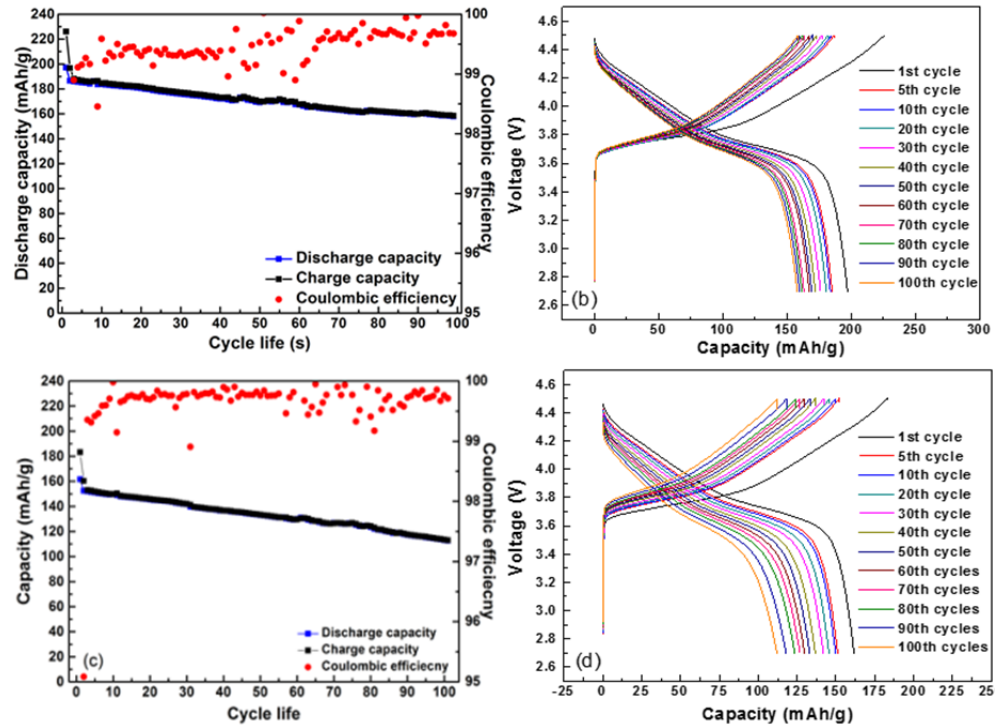


Figure IV - 247: Capacity retention and voltage profile of UT-Austin high capacity cathode, UTC#0/Li half cells cycled at RT between 2.7-4.5 V, C/5 using (a), (b) Gen 2 electrolyte and (c), (d) fluorinated electrolyte

Due to the high voltage tolerance of the fluorinated electrolyte, we also tested the half cell with increased cut-off voltage at 4.8 V, as shown in Figure IV - 248 to see whether it is capable of delivering extra capacity. Indeed, the initial capacity of the cathode half cell sees a dramatic 38% increase relative to the cell with cut-off voltage set at 4.5 V, as shown in Figure IV - 248.

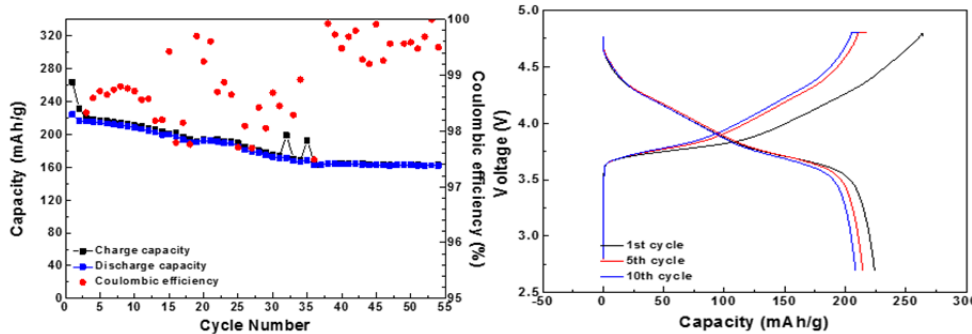
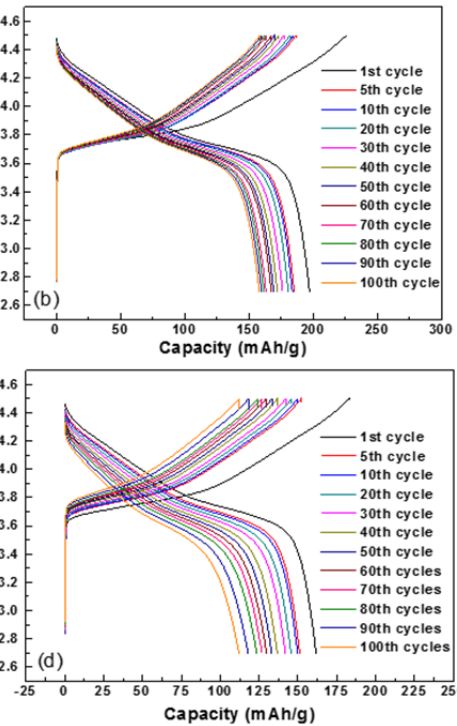


Figure IV - 248: Capacity retention and voltage profile of UT-Austin high capacity cathode UTC#0/Li half cells cycled at RT between 2.7-4.8 V, C/5 using fluorinated electrolyte

In the third quarter, with the new batch of cathodes from UT-Austin, UTC-E1, we investigated the effect of

in Figure IV - 247c and Figure IV - 247d. The capacity retention of the fluorinated electrolyte cell is slightly worse than the Gen 2 electrolyte cell, but the coulombic efficiency is slightly higher than the Gen 2 electrolyte cell. Moreover, the initial specific capacity of the fluorinated electrolyte cell is notably lower than the Gen 2 electrolyte cell.



However, the capacity retention and the coulombic efficiency are both worse than the cell with cut-off voltage at 4.5 V. Further investigation is needed to examine the poor capacity retention and low coulombic efficiency is whether due to electrolyte/electrode interface problem or due to the instability of the electrode caused by over delithiation.

fluorinated ether as an additive in the conventional Gen 2 electrolyte. The fluorinated ether F-EPE was added

into the Gen 2 electrolyte (LiPF_6 in EC/EMC = 3/7 by weight) at 5% by weight as an additive. The cathode half cell using Gen 2 and Gen 2 + 5% F-EPE were tested at cut off voltage of 4.5 V and 4.8 V at both RT and 55 °C, and the results are shown in Figure IV - 249. The cell with 5% F-EPE showed no difference from the

Gen 2 control electrolyte at both 4.5 V (Figure IV - 249a) and 4.8 V (Figure IV - 249b) cut-off voltages when cycled at RT, but at 55 °C, the cell with 5% of F-EPE showed better capacity retention as illustrated in Figure IV - 249c and Figure IV - 249d.

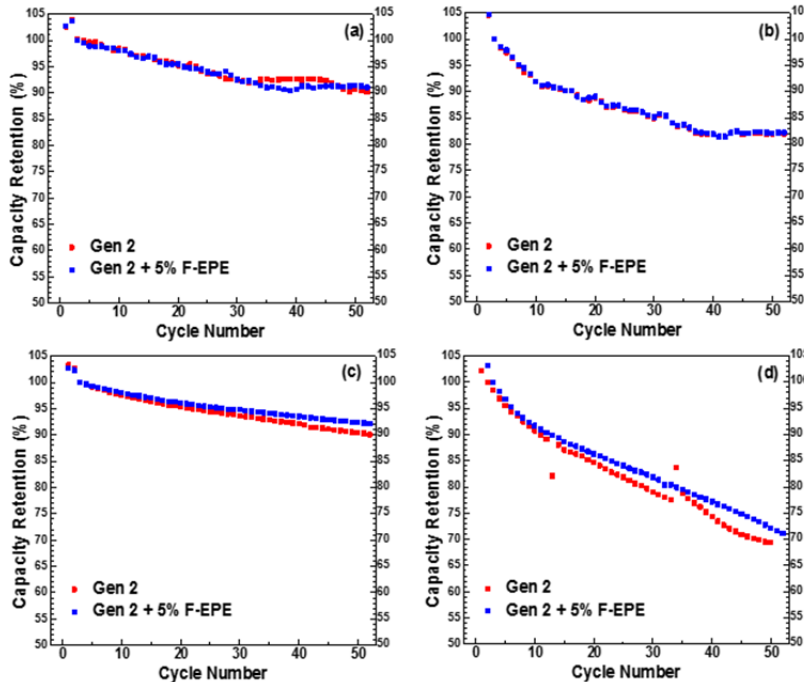


Figure IV - 249: Capacity retention profiles of UT-Austin high capacity cathode/Li half cells cycled at RT with cut-off voltage at (a) 2.7 V - 4.5 V and (b) 2.7 V- 4.8 V and at 55 °C with cut-off voltage at (c) 2.7 V - 4.5 V and (d) 2.7 V - 4.8 V using Gen 2 and Gen 2 + 5% F-EPE electrolytes

We also conducted research on Si anode side and have screened a couple of additives to improve the property of the Gen 2 electrolyte and have evaluated a fluorinated electrolyte HVE 1 using the baseline Umicore Si material (from Penn State). The electrode was fabricated with 50% silicon, 25% Super P, and 25% PAA as binder. The dQ/dV profiles of the 1st cycle formation of Si/Li half cells using Gen 2 electrolyte and fluorinated electrolyte with different additives are

summarized in Figure IV - 250a and Figure IV - 250b, respectively. Most of the additives did not affect the dQ/dV of Gen 2 electrolyte, except for F-EPE which makes SEI formation earlier during discharge process. The addition of LiDFOB or VC to HVE 1 electrolyte showed an obvious decomposition peak at 1.9 V and 2.0 V, respectively, indicating the formation of the artificial SEI on the surface of Si anode.

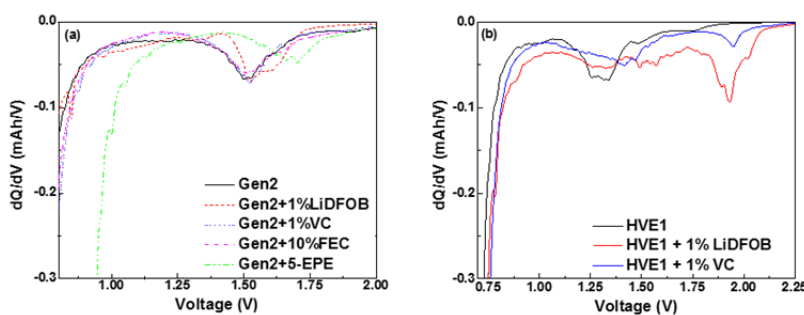


Figure IV - 250: Differential capacity plots of the 1st cycle formation of Si/Li half cells using (a) Gen 2 electrolyte with LiDFOB, VC, FEC and EPE as additives and (b) HVE1 electrolyte with LiDFOB and VC as additives

Si/Li cell performance of most of the electrolytes studied above is inferior than or at the same level with the Gen 2 control electrolyte, except for Gen 2 + 10% FEC shows improvement over the control. The cycling performance of Si/Li cells with Gen 2 and Gen 2 + 10%

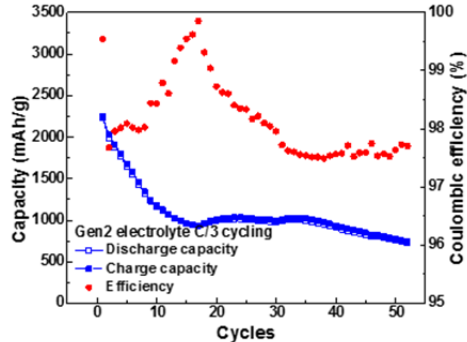


Figure IV - 251: Capacity retention profiles and Coulombic efficiency of Si/Li half cells at RT using (a) Gen 2 electrolyte and (b) Gen 2 + 10% FEC electrolyte

The silicon electrode was characterized by TEM after the formation cycle. Compared with the pristine silicon particles, shown in Figure IV - 252a, which are mostly spherical, the cycled particles lost their original shape and have uneven surface coating layers (Figure IV - 252b). EDS investigation of the surface coating reveals that it contains majorly carbon, oxygen, fluorine as well as phosphorous, which indicates that both the additive FEC and the salt LiPF₆ participated the SEI formation process.

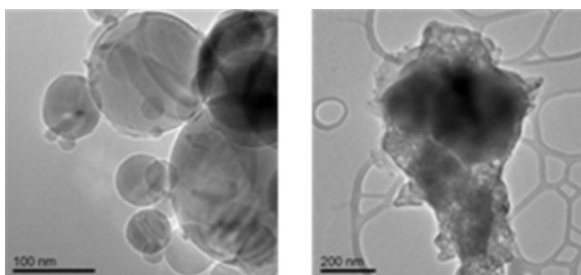
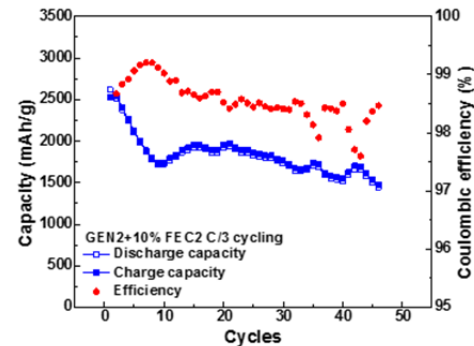
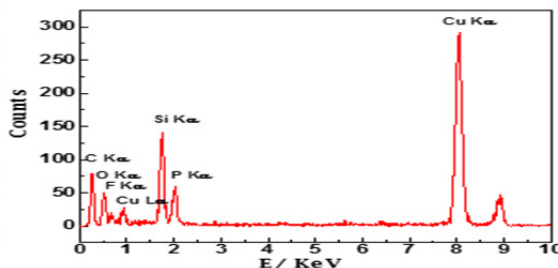


Figure IV - 252: TEM characterization of (a) pristine Si particles and (b) Si anode harvested from Si/Li half cell after formation in Gen 2 + 10% FEC electrolyte; (c) EDS spectrum of the edge coating on cycled Si particles

FEC electrolyte are shown in Figure IV - 251a and Figure IV - 251b. The addition of 10% FEC noticeably increased the overall capacity and coulombic efficiency of the anode half cell.



In the fourth quarter, with the newest batch of cathodes from UT-Austin named UTCE2, we compared the performance of fluorinated electrolyte FEC 2 (1.0 M LiPF₆ in FEC/F-EMC/F-EPE=3/5/2 by volume) with Gen 2 electrolyte. The cathode half-cell using Gen 2 and fluorinated electrolyte were tested at cut off voltage of 4.5 V and 4.8 V at both RT and 55 °C, and the results are shown in Figure IV - 253. The cell with fluorinated electrolyte showed better capacity retention in all conditions tested.



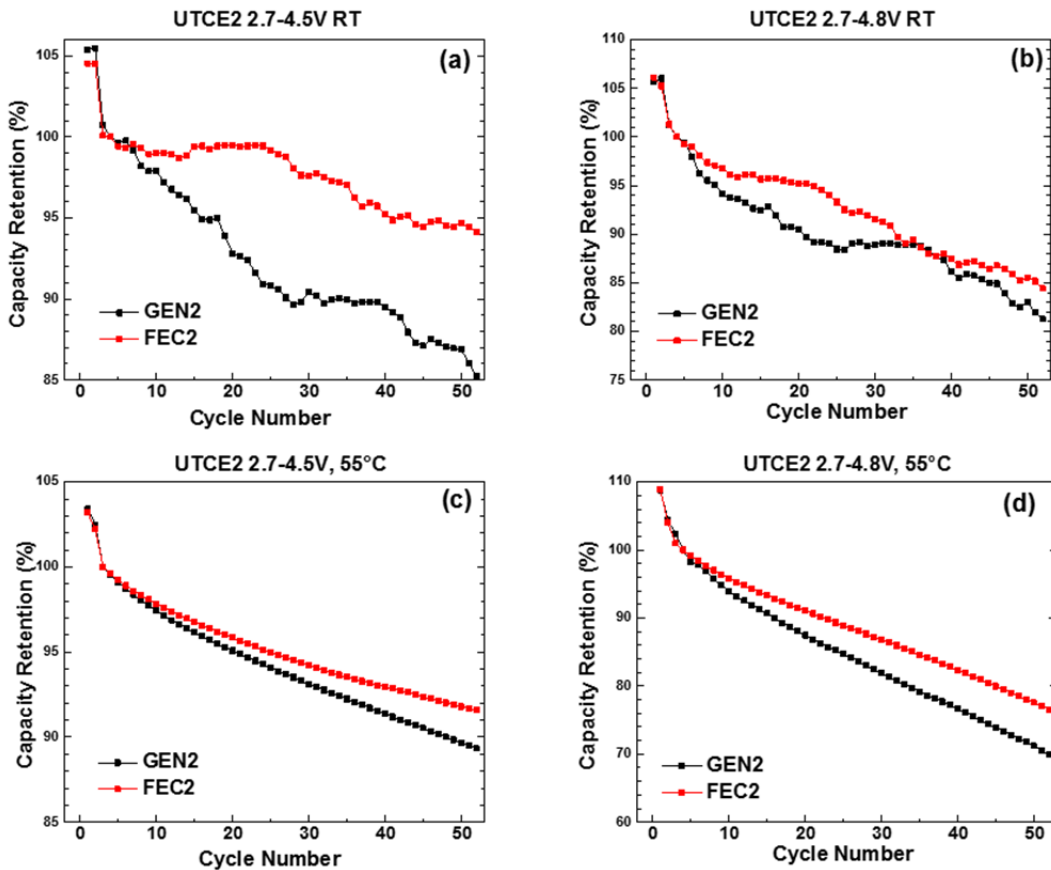


Figure IV - 253: Capacity retention profiles of UT-Austin high capacity cathode/Li half cells cycled with Gen 2 and FEC 2 electrolytes at RT with cut-off voltage at (a) 2.7 V - 4.5 V and (b) 2.7 V- 4.8 V and at 55 °C with cut-off voltage at (c) 2.7 V - 4.5 V and (d) 2.7 V - 4.8 V

We also conducted research on the PSU Si anode ($\text{SiO}_2\text{-C}$ material) and have screened a couple of additives to improve the performance of the baseline electrolyte (Gen 2+10% FEC by weight). Figure IV - 254a shows the chemical structure of the additives. The differential capacity plots of the 1st cycle

formation of $\text{SiO}_2\text{-C}/\text{Li}$ half cells using the baseline electrolyte with different additives are summarized in Figure IV - 254b. Based on the dQ/dV data, the SEI formation is significantly affected by the additives in that the peak intensities and positions are changed according to different additives.

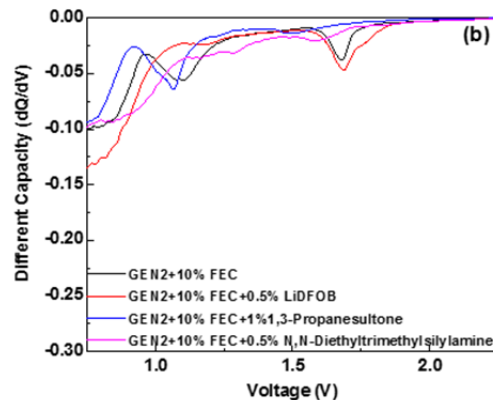
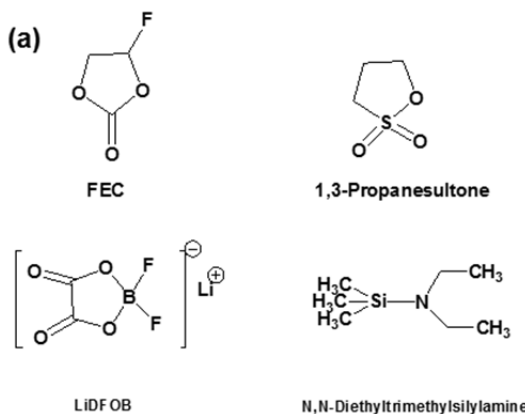


Figure IV - 254: (a) Chemical structure of different additives for $\text{SiO}_2\text{-C}$ anode; (b) Differential capacity plots of the 1st cycle formation of $\text{SiO}_2\text{-C}/\text{Li}$ half cells with Gen 2+10% FEC baseline electrolyte and with LiDFOB, 1,3-Propanesultone and N,N-Diethyltrimethylsilylamine as additives

The cycling performances of $\text{SiO}_2\text{-C}/\text{Li}$ cells with different additives are shown in Figure IV - 255. All 3 additives showed different degrees of improvement in

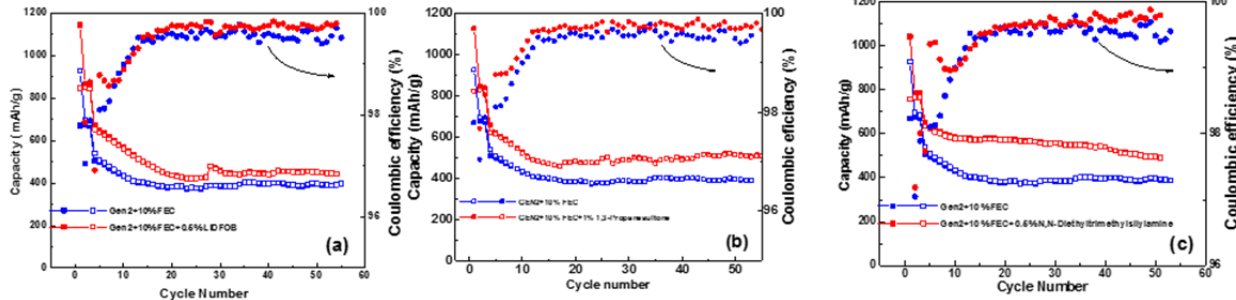


Figure IV - 255: Capacity retention and coulombic efficiency of $\text{SiO}_2\text{-C}/\text{Li}$ half-cells at RT using baseline plus (a) 0.5% LiDFOB, (b) 1% 1,3-Propanesultone and (c) 0.5% N,N-Diethyltrimethylsilylamine compared with the baseline Gen 2 + 10% FEC electrolyte

The harvested $\text{SiO}_2\text{-C}$ electrodes from the half-cells were characterized by SEM after the cycling test. Figure IV - 256a shows the surface morphology of the harvested electrode with baseline electrolyte. Figure IV - 256b, c, and d represents the morphology of the harvested electrodes from electrolyte with different additives. The morphology of the electrode surface is affected by the additives in all cases, which serves as another proof that the additives take effect on the anode.

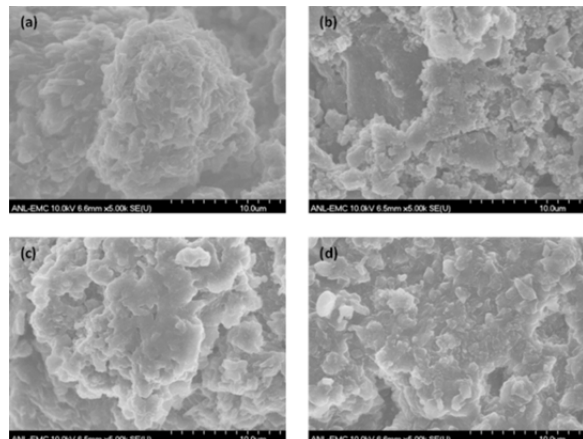
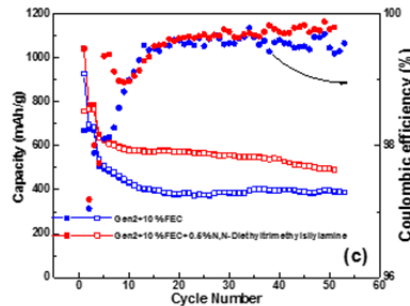


Figure IV - 256: SEM characterization of cycled $\text{SiO}_2\text{-C}$ anode harvested from $\text{SiO}_2\text{-C}/\text{Li}$ half-cells with (a) Gen 2+10% FEC baseline electrolyte, (b) baseline + 0.5% LiDFOB, (c) baseline + 1% 1,3-Propanesultone, and (d) baseline + 0.5% N,N-Diethyltrimethylsilylamine

Conclusions and Future Directions

Anode: The intermediate Si-based anode material, called B-Si/ $\text{SiO}_2\text{-2}^\circ\text{/C}$, developed in this quarter of the ABR project is capable of better performance when compared to B-Si/ $\text{SiO}_2\text{/C-325}$ and Si/ $\text{SiO}_2\text{/C}$ materials. This superior performance is attributed to active materials size reduction, which leads to short charge transport paths and thus increased material utilization.

terms of both capacity and coulombic efficiency over the baseline.



Furthermore, the high coulombic efficiency shown for the silicon anodes made with the interpenetrated gel polymer binder indicated that binder assisted in the formation of a relatively stable SEI layer on the silicon particles.

Electrode formulation and processing will be optimized to achieve high quality electrodes with both appropriate areal capacity and good cycling stability. Full cells will be fabricated and evaluated using intermediate anodes.

Cathode: The effects of the pH value on the electrochemical performance of Ni-rich cathode materials $\text{LiNi}_{0.8}\text{Co}_{0.1}\text{Mn}_{0.1}\text{O}_2$ using NaOH as a precipitating agent and $\text{LiNi}_{0.62}\text{Co}_{0.08}\text{Mn}_{0.23}\text{O}_2$ using Na_2CO_3 have been systematically investigated. It is found that the material prepared at $\text{pH} = 11.5$ with NaOH shows superior crystalline structure and exhibits relatively higher tap density as compared to those prepared at other pH values. In addition, the material prepared at $\text{pH} = 11.5$ shows the best electrochemical performance, including the highest initial discharge capacity and the best rate capability and cycling stability both at room temperature and at a high temperature of 55 °C. However, the long-term cycling performance is still not satisfactory. With the optimized synthetic conditions, the composition of Ni-rich cathode materials will be further optimized in order to achieve materials with enhanced cycling performance. Moreover, additional surface modifications will also be carried out to further enhance the surface structural stability of Ni-rich cathode materials.

The concentration-gradient cathode $\text{LiNi}_{0.62}\text{Co}_{0.08}\text{Mn}_{0.23}\text{O}_2$ we prepared with Na_2CO_3 shows superior stability to the constant-concentration material, indicating that the concentration-gradient structure probably can suppress the capacity fading issue. Since the capacity of the concentration-gradient cathode prepared with Na_2CO_3 is lower than that of our project target, our next step will be to optimize the synthesis conditions to obtain new concentration-gradient

cathodes with NaOH or KOH in order to improve their reversible capacity and long-term cycle life.

Electrolyte: For cells incorporating the newest batch of cathodes from UT-Austin, the fluorinated electrolyte is able to improve capacity retention. In regards to our investigation with the PSU Si anodes (SiO₂-C material), we conclude that electrolyte additives will definitely impact the SEI formation on the

active particles based on the differential capacity analysis. Additionally, the selected additives for this study are capable of improving the performance of the electrode material, although to different extents depending on the additive.

IV.D.6 High Energy High Power Battery Exceeding PHEV40 Requirements (TIAX)

Dr. Christopher Johnson (NETL Program Manager)

Dr. Jane Rempel (PI)
TIAX, LLC
35 Hartwell Avenue
Lexington, MA 02421

Subcontractor:
None

Start Date: 10/01/2013
Projected End Date: 09/30/2015

Objectives

The overall program objective is to demonstrate a lithium-ion battery system that meets and exceeds DOE's PHEV-40 performance and life goals.

Technical Barriers

The major technical challenge faced by Li-ion batteries is simultaneously meeting energy, power, and life targets for PHEV batteries over a wide temperature range.

Technical Targets

- Implement CAM-7TM/Si-based anode chemistry in Li-ion cells designed to achieve >200Wh/kg and >400Wh/L energy and >800W/kg and >1600W/L 10s pulse power targets under USABC PHEV battery testing procedures.
- Demonstrate performance of CAM-7/graphite system in baseline 18650 cells.
- Demonstrate Li-ion cells with higher energy and power capability than the baseline cell design
- Deliver baseline cells and improved cells to Argonne National Laboratory (ANL) for independent performance verification.
- Demonstrate that improved Li-ion cells have cycle life and calendar life that project to meeting PHEV-40 targets.

Accomplishments

- Delivered 18650 cells to ANL for independent testing with baseline design employing CAM-7/graphite electrodes.
- Improved the high temperature performance of CAM-7 material by tuning the dopant composition and distribution.
- Assessed the impact of electrode and cell design on cycle life of silicon-based anode materials.



Introduction

Li-ion cell energy density is largely determined by the properties of the active materials. The power capability is influenced by not only the active materials, but also the inactive materials such as the conductive carbons used in the electrode, the separator, and the electrolyte. Finally, the design of the electrodes (e.g., ratio of active material to conductive carbon to binder) also influences energy and power. Consequently, a system-level approach that marries selected active materials with suitable inactive materials and suitable electrode design is needed to meet DOE's PHEV-40 targets for simultaneously achieving high energy and power densities, and life.

Approach

Our overall approach is to combine TIAX's high-energy and high-power cathode material, CAM-7, and silicon-based anodes in electrode designs optimized for PHEV-40 application in cells using high-performance separators to meet the energy and power targets. CAM-7 is a high-nickel-content cathode material developed by TIAX with high discharge capacity and high rate capability. For example, with charge to 4.3 V in half cell versus Li metal, CAM-7 can provide > 200 mAh/g at low rates and > 130 mAh/g at 100 C discharge rate in suitably designed electrodes. With normal charge voltage to 4.2 V, this material exhibits very high discharge capacity and high power capability combined with excellent life at room temperature as well as high temperature cycling. We synthesize the CAM-7 cathode materials and implement them in electrode designs suitable for PHEV applications.

We are employing a different approach with Silicon-based anode materials. A number of materials suppliers are developing silicon-based Li-ion anode materials encompassing a wide range of approaches to simultaneously achieve high capacity and long life. In order to enhance the chance of success in this project, we proposed to source silicon materials from a wide range of suppliers, and engineer them into high-performance electrodes. We proposed to evaluate one or two down-selected materials in full-sized (multi-Ah) cells.

We have obtained high-performance separators from a number of different companies for evaluating with the CAM-7/silicon-based system.

At the end of this project, we will compare the CAM-7/silicon-based system against a baseline CAM-7/graphite system to demonstrate the potential for the CAM-7/silicon-based system to meet the PHEV-40 goals. Accordingly, to establish the baseline system performance, we fabricated and delivered 12 18650 cells with the CAM-7/graphite system for independent testing at Argonne National Laboratory (ANL). Performance of identical 18650 cells, retained and evaluated at TIAX, is reported in this summary.

The focus of year 1 was to optimize CAM-7 performance, evaluate and select suitable silicon anode materials, identify high-performance separators, and fabricate and test baseline 18650 cells.

Results

Baseline Cell Performance

12 baseline 18650 cells with our current standard CAM-7 cathode material, commercial graphite, and low-power separator were fabricated at TIAX and delivered to ANL for independent testing. A few cells from this cell build were retained and tested at TIAX. The results of this testing are summarized in Figure IV - 257, Figure IV - 258, and Figure IV - 259. The initial capacity of these cells was 1.7 Ah with a 1 C specific energy of 160 Wh/kg at room temperature. Note that the capacity and specific energy of these cells is limited by the internal diameter of the 18650 cans employed and the weight of these cans. The specific energy on a jelly-roll-only basis (i.e., without packaging) was 200 Wh/kg. We have also made 18650 cells with CAM-7 graphite with specific energy nearly 250 Wh/kg, verified in independent testing [ref: Allen JL, Allen JL, Delp SA, Jow TR. (2014). Evaluation of TIAX High Energy CAM-7/Graphite Lithium-Ion Batteries at High & Low Temperatures, U.S. Army Research Laboratory].

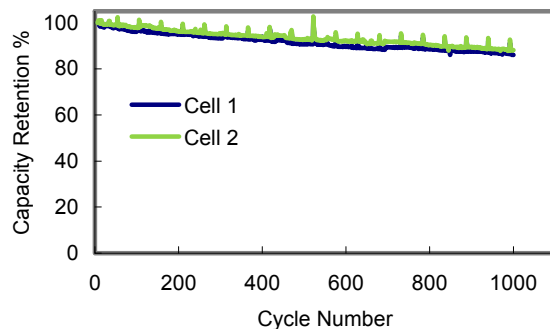


Figure IV - 257: Capacity retention during room temperature cycling of CAM-7/graphite system in baseline 18650 cells fabricated at TIAX. The cells are cycled at C/2 charge rate and discharged at 1C rate between 4.2 to 2.7V. Every 50 cycles, the C/3 and C/2 capacities are measured

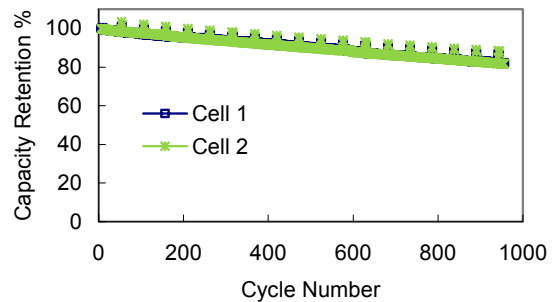


Figure IV - 258: Capacity retention during cycling at 45°C of CAM-7/graphite system in 18650 cells fabricated at TIAX. The cells are cycled at C/2 charge rate and discharged at 1C rate between 4.2 to 2.7V. Every 50 cycles, the C/20 and C/5 capacities are measured

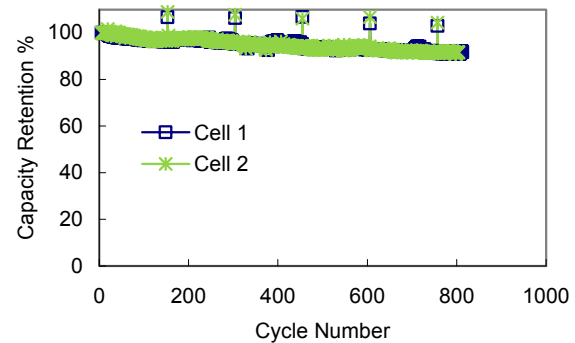


Figure IV - 259: Capacity retention during cycling at room temperature of CAM-7/graphite baseline system in 18650 cells fabricated at TIAX. The cells are cycled at C/2 charge rate and discharged at 1C rate between 4.1 to 2.7V. Note that cycling between 4.1 to 2.7 corresponds to 90% SOC swing during cycling. Every 50 cycles, the C/3 and C/2 capacities are measured

CAM-7 Cathode Material

In its current embodiment, CAM-7 cathode material has excellent properties for use in PHEV applications, and is indeed being featured in the roadmaps of two prominent global automotive

companies for their next-generation batteries. However, as with any material, additional improvements are possible. During this project, we further reduced the impedance growth during high temperature cycling. In order to facilitate rapid electrochemical testing of materials, we developed an electrochemical testing protocol that allows a high-fidelity characterization of impedance growth within a week of electrochemical testing, significantly faster than conventional protocols. We monitor the time spent at constant voltage during charge as an indicator of the impedance. Results from a particular matrix of experiments is summarized in Figure IV - 260.

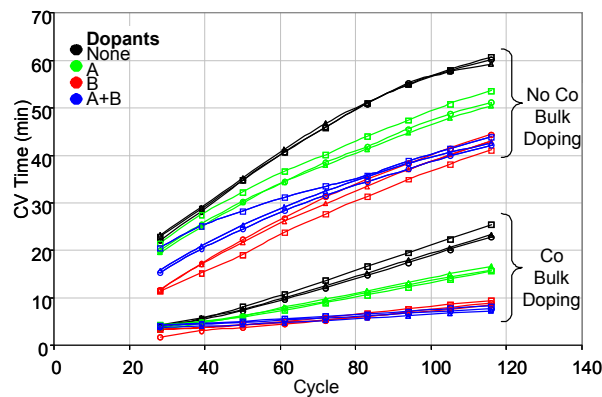


Figure IV - 260: Summary data showing the impact of dopant distribution on impedance growth of CAM-7 high-nickel cathode materials. Dopant A is placed in the bulk of the material, and dopant B at the surface. Measurements such as these were performed to develop a new composition of CAM-7 with very low impedance growth specifically for vehicle applications

Silicon-Based Anode Materials

As described above, we sourced eight different silicon-based anode materials from leading materials suppliers. Because of confidentiality agreements with the suppliers, we cannot share their identity or the composition of the silicon materials. The major focus in this project has been to engineer electrodes with these silicon-based anode materials for PHEV-40 application.

The different silicon-based materials were coated into electrodes at TIAX with identical electrode designs, and electrochemically evaluated under identical test conditions. The impact of electrode design, binder composition, electrolyte composition, voltage limits, and anode/cathode balancing, and pre-lithiation were evaluated initially in coin cells.

Previous calculations showed that in order for the silicon-based anodes to facilitate achievement of performance targets, they must be implemented in electrode designs with capacity > 1000 mAh/cc at an electrode loading > 2 mAh/cm², and operate with a cycling efficiency > 99.99%. Consequently, most of our testing has been performed in electrodes with initial capacity exceeding 1000 mAh/cc and loading exceeding 2 mAh/cm². Exemplar coin cell data showing the benefit of pre-lithiation are shown in Figure IV - 261. Although the capacity retention with pre-lithiation has dramatically improved, additional work is needed to optimize the silicon anode, electrolyte composition, and pre-lithiation levels to meet the PHEV-40 cycling targets.

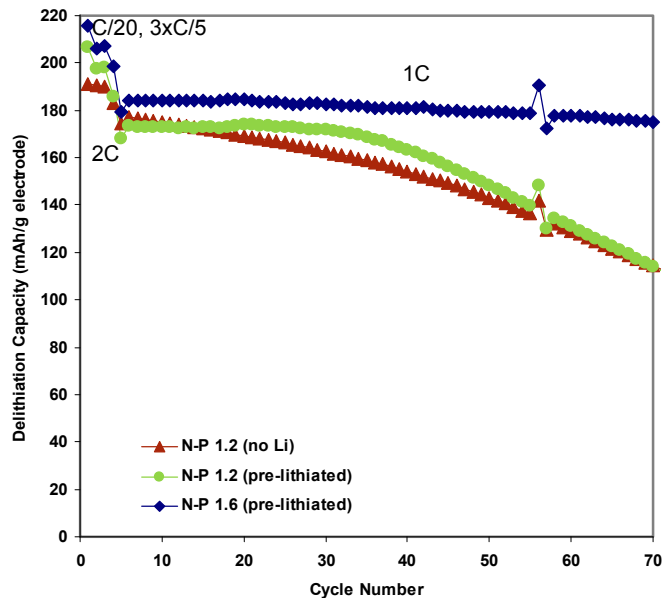


Figure IV - 261: Cycling results of CAM-7/silicon-based anode in coin cells showing the impact of anode to cathode ratio, and pre-lithiation on capacity retention

Conclusions and Future Directions

The TIAX approach of combining its high-performance CAM-7 cathode materials with silicon-based anode materials and high-performance separators can enable us to simultaneously meet the PHEV-40 targets for energy, power, and life. In this project, we have demonstrated the excellent cycle life of CAM-7/graphite 18650 cells both at room temperature and at elevated temperature cycling. Significant additional improvements in CAM-7 high temperature cycle life were obtained by modifying its composition. Silicon-based anode materials sourced from different suppliers are being engineered into electrodes that can meet the PHEV targets. We have evaluated the impact of electrode design, binder composition, electrolyte

composition, voltage limits, anode/cathode balancing, and pre-lithiation in coin cells.

Our focus going forward will be to down-select specific silicon material for further electrode engineering to meet the PHEV-40 targets. We will further optimize pre-lithiation approaches to obtain improved cycling of CAM-7/silicon-based cells. We will fabricate 18650 or multi-Ah pouch cells with CAM-7 and silicon-based anodes for evaluating against the PHEV-40 targets.

FY 2014 Publications/Presentations

1. 2014 DOE Annual Peer Review Meeting Presentation.

IV.E Process Development and Manufacturing R&D

IV.E.1 Process Development and Scale up of Advanced Cathode Materials (ANL)

Gregory K. Krumdick

Argonne National Laboratory
9700 South Cass Avenue
Argonne, IL 60439-4837
Phone: (630) 252-3952; Fax: (630) 252-1342
E-mail: gkrunderick@anl.gov

Collaborators:

YoungHo Shin, Argonne National Laboratory
Ozgenur K. Feridun, Argonne National Laboratory
Gerald Jeka, Argonne National Laboratory
Mike Kras, Argonne National Laboratory
Anthony Burrell, Argonne National Laboratory
Michael Thackeray, Argonne National Laboratory
Christopher Johnson, Argonne National Laboratory
Bryant Polzin, Argonne National Laboratory
Wenquan Lu, Argonne National Laboratory
Jason Croy, Argonne National Laboratory
Brandon Long, Argonne National Laboratory
Kumar Bugga, Jet Propulsion Laboratory

Start Date: June, 2010

Projected End Date: September, 2015

Objectives

- Evaluate and select the synthesis route, develop a customized process and scale-up to produce kilogram quantities of the target bench-scale advanced materials for basic research, market evaluation and high-volume manufacturing.
 - Select and develop scalable synthesis process with economic feasibility and produce target bench-scale materials with high quality and reproducibility.

Technical Barriers

Most advanced cathode materials like lithium and manganese rich metal oxide (LMR-NMC) materials have been synthesized in small quantity at the bench-scale with poor reproducibility and lack commercial availability. Sufficient quantity of these advanced materials with good quality is hard to get for basic

research and industrial evaluation, which needs evaluating synthesis route, customizing selected synthesis process and solving scale-up challenges to get high quality and reproducibility.

Technical Targets

- Set up and evaluate synthesis routes using conventional and emerging technologies for target bench-scale material.
 - Select better synthesis route by preliminary syntheses and their material evaluations.
- Develop a customized synthesis process for target bench-scale material.
 - Synthesize 100g intermediate scaled-up material for initial evaluation by collaborators.
- Identify and resolve constraints for the scale-up process of target bench-scale material.
- Optimize process and produce sufficient quantities of scaled-up material with equal or better quality than target bench-scale material.
 - Produce and deliver several kilograms of optimized scaled-up material.
- Compare the performance of scaled-up material to target bench-scale material by coin cell testing.
- Distribute synthesized materials to industry and R&D community.
- Obtain feedback from collaborators and modify the scaled-up material to get better performance.

Accomplishments

Scale-up of $\text{Li}_{1.2}\text{Mn}_{0.54}\text{Ni}_{0.13}\text{Co}_{0.13}\text{O}_2$

- Set-up and evaluation of synthesis routes using planetary ball mill, carbonate co-precipitation and hydroxide co-precipitation methods.
- Optimization of the selected process to generate material with high quality and reproducibility.
- Production of 1kg scaled-up carbonate cathode material (initial discharge capacity: 299 mAh/g) for surface coating application by JPL/NASA.
- Production of 2kg scaled-up carbonate cathode material (initial discharge capacity: 288 mAh/g) for pouch cell evaluation by JPL/NASA.
- Achievement of 20% increased capacity, 20% increased tap density and better cycle life of scaled-

- up material compared to JPL/NASA target specification.
- Performance evaluation of a modified scaled-up material with 2% AlF₃ surface coating by JPL/NASA from collaborator feedback.

Scale-up of Li_{1.14}Mn_{0.53}Ni_{0.28}Co_{0.19}O_y

- Set-up and evaluation of synthesis routes using carbonate and hydroxide co-precipitations.
- Synthesis of preliminary materials and evaluation of their physical and electrochemical properties.
- Achievement of improved capacity, tap density and cycle life compared to the target bench-scale material (by carbonate process).
- Delivery of preliminary materials to collaborator for performance check and decision to postpone further process development and scale-up.

Scale-up of Li_{1.05}Mn_{0.43}Ni_{0.52}Co_{0.05}O_y

- Set-up and evaluation of synthesis routes using carbonate and hydroxide co-precipitations.
- Synthesis of preliminary materials and evaluation of their physical and electrochemical properties.
- Achievement of improved capacity, tap density and cycle life compared to the target bench-scale material (by carbonate and hydroxide process).
- Coin cell evaluation of preliminary materials using an improved electrochemical testing protocol is ongoing prior to kilogram scale production.
- This material will become the baseline material for the upcoming DOE high voltage project.

Surface modification by dry coating process

- Set-up of pilot-scale dry coating system.
- Achievement of improved tap density and cycle life after dry coating of 1wt% Al₂O₃ on commercial lithium nickel oxide material.

Delivered materials:

- 10/30/13 – 5g Ni_{0.16}Mn_{0.67}Co_{0.16}(OH)₂ to ANL CSE for domain study.
- 10/31/13 – 100g Li_{1.45}Ni_{0.16}Mn_{0.67}Co_{0.16}O_y to JPL/NASA for evaluation.
- 11/11/13 – 500g Ni_{0.16}Mn_{0.67}Co_{0.16}(OH)₂ to ANL CSE for domain study.
- 01/17/14 – 100g Ni_{0.16}Mn_{0.67}Co_{0.16}CO₃ to ANL CSE for ion-exchange research.
- 01/20/14 – 300g Li_{1.37}Ni_{0.33}Mn_{0.67}O_y to ANL ES for ALD coating.
- 01/21/14 – 300g Li_{1.37}Ni_{0.33}Mn_{0.67}O_y to ANL ES for ALD coating.
- 01/30/14 – 1kg Li_{1.45}Ni_{0.16}Mn_{0.67}Co_{0.16}O_y to JPL/NASA for evaluation.
- 01/31/14 – 2kg Li_{1.45}Ni_{0.16}Mn_{0.67}Co_{0.16}O_y to JPL/NASA for evaluation.

- 02/03/14 – 400g Li_{1.45}Ni_{0.16}Mn_{0.67}Co_{0.16}O_y to ANL CSE for pouch cell evaluation.
- 02/04/14 – 50g Li_{1.45}Ni_{0.16}Mn_{0.67}Co_{0.16}O_y to ANL Material Screening Group.
- 03/17/14 – 50g Li_{1.45}Ni_{0.16}Mn_{0.67}Co_{0.16}O_y to ITN Energy Systems Inc. evaluation.
- 03/18/14 – 25g Li_{1.45}Ni_{0.16}Mn_{0.67}Co_{0.16}O_y to ITN Energy Systems Inc. evaluation.
- 05/20/14 – 10g Li_{1.37}Ni_{0.33}Mn_{0.67}O_y to ANL CSE for material evaluation.
- 06/30/14 – Cathode film Li_{1.06}Ni_{0.27}Mn_{0.54}Co_{0.19}O_y to ANL CSE for coin cell testing.
- 09/26/14 – 4g Li_{1.37}Ni_{0.33}Mn_{0.67}O_y to NanoResearch Inc. for evaluation.



Introduction

There is a strong need to get advanced cathode materials like lithium and manganese rich metal oxide (LMR-NMC) materials with high quality to the kilogram and tens-of-kilograms quantities for basic R&D purposes and industrial needs. However, these advanced materials lack commercial availability. To meet this need, evaluating synthesis routes, developing a customized process and resolving scale-up challenges are critical for the production of high-quality advanced materials with reproducibility and economic feasibility.

The physical and electrochemical properties of cathode material such as morphology, tap density, capacity, rate capability and cycle life are strongly affected by synthesis route and its process optimization though it has exactly same composition. This is the reason why process development and scale-up research is important and a critical bridge between basic R&D and commercialization.

Until recently, there was no systematic engineering research capability or program across the DOE complex or in industry to evaluate new synthesis routes and resolve constraints to the development of cost-effective process technology for the high-volume manufacture of advanced materials. Argonne's Materials Engineering Research Facility (MERF) enables a systematic engineering research to investigate emerging synthesis technologies together with conventional methods and develop a customized synthesis process for each target bench-scale material.

We are using improved continuous carbonate and hydroxide co-precipitation systems as conventional synthesis approaches and planetary ball mill as a rapid synthesis approach. Set-up and evaluation of emerging technologies such as advanced reactor system are ongoing. By selecting the best synthesis route and developing a customized synthesis process, production

of uniform high-quality material to the kilogram and tens-of-kilograms quantities is enabled.

This large stock of scaled-up material is used as a baseline material for basic research groups and further application such as surface coating. We are also developing an improved wet coating system in bench and pre-pilot scale to produce uniform surface coatings.

All scaled-up and surface-coated materials are characterized and electrochemically tested using coin half cell at the MERF. These results are validated by ANL Materials Screening Group and collaborators to confirm improved performance compared to the target bench-scale materials.

Approach

The first step for the process development and scale-up of advanced cathode material is to identify candidate cathode materials of interest to the ABR program participants including materials produced by the oxalate, carbonate, hydroxide or other processes. A database of materials to be scaled has been developed and maintained and is used to rate and prioritize candidates for scale-up. These candidates are ranked based on electrochemical performance, process complexity and interest level of basic researcher and battery industry.

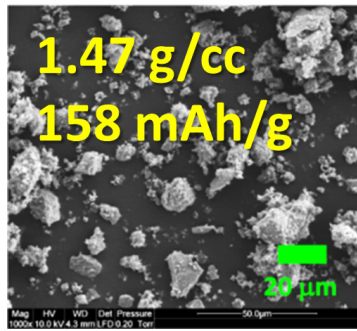


Figure IV - 262: Preliminary synthesis by planetary ball mill

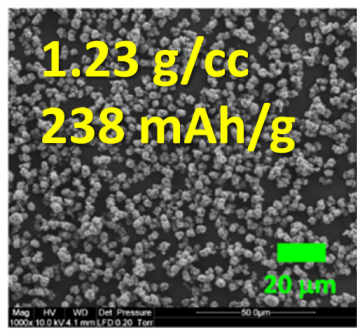


Figure IV - 263: Preliminary synthesis by hydroxide co-precipitation

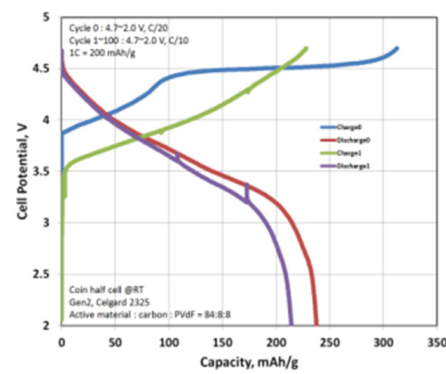
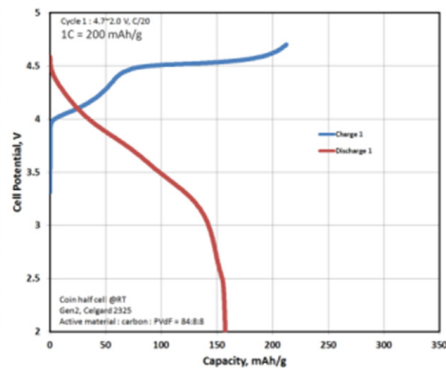
In FY13, we successfully completed the process development, scale-up and kilogram production of $\text{Li}_{1.14}\text{Mn}_{0.57}\text{N}_{0.29}\text{O}_2$ using the carbonate co-precipitation process. For the scale-up of $\text{Li}_{1.2}\text{Ni}_{0.13}\text{Mn}_{0.54}\text{Co}_{0.13}\text{O}_2$, evaluating synthesis routes, developing a customized synthesis process and optimizing operation variables were carried out. 100g of intermediate product was delivered to JPL/NASA for initial material evaluation.

In FY14, we successfully produced and delivered 3kg scaled-up product of the $\text{Li}_{1.2}\text{Ni}_{0.13}\text{Mn}_{0.54}\text{Co}_{0.13}\text{O}_2$ using the carbonate co-precipitation process. Our next two materials, the layered-layered spinel ($\text{Li}_{1.14}\text{Mn}_{0.53}\text{Ni}_{0.28}\text{Co}_{0.19}\text{O}_y$) and layered-layered ($\text{Li}_{1.05}\text{Mn}_{0.43}\text{Ni}_{0.52}\text{Co}_{0.05}\text{O}_y$) materials were selected and synthesized via carbonate and hydroxide co-precipitation processes.

Results

Scale-up of $\text{Li}_{1.2}\text{Mn}_{0.54}\text{Ni}_{0.13}\text{Co}_{0.13}\text{O}_2$

As an initial step for the process development and scale-up, preliminary syntheses were carried out using planetary ball mill, hydroxide and carbonate co-precipitations to select a better synthesis route for higher material quality.



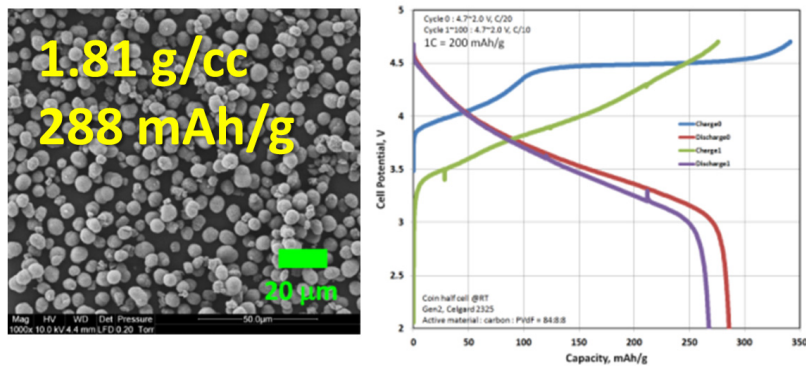


Figure IV - 264: Preliminary synthesis by carbonate co-precipitation

As you can see in these results of preliminary synthesizes (see Figure IV - 262, Figure IV - 263, and Figure IV - 264), physical and electrochemical properties of cathode material vary according to

synthesis process though it has exactly same composition. (See Table IV - 24.)

Table IV - 24: Summary of hydroxide cathode synthesis

Manufacturer	ANL ES20130715	ANL ES20130805	ANL ES20130923	ANL ES20131004	ANL ES20131105
Scale / Status	Pre-pilot				
Production date	7/15/2013	8/05/2013	9/23/2013	10/04/2013	11/05/2013
C A T H O D E	SEM x3,000				
	SEM x50,000				
	D ₁₀ /D ₅₀ /D ₉₀ [μm]	5.2/9.5/17.4	3.0/5.4/9.9	3.3/6.5/12.1	3.0/5.1/9.0
	Tap density [g/cc]	0.66	0.99	1.06	1.23
	1 st disch. cap. [mAh/g]	263.6	249.8	227.6	237.7

As you can see in these results, the tap densities of hydroxide cathode materials are lower than the target specification of JPL/NASA (tap density: > 1.5 g/cc) and there is a tendency that increased tap density resulted in a decrease in capacity.

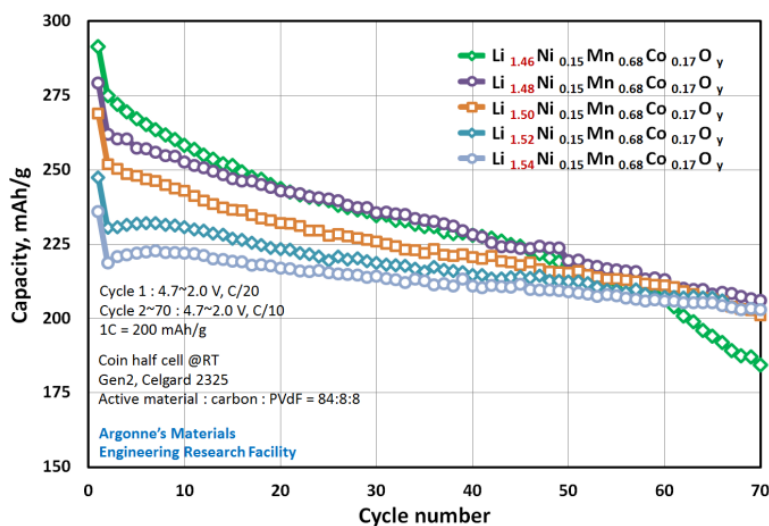
To meet the critical target specification of JPL/NASA (1st discharge capacity: ~ 240 mAh/g, tap density: > 1.5 g/cc), we decided to change the synthesis route from hydroxide co-precipitation (JPL/NASA's synthesis method) to carbonate co-precipitation. (See Table IV - 25.)

Table IV - 25: Summary of carbonate precursor synthesis.

P R E C U R S O R	Production #	ES20130924	ES20131106	ES20131111	ES20131114
	Variable change	Preliminary experiment	Lower NH ₄ OH/TM	5kg precursor production	
	Rxn temp. [°C]	35.2	35.2	36.0	37.4
	Na ₂ CO ₃ /TM ratio	1.05	1.05	1.05	1.05
	NH ₄ OH/TM ratio	0.1	0.03	0.03	0.03
	Reaction pH	8.5	7.7	7.8	7.9
	Operation time	12 hour	24 hour	30 hour	30 hour
SEM x1,000					
SEM x3,000					
D ₁₀ /D ₅₀ /D ₉₀ [μm]	0.2/7.0/10.5	0.2/7.9/11.8	3.2/7.0/10.7		
Tap density [g/cc]	1.50	1.52	1.60		

Using this 5kg carbonate precursor (ES20131111 + ES20131114), the effect of lithium content on cathode capacity and cyclability was evaluated to determine the

optimal lithium ratio of the scaled material. (See Figure IV - 265.)

**Figure IV - 265: Effect of lithium content on capacity and cyclability**

This result shows that lithium ratio has strong effect on initial capacity and capacity loss of cathode material. Based on this result, we decided to produce two grades of carbonate cathode materials. 1.5kg carbonate cathode with high initial capacity (ES20131111-1) was produced

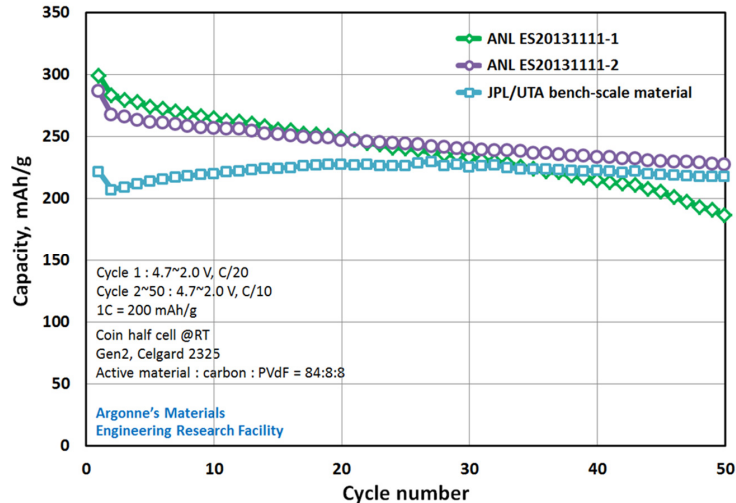
for surface coating application and 2.5kg carbonate cathode with good initial capacity and less capacity loss (ES20131111-2) was produced for pouch cell evaluation. (See Table IV - 26.)

Table IV - 26: Summary of carbonate cathode synthesis

	JPL/UTA Target Specification	UTA(18 mo.) uncoated	Commercial Scale-up	ES20130924 Scale-up carbonate	ES20131111-1 Scale-up carbonate	ES20131111-2 Scale-up carbonate
		Bench scale	Pre-pilot	Pre-pilot Preliminary 100g delivered	Pre-pilot Production 1 kg delivered	Pre-pilot Production 2 kg delivered
Composition (by ICP)	$\text{Li}_{1.5}\text{Ni}_{0.1625}\text{Mn}_{0.675}\text{Co}_{0.1625}\text{O}_2$	$\text{Li}_{1.8}\text{Ni}_{0.14}\text{Mn}_{0.68}\text{Co}_{0.19}\text{O}_y$	x	$\text{Li}_{1.48}\text{Ni}_{0.15}\text{Mn}_{0.68}\text{Co}_{0.17}\text{O}_y$	$\text{Li}_{1.49}\text{Ni}_{0.16}\text{Mn}_{0.67}\text{Co}_{0.18}\text{O}_y$	$\text{Li}_{1.47}\text{Ni}_{0.16}\text{Mn}_{0.67}\text{Co}_{0.16}\text{O}_y$
SEM x1,000	Uniform spherical morphology		x			
SEM x8,000						
$D_{10}/D_{50}/D_{90} [\mu\text{m}]$	x	1.2/11.1/29.3	x	4.0/6.7/11.4	3.8/6.4/10.8	3.8/6.3/10.7
Tap density [g/cc]	> 1.50	1.70	1.45 +	1.84	1.68	1.81
Initial disch. gravi. capacity [mAh/g]	> 240	228	223 +	289	299	288
Initial disch. vol. capacity [mAh/cc] **	> 360	388	323	532	503	521

** Calculated value based on tap density

+ Data from SPS Battery KDP meeting (June 25, 2012)

**Figure IV - 266: Capacity and cyclability summary**

As you can see in these results, we successfully scaled up $\text{Li}_{1.2}\text{Mn}_{0.54}\text{Ni}_{0.13}\text{Co}_{0.13}\text{O}_2$ using the carbonate co-precipitation process. 20% increased initial discharge capacity and 20% increased tap density were achieved compared to the target specification of JPL/NASA and ES20131111-2 cathode shows better capacity retention during 50 cycles. (See Figure IV - 266.)

This ES20131111-2 cathode was selected for the surface coating application by JPL/NASA and they applied 2wt% AlF_3 wet coating on this material. JPL/NASA sent back 2wt% AlF_3 coated ES20131111-2 material to us for material characterization and electrochemical evaluation, which is ongoing.

Scale-up of $\text{Li}_{1.14}\text{Mn}_{0.53}\text{Ni}_{0.28}\text{Co}_{0.19}\text{O}_y$

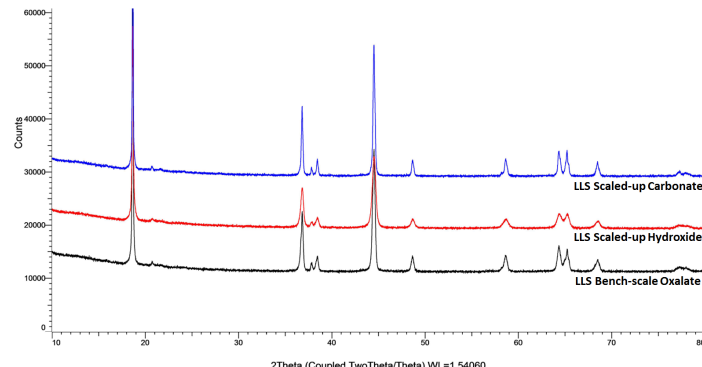
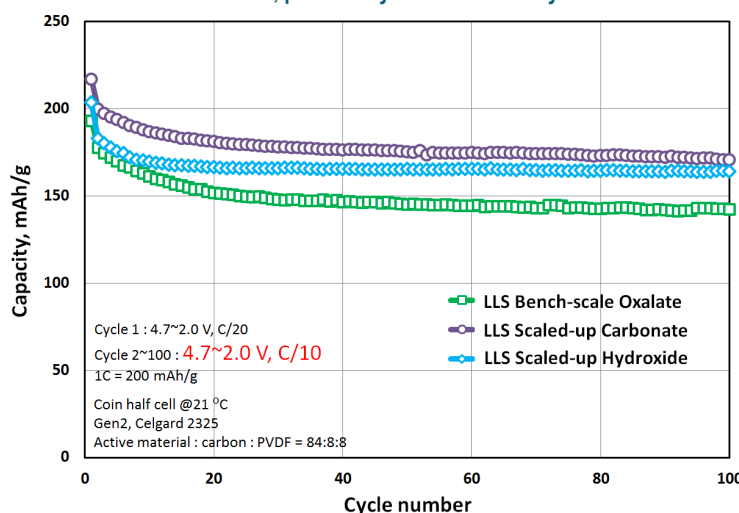
The layered-layered spinel material ($\text{Li}_{1.14}\text{Mn}_{0.53}\text{Ni}_{0.28}\text{Co}_{0.19}\text{O}_y$) was selected as the next

material for the process development and scale-up to help understanding the voltage fade issue of lithium and manganese rich metal oxide (LMR-NMC) materials. We are collaborating with Michael Thackeray's research group at ANL for this composition.

As you can see in these results, we synthesized carbonate and hydroxide cathode materials which meet the target specification. Although both carbonate and hydroxide cathode materials are preliminary products, they show improved capacity and good stability based on VF protocol. We delivered preliminary products to Michael Thackeray's research group at ANL to confirm their electrochemical performance. (See Table IV - 27, Figure IV - 267, and Figure IV - 268.)

Table IV - 27: Comparison of bench-scale oxalate, preliminary carbonate and hydroxide cathodes

	LLS target specification (Thackeray's group)	CSE LLS Oxalate	ES20140402 Scale-up Carbonate 1 st	ES20140710 Scale-up Hydroxide 1 st
		Bench scale	Pre-pilot Preliminary	Pre-pilot Preliminary
Composition (by ICP)	$\text{Li}_{1.1375}\text{Ni}_{0.28125}\text{Mn}_{0.53125}\text{Co}_{0.1875}\text{O}_y$	$\text{Li}_{1.05}\text{Ni}_{0.286}\text{Mn}_{0.519}\text{Co}_{0.195}\text{O}_y$	$\text{Li}_{1.063}\text{Ni}_{0.265}\text{Mn}_{0.542}\text{Co}_{0.193}\text{O}_y$	$\text{Li}_{1.206}\text{Ni}_{0.274}\text{Mn}_{0.534}\text{Co}_{0.191}\text{O}_y$
SEM x1,000	Max. capacity			
SEM x8,000	Min. voltage fade			
$D_{10}/D_{50}/D_{90} [\mu\text{m}]$?	6.3 / 12.3 / 22.3	5.2 / 9.6 / 16.8	2.4 / 4.8 / 8.8
Tap density [g/cc]	?	1.70	1.80	1.51
Initial disch. gravi. capacity [mAh/g]	> 200	193	218	202

**Figure IV - 267: XRD comparison of bench-scale oxalate, preliminary carbonate and hydroxide cathodes****Figure IV - 268: VF protocol comparison of bench-scale oxalate, preliminary carbonate and hydroxide cathodes**

Scale-up of $\text{Li}_{1.05}\text{Mn}_{0.43}\text{Ni}_{0.52}\text{Co}_{0.05}\text{O}_y$

The layered-layered material

($\text{Li}_{1.05}\text{Mn}_{0.43}\text{Ni}_{0.52}\text{Co}_{0.05}\text{O}_y$) was selected as the next material in collaboration with Michael Thackeray's research group at ANL. This composition was designed to have a small portion of Li_2MnO_3 -like domains in its structure and good stability with the highest layering structure. As an initial step for the process development and scale-up, preliminary syntheses were carried out using hydroxide and carbonate co-precipitations to

select a better synthesis route for higher material quality.

As you can see in these results, we synthesized carbonate and hydroxide cathode materials which show improved capacity and stability. Additional coin cell evaluations of preliminary materials are ongoing using an improved electrochemical testing protocol prior to kilogram scale production. (See Table IV - 28, Figure IV - 269, and Figure IV - 270.)

Table IV - 28: Comparison of bench-scale oxalate, preliminary carbonate and hydroxide cathodes

	4 th candidate Target spec. (Thackeray's group)	BL140804 JC1401 Oxalate	ES20140925 Pre-pilot Hydroxide 1 st	ES20140929 Pre-pilot Carbonate 1 st
		Bench-scale sample	Preliminary scaled-up	Preliminary scaled-up
Composition (by ICP)	$\text{Li}_{1.05}\text{Ni}_{0.5225}$ $\text{Mn}_{0.43}\text{Co}_{0.0475}\text{O}_y$	$\text{Li}_{1.03}\text{Ni}_{0.61}$ $\text{Mn}_{0.34}\text{Co}_{0.06}\text{O}_y$	$\text{Li}_{1.03}\text{Ni}_{0.52}$ $\text{Mn}_{0.44}\text{Co}_{0.05}\text{O}_y$	$\text{Li}_{1.07}\text{Ni}_{0.52}$ $\text{Mn}_{0.43}\text{Co}_{0.05}\text{O}_y$
SEM x1,000				
SEM x8,000				
$D_{10}/D_{50}/D_{90} [\mu\text{m}]$?	4.5 / 8.8 / 16.9	1.9 / 3.4 / 6.1	4.8 / 8.0 / 13.5
Tap density [g/cc]	?	1.04	0.97	1.39
Initial disch. capacity @10mA/g [mAh/g]	?	201.4	213.4	209.7
First cycle efficiency	?	87.5 %	88.4%	88.2 %

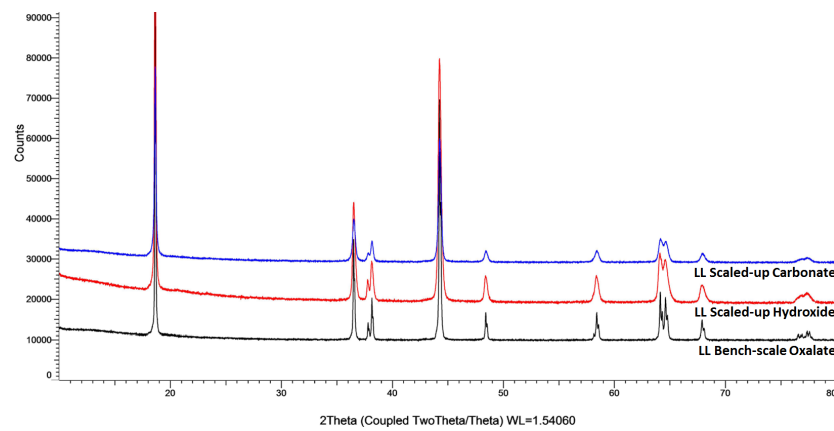


Figure IV - 269: XRD comparison of bench-scale oxalate, preliminary carbonate and hydroxide cathodes

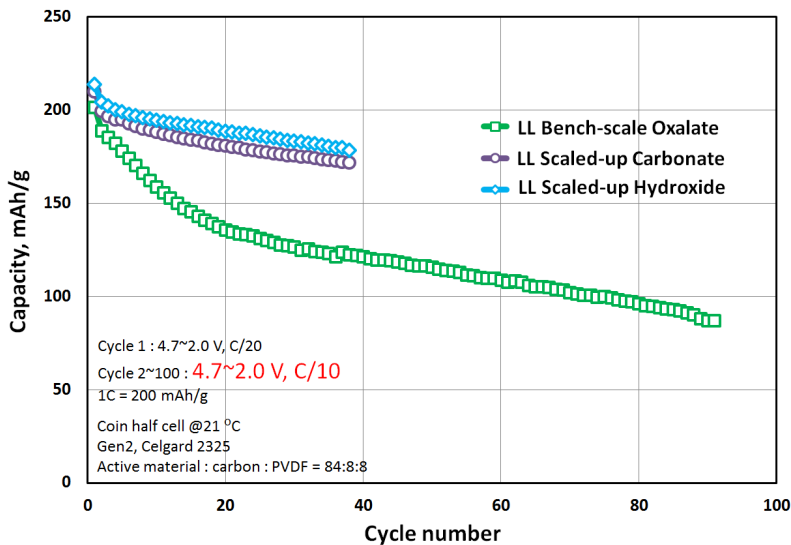


Figure IV - 270: VF protocol comparison of bench-scale oxalate, preliminary carbonate and hydroxide cathodes

Surface modification by dry coating

As another approach, to verify the positive effect of surface coating on cathode performance, we set up a pilot scale mechanofusion dry coater in collaboration with Christopher Johnson's research group at ANL. We then carried out 1 wt% Al_2O_3 coating on commercial lithium nickel oxide material (LNO).

Before dry coating

Commercial lithium nickel oxide (LNO)

$D_{50} = 8.2 \mu\text{m}$

Tap density = 2.58 g/cc

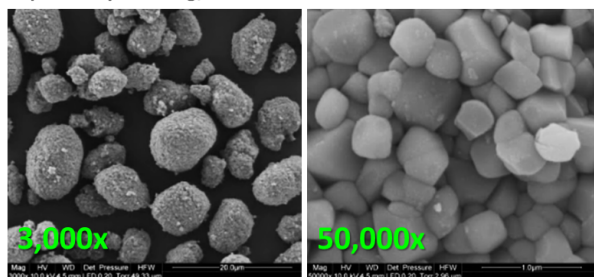


Figure IV - 271: SEM images of pristine LNO before dry coating

After dry coating

LNO coated with 1wt% Al_2O_3 (45 nm)

$D_{50} = 8.3 \mu\text{m}$

Tap density = 2.74 g/cc

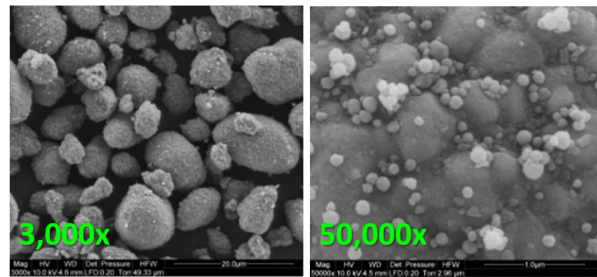


Figure IV - 272: SEM images of 1wt% Al_2O_3 coated LNO after dry coating

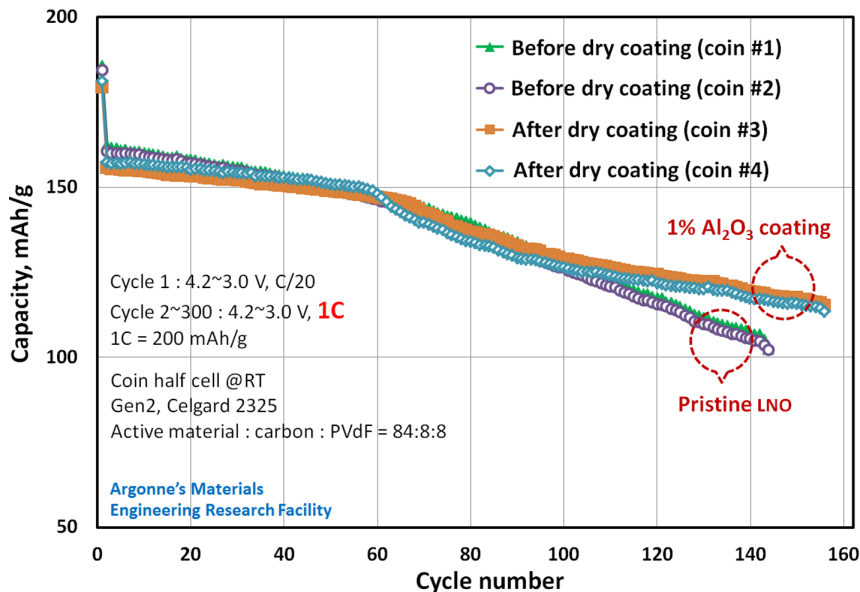


Figure IV - 273: 1C cyclability comparison of pristine and 1wt% Al_2O_3 coated LNO materials

As you can see in these results, the tap density of 1wt% Al_2O_3 coated material increase due to surface grinding and tiny particle formation. This 1wt% Al_2O_3 coated LNO material show better capacity retention than that of pristine material after 100 cycles. (See Figure IV - 271, Figure IV - 272, and Figure IV - 273.)

Conclusions and Future Directions

We successfully completed the process development, scale-up and kilogram production of $\text{Li}_{1.2}\text{Ni}_{0.13}\text{Mn}_{0.54}\text{Co}_{0.13}\text{O}_2$ with 20% increased capacity and tap density. JPL/NASA performed 2wt% AlF_3 wet coating on this scaled-up material and sent it back for material characterization and further collaboration about surface coating research. This 2wt% AlF_3 coated material shows better capacity retention at the voltage window between 4.7 and 2.0 compared to its pristine material.

We carried out preliminary syntheses layered spinel and layered layered materials using carbonate and hydroxide co-precipitation processes in collaboration with Michael Thackeray's research group at ANL. The preliminary scaled-up materials show improved electrochemical performance than the bench-scale oxalate samples. Further process development and scale up research is ongoing for these two bench-scale materials.

For surface modification of cathode material, we show that 1 wt% Al_2O_3 dry coating processes increase the capacity retention of pristine materials. Furthermore, we will optimize the dry coating process and develop an improved wet coating system in bench and pre-pilot scale to produce uniform surface coating. The scaled-up

high energy material will be tested using both dry and wet coating processes to achieve better stability.

In FY15, the next material, currently the gradient cathode material will be scaled to kilogram quantities. To evaluate a new emerging synthesis technology, we have recently been funded an LDRD project (#2015-132-N0) on an advanced manufacturing process which uses "Taylor Vortex Flow" to produce cathode precursors. As you can see in Figure IV - 274, Taylor vortices inside the reactor provides high mass transfer and homogeneous micro-mixing. In addition, this reactor shortens the reaction time with its strong agitation ability and removes dead-zones which thereby boosting the purity, density, particle size and distribution, crystallization degree and impurity removal ratio.

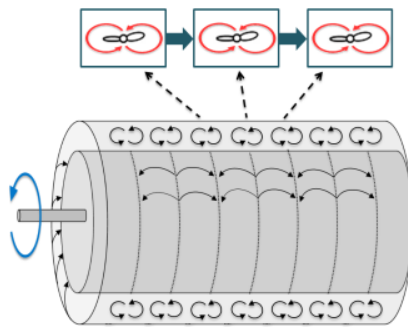


Figure IV - 274: Advanced Taylor Vortex Reactor.

By continuing to evaluate emerging manufacturing technologies we will be able to improve material performance while driving costs down. This will directly benefit the basic R&D groups and US battery manufacturers.

FY 2014 Publications/Presentations

1. "METHOD FOR PRODUCING SIZE SELECTED PARTICLES", Patent filed – April 30, 2014.
2. "Process development and scale-up of a cobalt free high energy cathode material", Advanced Automotive Battery Conference – February 3, 2014.
3. "Effect of secondary particle size and lithium ratio for $\text{Li}_x[\text{Ni}_{0.33}\text{Mn}_{0.67}]\text{O}_2$ and $\text{Li}_x[\text{Ni}_{0.15}\text{Co}_{0.17}\text{Mn}_{0.68}]\text{O}_2$ prepared by a carbonate co-precipitation method", Material Research Society – April 21, 2014.
4. "Synthesis of $\text{Li}_x\text{Mn}_{0.54}\text{Ni}_{0.13}\text{Co}_{0.13}\text{O}_y$ cathode materials for lithium-ion batteries via mechanochemical activation", 225th Electrochemical Society Meeting – May 11, 2014.
5. 2014 DOE Annual Peer Review Meeting Presentation.
6. "Scale-up of high energy cathode materials for electric vehicles at Argonne's Materials Engineering Research Facility", Materials Matters – September 2, 2014.
7. "Process development and scale-up of high energy cathode materials", The Battery Show – September 16, 2014.

IV.E.2 Process Development and Scale up of Advanced Electrolyte Materials (ANL)

Gregory K Krumdick (Program Manager)

Argonne National Laboratory

9700 South Cass Avenue

Argonne, IL 60439-4837

Phone: (630) 252-3952; Fax: (630) 252-1342

E-mail: gkrunderick@anl.gov

Collaborators:

Krzysztof (Kris) Pupek, Argonne National Laboratory

Trevor Dzwiniel, Argonne National Laboratory
Daniel Abraham, Argonne National Laboratory

Wenquan Lu, Argonne National Laboratory

Gao Liu, Lawrence Berkeley National Laboratory
Chris Orendorff, Sandia National Laboratory

Bob Powell, General Motors

Ion Halalay, General Motors

Jerry Martin, Boulderionics

Andrew Risco, Boulderionics

Ramin Amin-Sanayel, Arkema

Start Date: June 2010

Projected End Date: September 2015

Objectives

The objective of this task is to conduct process engineering research for scale-up of new advanced materials for Li-ion batteries. New, innovative materials are being constantly invented to improve safety, energy density, cycle, and calendar life of lithium ion batteries for HEV and PHEV applications. Up to this point, these materials have only been synthesized in small batches. Scaling up the original route used by discovery scientists involves modification of the bench-scale chemistry and process R&D to allow for the semi-continuous production of materials, development of an engineering flow diagram, design of a mini-scale system layout, construction of the experimental system and validation of the optimized process. The experimental system will be assembled and the materials will be manufactured in quantities sufficient for full scale industrial evaluation. The materials produced by the program will be analyzed to confirm chemical identity and purity. Analytical methods will be developed for quality control purpose. The electrochemical

performance of the materials will be validated to confirm that the properties match the original materials.

Technical Barriers

Advanced battery materials are primarily synthesized in small batches by discovery scientists who produce gram quantities of substances. The bench-scale processes are labor-intensive, time-consuming, and are not suitable for larger scale manufacturing. Furthermore, small-scale, un-optimized, not validated procedures produce inconsistent quality materials. High quality, uniform materials in sufficient quantity cannot be generated using bench-scale procedures. Therefore, process R&D and scale-up facility is required to manufacture quantities of the new materials that would allow for prototyping and thorough evaluation which is required prior to scaling to the next level.

Technical Targets

- Scale-up 4-6 new materials in FY14.
- Distribute synthesized materials to industry and R&D community.
- Investigate impurity profile effect on performance for selected electrolyte materials.

Accomplishments

- Scale-up work has been completed on the following materials:
 - Li-TDI (electrolyte salt).
 - LBNL-PEFM (binder for Si electrode).
 - LBNL-PFM (binder for Si electrode).
 - By request, an additional amount of LiDFOB was prepared using a MERF developed procedure.
- Electrochemical validation and comparison study has been completed on two new materials, RS5 and RS51 (the synthesis of the materials was completed and reported in FY13).
- Work on the following materials is ongoing:
 - GM Mn-Ion Trap (Separator Modifier).
 - SNL-PFPBO (electrolyte additive).
- We are in the process of establishing protocols for electrochemical evaluation to develop materials specification (minimum required purity and impurity profile).
 - Trace impurities analysis and electrochemical study of in-process materials will be used for

Li-FSI with collaboration with Boulder Ionics and Arkema.



Introduction

Researchers in the battery materials programs across the DOE complex refer to scale up as synthesis of battery materials in gram quantities, and with time consuming, multiple small-scale runs. There is a need to develop scale-up processes for battery materials (primarily lithium-ion based batteries) to the kilogram and tens-of-kilograms quantities at DOE labs to allow for full scale evaluation, support further research, and the transition of these technologies to industry. Currently, there is no such capability or program across the DOE complex that would allow accelerated transition of new materials and technologies from discovery stage to high-volume manufacturing.

Approach

A formal approach for process R&D and scale-up of advanced battery materials has been defined. This approach starts with the initial discovery of a new material and an initial electrochemical evaluation. This determines if the material is to be added to the inventory database, ranked and prioritized. At this point, the scale-up process begins with the feasibility study, followed by proof of concept testing, 1st stage scale-up and final 2nd scale scale-up. Go/No Go decisions are located after feasibility determination and electrochemical validation testing. (See Figure IV - 275.)

For each material scaled, we will develop a scalable manufacturing process, analytical methods and quality control procedures. We will also prepare a “technology transfer package” which will include:

- Summary of the original process used by discovery researchers to synthesize the material.
- Summary of the scalable (revised) process suitable for large scale manufacturing.
- Detailed procedure of the revised process for material synthesis.
- Analytical data/Certificate of Analysis for the material (chemical identity and purity).
- The material impurity profile.
- Electrochemical performance test data.
- Preliminary estimates of production cost.
- MSDS for the material.
- Material specifications.

We also make kilogram quantities of the material available for industrial evaluation and to the research

community. Samples are fully characterized chemically and electrochemically.

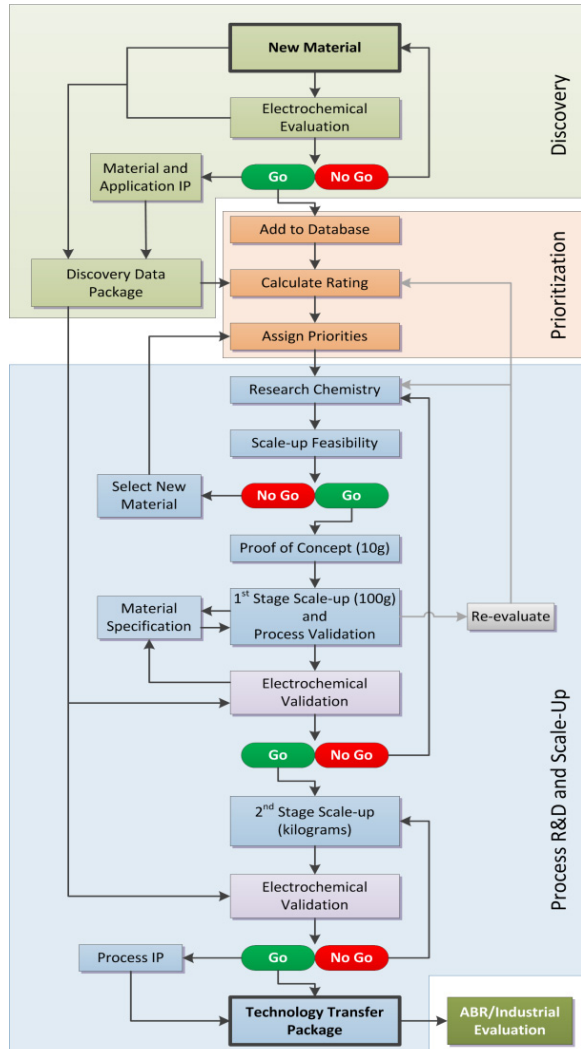


Figure IV - 275: Advanced Battery Materials Process R&D Workflow

Results

The milestones and due dates for Li-TDI (electrolyte salt) are shown in Table IV - 29.

Table IV - 29: Milestones and due dates for Li-TDI (electrolyte salt)

Li-TDI (electrolyte salt)	
MILESTONE	DATE
Assess scalability of disclosed process	10/15/2013
Develop and validate scalable process chemistry (10 g scale)	11/15/2013
First process scale up (100 g scale)	12/03/2013
Electrochemical validation	01/28/2014

The new salt, Li-TDI (see Figure IV - 276) was requested by Professor Wesley Henderson at North Carolina State University (NCSU) who was unable to obtain high purity material commercially or synthesize enough material to meet requests. The MERF developed a streamlined procedure and implemented new analytical in-process controls to monitor and optimize the procedure. Samples were submitted to NCSU and the data returned closely matched the electrochemical performance of the original sample.

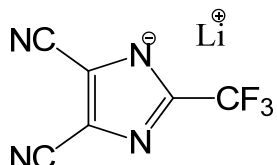


Figure IV - 276: Chemical structure of Li-TDI

The milestones and due dates for LBNL-PEFM (binder for Si electrode) are shown in Table IV - 30.

Table IV - 30: Milestones and due dates for LBNL-PEFM (binder for Si electrode)

LBNL-PEFM (binder for Si electrode)	
MILESTONE	DATE
Assess scalability of disclosed process	10/30/2013
Develop and validate scalable process chemistry (10 g scale)	04/30/2014
First process scale up (100 g scale)	Pending evaluation

The conductive polymeric binder for silicon electrodes for Li-ion batteries (see Figure IV - 277) was developed by Lawrence Berkeley National Lab (LBNL).

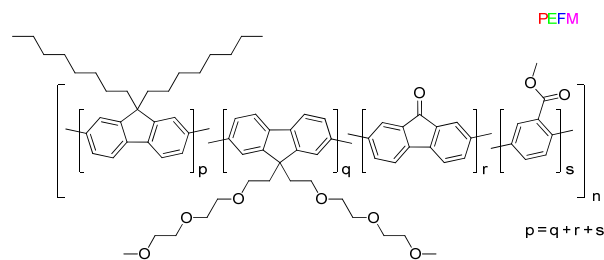


Figure IV - 277: Chemical structure of PEFM

The material was originally made only in gram quantities due to complex, multi-step process required for the synthesis.

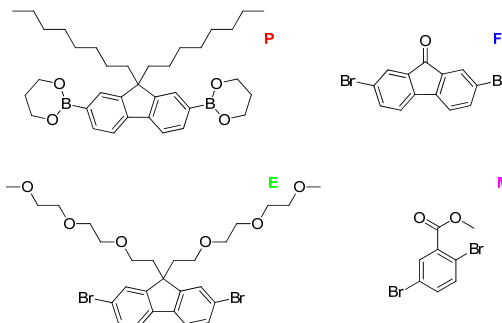


Figure IV - 278: Chemical structures of PEFM co-polymers

The co-polymer "E" (see Figure IV - 278) is not commercially available. The published procedure to make "E" requires advanced purification techniques that are not scalable. MERF developed simplified, scalable procedure for manufacturing the material in high yield and purity. The co-polymerization process was investigated and optimized to deliver material that match performance of the original sample. Several batches were synthesized and samples submitted to LBNL (Gao Liu) and ANL Materials Screening Group (Wenquan Lu) for evaluation.

The milestones and due dates for LBNL-PFM (binder for Si electrode) are shown in Table IV - 31.

Table IV - 31: Milestones and due dates for LBNL-PFM (binder for Si electrode)

LBNL-PFM (binder for Si electrode)	
MILESTONE	DATE
Assess scalability of disclosed process	10/30/2013
Develop and validate scalable process chemistry (10 g scale)	04/30/2014
First process scale up (100 g scale)	Pending evaluation

The conductive polymeric binder for silicon electrodes for Li-ion batteries (see Figure IV - 279) was developed by LBNL.

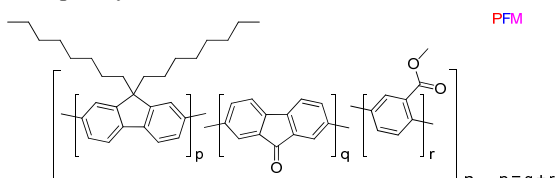


Figure IV - 279: Chemical structure of PFM

Several parameters of the synthesis procedure were investigated and optimized. (See Figure IV - 280.)

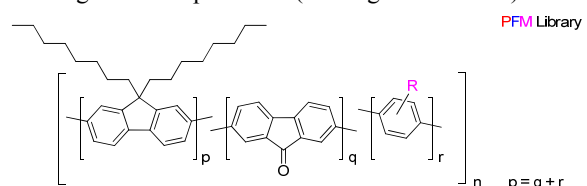


Figure IV - 280: Chemical structure of PFM derivatives

Additionally, a structurally diverse library of 6 different PFM-type co-polymers was synthetized to investigate structure-property relationships. Specifically, the R substituent in the “M” moiety of the co-polymer was varied to modulate electron density and adhesion. Samples of the PFM and modified PFM binder were submitted to LBNL (Gao Liu) and ANL Materials Screening Group (Wenquan Lu) for evaluation. The test conducted at LBNL confirmed that material manufactured by MERF match the performance of the original material.

The milestones and due dates for GM Mn-Ion Trap (Separator Modifier) are shown in Table IV - 32.

Table IV - 32: Milestones and due dates for GM Mn-Ion Trap (Separator Modifier)

GM Mn-Ion Trap (Separator Modifier)	
MILESTONE	DATE
Assess scalability of disclosed process	02/14/2014
Develop and validate scalable process chemistry (10 g scale)	04/14/2014
First process scale up (100 g scale)	07/14/2014
Second process scale up (kg scale)	Pending evaluation

Aza-crown ether modified styrene-divinylbenzene co-polymer (see Figure IV - 281) was invented by General Motors (GM) as a separator additive to prevent migration of Mn ions. MERF prepared several co-polymers in 100 g+ scale (Step 1) with different cross-linking ratios and investigated a scalable derivatization process (Step 2) that minimizes use of the expensive aza-crown ether.

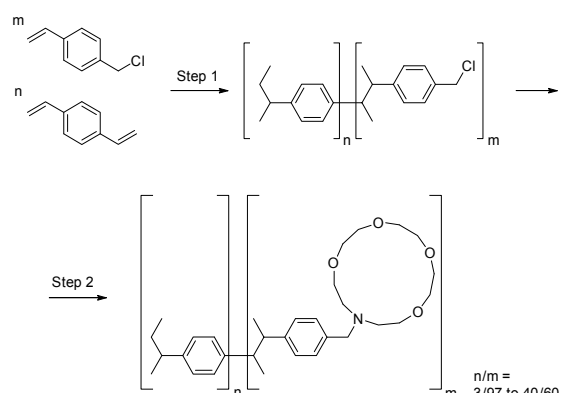


Figure IV - 281: Chemical synthesis and structures of GM's separator modifier

Samples of the material (ranging from 5 g to 80 g) were delivered to GM (Ion Halalay) for electrochemical evaluation.

The milestones and due dates for SNL-PFPBO (electrolyte additive, salt) are shown in Table IV - 33.

Table IV - 33: Milestones and due dates for SNL-PFPBO (electrolyte additive, salt)

SNL-PFPBO (electrolyte additive, salt)	
MILESTONE	DATE
Assess scalability of disclosed process	09/15/2014
Develop and validate scalable process chemistry (10 g scale)	12/15/2014
First process scale up (100 g scale)	02/15/2015

The lithium salt of PFPBO (see Figure IV - 282), originally developed as an anion binding agent (ABA), was studied by Chris Orendorff at Sandia National Lab (SNL) as an additive or replacement for LiPF₆. The MERF is currently working on understanding the reaction parameters, optimizing procedures, and developing analytical methods for in-process control and characterization of the final product.

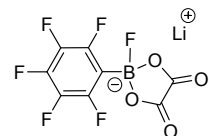


Figure IV - 282: Chemical structure of PFPBP

Conclusions and Future Directions

The technology transfer package for CWU-FRION was created. Sale-up work on Li-TDI was completed. Process R&D on conductive binders for Si electrode (LBNL-PFM and LBNL-PEFM) was completed. The materials were electrochemically evaluated in collaboration with Argonne’s CAMP facility. High purity LiDFOB was synthetized and samples were submitted to support industrial research. Polymers for GM Mn-ion trapping project were prepared and submitted for evaluation. Further work on this project at MERF is pending results from electrochemical performance testing. Additional materials to scale will be added after discussions with the project sponsor.

4-6 electrolyte materials are targeted for scale-up in FY15.

In addition, a detailed trace impurity analysis and electrochemical study of Li-FSI (see Figure IV - 283) will be conducted in collaboration with Boulderionics. The objective of this project is to develop battery grade specification for the materials by correlating impurities level and profile with electrochemical performance.

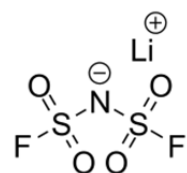


Figure IV - 283: Chemical structure of Li-FSI

Currently there are no commercial manufacturers of the material on industrial scale. Since the material can be manufactured using different processes, the purity and impurity profile may vary from vendor to vendor. The objective of the project is to develop specifications for the materials by correlating impurity levels and profiles with electrochemical performance. We will acquire samples of the material and conduct a comparative electrochemical performance study and trace impurity analysis to establish minimum purity (specification) required for acceptable performance.

Standardized protocols for validation of electrochemical performance for various classes of materials (electrolyte solvents, additives, redox shuttles) are being developed.

Seventy nine samples, totaling 9,700 g of battery grade materials have been provided to industry and scientific community for evaluation and to support further research (32 samples, 1,900 g in FY14 alone).

of Lithium-Ion Batteries Used in Electric Vehicles, K. Amine, T. Gozdz, G. Krumdick, Z. Zhang, T. Dzwiniel, K. Pupek, L. Zhang.

FY 2014 Publications/Presentations

1. Patent Application 14/171,556, filed Feb 3 2014, High Voltage Redox Shuttles, Method for Making High Voltage Redox Shuttles, T. Dzwiniel, G. Krumdick, K. Pupek.
2. Patent Application 14/266,052, filed Apr 30 2014, Process for the Production of Low Flammability Electrolyte Solvents, T. Dzwiniel, G. Krumdick, K. Pupek.
3. *From beaker to bucket: The safe scale-up of organic electrolyte materials.* Dzwiniel, T.; Pupek, K.; Krumdick, G. J. Chem. Health & Safety 2014, 21, 8.
4. Scale-up of High Voltage Redox Shuttles. Dzwiniel, T.; Pupek, K.; Krumdick, G. Materials Science & Technology 2014 Pittsburgh, PA, October 15, 2014.
5. Safe Large-Scale Synthesis of Advanced Battery Materials. Dzwiniel, T.; Pupek, K.; Krumdick, G. Battery Power 2014, Denver, Colorado, August 6-7, 2014.
6. Scale-up of High Voltage Redox Shuttles. Dzwiniel, T.; Pupek, K.; Krumdick, G. 14th Advanced Automotive Battery Conference (AABC) Atlanta, Georgia, February 3-7, 2014.
7. Safe Electrolyte Solvents: Flash Point Analysis of New Silicon-Based Solvents for Lithium-Ion Batteries. Dzwiniel, T.; Pupek, K.; Krumdick, G. Tactical Power Sources Summit, January 26-27, Washington D.C., 2014.
8. 2014 DOE Annual Peer Review Meeting.
9. R&D 100 Award 2014 for Argonne's Advanced Redox Shuttle Additive for Overcharge Protection

IV.E.3 Roll-to-Roll Electrode Processing NDE for Advanced Lithium Secondary Batteries (ORNL)

Peter Faguy (ABR Program Manager)

David L. Wood III, Debasish Mohanty, Jianlin Li, Shrikant Nagpure, and Claus Daniel

One Bethel Valley Road
P.O. Box 2008, MS 6065
Oak Ridge, TN 37831-6065
Phone : (865) 574-1157; Fax: (865) 241 4034
E-mail: wooddl@ornl.gov

Collaborators:

Mike Ulsh, Guido Bender and Bhushan Sopori (NREL); Frank Reilly (Ceres Technologies); Mike Wixom (Navitas Systems); David Telep (XALT Energy); Elena Shembel (Enerize); Jerry Forbes (Frontier Industrial Technology)

Subcontractor:

National Renewable Energy Laboratory

Start Date: October 11, 2011

Projected End Date: September 30, 2014

Objectives

- Reduce lithium ion battery system cost by implementing in-line non-destructive evaluation (NDE) and electrode QC.
- Quantification of effects of different defect types on rate performance and cell lifetime.
- Collaboration with NREL to establish in-line thermal diffusivity and optical reflectance methods.
- Installation of in-line, cross-web laser sensing for wet electrode thickness monitoring.
- Installation of IR thermography for dry electrode coating defects (agglomerates, pinholes, blisters, divots, metal particles, etc.)

Technical Barriers

- Electrode materials processing cost and in-line quality control.
- Cell calendar life, rate performance, and capacity retention.

Technical Targets

- Implementation of critical QC methods to reduce scrap rate by *creating feedback loops* (to meet \$300/kWh 2015 VTO storage goal for PHEVs).
- Quantification of various defect effects on cycle life (to achieve 3000-5000 cycles for PHEVs by 2015 and 750 cycles for EVs by 2020).
- Integrate electrode defect performance findings with NDE and QC development to advance lithium secondary battery manufacturing science.

Accomplishments

- Developed methods to generate different electrode coating defects such as pinholes, blisters, large agglomerates, divots, and metal particle contaminants for evaluation in full coin cell test matrix.
- Obtained comprehensive, statistically representative full coin cell data on different types of electrode coating defects to determine which type of defects cause cell failures or substandard performance.
- Installed in-line optical laser thickness measurement (at oven inlet) and IR thermography (at oven outlet) equipment on ORNL slot-die coating line for use in routine electrode QC.
- Investigated and correlated IR thermography electrode QC data with full coin cell statistical data quantifying capacity fade.
- Collaborated with NREL on establishing a method for measuring in-line electrode porosity based on thermal and structural properties; porosity is extracted from a mathematical model that simulates thermal response of white-light back-heated electrodes.



Introduction

Due to high scrap rates of 10-20% or more associated with lithium secondary cell production, new methods of quality control (QC), which have been successful in other industries, must be implemented. Often flaws in the electrodes are not detected until formation cycling when the entire series of manufacturing steps has been completed (significantly

increasing the value added of the cells), and the associated percentage of defective cells drive the costs of lithium secondary cells to an unacceptable level. If electrode flaws and contaminants could be detected in-line near the particular processing steps that generate them, then the electrode material could be marked as unusable and the processing equipment could be adjusted to eliminate the defects more quickly. ORNL has investigated several in-line analysis methods such as: 1) optical laser thickness sensing of wet electrodes for improved homogeneity across and down the web; 2) thermal IR imaging for detection of electrode thickness inhomogeneity and coating defects such as pinholes, blisters, divots, large agglomerates, and metal contaminants; 3) active IR thermography with white-light heating to measure in-line porosity through thermal diffusivity modeling; 4) optical reflectance for identifying surface coating defects; 5) X-ray fluorescence spectroscopy (XRF) for electrode transition-metal composition and areal weight uniformity; and 6) systematic performance investigation of the effects of different coating defects in full coin cell format. These in-line methods have been effectively utilized in other industries such as photovoltaic, flexible electronics, and semiconductor manufacturing, but the equipment and measurement methods must still be tailored for lithium secondary cell production. In previous annual reports (FY12 and FY13), we have delineated: 1) successful implementation of laser caliper technology to monitor wet electrode thickness during slot-die coating; 2) implementation of IR thermography for detecting flaws in the dried electrode exiting the slot-die coater oven; and 3) reaching a no-go decision on the feasibility and suitability of in-line XRF for detecting metal particle contaminants and electrode areal weight due to line-speed incompatibility. However, there is extremely limited understanding of the effect of different types of defects on cell performance and cycle life in order to establish electrode pass/fail criteria. The goal of this report is to present a thorough investigation correlating coating defect nature, electrochemical performance, and electrode microstructure as it relates to developing the methods needed to identify them on the coating line.

Approach

Our approach is to intentionally create different types of defects in the ABR baseline NMC 532 active material during coating and electrochemically evaluate the electrodes to obtain a comprehensive understanding between the defect nature and electrochemistry. In order increase understanding, cells were disassembled after electrochemical testing for microstructural analysis.

In addition, ABR baseline NMC 532 cathodes and ConocoPhillips A12 anodes were supplied to NREL for active IR thermography and optical reflectance

measurements. First, it had to be determined that the temperature response of the electrodes after white-light excitation could be accurately measured. Next a mathematical model was developed based on the thermal and structural properties of the electrodes that simulated the thermal responses based on material IR emissivities. The model calculates thermal diffusivity, which will in turn be used to extract porosity. The IR thermography experiments included a stationary steady-state response, a pseudo-steady state response where the white-light was turned off, and an in-line transient response of the electrode web moving past the white-light source. Proof-of-concept optical reflectance experiments showed various surface defects not visible with optical CCD cameras.

Results

1. Intentional creation of defects in NMC electrodes during slot-die coating and IR thermography detection

Different electrode defects were intentionally created during the NMC 532 coating process consisting of blisters, exaggerated non-uniform coating, metal-particle contaminants, divots, large agglomerates, and pinholes (Figure IV - 284). First, we implemented IR thermography to show changes in emissivity in the defective regions. Figure IV - 285 shows the optical and corresponding IR thermography images of the NMC 532 electrodes with various defects. Depending on the nature of the defects, the emissivity decreases or increases. For example, emissivity increases where a blister or agglomerate is located (Figure IV - 285e-f) where heat cannot be released as quickly. Emissivity decreases where pinholes, exaggerated non-uniform coating, or metal contaminants (Figure IV - 285a-b, Figure IV - 285c-d and Figure IV - 285g-h) are located where heat is released from the coating surface more quickly. These results show the capability of the IR thermography method to distinguish between different types of defects based on emissivity differences.

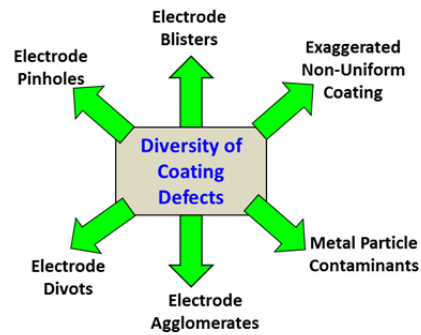


Figure IV - 284: Examples of different types of NMC 532 electrode defects that were intentionally created during slot-die coating

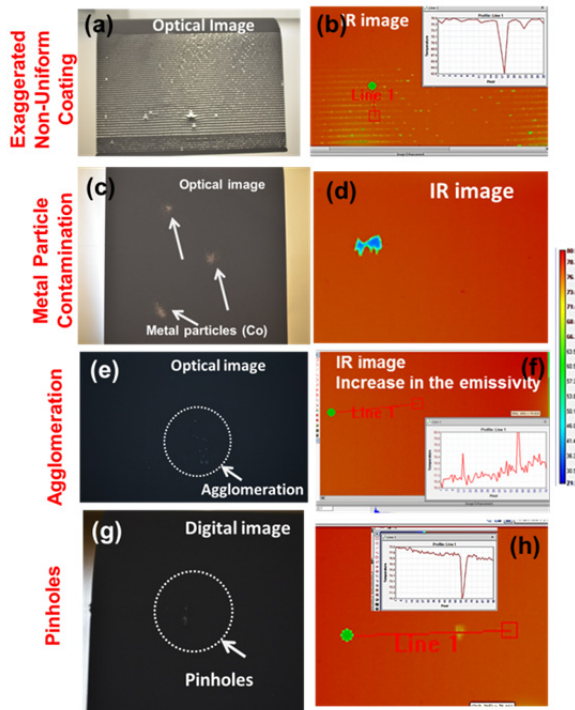


Figure IV - 285: Optical and IR images of intentionally introduced coating defects: exaggerated non-uniform coating (a, b), metal particle contamination (c, d), large agglomerates (e, f), and pinholes (g, h). The emissivity values in the IR thermographs increase or decrease depending on the nature of defects

2. Effect of defects on electrochemical performance

To understand how these defects alter the cell performance, electrochemical testing was conducted: 1) rate capability and subsequent columbic efficiency; and 2) high-rate 2C discharge capacity testing over 150 cycles, and 5C discharge capacity testing over 150 cycles in a full coin cell configuration (vs. ConocoPhillips A12 graphite). After cycling, the data from the defective NMC 532 electrodes were compared with the non-defective baseline NMC 532 electrodes. Each data point is the average of five different cells tested under identical conditions with t -distribution error bars.

2.1. Rate capability and columbic efficiency testing

a) Exaggerated non-uniform coating:

Rate capability is shown in Figure IV - 286a and columbic efficiency is shown in Figure IV - 286b for the defective electrode having an exaggerated non-uniform coating (vs. the non-defective baseline NMC 532 coating). From Figure IV - 286a it is clear that the gravimetric capacity for the defective electrode is 10-20% less (especially at higher c -rate) as compared to the non-defective electrode, and the full cell capacity for

defective electrode is 60-70% lower than the non-defective electrode. Since half of the active material is missing in the coating, intuition would suggest the full cell capacity should only be ~50% of the non-defective baseline. It is this 10-20% reduction in gravimetric capacity that contributes to the additional full cell capacity reduction. In addition, the columbic efficiency at different C rates of the defective electrode is slightly less than the baseline non-defective electrode. It is thought that this behavior is primarily due to the improper N/P ratio. Normally it should be 1.1, and in the case of these cells it is >2.

b) Electrode agglomeration:

Figure IV - 287a-b shows the rate capability and columbic efficiency, respectively, at different C rates of the NMC 532 electrode having agglomeration defects (vs. the base line non-defective NMC 532 electrode). Surprisingly, both the gravimetric and full cell capacities in the case of the defective electrode are somewhat higher than the baseline electrode; however, the columbic efficiency for the defective electrode is significantly lower than the baseline electrode. This result indicates that electrode agglomerates have a negative impact on the columbic efficiency (capacity retention), but not on short-term rate capability.

c) Metal contaminants:

Figure IV - 288 shows the effect of Co metal contaminants on rate performance and columbic efficiency. From Figure IV - 288a it is clear that the presence of Co powder substantially decreases the gravimetric and full cell capacity and has a detrimental effect on columbic efficiency. Not surprisingly, several of the cells failed to deliver measurable capacity above 2C. Our hypothesis for this deleterious electrochemical performance is participation of metal particles in the electrochemical reactions to form metallic alloys, which impede lithium diffusion pathways for the lithiation and delithiation reactions and cause significant irreversible capacity loss.

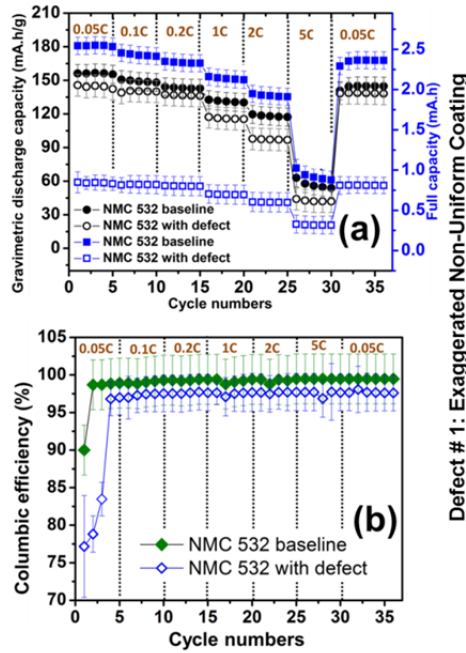


Figure IV - 286: Rate capability (a) and columbic efficiency (b) data from exaggerated non-uniform coating (open symbols) compared with non-defective baseline NMC 532 electrodes (closed symbols). In figure a, blue symbols are full discharge capacity and black symbols are gravimetric capacity

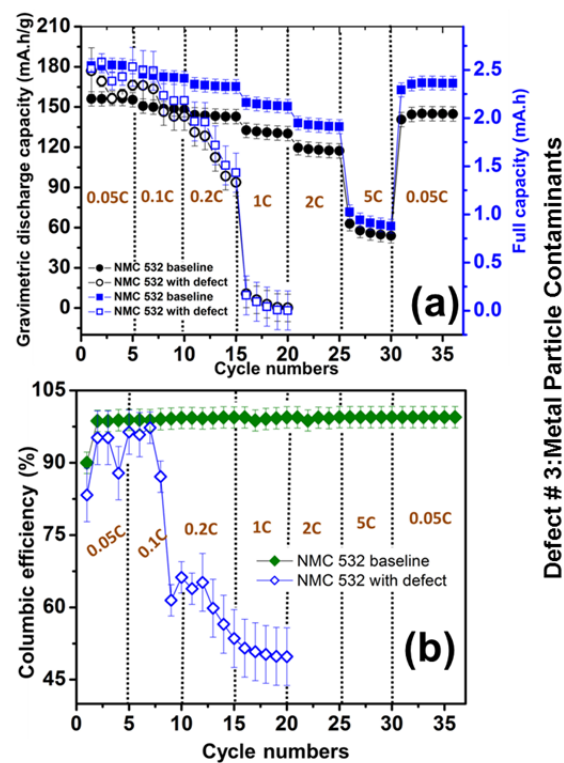


Figure IV - 288: Rate capability (a) and columbic efficiency (b) from metal particle contamination (open symbols) compared with non-defective baseline NMC 532 electrodes (closed symbols). In figure a, blue symbols are full discharge capacity and black symbols are gravimetric capacity

d) Systematic non-uniform coating

In order to obtain better understanding on the effect-missing-coating experiments discussed in Section 2.1a, a special shim for the ORNL slot-die coater was designed where two controlled geometries of missing coating area could be produced: 1) a 6-mm width stripe without coating (1x large defective area denoted as “Sample 1x”); and 2) three parallel 2-mm stripes without coating (3x small defective areas denoted as “Sample 3x”). In Figure IV - 289, a schematic of the customized shim and the corresponding IR thermography image for the electrode that was produced using the shim is shown. Figure IV - 290 and Figure IV - 291 show the comparison of electrode performance from Samples 1x and 3x, respectively, as compared to the baseline non-defective NMC 532 electrode. It was found that when the uncoated width was greater (Sample 1x), this cell suffered more so at high C rates than did Sample 3x. The columbic efficiency exhibited a similar trend for both Samples 1x and 3x.

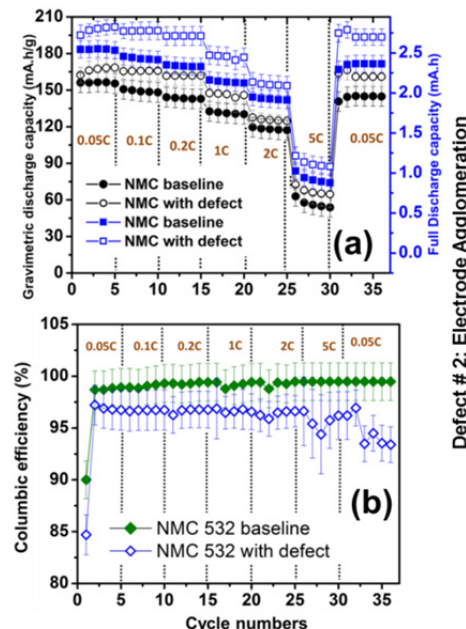


Figure IV - 287: Rate capability (a) and columbic efficiency (b) from agglomerated electrodes (open symbols) compared with non-defective baseline NMC 532 electrodes (closed symbols). In figure a, blue symbols are full discharge capacity and black symbols are gravimetric capacity

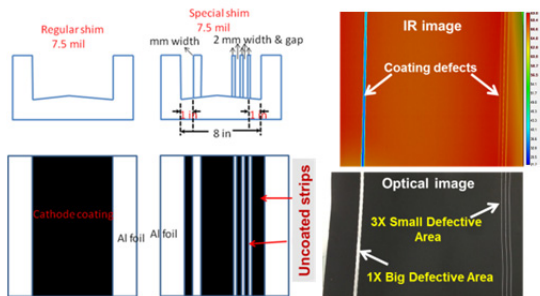


Figure IV - 289: Specially designed shim having a 6-mm uncoated stripe (1x large defective area) and three 2-mm uncoated stripes (3x small defective areas). The corresponding optical and IR thermography images are shown on the right

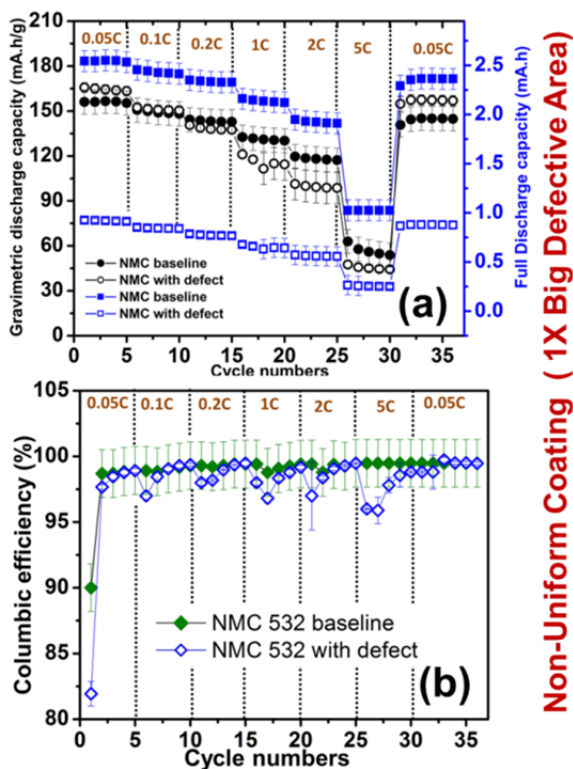


Figure IV - 290: Rate capability (a) and columbic efficiency (b) from the defective electrodes prepared from the special shim creating Sample 1x (open symbols) compared with non-defective baseline NMC 532 electrode (closed symbols). In figure a, blue symbols are full discharge capacity and black symbols are gravimetric capacity

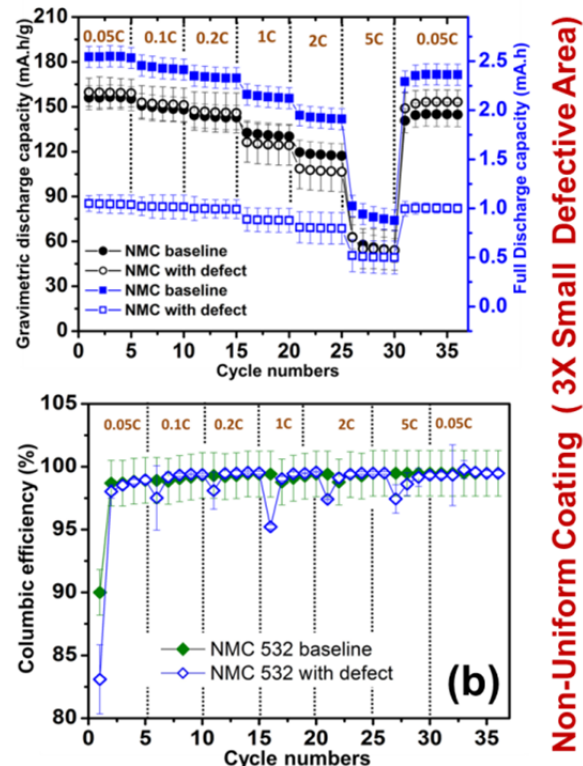


Figure IV - 291: Rate capability (a) and columbic efficiency data from the defective electrode prepared from special shim set creating 3X small defective non-coated area compared with the non-defective baseline NMC 532 electrodes (closed symbols). In figure a, blue color symbols represent full discharge capacity, black symbols represent the gravimetric capacity. The defective electrode shows lower capacity compared to baseline NMC 532 electrode at high-rate

2.2 High-rate (2C and 5C), short-term capacity fade testing

Capacity fade experiments for the various defective electrodes were performed at 2C and 5C discharge rates and compared with the baseline non-defective NMC 532 electrode. We chose four different types defects for longer-term cycling analysis: a) electrode agglomeration; b) 1x large (6 mm) defective area from the special shim coating (Sample 1x); c) 3x small (2 mm parallel) defective areas from the special shim coating (Sample 3x); and d) metal particle contaminants. The detailed results are summarized in Table IV - 34.

a) Large electrode agglomerates:

Figure IV - 292a-b shows capacity fading results at 2C and 5C discharge rates, respectively, for the baseline NMC 532 electrode and the electrode having large agglomerates. It was observed that ~80% of full-cell gravimetric capacity was retained after 60 2C cycles for the baseline NMC 532 electrode, whereas in the case of the agglomerated electrode, 12% gravimetric and 6%

full-cell capacity were retained after 200 cycles. At a discharge rate of 5C, the baseline NMC 532 electrode showed 75% gravimetric capacity retention and 58% full-cell retention after 200 cycles. In contrast, only ~14% discharge capacity retention (full cell and

gravimetric) was observed for the case of electrodes with agglomeration. These results show that coating agglomerates **must** be eliminated during the electrode dispersion preparation steps.

Table IV - 34: Summary of short-term capacity fade data at 2C and 5C discharge rates for non-defective baseline NMC 532 electrode and various defective electrodes

Electrodes	Discharge rate: 2C		Discharge rate: 5C	
	Gravimetric Capacity retention (%)	Full Capacity retention (%)	Gravimetric Capacity retention (%)	Full Capacity retention (%)
Baseline	80% after 60 cycles	77% after 60 cycles	75% after 200 cycles	58% after 200 cycles
Non-Uniform Coating (1X Big defective area)	60% after 200 Cycles	40% after 200 cycles	45% after 200 cycles	60% after 200 cycles
Non-Uniform Coating (3X Big defective area)	27% after 200 cycles	30% after 200 cycles	7% after 200 cycles	4% after 200cycles
Agglomerates	12% after 200 cycles	6% after 200 cycles	14% after 200 cycles	12% after 200 cycles
Pin holes	75% after 200 cycles	78% after 150 cycles	50% after 200 cycles	12% after 200 cycles
Metal contaminants	Zero capacity	Zero Capacity	Cell failure	Cell failure

*b) Non-uniform coating with missing stripes
(Samples 1x and 3x):*

Figure IV - 292c-d and Figure IV - 292e-f show the capacity fading comparison of the baseline NMC 532 electrodes *vs.* Samples 1x and 3x, respectively, for 2C and 5C discharge rates. Analysis shows that the capacity degradation rate was higher for the case of electrodes having greater interfacial length (Sample 3x) as compared to the smaller interfacial length (Sample 1x), with “interfacial length” being defined as the total length between the coating and stripe(s). At a discharge rate of 5C, the full-cell capacity retention was only 4% after 200 cycles for Sample 3x, whereas 60% full-cell capacity retention remained for Sample 1x after the same number of cycles. This finding verifies that it is the number of spots with missing coating (divots, blisters, etc.) in a given region of the web that is critical, not the size of the spot itself, which suggests that there is a long-term performance phenomenon related to the

uncoated interface. An investigation into this hypothesis is ongoing.

c) Metal particle contaminants

Capacity fade results from the electrode with metal particle contaminants (Co powder) compared to the baseline NMC 532 electrode are shown in Figure IV - 292g-h. Zero capacity was observed after only 3 cycles when operated at a discharge rate of 2C, and the cells were not stable enough for any cycling when discharged at 5C. These findings demonstrate that metal contaminants such as Cu and Al flakes from foil slitting operations and stainless steel particulates from dispersion mixing tanks (and any other airborne metallic dust) must be avoided in the electrode coatings at all costs, which is in contrast to the findings in Sections 2.2a-b where capacity fade rates increased substantially but did not cause complete cell failure early in life.

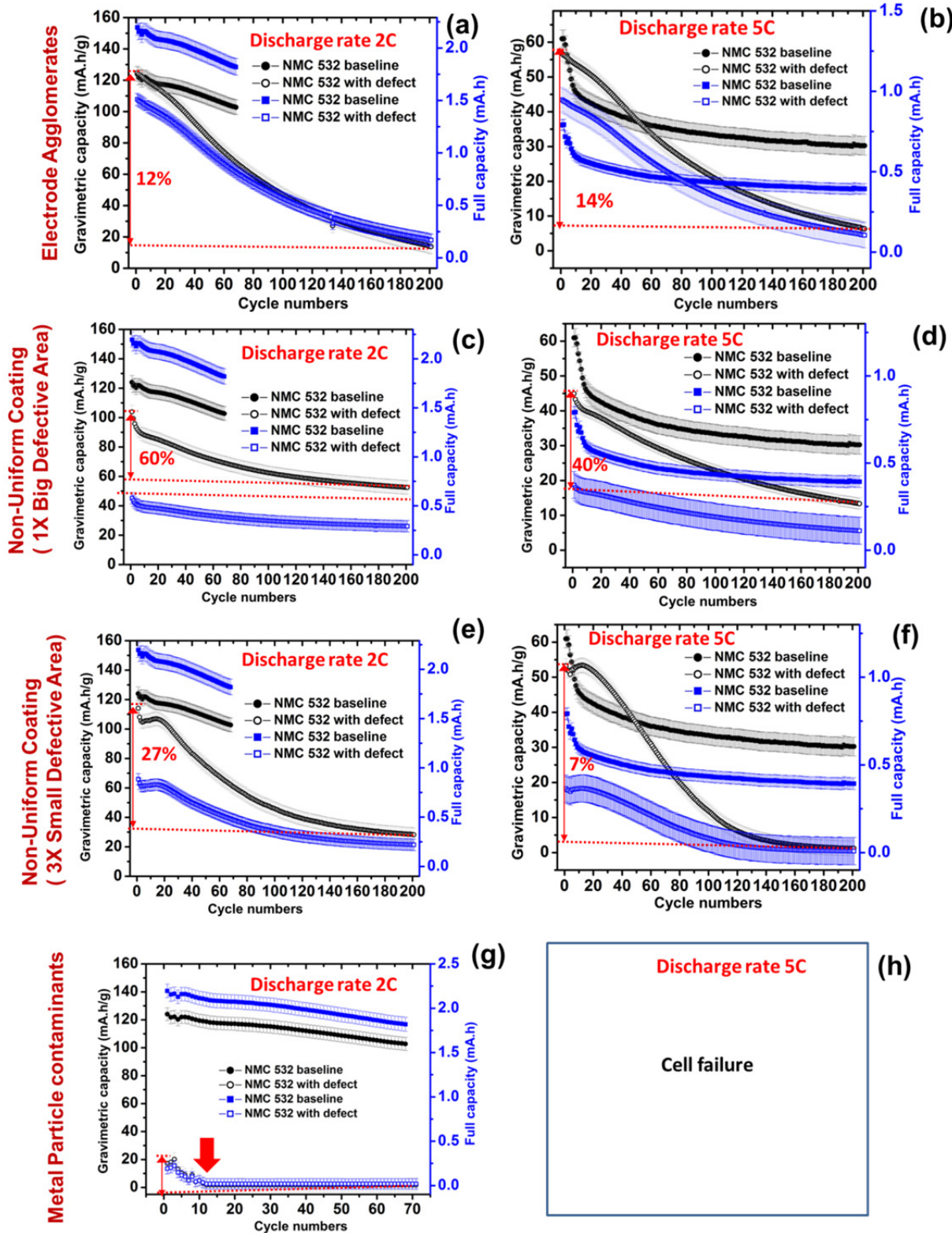


Figure IV - 292: Short-term capacity fade data for various defective electrodes (open symbols) where defect types are labeled to the left of each figure row compared with non-defective baseline NMC 532 electrodes (closed symbols) at 2C (left column) and 5C (right column) discharge rates. Blue symbols are full-cell discharge capacity and black symbols are gravimetric capacity

3. Understanding the relationship between defect microstructure and electrochemistry

To investigate the reason for poor electrochemical performance of certain defective electrodes, microscopic and X-ray mapping investigation are underway. In Figure IV - 293, we show SEM micrographs from the non-defective baseline NMC 532 electrode (Figure IV - 293a) and an electrode with agglomeration defects (Figure IV - 293b). Corresponding energy dispersive spectroscopy (EDS) elemental maps are shown in the bottom left and right of Figure IV - 293, as well, with the figure labels corresponding to 1 for C, 2 for Co, 3 for Mn, and 4 for Ni. In the Figure IV - 293b SEM image, it is clear that the agglomerated regions are C rich, which is further supported by the EDS X-ray mapping. These C-rich regions could block lithium diffusion pathways, and, hence, significant capacity degradation was observed (see Figure IV - 292a-b).

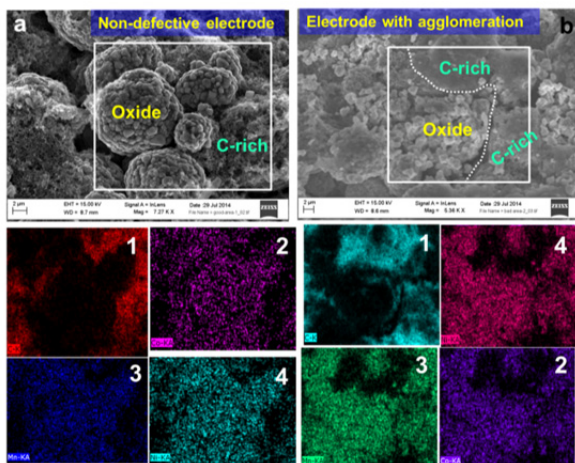


Figure IV - 293: SEM micrographs from non-defective baseline NMC 532 electrode (a) and defective electrode with large agglomerates (b). Carbon-rich areas are highlighted. Corresponding EDS X-ray maps from the respective SEM images are shown below (1 for C, 2 for Co, 3 for Mn, and 4 for Ni)

To obtain insight into the poor electrochemical performance for Sample 3x (three 2-mm parallel stripes of missing coating), an SEM image was analyzed at the interface between the coated and uncoated regions. It was observed that the interface had a maldistribution of active material as depicted in Figure IV - 294. Our hypothesis is that the more the interfacial length (total length between coated and uncoated areas) in a coin cell cathode, the less active material that is present in those spots. Hence, capacity fade is faster for those samples due to an, as yet, unexplainable phenomenon likely related to excessive local N/P ratios.

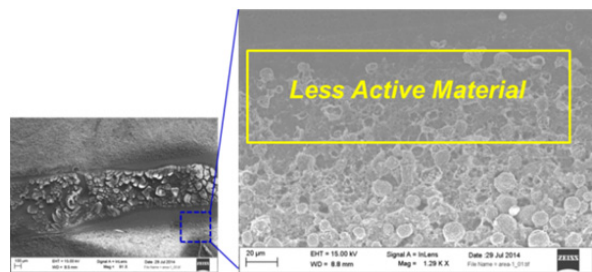


Figure IV - 294: SEM micrograph from the interfacial length between the coated and uncoated areas from Sample 3x showing less active material at the interface. It is also noted that the z-direction profile of the coated interfacial length is sloped downward towards the uncoated area, which could further alter the local N/P ratio and increase local contact resistance

4. Active IR thermography and optical reflectance for in-line electrode NDE

In collaboration with NREL and leveraging their significant Fuel Cell Technologies Office (FCTO) funding for in-line NDE for polymer electrolyte fuel cell (PEFC) components, ORNL has co-developed active IR thermography for measuring in-line lithium-ion electrode porosity via thermal diffusivity and optical reflectance for detecting coating surface defects.

4.1 Active IR thermography with white-light excitation

The major objective of this work is to check the feasibility of thermography-based imaging as an inspection tool for lithium-ion electrodes. A combined approach that includes experimental and modeling studies has been developed to correlate the observed temperature response from (backside) white-light excitation with fundamental properties of the electrodes. Several experiments have been performed to date with the ABR baseline ConocoPhillips A12 anode (two samples with similar areal weight and different porosities) and TODA America NMC 532 cathode (two samples with different areal weights and porosities):

- Stationary web (steady state temperature profile with constant white-light excitation).
- Stationary web (transient temperature decay after white-light excitation was switched off).
- Moving line speed of 0.5 ft/min (“pseudo steady state” where web passes by continuous white-light heating).

Development of a micro-scale model that describes the thermal response of an electrode based on the thermal conductivity, heat capacity, and density of the electrode constituents has been completed. In addition, a macro-scale model that describes the temperature response of the coated web passing by the white-light excitation source has been developed. The modeled temperature response is then fit to the experimental data from the three cases described above.

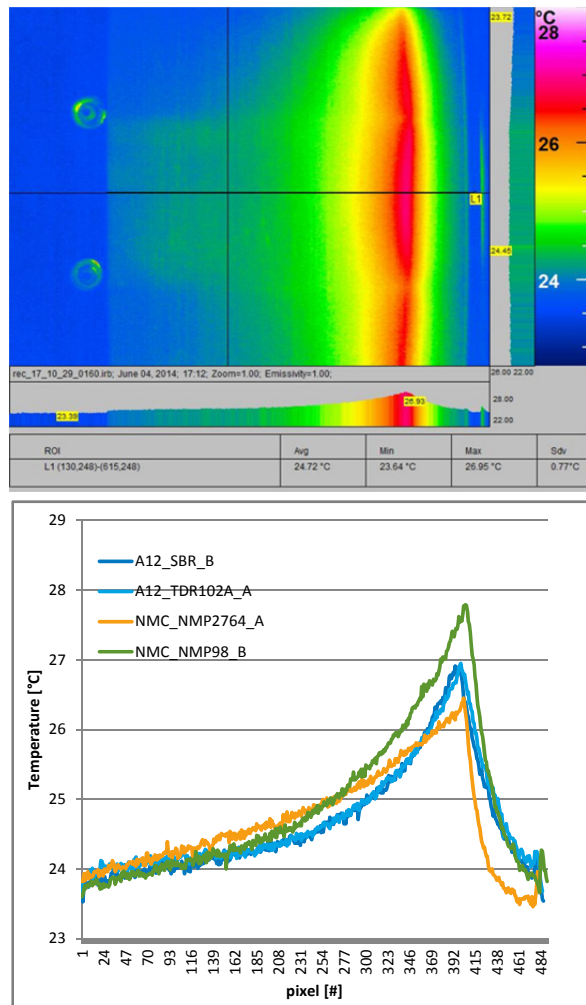


Figure IV - 295: Top – Temperature profile (from IR emissivity) of an A12 anode sample moving right to left past the excitation source (red color) showing a maximum temperature rise of ~27°C. Bottom – “Pseudo-steady-state” temperature profiles of all four anode and cathode samples moving at 0.5 ft/min past excitation source. Dark blue line is A12 anode with high porosity, light blue line is A12 anode with lower porosity, orange line is thick NMC 532 cathode with lower porosity, and green line is thin NMC 532 cathode with high porosity)

For the pseudo-steady state case (temperature profile for a designated web length does not change with respect to the white-light source position), it was observed that porosity of the A12 anode samples did not have an effect on the temperature profile since graphite has such as high thermal conductivity. However, areal weight and porosity had a significant effect on the much more thermally resistive NMC 532 cathodes. It is seen in Figure IV - 295(bottom) that the thick cathode with lower porosity exhibited a maximum temperature rise much lower (~1.5°C) than the thin, high-porosity cathode. This data confirms that the temperature response based on IR emissivity of the coatings can be

used for distinguishing differences between electrode areal weight and porosity.

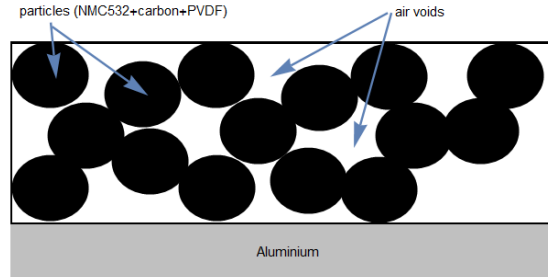


Figure IV - 296: Top – Micro-scale model of NMC 532 cathode assuming a thin, uniform binder around active-material/conductive-additive agglomerates deposited on Al foil. Bottom – Preliminary modeling of the effect of line speed on the temperature profile of a given electrode composition

For the micro-scale model, we assume the material structure is a laminate of particle composite and metal backing. (See Figure IV - 296.) To predict anisotropic thermal properties of such a structure we employ the Mori-Tanaka based estimates for the particle composite and the series-parallel resistance equations for the laminate. Macro-scale modeling of the bulk (cm-length scale) material properties is based on the moving web passing by the white-light excitation source experimental setup in pseudo-state-state fashion. The effective properties of the electrode (micro-scale model) are transferred to macro-scale model, and we compute numerical solutions to a heat equation to predict temperature distribution of the moving electrode. Model results fitting the experimental data are forthcoming in early FY15. By knowing the thermal conductivity, heat capacity, and absolute density of the electrode constituents, as well as the electrode bulk density and areal weight, in-line porosity can be extracted from the model fit to the measured pseudo-steady-state temperature profile based on IR emissivity. The remaining critical questions for this work in FY15 are can the measurement system be successfully installed on the ORNL slot-die coating line and is the technique compatible with line speeds of 20-60 ft/min.

4.2 Optical reflectance of electrode surface defects

The main objective of this work has been to develop a technique for lithium-ion electrode surface structure and morphology evaluation. A feasibility study with ABR baseline anode and cathode samples has been completed and imaging of electrode surface structures identified defects not detectable with conventional NDE inspection equipment such as CCD cameras. (see Figure IV - 297.) By the end of FY15, it is intended to implement this technique on the outlet of the ORNL slot-die coater.

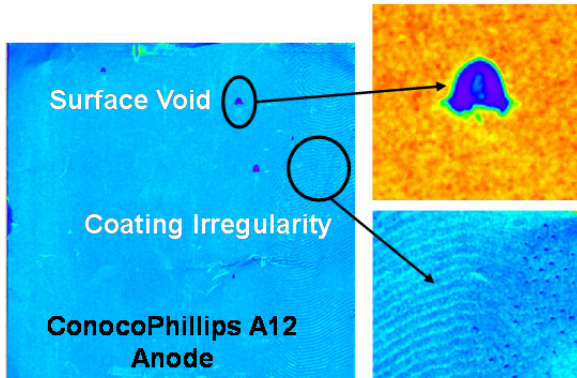


Figure IV - 297: Optical reflectance data identifying voids and coating streaks on the surface of a ConocoPhillips A12 anode that are not visible with conventional CCD camera line inspection equipment

Conclusions

- IR thermography and laser caliper techniques have provided valuable QC information during slot-die coating of electrodes, vastly improving the quality of routinely produced BMF anodes and cathodes.
- Different types of defects such as large agglomerates, metal particle (Co powder) contamination, and missing coating areas were intentionally and successfully introduced into the ABR baseline NMC 532 cathodes for obtaining insight into electrochemical performance effects.
- Rate capability testing, Coulombic efficiency, and high-rate capacity fading were statistically investigated for four different types of defects.
- Cathode agglomerates did not have a great effect on full cell discharge capacity, but aggravated cycle efficiency.
- Excessive metal particle contaminants (in this case, Co powder) had an extremely negative effect on performance, especially at higher C rates.
- Exaggerated cathode coating inhomogeneities (strips with missing coating) resulted in disproportionate drops in cell total capacity.
- Inhomogeneous cathode coating (especially missing areas and agglomerates) leads to

unbalanced N/P ratio, which affects gravimetric capacity and reduces Coulombic efficiency.

- Microstructures from defective areas were analyzed via SEM and EDS for understanding the observed electrochemical performance deterioration, especially for the cases of large agglomerates and missing coating stripes. Both of these defect types significantly contribute to high-rate capacity fade mainly due to N/P ratio imbalances and active material maldistribution.

FY 2014 Publications and Presentations

1. D. L. Wood III, D. Mohanty, Jianlin Li, C. Daniel, S. Nagpure, "Roll-to-Roll Electrode Processing NDE and Materials Characterization for Advanced Lithium Secondary Batteries," 2014 DOE Annual Merit Review, Washington, DC, June 18, 2014.
2. D. Mohanty, J. Li, R. Born, L.C. Maxey, R.B. Dinwiddie, C. Daniel, and D.L. Wood, "Non-Destructive Evaluation of Slot-Die-Coated Lithium Secondary Battery Electrodes by In-Line Laser Caliper and IR Thermography Methods," *Analytical Methods*, **6**, 674–683 (2014).
Highlighted in back cover of the journal:
<http://pubs.rsc.org/en/content/articlelanding/2014/ay/c4ay90003k/unauth#!divAbstract>
3. D. Mohanty, J. Li, C.L. Maxey, R.B. Dinwiddie, C. Daniel, and D. Wood, "In-Line Non-Destructive Testing of a Lithium-Ion Battery Electrode by Laser Caliper and Thermography," 2013 MRS Fall Meeting & Exhibit, Boston, Massachusetts, December 1-6, 2013.
4. D. Mohanty, J. Li, R. Born, C.L. Maxey, R.B. Dinwiddie, C. Daniel and D.L. Wood, "Reducing the Scrap Rate in Lithium-Ion Battery Manufacturing by Implementing In-Line Non-Destructive Electrode Evaluation Techniques," 3rd International Conference and Exhibition on Materials Science & Engineering, San Antonio, Texas, October 6-8, 2014.
5. D. Mohanty, J. Li, S. Nagpure, D.L. Wood, III, and C. Daniel, "Correlating Electrode Defects with Electrochemical Performance of Lithium-Ion Batteries," 2015 MRS Spring Meeting & Exhibit, San Francisco.

IV.E.4 Overcoming Processing Cost Barriers of High Performance Lithium Ion Battery Electrodes (ORNL)

Peter Faguy (ABR Program Manager)

David L. Wood, III, Jianlin Li, Claus Daniel, Shrikant Nagpure, and Debasish Mohanty

Oak Ridge National Laboratory
One Bethel Valley Road
P.O. Box 2008, MS-6065
Phone: (865) 574-1157; Fax: (865) 241-4034
E-mail: wooddl@ornl.gov

Collaborators:

Andy Jansen and Bryant Polzin (ANL); Chris Orendorff (SNL); David Telep and Fabio Albano (XALT Energy); Mike Wixom (Navitas Systems); James Banas (JSR Micro); Gregg Lytle (Solvay Specialty Polymers); Feng Gao and Alan Goliaszewski (Ashland, Inc.); Stuart Hellring, Jack Burgman and Terry Hart (PPG Industries); Mark Wanta (Superior Graphite); Rob Privette (XG Sciences); Tracy Albers (GraTech International); Bharat Chahar (Zenyatta Ventures)

Start Date: October 1, 2011

Projected End Date: September 30, 2014

Objective

To transform lithium ion battery electrode manufacturing by eliminating the costly, toxic organic NMP solvent.

Technical Barriers

Elimination of Expensive Solvent and Recovery System:

Electrode suspensions for lithium ion batteries are currently formulated using expensive polyvinylidene fluoride (PVDF) binder and expensive, toxic, and flammable N-methylpyrrolidone (NMP) solvent. It is desirable to replace these components with water and water-soluble binders, but methods of mass production of these suspensions are currently underdeveloped. The major problems with aqueous electrode dispersions are: 1) agglomeration of active-phase powder and conductive carbon additive; 2) poor wetting of the dispersion to the current collector substrate; 3) cracking of the electrode coating during drying resulting in poor

device performance and short life; and 4) increased adsorbed water on the active cathode particle surfaces. NMP based processing results in good performance, but it has the inherent disadvantages of high solvent cost, long drying times, and the requirement for explosion proof processing equipment and solvent recovery. Initial projections of the minimum cost savings associated with changing to water and water-soluble binder are 14-15% of the (pouch) cell manufacturing steps, or a reduction from \$0.873/Ah to \$0.746/Ah. That translates to 7-8% cost reduction on the lithium-ion battery (LIB) pack level. Improvements in this effort have been shown to be chemistry-agnostic and with little additional effort are adaptable to any electrode chemistry.

Technical Targets

- Low-cost, green manufacturing methodology for lithium ion battery (LIB) anodes using aqueous suspensions (to meet 2015 USABC storage goal of \$300/kWh for PHEVs).
- Correlation of properties of dispersions and electrode coatings to cell performance and advancement of energy storage manufacturing science.
- Lifetime of 10 years and 1000 cycles at 80% DOD for EVs and 5000 deep discharge cycles for PHEVs.

Accomplishments

- Establishment of detailed cost calculation for thick electrode processing and formation cycling (published in *Journal of Power Sources*).
- Evaluation of three water-soluble binders in full coin cells and down-selection of one for further evaluation.
- Evaluation of three conductive carbon additives with down-selected water-soluble binder for aqueous processed electrodes.
- Manufacturing of aqueous processed TODA NMC 532 and CP A12 anodes for collaboration with ANL on electrode thickness performance study.
- Matched full coin cell performance through 100 cycles (0.2C/-0.2C) of aqueous suspension and water-soluble binder to NMP/PVDF based suspensions for CP A12 and TODA NMC 532 electrochemical couple.
- Matched pouch cell (≥ 3 Ah capacity) performance through 100 cycles (0.2C/-0.2C) of aqueous

suspension and water-soluble binder to NMP/PVDF based suspensions for CP A12 and TODA NMC 532 electrochemical couple.



Introduction

The complex suspensions used during electrode processing, containing solvent, active graphite, conductive carbon, polymer binder, and perhaps a dispersant (surfactant), must be optimized using colloidal dispersion science. These components have different surface interactions with the solvent and dispersant, and each dispersion must be tailored based on surface charges, rheology, material constituents, order of addition, mixing protocol, coating method, and drying protocol. Regardless of organic or aqueous suspension, much development is still required to optimize these formulations for uniform coatings, reduce the cost associated with making the electrodes, and correlate suspension properties to electrode performance.

In conventional lithium ion batteries, PVDF is used as the electrode binder because of its electrochemical stability over a large potential window, and NMP is used as the solvent of electrode suspension. The advantage of using this organic system is that extensive research has been carried out on the resulting electrode microstructure and cell performance. However, there are still areas related to this conventional suspension that are relatively unexplored such as performance effects of solids loading, order of component addition, coating parameters, and drying conditions when materials are varied. The PVDF/NMP system has some disadvantages that make researching replacements attractive, most notably its cost. PVDF also has low flexibility, which can lead to breaking of the physical bond between active graphite and conductive carbon during long-term cycling. It contains fluorine, which is a source of producing stable LiF as a degradation product. The LiF may adversely interact with the otherwise stable solid electrolyte interface (SEI) layers. The use of NMP requires a process of recovery and treatment of the organic vapors for disposal or recycling. Therefore, there is increasing interest in switching the fabrication of composite electrodes from an organic route to an aqueous route. Compared to the organic route, the aqueous route is significantly more economically and environmentally friendly. For example, the cost of NMP in bulk quantities is ~\$1.5-2.0/L, whereas deionized water is only \$0.015/L.

In our previous work, it was successfully demonstrated that the TODA NMC 532 cathodes can be fabricated through aqueous processing, and excellent electrode performance was achieved in half cells.

Standard drying protocols have also been confirmed as sufficient to remove residual moisture from aqueous processed electrodes to match performance of NMP-based processing. However, long-term performance in full coin cells and large format pouch cells has not yet been verified. In FY14, full coin cells with all aqueous processed electrodes were assembled and tested.

Aqueous processed NMC 532 cathodes were also tested in 3 Ah pouch cells and delivered comparable performance to those from NMP-based processing. The effect of different types of conductive additives was investigated with two different carbon blacks and a graphene nanoplatelet material. Finally, a thorough analysis was completed on electrode processing cost comparison between NMP-based and aqueous processing, including the effect of electrode thickness and formation cycling and which has been predominantly overlooked by the lithium-ion research community.

Approach

Subtask 1. Cost analysis of aqueous processing:

A detailed processing cost was established for LIB electrodes via aqueous processing which included doubling electrode thickness and the impact of reducing formation time. The model includes a step-by-step approach on how to realize processing cost reduction in existing LIB manufacturing plants using NMP-based (baseline) processed thin electrodes and a standard 10-14-day wetting and formation process. This cost analysis was compared to other models such as the ANL “BatPaC” and TIAX studies.

Subtask 2. Electrode performance in full coin cells and large format pouch cells: The NMC 532 cathode was coupled with the CP A12 anode, and both electrodes were fabricated via aqueous processing. Both rate performance and cyclability were characterized and compared to the baseline NMP processed electrodes. The electrodes and cell testing were performed at the DOE Battery Manufacturing R&D Facility at ORNL (BMF).

Subtask 3. Rate performance study in aqueous processed electrodes: The rate performance of NMC 532 and CP A12 via aqueous processing was investigated in collaboration with ANL. Both electrodes with various areal loadings were fabricated through aqueous processing and sent to ANL for performance testing. The rate performance was compared to the baseline electrodes, and processing effects on electrode performance were verified.

Subtask 4. Conductive additive screening: Three conductive additives were selected to fabricate NMC 532 cathodes with a down-selected water soluble binder and their electrode performance (rate capability and

short-term capacity fade) was compared to the baseline NMP processed electrodes.

Results

Cost modeling of LIB electrode processing:

Electrode processing cost was analyzed for conventional NMP-based processing (baseline) and our proposed aqueous processing plus doubling the electrode thickness. Figure IV - 298 shows a graphical summary of the baseline calculations and reduced costs (combination of aqueous processing, thick electrodes, and reduced wetting and formation time). Please refer to our article ("Prospects for reducing the processing cost

of lithium ion batteries," *Journal of Power Sources*, **275** (2015) 234-242) for detailed analysis. The battery pack cost can be reduced from \$503/kWh-usable with baseline "thin NMP processing" to \$370/kWh-usable with thick aqueous processing, together with a significantly reduced formation-cycle time. The major cost reduction came from two parts: 1) reduction in current collectors and separators from \$114.6 to \$58.0/kWh-usable, which resulted from doubling the electrode thickness; 2) electrode processing from \$51.6 to \$3.1/kWh-usable enabled from replacing NMP with water, reducing energy consumption in electrode drying (time and air flow), and eliminating NMP recovery.

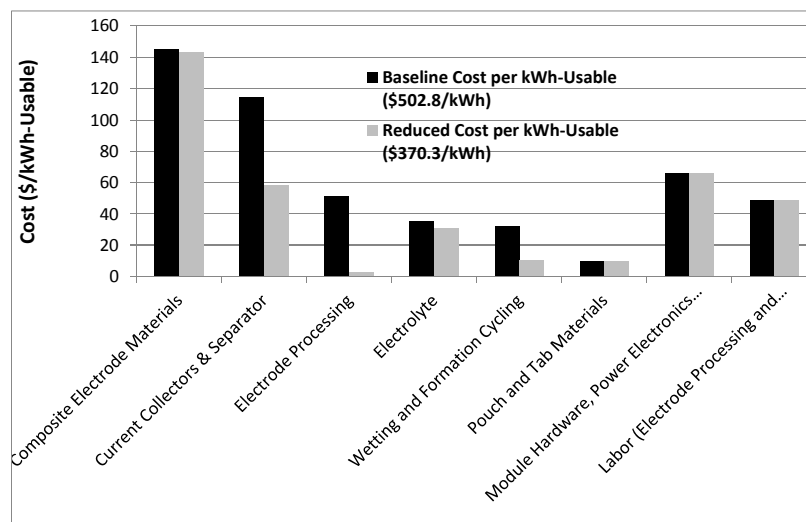


Figure IV - 298: Comparison of baseline and reduced pack costs (per kWh-usable basis) from the ORNL model. "Reduced" cost is associated with implementing aqueous processing, thick electrode coatings, and reduced wetting and formation times

Electrode performance validation: The TODA NMC 532 cathode via aqueous processing was evaluated in full coin cells with CP A12 natural graphite as the anode. Two water soluble binders, TRD202A from JSR Micro and PVDF Latex from Solvay Specialty Polymers, were selected as the binders for the cathode. The graphite anode was also fabricated via aqueous processing with PVDF Latex as the binder. Cathode areal loadings were 11-15 mg/cm², and anode areal loadings were controlled appropriately to maintain an electrode balance of N/P=1.0-1.2. Celgard 2325 was used as the separator, and the electrolyte was 1.2 M LiPF₆ in ethylene carbonate/diethyl carbonate (3/7 wt fraction). The cells were cycled at various C rates (1C was defined as 160 mA/g) for rate performance evaluation followed by 100 cycles at 0.2C/-0.2C for establishing short-term capacity fade.

Figure IV - 299 shows the electrode performance of full coin cells. The black curve denotes the baseline PVDF binder with NMP solvent. Each curve was averaged from at least three cells (with 2σ error bars).

The electrodes from the baseline PVDF/NMP and aqueous processing exhibited comparable rate performance except at high C-rates, which could be due to different cathode architectures resulting from contrasting binder interactions with the particulate phases. To achieve desirable electrode performance at high C rate, the binder needs to be optimized for molecular weight and concentration. Interestingly, the electrode with TRD202A delivered superior performance over the baseline at high C rates. In addition, both aqueous processed electrodes exhibited identical cyclability to the baseline at low C rate, which indicates that the NMC 532 cathode from aqueous processing is a suitable approach to manufacturing cathodes.

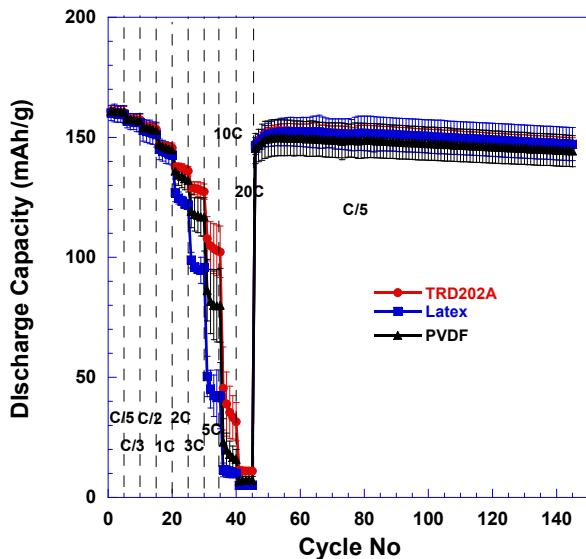


Figure IV - 299: Comparison of baseline NMP/PVDF processed electrodes and aqueous processed NMC 532 electrodes in full coin cells (CP A12 natural graphite anode)

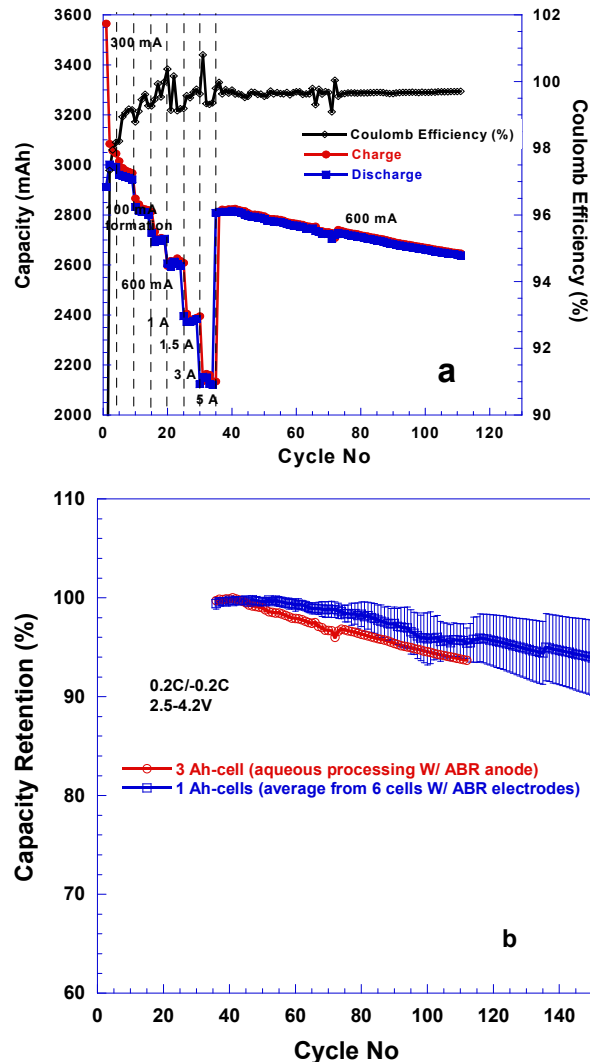


Figure IV - 300: (a) Aqueous processed NMC 532 rate performance and short-term capacity fade from a 3-Ah pouch cell with JSR Micro TRD202A as the binder; (b) comparison of capacity retention between cell from (a) and six baseline NMC 532 cathodes via PVDF/NMP baseline processing (2σ error bars)

The aqueous processed NMC 532 cathode with TRD202A as the binder was further scaled up into a 3-Ah pouch cell, and the rate capability and cycling performance is shown in Figure IV - 300. This cell demonstrated excellent rate performance and Coulombic efficiency; capacity retention after 100 cycles at 0.2C/-0.2C was compared to 6 baseline PVDF/NMP 1-Ah pouch cells in Figure IV - 300b. Capacity retention was nearly identical within experimental error and cell-to-cell variation. The observed excellent rate performance and cyclability in large format pouch cells demonstrates that aqueous processed electrodes can be scaled up and match the performance of baseline ABR pouch cells.

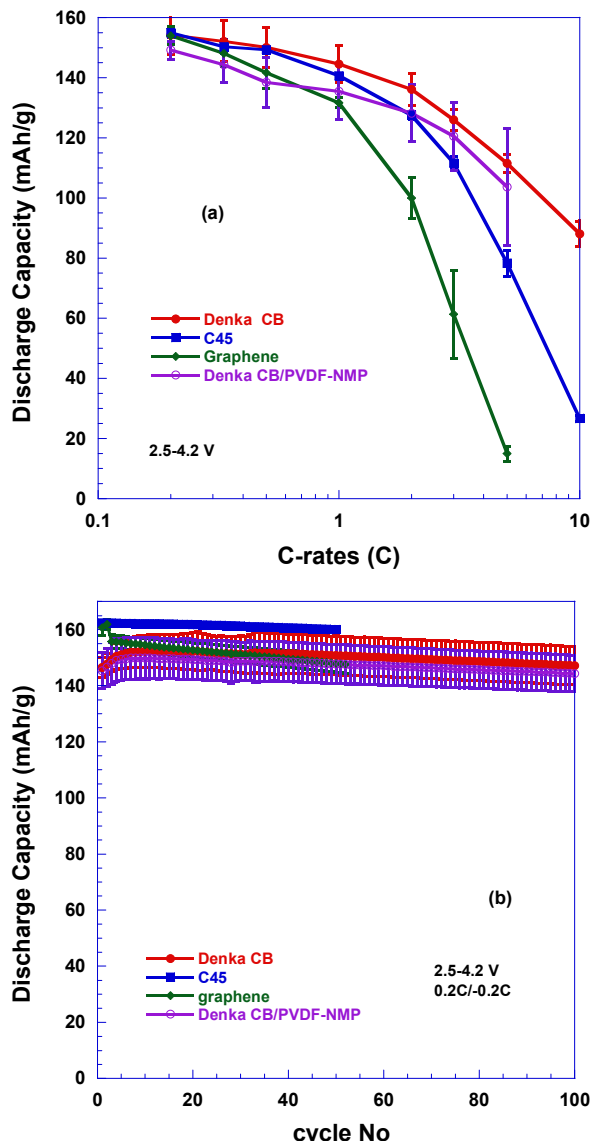


Figure IV - 301: (a) Half-cell rate capability of aqueous processed NMC 532 cathodes with different conductive carbon additives; (b) low-rate capacity fade in full coin cells coupled with CP A12 anodes via *a//aqueous processing*

Conductive additive screening: Three conductive additives were investigated including Denka carbon black, Super P C45 (C45), and a commercial graphene nanoplatelet material.

Figure IV - 301 shows the half-cell rate capability and the full-cell capacity retention of aqueous processed cathodes with these three conductive carbon additives. Half-cell rate capability is plotted in Figure IV - 301a, and performance was compared to the baseline Denka carbon black additive processed with PVDF/NMP. All electrodes demonstrated similar rate performance below 1C, but there was substantial deviation at higher rates. The cells with Denka carbon black exhibited better high-rate performance, which is ascribed to the higher

surface area than that of C45. The surface area of graphene is also much larger than that of C45; however, this electrode showed much lower rate performance, which could be due to non-optimized electrode formulation and architecture. With such high surface area, graphene nanoplatelets may require a higher content of binder to maintain sufficient electrode integrity and good adhesion between the cathode and current collector. The mixing protocol may also need to be adjusted accordingly to ensure a homogeneous cathode dispersion. The intent of this subtask was to verify that common (commercially available) conductive additives are compatible with aqueous processing and by no means advocates the use of a particular additive. In addition, this work also shows there is a great deal of optimization space in the power density realm related to binder and conductive additive selection (as evidence by the large spread in capacity in Figure IV - 301a – ~15 mAh/g for graphene nanoplatelets vs. ~115 mAh/g at 5C discharge rate).

Figure IV - 301b shows the low-rate capacity fade for the four cell groups, and it is seen that all conductive additive materials show good capacity retention and similar fading slopes except the cells with the graphene nanoplatelets. Our hypothesis for this behavior is that the graphene is not well dispersed yielding a coating with poor electrode/foil adhesion and particle cohesion (*i.e.* increased Ohmic losses during cycling).

Conclusions and Future Directions

ORNL developed a new cost model comparing the processing savings of ORNL thick aqueous electrode processing over conventional thin NMP-based electrode processing. It was demonstrated that the electrode processing cost (processing aide, solvent removal, and solvent recovery) can be reduced from \$51.6 to \$3.1/kWh-usable with aqueous processing due to the much lower boiling point of water, much higher vapor pressure of water, and ~25% lower heat of vaporization of water.

ORNL successfully fabricated NMC 532 cathodes with various commercially available water-soluble binders and conductive additives, validating the ubiquitous nature of the processing approach. These cathodes delivered comparable performance to those made by conventional NMP-based processing in full coin cells and large-format pouch cells. No negative performance effect on NMC 532 cathodes from aqueous processing has been observed through 100-150 low-rate (0.2C-/0.2C) cycles.

ORNL has established aqueous processing as our standard technique for electrode dispersion production and coating. We are also collaborating with PPG Industries on scaling this technology to industrial levels for domestic battery makers. In addition, ORNL has

obtained pre-prototype results on novel electrode architectures for thick cathodes (for example, including Nafion as a functional binder to enhance Li ion conduction at the triple-phase interface) to enable high energy density and simultaneous high power density. Resultant electrode structures will be further controlled via calendering optimization.

FY 2014 Publications and Presentations

1. Jianlin Li, Debasish Mohanty, Bradley Brown, Claus Daniel, and David Wood, “Fabrication and performance of $\text{LiNi}_{0.5}\text{Mn}_{0.3}\text{Co}_{0.2}\text{O}_2$ cathodes through aqueous processing with various binders”, 2014 Advanced Automotive Battery Conference, Atlanta, GA, February 3-7, 2014. (**Invited**)
2. D.L. Wood, J. Li, and C. Daniel, “Prospects for Reducing the Cost of Lithium Ion Electrode Processing and Pouch Cell Formation Steps,” *Journal of Power Sources*, 275 (2015) 234-242.
3. J. Li, D. Mohanty, C. Daniel, and D. Wood, “Aqueous Processing of $\text{LiNi}_{0.5}\text{Mn}_{0.3}\text{Co}_{0.2}\text{O}_2$ Composite Cathodes for Lithium-Ion Batteries,” 225th Meeting of The Electrochemical Society, Orlando, Florida, Abstract No. 194, May 11-15, 2014.
4. David L. Wood, III, Jianlin Li, Claus Daniel, Debasish Mohanty, and Shrikant Nagpure, “Overcoming Processing Cost Barriers of High-Performance Lithium-Ion Battery Electrodes,” DOE Annual Merit Review, Washington, DC, June 18, 2014.
5. Jianlin Li, David Wood, and Claus Daniel, “Enabling manufacturing composite cathodes through aqueous processing for lithium-ion batteries”, 3rd International Conference and Exhibition on Materials Science & Engineering, Oct. 6-8, 2014, San Antonio, TX.
6. David Wood, Jianlin Li, Claus Daniel, and Beth Armstrong, “Aqueous colloidal chemistry for low-cost, green manufacturing of lithium-ion battery electrodes”, MS&T’14, Oct. 12-16, 2014, Pittsburgh, PA. (**Invited**)

IV.E.5 Development of Industrially Viable ALD Electrode Coatings (NREL)

Robert Tenent

National Renewable Energy Laboratory
16253 Denver West Parkway
Golden, CO 80401
Phone: 303-384-6775
Email: Robert.tenent@nrel.gov

Subcontractor:
University of Colorado at Boulder

Start Date: October 2012
End Date: September 2014

Objectives

- The overall objective of the ABR program is to improve cycle life, abuse tolerance and reduce cost of advanced lithium-ion battery technologies for plug-in vehicles (PEV).
- Previous laboratory work conducted by NREL and the University of Colorado at Boulder has demonstrated that thin, conformal coatings of aluminum oxide on lithium ion battery electrodes formed by atomic layer deposition (ALD) can dramatically improve abuse tolerance and cycle life which in turn reduces ultimate cost.
- Current technology for performing ALD is not amenable to high throughput manufacturing methods and thus represents a high priced bottleneck in the implementation of ultrathin electrode coatings at a commercial scale.
- The objective of this current work* is the development of a system for deposition of thin protective electrode coatings using a novel “in-line” atmospheric pressure atomic layer deposition (AP-ALD) reactor design that can be integrated into manufacturing to address needs for improvement in rate capability, cycle life, and abuse tolerance in a cost effective manner.

Technical Barriers

- Lithium ion limited calendar and cycle life.
- Poor abuse tolerance of lithium ion batteries.
- High cost of lithium ion batteries.

Technical Targets

- Design and construct a prototype in-line ALD coater for deposition on porous substrates characteristic of cathode materials.

Accomplishments

- Constructed an in-line ALD reactor system for flexible substrates compatible with existing commercial battery electrode coating facilities.
- Demonstrated controlled deposition of aluminum oxide on a flexible substrate at an effective processing line speed of >400 ft/min, nearly an order of magnitude higher than current industrial processes.
- While further experimentation is warranted with additional funding, these results indicate that integration of in-line ALD coating within current industrial processes is feasible.



Introduction

In previous work, NREL, in partnership with the University of Colorado, has shown that extremely thin, conformal coatings of aluminum oxide deposited with the Atomic Layer Deposition (ALD) technique are capable of dramatically improving cycleability of lithium-ion cells. This project seeks to convert the common ALD processing format into a new reactor geometry that is compatible with battery electrode manufacturing.

As part of this effort for FY14, NREL and the CU-Boulder team working with limited carryover funding has successfully completed design and construction of a new in-line ALD reactor. Work in this area has focused on modification of previous reactor designs to build a system capable of assessing the ability to obtain ALD-type coating processes in an in-line format and under acceptable battery manufacturing conditions. Earlier reactors were constructed to conduct initial feasibility testing of the ALD process when converted to an in-line format and with deposition occurring at atmospheric pressure; however, these early designs focused on planar substrates. More recent work has focused on creating a system that is capable of deposition onto moving coated battery electrode foils, as used in present manufacturing. Special emphasis was placed on designing a system to understand the impact of coating on porous substrates.

Approach

ALD coating methods are conducted by sequential and separate exposure of a sample substrate surface to gas phase precursors that react to form a film. Deposition is typically performed in a closed reactor system at mild

vacuum as shown in Figure IV - 302. Precursor exposure steps are conducted in a single chamber and are separated in time. In a typical exposure “cycle” a sample is exposed to one precursor and the chamber is then purged with inert gas prior to exposure to the second precursor that completes the coating reaction. The “cycle” ends with another extensive inert gas purging step before the process can be started again. Film growth takes place by repeating this cycling precursor exposure process multiple times. The sequential and separate exposures are key to achieving the excellent conformal film deposition on highly textured substrates for which the ALD technique is known. ALD coatings have become common in the semiconductor industry for integration in microelectronics.

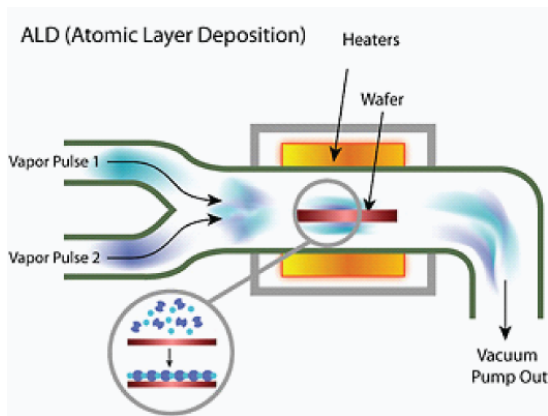


Figure IV - 302: A typical ALD chamber with sequentially separated precursor exposures that draws out overall processing time

As an alternative to the temporal separation of precursor exposure in the same reaction chamber, our work proposes a *spatial* separation of precursor exposure steps that is more consistent with “in-line” processing techniques. Figure IV - 303 shows a simplified conceptual schematic of our proposed apparatus.

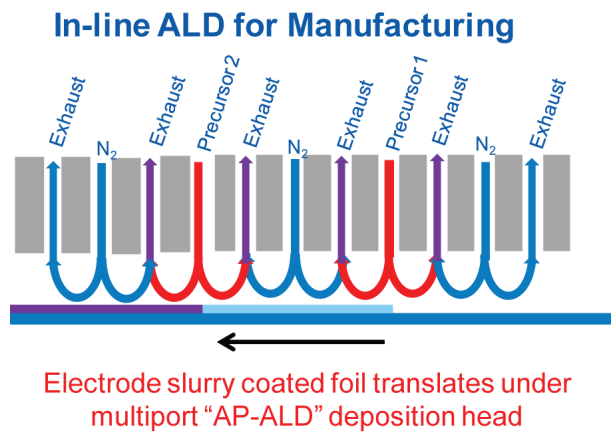


Figure IV - 303: A simplified schematic demonstrating the in-line spatial ALD concept

Our “spatial” ALD approach employs a multichannel gas manifold deposition “head” that performs sequential exposure of precursor materials as an electrode foil

translates beneath it. It is important to note that similarly designed deposition heads are currently employed by glass manufacturers for production of a variety of coated glass products using high-volume, in-line atmospheric pressure chemical vapor deposition (AP-CVD). Our approach leverages this existing knowledge base as well as our ALD expertise in order to enable in-line ALD coating that will allow the transfer of our previously demonstrated ALD-based performance improvements to larger format devices.

Results

Push-Pull Reactor Design

Current Li-Ion battery electrode are *porous*. A crucial factor for successful coating of these electrodes using in-line ALD technique is the ability to coat *porous* substrates. Coating of a porous substrate presents a specific technical challenge, as precursor materials must be able to fully penetrate as well as be removed from the porous film as rapidly as possible to enable high processing line speeds. This requires that the porous film be exposed to alternating high and low gas pressure regimes at different stages of the deposition process. At high local pressures (viscous flow conditions), a high number of gas phase collisions drive penetration of precursor gases into the film, while low local pressures (molecular flow conditions) allow rapid removal of unreacted precursor prior to the next precursor exposure step. We have termed the rapid progression through alternating high and low local pressure regimes the “push-pull” reactor design. A fundamental schematic of the “push-pull” reactor concept is shown in Figure IV - 304. In addition to precursor introduction and exhaust channels, the system is also designed with a nitrogen gas window that is pressured higher than the dosing precursors in between the precursor ports. This nitrogen gas purge will ensure that there is no cross talk between the different reactants that would lead to bulk film deposition.

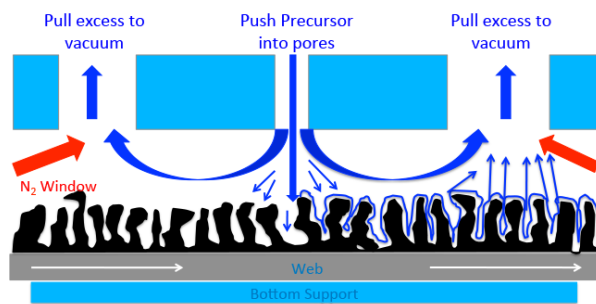


Figure IV - 304: A simple schematic demonstrating the alternate high and low pressure regimes present in the “push-pull” reactor concept

Digital Modular Roll-to-Roll System Design

As shown schematically earlier, a linear translational roll-to-roll design was initially considered for our “push-pull” deposition system. However, it was determined through earlier results and discussions

with additional roll to roll (R2R) processing experts that a linear design would not be capable of maintaining adequate tension on the web substrate during the “push-pull” deposition process. An improved format is a rotating drum-in-drum design as shown in Figure IV - 305. In the drum-in-drum system, a rotating inner drum on which substrates are mounted is set inside a fixed outer drum that contains all gas sources as well as purge and exhaust lines. The inner drum rotates the web radially while maintaining sufficient tension on the line to ensure accurate gas head to substrate spacing.

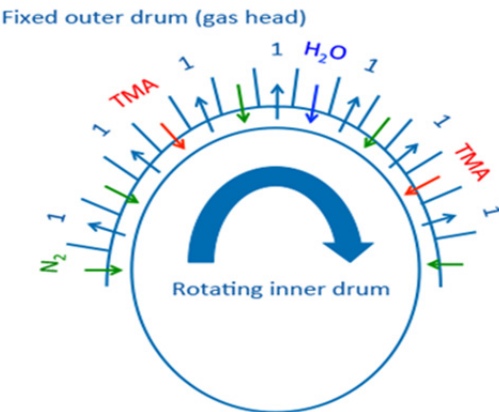


Figure IV - 305: Schematic representation of the "digital modular" design concept

In order to maximize reactor flexibility and enable extensive deposition condition optimization work, we have adopted what we term a “digital modular” system design. Figure IV - 306 shows a more detailed schematic of the drum-in-drum reactor design and demonstrates the digital modular design. To implement the “digital modular” design, the fixed outer drum of the reactor is faceted and has slots drilled every 2.5 cm. Precursor introduction as well as reactant exhaust occurs through the attachment of specific “modules” to these slots. Precursor dosing and vacuum exhaust modules have been fabricated that are able to fit to any of the slots in the external drum. This design will allow the modules to be moved interchangeably on the external drum to allow the maximum amount of variability in dosing and vacuum modules spacing. This enables extensive experimentation across a broad range of deposition conditions in order to optimize performance.

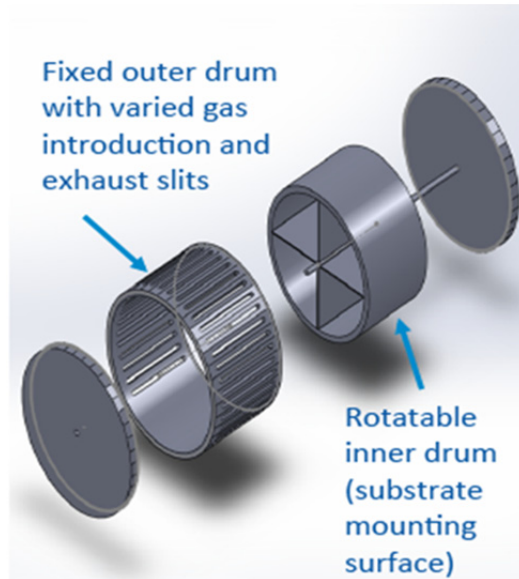


Figure IV - 306: Diagram of drum-in-drum reactor format

Module Design

Computational flow dynamics simulations were conducted to optimize the precursor introduction module design in order to ensure uniform precursor exposure to the moving substrate across the sample surface. As an example, Figure IV - 307 shows output from CFD calculations as well as the final constructed precursor introduction module. Our simulations showed that under expected deposition conditions, a minimum height of 2" was required for the precursor concentration to become uniform across the entire width of the module. Modules were constructed at a height of 5" in order to allow sufficient time and space for the precursor concentration to become uniform.

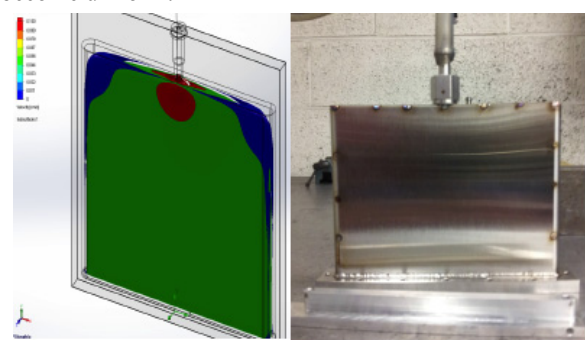


Figure IV - 307: Computational flow dynamic simulation of gas flow through the precursor introduction module and final construction

As discussed previously, another benefit of using the modular slot design is that blank modules can be added to modify channel spacing, furthermore, new modules can be added in the future without having to modify the main deposition head. As an example additional modules are

being designed that will allow for the use of in-situ diagnostics including pressure sensing and mass spectrometry as well as a module that will enable in-line plasma assisted deposition.

Reactor Construction and Assembly

Following the design phase, reactor parts were fabricated, assembled and tested. Figure IV - 308 shows the final assembled reactor before and after sample loading. Initial demonstration of reactor functionality was conducted through deposition of aluminum oxide onto flexible plastic films. While these films do not necessarily mimic the high porosity desired for a battery electrode, they were chosen as an initial candidate sample to allow initial deposition properties to be determined which could then be later refined for porous substrate depositions.

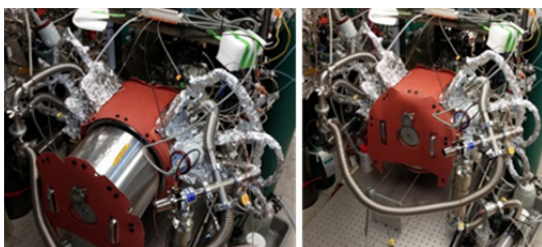


Figure IV - 308: Final construction and sample loading of in-line ALD reactor

Initial reactor set up included only two separate “channels” for precursor introduction to the sample. One channel for trimethyl aluminum and a second for ozone as the secondary reactant. Ozone was chosen as precursor to help minimize the introduction of water to eventual battery electrode substrates as well as for the ability to ramp deposition rates to higher speeds which should enable coating at high processing line speeds. Figure IV - 309 shows the measured thickness of aluminum oxide grown under fixed deposition conditions for a specific number of reactor rotations (or ALD cycles; 1 cycle per rotation). Note that film thickness increases linearly with the number of ALD cycles. This data has been fit to show film growth on a per reaction cycle basis (GPC, “growth per cycle”). The data in Figure IV - 309 achieved deposition rates per cycle typical with those observed on flat silicon substrates. It is important to note that the data shown in Figure IV - 309 was collected at a reactor rotation rate of 100 revolutions per minute that translates to an effective processing line speed of 400 ft per minute. Typical processing line speeds for state of the art battery manufacturing is near 50 ft per minute. These results prove that ALD coating can be conducted in a well controlled fashion at line speeds well above traditional battery electrode coating processes and thereby are not likely to present significant bottle necks when integrated with existing commercial lines. Further demonstrations need to be conducted to assess the impact of film porosity on the ability to effectively deposit coatings at high effective line speeds. Work of this nature is planned using typical porous

substrates as well as battery electrodes upon availability of sufficient funds.

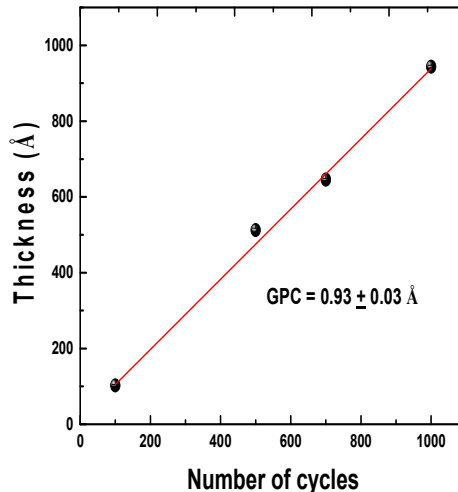


Figure IV - 309: Measured thickness of aluminum oxide deposited using in-line ALD showing linear film growth at ~400 ft/min line speeds

Conclusions and Future Directions

In FY14, the NREL/CU team designed and completed construction of a new in-line ALD based electrode coating reactor. Testing of the unit indicated that thin layers of aluminum oxide could be deposited on flexible substrates in a well-controlled fashion and at effective processing line speeds in excess of 400 ft per minute without loss in coating performance. This result indicated that practical integration of in-line ALD coating with state of the art commercial electrode coating facilities is reasonable. Additional work needs to be conducted to assess the impact of sample porosity on the ability to coat electrodes effectively. If additional funding can be obtained for a continuation of this effort into FY15, experiments will be conducted to determine optimal parameters for conformal coating on porous substrates. This work will entail detailed Design of Experiment methods used to determine optimal conditions to ensure conformal coating of a moving porous substrate. The output from this work will identify acceptable conditions for conformal coating of materials in an in-line format. Experiments will initially be conducted with model porous substrates with well-known geometries that will enable detailed measurements of coating quality. Following this initial optimization work, the NREL/CU team will partner with other ABR collaborators to coat larger format battery electrodes. Larger format electrodes will be fabricated into cells for testing at the NREL/CU laboratories as well as within collaborating labs.

It is anticipated that in a later stage, the NREL/CU team will partner with electrode and battery manufacturers and other organizations to integrate the new reactor design into a battery electrode coating process. Toward that end,

the existing reactor was intentionally designed to enable integration with further R2R processing capabilities.

FY 2014 Publications/Presentations

1. Manuscript entitled “Spatial Atomic Layer Deposition on Flexible Substrates Using a Modular Rotating Cylinder Reactor” submitted to the *Journal of Vacuum Science and Technology* (currently under review).

